NANOFLUIDS BASED ON MOLTEN NITRATES FOR THERMAL ENERGY STORAGE AND HEAT TRANSFER IN CONCENTRATED SOLAR POWER

M. Belén Muñoz Sánchez

2017

Nanofluids based on molten nitrates for thermal energy storage and heat transfer in concentrated solar power

Submitted for the in fulfilment of the requirements for the degree of PhD in Engineering of Materials and Sustainable Processes at the University of the Basque Country (UPV/EHU) by:

M. Belén Muñoz Sánchez

Supervisors:

Dr. Ane Miren García Romero

Dr. Francisco Javier Nieto Maestre

October 2017

zabalduz

tecnalia Inspiring Business

"Sabio no es quien sabe muchas cosas, sino quien actúa sabiamente. Es un modo elegido de ser, el talento para hacer las preguntas adecuadas y buscar las buenas respuestas. Es la poética del vivir"

José Antonio Marina

AGRADECIMIENTOS

Esta tesis es el final de un largo camino que comenzó hace algo más de cuatro años. Muchas personas me han acompañado a lo largo de esta aventura científica. Todas ellas han participado en alguna medida en la historia oculta entre líneas de esta tesis. Por eso, y por seguir a mi lado, merecen mi más sincero agradecimiento.

En primer lugar, quiero tener un enorme reconocimiento para la labor de mis dos directores: la Dra. Ana García y el Dr. Javier Nieto. Muchísimas gracias a Ana por "adoptarme" como doctoranda en un momento decisivo de toda esta historia. Por mover cielo y tierra a nivel interno de la Universidad siempre que lo he necesitado. Por tener un espíritu crítico que no ha hecho otra cosa que hacerme avanzar por el buen camino a pesar de las dificultades que he encontrado por el camino. Javi, ya sabes que gran parte de esta tesis también es tuya. Hemos formado un equipo estupendo. Por todos los días que hemos pasado tratando de descifrar los misterios de esta investigación. Por hacer más agradables los malos días y estupendos los buenos. Por creer en mí y hacerme de soporte frente a las dificultades que he tenido en este camino. Aunque las palabras se me quedan muy cortas, por todo eso quiero darte un inmenso gracias.

Quiero tener una mención especial para Iñigo Iparraguirre, porque sin él esto nunca hubiera sido posible. Por "pelearse" mucho con Matrix para poder darme una acogida excepcional cuando llegué a Tecnalia. Porque me ha aportado mucho con su visión comercial y amplios conocimientos técnicos de la energía solar. Y por su especial valoración y reconocimiento a mi trabajo y mi esfuerzo cada día.

A los compañeros de Tecnalia que con su saber hacer y experiencia han hecho posible obtener muchos de los resultados de esta tesis. A Izaskun Marañon y Gorka Imbuluzqueta, por su continuo esfuerzo y empeño por medir correctamente las sales en el DSC. A Alfredo Pacheco y Margot Llosa, por ser tan afables y cercanos y brindar su ayuda desinteresada con el DLS, microestructura e interacción de sales y nanopartículas. A Carmen del Río y Ana Rodríguez por las medidas de ICP y contaminantes y a Iñigo Ibañez por ayudarme siempre con una sonrisa y buen humor.

También una pequeña mención a todos los compañeros que desde mi llegada se esforzaron por hacerme más fácil mi adaptación a todos los niveles: Gorka, Carol, Saioa, Amets, Naiara, Iker, Uxoa y Oihana. Un agradecimiento también a Laura, Jokin y Amal, con los que he pasado muy buenos ratos durante mis últimos meses en Tecnalia.

Al Dr. Enrique Julià de la Universitat Jaume I, por su inestimable ayuda y apoyo todos estos años. Parte de los resultados de esta tesis se han completado gracias a tu colaboración. Fue una bonita casualidad conocernos allá por 2014.

RESUMEN

El suministro de energía es un tema de vital importancia que afecta especialmente a la sociedad debido a la emisión de Gases de Efecto Invernadero (GEI) y la necesidad de reducir el uso de combustibles fósiles. Es bien conocido que estas emisiones contribuyen al cambio climático y el calentamiento global, al mismo tiempo que conducen a una seria degradación del entorno y provocan enfermedades. Además, existen otras cuestiones serias relacionadas con el uso de fuentes de energía no renovable, como la seguridad en la cadena de suministro y su disponibilidad limitada.

En este contexto, la energía solar de concentración (CSP, por sus siglas en inglés) destaca como una opción muy valiosa dentro del marco de las energías renovables. Su disponibilidad es su característica principal comparada con otras energías alternativas. La energía solar no está disponible bajo demanda cuando y donde es necesaria. Como consecuencia, la mayoría de las plantas CSP cuentan con un sistema de almacenamiento térmico. Este sistema almacena la energía térmica como calor sensible, a través de dos tanques a diferentes temperaturas llenos con una sal fundida (Sal Solar, $NaNO_3$:KNO_3 60:40 %masa). El mismo material se utiliza como fluido de transferencia térmica para transportar el calor del campo solar al bloque de potencia. La madurez de esta tecnología está más que probada después de varias décadas desde que la primera planta CSP se puso en funcionamiento. Sin embargo, existen aún muchas oportunidades para desarrollar nuevos métodos de almacenamiento térmico o mejorar los que existen actualmente.

Las modestas propiedades termofísicas (calor específico y conductividad térmica) están entre las principales desventajas de la Sal Solar utilizada actualmente, lo que obliga al uso de una gran cantidad de sal para poder almacenar calor durante el tiempo necesario. Varias soluciones se han propuesto, como el uso de otras sales inorgánicas dentro de complicados sistemas de almacenamiento térmico para alcanzar una tasa de transferencia de calor adecuada. Recientemente, ha emergido una opción que considera el uso de la nanotecnología. Esta solución consiste en añadir pequeñas cantidades de nanopartículas a las sales para mejorar su comportamiento térmico. Estos innovadores materiales se han denominado como nanofluidos basados en sales fundidas o materiales de cambio de fase nanomejorados, dependiendo del método empleado para almacenar la energía térmica: calor sensible o latente, respectivamente.

Esta tesis analiza detalladamente el diseño, síntesis y caracterización de estos materiales. Su reciente descubrimiento, unido a las dificultades técnicas de trabajar con sales fundidas, han ocasionado que ciertas propiedades apenas se hayan estudiado. Se ha puesto especial atención en el desarrollo de un método preciso para medir el calor específico y un proceso de síntesis adecuado y escalable. La caracterización de los materiales incluye propiedades térmicas como el calor específico, la conductividad térmica, el calor latente y la temperatura de cambio de fase. También se han estudiado otras propiedades interesantes como la estabilidad de las nanopartículas en la sal fundida durante largos periodos y su comportamiento reológico.

ABSTRACT

Energy supply is a vital issue which specially concerns the society regarding the emission of GreenHouse Gases (GHG), and the need to reduce the use of fossil fuels. Such emissions are known to consequently contribute to the climate change and global warming, while at the same time they can lead to serious degeneration of the living environment and diseases. Moreover, there are also other serious issues related to the use of non-renewable fossil fuel feedstock, particularly the security of supply and their limited availability.

In this context, the Concentrated Solar Power (CSP) emerges as a high valuable option inside the frame of renewable energies. Its dispatchability is its main feature in comparison to other alternative energies. Solar energy is not available on-demand, when and where it is needed. As a result, the majority of the CSP plants are supplied with a thermal energy storage (TES) system. This system stores the thermal energy as sensible heat, by means of two tanks at different temperatures filled with a molten salt (Solar Salt, $NaNO_3$:KNO_3 60:40 wt%). The same material is used as Heat Transfer Fluid (HTF) to transport the heat from the solar field to the power block. The maturity of this technology is certainly proven after several decades the first CSP plant came into operation. However, there are still many opportunities to develop new methods of heat storage and to improve the presently existing ones.

The poor thermophysical properties (specific heat and thermal conductivity) of the currently used Solar Salt is one of the main drawbacks, which compels the use of a huge amount of salt to store the thermal energy for the required time. Several solutions have been proposed, such as the utilization of other inorganic salts (as sensible or Phase Change Materials (PCMs)) inserted into complicated TES devices to achieve an adequate heat transfer rate. In recent years, a new attempt considering the potential of nanotechnology has arisen. This solution consists of adding tiny quantities of nanoparticles to the salts to improve their thermal performance. These innovative materials are named as Molten Salt-Based Nanofluids (MSBNFs) or Nano-enhanced PCMs (NePCMs) depending on the method employed to store the thermal energy: sensible or latent heat, respectively.

This PhD thesis goes into detail about the design, synthesis and characterization of these materials. Their recent discovery, together with the technical difficulties of working with

molten salts made some properties to be hardly studied. The development of a precise method to measure the specific heat and a suitable and scalable synthesis procedure is considered with a special attention. The characterization of the materials involves the thermal properties such as the specific heat, thermal conductivity, latent heat and phase change temperature. Other interesting properties such as the stability of the nanoparticles in the molten salt in the long term and the rheological behaviour of these materials are also addressed.

INDEX OF CONTENTS

ANNEXES   357

INDEX OF FIGURES

INDEX OF TABLES

ABBREVIATIONS

ASS	Analytical Solar Salt
ASN	Analytical Sodium Nitrate
ANPs	Alumina Nanoparticles
CSP	Concentrated Solar Power
DLS	Dynamic Light Scattering
DSC	Differential Scanning Calorimetry
dTG	Differential Thermogravimetry
EDX	Energy-Dispersive X-ray spectroscopy
HTF	Heat Transfer Fluid
ISS	Industrial Solar Salt
ISN	Industrial Sodium Nitrate
LFA	Laser Flash Analysis
MDS	Molecular Dynamics Simulation
MDSC	Modular Differential Scanning Calorimetry
MSBNFs	Molten Salt-Based Nanofluids
MT	Melting Temperature
NEPCMs	Nano-Enhanced Phase Change Materials
NPs	Nanoparticles
PCMs	Phase Change Materials
PI	Polydispersity Index
QBSD	Quadrant Back-Scattering Detector
RRT	Round Robin Test
RSD	Relative Standard Deviation

RSS	Refined Solar Salt
RSN	Refined Sodium Nitrate
SD	Standard Deviation
SE	Secondary Electrons
SEM	Scanning Electron Microscopy
SiNPs	Silica Nanoparticles
S/V	Surface to Volume ratio
TEM	Transmission Electron Microscopy
TES	Thermal Energy Storage
TGA	Thermogravimetric Analysis
XRD	X-Ray Diffraction
ZP	Zeta Potential
Z-ave	Zeta-average diameter

Chapter 1

INTRODUCTION, GENERAL BACKGROUND AND MOTIVATION

1 INTRODUCTION, GENERAL BACKGROUND AND MOTIVATION

1.1 INTRODUCTION

Energy supply is a vital issue which specially concerns the society regarding the emission of GreenHouse Gases (GHG) and the need to reduce the use of fossil fuels. Such emissions are known to consequently contribute to the climate change and global warming, while at the same time they can lead to serious degeneration of the living environment and diseases. Moreover, there are also other serious issues related to the use of non-renewable fossil fuel feedstock, particularly the security of supply and their limited availability.

The worldwide economic crisis since 2008 added additional challenges, leading the governments to establish new policies and financial incentives to support the implementation and development of renewable energies. The European Commission has set a target of achieving a 20% of the total energy consumption from renewable sources by the year 2020 [1], which will stabilize the CO_2 emissions, thus reducing the contribution to the global warming.

Because of the use of fossil fuels, the current global CO_2 emissions (2012) are $32.3 \cdot 10^9$ tonnes per annum (tpa), showing an alarming annual increment when compared to the $28.2 \cdot 10^9$ tpa emitted in 2005. Without effective measures to reduce this tendency, it has been forecasted that the CO_2 emissions related to the energy consumption in the planet will further increase to $35.6 \cdot 10^9$ tpa in 2020 and $43.2 \cdot 10^9$ tpa in 2040 [2].

The imposed reduction in CO_2 emissions will require the immediate assumption of drastic measures. Among others, the development of highly-efficient energy capture, storage and re-use methods will be crucial in the next future. In the present situation, there is indeed a considerable scope for improving the energy efficiency. In the short or medium term, waste heat recovery and high temperature thermal energy storage can provide a huge leap to increase the energy efficiency. Currently existing power plants can use high temperature thermal energy storage to improve the energy balance of their operations, since the implementation of thermal storage will increase the flexibility and availability of heat and electricity in traditional or new power plants [3]. A report of the CSP Alliance gathers several studies where the Concentrated Solar Power (CSP) plants with thermal storage show a higher capacity value (selling price of the output electricity) than those without it (around 20 $/kWh of difference) [4].

In this context, the CSP emerges as a high valuable option inside the frame of renewable energies. This technology uses mirrors to reflect and concentrate sunlight onto the receivers. These receivers collect the concentrated solar energy and convert it into high-temperature heat used to generate steam that is driven to a turbine for producing electrical power. The main feature of the

current CSP plants under operation is their dispatchability. Solar energy is not available on-demand, when and where it is needed. As a result, the majority of the CSP plants are supplied with Thermal Energy Storage (TES) systems. In this way, the solar energy is harvested when it is available, it is stored and then it is used when it is required, in the desired amounts and in a manner that is comparable to or better than conventional power plants. This is possible thanks to the development and industrial implementation of efficient and robust TES systems. Several decades after the first CSP plant came into operation, the maturity of this technology is undoubtedly proven. However, there are still many opportunities to develop new methods and to improve the presently existing ones.

1.2 GENERAL BACKGROUND

1.2.1 Concentrated Solar Power (CSP)

1.2.1.1 The basic concept

The solar radiation arriving at the Earth's surface is composed of fairly scattered energy wavelengths. The photons comprising the solar radiation can be converted directly to electricity in photovoltaic devices

These photons can also be used in CSP plants, where the solar radiation heats up a fluid that is used to drive a thermodynamic cycle. In these plants, it is necessary to concentrate the sunlight, using mirrors or optical lenses, to create a sufficiently high energy density and temperature level. Various strategies have been adopted for concentrating and capturing the solar energy in CSP technologies, giving concentrations of 25–3000 times the intensity of sunlight [5].

Concentrating systems (which are sometimes also used in photovoltaic devices) can only make use of direct radiation, and are therefore applicable in areas with clear weather. In cloudy or dusty areas, photovoltaic technologies (PV) without concentration are likely to be preferred [5]. Taking into account the Levelized Cost of Electricity (LCE), the price of kWh_{th} is lower in the case of PV technologies. However, the main advantage of the CSP with respect to PV technologies is its dispatchability. The TES system allows producing energy during the night or cloudy periods.

A CSP plant comprises four main sub-systems, as schematically shown in Figure 1-1: the concentrating system, the solar receiver, the storage and/or supplementary firing ("back-up system") and the power block. They are linked together by a Heat Transfer Fluid (HTF) radiation transfer or fluid transport.
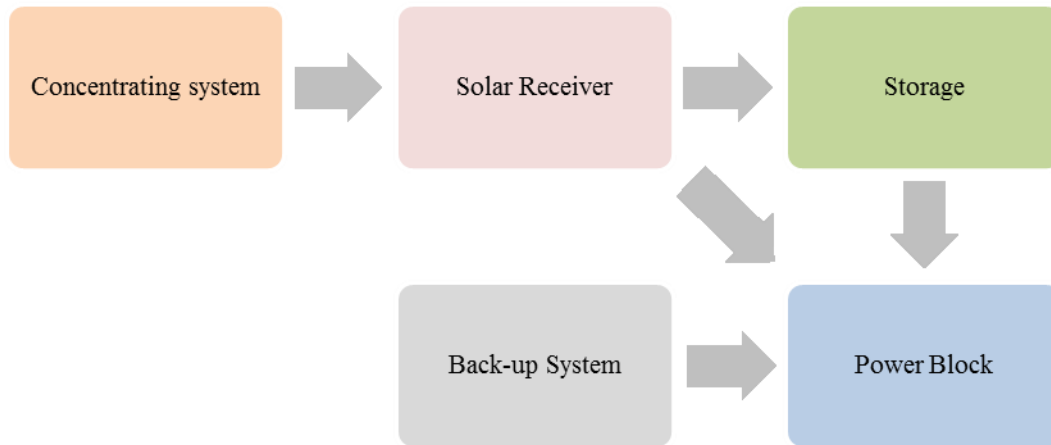
Figure 1-1. Main components and sub-systems of a CSP plant including storage. Based on [3].

The solar receiver absorbs the concentrated solar energy and transfers it to the HTF. Then, the HTF is used to deliver high-temperature heat to the power block and/or to store solar heat in a hot storage tank. The HTF in the solar field and the power block working fluid may be the same, as in a CSP plant using Direct Steam Generation (DSG) [5].

1.2.1.2 The four CSP technologies

As illustrated in Table 1-1, there are four CSP technologies that can be classified according to the method used to focus the sun's rays and also according to the receiver technology.

Regarding the method to focus the rays, there are two main systems: systems with a line focus (Parabolic Trough and Linear Fresnel) and systems with a point focus (Tower and Parabolic Dish). On the former systems, the sun rays are received in mirrors that track the sun along one axis and reflect the received rays to the focus, which remains on the same place whatever the sun position along the day. In those systems with a point focus, sun rays are received on mirrors that focus to the same point. The mirrors track the sun along two axes in order to harvest all the solar radiation along the day.

Regarding the receiver, two different technologies are presently used, fixed receivers and mobile receivers. The receivers are fixed in Linear Fresnel systems and in the Tower systems. The first consists of several plane mirrors parallel to the receiver where the sun rays are reflected. The Tower systems are composed of heliostats which are tracking the sun position and focus to the tower. Mobile receivers are used in Parabolic Trough and Parabolic Dish systems. In the former case, the receiver consists in a parabolic reflector with the line receiver placed on their parabolic focus. In the Parabolic Dish system, the receiver is not a line but a point. Figure 1-2 provides pictures of the solar receivers for each of the technologies.

Table 1-1. The four CSP technologies (based on [5]. Images from https://energy.gov/eere/sunshot/solar-multimedia).
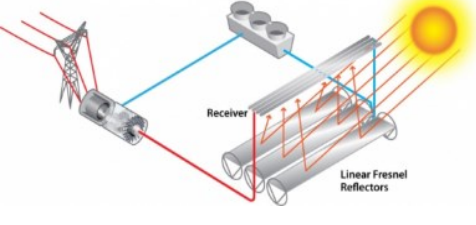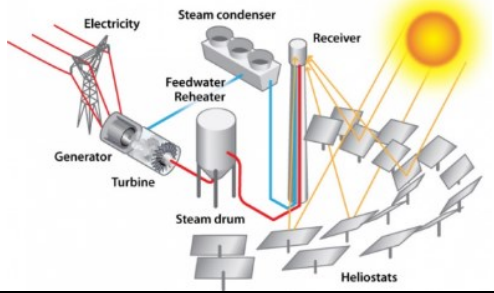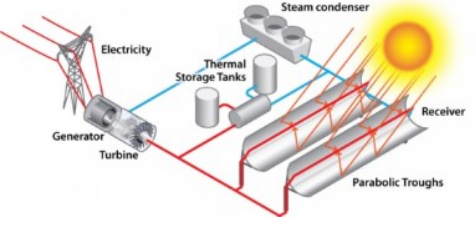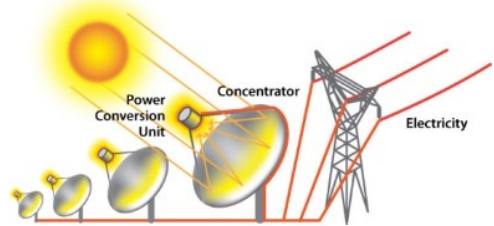
	FOCUS TYPE	
RECEIVER	Line focus	Point focus
Fixed	Lineal Fresnel 	Tower (central receiver systems)
Tracking/ Aligned	Parabolic Trough 	Parabolic dish

Figure 1-2. A) Tower power. Gemasolar plant in Andalucia, Spain (Torresol Energy) [5]. B) Parabolic dish (DLR, Markus Steur) [5]. C) Solar receiver for trough technology (Ultimate Trough® test loop installation, California) with permission from schlaich bergermann partner. D) Solar receiver for Linear Fresnel technology (Plataforma Solar de Almería (PSA) [6].

In each technology, various options exist for the HTF, the storage technology, and the thermodynamic cycle.

Synthetic oil and saturated steam are used as HTFs in commercial plants, while molten salt and superheated steam have come more recently into the market. The use of air (either at atmospheric pressure or pressurized) and of other pressurized gases (for example, CO_2 and N_2) is under development, while helium or hydrogen are used in the Parabolic Dish systems.

Presently, liquid molten salt is the only commercial option for the thermal storage of the captured radiation to last some hours in order to better match the electricity production to the demand. Steam is sometimes used for short time (less than 1 hour) storage.

Two types of thermodynamic cycles are currently employed for the production of energy: steam Rankine cycles, and Stirling cycles for parabolic dish concentrators [7]. Brayton cycles are presently under development. In these cycles a gas turbine is driven by pressurized gas heated by the solar collector. The combination of a Brayton cycle that supplies its waste heat to a Rankine cycle promises to achieve the best efficiency of all systems, and thus the highest electrical output per square meter of collector field [5].

1.2.1.3 Current performance and development status

As of December 2016, the CSP market has a total capacity of 8784 MWe worldwide, among which 4800 MWe is in operation, 1260 MWe is under construction and 2709 MWe under development. Spain has a total operational capacity of 2304 MW, making it the world's leading country in CSP. USA follows Spain, having a total capacity of 1745 MW (Figure 1-3). Interest has grown in India, Chile, South Africa, Australia, China and a few Middle East countries [8]. Parabolic trough systems are currently the most largely proven CSP technology and dominate the global market, being installed in more than 80% of the CSP plants in operation and under construction. Tower systems have just started to be introduced into commercial applications while the Linear Fresnel plants are currently making the transition to commercial applications. Parabolic dishes are at the early demonstration stage [9].
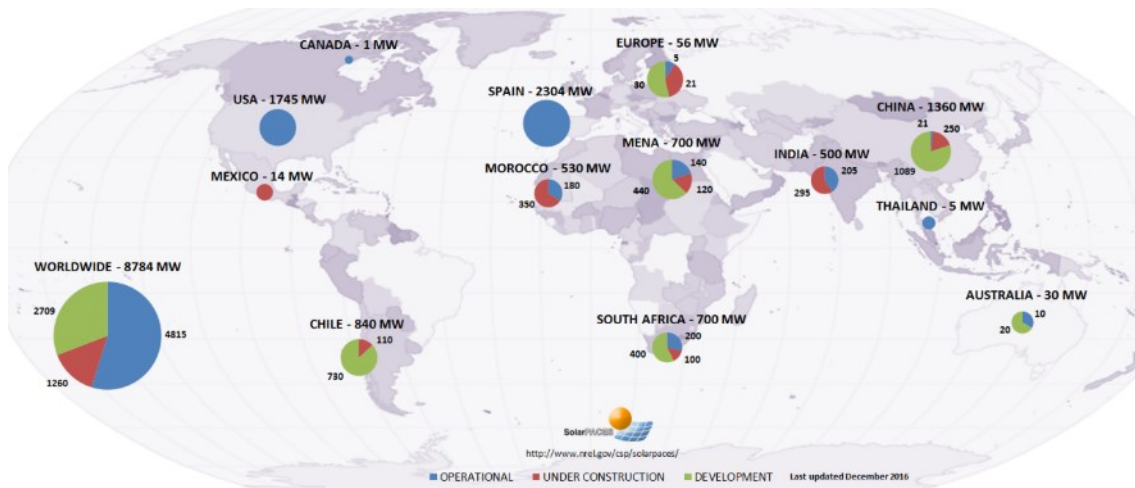
Figure 1-3. CSP Projects around the world (December 2016) [8].

1.2.2 Thermal Energy Storage (TES) technologies

1.2.2.1 The basic concept

A distinctive characteristic of CSP is the inherent option to incorporate TES. The main value of adding TES is that it enables a CSP plant to provide 'dispatchable power', helping the grid operator to reliably match supply and demand.

The basic concept of using TES to extend the hours of generation of a CSP plant is illustrated in Figure 1-4. The CSP plant includes a solar field which is larger than would otherwise be needed to drive the steam turbine at full capacity during daylight. The excess heat generated during the sunnier part of the day is sent to storage, which can then be drawn on later in the day to meet demand for electricity when the sun is no longer shining, thus improving the usage of the power block, and therefore the productivity of the plant. Depending on the extent to which the solar field is over-sized in relation to the turbine capacity, incorporating thermal storage capacity can extend the operating period of the CSP plant by a few hours after sunset up to 24 hours.
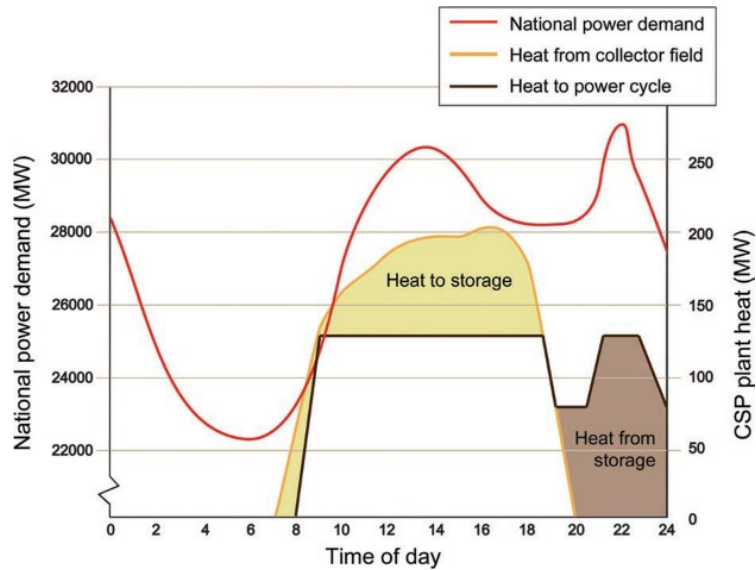
Figure 1-4. Extending operating hours of a 50 MWe CSP plant with thermal storage to follow the demand curve of a normal mid-summer day in Spain. Demand curve derived from RED Electrica de España and CSP load from computer simulation (https://demanda.ree.es/demandaEng.html) [5].

According to the method of storing the thermal energy, TES can be classified as sensible heat storage, latent heat storage and thermochemical storage.

1.2.2.2 Sensible heat storage

In sensible TES systems, the thermal energy is stored by raising the temperature of the storage medium, which is typically either a solid or a liquid. The thermal energy is released by lowering the temperature of the storage medium. The amount of energy stored depends on the quantity of the storage material (m), the specific heat capacity of the material (c_p) and the temperature change (ΔT) and it is determined by Eq. 1-1. All the TES systems currently installed in CSP plants use sensible storage, e.g. by storing the thermal energy in oil, molten salt, steam, ceramic or graphite.

$$Q = mc_p\Delta T \qquad\qquad \text{Eq. 1-1}$$

The state-of-the-art on the use of storage material for CSP plants is the so called "molten salts". For example, mixtures of nitrate salts such as Hitec® (40 wt% $NaNO_2$, 53 wt% KNO_3, 7 wt% $NaNO_3$), Hitec XL® (48 wt% $Ca(NO_3)_2$, 45 wt% KNO_3, 7 wt% $NaNO_3$) and Solar Salt (60 wt% $NaNO_3$, 40 wt% KNO_3) [10] have been commercially deployed in Parabolic Trough and Tower Systems. Synthetic oils (Therminol VP-1™ [11], Dowtherm™ [12], etc.) were the common working fluid in trough plants before the use of molten salts as HTF emerged (CSP plant Gemasolar (Spain), 2010). Solar Salt is relatively cheap and has the highest maximum operating temperature; however, it freezes at 220 °C, which in some cases requires quite expensive anti-freeze systems. Hitec and Hitec XL have a more desirable freezing temperature of 120–140 °C and are able to withstand a temperature limit of over 500 °C.

1.2.2.3 Latent heat storage

A latent TES stores and releases the thermal energy as latent heat during a material phase change. The materials employed for this purpose are known as Phase Change Materials (PCMs). Adequate materials for PCMs take advantage of the large latent heat that can be stored/released by changing a material from one phase to another (generally solid to liquid). Latent Heat Storage TES (LHTES) has attracted considerable attention for CSP applications over the past decade [6]. The amount of the energy stored is governed by, both the specific heat and the phase change enthalpy, and can be calculated by Eq. 1-2.

$$Q = m\big[c_{p,s}(T_m - T_s) + h + c_{p,l}(T_l - T_m)\big] \qquad \text{Eq. 1-2}$$

where $c_{p,s}$ and $c_{p,l}$ are the average specific heats of the PCM in solid and liquid phases, respectively, T_m is the melting temperature, h is the phase change enthalpy, and T_s and T_l are temperatures of the solid and liquid PCM, respectively.

Due to the nature of phase change, a large energy is absorbed/released to change the materials from solid to liquid (or viceversa), without changing the temperature of the system. Therefore, a LHTES system can offer nearly isothermal heat storage/releasing. If a temperature gradient is sought, LHTES offers a considerably higher storage density compared to a sensible storage system with the same temperature change. As a result, it enables a smaller (and potentially cheaper) storage system compared to a sensible storage system. Currently, no commercial LHTES system has been used in utility-scale CSP applications.

Due to the high temperature requirements for CSP systems, inorganic salts/salt eutectics and metals/metal alloys are potential PCMs [13,14]. Salts have been the most studied PCMs to reduce the cost of thermal storage. However, salts have low thermal conductivity, which limits the heat transfer between the HTF and the PCM, particularly during discharging. This restricts the actual use of the system. Considerable efforts have been made to enhance the heat transfer within PCM storage systems, including extending the heat transfer surface by encapsulating the PCM [15,16], adding fins to the wall of the heat exchanger tubes [17], adding heat pipes or thermosiphons in the system [18] and composing high thermal conducting composite materials into the PCM [19]. Inexpensive metals and metal alloys containing zinc, aluminum, copper, magnesium and silicon, have also been investigated [20,21]. Since they are high thermal conducting materials, heat transfer is enhanced with respect to molten salt-based PCM. However, their higher fire risk, cost and density in comparison to inorganic salts reduce its applicability.

1.2.2.4 Thermochemical energy storage

In thermochemical storage the energy is stored by means of a reversible chemical reaction (Eq. 1-3)

$$AB + Heat \Leftrightarrow A + B$$ Eq. 1-3

In the endothermic reaction, generally a chemical reactant AB absorbs the heat supplied from the solar field and is dissociated into two products, A and B, which can be stored separately. In the reverse process (exothermic reaction), the chemicals A and B are put in touch to produce AB, with a heat release. The amount of heat stored in a thermochemical process is given by Eq. 1-4 [22].

$$Q = a_r m \Delta H$$ Eq. 1-4

where, a_r is the fraction reacted, m is the mass of the reactant AB and ΔH is the heat of reaction per unit mass. Thermochemical storage possesses high energy density, much higher than the latent heat or sensible storage processes, and negligible heat loss, which potentially offers a long-term storage option with relatively small storage volume. The sorption processes are usually able to store low and medium grade heat at a temperature below 400 °C and the heat of reaction is typically between 20 and 70 kJ·mol^{-1}. The investigated processes include metal salts with water, ammonia, methanol or methyl-ammonia and metal alloys with hydrogen. Other type of chemical reactions allow the energy to be stored at temperatures over 400 °C with a higher heat of reaction, from 80 to 180 kJ·mol^{-1} [23].

The volumetric energy density of thermochemical TES is 5–10 times higher than latent and sensible TES respectively [9]. Compared to sensible and latent heat storage, thermochemical storage is still at a very early stage of development and so far most of the systems were only tested at a laboratory scale for short discharging periods. Large-scale experiments are required to prove the efficiency and economic feasibility of the thermo-chemical storage system for both short and long-term storage.

1.2.2.5 Types of TES systems

TES systems in CSP plants can be classified as active or passive systems [22,24] (Figure 1-5).

- An active storage system is mainly characterized by forced convection heat transfer into the storage material. The storage medium itself circulates through a heat exchanger, a solar receiver or a steam generator. This system uses one (thermocline) or two tanks as storage media. Active systems are subdivided into direct and indirect systems. In a direct system, the HTF also serves as the storage medium; while in an indirect system, a second medium is used for storing the heat (Figure 1-6).

- <u>Passive storage systems</u> are generally dual medium storage systems: the HTF passes through the storage only for charging and discharging a solid material. The HTF carries energy received from the energy source to the storage medium during charging, and receives energy from the storage when discharging (these systems are also called regenerators). The main disadvantage of regenerators is that the HTF temperature decreases during the discharging as the storage material cools down. In addition, the heat transfer is rather low as usually there is no direct contact between the HTF and the storage material and the heat is transferred via a heat exchanger.
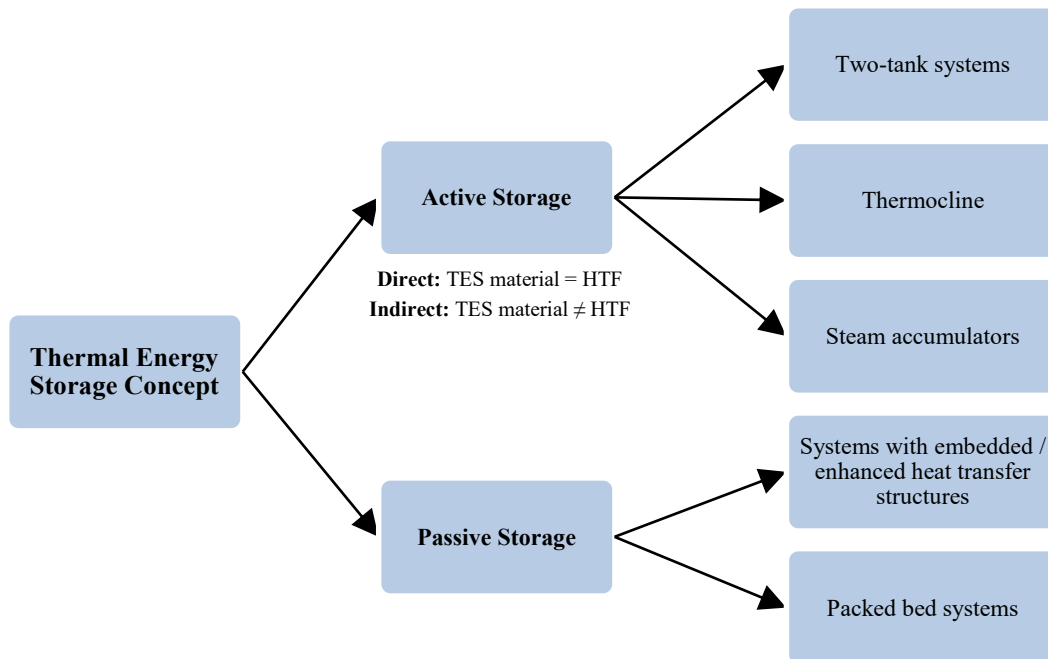
Figure 1-5. Categorization of the TES systems according to Kuravi and his colleagues. Adapted from [22].
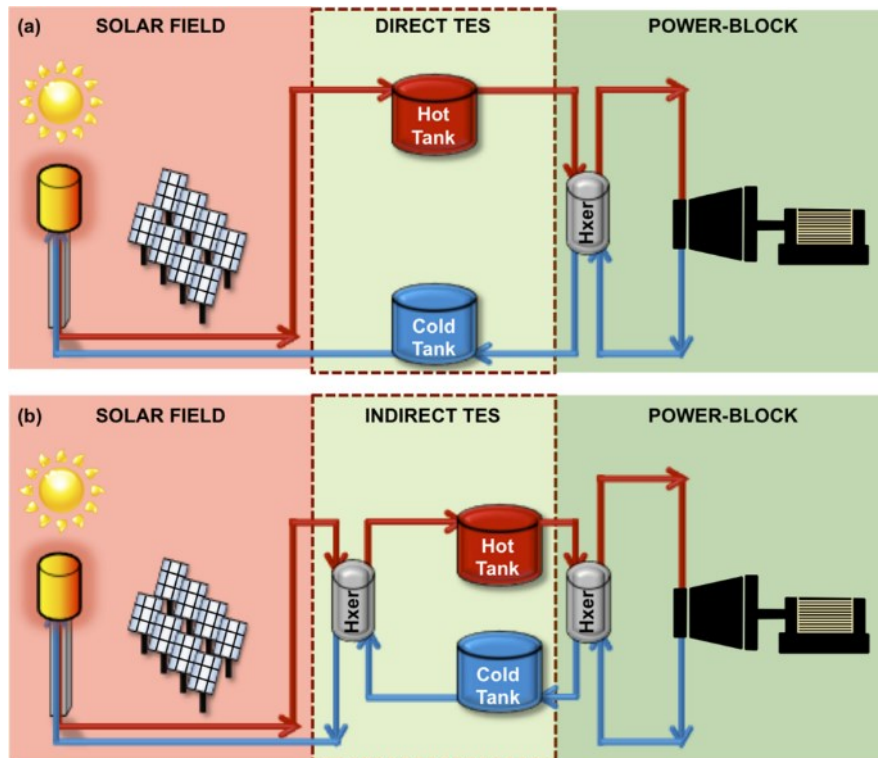
Figure 1-6. Schematic view of (a) a two-tank direct TES system, which uses the same HTF in the solar energy receiver and in the TES system and (b) an two-tank indirect TES system, which uses different HTFs in the solar energy receiver and in the TES system, requiring an additional heat exchanger [25].
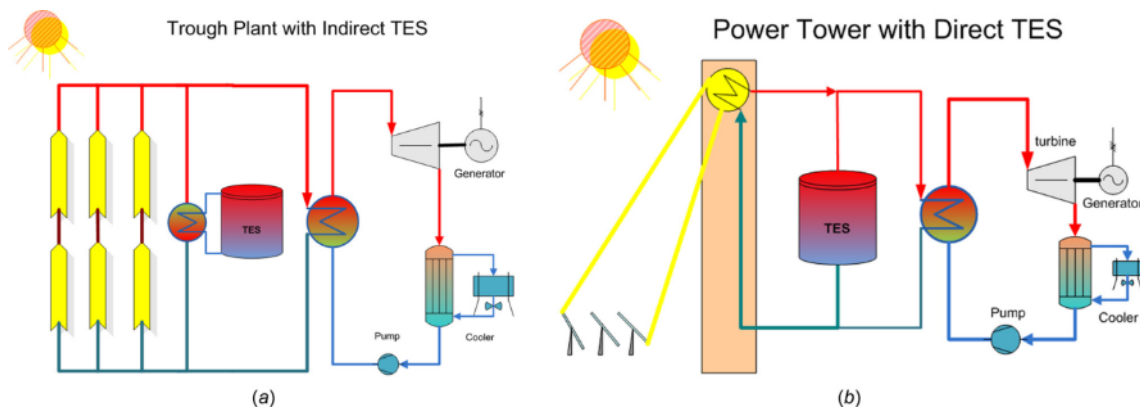
Figure 1-7. Thermocline indirect (a) and direct (b) integration of TES in a CSP system [26].

The storage system most commonly used in commercial Parabolic Trough plants, uses a two-tank, indirect storage approach (Figure 1-7b). The thermal oil emerging from the solar collector may be diverted to a heat exchanger, where its heat is transferred to the heat storage medium – molten salt. The hot salt can subsequently be used to heat the thermal oil instead of the solar field. The molten salt is a mixture of sodium and potassium nitrate (60:40 wt%), also called Solar Salt, with a melting temperature around 238 ºC. The salt is transferred between the "cold" and the "hot" tank, which are at temperatures about 291 and 384 ºC respectively. This technology was first implemented on the CSP plant of Andasol I (Spain) which is based on the Parabolic Trough

technology. An amount of 28,500 tonnes of Solar Salt for a total storage capacity of 1010 MWh are confined inside two tanks of 14 meters high and 36 meters of diameter. This system provides 7.5 to 8 hours of thermal energy.

An alternative two-tank system uses direct storage: the HTF also acts as the TES medium (Figure 1-7a), removing the need for a heat exchanger, and hence reducing the cost and increasing the overall efficiency. The technical feasibility of this option has been demonstrated for thermal oil in a Parabolic Trough plant (the SEGS-1 plant in California), and for molten salts in a Parabolic Trough demonstration plant (the ARCHIMEDE plant in Sicily, Italy) and in central receiver plants (the SolarTwo plant in California and the Gemasolar plant in Spain). In practice, direct storage using thermal oil is limited to operating temperatures below 400 °C due to the thermal stability of the oil, and to low capacity systems due to the fire hazard associated with storing large quantities of hot oil. Molten salts have been proven to operate at temperatures up to 570 °C, reducing the amount of salt needed, but long-term experience of the reliability of the concept is not yet available. In this option, the "cold" and "hot" tanks filled-in with the Solar Salt work at temperatures of 290 ºC and 565 ºC, respectively.

A single thermocline tank storage, which eliminates the need to have a second tank, enables a potential cost reduction of 35% compared to the two-tank storage [9]. In the thermocline systems, the hot and cold fluids are stored in the same tank, separated due to the thermal stratification [24]. Also, research has been conducted to use low-cost filler materials to reduce the overall required amount of the relatively higher cost molten salt storage medium [24].

In the active storage systems with steam accumulators, charging takes place when superheated steam or saturated water enters a pressurized storage tank that initially contains saturated steam and saturated water. The discharging process takes place by reducing the pressure in the storage tank. This results in the production of saturated steam that decreases in pressure as the discharging process occurs. Steam accumulators are well-suited for CSP plants with DSG: steam is produced directly in the solar field and then used in the power block to produce electricity. Steam that is produced in excess can be diverted to the steam accumulator.

Passive storage systems are mainly solid storage systems (concrete and castable materials). In the case of concrete storage, the solar energy of the solar field is transferred from the HTF to the solid storage material system. The storage material contains a tube heat exchanger to transfer the thermal energy from the HTF to the storage (Figure 1-8). A tubular heat exchanger is integrated into the storage material (Figure 1-9).

This heat exchanger corresponds to a significant share of the investment costs. The design of the geometry parameters, like the tube diameter and the number of pipes, is very important for the

performance of the TES system.
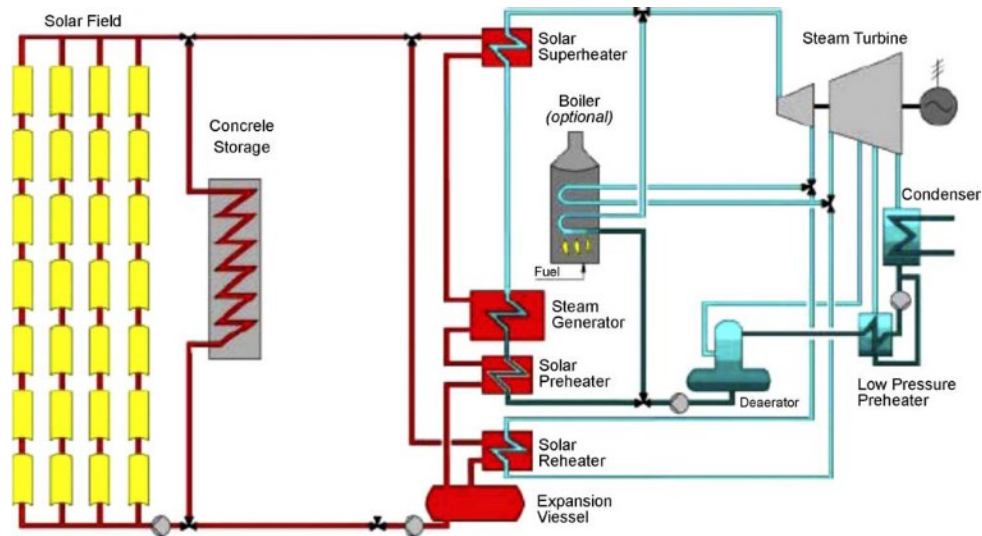
Figure 1-8. Scheme of a parabolic through power plant, with concrete (or castable ceramics) storage system [24].

Figure 1-9. View of the tubular exchanger into the concrete beam [27].

1.2.2.6 Challenges and cost reduction of the current two-tank system

As detailed in the TES systems analysis, the most widely implemented system nowadays is the two-tank indirect configuration. Indeed, this system presents drawbacks regarding the overall plant performance and costs. The use of molten salts as HTF and storage material at the same time eliminates the need for expensive heat exchangers. In this way, the solar field can be operated at higher temperatures than with the current HTFs, increasing the temperature drop across the turbine. Higher temperature drops increase the efficiency of the turbine power-cycle and the stored energy density of the sensible portion of the TES system. These advantages are signaled on Figure 1-10.
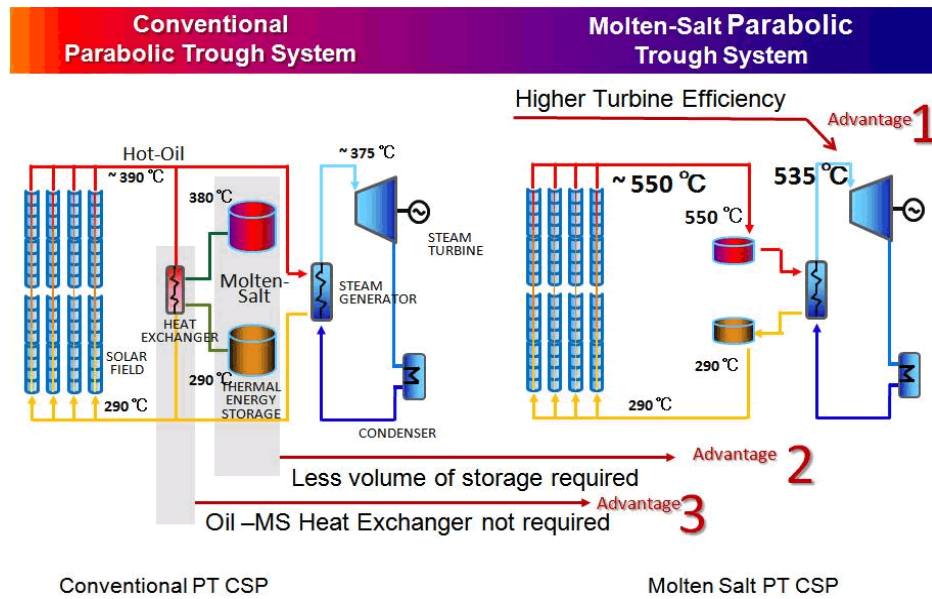
Figure 1-10. Advantages of an active two-tank TES system according to Chiyoda Corporation (https://www.chiyoda-corp.com/technology/en/green_energy/solar_energy.html)

Nevertheless, the molten salts freeze at relatively high temperatures (120–220 ºC), and this means that special care must be taken to ensure that the salt does not solidify in the solar field piping during the night. Hence, the protection and maintenance against the salt freezing has to be carefully planned and managed, increasing maintenance and operation costs [24]. On the other hand, results reported by D. Kearney concluded that the use of the molten salt as a HTF made economic sense only if the solar plant included a thermal storage system [28].

A relatively easy way to improve the economics of this system is to increase the heat capacity of the storage fluid. The minimum required heat capacity for a sensible storage material is a function of the temperature drop across the turbine. The heat capacity and the temperature drop together determine the stored energy density of the TES system. Other factors are the costs of the storage material, the tank and the piping materials that are required for the TES system. For the two-tank storage system, the low-temperature tank is normally at 300 ºC, so the temperature drop across the power block is determined by the maximum operating temperature [29].

In view of these potential advantages and savings, the increase of the specific heat of molten salts has been a new field of research in the last few years. The addition of tiny amounts of nanoparticles to these molten salts has demonstrated to produce enhancements of their specific heat. These materials are known as Molten Salt-Based Nanofluids (MSBNFs) or Nano-enhanced PCMs (NePCMs) and have attracted the attention of many research groups worldwide.

1.3   MOTIVATION

As stated on the previous introduction, the insufficient thermal properties of the molten salts can potentially be improved by doping them with nanoparticles. The inclusion of nanoparticles at minute concentrations has been claimed to significantly enhance the thermal conductivity and the specific heat capacity of the molten salts [30–32].

Thus, this thesis will focus on the addition of silica and alumina nanoparticles to the molten Solar Salt to enhance its specific heat capacity and thermal conductivity. Solar Salt is the currently used storage and HTF material in the direct two-tank TES systems.

Besides, Sodium Nitrate has been selected as PCM to study how their phase change properties (latent heat and melting temperature) are affected by the presence of the nanoparticles. This PCM is considered a good candidate to be used in DSG solar power plants, because of the proper match between its melting temperature (306 ºC) and the phase change temperature of the steam (310 ºC at a pressure of 100 bar) [33,34]. Some authors have studied how the phase change properties are influenced by the addition of nanoparticles to inorganic salts with controversial results [31,32,35–40]. However, the addition of nanoparticles to the Sodium Nitrate has not been investigated so far.

The general focus of this thesis is to develop MSBNFs or NePCMs as close as possible to the current industrial requirements of the CSP technology.

1.4   OBJECTIVES

The present thesis aims to strengthen and to provide new knowledge in the field of TES and heat transfer by molten salts on the CSP plants. The main objective is to develop a nanostructured material based on nitrate salts with improved thermophysical properties, suitable to be employed as HTF and TES in CSP plants. Therefore, the synthesis procedure and the raw materials have been selected with the objective of a future commercial implementation. This material is intended to be used as sensible and latent storage media, and/or HTF in the thermosolar plants. This will be accomplished by fulfilling the following research objectives:

- To develop precise and reproducible methods to characterize the specific heat and the nanoparticle size distribution in nanofluids or NePCMs based on nitrates.

- To precisely characterize the thermal properties of the nitrate salts of commercial purity which are further used in the thesis. The quantity and nature of their contaminants has a particular consideration.

- To properly select and analyze the nanoparticles (SiO_2 and Al_2O_3) which are further added to the nitrate salts. The absence of chemical interactions with the molten salt is foreseen.

- To develop a new synthesis method of the nanofluid or the NePCM ahead of the current state-of the-art, by reducing the amount of water and energy required to perform the process. The method also aims to keep the size of the nanoparticles at the nanometric scale, by avoiding their clustering and agglomeration during the preparation.

- To analyze the thermal properties of the developed nanofluids or NePCMs: the specific heat, the latent heat and the thermal conductivity. Specifically, the behavior of the material under the following cases is studied:

→ The influence of the nanoparticle percentage (0.5, 1.0 or 1.5 wt%) on the specific heat, latent heat and thermal conductivity of the material.

→ The influence of the synthesis method, the size and shape of the nanoparticles, and the base salt on the specific heat.

- To evaluate the stability of the nanoparticles on the molten salt in the long term.

- To determine the rheology of the nanofluids under variable shear rates and temperatures, studying the suitability of the rheological methods performed.

In summary, this thesis is conceived to study the most important aspects concerning the industrial application of the MSBNFs or NePCMs based on nitrates.

1.5   STRUCTURE OF THIS DOCUMENT AND METHODOLOGY

This thesis has been organized in nine chapters (Figure 1-11): The Chapter 1 consists of a brief introduction and a general background of the thermosolar and TES technologies. Chapter 2 presents an in-depth literature review on the molten salt-based nanofluids up to the present date. Chapter 3 describes the inorganic salts and nanoparticles used on the thesis as well as every experimental method employed for their characterization. Chapter 4 details the experimental study carried out to set up the synthesis procedure. Chapter 5 gathers the results of the thermal properties of Solar Salt-based nanofluids: thermal cycling, specific heat and thermal conductivity. Chapter 6 is devoted to the thermal properties of the Sodium Nitrate-based NePCMs. Chapter 7 deals with the stability of the nanoparticles suspended in the molten salt in the long term. Chapter 8 analyzes the rheological behaviour of the nanofluids. Chapter 9 gathers the main conclusions of the thesis and displays the challenges and future works in this research field.

The scientific contributions (journal articles and conference proceedings) have been included along the text. A comprehensive list of them is detailed at the end of the document.
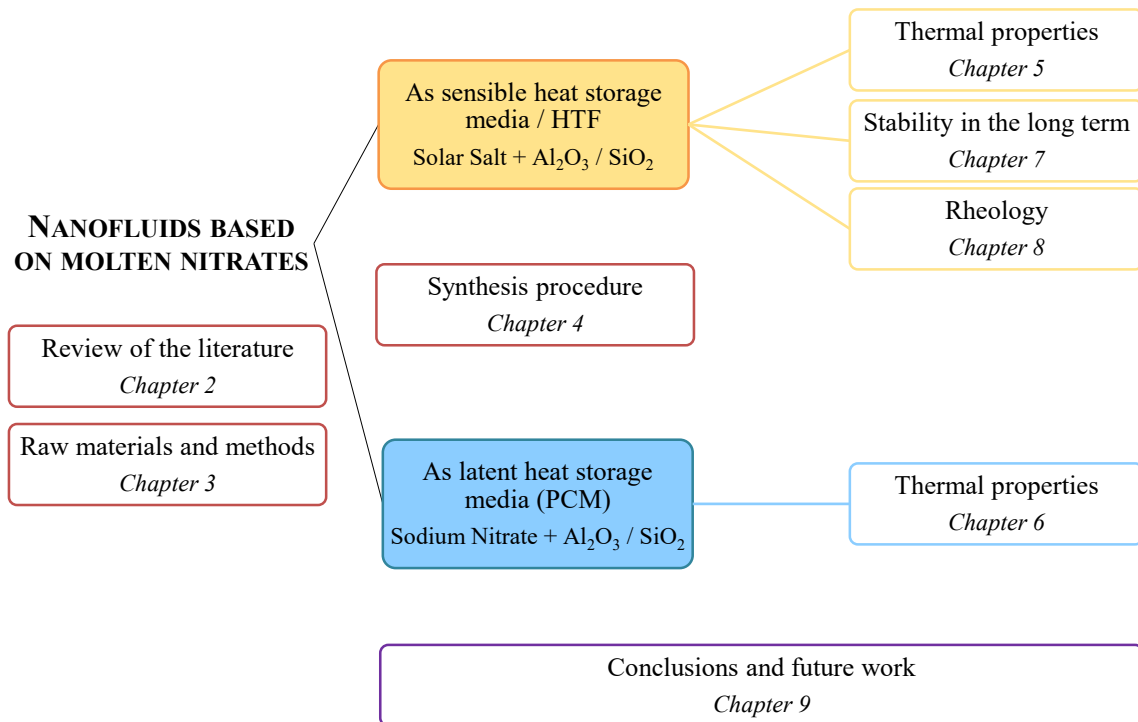
Figure 1-11. Organization of the thesis

.

Chapter 2

MOLTEN SALT-BASED NANOFLUIDS AS
EFFICIENT HEAT TRANSFER AND
STORAGE MATERIALS AT HIGH
TEMPERATURES. AN OVERVIEW OF THE
LITERATURE

2 JOURNAL CONTRIBUTION 1. MOLTEN SALT-BASED NANOFLUIDS AS EFFICIENT HEAT TRANSFER AND STORAGE MATERIALS AT HIGH TEMPERATURES. AN OVERVIEW OF THE LITERATURE

Authors: Belén Muñoz-Sánchez, Javier Nieto-Maestre, Iñigo Iparraguirre-Torres, Ana García-Romero and Jose M. Sala-Lizarraga

Abstract: The research in the field of nanofluids has experienced considerable advances from their discovery two decades ago. These liquid mixtures with tiny quantities (<10% in volume) of nanometric size solid particles (<100 nm) in suspension have a great potential for thermal management applications due to their excellent thermophysical properties. The so-called traditional nanofluids (based on water or industrial oils) have been extensively studied so far with a special focus on the enhancement observed in their thermal conductivity. Experimental results, mechanisms and models regarding these materials have been published and reviewed on a large number of articles. A new kind of nanofluids based on inorganic salts has been developed in the last few years with the aim of storing and transferring thermal energy at high temperatures. These Molten Salt-Based Nanofluids (MSBNFs) are characterized by a considerable increase of their specific heat due to the presence of particles at the nanometric scale. On the contrary, the specific heat of the traditional nanofluids is lower compared to that of the base fluid. This surprising behaviour has caused an opened debate in the scientific community, which is currently dealing with these controversial results and the lack of theories and models for these materials. This article reviews the published scientific contributions on MSBNFs. The influence of several facts on the specific heat is deeply analysed, as well as the synthesis methods. Other important aspects related to the behaviour and development of the MSBNFs such as the stability of the NanoParticles (NPs) in the molten salt, their latent heat, viscosity and thermal conductivity, have also been reviewed in this article. Finally, the difficulties and challenges concerning the further development of these materials have been summarized and the main conclusions have been listed.

2.1 INTRODUCTION

Nanotechnology has become a worldwide revolution in the last decades. The possibility of manipulating materials at the atomic and molecular level has led to achieve extraordinary attributes and features unimagined before.

In the framework of this broad field of research, nanofluids emerged recently as a promising material for thermal transfer and storage. They are composed of a base fluid where nanometric sized solid particles (less than 100 nm) are dispersed in volume concentrations typically lower than 10% [41]. The inclusion of nanostructures into a fluid causes an anomalous increment of its heat transfer rate, with particular incidence on its thermal conductivity [42,43]. The addition of

particles in the range of microns or millimetres to a fluid with the aim of improving its thermal properties is not a new idea. Maxwell was the first researcher who proposed a model for solid particles suspended in a fluid in 1873. In spite of their theoretical benefits regarding heat transfer features; these mixtures are limited on their practical application due to the particle sedimentation, the increment of the pressure drop in pipelines and the erosion they can produce [44–47]. In contrast to this situation, nanofluids have overcome the issue of stability because of the Brownian motion shown by nanostructures suspended in a liquid. These materials were first defined by Choi and Eastman in 1995 [42]. Goldstein and co-workers [48] specified that these particles may be in colloidal suspension. The initial experiments carried out by Choi and colleagues [43] consisted on dispersing CuO NPs in water to a concentration of 5% vol. An improvement of 60% was achieved compared to the thermal conductivity of the water. In addition, the new fluid gave excellent suspension results, with no significant settling of NPs.

The increment of the thermal conductivity has been also accomplished by many other researchers on a wide diversity of nanofluids. Carbon-based nanostructures and/or ceramic and metallic NPs have been used as additives to the base fluids. A large number of publications has been devoted to the research of water-based nanofluids [41,45]. In addition, other base fluids, such as ethylenglicol [49–51] and several kinds of engine oil [52,53] have been employed. They are known as traditional nanofluids.

However, several industrial processes require the application of fluids which operate at temperatures higher than those suitable for the above mentioned fluids. They are of special importance in Concentrated Solar Power (CSP) plants because their production depends on the efficient conversion of the thermal energy coming from the sun into electricity at temperatures higher than 300 ºC. The transport of the thermal energy is currently done through industrial oils, known as Heat Transfer Fluids (HTFs), which are thermally stable up to 400 ºC. The use of molten salts as HTFs has been put on practice in the last few years [10,54]. It allows working in a wider temperature range, thus increasing the process efficiency. Besides, the use of molten salts as Thermal Energy Storage (TES) material has been a common practice in CSP [24,55]. The main advantages of using molten salts for these applications are their low cost and thermal stability up to higher temperatures (>550 ºC). On the other hand, their poor heat transfer rate limits their industrial implementation. The improvement of their thermophysical properties (the specific heat, c_p, and the thermal conductivity, k) is the key to push forward the TES systems and new HTFs in CSP facilities.

With the aim of fulfilling this need, a new kind of nanofluid was developed six years ago by Shin and Banerjee at the University of Texas at Arlington [56]. They utilized an inorganic salt (the eutectic mixture Li_2CO_3-K_2CO_3 62:38 mol) as the base fluid and SiNPs as the addition material.

The specific heat of the developed mixtures presented the maximum enhancement (+100% of the base material) when only 1% by weight of NPs were mixed with the salt. The authors suggested that costs might be cut off by 50%, due to a combination of higher operating temperatures (higher thermodynamic efficiency) and the diminution in the amount of material required to store the same thermal energy. This work was the seed of the subsequent investigation of MSBNFs for many scientists around the world. The synthesis procedure and the specific characterization methods for these novel nanostructured materials were established by this research group for the first time. Several combinations of inorganic salts and different NPs can be presently found in the technical literature (Table 2-1). The results of the reported specific heat and other properties are controversial. Besides, the mechanisms which govern the interaction between the NPs and the molten salt are not still well-known nor understood. As a result, they are under the critical eye of the scientific community.

As mentioned before, the main purpose of MSBNFs is the thermal energy storage and transfer in CSP plants. This material can be used on three different ways for this application: 1) as sensible storage media 2) as HTF and 3) as latent heat storage media (also known as Nano-enhanced Phase Change Materials, NePCMs). The desirable features of MSBNFs are listed below:

- Enhanced heat transfer properties compared to the base fluid: higher thermal conductivity, higher specific heat and higher latent heat.
- Stability of the NPs dispersion in the molten salt during long periods of time.
- Stability and no degradation of the nanostructured material under thermal cycling.
- Small or negligible increment of the viscosity due to the presence of NPs to allow an efficient pumping of the nanofluid.
- Chemical compatibility and absence of physical erosion with the container materials.

This review provides a comprehensive summary of the materials, the synthesis procedures and the thermal and rheological properties of MSBNFs according to the scientific publications up to date. The theoretical models which explain the increment of specific heat and the molecular simulation results are also described. Finally, the main challenges of these novel nanostructured materials are listed. The present study complements and enriches the information published in recent reviews [57,58]. The novelty of our study is the detailed analysis of the factors affecting the specific heat of MSBNFs such as the NPs concentration, their shape and nominal size, the synthesis procedure and the base salt employed. In addition, we have reviewed for the first time the latent heat, the thermal and long-time stability, the thermal conductivity, the microstructure, the chemical compatibility and the cost estimation of MSBNFs.

2.2 THEORETICAL MECHANISMS AND SIMULATIONS

The study of MSBNFs is a relatively recent field of research, which is on its infancy. Until now, the major efforts of the research works have been focused on obtaining empirical results (Section 2.5). The proposal of suitable models and mechanisms to elucidate the heat transference through these materials is still scarce. A brief review of the available models and computational simulations is reported below. These works are focused on modelling the enhancement of the specific heat of MSBNFs since this is the most significant feature of these materials.

2.2.1 Mechanisms of specific heat enhancement

The prediction of the specific heat of traditional nanofluids is usually made through the assumption of a thermal equilibrium between the NPs and the surrounding fluid. The model proposed in the Eq. 2-1 by Pak and colleagues [59] was improved by Zhou and co-workers in 2008 [60] with the Eq. 2-2 to match more accurately their experimental results of alumina-water nanofluids. These expressions take into account the amount of the base fluid and NPs and the value of their specific heat respectively.

$$c_{p,nf} = \phi c_{p,np} + (1 - \phi)c_{p,bf} \qquad \text{Eq. 2-1}$$

$$c_{p,nf} = \frac{\phi \rho_{np} c_{p,np} + (1 - \phi)\rho_{bf} c_{p,bf}}{\phi \rho_{np} + (1 - \phi)\rho_{bf}} \qquad \text{Eq. 2-2}$$

where c_p is the specific heat (kJ·kg^{-1}·K^{-1}), ϕ is the volume fraction and ρ is the density (kg·m^{-3}). Subscripts *nf*, *np*, and *bf* denote nanofluid, nanoparticle and base fluid, respectively.

Most of the experimental results of conventional nanofluids are in agreement with the Eq. 2-2. The conventional nanofluids show a low specific heat due to the poor specific heat of the NPs (in general, $c_{p,np}$<2 kJ·kg^{-1}·K^{-1}) compared to the base fluid (i.e. the specific heat of water is 4.2 kJ·kg^{-1}·K^{-1}).

Nevertheless, in the MSBNFs the disparity between the experimental results and those predicted by the Eq. 2-2 has been described on several works [37,56,61–64]. In this case, the specific heat of both the inorganic salt and the ceramic NPs is very similar (<2 kJ·kg^{-1}·K^{-1}).

Shin and Banerjee [63] were the first researchers on proposing three theoretical models based on the previous heat transfer theories to explain these anomalous results (Figure 2-1). These mechanisms are focused on the interactions between the NPs and the liquid salt at a molecular level and may occur independently from one another. Several articles discuss these three models, along with the experimental results [31,39,56,57,65–67].

Mode I. Higher specific heat capacity of NPs than the bulk material. There are both theoretical [68] and experimental [69] evidences which support that the specific heat of NPs is enhanced with the reduction in size. The reason is that the atoms placed onto the surface of the NPs are less confined and their low vibration led the NPs to have a higher surface energy. These atoms have quantized energy which is constrained by the NPs size. Increments up to 25% of the specific heat of ANPs were observed compared with the value of the bulk material [69].

Mode II. Solid–fluid interaction energy. The existence of a great interfacial thermal resistance between NPs and the ions of the molten salt may increase the thermal storage potential of the nanofluid. This interfacial thermal resistance (known as Kapitza resistance) is due to the high surface area per unit mass, distinctive of NPs, and negligible at the macroscale [70].

Mode III. ''Layering'' of liquid molecules at the NPs surface. The ions of the molten salt surrounding the NPs surface are ordered forming a special "semi-solid" liquid layer. It has superior thermal properties compared to the bulk liquid. Their thickness has been estimated by Molecular Dynamics Simulation (MDS) to be around 2-5 nm [63]. The amount of created "liquid layers" depends on the surface energy of the NPs. The existence of these peculiar structures was experimentally demonstrated by Oh and co-workers [71] with Transmission Electronic Microscopy (TEM). The images showed that the layers of liquid aluminium are adhered over a sapphire surface (Figure 2-2). In this way, there is a certain NPs size which may maximize the number of liquid layers adhered to its surface and achieve a maximum improvement of the specific heat.
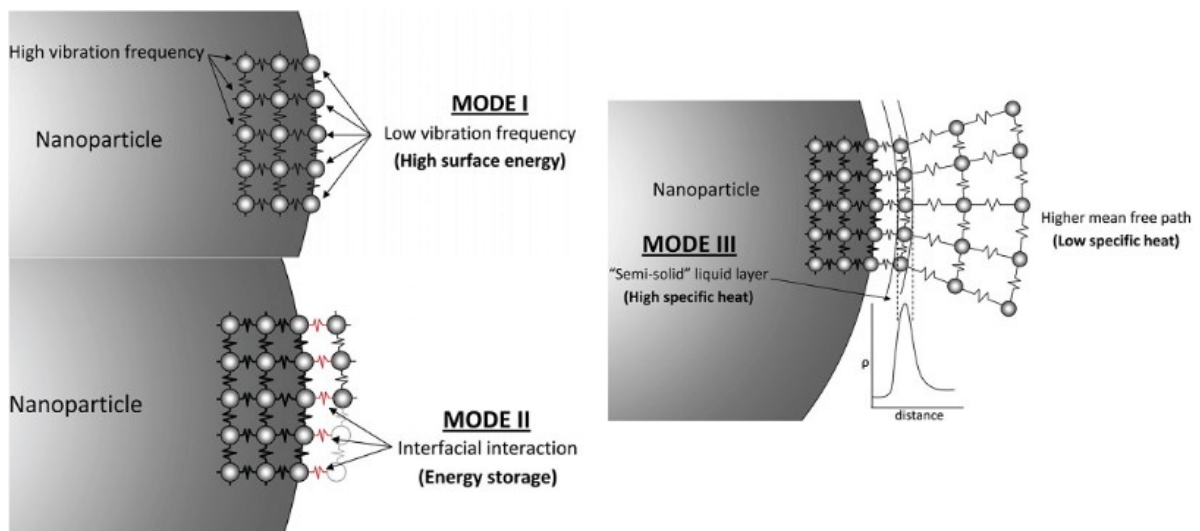
Figure 2-1. Models proposed by Shin and Banerjee for the enhancement of specific heat on MSBNFs. Reprinted with permission from [63].
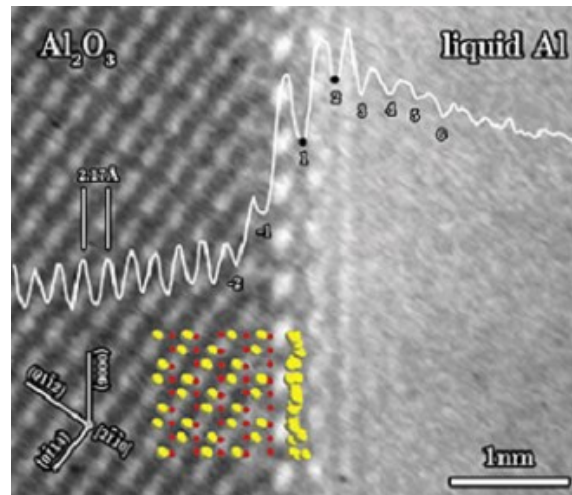
Figure 2-2. Semi solid layers of liquid aluminium at the interface of sapphire. Reprinted with permission from [71]

M. Thoms [40] considered the models of Shin and Banerjee and discussed in depth the concepts and hypothesis about the adsorption of molecules at the liquid-solid interface. This author demonstrated experimentally the strong influence of the NPs size on the specific heat of MSBNFs. The existence of an adsorbed layer of salt ions around the NPs was proposed and its thickness was estimated to be around 5-7 nm.

In addition Shin, Tiznobaik and Banerjee [72] proposed a general model to describe the specific heat enhancements in the MSBNFs. Fractal-like structures composed of ions of the inorganic salts have been observed in this kind of nanofluids (depicted in Figure 2-3. More examples included in Section 2.5.5). These special nanostructures possess superior thermal properties and are thought to be responsible of the high specific heat of the MSBNFs. The amount of the described structures is higher than the NPs concentration, which means that are also constituted by the salt components. Each ion establishes a different electrostatic interaction with the NPs and a concentration gradient on the NP surface occurs (Figure 2-4).
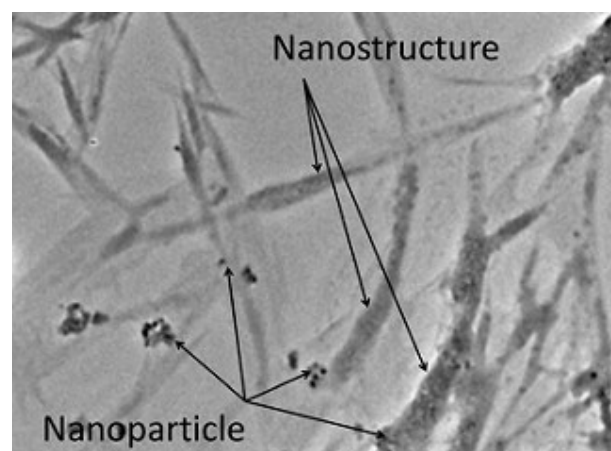
Figure 2-3. A high-resolution TEM of the NPs and the nanostructures. Reprinted with permission from [72].
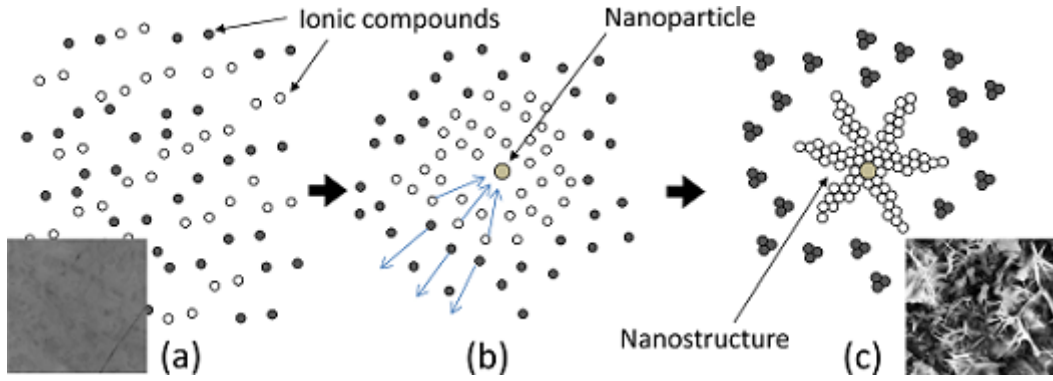
Figure 2-4. (a) Homogeneously dispersed ionic compound. (b) One component is more attracted to the NP surface due to the difference in electrostatic interactions. (c) The component on the NPs surface starts to crystallize and forms a nanostructure. Reprinted with permission from [72].

They theorized that these special nanostructures have a substantial effect on the specific heat of the whole material and must be considered in the model predictions. Hence, they proposed the inclusion of a new term on the Eq. 2-2, which was rearranged as appears on the Eq. 2-3:

$$c_{p,t} = \frac{m_{np}c_{p,np} + m_{ns}c_{p,ns} + m_{\bar{f}}c_{p,\bar{f}}}{m_{np} + m_{ns} + m_{\bar{f}}}$$

Eq. 2-3

where c_p is the specific heat (kJ·kg^{-1}·K^{-1}) and m is the mass (kg). Subscripts t, np, ns and $\bar{f}$ denote the nanomaterial, the nanoparticle, the nanostructure and the remaining base fluid (without the nanostructure), respectively.

On the other hand, Lu and Huang [61] studied for the first time the influence of the NPs size on the specific heat of Solar Salt (NaNO$_3$-KNO$_3$ 50:50 mol) doped with ANPs. In addition to the experimental results (described in Section 2.5.1.2), they proposed a model based on the Eq. 2-2, considering the contribution of the nanolayer on the NPs surface theorized by Shin and Banerjee [63] (Eq. 2-4):

$$c_{p,m} = \frac{c_{p,layer}W_{layer} + c_{p,np}W_{np} + c_{p,f}(W_f - W_{layer})}{W_{nf}}$$

Eq. 2-4

where c_p is the specific heat (kJ·kg^{-1}·K^{-1}) and W is the weight (kg). Subscripts m, $layer$, np, f and nf denote the nanomaterial, the nanolayer, the nanoparticle, the base fluid and the nanofluid, respectively.

They observed experimentally a reduction of the specific heat of the nanofluid compared to the base fluid. This diminution was more pronounced for a nanofluid containing smaller NPs. There is a higher contribution of the nanolayer as the NPs size is reduced for a certain NPs concentration.

Their experimental results fit perfectly with the Eq. 2-4.

All these models were recently gathered and studied in detail by Khanafer and colleagues [73]. They analysed first the existing models for the traditional water-based nanofluids. Then, they discussed the mentioned contributions to formulate a prediction of the specific heat of MSBNFs. In view of the incongruences between different researchers, they remarked the fact that more experimental and theoretical investigation is needed.

Ho and Pan [66] developed an interesting model to calculate the interfacial area of the NPs in a nanofluid composed of the Hitec salt (KNO_3-$NaNO_3$-$NaNO_2$, 53:40:7 mol) and ANPs. This parameter is a reliable predictor of the specific heat enhancement of the MSBNFs since the interfacial interactions between the NPs and the salt are the key of the proposed model. The authors analysed exhaustively the NPs size with Scanning Electronic Microscopy (SEM) images and established the amount of isolated and agglomerated NPs. An expression of the available interfacial area was proposed from these data which takes into account the contribution of both individual NPs and clusters.

Riazi and his colleagues [58] reviewed recently the specific heat of ionic liquids and MSBNFs. The interaction between the salt ions and the NPs were detailed extensively, with a special emphasis on the colloidal stability of the NPs on the molten salts. The three models proposed by Shin and Banerjee [63] were analysed and the inconsistencies between the results from different investigations were outlined.

2.2.2 Molecular Dynamics Simulation (MDS)

MDS is a powerful tool which provides information about the movement of atoms and molecules in a certain system. This is of special interest to compute some properties in MSBNFs which cannot be experimentally determined such as the heat transport at molecular level or the features of the nanolayer. In spite of its utility, a small number of studies have applied this technique to MSBNFs up to this date.

Shin [30] performed the simulation of the interfacial thermal resistance of the eutectic mixture of carbonates (Li_2CO_3-K_2CO_3 62:38 mol) mixed with two different nanostructures: on one hand carbon nanotubes (CNT) and on the other hand SiNPs. The interfacial thermal resistance of the NPs may act as a thermal barrier to the improvement of the effective thermal conductivity. The objective was to determine the optimal size of the NPs which maximized the effective thermal conductivity). With regard to the CNT nanofluid, no significant differences of the interfacial thermal resistance were observed with variations of the initial NPs temperature, the number of

atoms in the system and the size of the CNT. The independency between the thermal conductivity and the NPs size was also analyzed on the simulations performed with silica-based nanofluids. These simulations showed that the "nanolayer" composed of the salt molecules and developed around the NPs surface possess higher density than the bulk molten salt.

The interfacial thermal resistance of the eutectic mixture of carbonates (Li$_2$CO$_3$-K$_2$CO$_3$ 62:38 mol)-based nanofluids was also analysed by Jung [74]. First, a model for the enhancement of the specific heat was proposed and MDS was applied to several nanofluids (gold-water, sapphire-liquid Al, copper-liquid Ar). These simulations were further compared to the eutectic mixture of carbonates with addition of SiNPs. According to the results, the author outlined the following conditions which may cause the specific heat enhancements on MSBNFs: the specific heat of the compressed phase (nanolayer) must be greater than the liquid phase, the NPs density must be as low as possible, the density difference between the nanolayer and NPs must be maximized and the NPs size must be under a critical threshold (5-6 nm). The interfacial thermal resistance of nitrate-based nanofluids was also investigated. The solvent composition (KNO$_3$-NaNO$_3$ 40:60 wt% and 60:40 wt%), the NPs nature (Al$_2$O$_3$, SiO$_2$, SiC and Single-Wall Carbon NanoTubes (SWCNT)) and the NPs size were the factors analysed. A mixture of the eutectic mixture of carbonates and SWCNT was also simulated to compare the results with those of the nitrates. The MDS led to several conclusions about the interfacial thermal resistance of NPs in molten nitrates: independency of the NPs size, weak correlation with fluid composition and the SWCNT were the NPs with the highest interfacial thermal resistance. On the other hand, the carbonate-based nanofluids offered lower thermal resistance than the nitrate-based ones.

The effect of the solvent composition on the specific heat of MSBNFs was also studied by Jo and Banerjee [65]. The eutectic mixture of carbonates (Li$_2$CO$_3$-K$_2$CO$_3$ 62:38 mol) was the base fluid with the addition of graphite NPs. MDS gave information about the molecular structure of the nanofluid: the existence of a void around the NPs surface surrounded by the compressed layer was demonstrated. The chemical composition of the salt was different at the nanolayer and at the bulk. The results of these simulations were then correlated to the experimental evaluation of the nanofluid. The size of the compressed layer was estimated to be around 10-13 Å and seemed independent of the chemical composition of the salt. Besides, the concentration of K$^+$ ions in the nanolayer was higher than in the bulk liquid due to the higher adhesion forces between this element and the graphite NPs. These findings reinforced the idea of the existence of a supplementary thermal storage mechanism in the MSBNFs due to the special properties of the nanolayer.

The eutectic mixture of carbonates (Li$_2$CO$_3$-K$_2$CO$_3$ 62:38 mol) was doped with Multi-Wall Carbon NanoTubes (MWCNT) in [75]. The change on the salt composition between the nanolayer

and the molten salt were also observed. It was found that the higher the content of Li_2CO_3 in the carbonate mixture, the smaller the density of the nanolayer. Similarly to a previous work by the same authors [65], a chemical composition gradient was observed in the compressed phase, where K^+ had preference to be adsorbed rather than Li^+.

MDS was performed for SiNPs into the eutectic mixture of carbonates as the base salt [76] indicated an interfacial thermal resistance of $3.97 \cdot 10^{-9}$ $m^2 \cdot K \cdot W^{-1}$. The critical NPs size (15 nm) was deduced from this parameter. With higher NPs diameter the interfacial thermal resistance can be neglected and the effective thermal conductivity is maximized.

In the doctoral dissertation of Nagaraj [77] a deep revision of the models of Shin and Banerjee [63] was performed and MDS was applied to calculate the interfacial thermal resistance and the interactions encountered in a nanofluid of Solar Salt ($NaNO_3$-KNO_3 50:50 mol) and SiNPs. The formation of the nanolayer around the NPs was confirmed.

Miliozzi and colleagues [78] run a simulation of pure sodium nitrate in the solid and in the liquid state. The main focus was to know the material performance during the melting process since they propose a NePCMs based on molten nitrates. The simulation of the melting and solidification of the pure $NaNO_3$ is a necessary step to perform MDS with sodium nitrate-based nanofluids in the future.

2.3 MATERIALS

Nanofluids are composed of a base fluid and a nanoadditive which is intended to improve its thermal properties. The range of potential combinations of additives and fluids is enormous. Nanofluids are usually categorized by the kind of nanomaterial employed [44,45,79,80].

Theoretically, any solid nanostructure with suitable features can be used as an additive to the base fluid [44]. These nanostructures can be classified into four groups according to their nature [44,81]: carbon-based nanostructures (carbon and graphite nanofibers, graphite nanoplatelets, graphene flakes), carbon nanotubes (single- or multi-walled), nanoparticles [79,80] (ceramic, metallic, metallic oxides) and nanowires (i.e. silver nanowires). Among them, the ceramic NPs have been selected as addition in most of the publications about MSBNFs. Some few exceptions use carbon-based nanostructures [65,75,82–84]. Due to this generalized tendency and simplicity, the word "nanoparticles" (NPs) is used from now on to denote both the NPs and the nanostructures.

The base fluids that have been traditionally employed are water, engine oil, silicon oil, acetone,

decene and ethylene glycol [44,45,85]. The use of molten salts with high melting point as primary fluid is quite recent. To the authors' knowledge, the first scientific publication on the field is the doctoral dissertation of Malik [62] in 2010, where a nanofluid composed of Solar Salt (NaNO$_3$-KNO$_3$ 50:50 mol) and alumina nanoparticles (Al$_2$O$_3$) was analysed. The need of improving the thermal features of the storage salts for CSP has undoubtedly played a major role on the current scientific interest on MSBNFs. In addition, other industries (i.e. the nuclear) could be also benefit from using these kind of nanofluids [86].

Because of the high melting temperatures of inorganic salts and its aggressive nature, the requirements of the potential NPs are more severe than those needed for traditional nanofluids. The key requisites are a small average diameter, stability at high temperatures, and a strong affinity to the adsorbate [40]. It is essential to ensure the physical and chemical stability of the NPs in this type of medium. On one side, they must be able to withstand high temperatures without softening or suffering deformations. On the other side, the absence of chemical reactions of the NPs with the molten salts at the operating temperatures must be guaranteed. Additionally, the NPs must be insoluble in the salt medium in order to avoid particle coarsening due to the Ostwald ripening [87].

In view of the mentioned conditions, only some candidate materials can be employed in molten salts systems. Ceramic nanoparticles, specifically metal oxides, have focused the attention of the majority of the researchers working on MSBNFs. In fact, these were the first materials to be mixed and evaluated in the traditional nanofluids, primarily because of their ease of fabrication, low cost and chemical stability in solution [45]. The combinations of inorganic salts and NPs studied by each research group have been gathered in Table 2-1. At this point, the reader is warned that the composition of the mixture of nitrates known as Solar Salt slightly varies depending on the selected source. For the sake of ease, a unique composition of 50:50 mol is considered from this point. The same is applied the eutectic mixture of carbonates (Li$_2$CO$_3$-K$_2$CO$_3$ 62:38 mol) which has been also extensively used as base salt.

Table 2-1. Summary of the experimental works on MSBNFs including the base fluid and the NPs utilized.

Research institution and country	Base fluid (composition)	Melting temperature, ºC	NPs	Supplier, nominal size	Ref.
ENEA, Italy	Solar Salt NaNO$_3$-KNO$_3$ (50:50 mol)	222	Al$_2$O$_3$	Aeroxide AluC, Evonik, 13 nm (SEM)	[36,37]
			SiO$_2$	Aerosil 300, Evonik, 7 nm (SEM)	[36,37]
				---, 5-15 nm	[78]
			TiO$_2$	Sigma-Aldrich, 20 nm	[36]
				---, 21 nm	[78]
			SiO$_2$-Al$_2$O$_3$	Aerosil Cok84, Evonik, 2-20 nm (SEM)	[36,37]
			SiO$_2$-TiO$_2$	---, 5-15-21 nm	[78]
	KNO$_3$	334	Al$_2$O$_3$	Aeroxide AluC, Evonik, 13 nm (SEM)	[37,39]
			SiO$_2$	Aerosil 300, Evonik, 7 nm (SEM)	[37,39]
			SiO$_2$-Al$_2$O$_3$	Aerosil Cok84, Evonik, 2-20 nm (SEM)	[37,39]
Texas A&M University, EEUU	BaCl$_2$-NaCl-CaCl$_2$-LiCl (15.9:34.5:29.1:20.5 mol)	378	SiO$_2$	---, 26 nm (TEM)	[63]
				Melorium Tech, 10 nm	[30]
	KCl-CaCl$_2$-LiCl (44.2:50.5:5.3 mol)	340	SiO$_2$	Melorium Tech, 10 nm	[88]
	Li$_2$CO$_3$-K$_2$CO$_3$ (62:38 mol)	488	Al$_2$O$_3$	---	[32,89]
			SiO$_2$	Melorium Tech, 10 nm, 1-20 nm (TEM)	[30,56,76,90–92]
				---	[32,93]
			MWCNT	Melorium Technologies, ϕ=10-30 nm, L=1.5 µm	[75,76,84,94,95]
			Graphite	Sigma Aldrich, ϕ=50 nm	[65,94]
			TiO$_2$	Melorium Tech, 10 nm declared, 20-30 nm measured	[96]

Table 2-1. Summary of the experimental works on MSBNFs including the base fluid and the NPs utilized.

Research institution and country	Base fluid (composition)	Melting temperature, ºC	NPs	Supplier, nominal size	Ref.
	Solar Salt NaNO$_3$-KNO$_3$ (50:50 mol)	222	Al$_2$O$_3$	---	[38,62]
				---, 40 nm	[97]
				Alfa Aesar, 50 nm	[74]
			SiO$_2$	---	[38]
				Melorium Tech, 10 nm declared	[74]
			TiO$_2$	Melorium Tech, 10 nm	[74]
			Mica	Spectrum Inc., 45 μm	[74]
	KNO$_3$-LiNO$_3$ (58.8:41.2 mol)	130	SiO$_2$	Melorium Tech, 10 nm declared	[74]
	LiNO$_3$-NaNO$_3$ (45:55 mol)	192	SiO$_2$	Melorium Tech, 10 nm declared	[74]
	LiCl-LiNO$_3$ (12.5:87.5 mol)	244	SiO$_2$	Melorium Tech, 10 nm declared	[74]
University of Texas at Arlington, EEUU	Li$_2$CO$_3$-K$_2$CO$_3$ (62:38 mol)	488	Al$_2$O$_3$	Melorium Tech, 10 nm	[98,99]
			SiO$_2$	Melorium Tech; 5, 10, 30 and 60 nm	[67,100,101]
				Melorium Tech, 10 nm declared, 23 nm measured	[99,102]
				Alfa Aesar, ---	[103]
			MgO	Melorium Tech, 10 nm	[99]
	Solar Salt NaNO$_3$-KNO$_3$ (50:50 mol)	222	SiO$_2$	Melorium Tech; 5, 10, 30 and 60 nm	[104–106]
	Hitec XL Ca(NO$_3$)$_2$-NaNO$_3$-KNO$_3$ (49:30:21 mol)	120	SiO$_2$	Melorium Tech; 5, 10, 30 and 60 nm	[107–109]

Table 2-1. Summary of the experimental works on MSBNFs including the base fluid and the NPs utilized.

Research institution and country	Base fluid (composition)	Melting temperature, ºC	NPs	Supplier, nominal size	Ref.
	$LiNO_3$-$NaNO_3$-KNO_3 (38:15:47 mol)	<100	SiO_2	Melorium Tech, 60 nm measured	[110]
	$LiNO_3$-KNO_3-$NaNO_3$-KNO_2 (9:33.6:42.3:15.1 wt%)	<100	SiO_2	Melorium Tech; 5, 10, 30 and 60 nm	[111]
MIT, EEUU	$NaNO_3$	308	Al_2O_3	---	[87]
			SiO_2	---	[87]
			TiO_2	---	[87]
	NaCl-KCl (50:50 wt%)	658	Al_2O_3	---	[87]
			SiO_2	---	[87]
			TiO_2	---	[87]
	Li_2CO_3-K_2CO_3 (62:38 mol)	488	SiO_2	Sigma Aldrich, 5-15 nm	[40]
	Hitec KNO_3-$NaNO_3$-$NaNO_2$ (53:40:7 mol)	141	SiO_2	Sigma Aldrich, 5-15 nm	[40]
	$LiNO_3$	254	Al_2O_3	Nanostructured and Amorphous Materials, Inc., 10 and 200 nm	[40]
National Chiao Tung University, Taiwan	Solar Salt $NaNO_3$-KNO_3 (50:50 mol)	222	Al_2O_3	Sigma-Aldrich, 13 and 90 nm	[61]
National Tsing Hua University, Taiwan	Hitec KNO_3-$NaNO_3$-$NaNO_2$ (53:40:7 mol)	141	Sn@SiO_2	---	[82,83]
			Al_2O_3	Sigma–Aldrich Co. LCC, <50 nm, water nanofluid 20 wt%	[66]
North China Electric Power University, China	Solar Salt $NaNO_3$-KNO_3 (50:50 mol)	222	MWCNT	---	[83]
			Gold	Ted pella, 5 and 10 nm	[83]

Table 2-1. Summary of the experimental works on MSBNFs including the base fluid and the NPs utilized.

Research institution and country	Base fluid (composition)	Melting temperature, ºC	NPs	Supplier, nominal size	Ref.
Universidad Jaume I, Spain	Solar Salt NaNO$_3$-KNO$_3$ (50:50 mol)	222	SiO$_2$	SiO$_2$ Cristalline, Sigma Aldrich, 12 nm SiO$_2$ Amorphous, Nanostructured & Amorphous Materials, Inc., 20 nm	[112]
				SiO$_2$ Cristalline, Sigma Aldrich, 12 nm	[64,113]
University of Leeds, UK	Solar Salt NaNO$_3$-KNO$_3$ (50:50 mol)	222	CuO	Nanophase Technologies Corporation, 29 nm	[31]
				QinetiQ Nanomaterials Limited, 29 nm	[114]
			TiO$_2$	NanophaseNano Tek, 34 nm Sigma-Aldrich (TiOSO$_4$)	[31,35,115]
			ZnO	Nano-structured and Amorphous materials, 40 nm	[31]
			SiO$_2$	Sigma Aldrich, 5-15 nm	[31]
			Cu	United State Research Nanomaterials, 70 nm	[31]
University of the Basque Country / Tecnalia Research and Innovation, Spain	Solar Salt NaNO$_3$-KNO$_3$ (50:50 mol)	222	SiO$_2$	Sigma Aldrich, LUDOX® SM-30, ---	[116]
			Al$_2$O$_3$	Kawaken Fine Chemicals, Co., Alumisol-10A, ---	[117–119]
University of New Wales, Australia	Solar Salt NaNO$_3$-KNO$_3$ (50:50 mol)	222	SiO$_2$	Sigma Aldrich, 12-20 nm Nanocomposix, 20 nm In-house, 20 nm	[120]
Abengoa Research, Spain	Solar Salt NaNO$_3$-KNO$_3$ (50:50 mol)	222	MWCNT	Iolitec, ϕ=10-20 nm, L=5-15 µm	[121]

2.4   SYNTHESIS METHODOLOGY

The manufacturing process of MSBNFs is of critical importance since it has a direct impact on the subsequent properties of the material [37,56,65] (see Section 2.5.1.3). The process of combining the NPs with the salts must achieve the following objectives:

- To obtain a homogenous dispersion of NPs into the salt matrix.

- To maintain the NPs size in the nanometric range, avoiding agglomeration and clustering through every synthesis step.

This section presents the procedures commonly used to prepare the traditional nanofluids; the usual stabilization techniques and their evaluation. The aim is to provide a general knowledge on the subject. The specific methods for the synthesis of MSBNFs are detailed and reviewed next.

2.4.1   Common methods of producing nanofluids

There are two different methods which have been commonly used to produce the traditional nanofluids: the single-step and the two-step method.

The <u>two-step method</u> for preparing nanofluids is a step-by-step method which separates the nanofluids synthesis from the preparation of the NPs [44]. The NPs are first produced as a dry powder and then dispersed into the fluid in a second processing step. Some authors suggested that the two-step process is more suitable to prepare nanofluids containing oxide NPs than those containing metallic NPs [46,122] because of the higher stability on solution of the oxides. Since several companies have already scaled up the synthesis techniques to produce nanopowders, there are potential economic advantages in using such powders. An important problem that needs to be solved is the stabilization of the suspension prepared with these powders [44,123]. Stability is inherently related to the preparation of suspensions since the individual particles tend to quickly agglomerate before a complete dispersion can be achieved. This is due to the strong Van der Waals forces among the NPs. Ultrasonic vibration and other techniques are commonly used to obtain a better NPs dispersion and stability, as explained later. In spite of such disadvantages this process is still popular because of its economic interest [122,124].

To produce nanofluids with improved stability, the one-step methods have been developed [44,45]. The <u>single-step methods</u> are processes where the preparation of the NPs and the synthesis of the nanofluid are done at the same time. The NPs are directly prepared by Physical Vapour Deposition (PVD) or by a wet chemical method [46]. The PVD technique consists of condensing the nanophase powders from the vapor phase directly into a flowing low-vapor–pressure fluid.

In the one-step method the process stages of drying, storage, transportation and dispersion of the NPs are avoided. Consequently, the agglomeration is minimized and the nanofluid stability is increased. The main disadvantage of this method is that only fluids with low vapour pressure are suitable for the process, which limits its application [44,46,122]. Besides, undesired residual reactants remain in the nanofluids due to their incomplete reaction. The presence of these impurities may hinder the positive effect of the NPs addition to the molten salts [123].

The corrosive nature of the molten salts makes difficult the synthesis of the MSBNFs by the single-step method. In addition, the manipulation of the liquid salts at high temperatures is expensive and involves health risks. Therefore, the two-step procedure is generally used as described later in Section 2.4.3.

2.4.2   Stabilization techniques

One of the major challenges during the nanofluid preparation is to assure that the NPs remain dispersed into the base fluid. The stability of a nanofluid depends mainly on the characteristics of the suspended NPs, such as the particle morphology or its chemical structure. The base fluids and the NPs should be chosen properly to achieve a long-time stable suspension [45].

The Stokes law (Eq. 2-5) predicts the sedimentation rate of spherical particles into a fluid under stationary conditions.

$$V = \frac{2R^2}{9\mu}\left(\rho_P - \rho_L\right) \cdot g \qquad \text{Eq. 2-5}$$

where V is the particle's sedimentation velocity; R is the spherical particle's radius; μ is the liquid medium viscosity; ρ_P and ρ_L are the particle and the liquid medium density, respectively and g is the acceleration of gravity.

According to this expression, some strategies are effective on reducing the velocity of sedimentation and preventing the NPs agglomeration: maintain the NPs size as small as possible, increase the fluid viscosity and diminish the density difference between the NPs and the fluid.

In addition, there are several experimental techniques which successfully increase the NPs stability along the time. The most common methods used in conventional nanofluids are:

-   Addition of surfactants. These substances improve the wettability between the nanostructures and the fluid. A good dispersion of the NPs is achieved with a tiny quantity of surfactants, making this option simply and economical [45,46,122,123]. However, some important drawbacks have been reported when using surfactants, like the contamination of the base fluid, the foam

generation with the rising temperature and a higher thermal resistance between the NPs and the fluid [123]. The surfactants presently available are organic-based substances that cannot whistand temperatures higher than 200 ºC [45,46,87,122]. As a result, their use is not suitable in the synthesis of MSBNFs.

- Surface modification techniques. The NPs can be functionalized by adding chemical groups attached to their surface, avoiding the use of surfactants. These functional groups are selected according to the chemical nature of the components of the suspension [122,123].

- pH control. The nanofluid stability is directly related to its electrokinetic properties. Stability can be achieved by a suitable surface charge density in the NPs (the electrical potential difference between the inner and outer surface of the dispersed phase in a colloid). The concepts of the IsoElectric Point (IEP) and the zeta potential play a crucial role in this stability strategy, as addressed by the international research community [5,6,77,78]. The theories behind this electrostatic stabilization are well developed and detailed for aqueous solutions. However, they are not valid for high ionic concentration media such as molten salts and require modifications [87].

- Ultrasonic vibration. In this technique, the stability is gained by breaking the agglomerates with a physical stimulus rather than using a steric or electrostatic stabilization. UltraSound (US) energy is able to disaggregate the agglomerated NPs. This disaggregation has not been achieved by other physical methods like magnetic or high shear stirring [45,46,122]. Ultrasonic baths and probes are of common use to disperse NPs in salt aqueous solutions during the preparation of MSBNFs as detailed in the following section.

2.4.3   Production of MSBNFs

All the analysed studies about the MSBNFs use the aforementioned two-step method. In general terms, four basic steps are followed to complete the synthesis process:

1. **Solid mixing.** Weighing and mixture of the inorganic salt and the NPs in the solid state.
2. **Dissolution.** Addition of a certain quantity of distilled water to dissolve the salt.
3. **Stabilization.** NPs stabilization through the use of the ultrasonic power.
4. **Drying.** Water evaporation to obtain the final sample.

The principal concern on the production of MSBNFs is the scalability of the process. The described procedure is mainly conceived at a laboratory level. The large energy consumption required for removing this huge quantity of water and for the stabilization through ultrasonic waves is the main barrier to its industrial implementation. In addition, there are many variables which are difficult to control regarding the reproducibility of the method such as the power of sonication, the drying temperature and time and the solution concentration. Fortunately, some

authors [66,87,110,115] have described other alternative processes which result more cost-effective and with industrial interest.

Commercial NPs in the form of dry powder are of common use [31,35,39,40,61,64,74,75,87,97,99,102,110–114,125] while some few researchers begin the process by using commercially available water-based nanofluids where the NPs are homogenously dispersed [66,83,89]. On the first case, the salt and the NPs are weighed and mixed in the solid state according to the desired concentration of each other. This technique requires a certain quantity of water to be properly carried out, and as a result distilled water is added to this combination. The most common mass ratio between the solid material and the mixing water is usually 1:100 [30,32,38,39,56,63,67,74,90,98,99,102,104,105,107,108,112], although the water amount has been reduced in other publications [40,61,64,78,83,113]. The reason for these differences is mainly related to the different US stirring conditions employed by different authors

Ultrasonic stirring is employed to obtain and stabilize a good dispersion of the NPs into the fluid. This technique has demonstrated to be suitable to break the possible NPs clusters, generated and stabilized by the strong Van der Waals forces existing between them [46]. However, it has been reported that there is an optimal sonication time. If this time is exceeded, agglomeration may occur and this would affect the thermal properties of the synthetized material [46]. The sonication time can be noticeably reduced from hours to minutes if an ultrasonic probe is employed rather than an ultrasonic bath. Most of the researchers who are using the bath require sonication times higher than an hour, while only a few minutes are necessary with the aid of an ultrasonic probe [64,78,87,112,113].

The sonication step is not required if a water-based nanofluid is employed as a source of the NPs instead of the NPs in the form of a solid powder [66,126,127].

The last stage in the synthesis procedure consists of removing the water by simple evaporation. The aqueous solution is typically poured into a Petri dish and then heated on a hot plate. The solid sample is removed after by mechanical scrapping. Different drying times (from 2 hours to overnight) and heating temperatures (60-200 ºC) have been reported in the literature. In this step, the boiling of water has to be avoided to prevent the agglomeration of the NPs. The physical collisions between them proved to cause the degradation of the specific heat [30,38,40,56,98,113]. Schuller and colleagues [32] explored other alternatives to the drying stage. The water on nitrate-based nanofluids was removed by the spray drying method. The obtained materials offered a higher specific than those synthesized by the traditional method (see Section 2.5.1.3). On the other hand, nanofluids based on the eutectic mixture of carbonates (Li_2CO_3-K_2CO_3 62:38 mol) were submitted to a low temperature vacuum evaporation by these authors [32]. Spots of material were observed on the jar walls as a result of the violent boiling.

The specific heat of these materials was not reported, and the method was discarded.

Some authors have investigated other alternative mixing methods. The possibility of a direct blending of the NPs with the salts on their molten state has been evaluated [37,66,87,110]. A specific experimental set up was developed by Somani [87] (Figure 2-5). The NPs were initially dispersed in acetone by means of US. This nanofluid was injected into the bulk of molten nitrates and the NPs remained in the liquid while the acetone vaporized quickly. Finally, an ultrasonic probe was employed to disperse the NPs.
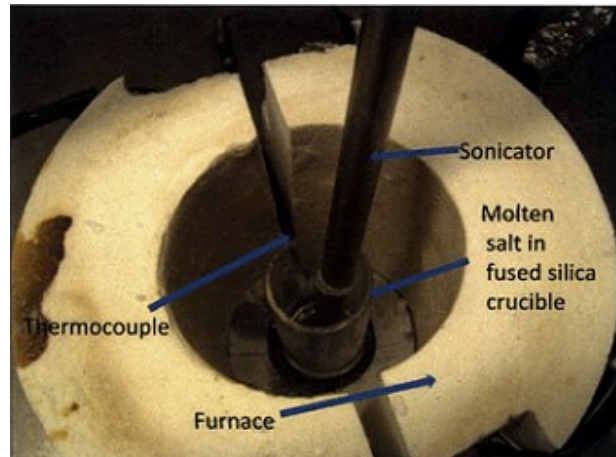
Figure 2-5. Experimental setup for dispersing the NPs in molten salts. Reprinted with permission from [87].

Ho and Pan [66] designed also a specific device (scheme shown in Figure 2-6) to perform the synthesis. First, a certain quantity of ANPs from a commercial water-based nanofluid was added to the solid salt. The mixture was melted and stirred for three hours in the stainless steel crucible of the device. The nanofluid was collected through three sampling tubes which were filled and cooled under forced convection until the salt solidification. The time reduction of the salt crystallization helped to reduce the NPs precipitation. The authors underline the good reproducibility of the results obtained with their production system.
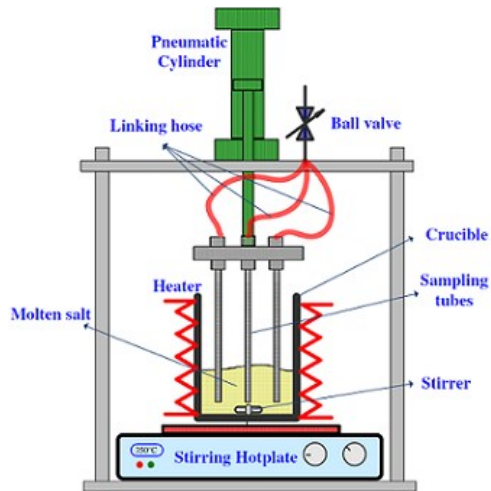
Figure 2-6. Schematic diagram of a device to synthetize the MSBNFs. Reprinted with permission from [66].

An extrusion machine for polymers was employed by Chieruzzi and coworkers to synthesize nanofluids based on Solar Salt ($NaNO_3$-KNO_3 50:50 mol) [37]. The salt and the NPs were mixed in the proper quantities in the solid state and placed inside the device were the material was heated at 300 ºC for 30 min with stirring. According to the published SEM images of the material, the NPs dispersion was poor. On the contrary, the same nanofluid synthesized by the traditional hot plate method showed better homogeneity.

The process followed by Seo and Shin [110] consisted in precisely weighing and mixing in the solid state a ternary nitrate salt with SiNPs. The mixture was placed inside a glass bottle and heated onto a hot plate at 300 ºC for 1 h. The nanofluid was synthesized four and the specific heat results were similar, which proved the reproducibility of this procedure.

Schuller [32] and Lasfargues [31,35,114] mixed the dry solid salt and the NPs with the aid of steel balls. The major advantage of this procedure resides on its scalability and the chance to produce high amounts of MSBNFs. The main issue is the presumable heterogeneous dispersion of the NPs, although it is difficult to quantify [31]. Considering this issue, as well as the potential nanofluid contamination by the milling balls, the aqueous traditional method was definitely preferred by the authors [32].

Finally, a pioneering work with the one-step synthesis method has been recently published [115]. A precursor of TiO_2 NPs and Solar Salt ($NaNO_3$-KNO_3 50:50 mol) were milled in solid and the mixture was heated at 450 ºC for 30 minutes. The samples were then cooled down to promote a rapid crystallization of the salt. The resultant material seems to be homogeneous and the specific heat was enhanced (see Section 2.5.1.1).

2.5 PROPERTIES

The characterization of MSBNFs has been mainly focused on the study of the specific heat and the influence of several factors on this property. Besides, the stability of the NPs dispersion in the molten salt, their latent heat (to act as NePCMs), the viscosity, the thermal conductivity and the material costs have also been studied by several researchers and reviewed in the following sections.

2.5.1 Specific heat

The influence of NPs on the specific heat of molten salts has been analysed in most articles dealing with MSBNFs. According to the models described on Section 2.2.1, the specific heat is generally enhanced when the molten salts are combined with the NPs. However, many authors have evidenced a decrease [30,36,37,40,61] of this property, instead of an increase. The inconsistences between the results obtained for the same nanofluid is of common occurrence. This may be probably related to differences on the raw materials, the synthesis procedures or the characterization methods employed to determine the specific heat. In this sense, it is of high importance to assure the accuracy of the selected measuring method [31,39,62].

The subsequent paragraphs examine in detail the influence of the most relevant factors on the enhancement of the specific heat of MSBNFs.

2.5.1.1 Influence of the NPs percentage

The change on the specific heat caused by the addition of NPs to the base salt in different quantities is the aspect most widely analysed through the reviewed literature. The aim of these studies is to find out the percentage which maximizes the specific heat for a certain combination of inorganic salt and NPs. This amount of NPs is highly variable depending on the analysed research, probably due to the differences on the NPs size among the materials. This detail is not usually found on the literature.

The combination of Solar Salt ($NaNO_3$-KNO_3 50:50 mol) and different amounts of SiNPs has been extensively studied. Figure 2-7 gathers the results of several publications about the increment of the specific heat versus the NPs percentage for this mixture. The maximum enhancement (31.1%) was obtained by Mondragón and colleagues [112] with 0.5 wt% of SiNPs. The authors proved that the NPs were well dispersed into the salt matrix with this amount, maximizing the interfacial area to interact with the salt components. A lower NPs concentration will lead to much dispersed and isolated NPs and higher quantities to agglomeration. However, other authors reported that the specific heat was maximized when the NPs quantity was 1 wt% [36,37,64,113], while the use of smaller or larger NPs concentration produced negligible effects,

or even a drop of the specific heat. Jung [74] attained a maximum increase of 23.3% of the specific heat when 2 wt% NPs was used.. Milozzi and co-workers [78] did not found significant differences when adding 1% or 3 wt% of SiNPs. Finally, Lasfargues [31] obtained small increments in comparison to those determined by other researchers, with a minimum at 1 wt% (-0.42%) and a maximum at 0.5 wt% (4.26%).
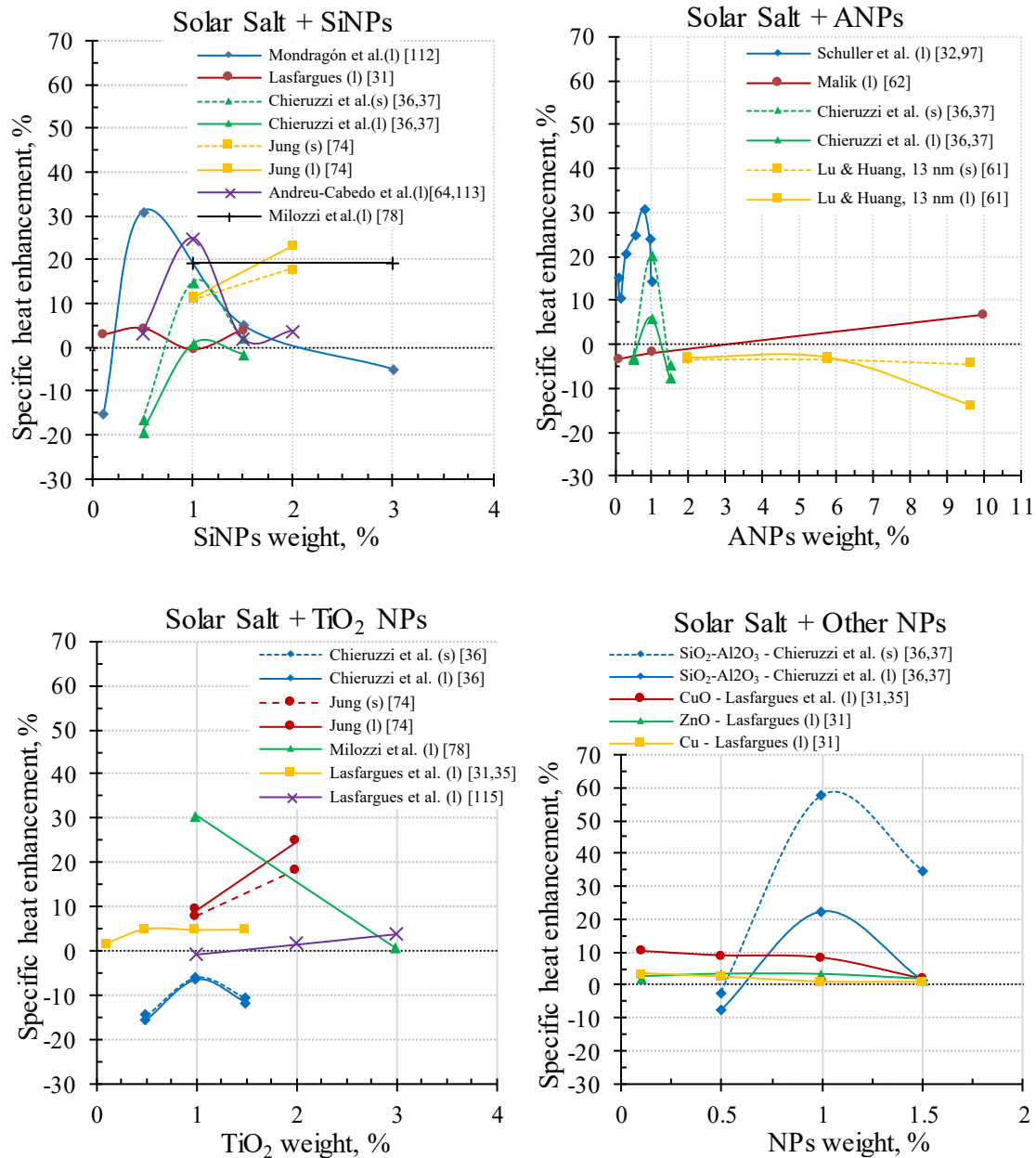
Figure 2-7. Specific heat enhancement vs. the concentration of different NPs mixed with the Solar Salt (NaNO$_3$-KNO$_3$ 50:50 mol). (s): measurement in the solid state, (l): measurement in the liquid state.

The mixture of ANPs and the Solar Salt (NaNO$_3$-KNO$_3$ 50:50 mol) has also been analysed in several studies. The results published in the reviewed articles about the specific heat enhancement as a function of the NPs percentage have been graphically gathered on Figure 2-7. The most

extensive work on this mixture were performed by Schuller and colleagues [32,97], who found the best results with an addition of 0.7 wt% of ANPs. They established a parabolic correlation between the specific heat and the NPs concentration, as shown in Figure 2-7 up right. Chieruzzi and colleagues [36,37] reported values that also fit into a parabolic correlation. They also found that the maximum enhancement takes place for 1 wt%, both in the solid and in the liquid states. However, the results reported by Malik and colleagues [62] and by Lu and Huang [61] did not match to this type of correlation. The maximum enhancements were obtained with 5.8% [61] and 10 wt% [62] in liquid respectively. Lu and Huang [61] reported a decrease of the specific heat for any of the studied percentages (2.0, 5.8 and 9.6 wt%) compared to the base salt. No dependence of the NPs concentration was found on the specific heat but there was a direct relation with the NPs size as analysed in Section 2.5.1.2. The nanolayer effect (described in Section 2.2.1) was suggested as the main mechanism involved on the process.

The discrepancies between the results obtained by different authors were also observed in nanofluids composed of the Solar Salt ($NaNO_3$-KNO_3 50:50 mol) with TiO_2 NPs (Figure 2-7). The additon of 1 wt% of nano-titania, lead to a specific heat enhancement of 30.5% [78], 9.3% [74], 4.7% [31,35] and 6.3% [36,37] in works carried out by different authors.

The Solar Salt ($NaNO_3$-KNO_3 50:50 mol) was also combined with other NPs (Figure 2-7). A mixture of SiO_2-Al_2O_3 (82:18 wt%) was added to the salt with excellent results [36,37]. The specific heat was improved by 22.5% in the liquid state with a concentration of 1 wt% The authors considered the formation of the semi-solid nanolayer around the NPs surface as the main mechanism to explain this increment. SEM images showed a homogeneous distribution of NPs and no evidence of clusters for this concentration, while this was not the case for the nanofluids containing 0.5 and 1.5 wt% of silica-ANPs.

Lasfargues [31] studied the addition of ZnO, CuO and Cu NPs to the Solar Salt ($NaNO_3$-KNO_3 50:50 mol). The nanofluids containing different amounts of these NPs showed the same enhancement of the specific heat, with the exception of the nanofluids containing high amounts of CuO NPs (> 1 wt%).

The eutectic mixture of Li_2CO_3-K_2CO_3 with the addition of several quantities of SiNPs was studied by Thoms [40] and Shin and coworkers [76]. The effect due to adding was studied in both of them. The maximum increments of specific heat were obtained with 1% [76] and 2 wt% [40] respectively. In contrast, other percentages (0.1, 0.5 and 2.0 wt%) did not improve this thermophysical property [76]. This behaviour is very similar to that found in the previous works [36,37,64,113] with the Solar Salt ($NaNO_3$-KNO_3 50:50 mol) as the carrier fluid and SiNPs.

Other nanofluids were synthetized by adding MWCNT in concentrations of 0.05, 0.1, 0.5 and 1.0

wt% to the eutectic mixture of carbonates (Li_2CO_3-K_2CO_3 62:38 mol) [76]. The enhancement of the specific heat was 9% in nanofluids with ≤0.1% of MWCNT and 17% for those containing ≥0.5%. The authors hypothesize that the optimum concentration for this nanofluid is higher than 1.0%.

2.5.1.2 Influence of the NPs size and morphology

Several studies have dealt with the effect of the NPs nominal size on the specific heat of MSBNFs. The results reported on the analysed articles have been gathered in Figure 11. It shows the variation of the nanofluid specific heat versus the NPs size. Two types of particles have been evaluated in these works, alumina and SiNPs.

An interesting investigation was performed by Lu and Huang with Solar Salt ($NaNO_3$-KNO_3 50:50 mol) and ANPs [61]. Spherical NPs of two different sizes, 13 and 90 nm diameter were added respectively. The nanofluids containing the smaller NPs showed a lower specific heat. A new model to compute the specific heat of MSBNFs was developed. This model accounted the nanolayer effect (Section 2.2.1). The experimental results showed that the nanolayer contribution is higher with smaller NPs. The specific heat of this nanolayer is between that of the solid (1.04 $kJ \cdot kg^{-1} \cdot K^{-1}$) and the molten salt (1.59 $kJ \cdot kg^{-1} \cdot K^{-1}$). Consequently, the nanofluid containing 13 nm ANPs showed smaller specific heat than the salt without nanoparticles. The nanofluid with larger particles had almost no variation of the specific heat in comparison to the raw salt.

Two nanofluids made of $LiNO_3$ with ANPs of 10 nm and 200 nm diameter respectively, were analysed by Thoms [40]. A trend similar to that reported by Lu and Huang was found, with a decrease of the specific heat for the nanofluid with 10 nm NPs, and a negligible enhancement for that containing 200 nm NPs. The authors considered that the effects of the absorbed layer on the bigger NPs are negligible due to their reduced available interfacial area compared to the same weight of the small NPs. It is remarkable that the salt specific heat decreases when the ANPs are added. The smaller the NPs, the larger the reduction of the specific heat is. Solely when very large particles are added, the specific heat increases slightly (less than 4%).

The works carried out with SiNPs of several sizes showed an increment of the salt specific heat with the addition of the NPs. Dudda and Shin [104–106] added 1 wt% SiNPs of four different sizes (5, 10, 30 and 60 nm) to the Solar Salt ($NaNO_3$-KNO_3 50:50 mol). A rise on the specific heat was observed as the NPs size increases (10% increase by adding 5 nm NPs, 28% increase with 60 nm NPs). The presence of special nanostructures with enhanced thermal properties (Figure 2-3) was confirmed by SEM images. The amount of these nanostructures increased with a higher NPs size. The authors suggested that too small NPs have more difficulties to be properly dispersed and tend to agglomerate. This may reduce the effective surface of the NPs and impede

the formation of a sufficient amount of the mentioned special nanostructures.

The salt Hitec XL, composed of $NaNO_3$, KNO_3 and $Ca(NO_3)_2$ (49:30:21 wt%) was employed as the base salt on the studies carried out by Devaradjane and Shin [107,108]. Like in the study described on the previous paragraph, SiNPs of four different sizes were added, in a concentration of 1 wt% The maximum increase of the specific heat (34%) was obtained on the nanofluids containing 10 nm NPs, as shown in Figure 2-8.

S. Changla [111] studied the nanofluid formed by 1 wt%-SiNPs and the $(Li,K,Na)NO_3$-KNO_2 salt. The formerly commented trend, regarding the NP size, was also reported in this study. The explanation to these results has not been clearly demonstrated by any of the authors.

When SiNPs (5, 10, 30 and 60 nm) were mixed with Li_2CO_3-K_2CO_3 [67], no dependence of the NPs size was observed. The specific heat increased around 25% in all nanofluids. A needle like structure, with large specific surface area, was observed by SEM, independently of the NPs nominal size. We consider that this difference in trend with the previous studies may be due to the crystallographic structure of these SiNPs, though there are not experimental evidences.

Riazi and colleagues [120] conducted a pioneering study about the influence of the NPs shape on the specific heat of MSBNFs. SiNPs from different sources and morphologies were mixed with the Solar Salt ($NaNO_3$-KNO_3 50:50 mol) to create three different nanofluids. The specific heat results clearly demonstrated a strong dependence of the NPs morphology. The highest enhancement (17.6%) occurred in the material containing the smaller (19-92 nm) and more spherical SiNPs (nanosalt B). On the contrary, the specific heat remained unchanged compared to the specific heat of the raw Solar Salt in those cases where the added SiNPs were highly agglomerated, forming large clusters (nanosalt A and C).
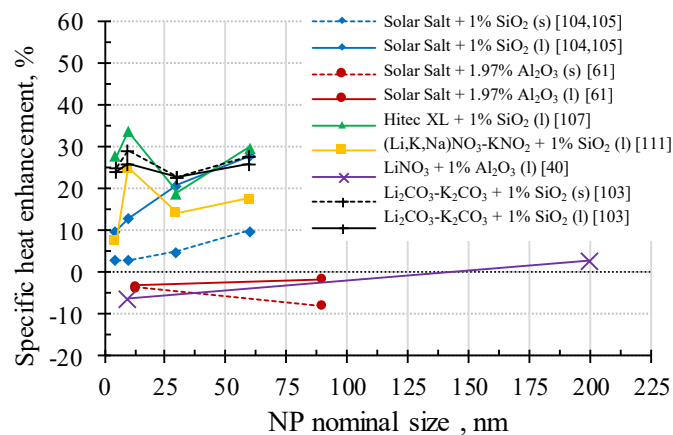
Figure 2-8. Specific heat enhancement vs. the NPs nominal size for different nanofluids. (s): measurement in the solid state, (l): measurement in the liquid state.

As detailed on the previous paragraphs, the relationship between the nominal NPs size and the nanofluid specific heat is controversial. Most of the analysed publications [40,61,104–106] found better specific heat results by adding higher NPs to the base salt (results limited to the particle size ranges selected on each case). However, other authors [120] reported the opposite trend or even the absence of relationship between the NPs size and the specific heat enhancement [67,108,109,111]. The influence of the agglomeration on the specific heat was demonstrated by Riazi and coworkers [120], where the NPs sizes in the final nanofluid were measured by TEM. Therefore, it is worth mentioning that in many cases the nominal NP size is not maintained after the nanofluid synthesis. A certain degree of agglomeration occurs, and the effective particle size can be very different from the original size. The mentioned research works did not measure the NPs size on the final material, with the exception of [120].

2.5.1.3 Influence of the synthesis procedure

Several methods have been employed to produce the MSBNFs. The hot plate method has been the most widely used procedure, but other manufacturing methods were tried. The synthesis procedure has a strong influence on the NPs dispersion inside the salt matrix. It also has a crucial influence on the agglomeration or clustering of the particles, and therefore on the final effective NP sizes in the final material. These two factors greatly determine the specific heat of the nanofluid.

The impact of minor modifications on the traditional hot plate-method was analysed by Shin and Jo [56,65] with Li_2CO_3-K_2CO_3 based nanofluids. Shin and colleagues [56] added 1 wt% of SiNPs to the salt and dried the aqueous solution at 60 ºC and at 100 ºC. The results were significantly better on the drying at the lower temperature (101% of enhancement) than at the higher (74%). The higher specific surface in nanofluids dried at 60 ºC is the factor considered by the authors.

Jo and coworkers [65] added 0.1 wt% of graphite NPs to the eutectic mixture of carbonates (Li_2CO_3-K_2CO_3 62:38 mol). The dispersion was dried by two different methods, a Petri Dish (Method 1) and in a glass vial (Method 2). The carbonate nanofluids which were dried on the Petri Dish (higher surface) achieved a larger enhancement of the specific heat as shown in Figure 2-9A. According to the authors, the glass vial has a smaller drying surface and a longer time is needed to dehydrate the samples. Consequently, the NPs tend to be more agglomerated in the aqueous solution with the use of this method. The homogeneity of these nanofluids is very poor and the specific heat is worse than the nanofluids dried on the Petri Dish.
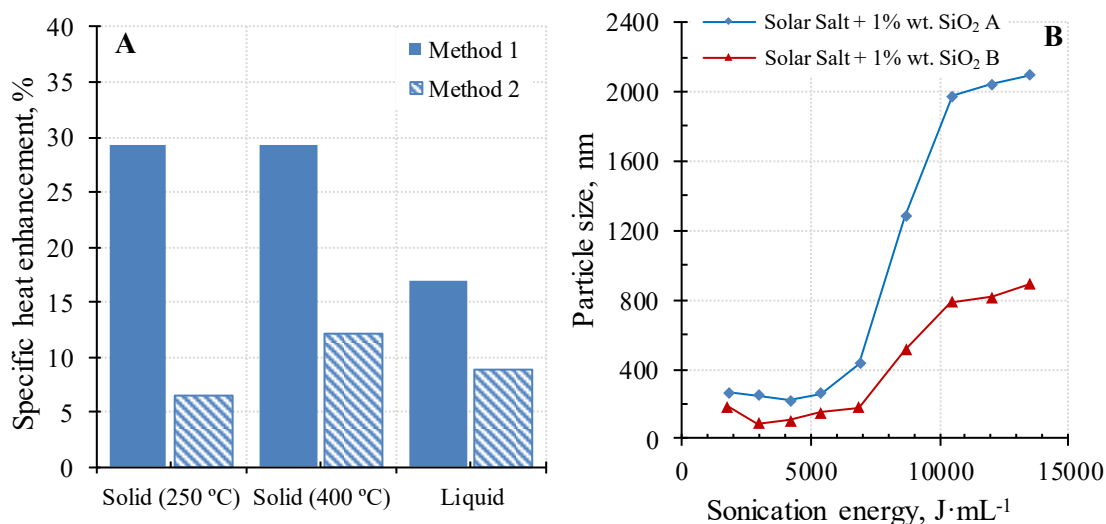
Figure 2-9. **A:** Specific heat enhancement of Li_2CO_3-K_2CO_3 (62:38 mol) and 1 wt% of SiNPs synthesized by drying in a hot plate (Method 1) or in a glass vial (Method 2). Adapted from [65]. **B:** Mean particle size of a 1 wt% SiO_2 – Solar Salt nanofluid vs. the sonication energy. Two types of SiNPs were used. Adapted from [120].

Modifications on the drying stage were also evaluated by Schuller and coworkers [32]. The spray drying method was compared to the traditional drying onto a hot plate, to remove the water on nanofluids of Solar Salt ($NaNO_3$-KNO_3 50:50 mol) with ANPs. The increment of the specific heat on the spray dried materials was around 30-40%, depending on the amount of NPs. The same synthesis was replicated and the nanofluids were dried on the hot plate at 100 ºC. A specific heat enhancement between 10-20% was achieved in this case. Any explanation is given by the authors to this behaviour.

With the aim of reducing the amount of the water employed to dissolve the salts and to disperse the NPs, the influence of this parameter was studied [126]. Three nanofluids of Solar Salt ($NaNO_3$-KNO_3 50:50 mol) and 1 wt% SiNPs were synthetized with a different amount of mixing water (31.60, 6.50 and 0.97 mL of water per g of dry material). The specific heat of the nanofluids synthesized with the highest and the lowest amount of water were of the same order (1.613 and 1.575 $kJ \cdot kg^{-1} \cdot K^{-1}$) while the intermediate nanofluid gave lower specific heat results (1.384 $kJ \cdot kg^{-1} \cdot K^{-1}$). It was considered that these differences were related to the degree of agglomeration of the NPs on each nanofluid.

Riazi and his coworkers analysed the effect of the sonication power on the NPs agglomeration [120]. They used the Solar Salt ($NaNO_3$-KNO_3 50:50 mol) with the addition of 1 wt% of two kinds of SiNPs. The effective NP sizes in the final nanofluid were measured with Dynamic Light Scattering (DLS). An optimum US energy was reported (Figure 2-9B), which led to a minimum value of the particle size (4000 $J \cdot mL^{-1}$ for Silica A and 3000 $J \cdot mL^{-1}$ for Silica B). An important increase of the clustering occurred when the sonication energy was higher than 7000 $J \cdot mL^{-1}$ on these two nanofluids.

The work by Chieruzzi and colleagues [37] compared the results obtained with an innovative procedure and those by the common hot-plate method. Solar Salt (NaNO$_3$-KNO$_3$ 50:50 mol)-based nanofluids with silica, alumina and silica-ANPs were synthesized by extrusion at high temperature, as detailed in Section 2.4.3. With independency of the NPs concentration, a diminution of the specific heat (compared to the pure Solar Salt) was observed on the nanofluids produced by this technique. On the contrary, the specific heat increased when the nanofluid was synthesized by the traditional method (e.g. an increment of 10.7% and 5.9% respectively for ANPs). The poor dispersion of the NPs into the molten salt obtained by means of the extrusion machine was claimed to be the main reason for this behaviour.

2.5.1.4 Influence of the base salt composition

Some studies analysed the specific heat of MSBNFs containing the same NPs but changing the base salts. Solar Salt (NaNO$_3$-KNO$_3$ 50:50 mol) and KNO$_3$ were evaluated in [37], mixed with SiO$_2$, Al$_2$O$_3$ and a mixture of both (SiO$_2$- Al$_2$O$_3$, 85:15) in a concentration of 1 wt% The increase of the specific heat was different in the two nanofluids, especially when the salt was mixed with alumina + SiNPs (Figure 2-10A). It was suggested that the difference might be due to the Na$^+$ cations in the Solar Salt and their specific interaction with the NPs. S. Jung [74] investigated the specific heat of four nitrate-based nanofluids with 1 wt% of SiNPs. The presence of Li$^+$ as the unique cation seems to be advantageous (Figure 2-10B). According to the author, the compressed phase contributes to the global specific heat in a different extension depending on the base salt.
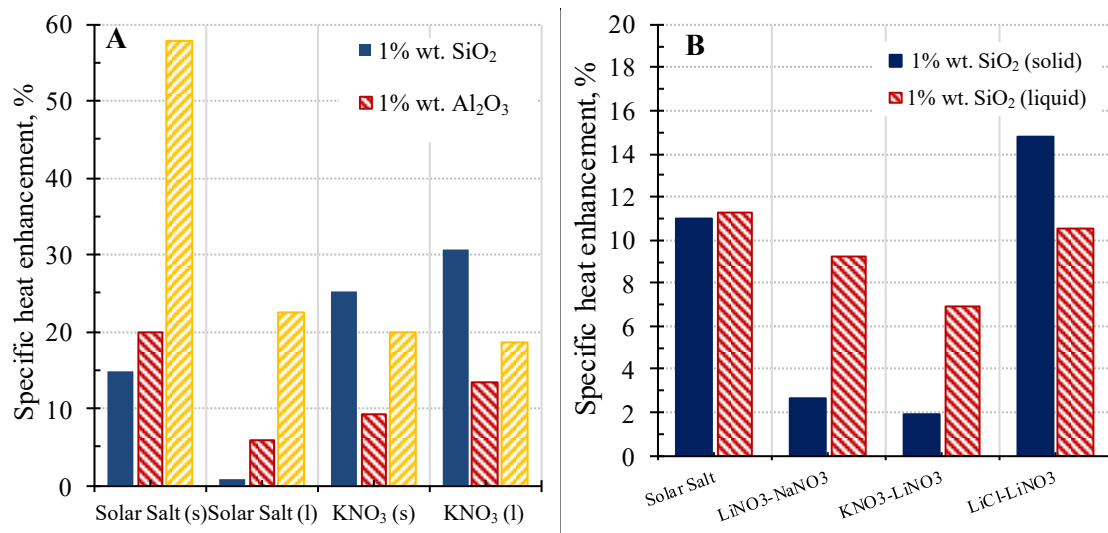
Figure 2-10. Specific heat enhancement vs. the base salt of MSBNFs. Adapted from [37] (A) and [74] (B).

In other approach, Jo and Banerjee [75] evaluated the influence of the composition of a carbonate binary salt on the final results. In this study, Li$_2$CO$_3$ and K$_2$CO$_3$ were mixed in different proportions and a correlation of the specific heat with its composition was suggested [128]. The

nanofluids were constituted by adding 1 wt% of MWCNT to five different mixtures of carbonates. The authors proved that there is a minimum of the specific heat for the eutectic mixture of carbonates (Li$_2$CO$_3$-K$_2$CO$_3$ 62:38 mol) as can be seen in Figure 2-11A. These experimental results were in agreement with their MDS calculations. The research with the binary mixture of carbonate and 1 wt% of SiNPs confirmed just the opposite trend (Figure 2-11B). The specific heat was enhanced near the eutectic composition of the carbonate mixture. The results did not agree with the predictions of the simple rule of mixtures (Eq. 2-2), although the nanofluids containing low or high content of Li$_2$CO$_3$ showed a little increment (or even a decrease) of the specific heat, matching the conventional specific heat model (Eq. 2-2).
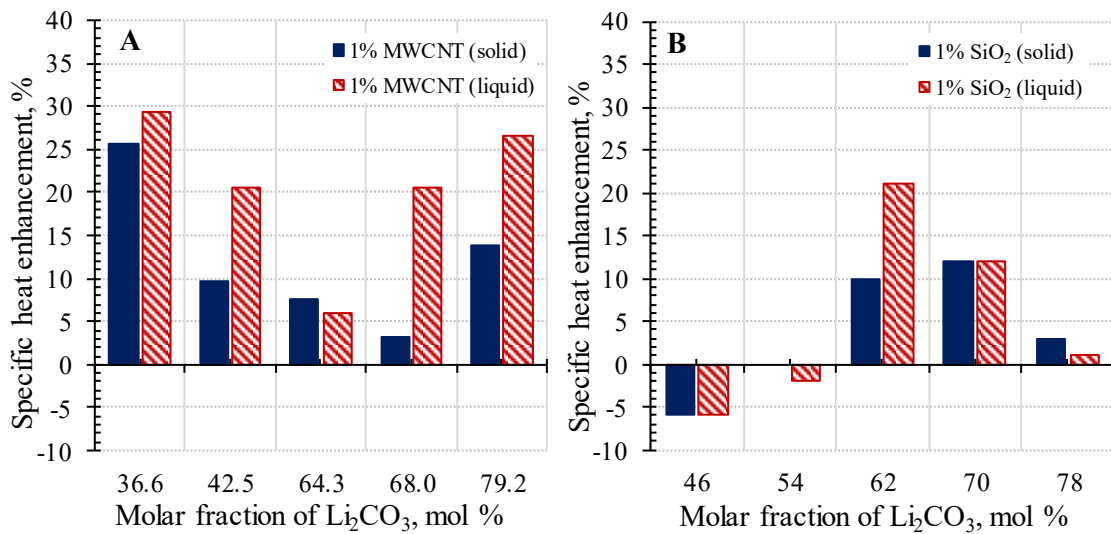
Figure 2-11. Specific heat enhancement of the mixtures of carbonates (Li$_2$CO$_3$-K$_2$CO$_3$) with 1 wt% MWCNT (A) and 1 wt% SiNPs (B) vs. salt composition. Adapted from [75] (A) and [30] (B).

In a different approach, Tiznobaik and Shin [103] studied the influence of impurities on the specific heat. A nanofluid containing the eutectic mixture of carbonates (Li$_2$CO$_3$-K$_2$CO$_3$ 62:38 mol) and 1 wt% of SiNPs was produced and its thermal analysis revealed an increase of 26% on the specific heat compared to the base carbonate salt. However, this improvement disappeared when a minute concentration of NaOH (0.02 wt%) was added to the same material. According to the authors, an excess of OH$^-$ ions may hinder the interaction between the NPs and the components of the base salt. This would cause the absence of the nanostructure with superior thermal properties and therefore, the similarity of the specific heat to the base salt. This premise was demonstrated by SEM images.

2.5.2   Latent heat and melting temperature

The thermophysical characterization of MSBNFs to be used as NePCMs is still scarce. The Solar Salt (NaNO$_3$-KNO$_3$ 50:50 mol) is the base fluid in most studies [31,32,35–38] while KNO$_3$ [37,39] and Hitec salt (KNO$_3$-NaNO$_3$-NaNO$_2$, 53:40:7 mol) nanofluids [40] have received much

less attention. The results usually include the latent heat, the melting and the onset temperature of the base salt and the nanofluid. For an easier comparison and analysis, the results of the latent heat of Solar Salt based-nanofluids published on the different articles have been gathered in Figure 2-12. In general, the results followed two general trends. On one side, the latent heat decreased with a higher amount of NPs [31,35]. All the studied NPs fulfilled this tendency, showing slight latent heat increments (maximum ≈ 5%) or even a reduction of this property. On the other hand, a parabolic correlation between the latent heat and the NPs concentration was observed [36,37]. The nanofluids containing 1 wt% of NPs achieved the maximum increment of latent heat for all kinds of NPs. They also offered the highest enhancement of the specific heat, and the authors suggested that these facts might be related. The combination of KNO_3 and 1 wt% of SiNPs offered a high enhancement of the latent heat (12%), while the addition of Al_2O_3 or SiO_2-Al_2O_3 resulted in a decrease (-9%) [37,39]. In addition, every of the previous studies found that the onset melting temperature did not change with the addition of the NPs. The melting range was broader than that of the base salt, with a slight increase on the peak-temperature melting point.

The reason of this behaviour is still unclear. Chieruzzi and coworkers [36,39] suggested that the latent heat enhancement may be due to the existence of layers of small agglomerates where the NPs would be confined. These agglomerates may need higher energy to be melted, which would increase the latent heat. The results obtained by Lasfargues and his colleagues [31,35] support this affirmation. They also suggested that the dispersion of NPs and the presence of clusters may raise the entropy of the fluid and affect its thermophysical properties.
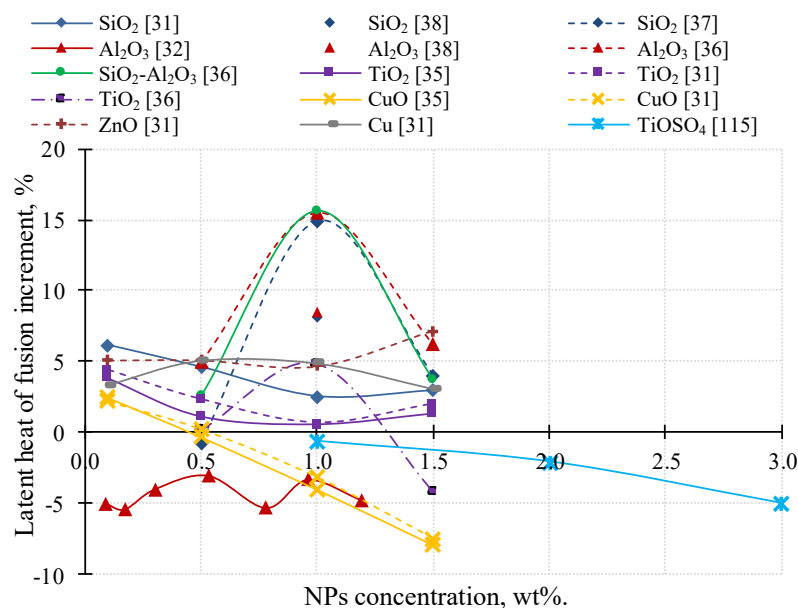
Figure 2-12. Latent heat increment vs. the NPs concentration on Solar Salt ($NaNO_3$-KNO_3 50:50 mol)-based nanofluids.

2.5.3   Long-term stability

The thermal properties of the MSBNFs must be invariant over time. Otherwise, the potential applications of these materials would be highly reduced due to the impossibility of maintaining these improved thermal characteristics. Some authors have carried out stability tests to verify the behaviour of MSBNFs along the time, both as a fluid [31,32,38,87,112] and as NePCMs [32,64,89,113].

In the first case, the material is always in the liquid state. As a consequence, the NPs embedded in the molten salt may collide between them due to their characteristic Brownian motion. As a result, they can constitute agglomerates of different sizes. If these aggregates reach a certain size, they will settle down and NPs will no longer be present in the bulk of the molten salt, except of a negligible quantity. This sample will lose its extraordinary heat transfer properties because of the high heterogeneity caused by the agglomeration and settling of the NPs. Therefore, the challenge is to maintain the unique attributes of these materials in the long term, preventing their agglomeration. The process of agglomeration and settling of the NPs is modelled by the Eq. 2-5 as explained previously, in Section 2.4.2.

If the material is analysed as NePCMs, in addition to the required stability on the liquid stage, the nucleation and crystallization stages should also be taken into account. These processes may change the settling mechanism of the NPs since their Brownian motion is physically limited by the nucleation and subsequent growth of the salt crystals.

The stability evaluation is usually studied by comparing the initial and the final specific heat of the nanofluid. The salt is maintained in the liquid state for some hours [31,87,112] or cycled between two temperatures (with a phase change in the temperature interval [32,64,89,113] or without phase change [32,38]).

A nanofluid of Solar Salt (NaNO$_3$-KNO$_3$ 50:50 mol) and 0.5 wt% of SiNPs was maintained at 500 °C for 12 hours by Mondragon and coworkers [112]. A lower specific heat was measured on the upper part of the sample after this treatment. However, the bottom portion of the sample remained with the same value (Figure 2-13A). The authors attributed the decrease on the specific heat to the setting of the NPs.
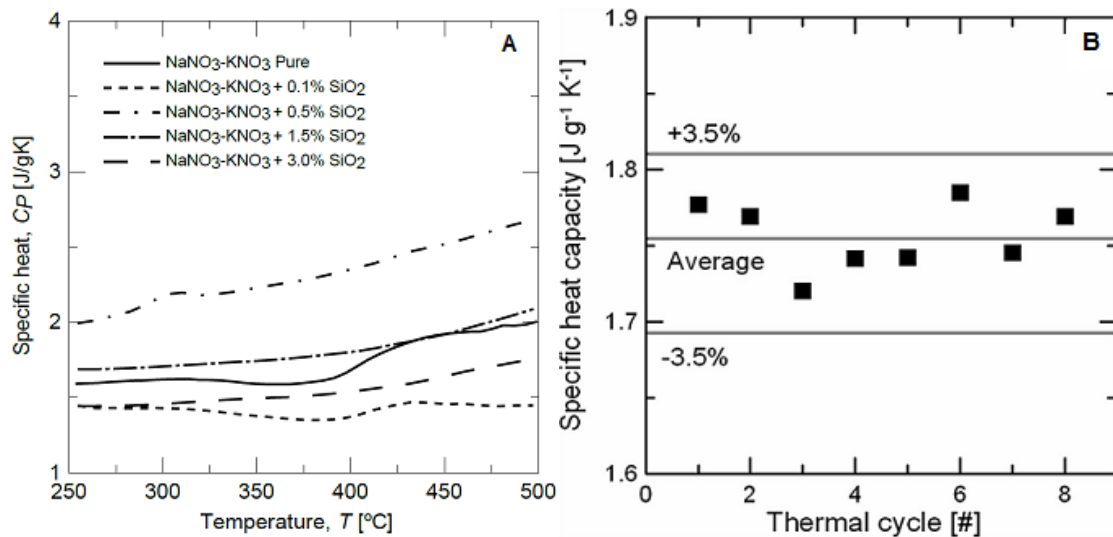
Figure 2-13. Stability of SiNPs in Solar Salt on the liquid state (A) [112] and after several thermal cycles (B) [113]. Reprinted with permission.

The study performed by Andreu-Cabedo and her colleagues [64,113] demonstrated that the 1 wt% silica- Solar Salt (NaNO3-KNO3 50:50 mol) nanofluid was stable when submitted to eight thermal cycles between 160 and 420 ºC, to know its behaviour as NePCMs. The mean specific heat of the liquid state (250-420 ºC) was always comprised on the test uncertainty, as can be seen in Figure 2-13B.

Contradictory results were found by Schuller and Betts [32,38], which evaluated the stability of a similar nanofluid (Solar Salt and 1% SiNPs). It was thermally cycled three times in the liquid state between 300 and 450 ºC for 6 hours. The material was unstable when the temperature rose above 400 ºC, showing a gradual decrease of the specific heat with each cycle. On the opposite side, these authors reported that the addition of ANPs to the Solar Salt was stable and the specific heat remained constant all along the tests performed. The reason of this different behaviour is still unknown.

The stability test of the Solar Salt (NaNO3-KNO3 50:50 mol) doped with ANPs from [32,38] was performed at a larger scale (with several grams of nanofluid) and a longer experimental time (up to 448 cycles) [32]. The samples analysed were extracted from the upper, the middle and the lower part of the container. The specific heat of this nanofluid remained constant through multiple cycles, and almost independent of the analysed area (Figure 2-14A). The authors considered that the settling of the NPs did not occur in this case.

The stability of a nanofluid made of the eutectic mixture of carbonates (Li2CO3-K2CO3 62:38 mol) and 1 wt% of ANPs [32,89] was also evaluated. The tendency was the opposite as the previous research. The thermal cycling caused the settling of NPs and their accumulation on the

container walls. The specific heat of the cycled nanofluid was always higher than the base salt and the uncycled material. The ANPs concentration was measured on each sample and had no influence on the specific heat results.
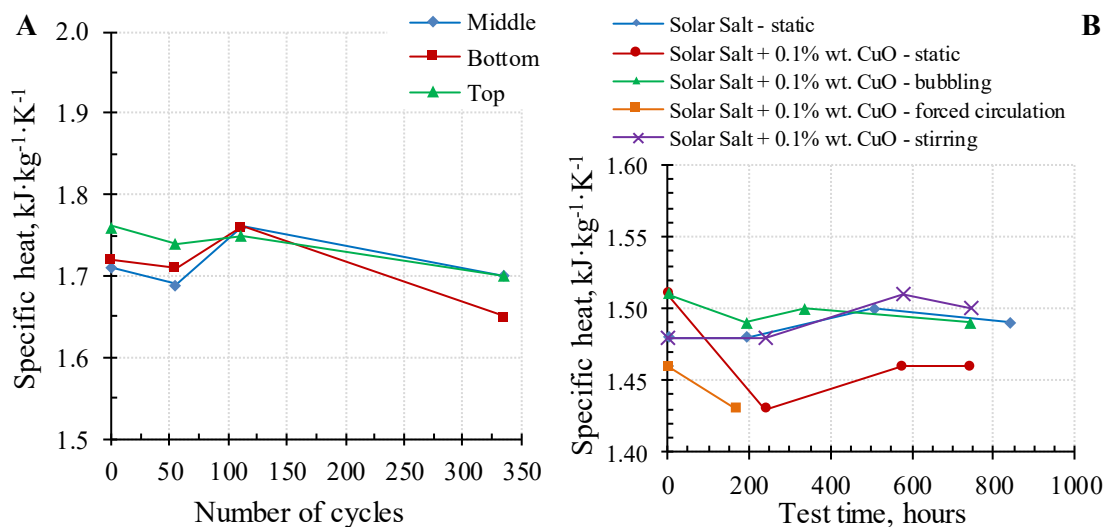
Figure 2-14. A: Specific heat vs. the number of cycles and the sampling area in Solar Salt with 1 wt% ANPs. The material was cycled between 300 and 400 ºC for 6 hours in each cycle. Adapted from [32].
B: Specific heat vs. the test time at 300 ºC for different stabilization techniques. Adapted from [31].

Three strategies (bubbling, forced circulation and mechanical stirring) were investigated to improve the stability of Solar Salt ($NaNO_3$-KNO_3 50:50 mol) with 0.1 wt% of CuO NPs [31]. The nanofluid was maintained at the liquid state at 300 ºC. The study started by analysing the behaviour of the material under static conditions. Accumulation of the NPs at the bottom was observed after 840 hours. The specific heat was significantly reduced in comparison to the initial values (Figure 2-14B). Mechanical stirring provided a great NPs dispersion (according to SEM images) and the specific heat remained at the initial value and even increased as the test progressed. The other evaluated techniques were less effective on maintaining the initial thermophysical properties (specific heat, melting point and latent heat of fusion).

Turbidity measurements were used in an exhaustive study [87] to evaluate the stability of $NaNO_3$ with silica, alumina and titania NPs respectively. A direct correlation was found between the test temperature and the NPs agglomeration rate. This behaviour is attributed to the increase in thermal energy of the NPs with temperature and their perikinetic collision rate constant. In addition, the density and the viscosity of the medium are reduced at higher temperatures. As a consequence, the settling rate rises and agglomeration is produced. However, other factors such as the initial NPs size and their concentration showed a weaker influence on the settling and the agglomeration rate. Finally, this study was reproduced using a mixture of NaCl-KCl (50:50 wt%) as the base-salt. In this case, the setting rate was increased due to the lower viscosity and density of this chloride salt in comparison to the $NaNO_3$.

2.5.4 Thermal conductivity

The research on MSBNFs has been mainly focused on the increase of the specific heat, as reported in the precedent sections. However, the expected increase on the thermal conductivity has also been studied, although in much shorter depth. The high melting temperature and the corrosive nature of the molten salts and MSBNFs hinder the measurement of this thermophysical property. Nevertheless, several studies have determined the thermal conductivity of MSBNFs in the solid state. Their values have been compared with those of the pure inorganic salts.

D. Shin [30,102] employed the Laser Flash Analyser (LFA) technique to register the thermal diffusivity of the eutectic mixture of carbonates (Li_2CO_3-K_2CO_3 62:38 mol) with 1 wt% of SiNPs, in the solid state. The thermal conductivity was then calculated according to the Eq. 2-6 [31].

$$k = \alpha \rho c_p$$
<div align="right">Eq. 2-6</div>

where k is the thermal conductivity (W·m^{-1}·K^{-1}), α is the thermal diffusivity (m^{2}s^{-1}), ρ is the density (kg·m^{-3}) and c_p is the specific heat (kJ·kg^{-1}·K^{-1}).

A significant enhancement of this property was achieved with independency of the test temperature, achieving an increment of 47%, 36% and 37% above that of the pure carbonate, as shown in Figure 2-15. The theoretical models of Hamilton-Crosser and Maxwell-Garnett did not forecast any increase of the thermal conductivity. The author suggested that this unexpected result is due to the percolation networks observed on the SEM images (Section 2.5.5).
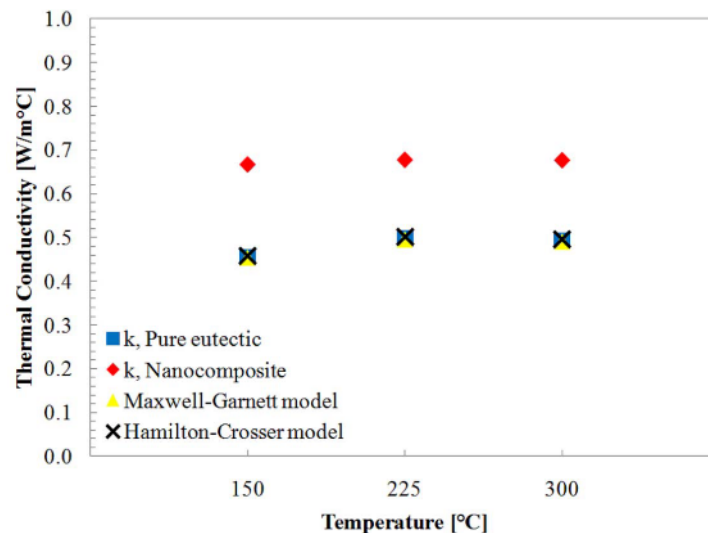
Figure 2-15. Thermal conductivity of the eutectic mixture of carbonates (Li_2CO_3-K_2CO_3 62:38 mol) and 1 wt% of SiNPs. Comparison with the theoretical models. Reprinted with permission from [30].

On the contrary, no increase of the thermal conductivity was found in the nanofluids constituted by Solar Salt ($NaNO_3$-KNO_3 50:50 mol) and ANPs in several concentrations [32]. The thermal diffusivity of the plain salt and the nanomaterials was measured by the LFA method at five different temperatures (65, 85, 105, 125 and 145 ºC). The thermal conductivity was calculated with this information. Table 2-2 shows the thermal conductivity obtained at 145 ºC. A decrease of the value with respect to the base salt was found with independency of the amount of NPs.

Table 2-2. Thermal conductivity of the Solar Salt with ANPs at 145 ºC. Adapted from [32].

Concentration of ANPs, %	Thermal conductivity k, $W \cdot m^{-1} K^{-1}$	Enhancement, %
0.00	0.61	---
0.09	0.46	-24.59
0.17	0.53	-13.11
0.30	0.44	-27.87
0.53	0.46	-24.59
0.78	0.52	-14.75
1.19	0.46	-24.59

2.5.5 Nanofluid microstructure

As explained in Section 2.2.1, the heat transfer properties manifested by MSBNFs are based on the changes induced by the NPs in the base salt. Specifically, the surface interactions between the nanometric particles and the salt ions are responsible of the thermal transfer enhancement. The analysis of the nanofluid microstructure on the reviewed articles encompasses the following objectives:

- To confirm the presence of the nanostructures generated in the surroundings of the NPs. They are presumably constituted by ions of the base salt which are aligned and ordered around the NPs surface acting as nucleation sites for crystallization. These nanostructures look like long needles or networks over the amorphous salt crystals. They have been observed through SEM [30,63,67,90,91,98,99,104,105,107,110,114] (Figure 2-16) or TEM images [30,56,72,74,84,91,102] by several researchers (Figure 2-3 and Figure 2-17). It is not possible to know if these nanostructures are present in the same extension or aspect in the real nanofluid since the microstructure is analysed in the solid state.
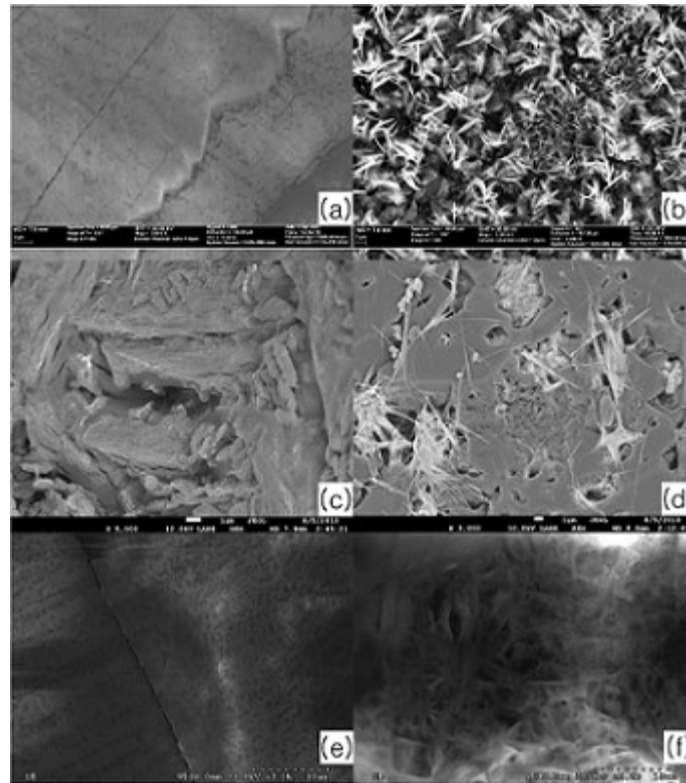
Figure 2-16. SEM images of the pure eutectic mixture of carbonates (Li_2CO_3-K_2CO_3 62:38 mol) (a,c,e) and the nanostructures observed after the addition of silica (b), alumina (d) and magnesia NPs (f). Reprinted with permission from [99].
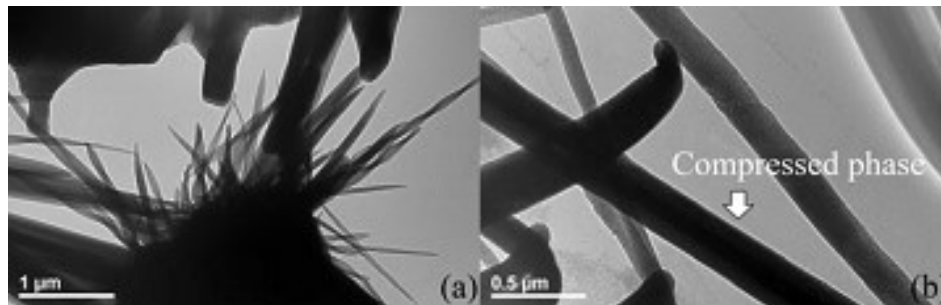
Figure 2-17. TEM images of the eutectic mixture of carbonates (Li_2CO_3-K_2CO_3 62:38 mol) with SiNPs. The needle shaped structures are clearly observed. Reprinted with permission from [56].

- To have an approximate measurement of the individual NPs and the clusters size into the molten salt. This information is relevant to know the available surface of interaction and thus, the likelihood to generate the mentioned nanostructures. The analysis of this parameter has been usually carried out with SEM images [30,61,63,66,90,113] (Figure 2-18) and the DLS technique [64,78,112,113,118,120,126,127]. As indicated before, the evaluation of the size is not highly representative since a tiny amount of the sample is analysed. In addition, the accuracy of the measurement by means of the SEM images and by DLS has strong limitations. On the SEM, the biggest particles or agglomerates are more likely to be found. On the DLS, the analysis requires the dissolution of the sample in water, which can cause the break of NPs clusters originally present in the sample.
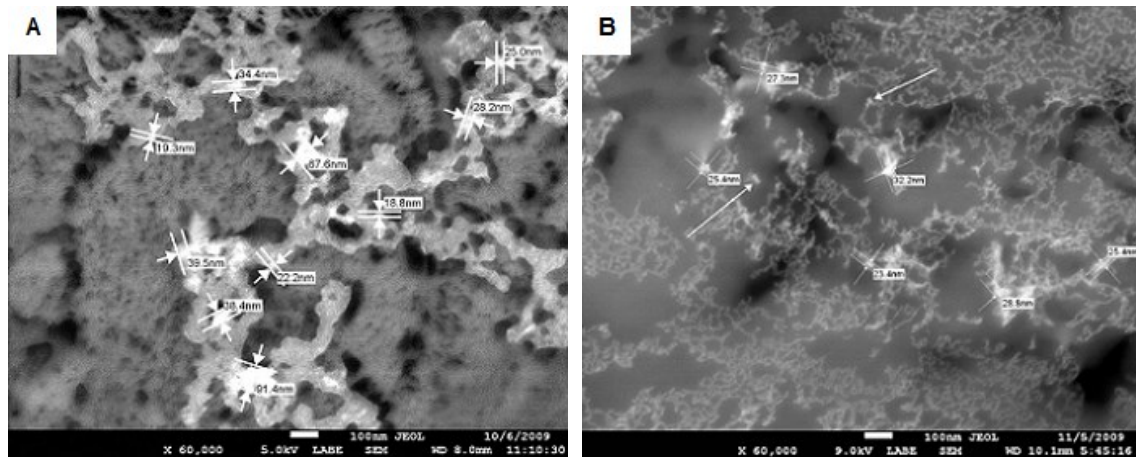
Figure 2-18. SEM images of silica-based nanofluids with A) Li$_2$CO$_3$-Na$_2$CO$_3$ [90] and B) BaCl$_2$-NaCl-CaCl$_2$-LiCl [30,63] as the base salts respectively. A network substructure is observed, interconnecting the SiNPs. Reprinted with permission from [30,63].

- <u>To evaluate the dispersion of NPs into the molten salt matrix.</u> A homogeneous distribution is highly desirable, to avoid great differences of thermal transfer between different regions of the material. SEM with Energy Dispersive X-Ray Spectroscopy (EDX) mapping has been used to know the elemental composition of a certain area of the material [35,39,61] (Figure 2-19). It is worth mentioning that the nanofluid microstructure has always been studied with the material on solid state. This indirect characterization is mainly due to the inexistence of suitable techniques or commercial devices working at high temperatures to know the real appearance of NPs into the molten salt [113].
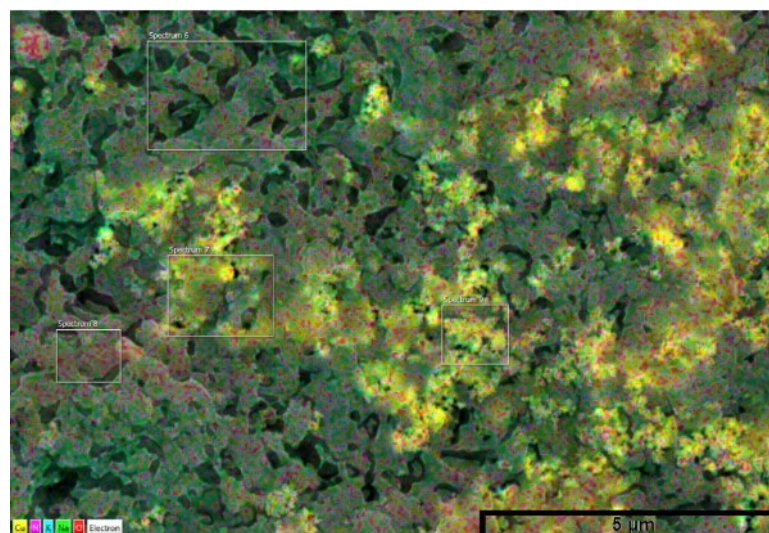
Figure 2-19. EDX mapping of the Solar Salt (NaNO$_3$-KNO$_3$ 50:50 mol) with 0.1 wt% CuO NPs (Yellow—Cu, Violet—N, Blue—K, Green—Na, and Red—O). Reprinted with permission from [35].

2.5.6   Viscosity

The knowledge of the rheological properties of MSBNFs is of high importance for their industrial operation. The ideal nanofluid is expected to possess improved thermal characteristics as well as a low viscosity to avoid an increase of the pressure drop and the required pumping power [44–46,129,130]. The rise in viscosity by the introduction of the NPs into the molten salt has to be avoided, or at least minimized. A commitment should be reached between the faster heat transfer rates and the higher costs associated to the fluid pumping [74]. In addition, the nanofluid stability is also influenced by the viscosity of the medium and this factor should be also taken into account to develop a stable material through its lifetime [45,87]. The research on the rheological properties of MSBNFs is still scarce. The research reported in this area focus on evaluating the dependence of the viscosity on the NPs concentration, the temperature and the shear rate.

Jung [74] analysed the viscosity of nanofluids based on Solar Salt ($NaNO_3$-KNO_3 50:50 mol). The shear rate varied from 1 to 1000 s^{-1} and the tests were carried out at 300, 350 and 400 ºC. SiNPs were added in a concentration of 0.5 and 1 wt% The pure Solar Salt showed a Newtonian behaviour whereas the nanofluids exhibited a shear thinning behaviour. For a certain shear rate, the nanofluid viscosity increased with the rise in the NPs concentration (Figure 2-20A). For a certain temperature (350 ºC), the viscosity decreased asymptotically when increasing the shear rate (Figure 2-20B).
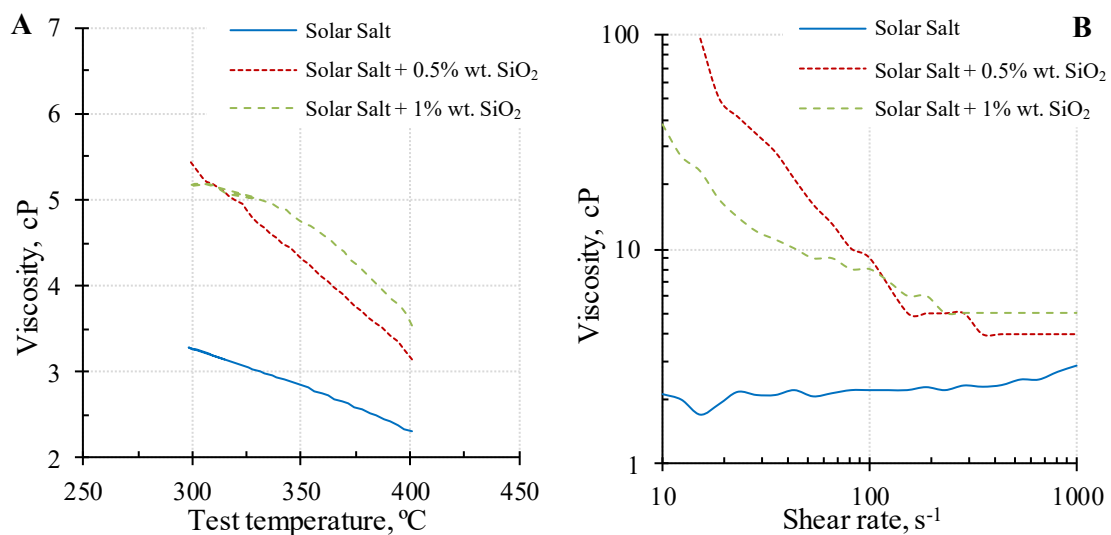
Figure 2-20. Viscosity of the pure Solar Salt ($NaNO_3$-KNO_3 50:50 mol) and its mixture with 0.5 and 1 wt% of SiNPs vs. test temperature at 1000 s^{-1} (A) and vs. the shear rate at 350 ºC (B). Adapted from [74].

Jo and Banerjee [84] reported a high increment of the viscosity in nanofluids composed by the eutectic mixture of carbonates (Li_2CO_3-K_2CO_3 62:38 mol) with MWCNT in different concentrations. For example, the addition of 5 wt% of MWCNT led to an increment of the

viscosity up to 130% (shear rate of 1000 s^{-1}). The nanostructure agglomeration is responsible of this huge viscosity rise. The shear thinning behaviour was more evident at low shear rates and for nanofluids with higher MWCNT quantity. The Krieger–Dougherty model of viscosity, which accounts for the agglomeration, was used to predict the results. However, P. Estellé [131] proposed a modification in that model to consider the fibre-shape of MWCNT, which lead to a better fit of the experimental results.

The Solar Salt (NaNO$_3$-KNO$_3$ 50:50 mol) was utilized as the base fluid by Lasfargues and co-workers [31,114] with 0.1 wt% of CuO NPs. The shear rate varied from 100 to 1000 s^{-1} and the temperature range was established between 250 and 450 °C. A mathematical relation between the viscosity and temperature was deduced for the base salt with high accuracy [114] (Figure 2-21A). Both the Solar Salt and the CuO nanofluids showed a Newtonian behaviour, characterized by a constant viscosity with increasing shear rates (Figure 2-21B). The addition of NPs increased the viscosity of the Solar Salt as reported in the precedent studies [74,84]. According to the authors, additional energy is needed to move the NPs due to the existence of a vortex on their surface, which may explain the increment of viscosity. The shear rate, the shape of the particles, their concentration and the kind of NPs may have an impact on the viscosity of the final nanofluid.
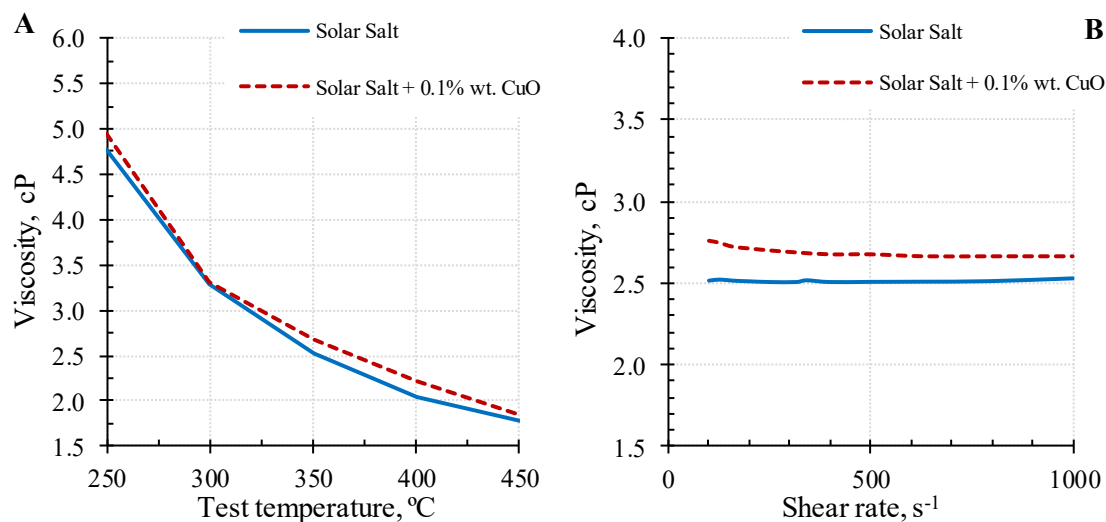
Figure 2-21. Viscosity of the pure Solar Salt and its mixture with 1 wt% CuO NPs vs. the test temperature at 1000 s^{-1} (A) and versus the shear rate at 350 °C (B). Adapted from [114].

To summarize, the works of Jo, Banerjee [84] and Jung [74], indicate that the addition of the NPs may lead to changes on the Newtonian behaviour of the molten salts. In addition, the viscosity is greatly increased by the presence of the NPs. Lasfargues [31,114] found the opposite tendency. This may be due to many factors which influence the rheological performance of MSBNFs, such as the shape of the particles, their size and concentration, the nature of the base fluid, the test temperature and the tested shear rates. Lasfargues [31] considered that the possible clusters of the NPs existing in the nanofluid are broken in individual NPs with high shear rates (>100 s^{-1}).

According to this author, the rheological performance of the nanofluid is the same as the base salt.

2.5.7   Corrosion

The influence of the NPs on the corrosive behaviour of molten salts was studied by Schuller and coworkers [32,93]. The eutectic mixture of carbonates (Li$_2$CO$_3$-K$_2$CO$_3$ 62:38 mol) was doped with 1 wt% of SiNPs. The nanofluid was introduced in stainless steel 304 containers to perform static corrosion tests. The exposure times were 2, 4 and 6 weeks at 520 ºC for both, the nanofluids and the pure salt. The results gave a clear indication of the non-corrosive nature of the carbonate-based nanofluid for the evaluated steel. Figure 2-22 shows the corrosion rate determined on the pure and the doped salt. The reduction of the corrosion rate is clearly observed, with a mass loss reduction of 37, 59 and 49% for testing periods of 2, 4 and 6 weeks respectively. The authors considered two main hypotheses. The first one refers to the quick formation of a complex between the SiNPs and the salt which may act as a passive layer, thus preventing further corrosion. The second possibility is the migration of the SiNPs to the walls of the container and the formation of a physical barrier which may reduce the corrosion.
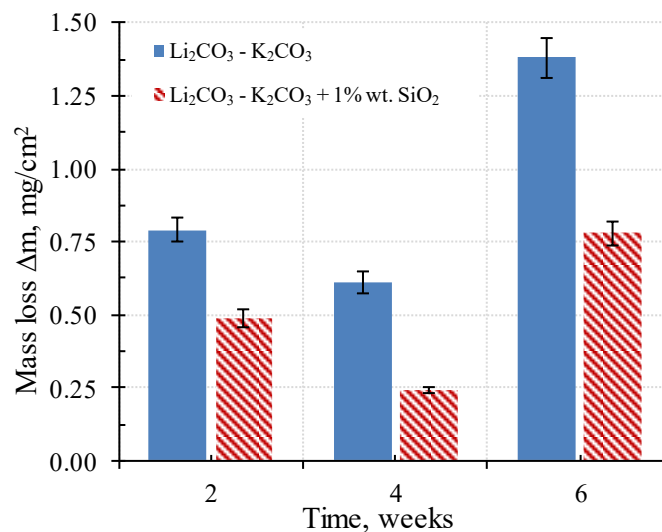
Figure 2-22. Total mass loss of the raw carbonate and the SiNPs-doped carbonate. Adapted from [32,93].

2.5.8   Economic evaluation

The further industrial implementation of the MSBNFs in CSP is currently remote and a wider and deeper characterization of these materials is needed first. Although this research topic is still on its first steps, the industrial interest can be boosted by demonstrating the cost reduction of the new material in comparison to the currently employed thermal storage solutions.

A few brief economic evaluations have been found through the scientific literature. The material costs as well as the savings produced by its improved thermal properties are considered.

The researchers from Texas A&M University [32,62] employed a figure of merit developed by the Department of Energy of the United States (DOE) to calculate the material cost (Eq. 2-7):

$$Media\ cost \left[\frac{\$}{kWh_t}\right] = \frac{Material\ costs \left[\frac{\$}{kg}\right]}{Average\ c_p \left[\frac{kJ}{kgK}\right] x\ \Delta T\ [K]\ x\ 2.778 \cdot 10^{-4} \left[\frac{kWh_t}{kJ}\right]} \qquad \text{Eq. 2-7}$$

An economic simulation was performed with the Solar Salt (NaNO$_3$-KNO$_3$ 50:50 mol) and ANPs according to Eq. 2-4. The considered NPs concentrations were 10, 25 and 50 wt% respectively. The theoretical economic benefit based on the specific heat improvement was related to the material cost compared to the plain Solar Salt (Figure 2-23). The predicted increment of the cost of Solar Salt-based nanofluids for different percentages of ANPs are gathered in Table 2-3.
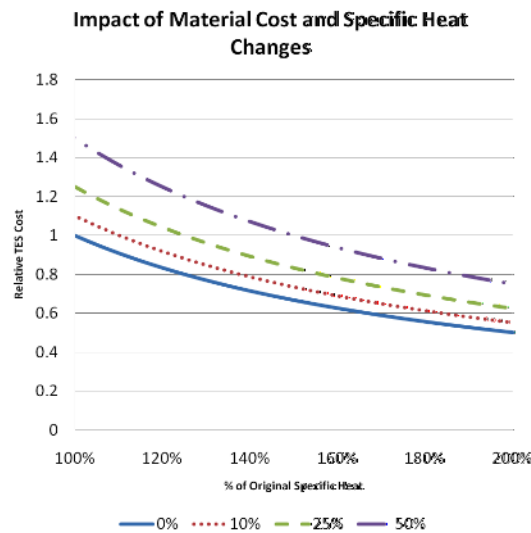
Figure 2-23. Relative TES material costs according to the increment of the specific heat and the manufacturing cost increase. Reprinted with permission from [32,62].

Table 2-3. Predicted cost increase (%) for a nanofluid of Solar Salt (NaNO$_3$-KNO$_3$ 50:50 mol) with ANPs. Adapted from [62].

Mass fraction Al$_2$O$_3$, %	Increase in material cost, %	c$_p$ increase leading to a 20% reduction of global costs
0.1	0.9	126
1.0	8.8	136
10	87.6	235

Miliozzi and coworkers [78] briefly discussed the cost of MSBNFs. The difficulty of conducting an accurate economic analysis of a roughly characterized material is emphasized. The considered scenario included an increase of the specific heat capacity of 20-30% (which was indeed experimentally determined). This involves a tank volume reduction, but the potential savings

cannot be precisely quantified. The main barrier is the absence of information about the thermal diffusivity of the material. The calculated increment of the manufacturing costs was lower than 2%. Some other costs should be added to it, such as the hypothetical industrial synthesis process, which has not yet been fully identified.

2.6 CURRENT CHALLENGES AND FUTURE WORK

The researchers working on MSBNFs must face several issues to create a solid knowledge and establish the future research topics on the field. In line with the features analysed through this review, the main barriers of MSBNFs and their possible solutions are laid out in the following paragraphs:

- **Characterization of the starting materials.** The information about the properties of inorganic salts and NPs is very scarce or absent. Specific data of the actual nanoparticle size and shape is of great importance because of its influence on the final properties. In addition, the chemical compatibility between the salt and the NPs must be evaluated to guarantee the absence of future undesirable reactions.

- **Scalability and reproducibility of the synthesis procedure.** The most common method to produce MSBNFs requires the use of huge quantities of water and ultrasonic power in a batch procedure. This procedure greatly hinders the industrial scalability and reproducibility of the method. Novel processes are needed to overcome these drawbacks, such as the direct mixing of NPs with the liquid salts at high temperatures. The key is to achieve a homogenous dispersion of the NPs in the salt.

- **Long-term stability of the NPs in the molten salt.** Some studies have demonstrated that the NPs immersed into a molten salt suffer from agglomeration and settling after a few hours. Unfortunately, any feasible solution to delay or eliminate this issue has been proposed on the scientific literature until now. A deeper knowledge of the interactions between salts and NPs at a molecular level is necessary to advance in this matter. The use of physical techniques such as ultrasounds or mechanical stirring to break the agglomerates could be the answer. In addition, the use of novel functionalized NPs with surface modifications may also considerably reduce their agglomeration into the molten salt.

- **Standardization of measuring methods.** The characterization of the thermophysical properties under standardized procedures is highly desirable to compare the results of different

researchers. The huge number of methods found in literature to characterize the specific heat of MSBNFs makes difficult to draw comparisons, trends or conclusions for particular systems of salt-nanoparticle. The same situation occurs regarding other properties, such as the latent heat or the viscosity.

- **Devices for the characterization of high temperature fluids.** Nowadays it is impossible to characterize some properties of MSBNFs because there are not commercial devices which can stand the high temperature and the corrosive nature of the molten salts. Particularly, the current methods to analyse the thermal conductivity are not technically suitable for fused salts. The same problem occurs to measure the nanoparticle size when the salt is on the liquid state. The analysis through indirect measurements (SEM, DLS, LFA), or the design of self-made apparatus, have been the applied solutions so far, with high limitations in terms of accuracy and representativeness.

- **Influence of the nanoparticle size.** The relationship between the nanoparticle size and the specific heat of the nanofluid is not yet clear. As mentioned before, the initial size and shape of the NPs has not frequently been reported in the published articles, although the size that the NPs or the clusters have on the final material is reported on most publications. This size is analysed with SEM images or DLS in a few cases. In both techniques the material is on the solid state, thus, the absence of the real state of the sample makes it difficult to confirm or discard this dependence.

- **Viscosity.** The rheological properties of MSBNFs are critical for a possible industrial application. Feasible and economical solutions must be developed to avoid an excessive increment of the viscosity. Nanofluids with higher viscosity than the base fluid lead to the increase of the pressure drop and consequently will require the use of pumping power.

- **Corrosion and erosion of containment materials.** To the best of our knowledge, this issue has not yet received relevant attention from the scientific community of MSBNFs. Although these aspects have been studied for traditional nanofluids [129], it is necessary to know if the corrosive nature of the salt suffers of any change due to the presence of NPs. In addition, there may be physical erosion of pipes or tanks with the nanofluid movement.

- **Theoretical models and simulations.** As explained in Section 2.2, some models have been proposed to justify the unusual high values of the specific heat of MSBNFs. In addition, MDS performed for some systems gives an initial idea of the processes which take place. However, a further development of these models and simulations with a higher number of combinations of

salt-nanoparticle is necessary. The obtained predictions must be confirmed by experimental results and vice versa. More investigations involving their own simulation and experimental work at the same time are needed.

- **Economical evaluation.** The likelihood of implementing these materials in the future is strongly dependent on their final cost. Although some cost-estimation has been found in the literature survey, much economic analysis remains yet to be performed. For example, a balance between the enhancement of thermal properties and the amount of NPs necessary to achieve it has not yet been determined. The inclusion of a high percentage of nanomaterials in the molten salts may fold the specific heat by several times but the cost might increase to an unacceptable level. Other aspects, such as the viscosity and the corrosion, should be taken into account as well. As emphasized before, the economic impact of the synthesis procedure must be seriously considered.

Chapter 3

RAW MATERIALS AND EXPERIMENTAL METHODS

3 RAW MATERIALS AND EXPERIMENTAL METHODS

3.1 INTRODUCTION

The present Chapter covers two objectives. First, the main features of the base salts and the nanoparticles selected for the study are detailed. Then, the methods and techniques used in the raw materials and nanofluids characterization are described with precision. All of them are gathered here as a compendium, since each of them is described again on the following chapters of results. The initial experiments which were carried out to optimize some of these methods are also included (Journal contribution 2 and Conference contribution 1 and 2). Finally, the characterization of the nitrates and the nanoparticles is explained. Most of the results included on this chapter have been used on the subsequent Chapters devoted to nanofluids characterization because they are the reference values to determine the improvement and/or modification obtained in the nanofluids. At the end of this Chapter, the Conference contribution 3 about the characterization of solar salt and boehmite nanoparticles has been reproduced.

3.2 RAW MATERIALS SPECIFICATIONS

In this section, the main features of the materials employed through the thesis are detailed. This will provide a clear insight on their properties to study their influence on the further synthetized nanofluids.

3.2.1 Salts

3.2.1.1 Sodium nitrate

Sodium nitrate ($NaNO_3$) is an inorganic salt found in natural deposits in few parts of the world, mainly in the Atacama Desert, in Chile [132]. Presently, it is synthetically produced for industrial applications [133]. At room temperature, its physical aspect is a white crystalline solid, odourless and colourless, moderately hygroscopic, saline in taste, and very soluble in water, ammonia and glycerol. Sodium nitrate is used as a fertilizer and in a number of industrial applications, including the manufacture of glass, explosives, and charcoal briquettes, as well as in the production of potassium compounds.

Sodium nitrate can be found on several grades of purity. Table 3-1 shows the grades of sodium nitrate employed in this investigation and their main specifications according to the manufacturers [134–136].

Table 3-1. Chemical composition, purity and supplier of the different $NaNO_3$ grades used in this work [134–136].

SODIUM NITRATE, $NaNO_3$			
Grade	Analytical (ISN)	Refined (RSN)	Industrial (ISN)
Supplier	Labkem	SQM	SQM
Melting point, ºC	n.s.	308	n.s.
Purity, %	≥ 99.5	≥ 99.5	≥ 98
Cl^-, ppm	≤ 5	≤ 800	≤ 6000 (total Cl)
ClO^{3-} / ClO^{-4}, ppm	≤ 30	≤ 350	n.s.
IO^{3-}, ppm	≤ 5	n.s.	n.s.
PO_4^{3-}, ppm	≤ 2	n.s.	n.s.
SO_4^{2-}, ppm	≤ 30	≤ 1000	≤ 5000
CO_3^{2-}, ppm	n.s.	≤ 1000	≤ 1000
OH^-, ppm	n.s.	≤ 2000	≤ 2000
NO_2^-, ppm	≤ 2	≤ 200	≤ 200
NH_4 salts, ppm	≤ 20	n.s.	n.s.
Pb, ppm	≤ 5 (total heavy metals)	≤ 5	≤ 5
Cd, ppm	n.s.	≤ 1	≤ 1
Cr, ppm	n.s.	≤ 0.5	≤ 0.5
Hg, ppm	n.s.	≤ 0.5	≤ 0.5
As, ppm	n.s.	≤ 0.5	≤ 0.5
Mg^{2+}, ppm	≤ 10	≤ 200	≤ 1000
K^+, ppm	≤ 50	n.s.	n.s.
Ca^{2+}, ppm	≤ 20	≤ 20	≤ 100
Fe, ppm	≤ 2	≤ 10	≤ 10
Insoluble in H_2O, ppm	≤ 50	200	500
Moisture, %	≤ 1	0.1	0.1

n.s.: not stated.

3.2.1.2 Potassium nitrate

Potassium Nitrate (KNO_3) is found as a colourless transparent crystalline solid or as a white powder. It is soluble in hot water (1480 g/L at 80 ºC) but slightly soluble in cold water (808 g/L at 10 ºC). It releases oxygen when it decomposes on heating (400 ºC). It is a strong oxidizer and reactive with reducing agents, combustible materials, organic materials or metals. Potassium nitrate is a synthetic product, prepared commercially by the reaction of potassium chloride with sodium nitrate. It is used in the manufacture of gunpowder. It is also used in explosives, fireworks, matches, and fertilizers, and as a preservative in foods, especially meats. It is also sometimes used in medicine as a diuretic. Potassium nitrate is also used to produce optics glass and high grade craft glassware. Table 3-2 gathers its chemical composition [137–139].

Table 3-2. Chemical composition, purity and supplier of the different KNO_3 grades [137–139].

POTASSIUM NITRATE, KNO₃			
Grade	Analytical (APN)	Refined (RPN)	Greenhouse (Multi-K GG) (IPN)
Supplier	Labkem	SQM	Haifa
Melting point, ºC	n.s.	333	n.s.
Purity, %	≥ 99.8	≥ 99.6	n.s.
Cl^-, ppm	≤ 5	≤ 1000	n.s.
ClO^{3-} / ClO^{-4}, ppm	≤ 30	≤ 100	n.s.
IO^{3-}, ppm	≤ 5	n.s.	n.s.
PO_4^{3-}, ppm	≤ 2	n.s.	n.s.
SO_4^{2-}, ppm	≤ 30	≤ 500	n.s.
CO_3^{2-}, ppm	n.s.	≤ 200	n.s.
OH^-, ppm	n.s.	≤ 100	n.s.
NO_2^-, ppm	≤ 5	≤ 200	n.s.
NH_4 salts, ppm	≤ 20	n.s.	n.s.
Pb, ppm	≤ 5 (total heavy metals)	≤ 5	n.s.
Cd, ppm	n.s.	≤ 1	n.s.
Cr, ppm	n.s.	≤ 0.5	n.s.
Hg, ppm	n.s.	≤ 0.5	n.s.
As, ppm	n.s.	≤ 0.5	n.s.
Mg^{2+}, ppm	≤ 10	≤ 100	n.s.
K^+, ppm	≤ 50	n.s.	n.s.
Ca^{2+}, ppm	≤ 20	≤ 20	n.s.
Fe, ppm	≤ 2	≤ 10	n.s.
Insoluble in H_2O, ppm	≤ 50	≤ 100	700
Moisture, %	≤ 0.2	0.1	≤ 0.2

n.s.: not stated.

3.2.1.3 Solar Salt

The TES material currently implemented in the CSP plants is called Solar Salt. It has been chosen as the base fluid in this thesis. It consists of a non-eutectic mixture of sodium and potassium nitrate (60:40 wt%). In Figure 3-1 the phase diagram of this blend is shown [140] and the composition of the Solar Salt is signalled (x_{NaNO3}=0.64 molar fraction). According to this figure, the blend starts melting at 224 ºC and ends at 238 ºC. The use of this mixture instead of the eutectic one as TES material in the thermosolar energy plants is based only on economic considerations, due to the higher cost of KNO_3 in comparison to the $NaNO_3$ cost.
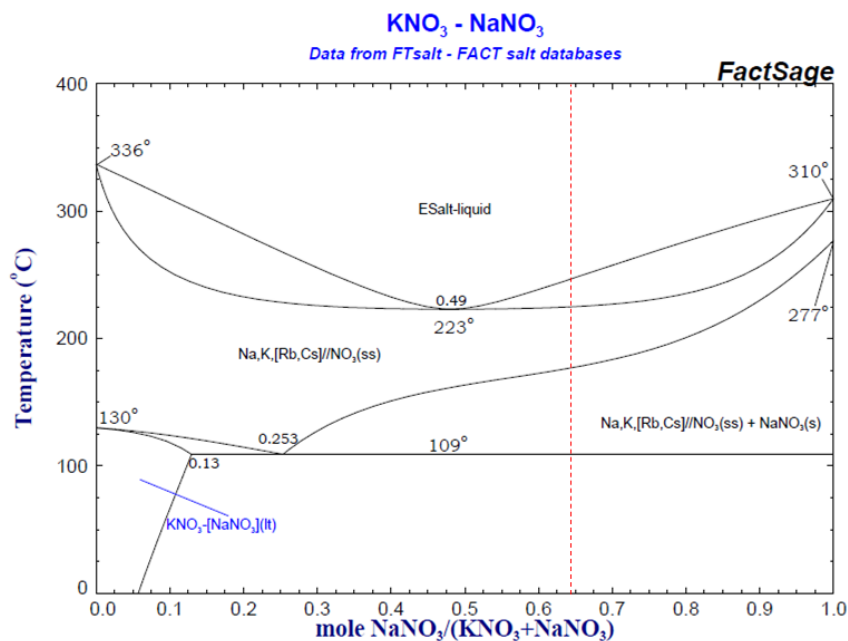
Figure 3-1. Phase diagram of the mixture of sodium and potassium nitrate [140]. The red line is the composition of the Solar Salt used as the base fluid on this thesis.

Three Solar Salt mixtures were prepared by mixing sodium nitrate and potassium nitrate to a ratio 60:40 wt% respectively. Each mixture was produced with the raw materials corresponding to a similar purity grade. Table 3-3 gathers the composition of these three mixtures. All of these blends were prepared in the same manner: the initial sodium nitrate and potassium nitrate were dried in an oven at 100 ºC for at least two hours to remove their humidity. Then, the required quantities of each salt were precisely weighed on a scale (ME204/M, Mettler-Toledo). Finally, the mixtures were melted at 396 ºC for 30 minutes into a furnace (Nabertherm) to ensure their homogeneity. Once the melting program was finished, the salts were extracted from the furnace and left to cool down at room temperature until their complete solidification. The samples were then crushed and milled into a mortar to obtain a fine powder.

Table 3-3. Solar Salt mixtures made of different grades of sodium nitrate and potassium nitrate.

	SOLAR SALT ANALYTICAL GRADE	SOLAR SALT REFINED GRADE	SOLAR SALT INDUSTRIAL GRADE
Acronym	ASS	RSS	ISS
$NaNO_3$ Analytical Grade	X		
$NaNO_3$ Refined Grade		X	
$NaNO_3$ Industrial Grade			X
KNO_3 Analytical Grade	X		
KNO_3 Refined Grade		X	
KNO_3 Greenhouse Grade			X

3.2.2   Nanoparticles

As established in the previous Chapter 2, only ceramic nanoparticles are able to withstand the high temperatures and corrosive nature of the molten salts. Alumina and silica nanoparticles belong to this group. They have been widely employed in contact with molten salts by many researchers, showing promising results. Therefore, the present study selected these nanoparticles with the aim of having a solid bibliographic background for a further comparison of the results.

3.2.2.1 Alumina nanoparticles

The source of alumina nanoparticles employed in the present study is a commercial water-based nanofluid (Alumisol-10A, Kawaken Fine Chemicals, Co.). This solution contains 10 wt% of boehmite nanoparticles. The technical features of this product are listed in

Table 3-4. The nanoparticle size distribution and the TEM image provided by the manufacturer are depicted in Figure 3-2. The product is synthesized by the manufacturer employing the sol-gel method using aluminum alcoxides as raw materials.

Table 3-4. Main characteristics of the commercial nanoparticles dispersion employed in this study [141]..

ALUMISOL-10A	
Supplier	Kawaken Fine Chemicals
Al_2O_3, %	9.8 – 10.2
pH	3.4 – 4.2
Average particle diameter, nm	5 - 15
Stabilizer	Nitric acid
Appearance	Slight white liquid
Crystal system	Boehmite, (aluminium oxide hydroxide, γ-AlO(OH))
Viscosity, cp (25 ºC)	≤ 50
Specific surface area, $m^2 \cdot g^{-1}$ (5 h at 500 °C)	250.8
Specific surface area, $m^2 \cdot g^{-1}$ (5 h at 1000 °C)	115.8
Notes	Water solution
NO_3^-, ppm	7000
PO_4^{3-}, ppm	< 2
Other: (Ni, Cu, Ti, Ca, Mg, Cr, Li, Na, K), ppm	< 1
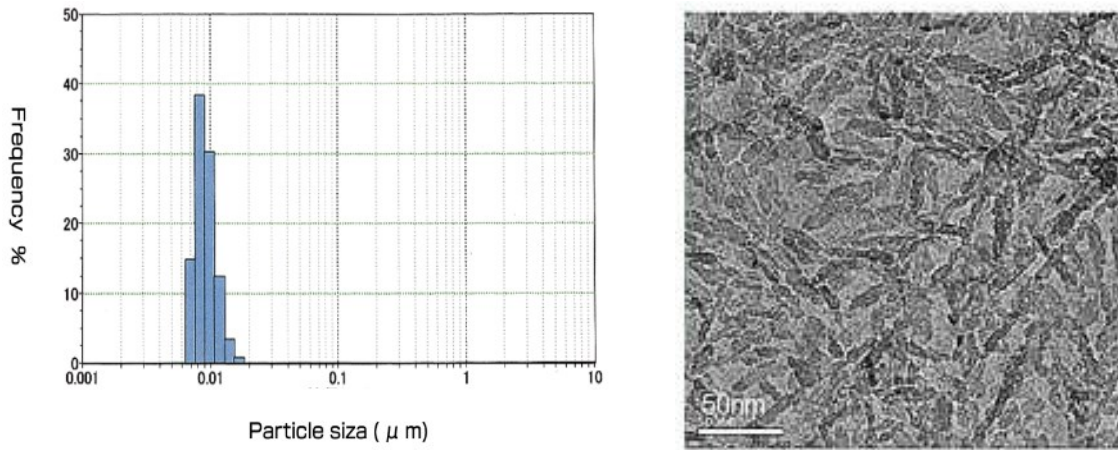
Figure 3-2. Nanoparticle size distribution (left) and TEM image (right) of the product Alumisol-10A [141].

The boehmite, is an aluminium oxihydroxide (AlOOH), precursor of the γ-Al$_2$O$_3$. It crystallizes on an orthorhombic dipyramidal lattice [142] and its structure consists of layers of the basic structural units plotted in Figure 3-3.
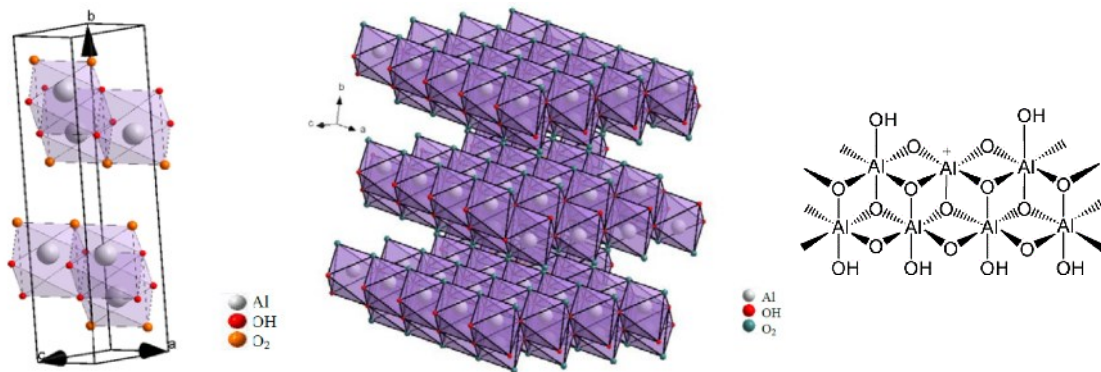
Figure 3-3. Schematic structure of boehmite: Basic structural unit (left), spacial configuration (middle and right) [142,143].

3.2.2.2 Silica nanoparticles

The product known as LUDOX® SM-30 (W. R. Grace & Co.-Conn) was used as the source of silica nanoparticles. It is a commercial aqueous colloidal nanofluid containing 30 wt% of silica nanoparticles [144,145]. According to the manufacturer, it contains discrete, spherical particles of amorphous silica in the low nanometer size range. The nanoparticles, dispersed in water, are non-porous and exhibit non detectable crystallinity. Besides, the product is designed to have a monomodal and narrow size distribution (Figure 3-4) which gives the advantage that all particles will have similar available surface for interacting with the molten salt media. The main characteristics of LUDOX® SM-30 are gathered in Table 3-5.
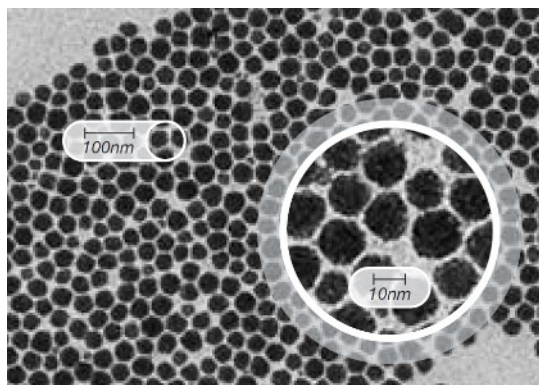
Figure 3-4. TEM picture of monodisperse LUDOX® colloidal silica [145].

Table 3-5. Chemical composition, properties and supplier of the silica nanoparticles [144].

LUDOX® SM-30	
Supplier	W. R. Grace & Co.-Conn
Counter ion	Na^+
Particle size, nm	7
SiO_2 Specific surface area $m^2 \cdot g^{-1}$	340
Silica content, SiO_2 wt%	30
Sodium content (wet basis), Na wt%	0.5
Sodium content (dry basis), Na wt%	1.7
pH	8-11

These small silica particles are formed by a dense silica core and a surface covered by silanol (Si-OH) groups. Because of their small particle size and high surface area, these silanol groups strongly interact with other chemical groups. However, for the same reason, the free colloidal silica particles are very unstable and tend to react with each other to form large agglomerates of silica gel, prone to settling. To prevent the aggregation and gelling, the silica particles in suspension are stabilized by inducing a charge on the surface to make the particles repel each other. The colloidal silica products are divided into grades, depending on the employed stabilization route. The alkaline grade silica is stabilized by treatment with bases (NaOH or NH$_4$OH) to provide a negatively charged surface, leaving the counter ions (Na^+ or NH_4^+) in solution to balance the charge on the surface, as illustrated on Figure 3-5. The LUDOX® SM-30 silica nanoparticles are stabilized with Na^+.

Table 3-6 shows the main features of these nanoparticles.
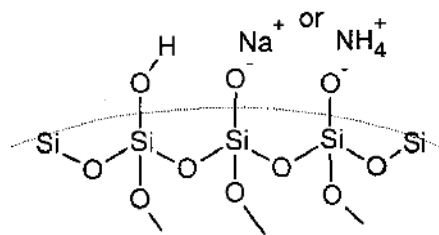
Figure 3-5. Structure of the colloidal silica nanoparticles [146].
In addition to LUDOX® SM-30, solid crystalline silica nanoparticles (Silica nanopowder, Sigma-Aldrich, St. Louis, MO, USA) were used to replicate the traditional synthesis method of the nanofluids.

Table 3-6. Main properties of the solid silica nanoparticles [147].

SILICA NANOPOWDER	
Supplier	Sigma-Aldrich
Purity, %	99.8
Diameter, nm	12
Surface area, $m^2 \cdot g^{-1}$	175-225
Boiling point, ºC	2230
Melting point, ºC	1600
pH	3.7 – 4.7
Water content, wt%	< 1.50
Trace metal analysis, ppm	≤ 2500

3.3   EXPERIMENTAL METHODS

3.3.1   Analysis of the salt impurities

The main impurities of the nitrate salts with non-analytical grade and the nanofluids based on them were analysed and quantified. The chemical analysis was performed in the laboratory of Tecnalia following the common procedures of determination for each compound. Specific analytical methods were carried out to determine each type of contaminant:

- **Chlorides:** The salt was dissolved in water and then analysed by Ionic Chromatography.
- **Sulphates:** The sample was dissolved in nitric acid and the total amount of sulphur was analysed by Inductively Coupled Plasma / Optical Emission Spectrometry (ICP/OES). The results are expressed as sulphates.
- **Phosphates:** The sample was dissolved in nitric acid and the total amount of phosphor was analysed by ICP/OES. The results are expressed as phosphates.
- **Nitrites:** The salt was first dissolved in ultrapure water. In this solution, the colorimetric method was performed according to the American Public Health Association (APHA) standard "4500-NO_2 –B: Nitrite by colorimetry. Standard Methods for the Examination of Water and Wastewater".

- Calcium and magnesium: The sample was dissolved in nitric acid and the total magnesium and calcium was analysed by ICP/OES in the solution thus obtained.

- Carbonates and hydroxides: The salt was first dissolved in ultrapure water. An acid-based titration was done over this solution with hydrochloric acid. The method was done according to the standards "UNE-EN ISO 9963-1:1996. Water quality. Determination of alkalinity. Part 1: Determination of total and composite alkalinity (ISO 9963-1:1994)" and "UNE-EN ISO 9963-2:1996. Water quality. Determination of alkalinity. Part 2: Determination of carbonate alkalinity (ISO 9963-2:1994)".

3.3.2 Nanoparticle size and Zeta Potential

The determination of the size of the particles dispersed on the salt-nanoparticle dispersions was carried out by means of Dynamic Light Scattering (DLS). This is a non-invasive, well-established technique for measuring the size of particles and macromolecules in the submicron region, down to below 1 nanometre. It is used to measure the size of the particles suspended in a liquid [148].

Particles in suspension undergo Brownian motion, a phenomenon influenced by particle size, sample viscosity and temperature. The Brownian motion is the random movement of particles in a liquid due to the bombardment by the molecules that surround them. Light scattering is a consequence of the interaction of light with particles and also with the electric field of the small particles or molecules. When such particles are illuminated with a laser, the intensity of the scattered light fluctuates at a rate that depends on the speed of particle movement.

The diameter measured in DLS is called the hydrodynamic diameter and corresponds to the diameter of a sphere with the same translational diffusion coefficient as the particle being measured. The hydrodynamic diameter depends not only on the size of the particle "core", but also on any surface structure, as well as on the type and concentration of any ions in the medium. In the case of non-spherical particles, DLS will give the diameter of a sphere that has the same average translational diffusion coefficient as the particle being measured (Figure 3-6). This means that, for example, in the ANPs (needle-shaped) the results cannot be considered as absolute numbers but only serve as a comparison between them.
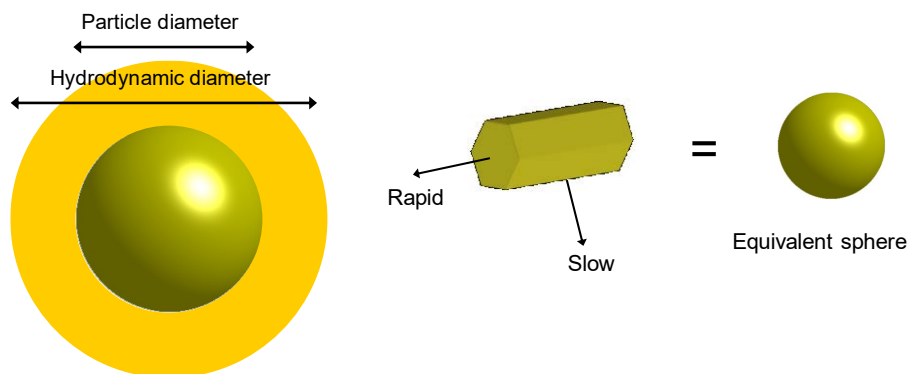
Figure 3-6. Example of hydrodynamic diameter (left) and equivalent sphere (right). The brown area around the particle are the molecules attached to its surface. Reprinted with permission from [149].

The result from a DLS experiment yields the intensity distribution of different particle size ranges. The intensity distribution is naturally measured according to the scattering intensity of each particle fraction or family. As a consequence, it can be overestimated, since a small amount of aggregation/agglomeration or the presence of a large particle species can dominate the distribution.

This can be converted, using Mie theory [148], to a volume or number distribution. That means a distribution describing the relative proportion of multiple components in the sample, based on their volume or number rather than based on their scattering (intensity).

When transforming an intensity distribution to a volume or number distribution, there are four assumptions that must be accepted: 1) all particles are spherical; 2) all particles are homogeneous (with the same composition and phase/crystalline nature); 3) the optical properties of the particles are known, i.e. the real & imaginary components of the refractive index and 4) there is no error on the intensity distribution.

An understanding of these assumptions is particularly important, since the DLS technique itself produces distributions with inherent peak broadening, so there will always be some error in the representation of the intensity distribution. As such, volume and number distributions derived from these intensity distributions are best used for comparative purposes, or for estimating the relative proportions where there are multiple modes, or peaks, and should never be considered absolute.

This is clearly illustrated in the Figure 3-7 for a sample consisting of equal numbers of particles with diameters of 5 nm and 50 nm. The number weighted distribution (plot on the left side) gives equal weighting to both types of particles, therefore emphasizing the presence of the fine 5 nm particles. The intensity weighted distribution (plot on the right side) has a signal one million times higher for the coarser 50 nm particles than for the 5 nm ones. Larger or aggregated particles show higher scattering intensity than the small particles, being proportional to r^6, which may lead to

misinterpretations. The volume weighted distribution (plot on the center of the figure) is intermediate between the two former cases, being the volume of the bigger particles 1000 times larger than the volume of the smaller ones (volume of a sphere is equal to $4/3\pi r^3$)
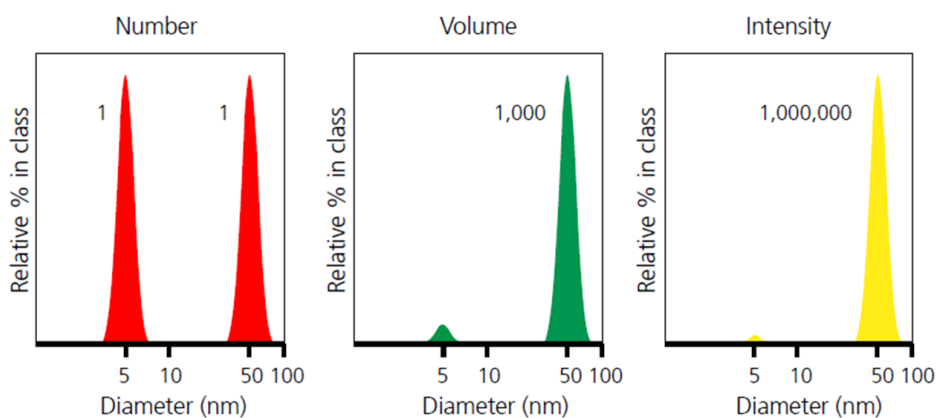
Figure 3-7. Example of number (left), volume (center) and intensity (right) weighted particle size distributions for the same sample [150].

In addition to the light scattering, the DLS device can measure the Zeta Potential (ZP) of a colloidal dispersion, which is used to evaluate stability of a fluid dispersion with nanoparticles. The ZP is a parameter which is related to the surface electrical charge, a property that all materials possess, or acquire, when suspended in a polar fluid (like water). It must be noted that only small, colloidal or nanosize particles can be suspended in a fluid, and it occurs due to an ionic-electrical stabilization between the particles and the fluid ions. An electrical double layer surrounds these small particles (Figure 3-8), locally forming an "ionic" concentration different from the ionic concentration of the solution. The electrical double layer is divided into two regions. The first region is called the Stern layer, formed by ions with charge opposite to that created onto the particle. The Stern layer is strongly bound to the particle and the ions move together with it. The second layer is known as the diffuse layer where the ions are less strongly attached [151]. The electric potential due to the surface charge at the outermost surface of the Stern layer is called the Stern potential. The electric potential at the end of the diffuse layer is the ZP. Thus, it is the potential difference between the dispersion medium and the outermost surface of the diffuse layer. At constant ionic strength of the medium, the higher the charge on the particle, the higher will be the ZP.
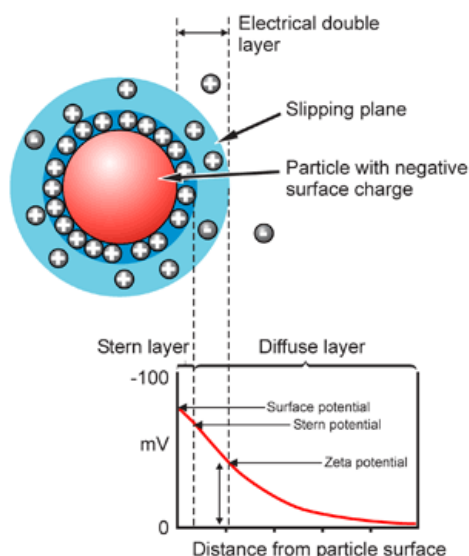
Figure 3-8. Scheme of the electrical double layer formed across a negatively charged colloidal particle. Reprinted with permission from [152].

In general, a high magnitude of the ZP (negative or positive) is an indication of an electrically stabilized system and the nanoparticles will not form clusters. When the ZP reaches zero (isoelectric point (IEP)) the nanoparticles tend to agglomerate. Larger information about the stability of colloidal dispersions and the ZP can be found in [148].

In this work, the DLS equipment used to characterize the nanoparticle size and its ZP was the Zetasizer Nano ZS (Malvern Instrument, Ltd. Malvern, UK). Tests were performed with 173° scattering angle. The analysis was performed on a liquid sample at room temperature. Therefore, the solid samples needed to be dissolved in distilled water prior to the measurement. The minimum and maximum concentration of the nanoparticles in this solution is related to their expected sizes, according to Malvern experts' advices (Table 3-7) [153]. The samples were dissolved in distilled water just before performing the experiment to avoid any interference on results due to the sedimentation of nanoparticles. This water was previously adjusted to the pH of stability of the nanoparticles, as will be explained later. Then, the specific cells of the equipment (the cells for measuring ZP are different from those required to measure the particle size distribution) were filled in with a little amount of the sample solution (around 1 mL) and placed inside the device. The measurement was repeated three times on each sample to evaluate the method accuracy. It is important to remark the impossibility of establish an equivalence between the nanoparticle dispersion into the molten salt and into the water solution measured in the DLS. The nanoparticle sizes measured with this method are considered as an approximation to the real ones, in absence of a device capable of measuring at the high working temperatures of the inorganic salts.

Table 3-7. Nanoparticle concentration on the measured solution according to their expected size. These values are recommendations from Malvern Instruments [153]

Particle size, nm	Minimum concentration	Maximum concentration
< 10	0.5 mg·mL^{-1}	Only limited by the sample material interaction, aggregation, gelation, etc.
10 – 100	0.1 mg·mL^{-1}	5% mass (assuming a density of 1 kg·m^{-3})
100 -1000	0.01 mg·mL^{-1}	1% mass (assuming a density of 1 kg·m^{-3})

Before doing the measurements, a Standard Operating Procedure (SOP) is defined having into account some features of both, the nanoparticles and the solvent: the Refractive Index (RI), the viscosity and the absorption (Table 3-8). The Refractive Index of a dilute solution of Solar Salt was measured by a manual refractometer and the viscosity was considered to be that of the distilled water at 25 ºC. The refractive indexes of both ANPs and SiNPs were found on the Zetasizer Nano ZS software, as well as the data for a dilute solution of Sodium Nitrate.

Table 3-8. Physical parameters of the Solar Salt, alumina and silica implemented on the measurement procedure.

	Solar Salt	Sodium Nitrate	Alumina (Al$_2$O$_3$)	Silica (SiO$_2$)
Refractive Index (RI)	1.343	1.331	1.760	1.460
Viscosity (cp)	0.8872	0.8919		
Absorption			0.100	0.000

The ZP of the solutions prepared with each type of nanoparticle was measured at different pHs. For each nanoparticle, several dispersions were prepared at different pHs ranging from 2 to 10. In every case, the pH was adjusted using nitric acid or sodium hydroxide diluted solutions. All the solutions were prepared at room temperature. The special cuvettes for the determination of ZP were carefully filled in with these solutions, avoiding the presence of air bubbles, to carry out the ZP measurements.

The previous experiments done to optimize this measurement method are detailed later in the Conference contribution 2 [118].

3.3.3 Thermal properties

3.3.3.1 Thermal stability

The Thermogravimetric Analysis (TGA) measures the absolute amount and the rate of weight change of a sample as a function of time or temperature in a controlled environment. TGA has a wide range of properties that can be measured such as thermal stability, oxidative stability, interaction with different atmospheres, moisture and volatile content, and sometimes the composition of multi-component systems. The three most important characteristics that TGA collects are the weight, the rate of weight change (differential thermogravimetry, dTG) and the

temperature. A dTG curve is generated as the first derivative of the weight with respect to temperature or time. The dTG curve can be used to provide both qualitative and quantitative information about the sample. Qualitative modes of analysis include identifying a material and distinguishing between two or more overlapping reactions. Quantitative modes include the analysis of the curve weight-time and the temperature at maximum weight loss/gain measurements [154].

In this research, the technique was used to verify the thermal stability of salts and nanoparticles in the working temperature range of TES at CSP plants and to guarantee the absence of reactions between them.

The following procedure was employed to determine the thermal stability of the raw Solar Salt, nanoparticles and Solar Salt-based nanofluids. About 20 mg of the dried sample was introduced in a platinum crucible specifically supplied for the TGA measurements. The crucible was placed in the TGA device (SETARAM SETSYS Evolution –1750, Setaram Instrumentation, France) and subjected to the following heating program. First, a heating-ramp from 20 ºC to 90 ºC at 5 ºC/min to remove humidity. This ramp was followed by a second heating-ramp from 90 ºC to 550 ºC at 2 ºC/min. Then, the sample was hold at the highest temperature for 3 hours and cooled again until 90 ºC (2 ºC/min). Finally, two additional heating and cooling cycles between 90 ºC to 550 ºC were applied in order to know if the weight losses were reversible or not.

The analyses were always carried out under air atmosphere instead of an inert one, to account for the worst scenario. The weight loss of the sample was precisely registered along the time with the thermobalance.

3.3.3.2 Specific heat

The specific heat of the Solar Salt, Sodium Nitrate, ANPs, SiNPs and the nanofluids composed of these materials was determined by means of Differential Scanning Calorimetry (DSC). This is a well-established measuring method which is used at a large scale in different areas of research, development, and quality inspection and testing. A large number of properties and transitions related to the exchange of heat can be quickly identified over a large temperature range. The temperature where changes or reactions occur can be determined, as well as the characteristic energy exchange taking part on the occurred phenomenon. To do these measurements only some few milligrams of sample are required. Measurements obtained by DSC allow to determine the heat capacity (specific heat), the heat of transition, some kinetic data, the purity of compounds, the phase transition temperatures and their latent heats, the glass transition of polymers; it can be used to identify substances, to set up phase diagrams and to determine degrees of crystallinity of a material [155].

There are three main DSC technologies presently available in the market, with several relevant different operational features. This study employs a DSC technique based on implementing a defined temperature program to two different samples simultaneously (the same T program at the same time), the sample under study and a reference sample. The apparatus measures the difference of the heat flow rate between the sample under study and the reference during the test, to reach the same predefined temperature on each moment.

DSC is the most widespread thermal analysis technique to measure the specific heat of a material. The american standard ASTM 1269E is one of the most utilized procedures to determine this property. The analysis is based on measuring -and comparing- the power to heat the sample and the power to heat a well-known reference material (usually sapphire) [32]. In recent years, a novel method known as Modulated Differential Scanning Calorimetry (MDSC) developed by TA Instruments has emerged as a reliable alternative. In this case, two simultaneous heating cycles are applied to the sample and the reference: a lineal cycle and a sinusoidal cycle "imprinted" onto the lineal cycle. The first cycle is measuring the total heat flow (comparable to the ASTM standard) while the sinusoidal (modulated) heating rate allows the direct calculation of the specific heat [156].

The MDSC method has been successfully employed by several researchers to determine the specific heat of the MSBNFs [32,38,89,97,104,105,107,110,111]. An exhaustive study concluded that the specific heat of MSBNFs obtained by these two mentioned methods were equivalent [38]. However, the MDSC method gives the specific heat of the material without the need of measuring an empty crucible.

3.3.3.2.1 Solar Salt and its nanofluids

The apparatus employed in this work to determine the specific heat of the Solar Salt and the nanofluids based on it was a Differential Scanning Calorimeter Q100 (TA Instruments) with autosampler. It was used to perform the specific heat measurements with MDSC under an isothermal procedure. First, the solid material was dried at 100 ºC at least for 2 hours in an oven to remove the ambient humidity. Then, around 30 mg of the sample were introduced in a T-zero aluminium crucible (Figure 3-9) which was heated on a hot plate before being hermetically sealed afterwards. The crucible filling and sealing was done inside a glove box filled (Unilab plus ECO Mbraun, 200 mbar, argon atmosphere). That guarantees the absence of O_2 (<0.5 ppm) and H_2O (<0.5 ppm). Once inside the DSC, the sample was first stabilized at the desired temperature for an isothermal period of 10 min to achieve the salt thermal equilibrium. The data collection was carried out for 20 min at the same temperature. Nitrogen was used as inert gas inside the device. The specific heat was measured at 196 °C (solid state), 296 ºC and 396 °C (both in liquid state). These temperatures correspond to the working temperatures of the Solar Salt in real conditions.

The temperature modulation of the DSC technique was set-up to 0.6 °C of amplitude and a period of 110 s in order to provide good sensitivity. Three different portions of each sample were measured to obtain a representative result. This measurement method proved to achieve a high precision, as demonstrated in the Journal contribution 2 and Conference contribution 1 [157,158].
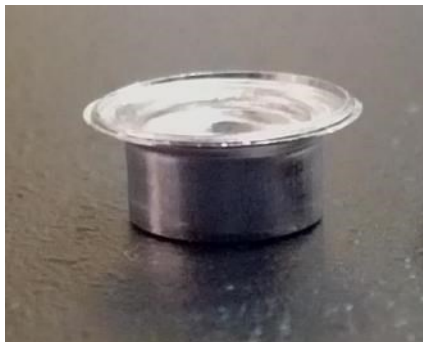
Figure 3-9. T-zero aluminium crucible utilized to the thermal analysis in DSC.

The experimental tests were always performed from the highest to the lowest temperature. Thus, a complete melting of the sample was achieved at the beginning of the experiment (melting temperature of the salt is 238 ºC), which is beneficial in order to obtain the results from the solid state over a compact piece rather than on the initial fine powder. Initially, the sapphire sample commonly used as the reference material was measured under the same protocol to find out the possible device divergence with the theoretical values [159] and to correct the final sample results. The thermal program described is depicted in Figure 3-10.
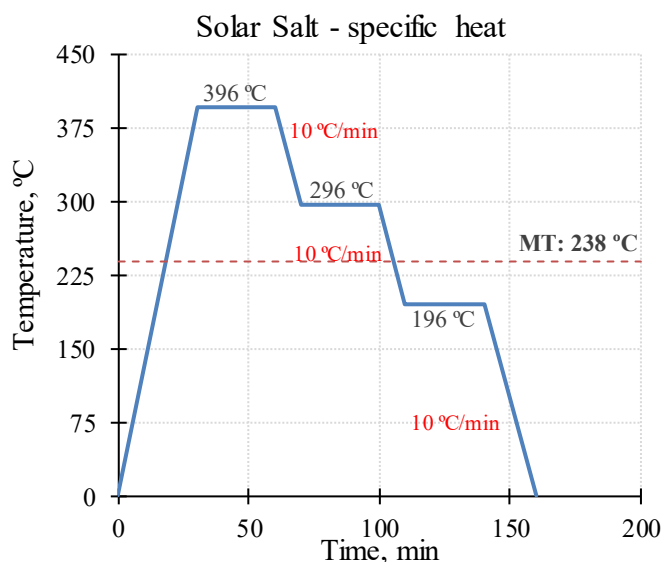
Figure 3-10. Thermal program used to measure the specific heat of the Solar Salt and its nanofluids. The temperatures of the isothermal periods, the cooling rate and the melting temperature (MT) of the Solar Salt are signalled.

3.3.3.2.2 Sodium nitrate and its nanofluids

The determination of the specific heat of the samples of Sodium Nitrate was done in a comparable manner to that of the Solar Salt. The sample preparation and encapsulation was exactly the same. The thermal program in the DSC (Figure 3-11) was adapted to the melting temperature of the Sodium Nitrate (308 ºC) and the objective of using it as PCM. Two isothermal steps at 326 ºC (liquid) and 256 ºC (solid) were conducted to know the specific heat in the liquid and the solid state, respectively. The conditions were the same that described for the Solar Salt samples, with a modulation of 0.6 ºC of amplitude and a period of 110 seconds. The samples were thermally equilibrated at the test temperature during 10 minutes prior to the data collection period (20 minutes).
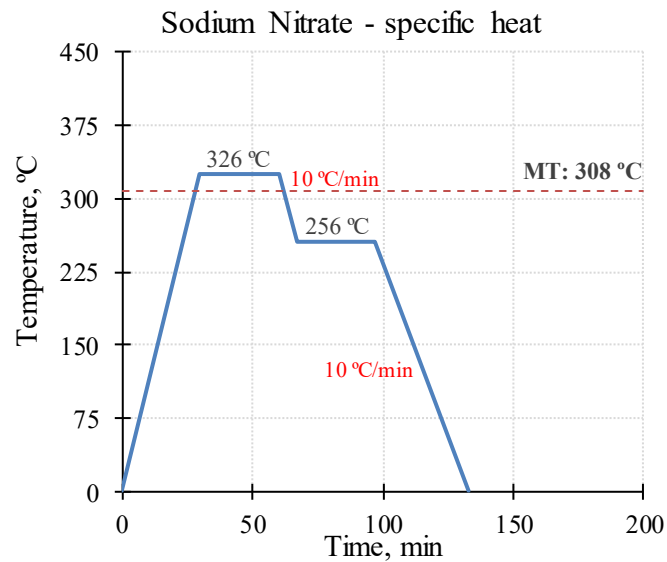
Figure 3-11. Thermal program used to measure the specific heat of the Sodium Nitrate and its nanofluids. The temperatures of the isothermal periods, the cooling rate and the melting temperature (MT) of the Sodium Nitrate are signalled.

3.3.3.3 Latent heat and melting temperature

The phase change properties (latent heat and melting temperature) of the Sodium nitrate and its nanofluids were measured with the aim of using these materials as NePCMs. The analysis was performed in the DSC just after measuring the specific heat as described in the precedent section. The sample was first melted by increasing the temperature up to 350 ºC, followed by two heating and cooling cycles between 350 ºC and 200 ºC at a heating/cooling rate of 10 ºC/min. The results of the latent heat and melting temperature were obtained from the second thermal cycle.

3.3.3.4 Thermal conductivity

The thermal conductivity of the salts and the nanofluids were indirectly determined by means of the thermal diffusivity, which was measured by means of the Laser Flash Analyzer (LFA) technique. This device works by shining a pulsed laser on the sample, which is absorbed by it, leading to a temperature rise at its surface and the propagation of the heat by conduction. The temperature distribution inside the sample depends only on the thermal diffusivity of the material if other conditions remain invariable. Further comprehensive information on this technique can be found elsewhere [160].

The relationship between the thermal conductivity (k) and the thermal diffusivity (α) can be calculated from the Eq. 3-1:

$$k = \alpha \, \rho \, c_p$$

<div align="right">Eq. 3-1</div>

where k is the thermal conductivity (W·m^{-1}·K^{-1}), α is the thermal diffusivity (m^2·s^{-1}), ρ is the density (kg·m^{-3}) and c_p is the specific heat (kJ·kg^{-1}·K^{-1}).

The specific heat of this Eq. 3-1 was obtained from the DSC measurements, as detailed in the precedent section. The density was calculated for each temperature and salt according to the correlations reported in the literature [161].

A laser flash device model LFA427 from Netzsch, with a temperature range from -150 ºC to 2000 ºC was used to measure the thermal diffusivity (α). The tests were conducted under a nitrogen atmosphere with a flow rate of 100 mL/min, a laser voltage of 500 V and a pulse period of 0.80 ms. A platinum holder (ϕ = 12.7 mm, Figure 3-12, left) suitable to contain the molten salt was used in this work. A sample of approximately 92 mg was used for each measurement. Figure 3-12, left shows the empty holder prior to the measurements. An external graphite coating (Figure 3-12, right) is necessary to increase both the absorption of the laser on the sample's front surface and the surface emissivity. A mathematical model considering a composite material structured on three layers (platinum + sample + platinum) is used by the device to calculate the thermal diffusivity [160]. Two portions of each salt or nanofluid were analysed in the LFA. Each of these portions were submitted to the explained experimental program twice. Then, all these data were used to calculate the mean thermal diffusivity and its Standard Deviation (SD), as well as the thermal conductivity results.
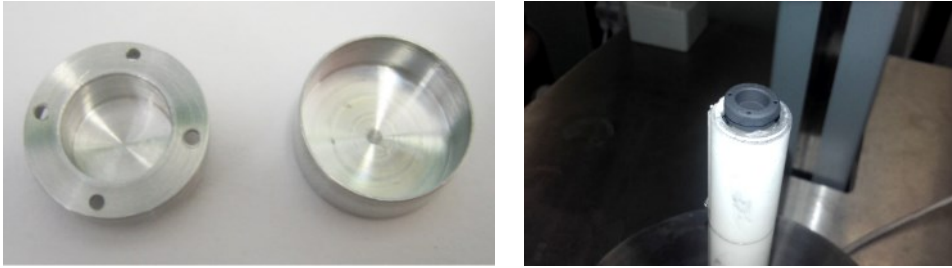
Figure 3-12. Platinum holder (pan and lid) used to contain the salt, empty (left) and coated before the analysis (right).

3.3.3.4.1 Solar Salt and its nanofluids

The study of the thermal conductivity of Solar Salt-based nanofluids nearly inexistent in the literature and the studies are focused in the specific heat. However, the thermal conductivity influences strongly the heat storage and transfer processes. Thus, it is of high interest the evaluation of the increase of this property on the Solar Salt due to the addition of the nanoparticles.

With this objective, the thermal diffusivity of the Solar Salt and its corresponding nanofluids were measured at 25 ºC, 196 ºC, 256 ºC and 396 ºC according to the method described previously. The measurement at 25 ºC was carried out with the aim of comparing the obtained results with those found on the published literature. The measurements were performed from the highest to the lowest temperature.

3.3.3.4.2 Sodium Nitrate and its nanofluids

As stated in the Chapter 1, Sodium Nitrate-based nanofluids are intended to be used as NePCMs due to its appropiate melting temperature (308 ºC) for DSG . The low thermal conductivity of the Sodium Nitrate is a serious drawback for its use as PCM, slowing down the heat transfer rate during the charging and discharging cycles. The addition of nanoparticles could increase this thermal conductivity and the thermal transfer.

To check this hypothesis, the thermal diffusivity of the Sodium Nitrate and its nanofluids were measured at 400 ºC (liquid state), following the described procedure.

3.3.4 Microstructure and composition

The study of the microstructure of the nanofluids is useful to broaden the knowledge of the changes induced by the nanoparticles in the base salt. In this sense, the microstructure of the nanofluid could be linked to the improvement of the thermal properties, as proposed by some authors [30,63,99]. The objectives of this characterization are: to analyse the existence of nanostructures in the salt between the nanoparticles, to confirm the nanoparticles sizes measured

by DLS and to evaluate the homogeneous dispersion of the nanoparticles into the matrix salt.

3.3.4.1 Transmission Electron Microscopy (TEM)

To identify the morphology of the nanoparticles the optical microscopes are unsuitable, and the SEM microscope presents large limitations due to their size range. Accordingly, the size and the shape of the SiNPs and ANPs were observed by means of TEM, using a device JEOL 2100 operating at a voltage of 100 kV.

3.3.4.2 Scanning Electron Microscopy (SEM)

The Scanning Electron Microscopy (SEM) was employed to characterize the nanoparticle clusters on the solid salt, both in the Solar Salt and the Sodium Nitrate-based nanofluids. The SEM analysis was carried out on a field emission scanning electron microscope (FESEM, JEOL, 7001F). Secondary Electrons (SE) and Back Scattered Electron (BSE) images were obtained for each sample, accounting for the relief and the composition of the salt surface respectively. Energy-Dispersive X-ray spectroscopy (EDX), an element analysis technique, was carried out when required.

SE were used to observe the topography of the specimen surface with high resolution. As the intensity of the generated secondary electrons varies depending on the angle of the incident electrons onto the specimen surface, subtle variations of the surface roughness modify the signal intensity, and correspondingly the image obtained on the screen. BSE are mainly used to observe the compositional differences of the specimen. In the case of a polycrystalline specimen, the differences in crystal orientation are observed as the contrast in the image. In addition, the elemental analysis of the images was performed by EDX. Characteristic X-rays generated from the specimen spot where the electrons impact, are detected by a semiconductor detector and converted into electric signals.

The three mentioned signals are originated at different depths on the sample. The electrons come from the main beam of electrons focused onto the sample surface, as seen in Figure 3-13.

The specimen preparation involves placing the sample in the form of solid powder on a microscopy slide. The samples to be tested must be conductive so, due to the low conductivity of the inorganic salts, the specimens were covered with a graphite layer prior to their characterization. Because of the low melting temperature of the nitrates, a voltage of 5 kV was used. A Working Distance (WD) around 10 mm was used to improve the resolution obtained with such a small voltage.
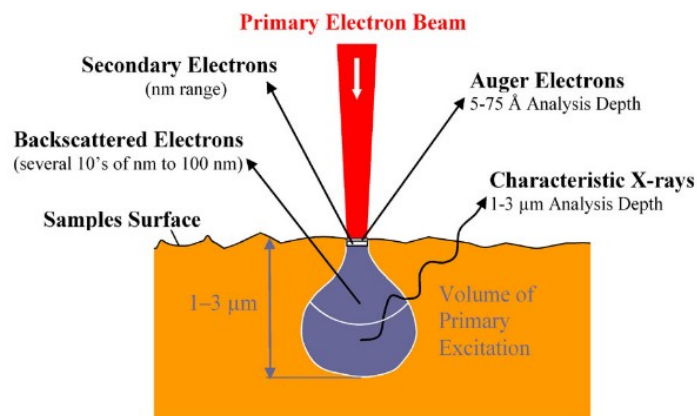
Figure 3-13. Electron beam and sample interaction. (Source: https://www.surfgroup.be/semedx)

3.3.4.3 Crystalline structure

X-ray diffraction (XRD) is generally used to identify the crystallographic composition of a crystalline sample. The intensity of the diffracted X-rays that impacted onto the sample surface is measured as a function of the incidence angle of the rays with respect to the sample surface. The angle of diffraction is related to the crystal lattice parameters. The XRD pattern of each compound is like its fingerprint. XRD is a well-known and mature technique and presently there is a large database of diffraction patterns corresponding to almost any available compound in the world [40]. The database has been formed by the diffraction patterns obtained by many researchers since the beginning of the last century. As a result, the XRD apparatus is aided with a computer system including a database with patterns. Information about the principles and the interpretation of the XRD can be found in books on Materials Science [162,163].

On the present study, a XRD device Bruker D8 Advance was used to evaluate the crystallinity of the nanoparticles, the salts and the nanodoped-salts. The X-ray source was the Cu Kα line (λ=0.154 nm). The angle was scanned with a step size of $0.03°$ and a step time of 2 second.

3.3.5 Long term stability

The stability of the nanoparticles into the molten salt is a great challenge of the MSBNFs. In the traditional nanofluids (based on water or oils) the nanoparticles are stabilized by functionalization or the addition of surfactants, which is very difficult in the MSBNFs due to the high working temperatures. The nanoparticles in the ionic media of the molten salt tend to collide between them, agglomerate and set down. Thus, after this process the nanoparticles may not be longer dispersed into the molten salt and the enhancements of the thermal properties may disappear.

Due to the novelty of the MSBNFs, there are not standard or agreed procedures to evaluate their stability in the long term. An experimental method has been designed, including the visual inspection of the molten nanofluid and its characterization by ICP (nanoparticle percentage), DSC (specific heat) and DLS (nanoparticle size).

The Solar Salt and its nanofluids were melted inside a glass flask and maintained in the liquid state (at 396 ºC) in a furnace for a certain period. Pictures of these flasks were taken after 0.5 h, 1 h and 5 h to further compare the aspect of the nanofluids. These periods of time were selected based on our own experience. In addition to this visual analysis, sampling was done at the same periods of time. As illustrated in Figure 3-14, these aliquots (around 10 mL) were extracted from the middle area of the liquid by a glass pipette and dropped on a glass surface. Once the picture and the sample were taken, the flask was returned into the furnace until the next sampling time. The samples were stored in a dry place for their further characterization, as detailed later.

It is worth mentioning that the sampling should be done in the liquid state rather than get the solid material after cooling it down. Otherwise, the nanoparticles may agglomerate at the bottom during the solidification process, making impossible to analyze their properties under real conditions. To check this assumption, the nanofluid was left at room temperature after finishing the stability test until its solidification. Then, the glass flask was broken and a portion from the middle of the whole sample was extracted and characterized in the same manner as the previous samples.
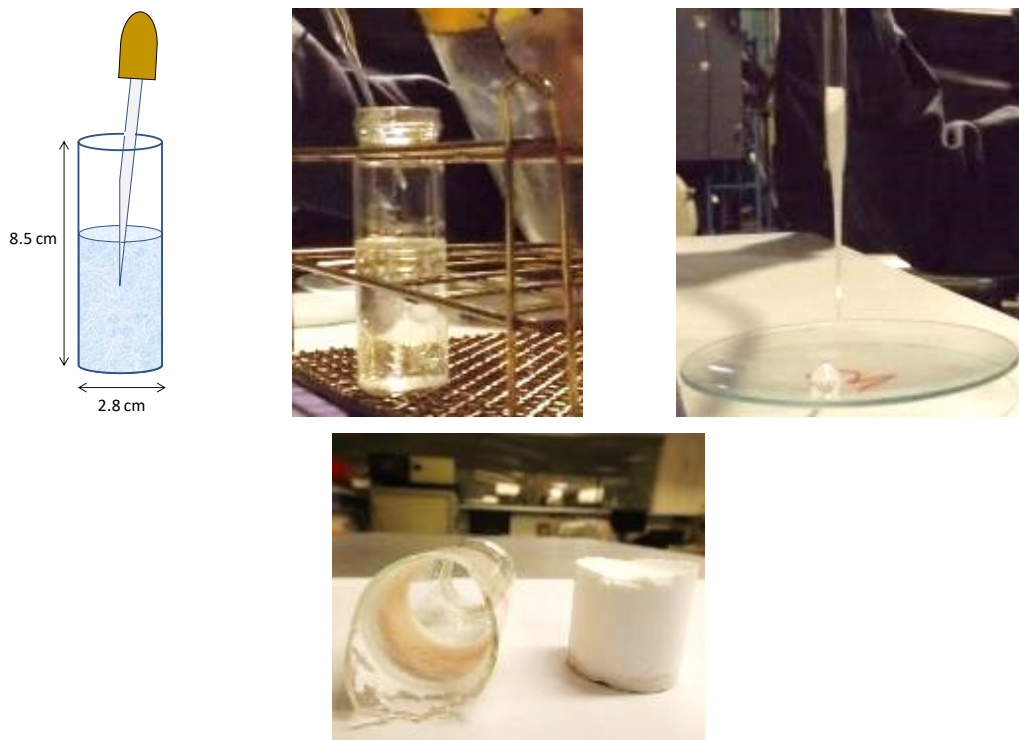
Figure 3-14. Development of the stability test: schematic representation and picture of the flask containing the nanofluid and dropping off the sample in a glass surface (up). Solid sample after the stability test (bottom).

After that, the quantity of ANPs or SiNPs on each nanofluid and its aliquots was measured to find out how many of them remained dispersed on the nanofluid core after a certain period of time. With this aim, the amount of aluminium and silicon was determined by ICP-OES (Thermo ICAP 7400 DUO) by an alkaline digestion. An amount of around 0.1 g of the solid sample was mixed with 1 g of lithium metaborate and put inside a platinum crucible. This mixture was melted in a furnace at 950 ºC for 20 minutes. The molten sample was then extracted in a beaker with an aqueous solution of HCl. The analysis was performed twice for each sample in order to obtain reliable results.

The mass concentration of Al_2O_3 and SiO_2 were determined from the percentages of Al and Si according to the Eq. 3-2 and Eq. 3-3, respectively.

$$\% \, Al_2O_3 = \frac{\% \, Al \cdot [Al_2O_3]_{mw}}{2 \cdot [Al]_{aw}}$$

Eq. 3-2

$$\% \, SiO_2 = \frac{\% \, Si \cdot [SiO_2]_{mw}}{[Si]_{aw}}$$

Eq. 3-3

where the percentages are expressed in mass fraction and *mw* and *aw* means molecular and atomic weight, respectively.

In addition, the nanoparticle size distribution and the specific heat were determined according to the procedures explained in the precedent sections.

3.3.6 Rheology

In spite of the thermal properties of the MSBNFs, their rheology is also of high importance for their industrial implementation as HTFs or in the TES system. The introduction of the nanoparticles into the molten salt may lead to a rise of the viscosity. This will increase the pumping energy required and could occasionally require design changes of some elements. A commitment should be reached between the larger heat transfer rates achieved by the MSBNFs and the higher pumping costs. In addition, heat transfer is directly affected by viscosity because the Reynolds number changes.

The viscosity and the shear stress of the Solar Salt and its nanofluids were measured under different shear rates and temperatures. The rheological study included two approachs:

- <u>Influence of the measuring system.</u> Two different configurations were used: coaxial cylinders and parallel plate. The rheometer features may impact the viscosity results, as reported by Jin et

al. [164]. A coaxial cylinder rheometer consists of an inner concentrically rotating cylinder with an outer stationary cylinder where the test sample is placed, according to the schema shown in Figure 3-15, left. On the other side, a parallel plate rheometer consists of two parallel disks where the sample is placed with an adjustable gap (Figure 3-15, right).

- <u>Influence of the nanoparticle concentration.</u> Nanofluids with RSS as the base fluid and different nanoparticle percentages were tested in one of the parallel plate rheometers. The results were evaluated with the theoretical predictions for these materials.
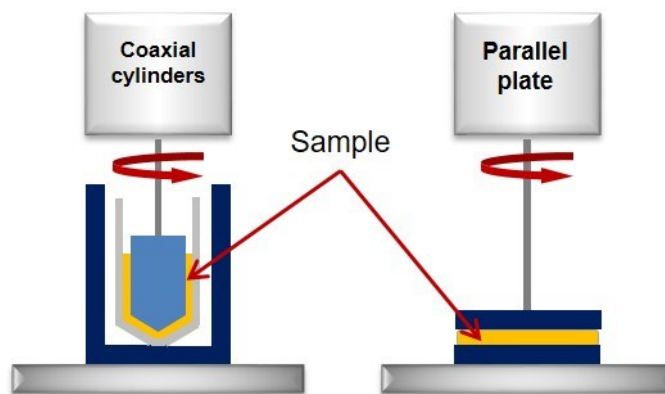
Figure 3-15. Schematic representation of the geometry of the rheometers used in this study: coaxial cylinders (left) and parallel plate (right).

The Table 3-9 summarizes the test conditions established for each of the three rheometers used in this study.

Table 3-9. Experimental conditions of the viscosity measurements carried out with the three rheometers.

	Rheometer 1	Rheometer 2	Rheometer 3
Device	DV-III Ultra, Brookfield Inc.	AR 2000ex, TA Instruments	MCR 3502, Anton Paar
Configuration	Coaxial cylinders	Parallel plate (45 mm)	Parallel plate (35 mm)
Shear rate range, s^{-1}	1-250	100-1000	1-250
Tested temperatures, ºC	250, 270, 290, 300	300, 350, 400	300, 350, 400
Sample amount, g	9	2	1.7
Time for thermal stabilization, min	60	5	5
Number of cycles (1 cycle = min-max-min shear rate)	3	5	2
Shear rate points per range	20	20	36
Time at each shear rate, s	10	10	--
Acquired data at each shear rate	2	1	1

3.3.6.1.1   Coaxial cylinders (Rheometer 1)

The viscosity of the undoped salts the nanofluids were measured with a programmable rotational rheometer (DV-III Ultra, Brookfield Inc., USA) coupled with a furnace (maximum temperature 300 ºC) and a temperature controller. The coaxial cylinders system consists of a cone spindle which is introduced in a sample chamber (Figure 3-16). This assembly is placed inside a closed thermal chamber during the high temperature measurements avoiding the evaporation of the sample. The shear rate testing range was comprised between 1 and 250 s^{-1}. The samples were tested at 250 ºC, 270 ºC, 290 ºC and 300 ºC (Test 1).

Following the recommendations given by the rheometer manufacturer, around 9 g of the solid sample were placed inside the stationary cylinder and melted at the lowest temperature, 250 ºC. After the sample was molten, the spindle was slowly inserted and put into contact with the molten flluid with special care to prevent the formation of any bubble that may alter the results. The sample was held at the test temperature for 60 minutes to reach its thermal equilibrium before collecting the data. Then, three increasing and decreasing shear rate cycles were applied to obtain the different steady state flow curves versus temperature. On each cycle, measurements were taken at 20 different shear rates, 6 points per each shear rate. Once this experimental procedure finished, a new experiment starts by heating up the same previous sample at the next target temperature, 270 ºC, reproducing the same experimental procedure to obtain measurements. This process is repeated at the different temperatures until the last experiment is carried out at 300 ºC. At each new temperature, the sample is thermally equilibrated again for 60 minutes prior to replicate the test. The mean shear stress, the mean viscosity and the Standard Deviation (SD) of the measurements were calculated for each analyzed shear rate. The results for very low shear rates, under 50 s^{-1}, were omitted due to their low repeatability (torque <10%), according to the Brookfield user manual [165].

Figure 3-16. Left: The spindle and the sample chamber used for the rheological tests (Rheometer 1). Right: General view of the rheometer. The spindle is hanged on the device which applies the rotational force and then immersed into the molten salt contained in the sample chamber.

3.3.6.1.2   Parallel plate (Rheometers 2 and 3)

It is well-known that the nanofluid viscosity values may differ depending on the employed rheometer geometry [164]. Thus, with the aim to determine if this could be the case in our samples and in order to attain reliable results, two high temperature rotational rheometers with parallel plate geometry were used. In these rheometers, the tests were done at higher temperatures (300 ºC to 400 ºC) than in the coaxial cylinder device. These temperatures are in the range of the real operating conditions. Unfortunately, the maximum working temperature of the previous rheometer was 300 ºC. The data obtained at this temperature is further used to compare the performance of the two rheometers.

On one side, the samples were measured with a rheometer AR 2000ex, from TA Instruments (Rheometer 2, Figure 3-17, left). About 2 g of the solid sample were placed between the parallel plates with a gap of 0.35 mm. The sample is heated up to the desired testing temperature and then analysed at shear rates between 10 and 1000 s^{-1}. The testing temperatures were 300 ºC, 350 ºC and 400 ºC. Five cycles of increasing and decreasing shear rates were performed on each temperature, to find out the possible time dependency. 20 shear rate measurement-points were defined on each cycle and each measurement lasted 10 s. Because of the little amount of sample needed, the thermal equilibrium is shortly reached. Fresh sample was put on the device to carry out the tests at each temperature.

The viscosity of the samples were also measured on the second parallel plate rheometer (Rheometer 3), an Anton Paar MCR 3502, where about 1.6 g of the solid sample were placed between the parallel plates of the rheometer, fixing a gap of 1 mm between them (Figure 3-17, right). The sample is heated up to the desired testing temperature, and then the test start. The shear rates employed ranged from 10 s^{-1} to 1000 s^{-1}. The testing temperatures were 300 ºC, 350 ºC and 400 ºC.

Figure 3-17. The rheometers with the parallel plate configuration. Rheometer 2: AR 2000ex (left) and Rheometer 3: MCR 302 (right).

It is worth mentioning that parallel plate rheometers require a precise amount of sample to attain reliable measurements (Figure 3-18). Underfilling the container may lead to errors and overfilling it may cause the loss of fluid [166]. The use of these two different rheometers was merely due to their availability on the laboratory at the time of performing the measurements. The main difference between them is the maximum possible shear rate to perform the experiments, while the rest of their features are similar and equivalent. The objective is to compare the results of the nanofluids analysed on each one with those of the coaxial cylinder rheometer.
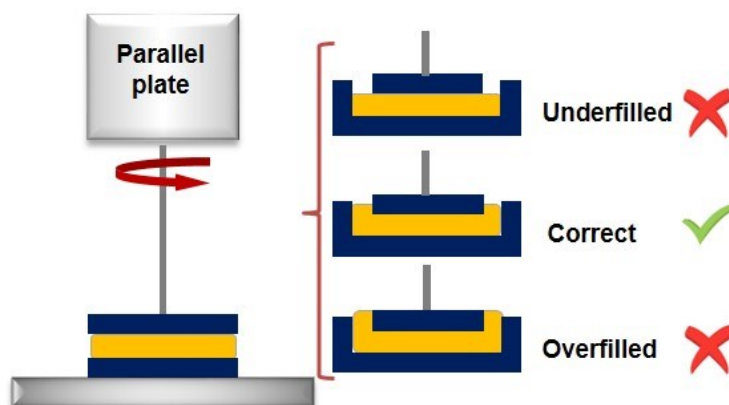
Figure 3-18. The amount of loaded sample into the parallel plate geometry is critical.

3.4 OPTIMIZATION OF EXPERIMENTAL METHODS

3.4.1 Introduction

The assurance of reproducible results with the experimental methods is an essential step before going on with the nanofluid characterization. This section is analysing the reproducibility and the optimization of the more important properties in this research: the specific heat and the nanoparticle size distribution.

The following subsections consist of the reproduction of three contributions concerning the precision and details of the methods used to measure mentioned properties.

3.4.2 Journal contribution 2. A precise method to measure the specific heat of Solar Salt-based nanofluids

Authors: Belén Muñoz-Sánchez, Javier Nieto-Maestre, Gorka Imbuluzqueta-García, Izaskun Marañón-García, Iñigo Iparraguirre-Torres and Ana García-Romero
Abstract: A novel material has been developed for thermal energy storage at high temperatures ([300 °C) with enhanced thermal transport and storage properties. It is considered more efficient than the current molten salts used in the concentrated solar power plants. It is composed of an inorganic salt doped with a small percentage of nanoparticles (NPs), which are claimed to increase the specific heat compared with that of the raw salt. Thus, a precise determination of this thermal property is essential to perceive this enhancement. The specific heat of solar salt (SS) and a mixture of SS with 1 mass% of alumina NPs have been measured by the differential scanning calorimetry (DSC) technique. An isothermal procedure based on modulated DSC has been established to perform the measurements. The influence of the type of crucible, the amount of sample inside the crucible and the presence of moisture on the scattering of the data has been studied. Reliable results with a low uncertainty (\10%) were achieved by the use of T-zero aluminium hermetic crucibles, the mass increment of analysed sample (30 mg) and the absence of moisture inside the crucibles.

3.4.2.1 Introduction

Molten nitrate salts have been of common use in CSP plants to store thermal energy as sensible heat for several decades [167]. More recently, these materials have also been proposed and employed as heat transfer fluid, HTF, to increase the operating temperature and thus the thermal efficiency of the system compared to the industrial thermal oils widely used in these plants [168]. Although the technology of molten salts for CSP is mature, their poor thermophysical properties (specific heat and thermal conductivity) are one of their most challenging problems. The addition

of tiny quantities of nanoparticles to the molten salts has proven to significantly increase their specific heat [38]. In order to quantify the expected enhancement, it is essential to conceive and develop a reliable and precise measurement method.

Differential Scanning Calorimetry (DSC) is the most widespread thermal analysis technique to measure the specific heat of a material. The large scattering of the results is one of the most important issues when measuring this property with a DSC device. There are many factors which could influence the uncertainty of the results within a certain extension. With the aim of establishing a systematic analytical procedure, it is essential to determine and control the sources of variability. In this sense, each material has a different behaviour depending on its nature. Accordingly, the experimental procedures should be adapted to its particular features.

The ASTM 1269E is the most extended procedure to determine the specific heat of a material. The determination is based on measuring -and comparing- the power to heat the sample and the power to heat a well-known reference material (usually sapphire) [32]. In recent years, a novel method known as Modulated Differential Scanning Calorimetry (MDSC) has emerged as a reliable alternative. In this case, two simultaneous heating rates are applied to the sample: lineal and sinusoidal. The first one is the total heat flow analogous to the ASTM standard while the sinusoidal (modulated) heating rate allows the direct calculation of the specific heat [156].

The MDSC method was successfully employed by several researchers to determine the specific heat on Molten Salt-Based Nano Fluids (MSBNF) [32,38,89,97,104,105,107,110,111]. An exhaustive study concluded that the specific heat of MSBNF obtained by these two methods were equivalent [38]. However, the scattering of the results and the associated uncertainty have been highlighted by numerous authors in this field [31,32,38,62,74]. Most of these publications only considered the deviations related to the measuring device. Betts [38] performed an extensive investigation about other sources of variability. The influence of the heating rate and the weight of the sample were analysed. As expected, the weight difference between the sample and the reference (sapphire) had influence on the measurement precision.

Presently, there is still a need to define a procedure suitable for the determination of the specific heat of MSBNF. Increasing the precision of these measurements is still a challenge for the scientific community. Consequently, the main objective of this work consists of establishing an adequate and reproducible procedure to measure the specific heat of SS-based nanofluids. The proposed procedure uses the MDSC method. The influence of factors such as the sort of crucible, the sample weight and the possible moisture contained in the sample was analysed in detail.

3.4.2.2 Materials and Methods

The specific heat of two materials was analysed: the material known as SS (a mixture of 60% $NaNO_3$ and 40% KNO_3 by weight) and the same salt doped with the addition of alumina NPs (1% by weight).

Pellets of industrial grade of $NaNO_3$ (≥98%, SQM industries) and KNO_3 (≥99%, Multi-KGG Greenhouse-grade, Haifa Group) were first crushed in a mortar to obtain a fine powder. The raw materials were dried in an oven at 100 ºC for two hours prior to weigh and then, mixed in the proper quantities to achieve the desired composition. Finally, the mixture was melted to homogenize the sample. The obtained material was hand-milled in a mortar, stored under dry conditions and then employed to perform the thermal analysis. The nanodoped material (SS1A) was prepared by dissolving the SS in deionized water, then adding the necessary amount of alumina NPs. The alumina nanoparticles consisted of a commercial aqueous suspension of 10 nm particles (Alumisol-10A, Kawaken Fine Chemicals, Co.). The water was then removed by heating at 100 ºC. The dried material was melted and cooled down at room temperature. The solid material was milled and manually stirred for homogenization. By milling and mixing the whole sample (about 10 g), the small portion which is filling the crucible (a few mg) is more homogeneous regarding its composition. The representative samples were obtained in this way.

A Differential Scanning Calorimeter (DSC, Q100, TA Instruments) was used to perform the specific heat measurements with Modular Differential Scanning Calorimetry (MDSC) under an isothermal procedure. Several milligrams of the sample were introduced in an aluminium crucible, which was hermetically sealed afterwards. The sample was first stabilized at the desired temperature by an isothermal period of 10 minutes to achieve the salt thermal equilibrium. The data collection was carried out during 20 minutes at the same temperature. The gas atmosphere inside the device to perform all the measurements was nitrogen. Each experiment included the measurement of the specific heat at three different temperatures: 196 ºC (solid state), 256 ºC and 396 ºC (both in liquid state). Following the recommendation of TA Instruments [169,170], the modulation was set up with 0.6 ºC of amplitude and a period of 110 s in order to provide good sensitivityeconds to attain a calibration constant, Kc_p, near to 1.00.

The experimental tests were always performed from the highest to the lowest temperature. Thus, a complete melting of the sample was achieved at the beginning of the experiment (melting temperature of the salt is 220 ºC), ensuring the good contact between the crucible and the material along the measurements, which would have not been the case if the measurements are taken with loose powder material.

By means of the above defined measuring procedure, the influence of the following empirical

parameters was studied: type of crucible (two different types evaluated), mass of the sample (two different amounts) and ambient humidity (three different conditions were employed). To evaluate the influence of these parameters six experiments were defined. The experimental conditions of these experiments are shown on Table 3-10. These experiments were carried out both, with the pure SS and with the SS1A. Each experiment was performed from three to six times with a new sample each time. The weight measurements were carried out using a scale with a precision of 0.01 mg (Mettler Toledo Excellence Plus XP205 Deltarange).

Table 3-10. Description of the experimental conditions.

Experiment reference	Crucible	Sample	Sample weight/mg	Atmosphere	Number of replicas
1	Traditional hermetic	SS, SS1A	10	Ambient	6
2	T-zero hermetic	SS, SS1A	10	Ambient	6
3	T-zero hermetic	SS, SS1A	30	Ambient	6
4	T-zero hermetic	SS	30	Ambient	3
5	T-zero hermetic	SS	30	Ambient (previous heating)	3
6	T-zero hermetic	SS	30	Inert (previous heating)	3

Before the experiments took place, a sapphire sample with a mass of 25.55 mg was measured following the same protocol to find out the possible device divergence with the theoretical values [159] and to correct the final sample results. The sapphire is the most used reference material to perform the calibration of DSC before testing any sample. Its specific heat value is between 0.0949 J g^{-1} K^{-1} and 1.3128 J g^{-1} K^{-1} depending on the temperature (-183.15 ºC to 1376.85 ºC). Höhne and colleagues [155] recommend calibrating the apparatus with a material of similar specific heat to that of the sample under study in order to obtain accurate results. Since the sapphire and the materials under evaluation correspond to ionically-bonded inorganic compounds, their specific heat belongs to a similar order of magnitude, which can be considered an acceptable approach for the development of the measurement and calibration procedure. The experimental specific heat obtained with sapphire at the temperatures of interest was compared to the theoretical values and a calibration constant, Kc_p (theoretical/measured) was calculated. Its value was provided to the device which had into account this little divergence to further correct the sample results.

The uncertainty of the measuring procedure and technique were evaluated by means of the sapphire measurements carried out for calibration. According to the obtained calibration constants Kc_p, the mean uncertainty was under 2%. The uncertainty due to the experimental materials production and sampling was evaluated by the following experiments.

3.4.2.2.1 Influence of the type of crucible

The results from the experiments reference 1 and 2 were used to study the influence of the crucible type on the specific heat determined by MDSC. Two kinds of aluminium crucibles were employed: the traditional hermetic crucible and the T-zero hermetic crucible (Figure 3-19). Six crucibles of each type were filled in with 10 mg of SS sample and then hermetically crimped. The SS and SS1A samples were analysed.

Figure 3-19. T-zero crucibles (left) and traditional crucibles (right). Both are hermetic and made of aluminium.

3.4.2.2.2 Influence of the weight of the sample

The influence of the amount of material on the specific heat was evaluated by producing the same experiment with a different amount of material in each case. The T-zero hermetic crucibles were used, with sample amounts of 10 mg and 30 mg. The results of the experiments referenced as 2 and 3 were used to carry out this study.

3.4.2.2.3 Influence of the sample moisture

The SS is a hygroscopic material and the presence of moisture inside the crucible may increase the scattering of the results. To evaluate this feature, three different experiments were devised (Experiments reference 4, 5 and 6 on Table 1). All these experiments were done with T-zero crucibles with 30 mg of SS, according to the best results obtained from the study of the two previous parameters. Three identical crucibles were analysed on each experiment. On the Experiment reference 4 they were sealed under a non-controlled atmosphere (the normal laboratory ambient). On the Experiment reference 5 they were first filled and heated on a hot plate (above 100ºC) before closing them. On the Experiment reference 6 all the material was inserted into a glove-box (Unilab plus ECO Mbraun, 200 mbar, argon atmosphere) and the crucibles were first filled and heated on a hot plate and then sealed under inert conditions. Although the crucibles of Experiment reference 5 and 6 were previously heated, they quickly lost this heat and were at ambient temperature when closing. This is due to their tiny size and material (aluminium). The existence of an underpressure on these crucibles is discarded.

In order to know the presence of moisture on these samples, the DSC was used to record the heat

flow around 120 °C. The enthalpy of fusion (ΔH_f) measured at this temperature is directly related to the water contained inside the crucible.

3.4.2.3 Statistical treatment of the measurements

In all the experiments carried out in this study the weight of the filled crucibles was registered before and after the experiments to determine if any sample leakage or mass loss could have occurred during the experiment.

The specific heat measurements were replicated three or six times depending on the experiment (Table 3-10) to study the data repeatability. These results were statistically treated afterwards. The mean value, the Standard Deviation (SD) and the Relative Standard Error (RSE) were calculated for each set of data, considering a Student's t-distribution with a 95% confidence interval. These parameters were obtained according to the Eq. 3-4, Eq. 3-5 and Eq. 3-6

$$SD = \sqrt{\frac{\sum_{i=1}^{n}(x_i - \bar{x})^2}{n-1}}$$

Eq. 3-4

where SD is the standard deviation, x_i is an individual measurement, $\bar{x}$ is the mean value of the sample and n is the number of replicas.

$$CI = \bar{x} \pm \Delta x = \bar{x} \pm t_{\alpha/2} \cdot \frac{SD}{\sqrt{n}}$$

Eq. 3-5

where CI is the confidence interval, $\bar{x}$ is the mean value of the sample, Δx is the amplitude of the interval, $t_{\alpha/2}$ is the percentile of the Student's t distribution with a significance level of α and $n\text{-}1$ degrees of freedom, SD is the Standard Deviation and n is the number of replicas.

$$RSE = \frac{\Delta x}{\bar{x}} \cdot 100$$

Eq. 3-6

where RSE is the Relative Standard Error, Δx is the amplitude of the interval and $\bar{x}$ is the mean value of the sample.

3.4.2.4 Results and discussion

3.4.2.4.1 Influence of the crucible type and the weight of the sample

The results of the specific heat collected from the MDSC measurements were analysed according to the mentioned statistical procedure. The mean value, the SD and the RSE are shown in Table 3-11 and for the SS and SS1A samples respectively.

According to these results some trends can be noted. The use of the traditional crucibles (Experiment reference 1) caused a high scattering of the specific heat results at any temperature. The RSE were around 40% in SS and slightly lower in SS1A. These values are far from the target value for reliability (RSE $\leq$ 5%). On the other hand, the scattering was greatly reduced by using the T-zero hermetic crucibles (Experiment reference 2). The RSE was in this case around 9% for both samples, which means that the SS specific heat uncertainty was cut off by 30% and the SS1A by 10% compared with previous RSE results. Although these errors are still higher than the objective, it denotes a clear improvement. The experiments also revealed that the temperature of the experiment had a large influence on the scattering of the results. The measurements on the solid state (196 ºC) showed higher RSE, probably due to the presence of metastable solid phases generated during the cooling process [171]. In the Experiment reference 3 the sample weight inside the T-zero hermetic crucible was increased from 10 to 30 mg. As shown in Table 3-11 and

Table 3-12, the RSEs were near the target and always under 10%. The RSEs of the samples SS1A were higher, as foreseen, because of the typical high heterogeneity of these nanostructured materials. The small percentage of nanoparticles employed in the composition (1 wt%), and the prone agglomeration of these particles, make it feasible that the small samples (mg) required for the measurements in the DSC, extracted from the same batch, could indeed present significant particle-percentage differences.

Table 3-11. Influence of the crucible type and the sample weight on the scattering of the specific heat determined on SS samples (SD = Standard Deviation, RSE = Relative Standard Error).

Temperature/°C		Experiment reference 1	Experiment reference 2	Experiment reference 3
		Traditional crucible, 10 mg	T-zero crucible, 10 mg	T-zero crucible, 30 mg
196	Mean specific heat/J g^{-1} K^{-1}	1.902	2.458	3.910
	SD/J g^{-1} K^{-1}	0.849	0.217	0.102
	RSE/%	46.86	9.26	2.75
256	Mean specific heat/J g^{-1} K^{-1}	1.992	2.521	3.707
	SD/J g^{-1} K^{-1}	0.800	0.228	0.236
	RSE/%	42.14	9.51	6.67
396	Mean specific heat/J g^{-1} K^{-1}	2.142	2.505	3.322
	SD/J g^{-1} K^{-1}	0.762	0.178	0.122
	RSE/%	37.34	7.47	3.85

Table 3-12. Influence of the crucible type and the sample weight on the scattering of specific heat determined on SS1A samples (SD = Standard Deviation, RSE = Relative Standard Error).

Temperature/°C		Experiment reference 1	Experiment reference 2	Experiment reference 3
		Traditional crucible, 10 mg	T-zero crucible, 10 mg	T-zero crucible, 30 mg
196	Mean specific heat/J g^{-1} K^{-1}	1.741	3.431	2.900
	SD/J g^{-1} K^{-1}	0.490	0.222	0.194
	RSE/%	29.56	10.29	7.01
256	Mean specific heat/J g^{-1} K^{-1}	1.633	2.855	2.686
	SD/J g^{-1} K^{-1}	0.381	0.152	0.026
	RSE/%	24.50	8.46	1.02
396	Mean specific heat/J g^{-1} K^{-1}	1.670	2.636	2.832
	SD/J g^{-1} K^{-1}	0.311	0.149	0.234
	RSE/%	19.52	8.98	8.67

There are two features of the SS that may affect the uncertainty of the specific heat results: its low thermal conductivity and its high surface tension [161]. The first property means a low heat transfer rate in the material. Thus, a good thermal contact is essential between the sample, the crucible and the thermocouple of the device. The second factor causes the molten salt to "climb" through the crucible walls, which is known as creeping. This causes an undesirable effect since part of the salt is leaving the bottom of the crucible and loses the contact with the thermocouple which registers the test temperature.

These two features are behind the different results found between the two kinds of crucibles. The dissimilar shapes of the traditional and the T-zero crucibles can be observed in Figure 3-19. A critical detail to be noticed is the flat shape of the T-zero crucible bottom. This feature allows a better thermal contact between the thermocouple and the crucible and, consequently, with the sample (Figure 3-20). The thermal energy is more homogenously carried through the sample and the results uncertainty become lower [40]. However, it is possible to reduce more the RSE in the measurements if the T-zero crucible is filled with a higher amount of the sample (30 mg). The explanation is related to the low viscosity and high surface tension of the SS. When the crucible is filled with 10 mg of the sample, some amount wicks up through the walls in the liquid state and the sensor may lose the contact with this part of the sample (Figure 3-21). If the T-zero crucible is filled with 30 mg of the sample most of its volume is full, so the wicking problem is negligible and the thermal energy transfer is consistent and reproducible. The described behaviour has been observed by Thoms [40]. Höhne and co-workers also state that better contact conditions and higher masses lead to a higher sensitivity of the DSC system [155].
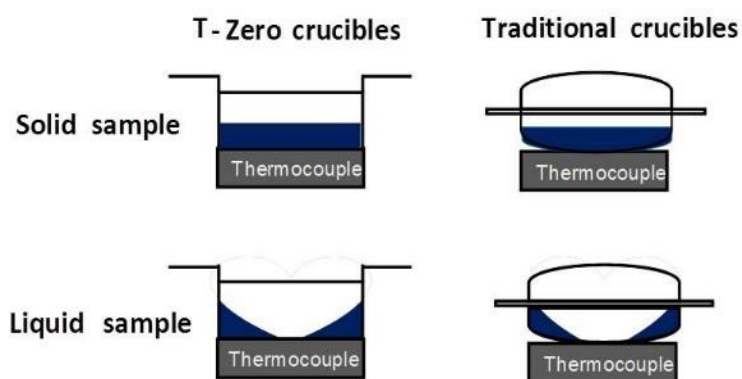
Figure 3-20. Schematic section of the T-zero and the traditional crucibles showing the difference in thermal contact. Adapted from [40].

Figure 3-21. Opened Tzero pan with 10 mg of sample after measurement. The presence of sample on the lid is clearly observed.

It is worth mentioning that the absolute specific heat of SS in these experiments are a bit higher than the literature values [38,61,74,97,104,105,113] despite the increasing accuracy achieved with Experiments reference 2 and 3. The salt absorbs water from the ambient since it is very hygroscopic and these experiments are done outside of a controlled atmosphere. As a consequence, the absolute specific heat may be influenced by the presence of residual water which turns into vapour at the tested temperatures (water vapour specific heat is around 2 J g^{-1} K^{-1} at this temperature range [172]).

Moreover, the increment of the specific heat of SS1A compared to SS is only achieved in the Experiment reference 2 (39, 13 and 5% for each temperature respectively). There is not a clear explanation for this trend yet. There is not a complete agreement in the scientific community about the enhancement of specific heat on molten salts containing nanoparticles. Our research group is currently doing an exhaustive research on this field to confirm if this is occurring systematically or only under very specific conditions.

3.4.2.4.2 Influence of the sample moisture

The impact of any possible moisture contained in the samples has been considered. The SS is a highly hygroscopic material [38], which causes the sample to absorb the humidity from the surroundings very quickly, depending on the ambient humidity and temperature. As a result, each sample prepared under ambient conditions can contain a different amount of salt and water, impossible to control or quantify, which means higher variability of the measurements performed by MDSC.

The results of specific heat, the mean values, the SD and the RSE are presented in Table 3-13 for the Experiments reference 4, 5 and 6 done with the SS. In agreement with these results, the samples which were closed under inert atmosphere (Experiment reference 6) produced the highest precision. The increased RSE of the Experiments reference 4 and 5 can be deemed to the presence of moisture. This is evidenced by the results of the latent heat determined on these experiments at 120 ºC (Table 3-13), which are directly related to the quantity of water contained in the samples.

A graphical analysis is shown in Figure 3-22. An important reduction of the moisture content is achieved by heating the sample inside the crucible before crimping it (Experiment reference 5). The absence of water is evidenced by the lack of a peak on the heat flow registered in Experiment reference 6.

The scattering of the data at the highest test temperature (396 ºC) is strongly influenced by the presence of water in the Experiments reference 4 and 5. The steam generated at this temperature may increase the pressure inside the hermetic crucible and distort the results of specific heat (which is calculated assuming a constant pressure).

In the Experiment reference 6, the RSEs have been greatly reduced compared to the Experiments reference 4 and 5. The errors are in the range of the RSE target (5%) at any temperature. However, it is still possible to increase the results precision if more replicas of the SS are analysed.

Table 3-13. Influence of the sample moisture on the scattering of the specific heat of SS samples
(SD = Standard Deviation, RSE = Relative Standard Error).

Temperature/ºC		Experiment reference 4	Experiment reference 5	Experiment reference 6
		Ambient	Previous heating + ambient	Previous heating + inert
196	Mean specific heat/J $g^{-1} K^{-1}$	1.632	1.605	1.502
	SD/J $g^{-1} K^{-1}$	0.040	0.011	0.038
	RSE/%	6.04	1.77	6.20
256	Mean specific heat/J $g^{-1} K^{-1}$	2.223	1.716	1.703
	SD/J $g^{-1} K^{-1}$	0.031	0.054	0.038
	RSE/%	3.45	7.78	5.54
396	Mean specific heat/J $g^{-1} K^{-1}$	1.619	1.659	1.666
	SD/J $g^{-1} K^{-1}$	0.121	0.155	0.015
	RSE/%	18.60	23.27	2.30
≈120	Enthalpy of vaporization/J g^{-1}	17.79	8.91	---
	SD/J g^{-1}	0.61	0.04	---
	RSE/%	8.51	1.16	---
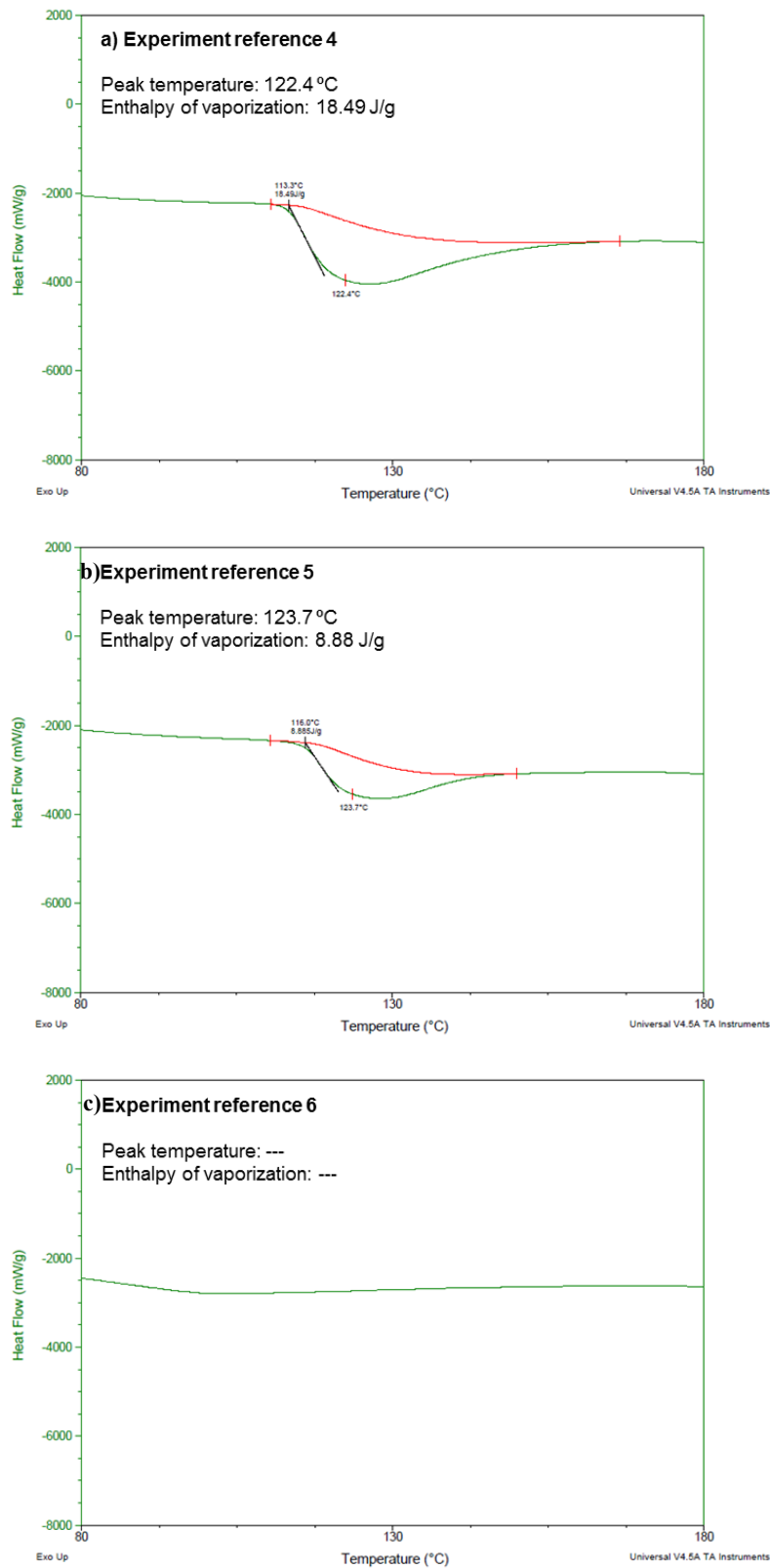
Figure 3-22. Heat flow at around 120 ºC of samples tested under experiments reference 4 (a), 5 (b) and 6 (c). Note the absence of water in Experiment reference 6 (crucible closed under inert conditions).

3.4.2.4.3 Analysis of the combined three factors

The Figure 3-23 shows graphically the RSE of the specific heat values determined on the SS samples analysed according to the three factors investigated on this research: crucible type, sample weight and moisture content. The error percentage is less than 10% in most cases. The best results (RSE≈5%) were found by using T-zero crucibles, filled in with 30 mg of sample and closed under an inert atmosphere (Experiment reference 6).
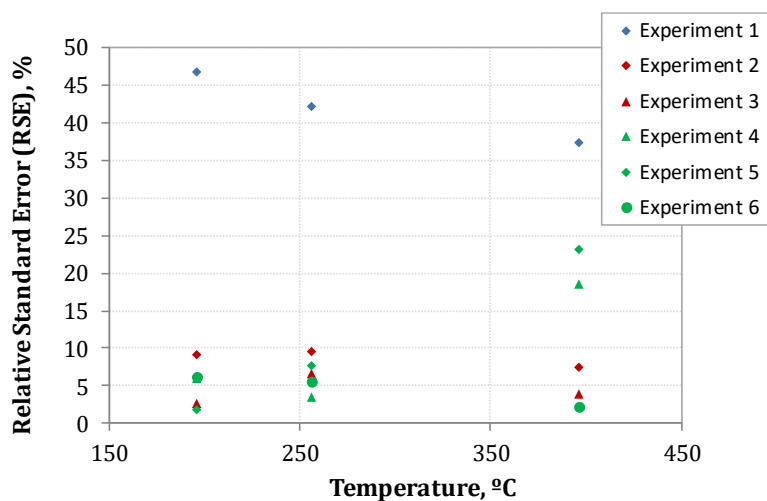
Figure 3-23. The specific heat uncertainty of the SS samples in the performed experiments.

For the sake of comparison, the specific heat of the same materials (SS and SS1A) determined by other authors are gathered in Table 3-14. The SD and RSE have been calculated and included on the table, as well as other important information, like the measurement method and the sample weight.

A graphical comparison of these data is presented in Figure 3-24, where the specific heat and the SD are represented versus the test temperature. The data from the Experiment reference 6 have also been included on the graph. These data cannot be directly compared with each other due to the lack of details about the employed DSC procedure, differences on the salt and the nanoparticle sources and purities as well as the particular details on the synthesis method. Focusing on the DSC method, the number of replicas ranges between three [38,61,97] and six [74]. It is noteworthy to comment that a higher number of measurements does not imply a higher accuracy on the specific heat determination, but increases the precision. The analysis of these results points towards the potential relevance of using a large amount of sample to reduce the uncertainty. The results obtained with larger samples masses (15-25 mg) [104,105] rendered lower uncertainty than those collected from a sample weight around 10 mg [38]. However, in most articles the amount of the sample used in the experiment has not been provided [61,74,97,113].

Table 3-14. Analysis of the uncertainty of specific heat results of SS and SS1A reported by different authors (SD = Standard Deviation, RSE = Relative Standard Error).

Sample	Temperature /°C	Mean specific heat/J g^{-1} K^{-1}	SD /J g^{-1} K^{-1}	RSE /%	N. of replicas	Sample weight/mg	Method	Ref.
SS	313	1.590	0.031	8.39	3	Unknown	Unknown	[61]
	313	1.600	0.012	3.23	3	Unknown	Unknown	[61]
	350	1.580	0.021	5.67	3	8-18	ASTM	[38]
	350	1.523	0.030	9.27	3	7-10	MDSC	[38]
	335	1.480	0.090	16.88	5	Unknown	ASTM	[113]
	170	1.210	0.020	4.59	5	15-25	MDSC	[104,105]
	350	1.470	0.020	3.78	5	15-25	MDSC	[104,105]
	350	1.470	0.042	12.29	3	Unknown	MDSC	[97]
	180	1.191	0.075	16.10	6	Unknown	ASTM	[74]
	373	1.315	0.099	19.35	6	Unknown	ASTM	[74]
SS1A	350	1.923	0.080	17.63	3	6-17	ASTM	[38]
	350	1.823	0.037	6.51	3	8-10	MDSC	[38]
	350	1.820	0.050	11.82	3	Unknown	MDSC	[97]
	180	1.324	0.015	3.15	5	Unknown	ASTM	[74]
	373	1.566	0.014	2.48	5	Unknown	ASTM	[74]
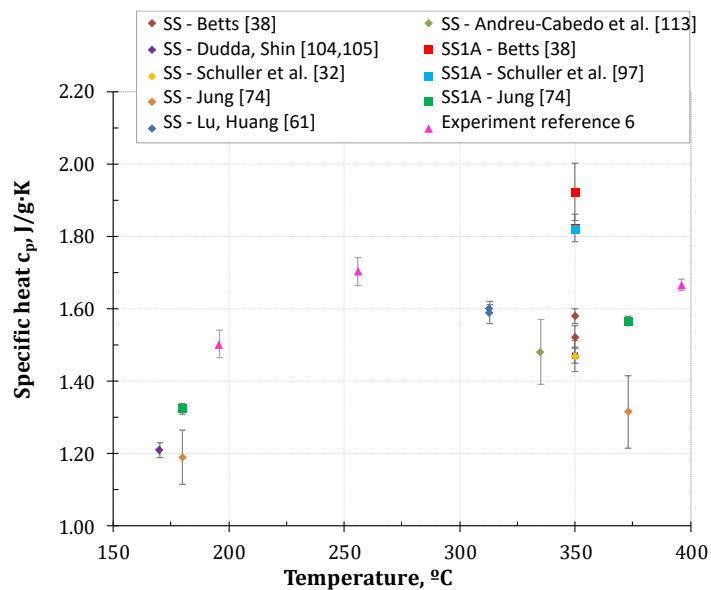
Figure 3-24. The specific heat (and the Standard Deviation, SD) of SS and SS1A versus the test temperature in the published articles. The data from the Experiment reference 6 are also included.

The influence of the kind of crucible has not been analysed on any of these articles, neither the potential presence of humidity on the sample. As a result, the amount of the sample inside the crucible is the crucial factor to reduce the scattering of the results on these measurements.

However, according to the results the absence of humidity during the preparation and the experimental manipulation of the samples is the most important factor to ensure a good precision.

Indeed, this factor could explain why the scattering is reduced when the amount of material employed is higher and the preparation and measurement is carried out without humidity control. If small amounts of material are used, the samples will be fully saturated by the moisture existing on the laboratory atmosphere. On the contrary, the water absorption of large samples will be relatively low and the global humidity percentage on large samples will be low in comparison to small samples.

As a result, the testing procedure developed in the present work requires a controlled atmosphere cabinet (glove-box) to carry out the sample preparation. Further research is required to quantitatively analyse the water uptake in relation to the atmospheric relative humidity of the laboratory. A deep knowledge of this aspect could lead to develop a new procedure that might not require the use of a glove-box.

It is worth mentioning that the authors have been recently involved in a Round Robin Test about the specific heat of Solar Salt [173]. Nine partners were taking part on the experiments, including universities, research centres and private companies. The sample provided by the organizers was analysed according to the procedure developed in this research and the values of specific heat were within the average. This may denote the suitability and accuracy of the present method at measuring this kind of samples.

3.4.2.5 Conclusions

The determination of the specific heat of SS and nanodoped SS by means of the DSC usually yields a large scattering of the results due to several different factors. This study has evaluated the potential influence of the kind of crucible used on the DSC, the weight of the sample and the moisture contained on the sample.

The use of flat-bottom crucibles (T-zero) instead of the traditional non-flat bottom crucibles helps in reducing the scattering of the results. This has been attributed to the better contact between the material and the crucible on the flat-bottom crucibles.

The weight of the sample is an important factor to reduce the scattering of the results. The use of large samples improves the precision of the results. Several factors could be responsible for this

behaviour, including the better contact between the sample and the sensor and the presumably lower humidity absorption percentage. However, further research is required to elucidate this assumption.

The moisture absorbed by the sample during the manipulation to prepare the DSC specimens has shown to be the crucial factor to reduce the scattering of the results. The RSE is below 5% when the samples have been treated to remove any absorbed humidity and the DSC specimens are prepared in a controlled atmosphere in absence of moisture.

The lowest scattering was found when the T-zero type crucibles were used, filled in with 30 mg of the sample and sealed under an inert atmosphere. The specific heat was determined according to a MDSC method with several isothermal stages. On these conditions, the RSE of the measurement is around (and even below) 5%, both for the SS and for the nanodoped SS (SS1A). This error represents a very low uncertainty.

A reliable and precise procedure to determine the specific heat with the MDSC method has been established. The approach developed by this work is suitable for a particular material composed of solar salt and 1% by weight of alumina nanoparticles. A relative error not larger than 5% can be guaranteed when following this procedure.

The samples should be prepared under an inert atmosphere. It is also recommended to use a large amount of sample (30 mg) and a T-zero hermetic crucible to improve the precision of the results.

The experimental MDSC program recommended for determining the specific heat of SS and nanodoped SS (SS1A) consists of an isothermal procedure with 10 minutes of thermal stabilization followed by 20 minutes of data collection. The modulation parameters are 0.6 ºC of amplitude and a period of 110 seconds.

3.4.3 Conference contribution 1: Round Robin Test on the Measurement of the Specific Heat of Solar Salt

Authors: Belén Muñoz-Sánchez, Javier Nieto-Maestre, José González-Aguilar, José Enrique Julia, Nuria Navarrete, Abdessamad Faik, Thomas Bauer, Alexander Bonk, María Elena Navarro, Yulong Ding, Nerea Uranga, Elisabetta Veca, Salvatore Sau, Pau Giménez, Pierre García and Juan Ignacio Burgaleta

Abstract. Solar salt (SS), a well-known non-eutectic mixture of sodium nitrate (60 wt%) and potassium nitrate (40 wt%), is commonly used either as Thermal Energy Storage (TES) material (double tank technology) or Heat Transfer Fluid (HTF) (solar tower) in modern CSP plants worldwide. The specific heat (c_p, kJ·kg^{-1}·K^{-1}) of SS is a very important property in order to support the design of new CSP Plants or develop novel materials based on SS. A high scientific effort has been dedicated to perform a suitable thermophysical characterization of this material. However, there is still a great discrepancy among the c_p values reported by different authors [174]. These differences may be due to either experimental error (random or systematic) or divergences in the starting material (grade of purity, presence of impurities and/or water). In order to avoid the second source of uncertainty (the starting material), a Round Robin Test (RRT) was proposed starting from a common material. In this way, the different methods from each laboratory could be compared. The study should lay the foundations for the establishment of a systematic procedure for the measurement of the specific heat of this kind of materials. Nine institutions, research centres and companies, accepted the proposal and are contributing with their results. The initiative was organized within the Workshop SolarPACES Task III – Material activity.

3.4.3.1 Introduction

A precise determination of the c_p of the Solar Salt is essential to fulfil both research and industrial purposes. The investigation of new TES materials, the design of novel industrial TES systems and the improvement of their effectiveness are based on this property. With these aims, the analytical technology is improving day by day to achieve more accurate results and reduce the measurement errors in order to comply with the requirements of industry. Nowadays, the most widespread thermal analysis technique to measure the c_p is the Differential Scanning Calorimetry (DSC).

The sources of uncertainty for the c_p measurement can be classified in two main groups:

- Device precision: the experimental errors from the devices employed in the measurement (balance, DSC or other calorimeter) and their use (human error), they are also divided in random and systematic.

- Starting material: the divergences on the starting material: lack of homogeneity, presence of impurities or moisture.

The experimental errors are not easily minimized. The device supplier (DSC or other) usually reports a certain error for the equipment. However, the final error is the sum of many factors. For example, the calibration of the equipments (balance, DSC) is very important, as well as the skills of the person who will perform the measurements. In most cases, the final error is strongly influenced by the method of measurement. The election of the measurement method should be adapted to the properties of the material. The provider usually recommends the proper method for the application requested by the customer. In this way, there are standards that are commonly accepted for specific materials, but the technology is advancing and these standards should be revised periodically.

In order to avoid the divergences on the starting material, it is strongly recommended to assure that the sample is representative of the starting material. Performing the measurements on different samples from the same starting material may reduce the errors due to the lack of homogeneity. In the case of thermal characterization, it is essential to remove traces of water from the sample prior to measurements. The presence of humidity may induce errors for two reasons: part of the weight introduced in the device for the c_p measurement corresponds to water, and that the c_p of water (4.18 $kJ \cdot kg^{-1} \cdot K^{-1}$ at 25ºC) is much higher than the sample one.

With the aim to compare different techniques of measurement, it is essential to eliminate the uncertainties due to the starting material. In this way, a RRT becomes a powerful tool to compare the methods and devices employed by different laboratories. The same sample is delivered to all the partners involved in the RRT. All the partners do the same conditioning treatment prior to analysis. Therefore, the errors can only be attributed to the equipments and the methods employed by each partner.

3.4.3.2 Aim

The aim of this work is to perform a RRT for the measurement of the c_p of SS. The different methods of measurement of c_p will be compared for this specific application.

3.4.3.3 Method

3.4.3.3.1 Sample Preparation and Conditioning

Sodium nitrate (Labkem, analytical grade) and potassium nitrate (Labkem, analytical grade) were dried at 100 ºC overnight in an oven (Raypa). A SS batch (120 g) was prepared by mixing 72 ± 0.1 g of sodium nitrate with 48 ± 0.1 g of potassium nitrate. (60:40 wt%). The mixture was homogenized and melted in a furnace (Nabertherm) at 350 ºC for ½ h. After being cooled, the SS was milled and stored under dry conditions.

Prior to the sample preparation, the SS batch was dried in an oven at 100 ºC for 1 hour. Nine samples were prepared by weighing enough quantity to perform the measurements (~ 2 g) from the SS batch under argon and dry atmosphere (<0.5 ppm O_2, <0.5 ppm H_2O) using a glovebox (mod. UNIlabplus ECO, Mbraun). Samples were closed inside the glovebox and stored under dry conditions. Samples were delivered to participants within silica gel in order to protect them from moisture. The samples were dried for 1 hour prior to be measured.

3.4.3.3.2 Standard ASTM E1269

The standard ASTM E1269 [175] is the most accepted procedure to measure the c_p of materials. Three different heat flow measurements are required for the specific heat calculation: blank curve (two empty crucibles), sapphire curve (a crucible with a certified sapphire disc in the sample side and an empty reference crucible) and sample curve (a crucible with salt in the sample side and an empty reference crucible).

The specific heat determination requires the use in the temperature program of an isothermal segment, followed by a dynamic segment where the data are collected, and a final isothermal segment because the signal needs to be stabilized (isothermals) before and after the dynamic segment.

3.4.3.3.3 MDSC Testing

TA Instruments developed an innovative technique [176] to measure the c_p based on the registration of the heat absorbed (or released) by the sample when a modulated heating rate (changing heating rate) is superimposed on top of a linear heating rate. This modulation is defined by the amplitude (A, ºC) and the cycle time (s). MDSC can be applied either on dynamic or isotherm methods. The main advantage of this technique is that one single experiment is required to obtain accurate results.

3.4.3.3.4 Calorimeter SETARAM

The principle of working of this calorimeter is similar to DSC, but in this case the volume of cell is 12 cm^3. The use of higher amounts of sample would hopefully lead to lower errors. This device allows a correct calibration of the measure thanks to its reference cell. It features a high precision Calvet 3D detector with a thermocouple network totally surrounding the reference cell and the sample cell so that heat flux could be measured in every direction. The calorimeter measures the heat flux difference between the sample and a reference material subjected to the same temperature variations under a controlled atmosphere, and thus allows calculating the corresponding c_p of the sample material.

3.4.3.4 Description of the Methods

The description of the methods used by the partners is shown in Table 3-15 (dynamic) and Table 3-16 (isotherm). The partner 1 performed several measurements using different methods, therefore it appears in four rows (2 dynamic and 2 isotherm). Basically, in dynamic methods, the measure of c_p is done during a heating or cooling ramp. Before and after the heating ramp, there is an isotherm step. The parameter ΔT means the interval of temperatures where the heating ramp is applied (between isothermal steps). The range of temperatures (Range T) is the complete range of measurement. In the case of isotherm methods, the measurements are performed as fixed temperatures also indicated. The parameter Est (min) indicates the time for stabilization at the temperature of measurement. The modulate parameters are also specified (amplitude and period) where MDSC was used.

Some other parameters about the crucible: the atmosphere (Atm) inside the crucible (argon or air), the material of the crucible (M), the type (hermetic or non-hermetic), the sample weight and the number of replica for the same starting material are also shown in Table 3-15 and Table 3-16.

Table 3-15. Description of dynamic methods used by different partners to perform the c_p analysis.

			PARAMETERS						CRUCIBLE				
				MDSC								Sample Weight	N
			Ramp	ΔT	A	t	Range T	Flow	Atm	M	Type		
P	Device	Method	ºC/min	ºC	ºC	s	ºC					mg	
1	Mettler Toledo (DSC2)	ASTM E1269	20	130	n.a	n.a.	370-500	N₂	Air	Al	40µl pinhole	10-15	6
1	TA Instruments (Q2000)	MDSC	5	320	0.5	60	80-400	N₂	Air	Al	T-zero	10-22	3
2	TA Instruments (Q2000)	MDSC	2	390	1	120	50-440	N₂	Ar	Al	T-zero	25	3
3	Netzsch (DSC 204)	ASTM E1269	10	300	n.a	n.a.	150-450	N₂	Air	Pt	no hermetic	22-25	3
4	Mettler Toledo (DSC1)	DIN 51007	30/10	50	n.a	n.a.	50-550	Air	Air	Al	40µl pinhole	25	4
5	Mettler Toledo (PDSC132)	ASTM E1269	10	50	n.a	n.a.	170-420	N₂	Air	Al	40µl pinhole	13	2
6	Mettler Toledo (DSC2)	ASTM E1269	20	50	n.a	n.a.	175-475	N₂	Air	Al	40µl sealed	20-21	4
7	Mettler Toledo (DSC2)	ASTM E1269	10	425	n.a	n.a.	25-450	N₂	Air	Pt	no hermetic	25	3

*P = Partner, Ramp = heating rate, ΔT = gradient of temperatures between isotherm steps. A = amplitude. t = period. Range T = range of measurement temperatures. Flow = flow gas during measurement. Atm = gas inside the crucible. M = material crucible. T-Zero = hermetic Al pan & lid from TA Instruments. N = number of replica

Table 3-16. Description of isotherm methods used by different partners to perform the c_p analysis. All measurements were performed under a constant N_2 flow in the device.

P	Device	Method	Est. min	Meas. min	A °C	t s	Temperatures °C	Atm	M	Type	Sample Weight mg	N
			\multicolumn{5}{c	}{MDSC}				\multicolumn{2}{c	}{}	
1	TA Instruments Q2000	MDSC	0	20	0.5	60	400/350/300	Air	Al	T-zero	10-22	3
1	TA Instruments Q2000	MDSC	2	15	0.5	60	400/350	Air	Al	T-zero	15-25	4
8	TA Instruments Q1000	MDSC	20	10	0.6	110	400/300/200	Ar	Al	T-zero	26-27	3

*P = Partner. Est. = stabilization time. Meas = measurement time. A = amplitude. t = period. Temp = measurement temperatures. Atm = atmosphere inside the crucible. T-Zero = hermetic Al pan & lid from TA Instruments. M = material. N = number of replica.

3.4.3.4.1 Specific Heat Result Analysis

The c_p results provided by the partners were statistically treated according to the following procedure [177]. The mean, the Standard Deviation (SD) and the Relative Standard Error (RSE) were calculated for each set of data, considering a Student's t-distribution with a 95% confidence interval. These parameters were obtained according to the Eq. 3-7, Eq. 3-8 and Eq. 3-9.

$$SD = \sqrt{\frac{\sum_{i=1}^{n}(x_i - \bar{x})^2}{n-1}} \qquad \text{Eq. 3-7}$$

where SD is the standard deviation, x_i is one of the individual measurements, $\bar{x}$ is the mean value of the sample and n is the number of replicas.

$$CI = \bar{x} \pm \Delta x = \bar{x} \pm t_{\alpha/2} \cdot \frac{SD}{\sqrt{n}} \qquad \text{Eq. 3-8}$$

where CI is the confidence interval, $\bar{x}$ is the mean value of the sample, Δx is the amplitude of the interval, $t_{\alpha/2}$ is the percentile of the Student's t distribution with a significance level of α and n-1 degrees of freedom, SD is the standard deviation and n is the number of replicas.

$$RSE = \frac{\Delta x}{\bar{x}} \cdot 100 \qquad \text{Eq. 3-9}$$

where RSE is the Relative Standard Error, Δx is the amplitude of the interval and $\bar{x}$ is the mean value of the sample. The RSE should not be confounded with the Relative Error (RE) that is calculated as the Absolute Error (AE) divided by the average of a finite number of samples:

$$RE = \frac{x_i - \bar{x}}{\bar{x}} \cdot 100 \qquad\qquad \text{Eq. 3-10}$$

The RE gives an idea of the dispersion of each individual measurement with respect to the average among them.

3.4.3.5 Results

The results reported by all the partners are shown in Figure 3-25. As it can be seen in the graphic, some c_p values are highly deviated from the average (inside red lines). The measurements resulted from the calorimeter SETARAM C80 were anomalous, and highly dispersed. Therefore, they are not presented. Further research should be done to achieve more confident results with this technique. A statistical analysis will be done.
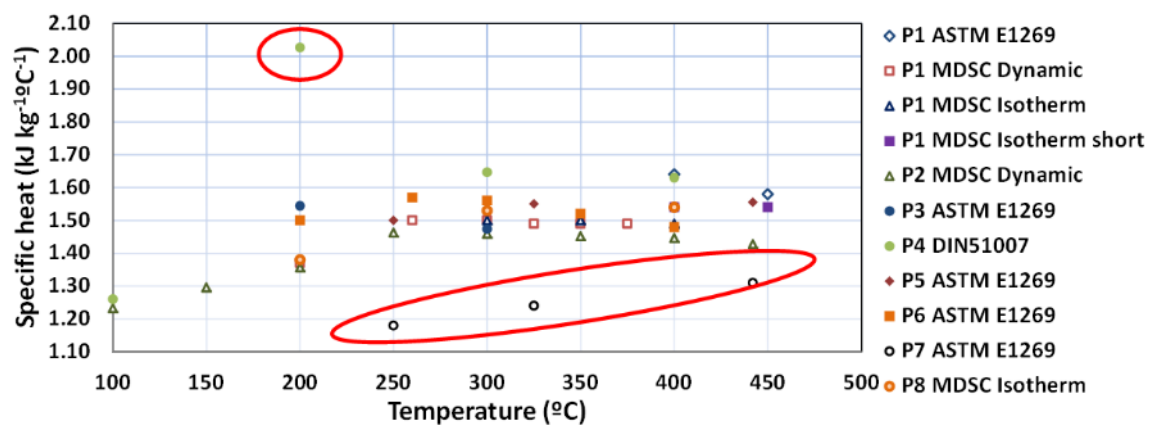
Figure 3-25. Results reported by the partners of the RRT on the measurement of c_p of SS.

In order to compare the accuracy of the results, three temperatures were selected (200 ºC, 300 ºC and 400 ºC), Figure 3-26 and Figure 3-27 show the SD and the RSE (%) calculated by the expressions Eq. 3-7 and Eq. 3-9 from the measurements reported by each partner. Partner 5 only provided two measurements (from two crucibles), the RSE is very high and no representative for this small number of samples. For this reason, it was omitted. The SD of Partner 5 is in the order of magnitude of the other partners.

The SDs are lower than 0.1 kJ·kg^{-1}·K^{-1} for all the partners except Partner 7, and in the order of 0.05 kJ·kg^{-1}·K^{-1} in most cases. Regarding to RSE (%), it was lower than 10% for all the partners except Partner 7. This limit of RSE (10%) can be considered too high. However, due to the low amount of measurements (in the order of 3-4 for most of the partners), it can be considered acceptable.
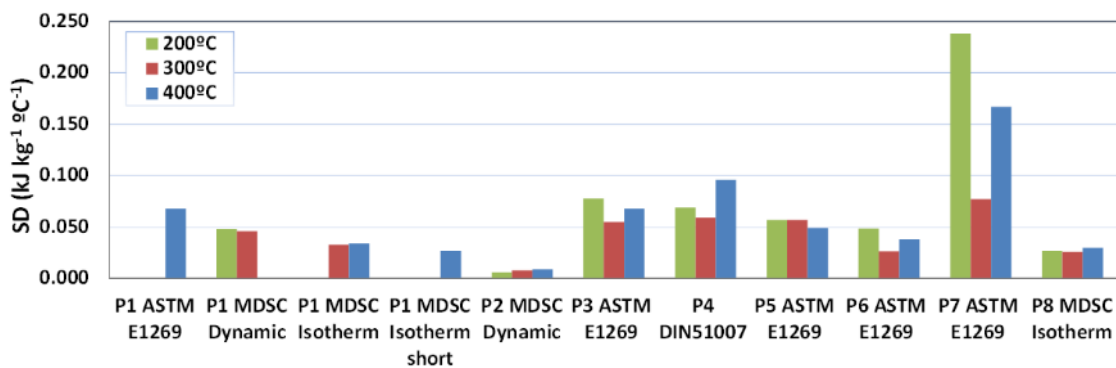
Figure 3-26. SD ($kJ \cdot kg^{-1} \cdot K^{-1}$) calculated from the results reported by each partner according to Eq. 3-7.
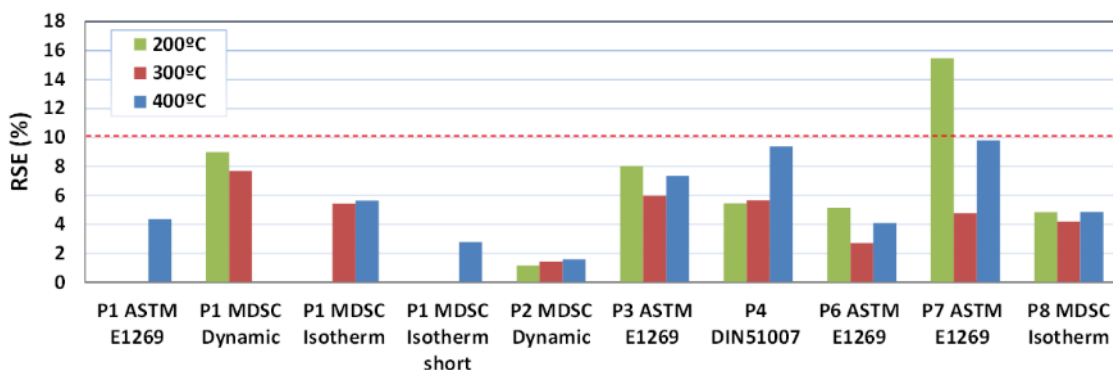
Figure 3-27. RSE (%) calculated from the results reported by each partner according to Eq. 3-9.

Table 3-17 shows the average of the c_p measurements at the three selected temperatures (200, 300 and 400 ºC) performed by all the partners. The average values shown in this table are graphically represented in Figure 3-25. Taking into account the measurements from all the partners, the SD and RSE are too high. This fact reveals a high dispersion between the results. The relative error (RE) of the measurement of each partner was calculated according to Eq. 3-10. REs from Partners 4 and 7 were higher than the rest (36.75% and 20.38% at 200ºC). Particularly, the c_p measurements of Partner 7 are more dispersed between them than the other partners' ones (Figure 3-26 and Figure 3-27). The origin of these deviations is not well known, but these results have been not considered for further statistical analysis. The revised results are shown in Table 3-18.

It can be concluded that the average values for the c_p of SS, according to the partners' results, are 1.442 $kJ \cdot kg^{-1} \cdot K^{-1}$ (200 ºC), 1.510 $kJ \cdot kg^{-1} \cdot K^{-1}$ (300 ºC) and 1.521 $kJ \cdot kg^{-1} \cdot K^{-1}$ (400 ºC). Table 3-18 shows an acceptable RSE, lower than 6% for the three temperatures. The c_p results are represented graphically in Figure 3-28, all the c_p measurements are within the interval between 1.20 and 1.65 $kJ \cdot kg^{-1} \cdot K^{-1}$. After the revision of results (Table 3-18), there are no REs higher than 10%, and most of them are lower than 5%.

There is some discrepancy on the c_p values at 200 ºC resulted from methods based on ASTM E1269 standard with respect to those derived from MDSC methods as shown in Figure 3-28. The MDSC methods produce lower results at this temperature than those produced by ASTM E1269-

based methods, independently of the temperature program used (dynamic or isotherm). At 200 ºC, the dispersion between the MDSC results is extremely low. The reason of this is not clear, maybe the lower conductivity of the salt in the solid state has an effect on the c_p measurement, or maybe there is an endothermic process like a change on crystallinity at this temperature, or the proximity of the melting point (220ºC). Even, it is not well-known which of the measured values is more accurate.

Table 3-17. Average values of c_p ($kJ \cdot kg^{-1} \cdot K^{-1}$) measurements performed by the partners.

	c_p ($kJ \cdot kg^{-1} \cdot K^{-1}$)			RE (%)		
	200ºC	300ºC	400ºC	200ºC	300ºC	400ºC
Partner 1 ASTM E1269			1.640			8.53
Partner 1 MDSC Dynamic	1.370	1.500		7.57	0.30	
Partner 1 MDSC Isotherm		1.500	1.490		0.30	1.40
Partner 1 MDSC Isotherm short program			1.540			1.91
Partner 2 MDSC Dynamic	1.357	1.459	1.446	8.45	2.44	4.31
Partner 3 ASTM E1269	1.544	1.474	1.480	4.17	1.44	2.06
Partner 4 DIN51007	2.027	1.647	1.630	36.75	10.13	7.87
Partner 5 ASTM E1269	1.500	1.550	1.555	1.20	3.64	2.91
Partner 6 ASTM E1269	1.500	1.560	1.480	1.20	4.31	2.06
Partner 7 ASTM E1269	1.180	1.240	1.310	20.39	17.09	13.31
Partner 8 MDSC Isotherm	1.380	1.530	1.540	6.90	2.30	1.91
Media	1.482	1.496	1.511			
SD	0.248	0.111	0.095			
RSE (%)	14.00	5.70	4.50			

Table 3-18. Average values of c_p ($kJ \cdot kg^{-1} \cdot K^{-1}$) measurements, removing Partner 4 and 7.

	c_p ($kJ \cdot kg^{-1} \cdot K^{-1}$)			RE (%)		
	200ºC	300ºC	400ºC	200ºC	300ºC	400ºC
Partner 1 ASTM E1269			1.640			7.80
Partner 1 MDSC Dynamic	1.370	1.500		4.98	0.69	
Partner 1 MDSC Isotherm		1.500	1.490		0.69	2.06
Partner 1 MDSC Isotherm short program			1.540			1.22
Partner 2 MDSC Dynamic	1.357	1.459	1.446	5.88	3.40	4.95
Partner 3 ASTM E1269	1.544	1.474	1.480	7.09	2.41	2.72
Partner 5 ASTM E1269	1.500	1.550	1.555	4.03	2.62	2.21
Partner 6 ASTM E1269	1.500	1.560	1.480	4.03	3.28	2.72
Partner 8 MDSC Isotherm	1.380	1.530	1.540	4.29	1.30	1.22
Media	1.442	1.510	1.521			
SD	0.082	0.038	0.061			
RSE (%)	5.95	2.32	3.35			
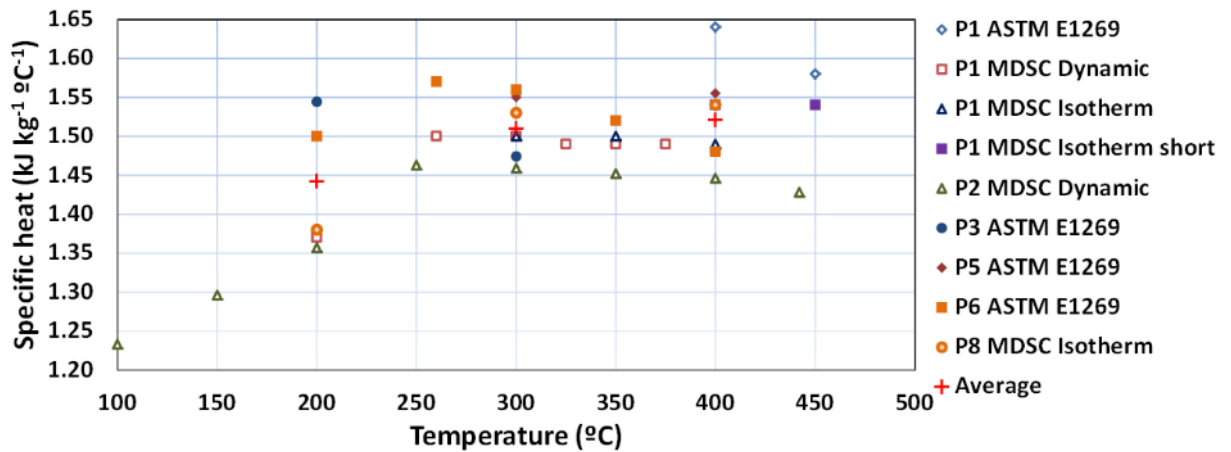
Figure 3-28. Results reported by the partners 1, 2, 3, 5, 6 and 8 on the measurement of c_p of SS.

In the liquid state, no conclusions can be deduced about the goodness of the methods used. The deviations are very low for almost all partners. Only Partner 1, using an ASTM E1269-based method gave higher c_p values at 400 ºC (1.64 kJ·kg⁻¹·K⁻¹) than the others. However, the measurements performed by Partner 1 following the ASTME1269 standard are very dispersed (SD > 0.05 kJ·kg⁻¹·K⁻¹).

3.4.3.6 Conclusions

A RRT on the measurement of the c_p of SS was done involving 9 Partners. Eight of them used DSC devices. One of the partners used a calorimeter SETARAM C80. Each partner performed the cp test according to their own criteria and routine. The usual standard ASTM E1269 employed to the cp determination in a wide diversity of materials was shown to be adequate for the Solar Salt in terms of low results scattering. In addition, the MDSC method developed by the DSC supplier TA Instruments, also demonstrated its suitability.

The next step on this research work will be the selection of the best measurement method with the standard ASTM E1269 and MDSC. All the partners will perform the tests under the same conditions to determine the cp of the Solar Salt with a high level of accuracy.

3.4.4 Conference contribution 2: Nanoparticle size evaluation through Dynamic Light Scattering (DLS) technique in a nitrate salt doped with ceramic nanoparticles

Authors: B. Muñoz-Sánchez, J. Nieto-Maestre, I. Iparraguirre-Torres, A. García-Romero

3.4.4.1 Introduction

Nanostructured materials have attracted great interest in recent years because of the unusual and exceptional properties showed by them due to the presence of additives at the nanometric scale. Among other properties, the thermal transfer rate is greatly improved compared to the base material which means the key to push forward the current technology of thermal energy storage (TES) systems.

In addition, a significant concern of the mentioned materials consists of developing suitable characterization methods since there are not standardized procedures which allow these nanostructured materials to be properly analysed. In particular, the present contribution deals with a material composed by an inorganic salt known as solar salt (60 wt% $NaNO_3$ – 40 wt% KNO_3) and boehmite nanoparticles (hydrated alumina, $AlOOH$) as an innovative medium to storage heat at high temperatures in concentrated solar power (CSP) plants. The presence of nanoparticles (not agglomerated) is thought to be the responsible of significant increments of the specific heat comparing to the base inorganic salt [72]. This can be detected through DLS, which is a particle size analysis technique based on the random Brownian motion of the nanoparticles. The objective of this research is to establish a suitable and reliable method of measuring the nanoparticle size based on the DLS technique applied to a nanostructured material containing boehmite nanoparticles in a matrix of solar salt. Moreover, through the study of the electrokinetic properties of the starting boehmite we will be able to stablish the best conditions to avoid nanoparticle agglomeration in the first steps of our synthesis procedure.

In this study, the particle size and the zeta potential of an aqueous dispersion of boehmite nanoparticles was analysed by DLS. The starting material was Alumisol-10A, an industrial water nanofluid of boehmite nanoparticles (10 nm, Kawaken Fine Chemicals, Co.). This suspension was diluted in water to obtain a concentration of nanoparticles of 0.5 $mg \cdot mL^{-1}$ (following the device manufacturer recommendations). The influence of six different pH (2, 3, 6, 8, 9 and 10) on suspension stability was studied.

Beside this sample, the final nanoparticle size and stability in the nanostructured material composed by solar salt doped with 1 wt% of boehmite nanoparticles was analysed. The synthesis

was performed as follows. Pellets of sodium nitrate (Industrial grade, SQM industries) and potassium nitrate (Multi-KGG Greenhouse-grade, Haifa Group) were mixed in the proper quantities to obtain the desired composition and then dissolved in water. After that, the necessary amount of boehmite water nanofluid was added to the salt aqueous solution. The water was removed by simple heating (100 ºC) and finally the material was melted at 450 ºC for half an hour to homogenize the sample. After cooling it at room temperature, the solid material was milled again and a representative portion was obtained. In order to perform the analysis, it is necessary to re-dissolve this solid material in water, since the measurement is always done over a liquid sample. Distilled water at the optimum pH (obtained from the experiments with boehmite explained in the previous paragraph) to avoid boehmite agglomeration was employed. The nanostructured samples were submitted to different experiments to evaluate the influence of several factors on the final results.

- <u>Nanoparticle concentration</u>: Solid sample was dissolved in water to obtain concentrations of 0.5, 0.1 or 0.01 mg·mL^{-1}.
- <u>Measurement repeatability</u>: Three replicas of the sample where analysed with the optimum concentration to find out the precision of the technique to evaluate the size of the nanoparticles.
- <u>Nanoparticle sedimentation</u>: The three previous replicas were analysed after 15 and 30 minutes of the first measurement to elucidate if there is nanoparticle agglomeration during sample preparation and testing.

3.4.4.2 Results and Discussion

The size results from DLS Malvern software were analysed with the same Standard Operating Procedure (SOP) both for the initial nanoparticles and the final material. This procedure has into account some features both of the nanoparticles (the refractive index and the absorption) and the solvent (the refractive index and the viscosity). Several parameters [178] such as Z-average (Z-ave), Polidispersity Index (PI), and the count rate were used to compare and evaluate the results accuracy. In addition, Z Potential (ZP) experiments allowed analysing the stability of boehmite nanoparticles with pH. The showed results correspond to the mean value of three measurements from which Standard Deviation (SD) and Relative Standard Deviation (RSD) have been calculated.

The <u>Z-ave</u> is defined as the intensity - weighted mean diameter derived from the cumulants analysis of sizes. In DLS this is the most important and stable number produced by the technique. If the Z-ave is decreasing with successive measurements the sample may be unstable.

The <u>PI</u> is a dimensionless measure of the broadness of the size distribution calculated from the cumulants analysis. Its value ranges from 0 to 1 being commonly in the range between 0.08 and

0.70. Values lower than 0.08 mean nearly monodisperse sample and greater than 0.70 indicate very broad distribution of particle sizes. The count rate is the number of photons detected and is usually stated in a "per second" basis. This is useful for determining the sample quality, by monitoring its stability as a function of time. If the count rate decreases with successive measurements could be due to particle sedimentation, creaming or dissolution. The ZP is a parameter which is related to the surface charge, a property that all materials possess, or acquire, when suspended in a fluid. A stable dispersion has a ZP lower than -35 mV and higher than 35 mV. The Iso Electric Point (IEP) is the pH corresponding to a ZP value of zero.

Regarding the initial nanoboehmite dispersion, the results of Z-ave, PI and ZP at different pH can be seen in Table 3-19. A graphical representation of the ZP of boehmite versus pH can be found in Figure 3-29.

Table 3-19. Initial nanoboehmite solution: Z-ave, PI and ZP results and dispersion parameters.

pH	Z-ave			PI			ZP		
	Mean (nm)	SD (nm)	RSD (%)	Mean	SD	RSD (%)	Mean (mV)	SD (mV)	RSD (%)
2	65.29	1.07	1.64	0.241	0.008	3.13	35.77	1.46	4.07
3	64.46	0.77	1.20	0.243	0.004	1.55	33.70	1.70	5.04
6	64.89	0.44	0.67	0.237	0.009	3.78	37.80	3.54	9.35
8	69.31	0.43	0.62	0.242	0.006	2.27	40.10	2.10	5.23
9	65.25	0.28	0.43	0.239	0.004	1.82	40.40	2.55	6.30
10	1439.00	55.15	3.83	0.943	0.019	2.02	-32.70	1.11	3.41

According to these data, some trends can be deduced. The size of boehmite nanoparticles is very similar (results are between 65-69 nm) at the pH range studied, except for pH 10. This behaviour is confirmed by ZP results. There is a change in the sign of ZP between pH 9 and 10, which means that nanoparticles are completely destabilized at pH>9 and this causes the agglomeration showed by the enormous increase of Z-ave result at pH 10. The IEP of this initial dispersion is around 9.5 as can be easily checked in Figure 15. The behaviour of ZP versus pH has been still described by other researchers [179] and results are quite similar to ours. As a final observation, the PI shows that the size distribution of boehmite nanoparticles is quite narrow. It is also worth mentioning that RSD are low (<5%) in the most of the results and only ZP data dispersion is a bit higher. Along with this behaviour, pH 2 can be established as the optimum to work with this kind of nanoparticles in aqueous solution since even Z-ave values are in the range of 65 nm as experiences with pH 3, 6 and 9, the ZP values with pH 2 are in the stable region (>35 mV) and have higher precision than other results. Moreover, the pH of the starting commercial nanofluid (Alumisol-10A) is 2 and it remains stable for months with any nanoparticle precipitation.

The second part of our study is done over the nanostructured samples. As it was stated before, the final solid sample needs to be re-dissolved in water before analysis. Thus, the first task is to find

out which nanoparticle concentration should be used in this aqueous dispersion. Following the DLS supplier instructions [153], there are some optimal concentrations depending on the expected nanoparticle size (Table 3-20).
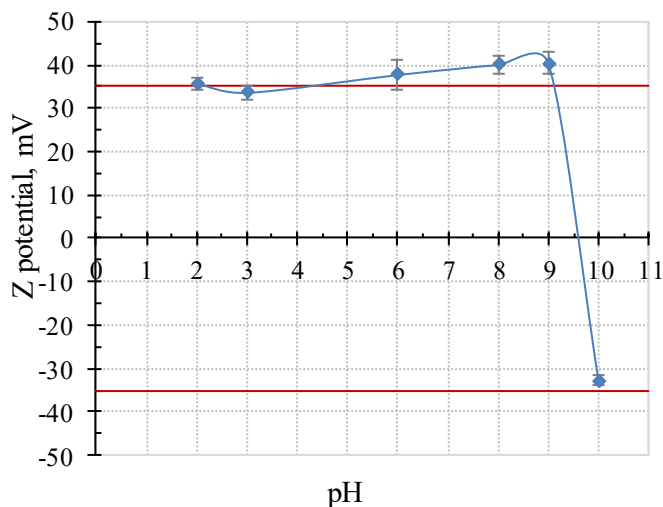
Figure 3-29. Initial boehmite solution: ZP versus pH.

Table 3-20. Nanoparticle concentration on the measured solution according to their expected size. These values are recommendations from Malvern Instruments [153]

Particle size, nm	Minimum concentration	Maximum concentration
< 10	0.5 mg·mL^{-1}	Only limited by the sample material interaction, aggregation, gelation, etc.
10 – 100	0.1 mg·mL^{-1}	5% mass (assuming a density of 1 kg·m^{-3})
100 -1000	0.01 mg·mL^{-1}	1% mass (assuming a density of 1 kg·m^{-3})

Starting from the nanostructured solar salt based material doped with 1% boehmite nanoparticles, three dispersions at different concentrations (0.1, 0.01 and 0.005 mg·mL^{-1}) were prepared. Results based on Z-ave as well as the corresponding PI are gathered in the Table 3-21 below. The intermediate nanoparticle concentration (0.01 mg·mL^{-1}) offered the lowest Z-ave and also the lowest SD. The quite high PI values point out the broadness and not monomodal nature of the size distribution.

Table 3-21. Influence of the nanoparticle concentration in Z-ave and PI of the nanostructured sample.

Nanoparticle concentration (mg·mL^{-1})	Z-ave			PI		
	Value (nm)	SD (nm)	RSD (%)	Value (nm)	SD (nm)	RSD (%)
0.1	2444.50	570.64	23.34	0.956	0.062	6.51
0.01	1872.00	90.51	4.83	0.773	0.168	21.77
0.005	2104.50	260.92	12.40	0.974	0.037	3.85

Our second objective is to analyse the repeatability of the nanoparticle size determination with the DLS technique. Three portions of the same solid sample were measured independently on the

device with the optimum concentration of 0.01 mg·mL^{-1}. Figure 3-30 shows that Z-ave values were consistent (maximum RSD 12.66%) with a difference of 237 nm between the highest and the lowest result.

Finally, it is well known that nanoparticles in dissolution may agglomerate and settle along the time specially when they are dispersed from the solid state without the aid of any mechanical system (e.g. ultrasonic power). This issue can lead to erroneous measurements (greater sizes than the real ones) and it is of interest to establish a maximum time to perform the test after re-dissolving the solid sample. To verify this factor, two more measurements of the three previous replicas were performed at 15 and 30 minutes after preparing the sample. The count rate results indicate that for replica 1, there is a decrease in this parameter with the time. This behaviour is not the same for the other two replicas (Figure 3-30). A possible explanation would be that fewer nanoparticles are present in the liquid to be analysed because they may be agglomerated, so the probability of being intercepted by the laser beam would be lower or even they are settled at the bottom of the cuvette. In any case, since there are variations with the time of measurement in the Z-ave values (Table 3-22), it is important to test the sample just after its dissolution.
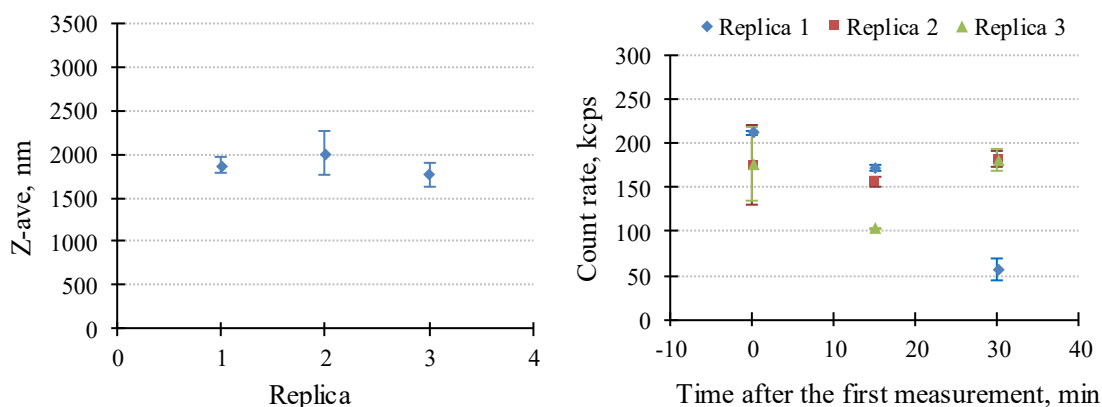
Figure 3-30. Study of repeatability (left) and evolution of the count rate with the time (right).

Table 3-22. Influence of the test time in the Z-ave results.

Time after the dissolution, min	Z-ave								
	Replica 1			**Replica 2**			**Replica 3**		
	Value (nm)	SD (nm)	RSD (%)	Value (nm)	SD (nm)	RSD (%)	Value (nm)	SD (nm)	RSD (%)
0	1872.00	90.51	4.83	2010.00	254.56	12.66	1773.00	136.47	7.700
15	1736.50	160.51	9.24	1904.00	94.75	4.98	1166.50	149.20	12.79
30	1028.00	12.73	1.24	2027.00	175.36	8.65	1639.50	6.36	0.39

3.4.4.3 Conclusions

The DLS technique has been used to characterize a nanostructured material composed by an inorganic salt doped with ceramic nanoparticles. The suitability and accuracy of this method to determine the nanoparticle size in this material has been studied and the optimal conditions to perform the analysis have been established. Boehmite nanoparticles are stable in the acid pH range showing an optimum working pH of 2. The nanostructured material showed a good repeatability regarding nanoparticle size with a dilution factor of 0.01 mg of nanoparticle per mL of water and nanoparticles remained stable in solution enough time to perform the measurement just after the sample preparation. The strength of this technique allows an easy and quick size determination requiring very low amount of sample. It would be interesting to compare the results with other size measurement techniques such as Scanning Electron Microscopy (SEM).

3.5   RAW MATERIALS CHARACTERIZATION

3.5.1   Salts

3.5.1.1 Analysis of the salts impurities

As described previously, the salts employed as TES materials in the CSP plants are not of analytical quality due to economic reasons. In this study, two different raw materials have been employed to synthetize the nanofluids made of sodium nitrate and potassium nitrate: the Refined Grade and the Industrial Grade. One pf the raw materials corresponds to the commercial Solar Salt currently used in the TES systems, while the other one corresponds to cheaper commercial Solar Salt, unsuitable because of corrosion problems with the materials of the storage tanks. It has been included in the study because the addition of nanoparticles may reduce the corrosion of this molten salt [32,93].

Working with commercial raw materials, non-analytical grades, is beyond the state-of-the-art (where high purity salts have always been used until now). As a result, it is required to analyse the presence of impurities as a new factor on the final properties of the nanofluids.

Chemical analysis was performed with the aim of having a precise quantification of the impurities on the raw salts. The most abundant pollutants on sodium and potassium nitrate are listed on Table 3-23. The analytical grade salts are not considered for this analysis since its low content of impurities is outside the detection limit of the used techniques.

The impurity content of the two types of Solar Salt mixtures, the Refined Solar Salt (RSS) and the Industrial Solar Salt (ISS) (Table 3-24), are calculated from the results showed on Table 3-23, according to the amount of sodium and potassium nitrate respectively. Figure 3-31 shows the different physical appearance of the molten Solar Salt depending on its purity.

Table 3-23. Analysis of the main impurities of $NaNO_3$ and KNO_3 on the refined, industrial and greenhouse grade.

	$NaNO_3$ Refined Grade (RSN)	$NaNO_3$ Industrial Grade (ISN)	KNO_3 Refined Grade (RPN)	KNO_3 Greenhouse Grade (IPN)
Chlorides (total), ppm	590	2,900	120	1,800
PO_4^{3-}, ppm	380	<50	<50	100
SO_4^{2-}, ppm	1,800	1,300	<50	<50
CO_3^{2-}, ppm	<100	220	<100	400
OH^-, ppm	<50	<50	<50	<50
NO_2^-, ppm	60	70	250	1,300
Mg^{2+}, ppm	64	460	4	3
Ca^{2+}, ppm	16	105	55	62

Table 3-24. Impurities of RSS and ISS calculated from those of the raw sodium and potassium nitrate.

	Solar Salt Refined Grade (RSS)	Solar Salt Industrial Grade (ISS)
Chlorides (total), ppm	400	2,460
PO_4^{3-}, ppm	230	40
SO_4^{2-}, ppm	1,080	780
CO_3^{2-}, ppm	<100	290
OH^-, ppm	<50	<50
NO_2^-, ppm	140	560
Mg^{2+}, ppm	40	277.2
Ca^{2+}, ppm	31.6	87.8
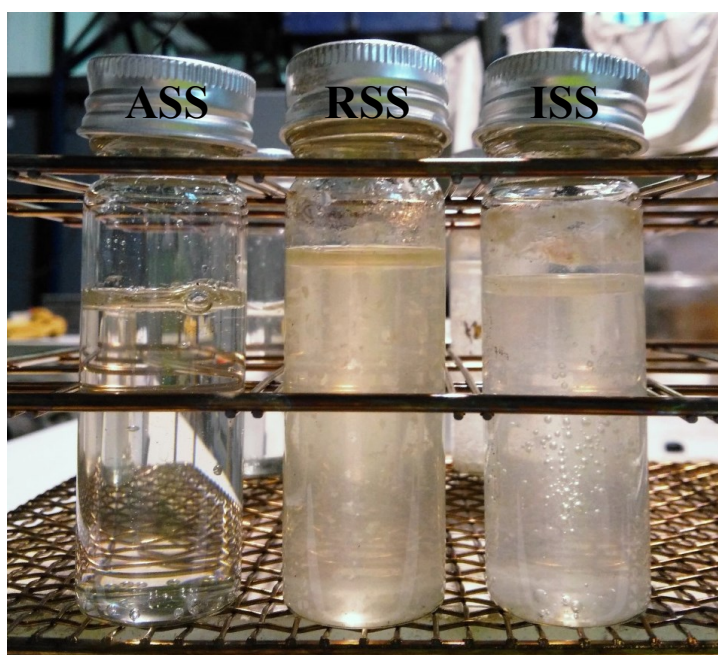
Figure 3-31. Visual appearance of the three Solar Salts in the molten state (396 ºC). ASS (left), RSS (middle), ISS (right). Solid impurities are clearly seen in RSS and ISS.

3.5.1.2 Thermal stability

Figure 3-32 shows the evolution of the weight of ISS and ISN under the thermal treatment described in the Section 3.3.3.1 of experimental methods. As expected, the weight loss in this temperature range is very small because the nitrates are thermally stable until 600 ºC [31,33,113,180]. According to the Table 3-25, the Solar Salt ISS suffered only a tiny weight loss (0.6%) near 550 ºC due to the start of its thermal decomposition, to yield nitrites and nitrogen oxides. Only the thermal stability of the ISS grade has been analysed because the differences between this grade and the ASS and RSS do indicate that they are thermally stable in the same range of temperatures. The weight loss of the ISN (Table 3-25) is also very small (1.2%), slightly higher than that of ISS, in agreement with the analysis of Bauer and co-workers [33].
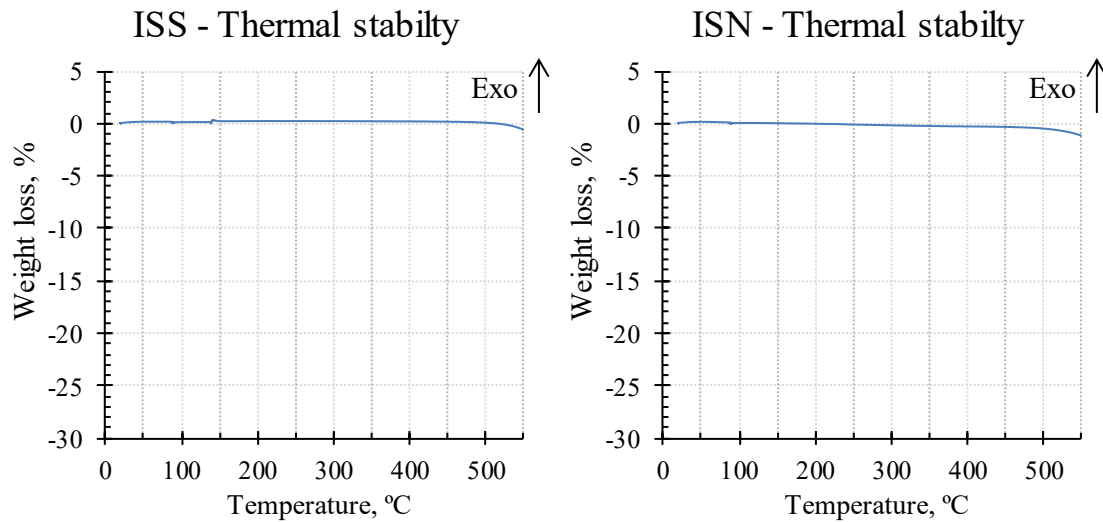
Figure 3-32. TGA measurement of the ISS (left) and the ISN (right) salts.

Table 3-25. Weight loss % at each temperature range for the TGA measurements of ISS.

Sample	Temperature interval, ºC	Weight loss, %	dTG* Minimum, ºC
ISS	20 -550	0.6	---
	Residue	99.4	---
ISN	20 -550	1.2	---
	Residue	98.8	---

*dTG = Differential Thermogravimetry

3.5.1.3 Specific heat

The salts specific heat was precisely measured according to the method described in the Section 3.3.3.2 of experimental methods. Table 3-26 shows the results of the three Solar Salts grades (different degree of purity). The specific heat values included on the table correspond to the average values determined on four batches of each salt. The obtained results agree with those published in the scientific literature [86,180] (Figure 3-33, around 1.550 $kJ \cdot kg^{-1} \cdot K^{-1}$ in liquid).

Table 3-26. Average value and standard deviation (SD) of the measured specific heat of the three Solar Salts used to prepare the nanofluids. Values determined at three different temperatures, one corresponding to solid phases and two corresponding to liquid.

Temperature, ºC	ISS		RSS		ASS	
	c_p, $kJ \cdot kg^{-1} \cdot K^{-1}$	SD, $kJ \cdot kg^{-1} \cdot K^{-1}$	c_p, $kJ \cdot kg^{-1} \cdot K^{-1}$	SD, $kJ \cdot kg^{-1} \cdot K^{-1}$	c_p, $kJ \cdot kg^{-1} \cdot K^{-1}$	SD, $kJ \cdot kg^{-1} \cdot K^{-1}$
196	1.398	0.044	1.406	0.046	1.397	0.058
296	1.521	0.042	1.557	0.043	1.564	0.046
396	1.528	0.046	1.569	0.038	1.572	0.061
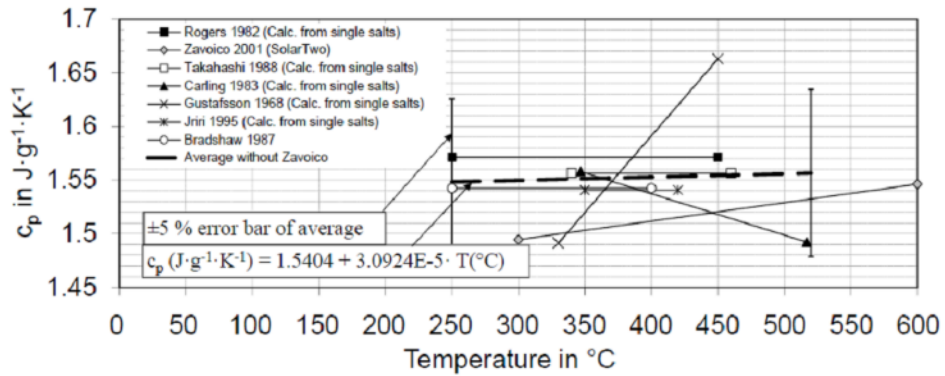
Figure 3-33. Specific heat of the Solar Salt according to the literature [180].

The specific heat of the Sodium Nitrate was also measured, both in the solid (256 ºC) and in the molten state (326 ºC). Results are gathered on the Table 3-27. The values are in agreement with the published ones [33] (Figure 3-34, an average value of kJ·kg^{-1}·K^{-1} is encountered at 326 ºC). The high c_p showed by the experimental results in the solid state is due to the proximity of the melting point.

Table 3-27. Average specific heat and standard deviation (SD) of the Sodium Nitrate used to prepare the NePCMs. Determined at two temperatures (one on solid state, one on liquid state).

Temperature, ºC	ISN		RSN		ASN	
	c_p, kJ·kg^{-1}·K^{-1}	SD, kJ·kg^{-1}·K^{-1}	c_p, kJ·kg^{-1}·K^{-1}	SD, kJ·kg^{-1}·K^{-1}	c_p, kJ·kg^{-1}·K^{-1}	SD, kJ·kg^{-1}·K^{-1}
256	2.826	0.069	2.453	0.051	2.431	0.034
326	1.606	0.024	1.679	0.053	1.776	0.043
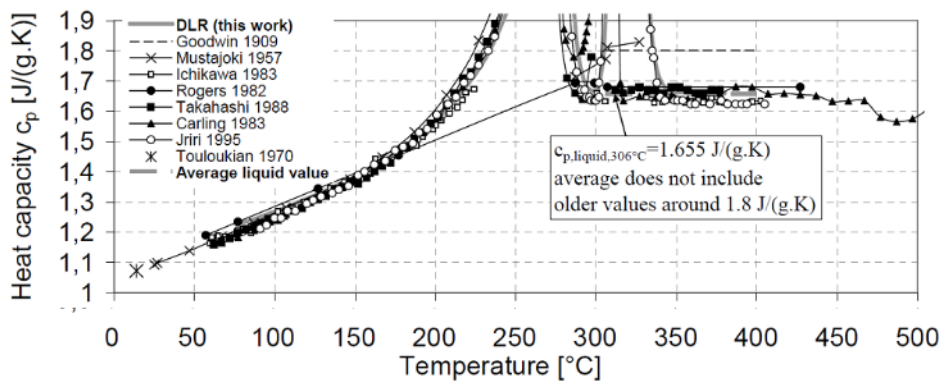
Figure 3-34. Specific heat of Sodium Nitrate according to the literature [33].

3.5.1.4 Latent heat

The Sodium Nitrate was characterized as PCM according to the method described in Chapter 3. The latent heat of fusion, the melting temperature, the latent heat of crystallization and the crystallization temperature were measured on the different Sodium Nitrate raw materials. The mean values and the SD are showed in Table 3-28. These thermophysical parameters are slightly different than those published in the literature, where the reported melting temperature is around 306 ºC and the latent heat of fusion is 178 kJ·kg^{-1} [33]. Regarding the latent heat of fusion, the

highest values corresponded to the ASN. The impure salts (RSN and ISN) attained lower values, and they seemed to be inversely related to the amount of impurities. This reduction on the phase change properties due to the presence of impurities is well known and has been demonstrated by Zhang and his colleagues [181]. It is associated to the lower crystallinity of these impure salts and thus, a more disordered internal structure and an easier melting process. On the crystallization stage, the latent heats are very similar to that of the fusion stage and have the same dependence of the salt purity. Regarding the melting temperature, the ASN has the highest value of the materials measured in this work. The RSN and the ISN progressively reduce this temperature with the increasing content of impurities. It is worth mentioning that the subcooling observed in the three salts is similar, which corresponds to a difference between the melting and the crystal nucleation temperatures around 10 ºC.

Table 3-28. Experimental results of the phase change features of the Sodium Nitrate: latent heat of fusion ΔH_f, latent heat of crystallization ΔH_c, melting temperature (T_m) and crystallization temperature (T_c). SD = Standard Deviation.

Salt	Fusion				Crystallization			
	ΔH_f, kJ·kg^{-1}	SD, kJ·kg^{-1}	Tm, ºC	SD, ºC	ΔH_f, kJ·kg^{-1}	SD, kJ·kg^{-1}	Tc, ºC	SD, ºC
ASN	180.53	1.15	310.98	1.03	181.43	1.15	300.79	0.42
RSN	161.65	3.04	307.07	0.00	163.20	0.85	296.28	0.35
ISN	124.67	3.06	300.01	0.27	126.37	3.27	292.19	0.81

3.5.1.5 Thermal conductivity

The thermal conductivity was indirectly measured through the thermal diffusivity in a LFA device, as detailed before. The Table 3-29 shows the thermal diffusivity (α) and conductivity (k) of the RSS, measured at the three usual temperatures. The results both for the α and k are very similar between them with independency of the solid or the liquid state of the salt. Compared with the literature values for these properties (illustrated in the Figure 3-35), the experimental thermal diffusivity results are higher (0.165 mm^2·s^{-1} at 296 ºC and 0.180 mm^2·s^{-1} at 396 ºC), while the thermal conductivity are very similar (0.48 W·m^{-1}·K^{-1} at 296 ºC and 0.50 W·m^{-1}·K^{-1} at 396 ºC). The differences could be attributed with the different techniques used by other authors and the non-analytical grade of the RSS.

Table 3-29. Thermal diffusivity and thermal conductivity of the RSS in the solid (196 ºC) and in the liquid state (296 ºC, 396 ºC). SD = Standard Deviation.

Temperature, ºC	RSS			
	α, mm^2·s^{-1}	SD, mm^2·s^{-1}	k, W·m^{-1}·K^{-1}	SD, W·m^{-1}·K^{-1}
196	0.203	0.009	0.441	0.047
296	0.201	0.009	0.465	0.024
396	0.212	0.010	0.499	0.052
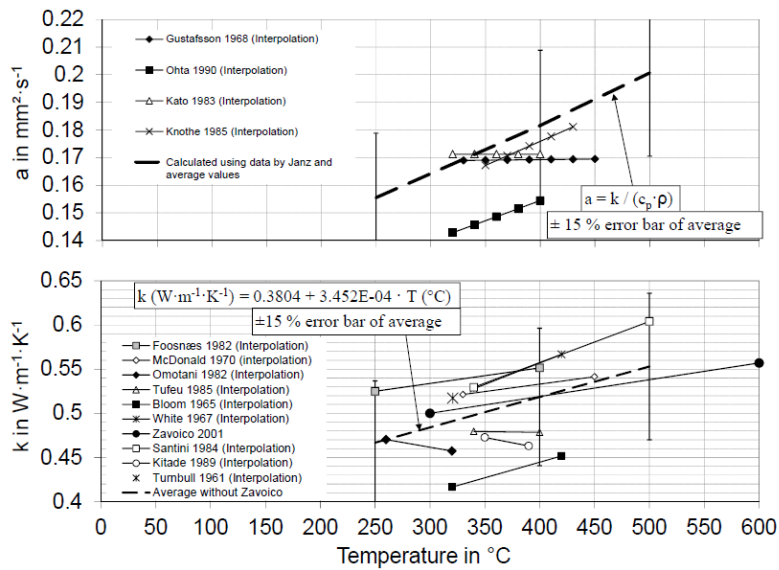
Figure 3-35. Thermal diffusivity and thermal conductivity of the Solar Salt according to the literature [180].

In addition, the thermal diffusivity and the thermal conductivity of the ASN were also analysed (see Table 3-30). In opposition to the RSS results, in this case there is a perceivable difference between the solid and the liquid state. According to the Figure 3-36, the experimental results of thermal diffusivity are similar to those found by Kobayashi et al. [33] in solid and Kato et al. [33] in liquid. With respect to the thermal conductivity, the experimental results in solid are higher than those appearing in the literature. This discrepancy could be due to the different crystal structure of the solid Sodium Nitrate [33]. The thermal conductivity in liquid is in the range found in other publications.

Table 3-30. Thermal diffusivity and thermal conductivity of the ASN in the solid (256 ºC) and in the liquid state (326 ºC). SD = Standard Deviation.

Temperature, ºC	ASN			
	α, mm^2·s^{-1}	SD, mm^2·s^{-1}	k, W·m^{-1}·K^{-1}	SD, W·m^{-1}·K^{-1}
256	0.169	0.003	0.882	0.037
326	0.195	0.004	0.604	0.047
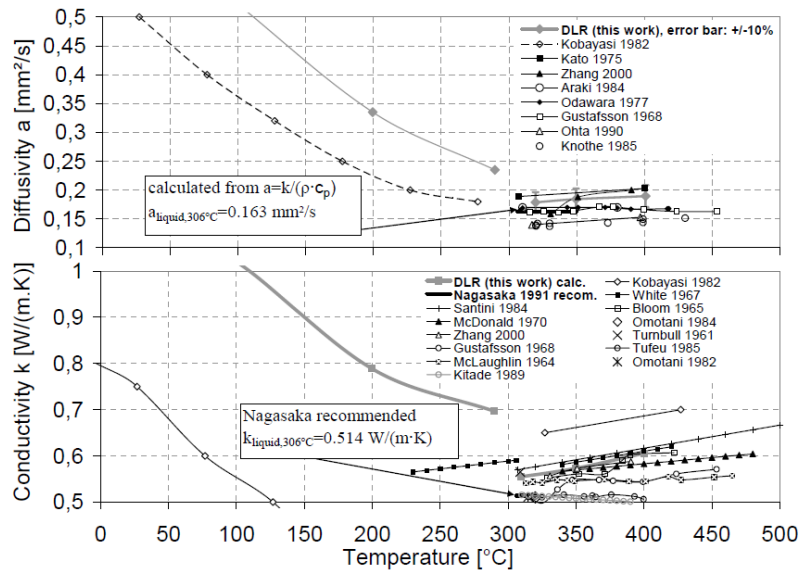
Figure 3-36. Thermal diffusivity and thermal conductivity of the Sodium Nitrate according to the literature [33].

3.5.1.6 Microstructure

The analysis of ISS by SEM revealed that the Solar Salt crystals are rounded-shape. Figure 3-37 shows two SEM images with 10,000x and 5,000x times of magnification and the EDX analysis of the ISS appears in Figure 3-38. These images were done with the QBSD backscatter electron detector, where changes in grey tones correspond to different salt compositions. Thus, the sodium nitrate crystals appear in a darker grey and the potassium nitrate ones. The obtained SEM images of the Solar Salt are quite similar to others described in diverse publications [31,74].
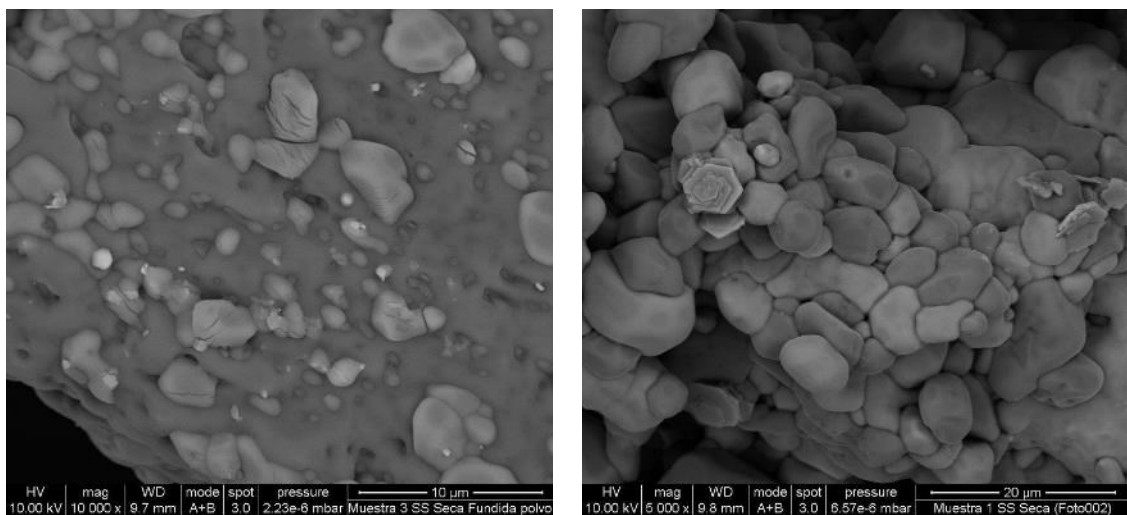
Figure 3-37. SEM images of the ISS done under QBSD with 10,000x (left) and 5,000x (right) of magnification. KNO_3 is seen as light grey and $NaNO_3$ as darker grey.

	ISS		
	Amount, wt%		
Element	**1**	**2**	**3**
K	51.77	100	100
O	38.37		
Na	6.59		
C	3.27		
Total	100	100	100
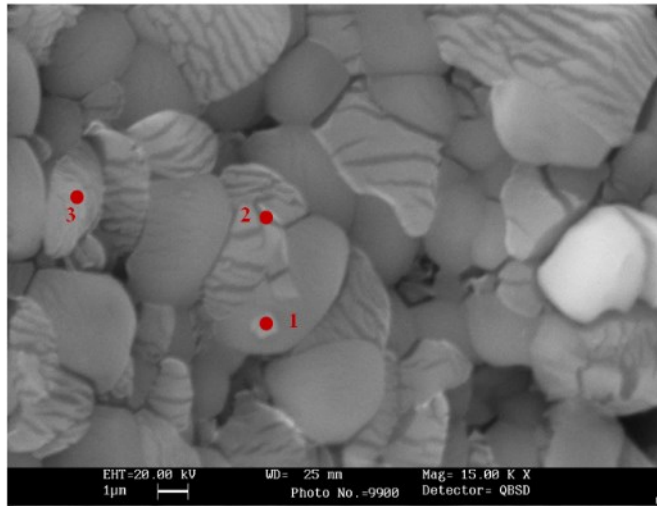
Figure 3-38. ISS image (SEM) with the EDX spot analysis on the locations indicated on the picture.

On the other hand, Figure 3-39 depicts the XRD spectrum of the ISS at room temperature. This crystallographic profile is coincident with the XRD spectra of KNO_3 and $NaNO_3$ of the reference database and the studies performed by Zhang [181] and Benages [171].
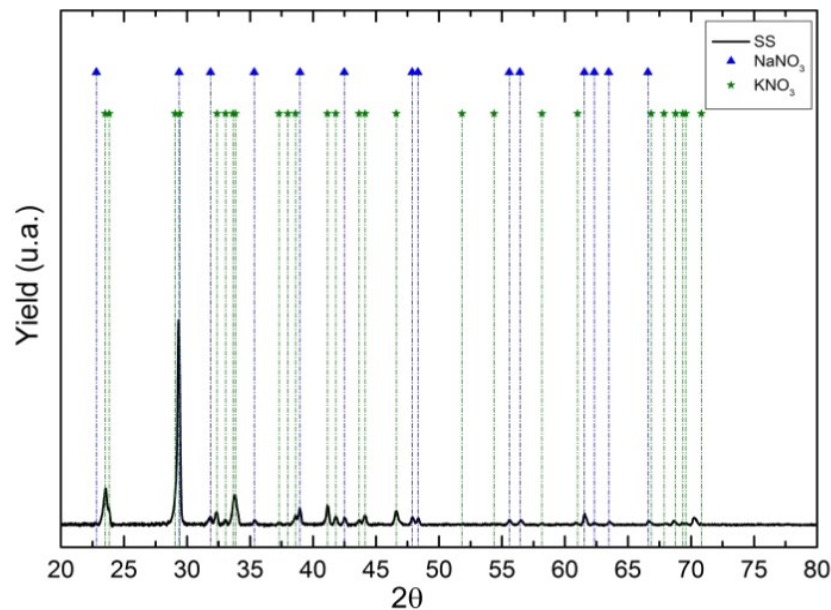
Figure 3-39. XRD spectra of the ISS. The diffraction peaks of both KNO_3 and $NaNO_3$ are depicted.

3.5.1.7 Stability in the long term

The thermal stability of the Solar Salt has been analysed in Section 5.1.2 and it is referred to the degradation of the sample due to high temperatures. However, the stability of the solid contaminants in the molten Solar Salt (non-analytical grade) is analysed in this section. This serves as a hint to further understand the stability of the nanoparticles on the molten Solar Salt depending on the purity of the latter.

The precipitation of the contaminants at the bottom of the flask in the RSS and the ISS is easily seen in the pictures showed in Figure 3-40. The contaminants precipitation was occurring later than 1 hour after the melting of the salt on the ISS. A little white cloud was noticed at the bottom of the flask while the remainder liquid had lost the turbidity seen on the previous pictures. On the other hand, the RSS was more transparent than the ISS from the beginning due to its lower content of impurities. Both RSS and ISS became clear after 5 hours due to the precipitation of the impurities. The analysis of the bottom part of the solid samples revealed the composition showed in the Figure 3-41 and the Figure 3-42. Sulphates, phosphates and magnesium were the impurities with a higher presence in the lowest part of both samples. For the RSS, phosphates were the most abundant substance while magnesium was for the ISS.
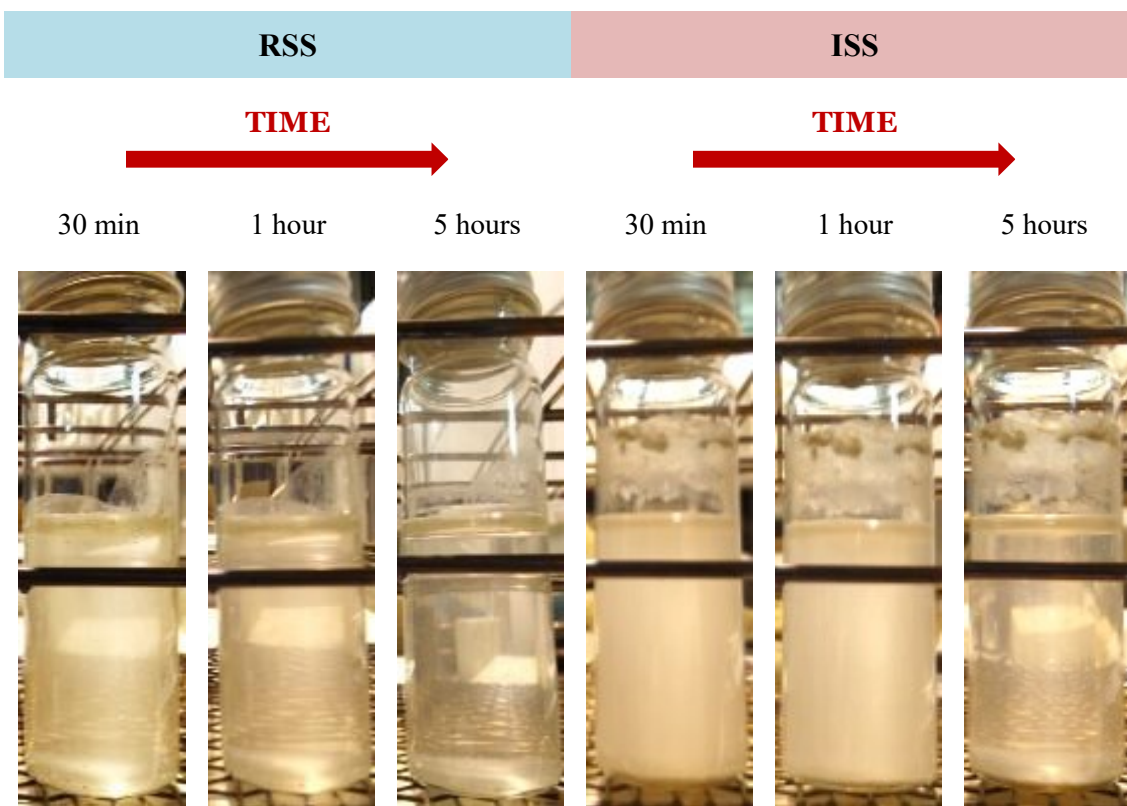
Figure 3-40. Pictures of the RSS and the ISS during the stability test. Impurities settle down at the bottom of the glass flask only after 5 h in the molten state.
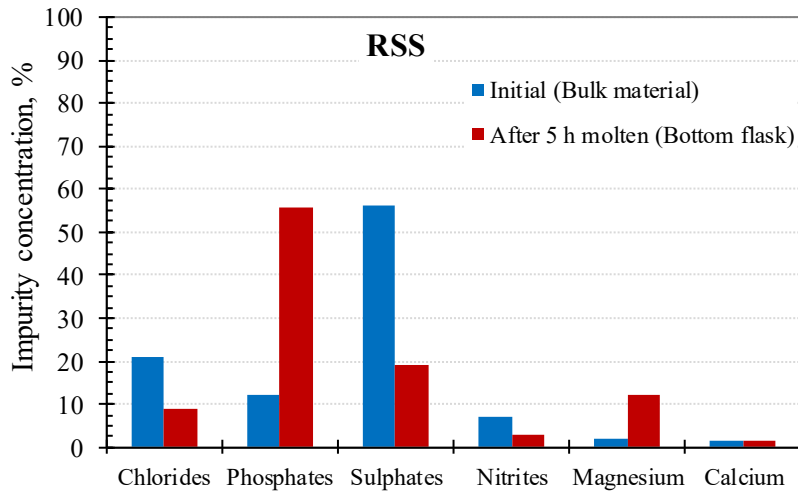
Figure 3-41. Comparison between the amount of initial contaminants in RSS and those settled down after 5 hours in the molten state.
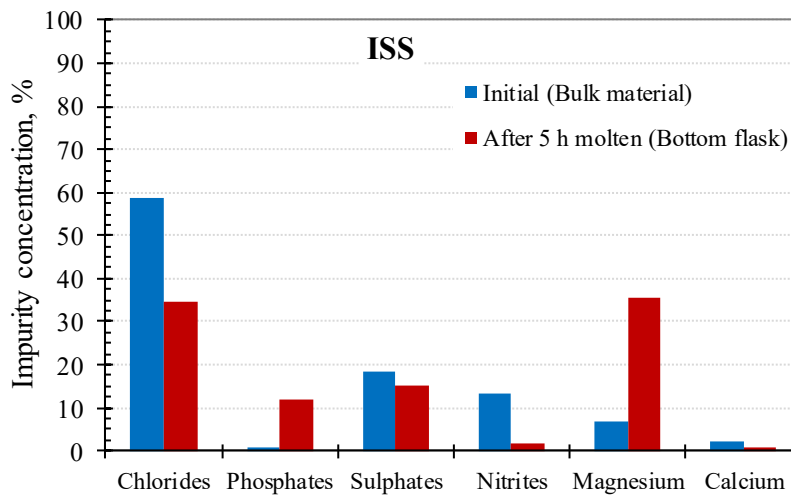
Figure 3-42. Comparison between the amount of initial contaminants in ISS and those settled down after 5 hours in the molten state.

3.5.1.8 Rheology

The rheology of the Solar Salts RSS and ISS are analysed according to the method described before. The influence of the shear rate and the temperature is evaluated on the results.

3.5.1.8.1 Influence of the shear rate

Generally, the rheological behaviour of fluids is evaluated by comparing the variation of the shear stress (τ) as function of the shear rate (γ). Depending of this relationship, the fluids are classified as "time-independent", "time-dependent" or "viscoelastic" fluids [182]. Most of the real fluids have a mixture of two or even three of these types.

Time-independent fluids are characterized by a specific shear stress under a certain shear rate, temperature and pressure. The flow curves of these fluids follow to the power law fluid model (Eq. 3-11) (also known as the Ostwald de Waele model) [183].

$$\tau = k \cdot \gamma^n$$
<div align="right">Eq. 3-11</div>

where k (Pa·s^n) is the consistency index and n is the flow behaviour index. Power-law fluids can be subdivided into three different types of fluids based on the value of their flow behaviour index:

n < 1 → Shear thinning or pseudoplastic, decreasing viscosity with higher shear rates

n = 1 → Newtonian, constant viscosity with higher shear rates

n > 1 → Shear thickening or dilatant, increasing viscosity with higher shear rates

Viscoelastic fluids are those with a behaviour characterized by the existence of a yield stress (τ_0) which must be exceeded before the fluid will deform or flow. Among the models developed to explain this kind of fluids, the Bingham rheological model (Eq. 3-12) is widely accepted. It implies that the fluid is a rigid material under low shear stresses and has a Newtonian behaviour after overcoming the yield stress [182,183].

$$\tau = \tau_0 + \mu_0 \cdot \gamma$$
<div align="right">Eq. 3-12</div>

where τ is the shear stress applied over the sample, τ_0 is the yield stress, μ_0 is the plastic dynamic viscosity and γ is the shear rate. The flow behaviour of some particulate suspensions is close to this expression [182].

The time-dependent fluids are more complex and their viscosity depends not only on the shear rate but also on the duration of shearing and their kinematic history.

3.5.1.8.1.1 Coaxial cylinder (Rheometer 1)

The Figure 3-43 up shows the lineal dependence between the shear stress and the shear rate between 250 ºC and 300 ºC for the RSS and ISS. The dependence of the viscosity with the shear stress is also included with the aim of clarification (Figure 3-43, down). A linear regression based on the Bingham rheological model (Eq. 3-12) fits this trend (see Table 3-31). The results correspond to the mean of the six data obtained at each shear rate. The Bingham rheological profile implies a constant viscosity once the yield stress has been overcome. In agreement with the high coefficients of determination (R^2 >0.99) found, it can be concluded that both salts show a Bingham profile. In the case of the ISS, the lineal fitting is not as good as in the previous samples. In the region of low shear rates (<100 s^{-1}) and at certain temperatures (290 ºC and 300 ºC) these materials show a shear thinning behaviour (Figure 3-43, up right). This could be related to the setting of the impurities at the bottom of the container since the salt has been in the molten state for several hours before collecting these data.
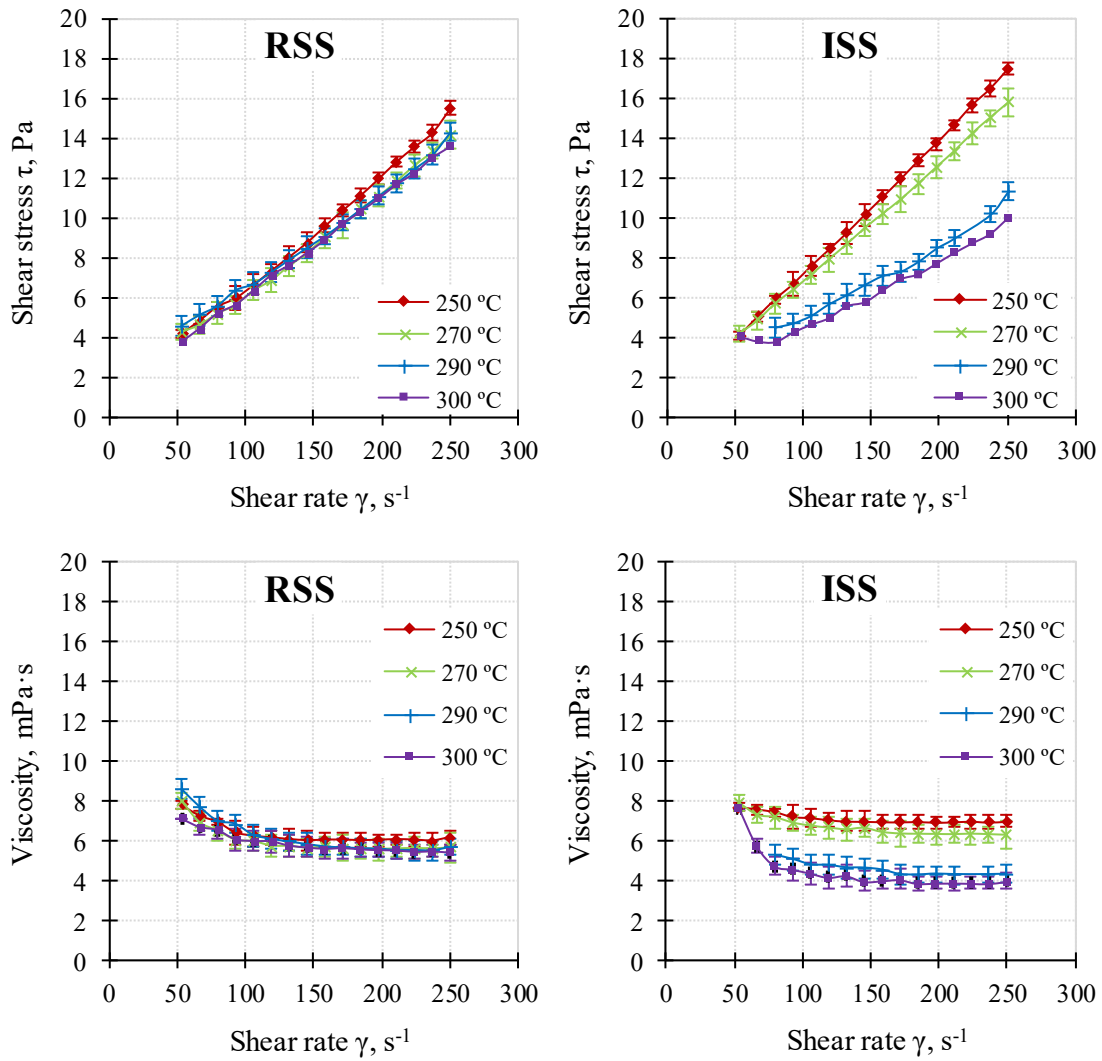
Figure 3-43. Up: Dependence between the shear stress (τ) and the shear rate (γ) on the RSS and ISS in the concentric cylinder method at temperatures between 250 ºC and 300 ºC. Down: Dependence between the viscosity (μ) and the shear rate (γ) on the RSS and ISS in the concentric cylinder method at temperatures between 250 ºC and 300 ºC. The error bars are the SD of the six measurements at each shear rate.

Table 3-31. Yield stress (τ_0), plastic dynamic viscosity (μ_0) and coefficient of determination (R^2) from the lineal regression according to the Bingham rheological model (Equation 1).

Temperature, ºC	RSS			ISS		
	τ_0, Pa	μ_0, Pa·s	R^2	τ_0, Pa	μ_0, Pa·s	R^2
250	0.8038	0.0568	0.9957	0.4249	0.0680	0.9996
270	1.0184	0.0514	0.9954	0.9391	0.0590	0.9996
290	1.7570	0.0478	0.9945	1.3852	0.0360	0.9930
300	1.1302	0.0498	0.9995	0.8813	0.0351	0.9950

The effect of the shear rate on the Solar Salt viscosity has been briefly studied on the scientific literature. All these studies employed analytical grade raw materials (Lasfargues et al. [31,114] and Jung et al. [74,95]). In those studies, the Solar Salt is described as a Newtonian fluid. On the contrary, these experimental results show that it is a Bingham fluid. The reason for these

differences could be related to the purity of the raw salts, where both, RSS and ISS, contain solid impurities which may modify their rheological profile, as pointed out by [183,184]. Other important factors responsible of the differences between our results and those obtained by other authors are the limited shear rate range employed in the present work (1-250 s^{-1}) In comparison to the wide shear rate range (1-1000 s^{-1}) used on most other articles and the rheometer configuration (a cone-plate geometry was employed on the other studies).

3.5.1.8.1.2   Parallel plates (Rheometers 2 and 3)

The Figure 3-44 up shows the lineal dependence between the shear stress and the shear rate between 250 ºC and 300 ºC for the RSS and ISS. The dependence of the viscosity with the shear stress is also included with the aim of clarification (Figure 3-44, down). In general, these flow curves can be fitted to the power law fluid model (Eq. 3-11). According to the Figure 3-44, several rheological performances can be noticed on these flow curves.

The tests performed on the RSS (Figure 3-44, left) reveal two different tendencies. At low shear rates (<100 s^{-1}) the fluids show a shear thinning behaviour, while at higher rates a shear thickening behaviour is displayed. As mentioned in the analysis of the results corresponding to the coaxial cylinder geometry, this change on the rheological behaviour may be related to the deagglomeration of impurities followed by a reagglomeration beyond a certain shear rate (100 s^{-1}). At shear rates lower than this value, the impurities are flow-oriented by the increasing shear rate and stays as individual particles. Beyond this point, the shear rate increases enough to make high energy collisions between the particles and they agglomerate again [182]. The good correlation of the shear thickening trend is shown on Table 3-32.

On the other side, the samples of ISS exhibit a clear Newtonian behaviour (Figure 3-44, right). Accordingly, suitable fittings are also obtained in this case (Table 3-32).

The Newtonian rheological profile of the Solar Salt proposed by Lasfargues et al. [31,114] and Jung et al. [74,95] is in agreement with the results of ISS. The upper shear rate employed on our study is the same employed by those authors (1000 s^{-1}), and the rheometer geometry (parallel plate) is more similar than the coaxial cylinder to the the cone-plate configuration employed by them. The non-Newtonian character of the RSS can be explained by the strong influence of the impurities at reduced shear rates in the small volume of sample required on the experiments. The higher shear rates used with the ISS may led to the discussed Newtonian behaviour and the inexistence of a shear thickening region at high shear rates (>250 s^{-1}).
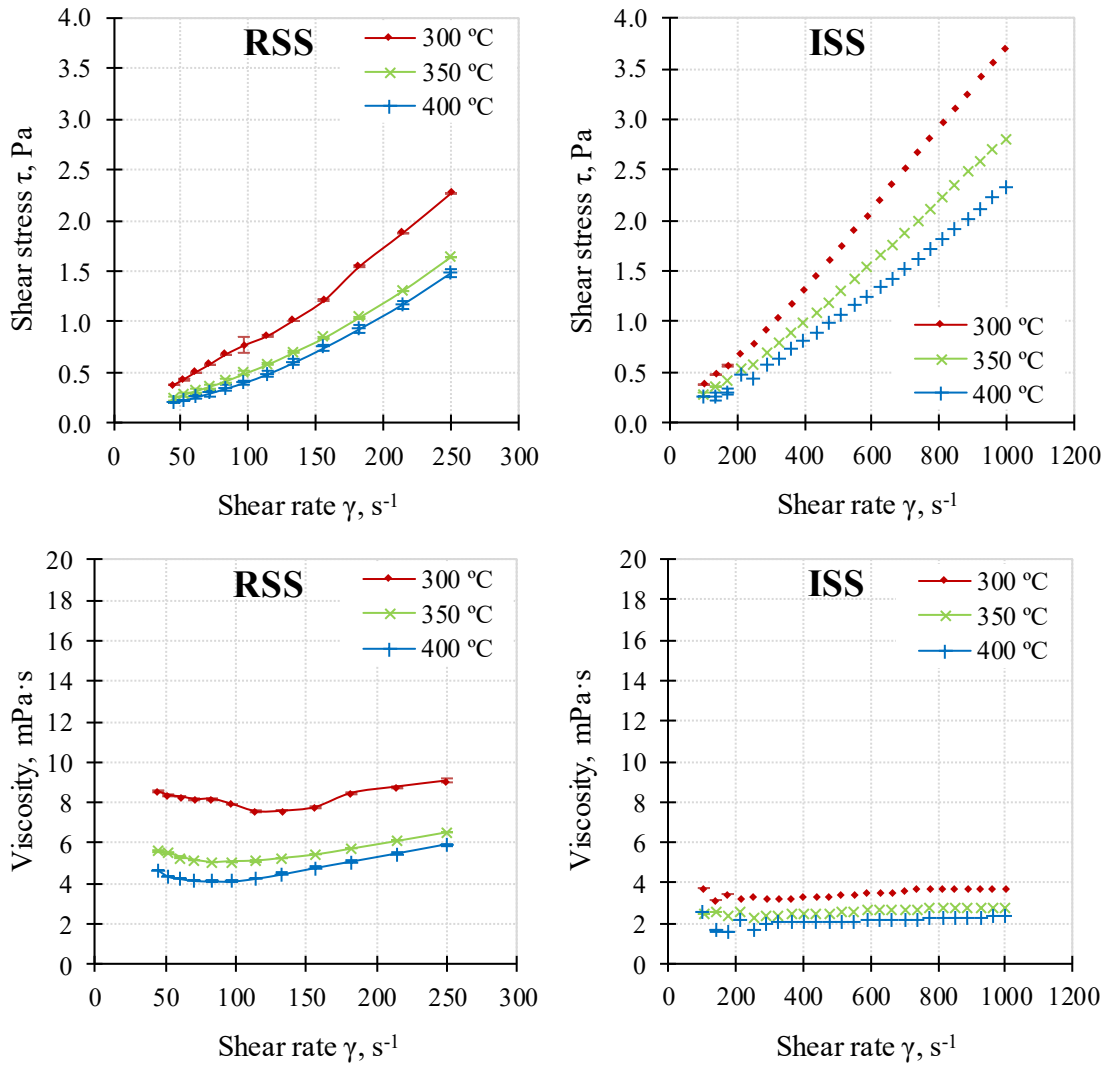
Figure 3-44. Up: Dependence between the shear stress (τ) and the shear rate (γ) on the RSS and ISS in the parallel plate method at temperatures between 300 ºC and 400 ºC. Down: Dependence between the viscosity (μ) and the shear rate (γ) on the RSS and ISS in the parallel plate method at temperatures between 300 ºC and 400 ºC. The error bars are the SD of the six measurements at each shear rate.

Table 3-32. Consistency index (k), flow behaviour index (n) and coefficient of determination (R^2) obtained when the experimental data are fitted to the power law fluid model (Eq. A.1). RSS-based nanofluids analysed between 1 and 250 s^{-1} (Rheometer 3) and ISS-based nanofluids analysed between 10-1000 s^{-1} (Rheometer 2).

	RSS			ISS		
Temperature, ºC	k, Pa·s^n	n	R^2	k, Pa·s^n	n	R^2
300	0.0041	1.1374	0.9972	0.0036	1.0000	0.9935
350	0.0014	1.2866	0.9973	0.0027	1.0000	0.9916
400	0.0007	1.3788	0.9983	0.0022	1.0000	0.9908

3.5.1.8.2 Influence of the temperature

The evolution of viscosity with the temperature usually follows an Arrhenius model, as seen in Eq. 3-13, although some authors use a simple polynomial regression [114,185].

$$\mu = A_0 \exp(E_{visc}/RT)$$
<div align="right">Eq. 3-13</div>

where μ is the viscosity, A_0 is a constant, E_{visc} is the activation energy for viscous flow, R is the universal constant for the perfect gases, and T is the absolute temperature. Eq. 3-13 is commonly transformed into a lineal relationship by means of logarithms and known as the Vogel, Tamman and Fulcher (VTF) Equation (Eq. 3-14) [45].

$$\ln\mu = A + 1000\frac{B}{T+C}$$
<div align="right">Eq. 3-14</div>

These three variables have a physical meaning: A is the result of calculating $\ln\mu$ at a very high (infinite) temperature, B is the energy barrier to be overcome after any rearrangement of liquid molecules and C is the temperature at which the viscosity is infinite [45].

3.5.1.8.2.1   Coaxial cylinder (Rheometer 1)
Figure 3-45 shows the mean viscosity of RSS and ISS determined for shear rates higher than 100 s^{-1} at different temperatures. It was observed that at shear rates between 100 and 250 s^{-1} the viscosity values remained constant for the two salts with this coaxial cylinder rheometer (Figure 3-43, down).

The viscosity of the undoped Solar Salt is around 5.70 mPa·s for the RSS grade and between 4.00 mPa·s and 7.00 mPa·s for the ISS grade. These viscosity values are higher than those reported by [164] for the analytical grade mixtures, probably due to presence of impurities on our salts. The viscosity of the RSS is independent of the test temperature, which is not in agreement with the commonly reported viscosity decrease when the temperature is risen.

3.5.1.8.2.2   Parallel plates (Rheometers 2 and 3)
Figure 3-45 shows the viscosity results of RSS at shear rates of 250 s^{-1} and the mean results for the ISS at shear rates from 300 s^{-1} to 1000 s^{-1} in the first salt and compared to those found in the literature. According to this Figure 3-45, the viscosity of the undoped RSS Solar Salt determined with the parallel plate rheometers lies in between 8.58 mPa·s and 6.43 mPa·s, and between 3.55 mPa·s and 2.17 mPa·s on the ISS grade. The RSS viscosity values determined in this work are much higher than those published in the literature [164], while those obtained with the ISS grade lie within the average viscosity reported on the literature at different temperatures. These differences lay on the selected shear rate range and the presence of impurities on the salts used in this study.
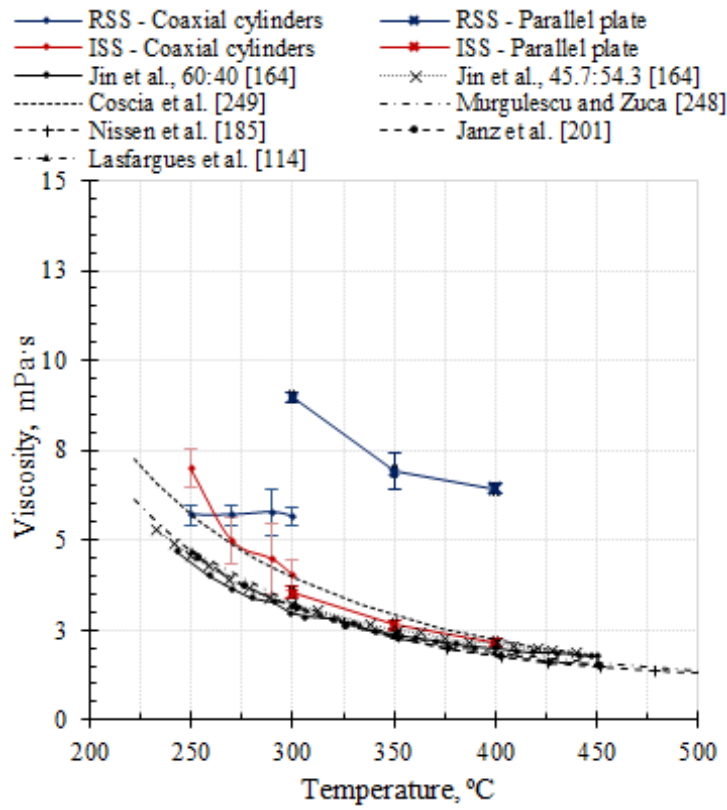
Figure 3-45. Viscosity versus temperature of the experimental results of the RSS and ISS in the coaxial cylinder and the parallel plate rheometer and the results published by other authors.

3.5.2 Nanoparticles

3.5.2.1 Thermal stability

3.5.2.1.1 Alumina nanoparticles

The thermal stability of boehmite nanoparticles is analysed in Figure 3-46 and Table 3-33 and reveals three different stages in our temperature range. The first weight loss (Δm=-11.3%) occurs between 20 and 90 ºC with a minimum around 80 ºC, due to the loss of humidity of the sample. A second step of dehydration (Δm=-13.3%) is observed in the range of 90-400 ºC with an endothermic peak in 390 ºC related to the desorption of intralaminar water located between boehmite nanoparticles. Finally, the boehmite starts the transformation in γ-Al_2O_3 that accounts the 5.6% of the mass loss. These changes are irreversible, as confirmed by the absence of weight change on the second and the third cycle of the thermal treatment. These results are in agreement with the specialized literature on this subject [186,187].

Figure 3-46. TGA measurement of the alumina nanoparticles.

Table 3-33. Weight loss % at each temperature range for the TGA measurements of alumina nanoparticles.

Temperature interval, ºC	Weight loss, %	dTG* Minimum, ºC
20 - 90	11.3	76
90 – 550 (1st cycle)	18.8	387
550 – 90 (2nd cycle)	< 0.5	---
90 – 550 (3rd cycle)	< 0.5	---
Residue	69.9	---

*dTG = Differential Thermogravimetry

3.5.2.1.2 Silica nanoparticles

The TGA and DTG curves of the silica nanoparticles are reported in Figure 3-47. The weight loss of the sample (Table 3-34) is characterized by two stages. The first region from room temperature to 90 ºC is linked with the loss of physically absorbed water from the surface of the nanoparticles (6.3 wt%). On the other hand, from 90 ºC to 550 ºC there is a lower mass loss (2.5 wt%) due to the chemically adsorbed water bonded to Si–OH through hydrogen bond. These results are in agreement with the thermal degradation of amorphous silica studied by Zhuravlev [188] and Liu and his co-workers [189].
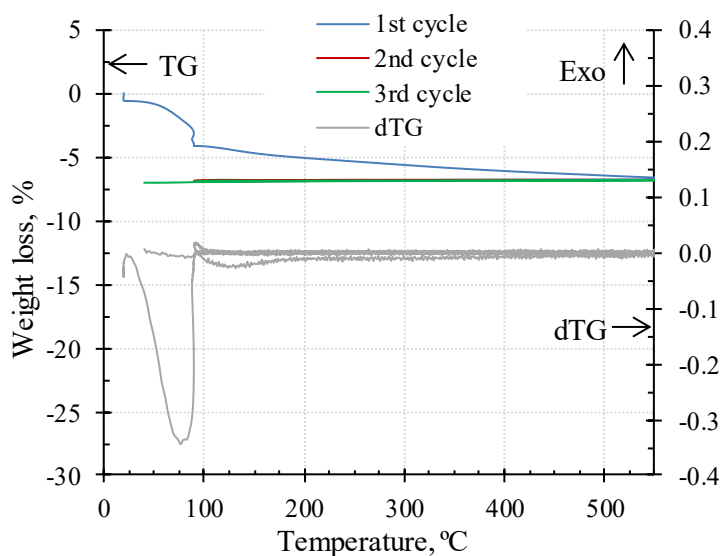
Figure 3-47. TGA measurement of the silica nanoparticles.

Table 3-34. Weight loss % at each temperature range for the TGA measurements of the silica nanoparticles.

Temperature interval, ºC	Weight loss, %	dTG* Minimum, ºC
20 - 90	6.3	69
90 – 550 (1st cycle)	2.5	---
550 – 550 (2nd cycle)	<0.5	---
550 – 550 (3rd cycle)	<0.5	---
Residue	91.2	---

*dTG = Differential Thermogravimetry

3.5.2.2 *Nanoparticle size and Zeta Potential*

3.5.2.2.1 Alumina nanoparticles

The alumina nanoparticles suspension (Alumisol-10A) was dissolved in water at different pH and measured with the DLS device according to the method described before. The Table 3-35 is gathering the results of the ZP, as well as the mean nanoparticle size (Z-ave) and the PI as a quality control of the measurement. A graphical representation of the ZP of Alumisol-10A as a

function of the pH can be found in the Figure 3-48. The red lines in this figure indicate the region of electrical stability of the nanoparticles (ZP≥35 mV and ZP≤-35 mV).

Table 3-35. Initial alumina nanoparticles (A10): Z-ave, PI and ZP results and dispersion parameters.

pH	Z-ave			PI			ZP		
	Mean (nm)	SD (nm)	RSD (%)	Mean	SD	RSD (%)	Mean (mV)	SD (mV)	RSD (%)
2	65.29	1.07	1.64	0.241	0.008	3.13	35.77	1.46	4.07
3	64.46	0.77	1.20	0.243	0.004	1.55	33.70	1.70	5.04
6	64.89	0.44	0.67	0.237	0.009	3.78	37.80	3.54	9.35
8	69.31	0.43	0.62	0.242	0.006	2.27	40.10	2.10	5.23
9	65.25	0.28	0.43	0.239	0.004	1.82	40.40	2.55	6.30
10	1439.00	55.15	3.83	0.943	0.019	2.02	-32.70	1.11	3.41

According to these data, some trends can be deduced. The size of the alumina nanoparticles is very similar (results are between 65-69 nm) in the pH range studied, except for pH 10. This behaviour is confirmed by the ZP results. There is a change in the sign of the ZP between pH 9 and 10, which means that nanoparticles are completely destabilized at pH>9 and this causes the agglomeration showed by the enormous increase of Z-ave result at pH 10. The IEP of this initial dispersion is around 9.5 as can be easily checked in Figure 14. The behaviour of the ZP versus pH for alumina nanoparticles has been still described by other researchers [20–23] and results are quite similar to ours. As a final observation, the PI shows that the size distribution of boehmite nanoparticles is quite narrow (<0.5). Accordingly, it is possible to work with this kind of nanoparticles in a pH range from 2 to 9 since their ZP is inside the region of electrical stability (≥35 mV). The pH of the original commercial aqueous nanofluid (A10) is between 3.4 and 4.2 according to the manufacturer and it remains stable for months without nanoparticle precipitation. The pH 2 was selected from that moment to work with alumina nanoparticles.

Figure 3-49 shows the alumina nanoparticles size distribution for the pH 2. It is a monomodal size distribution where the sizes range between 10 and 190 nm and the mode is located at 15.69 nm. Most of the nanoparticles (90%) are smaller than 21.70 nm. These nanoparticles sizes are higher than those offered by the supplier, probably due to some agglomeration after the addition of some water prior to the measurement in the DLS.
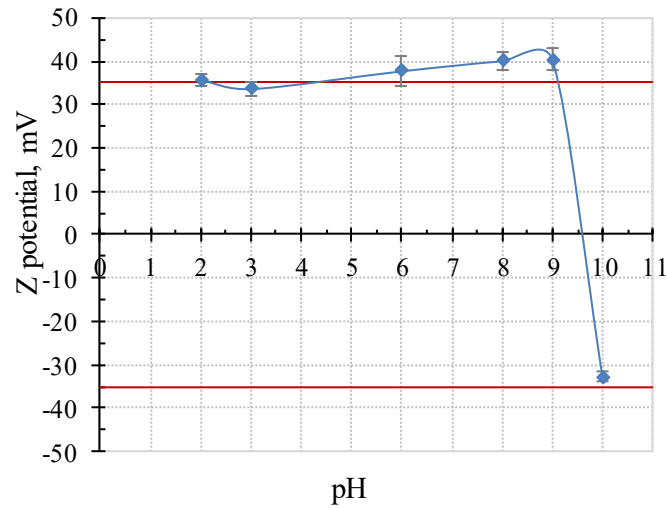
Figure 3-48. ZP versus pH of the alumina nanoparticle dispersion (Alumisol-10A).
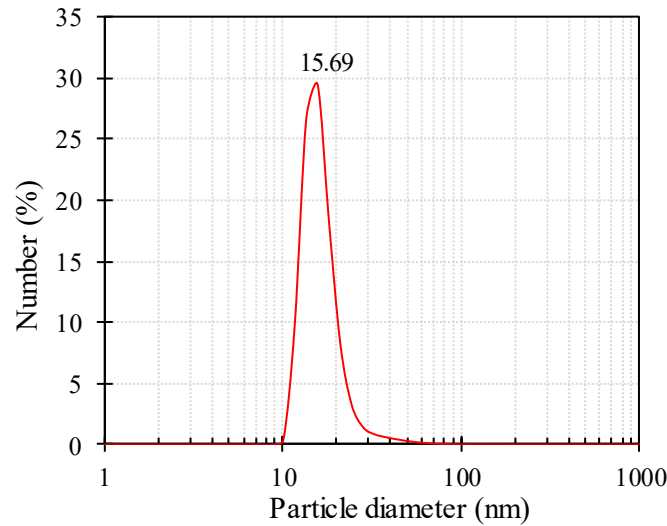
Figure 3-49. Nanoparticle size distribution of the alumina nanoparticles. The mode of the distribution is signalled on the graph.

3.5.2.2.2 Silica nanoparticles

The silica nanoparticles suspension (LUDOX® SM-30) was dissolved in water at different pH and measured with the DLS device according to the method described before. Table 3-36 is gathering the results of the ZP, as well as the mean nanoparticle size (Z-ave) and the PI as a quality control of the measurement. A graphical representation of the ZP of LUDOX® SM-30 in function of the pH can be found in the Figure 3-50. The red lines in this figure indicate the region of electrical stability of the nanoparticles (ZP≥35 mV and ZP≤-35 mV).

Table 3-36. Initial silica solution: Z-ave, PI and ZP results and dispersion parameters.

pH	Z-ave			PI			ZP, mV		
	Mean (nm)	SD (nm)	RSD (%)	Mean	SD	RSD (%)	Mean (mV)	SD (mV)	RSD (%)
2	47.25	1.00	2.11	0.328	0.007	2.11	-6.05	0.81	13.45
4	51.26	2.06	4.02	0.352	0.010	2.71	-34.65	1.06	3.06
6	53.36	0.88	1.66	0.358	0.003	0.79	-33.20	0.28	0.85
8	52.69	0.89	1.68	0.357	0.004	1.06	-34.75	0.92	2.65
9	51.93	2.14	4.11	0.350	0.018	5.09	-29.85	1.20	4.03
10	49.29	0.89	1.81	0.293	0.030	10.36	-36.75	5.87	15.97

According to these data, some trends can be deduced. The size of the silica nanoparticles is very similar (results are between 47-53 nm) at the pH range studied, with lower values at pH 2 and 10. This behaviour is confirmed by the ZP results. They are quite uniform around the value of -34 mV with independency of the pH. Only the sample dispersed in water at pH 2 is getting out this trend with a ZP value of -6 mV, which is inside the instability region and near from the IEP which may be close to a pH of 1.5. The behaviour of the ZP in function of the pH for silica nanoparticles has also been studied by Yoon [190] and Bumb [191] with quite similar results. As a final observation, the PI shows that the size distribution of silica nanoparticles is quite narrow (<0.5). Accordingly, it is possible to work with this kind of nanoparticles in a pH range from 4 to 10 since their ZP is inside the region of electrical stability (≤-35 mV). The pH 9 was selected to work with silica nanoparticles.

Figure 3-51 shows the alumina nanoparticles size distribution for the pH 9. It is a monomodal size distribution where the sizes range between 10 and 105 nm and the mode is located at 13.55 nm. Most of the nanoparticles (90%) are smaller than 25.40 nm.
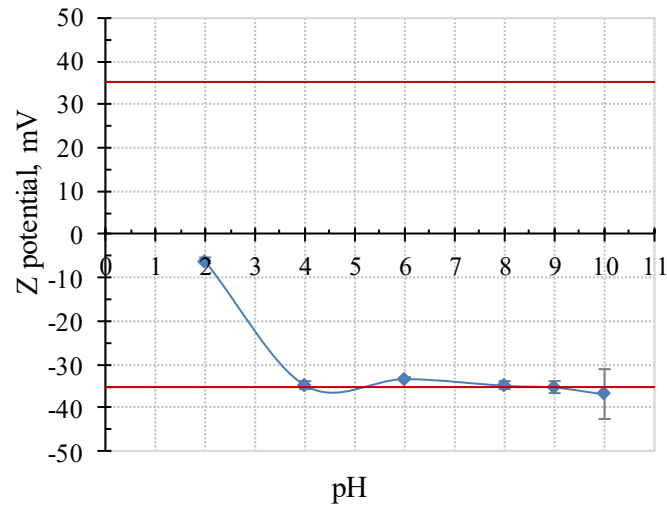
Figure 3-50. Initial silica solution: ZP versus pH.
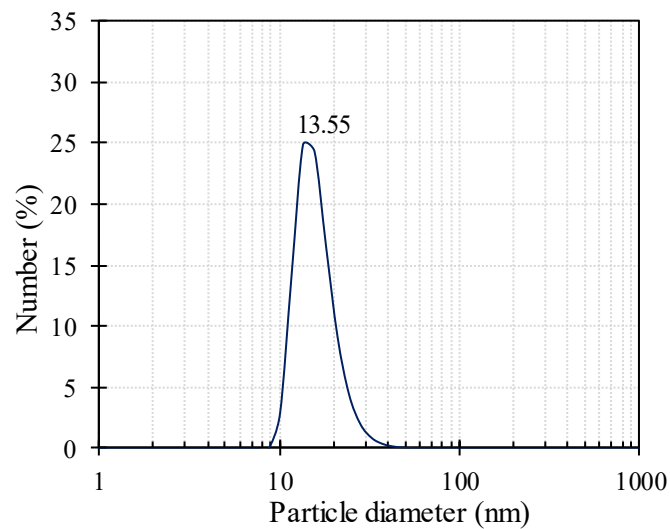
Figure 3-51. Nanoparticle size distribution of the silica nanoparticles. The mode of the distribution is signalled on the graph.

3.5.2.3 Specific heat

The specific heat of the nanoparticles was measured by DSC according to the thermal program detailed before. The objective was to have our experimental results to be further included on the model used to estimate the specific heat of the nanofluids.

3.5.2.3.1 Alumina nanoparticles

The specific heat of the alumina nanoparticles is exposed in Table 3-37. As showed along with our experimental results, the values appearing in the literature for the bulk material are lower than ours. This could be due to the increment on the specific heat of alumina nanoparticles with respect to the bulk material, as observed by Wang and his colleagues [192]. The comparison with their

results is not possible since they did not perform measurements at high temperatures.

Table 3-37. Specific heat of the alumina nanoparticles measured at the three temperatures of interest (SD = Standard Deviation) and comparison with the literature.

Temperature, ºC	Alumina nanoparticles		Furukawa et al. [193]	Auerkari [194]
	c_p, kJ·kg^{-1}K^{-1}	SD, kJ·kg^{-1}K^{-1}		
196	1.195	0.039	1.015	0.999
296	1.237	0.009	1.087	1.057
396	1.471	0.031	1.136	1.099

3.5.2.3.2 Silica nanoparticles

The specific heat of the silica nanoparticles is gathered in Table 3-38. As showed along with our experimental results, the values appearing in the literature for the bulk material are in agreement with ours.

Table 3-38. Specific heat of the silica nanoparticles measured at the three temperatures of interest (SD = Standard Deviation) and comparison with the literature.

Temperature, ºC	Silica nanoparticles		CRC Handbook [30]
	c_p, kJ·kg^{-1}·K^{-1}	SD, kJ·kg^{-1}·K^{-1}	
196	0.970	0.112	0.988
296	0.943	0.243	1.052
396	1.157	0.143	1.116

3.5.2.4 Microstructure and composition

3.5.2.4.1 Alumina nanoparticles

Figure 3-52 presents the TEM image of the initial alumina nanoparticle (Alumisol-10A). This figure gives an idea of the nanoparticle size which is in the range of that obtained by the DLS technique (Figure 3-49). On the other side, it can be deduced from the image that the morphology of the alumina nanoparticles consists of several layers arranged in a fiber-like structure.

Figure 3-52. TEM image of the alumina nanoparticles.

Figure 3-53 exhibits the recorded XRD patterns for the alumina nanoparticles before and after being heated at 450 ºC (as detailed before). The spectrum of the boehmite (AlOOH) nanoparticles (precursor of alumina) showed several peaks typical of this material as is supported by the XRD spectra database software of the device and the specialized literature [195,196]. After the thermal treatment, there is a decrease of the crystallinity and the pattern is more diffused. This is probably due to the loss of the intralaminar water and the incipient conversion to γ-Al_2O_3, which was revealed by the TGA tests results (Figure 3-46).
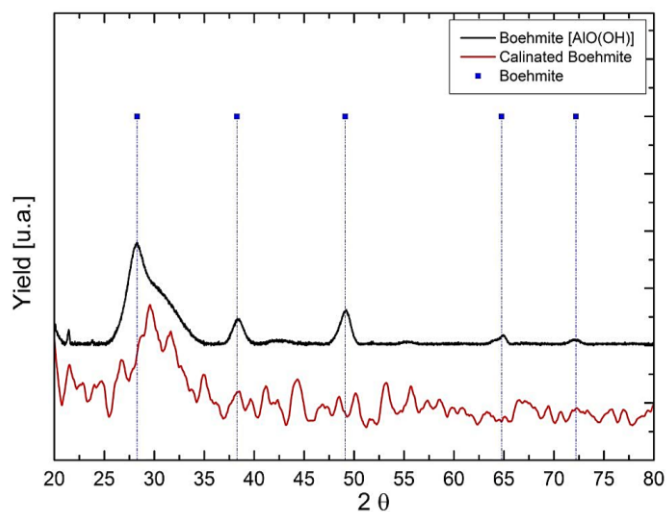
Figure 3-53. XRD spectra of boehmite before and after the calcination process.

3.5.2.4.2 Silica nanoparticles

Figure 3-54 presents the TEM image of the initial silica nanoparticles (LUDOX® SM-30). This figure gives an idea of the nanoparticle size which is in the range of that obtained by the DLS technique (Figure 3-51). On the other side, it can be deduced from the image that the morphology of the silica nanoparticles consists of spheres which are clustered together forming chains.
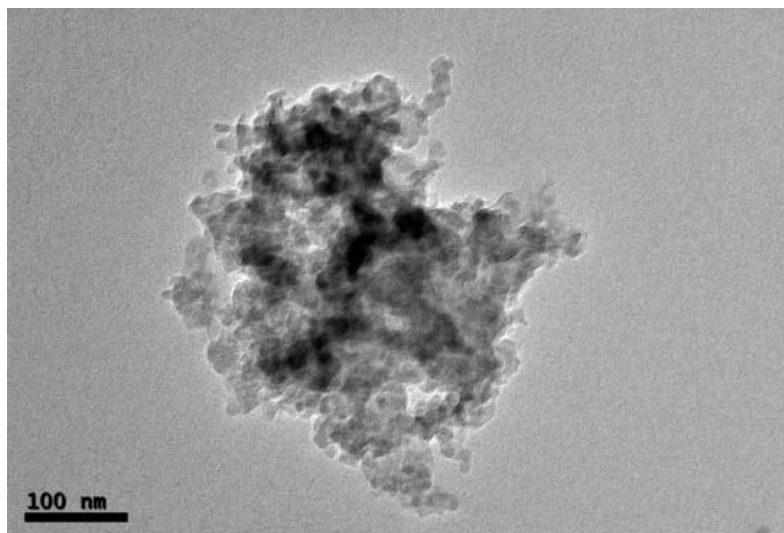
Figure 3-54. TEM image of the silica nanoparticles.

Figure 3-55 exhibits the recorded XRD patterns for the silica nanoparticles before and after being calcinated at 450 ºC (as detailed before). The spectrum of the silica nanoparticles showed that the material is amorphous, as declared by the supplier of the LUDOX® SM-30.
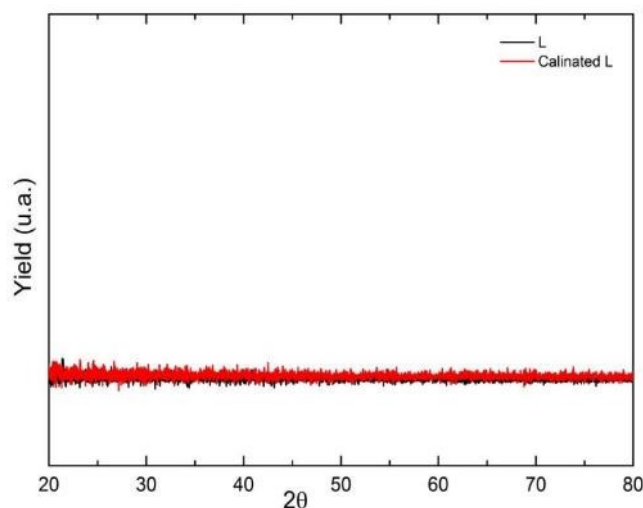
Figure 3-55. XRD spectra of the LUDOX® SM-30 before and after the calcination process.

3.5.3 Conference contribution 3: Preparation of Nanofluids Based on Solar Salt and Boehmite Nanoparticles: Characterization of Starting Materials

Authors: Belén Muñoz-Sánchez, Javier Nieto-Maestre, Iñigo Iparraguirre-Torres, José Ángel Sánchez-García, José Enrique Juliá and Ana García-Romero

Abstract. A nanofluid composed of Solar Salt (SS) and boehmite nanoparticles (A) in a concentration of 1% by weight, is proposed as thermal storage medium for Concentrated Solar Power (CSP) plants. A wide characterization of the raw materials has been done, focused on their thermal stability and the nanoparticle primary size and shape among other properties such as its specific heat and crystalline structure. Some features of the final nanofluids have been also investigated: thermal stability, nanoparticle sizes and their distribution and specific heat. The showed results confirm that these materials are thermally stable in the working temperature range both individually and combined. In addition, the synthesis procedure implemented is effective to keep the nanoparticle sizes in the nanometric range (<100 nm). These findings mean the first step to carry on research and characterization of this nanofluid.

3.5.3.1 Introduction

Feasibility of solar thermal technology has been widely demonstrated, becoming a safe bet in the energy mix. Growing interest from both public and private sector has led to achieve considerable advances and improvements in recent years. However, one of the critical factors to make this energy option more competitive is to extend plant operation time when sun is not available (cloudy weather or at night). This would allow to produce energy in a constant way and to adapt operation to energy demand. In this way, there is a need of storing the thermal energy when sun is shining to use it afterwards.

The current system employed in CSP plants consists of an inorganic salt composed of a eutectic mixture of sodium and potassium nitrate (60:40 by weight) which store the energy as sensible heat. It is known as SS and the configuration is the two-tank molten salt system. This salt is cheap, environmentally friendly and thermally stable at the temperatures of the CSP installation, which makes it interesting as thermal storage medium. However, its main drawback is its poor heat transfer rate due to the low thermophysical properties, such as the specific heat (c_P) and thermal conductivity (k) in the liquid state. This implies the need of a huge quantity of material to store the required energy for the solar plant. In this context, effective solutions are needed to increase the heat transfer characteristics of this material.

Nanofluids have been recently proposed as a successful answer to the mentioned issue. Nanofluids are described as liquid suspensions containing nanometre-sized particles (<100 nm).

They have been widely studied for the last twenty years as a way to increase the thermal conductivity of the base fluid. Inside this broad research topic, the specific study of molten-salt based nanofluids is quite recent (first works date from 2010 [56]) and this technology is still at its infancy. As a consequence, there are some controversial published results related to the c_p enhancement of the inorganic salts when nanoparticles are present. The mechanism that is governing this behaviour is still not very well-known, though it seems clear that the available nanoparticle surface area plays an important role [66,113].

In this work, a nanofluid based on SS containing boehmite nanoparticles in a concentration of 1% by weight is studied. In particular, we have developed a specific characterization of the initial materials as a starting point to create a nanofluid with improved thermal properties. Some other properties have been measured in the final material, mainly to assure that nanometric sizes are kept after the manufacturing procedure and the nanoparticles have not been highly agglomerated.

3.5.3.2 Experimental

3.5.3.2.1 Raw Materials

3.5.3.2.1.1 Boehmite nanoparticles

The starting material was Alumisol-10A, an industrial water nanofluid (Kawaken Fine Chemicals, Co.) containing 10% by weight of boehmite nanoparticles with a primary size of 10 nm according to the manufacturer.

3.5.3.2.1.2 Solar Salt

Solid pellets of sodium nitrate (Industrial grade, SQM industries) and potassium nitrate (Multi-KGG Greenhouse-grade, Haifa Group) were crushed in a mortar and mixed in the proper quantities to obtain the desired composition (60:40 by weight of $NaNO_3$:KNO_3).

3.5.3.2.2 Nanofluid Synthesis Procedure

Boehmite nanoparticles were included in the SS at a concentration of 1% by weight to create the nanostructured material (SS1A). The synthesis was performed as follows. Initial materials were dissolved in water to obtain initial solutions of 15% and 1% by weight for SS and A respectively. The necessary amounts of these solutions were mixed under agitation. The water was removed by simple heating (100 ºC) in a furnace and finally the material was melted at 450 ºC in an oven for 30 minutes to homogenize the sample. After cooling it at room temperature, the solid material was milled again and a representative portion was obtained.

3.5.3.2.3 Characterization Methods

3.5.3.2.3.1 Thermogravimetric analysis (TGA)

The thermal stability both of the starting materials (A and SS) and the final nanofluid (SS1A) was analysed. About 20 mg of the dried samples were put in a platinum crucible and heated in a TGA device (SETARAM SETSYS Evolution – 1750, Setaram Instrumentation, France). The heating program consisted of a first heating from 20 to 90 °C at 5 °C/min to remove humidity followed by a second stage from 90 to 550 °C at 2 °C/min. Then, the sample was maintained at the highest temperature for 3 hours. Finally, it was submitted to two thermal cycles of heating and cooling between 90 and 550 °C to know if possible changes are reversible or not. The analyses were always done under air atmosphere.

3.5.3.2.3.2 X-Ray Diffraction (XRD)

A XRD device Bruker D8Advance was used to have information about the crystal structure of the raw materials A and SS. For the boehmite, two different spectra were taken: after simple drying of Alumisol-10A (100 °C) and after applying the same thermal treatment of the nanostructured material (450 °C, 30 min) in order to know its final conformation. A comparison between the boehmite structure before and after this thermal program was done. In addition, SS spectrum was compared with other bibliographic sources.

3.5.3.2.3.3 Dynamic Light Scattering (DLS)

The nanoparticle size distribution of A and SS1A was characterized using the DLS technique (ZetaSizer nano ZS, Malvern Instruments, Ltd. Malvern, UK). The starting boehmite dispersion Alumisol-10A was used to measure the initial sizes and the final nanofluid SS1A was measured after melting, cooling it at room temperature and carefully milling. A certain quantity of distilled water is needed to be added to the sample prior to the analysis according to their nanoparticle expected size. The nanoparticle concentration was 0.5 mg per mL of water for the starting boehmite and 0.1 mg·mL^{-1} for the synthetized material, in agreement with Malvern experts' advices. The presence of dissolved nitrates in SS1A was taken into account into the operating procedure implemented on the device to analyse this sample.

3.5.3.2.3.4 Transmission Electron Microscopy (TEM)

The size and shape of primary boehmite nanoparticles were observed by means of TEM using a device JEOL 2100 operating at a voltage of 100kV. The elemental composition of boehmite was analysed by means of Energy Dispersive X-ray Spectroscopy using an EDX system (Oxford Instruments INCA Penta FETX3) attached to TEM.

3.5.3.2.3.5   Scanning Electron Microscopy (SEM)

The dispersion of nanoparticles in solid SS1A samples was evaluated using a field emission scanning electron microscope (SEM) (JEOL, 7001F). Specimens were metallized in a thermal evaporator. Secondary Electrons (SE) and Quadrant Back-Scattering Detector (QBSD) images and digital image processing were used to characterize the nanoparticle clusters in the solid salt. The elemental composition of the material was analysed by means of Energy Dispersive X-ray Spectroscopy using an EDX system (Oxford Instruments INCA Penta FETX3) attached to SEM.

3.5.3.2.3.6   Differential Scanning Calorimetry (DSC)

A DSC device (Q100, TA Instruments, US) was used to measure the specific heat (c_p) of the raw materials A, SS and SS1A through Modular Differential Scanning Calorimetry (MDSC) with an isothermal procedure. Three temperatures, 196 ºC (SS in the solid state), 256 ºC and 396 ºC (SS in the liquid state) were tested. Some milligrams of the sample were introduced in an aluminium pan hermetically sealed under an inert atmosphere. The samples were first stabilized at the desired temperature and then subjected to an isothermal period of 10 minutes to achieve the salt thermal equilibrium prior to the data collection (20 minutes). The modulation was set up with 0.6ºC of amplitude and a 110 seconds period according to the TA Instruments expert advices. The explained isothermal program was always performed from the highest to the lowest temperature. Thus, in the case of SS a complete melting of the sample was achieved at the beginning of the experiment (melting temperature 220ºC). In this way, the sample inside the crucible in the solid state behaves as a compact piece rather than the initial fine powder. The sapphire sample commonly used as the reference material was first measured under the same protocol to find out the possible device divergence and correct the final sample results.

Three different replicas were measured for each sample and the average c_p and its Standard Deviation (SD) were obtained.

3.5.3.3 Results and discussion

3.5.3.3.1 Thermal Stability

The first and most important step to validate the feasibility of a certain nanomaterial to be included in a matrix of molten salt is its thermal stability. It is essential to analyse both the possible changes of the nanomaterial and also those of the mixture with the salt at the working temperature range. Figure 3-56 shows the thermogravimetric (TGA) curves from 20 ºC to 550 ºC in the first thermal cycle for A, SS and the nanostructured material SS1A. The differential thermogravimetric (dTG) curve is also presented in the case of A to analyse the inflections in the TGA curve and

consequently the changes in the rate of weight loss.

The thermal analysis of boehmite nanoparticles revealed three different stages in our temperature range. The first weight loss (Δm=-8.4%) occurs between 20 and 90 ºC with a minimum around 80 ºC, due to the loss of humidity of the sample. A second step of dehydration (Δm=-13.3%) is observed in the range of 90-400 ºC with an endothermic peak in 390 ºC related to the desorption of intralaminar water located between boehmite nanoparticles. Finally, the boehmite starts the transformation in γ-Al_2O_3 that accounts the 5.6% of the mass loss. These results are in agreement with literature on this subject [186,187].

According to the curves, the SS is thermally stable and the weight losses are minor (0.6%). It is considered that formation of nitrites (the main mechanism of thermal degradation of nitrates) starts around 450 ºC but at temperatures lower than 600 ºC it occurs in a very little extension [33].

The curve which represents the SS1A sample is very similar to that of the SS and mass losses are slightly higher due to the presence of boehmite and its dehydration processes explained before.

The three samples registered neglectful weight losses (under the detection limit of the device) after their thermal cycling, so it is considered that any thermal events found in the first heating cycle are irreversible. This is of quite importance because a stable sample of solar salt with boehmite nanoparticles can be obtained by melting it at the suitable temperature. Therefore, it is considered that boehmite is a valid nanomaterial to be mixed with the solar salt.
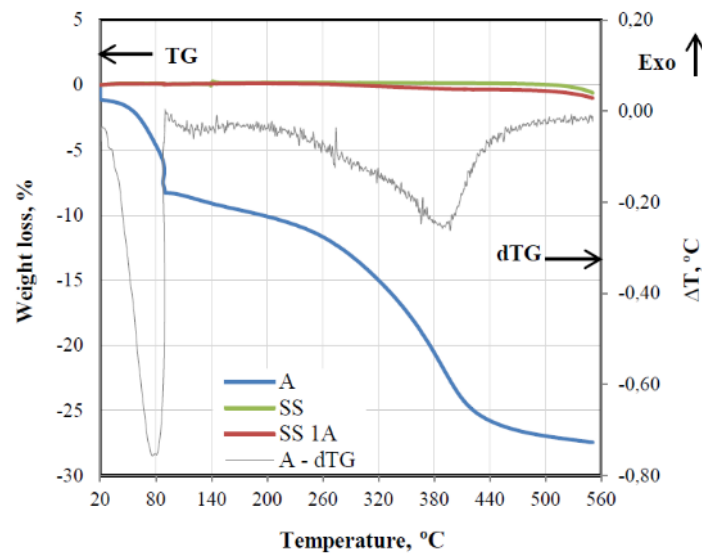
Figure 3-56. TGA-dTG curves of the initial boehmite (A), Solar Salt (SS) and solar salt with boehmite nanoparticles (SS1A).

3.5.3.3.2 Crystalline Structure

Figure 3-57 exhibits the recorded XRD patterns for A (before and after calcination) and SS. The spectrum of boehmite nanoparticles showed several peaks typical of this material as is supported by XRD spectra database software of the device and the specialized literature [33]. After the thermal treatment at 450 ºC, there is a decrease of crystallinity and the pattern is more diffused. This is probably due to the loss of intralaminar water and the incipient conversion to γ-Al_2O_3, which was revealed by the TGA tests results.

On the other hand, the peaks appearing in the SS spectra are also in agreement with the aforementioned database. This XRD pattern will be further employed in the nanostructured samples to get knowledge about possible changes happened in the crystalline structure of SS induced by the addition of boehmite.

(a) (b)
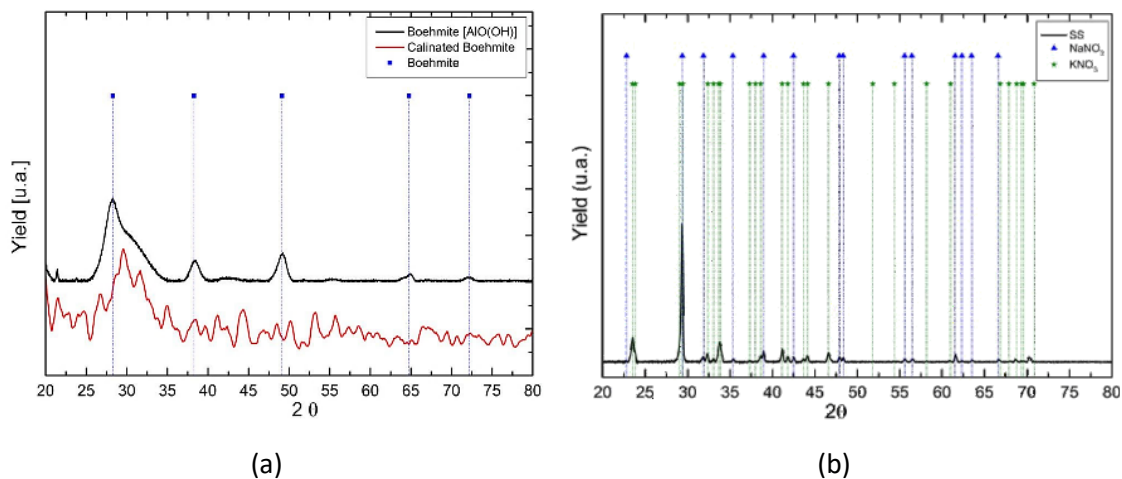
Figure 3-57. XRD spectra of boehmite before and after calcination process (a) and Solar Salt (SS) (b).

3.5.3.3.3 Nanoparticle Size, Morphology and Distribution

It is generally accepted that the nanoparticle size in the final synthetized material is the key factor responsible of the anomalous increment of the thermophysical properties in the molten-salt based nanofluids [66,113]. Therefore, it is of high importance to control and limit the nanoparticle agglomeration through the synthesis procedure in order to stay in the nanometric range (<100 nm). The nanoparticle shape may have also some influence on the further interaction with the anions and cations of the SS. The distribution of nanoparticles into the salt matrix is also interesting to discard a high heterogeneity of the sample.

The size distribution of A and SS1A obtained from DLS is shown in Figure 3-58. The boehmite initial sizes are in the range from 8 to 25 nm with a maximum in 13 nm. Bigger sizes are found in the sample SS1A due to the nanoparticle agglomeration occurred during the preparation of the nanostructured material. Most of the nanoparticles sizes falls in the interval 50 to 140 nm and the

maximum is located in 68 nm. A tiny quantity of the nanoparticles suffered a higher degree of agglomeration with a size around 712 nm.

Figure 3-59 presents two TEM images of the initial boehmite. On one side, the Figure 3-59 (a) gives an idea of the nanoparticle size which is in the range of that obtained by DLS technique. On the other side, it can be deduced from both images that the morphology of the boehmite nanoparticles consists of several layers arranged in a fiber-like structure.

Finally, SEM images of SS1A were examined to get knowledge about the clusters sizes and its distribution along the SS matrix. Images taken on the solid sample both with the SE and QBSD detector can be seen in Figure 3-60 (a) and (b) respectively, along with their elemental composition from EDX analysis. These images are similar to the ones published by other research groups working with nitrate salts [66,113]. The matrix of salt is seen as a group of globe-shaped crystals with two different grey tones corresponding to the components of SS ($NaNO_3$ in darker grey). This colour differences can only be seen in QBSD images (Figure 3-60 (b)). The nanoparticles appear embedded in the SS crystals with a different shape. The marked-red areas were analysed with EDX to confirm the presence of nanoparticles. In Figure 3-60 (a) an agglomerate of around 5 x 3 μm was found and its elemental composition revealed that aluminium is present in that area. Some quantity of chloride was also found because this element is contained in the industrial-grade nitrates which have been employed. The cluster analysed in the indicated area in Figure 3-60 (b) is about 1 μm in size and aluminium appears in the elemental composition. Some carbon appears due to contamination of the sample and little quantities of chloride were found again. It is worth mentioning that in both Figure 3-60 (a) and Figure 3-60 (b) the EDX analyses were also performed in areas outside those marked in red. No aluminium was found in those regions.

The analysed DLS results show that the manufacturing method followed to produce SS1A is adequate since most of the nanoparticles remains in the nanometric range in the final material. This is an important first step that would allow achieving an enhancement in c_p when further DSC analyses were done. In addition, the microscope images have confirmed the size distributions of nanoparticles both before and after adding them in the SS.
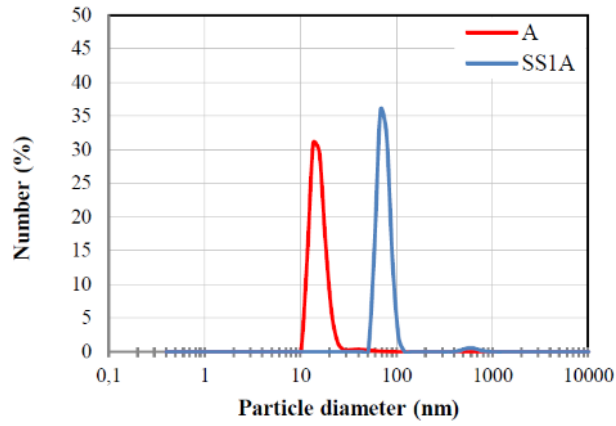
Figure 3-58. Boehmite nanoparticle size distribution for the initial boehmite (A) and the nanostructured material (SS1A).
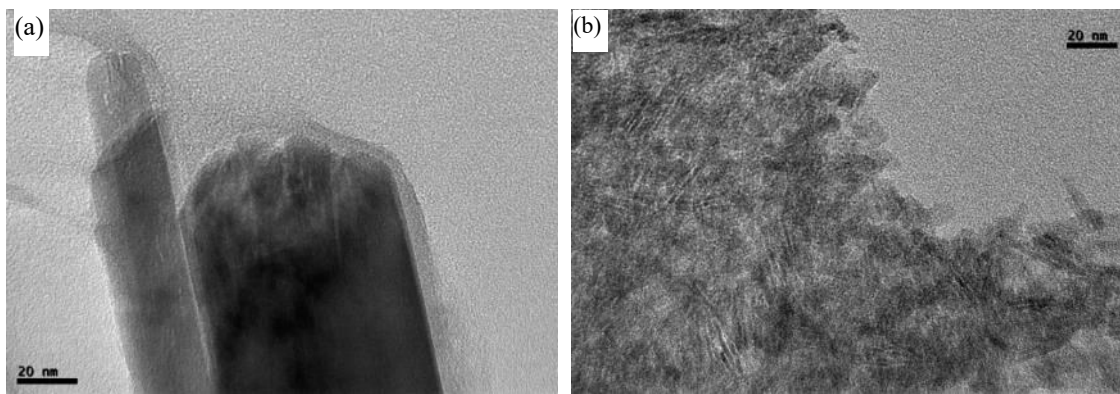
Figure 3-59. TEM images of boehmite nanoparticles.
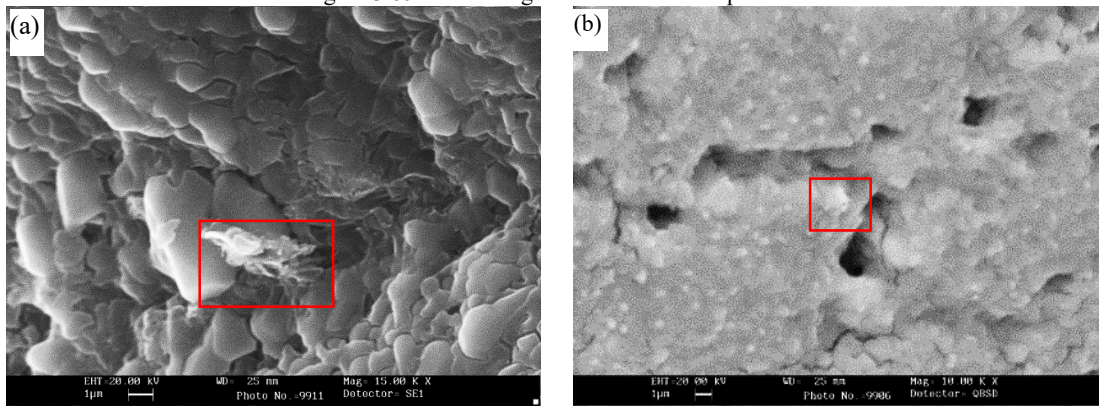
Element	Weight%	Atomic%
O	59.52	73.68
Na	13.13	11.31
Al	4.69	3.45
Cl	1.63	0.91
K	21.03	10.65
Totals	100.00	

Element	Weight%	Atomic%
C	13.67	23.81
O	33.17	43.36
Na	9.46	8.61
Al	1.48	1.15
Cl	8.93	5.27
K	33.28	17.80
Totals	100.00	

Figure 3-60. SEM images of SS1A and their EDX analysis. SE image (a) and QBSD image (b).

3.5.3.3.4 Calorimetric analysis

Our main objective consists of improving the thermal performance of the nanostructured material. This starts by measuring the c_p of the raw SS in a precise manner. These results would allow comparing the value of this thermophysical property in the pure salt with the salt containing nanoparticles. The c_p of raw boehmite has been also evaluated in order to establish a theoretical value of the specific heat of the mixture by applying the traditional mixing rule. Results of the specific heat capacity of A, SS and SS1A (theoretical and experimental) are presented in Table 3-39. In addition, the enhancements in c_p obtained with the addition of nanoparticles have been calculated from the experimental SS1A results. The collected data for the SS and A are in concordance with the results provided by the specialized literature [195,197]. The results indicate that A has a lower c_p than the SS and therefore, their mixture may have a decrease of this property with respect to the SS. However, an improvement has been obtained for any of the temperatures, being especially high in the solid state. The observed behaviour is in agreement with the findings of other authors [66,113]. Further work is needed to understand this performance and investigate the factors that are affecting this property.

Table 3-39. Specific heat and SD of boehmite (A), solar salt (SS) and final nanofluids (SS1A) at the studied temperatures.

Sample	Specific heat, c_p (kJ·kg^{-1}·K^{-1})		
	196 ºC	256 ºC	396 ºC
A	1.195 ± 0.039	1.237 ± 0.009	1.471 ± 0.031
SS	1.424 ± 0.020	1.552 ± 0.002	1.568 ± 0.025
SS1A (Theor.)	1.421	1.548	1.567
SS1A (Exp.)	1.693 ± 0.025	1.631 ± 0.027	1.618 ± 0.028
Enhanc. (%)	18.87	5.07	3.19

3.5.3.4 Conclusions

A novel nanomaterial composed by boehmite nanoparticles dispersed in a matrix of molten solar salt (an inorganic salt based on nitrates) is proposed as an effective thermal storage material in solar power plants. The initial materials have been characterized prior to the synthesis in order to know their suitability to the final application. Thermal analysis revealed that boehmite undergoes several dehydration events at the working temperature range but they seem to be irreversible. Solar salt remains stable with little weight changes at these temperatures. The crystalline structure was analysed by XRD and the loss of crystallinity may be related to the thermal dehydration of boehmite. In addition, DLS and TEM were employed to analyse the initial nanoparticle size (13 nm) and shape (laminar). The synthetized nanomaterial (SS1A) has been also characterized. Its thermal stability results to be very similar to that of the SS with no weight changes. Finally, the

nanoparticle size remains in the nanometric range (68 nm) after the mixing and manufacturing procedure, which is quite important to obtain improvements of the specific heat. This property was also analysed and enhancements were found both in the solid and the liquid state compared to the base SS. In addition, the specific heat results of both boehmite and the SS are in the range of the published values.

Further characterization of the nanostructured material is needed in order to understand the mechanism responsible of the enhancement of thermal properties respect to the base salt. Future work includes also the measuring of thermal conductivity, viscosity and cost estimation.

Chapter 4

SYNTHESIS PROCEDURE

4   SYNTHESIS PROCEDURE

4.1   INTRODUCTION

This Chapter details the procedure followed to obtain the nanofluids. The studies performed in this work show that the synthesis method followed to produce the MSBNFs or NePCMs largely determine the nanoparticle size into the molten salt and thus, the thermal performance of the nanofluid.

A new synthesis methodology has been developed, which is beyond the start-of-the-art. This procedure offers advantages In comparison to the traditional hot plate method commonly reported on the literature, as well as in comparison to a less usual method based on spraying the nanoparticles over the solid salt (Journal Contribution 3).

The method developed in this work was optimized as detailed in the Journal Contribution 3 and in the Conference Contribution 4.

4.2   JOURNAL CONTRIBUTION 3. BEYOND THE HOT PLATE METHOD FOR THE SYNTHESIS OF MOLTEN SALT-BASED NANOFLUIDS: DEVELOPMENT OF TWO INNOVATIVE PROCEDURES

Authors: Belén Muñoz-Sánchez, Javier Nieto-Maestre and Ana García-Romero
Abstract: The research on nanofluids with inorganic salts as the base fluid is increasing lately due to the high enhancements of specific heat showed by these materials. These increments are directly related to the high free surface of the nanoparticles interacting with the molten salts, which mainly depends on the nanoparticle percentage, size and shape. In order to achieve Molten Salt Based Nanofluids (MSBNFs) with the desired particle concentration and size-distribution, it is essential to pay attention to the synthesis procedure. The different variables involved (temperature, time, stirring…) should be carefully selected and the particle size-distribution monitored during the fabrication of the nanofluids. Two new production methods of Solar Salt-based nanofluids have been developed in this work, named as "sprayed nanoparticles" and "low-water hot plate". The results have been compared to those obtained by the traditional hot plate method. According to the nanoparticle size distribution and to the specific heat, the most effective synthesis method is the so called "low-water hot plate". Its novelty lies on the use of water-based nanofluids as a source of nanoparticles, rather than solid nanoparticles. This circumstance eliminates the need of ultrasounds to disperse the nanoparticles and reduces the mixing water required to carry out the process by 100 times. The second part of this research is devoted to the optimization of this synthesis procedure with the objective of producing the smallest possible nanoparticle size in the final nanofluid.

4.2.1 Introduction

Nanofluids are defined as the colloidal suspension of nanoparticles (size under 100 nm) into a base fluid. These composite materials were first synthetized by Choi and Eastman [42] in 1995 and their main attribute and novelty lies on the spectacular enhancement of the thermal conductivity compared with their base fluid. Therefore, these innovative materials have a high application potential on those industries involving thermal transfer and storage processes, such as the Concentrated Solar Power (CSP) technology.

The current solar power facilities face some challenges in terms of material designing. A molten inorganic salt (a mixture of molten nitrates called "Solar Salt") is used both, as Heat Transfer Fluid (HTF) to transfer the heat from the sun to the steam cycle and as Thermal Energy Storage (TES) material, to increase the working hours of the plant. The main drawbacks of this material are the low specific heat and thermal conductivity, which restraint the heat transfer rate desirable for this application.

In this case, the nanofluids technology could significantly overcome this issue. The materials consisting of a dispersion of nanoparticles into fused salts are known as Molten Salt-Based Nanofluids (MSBNFs) and constitute a research area inside the field of nanofluids. These MSBNFs were first synthetized by Shin and Banerjee [56] in 2010, who claimed a significant increase of the specific heat (100%) In comparison to the base salt. Since then, many investigations have supported this finding and the specific heat has been the most studied property on these materials.

Among other factors, the synthesis procedure of the MSBNFs has a direct impact on the thermal performance of the material, as revealed by several investigations [31,32,37,56,65,66,110,115,120]. The route followed to produce the material affects the nanoparticle size and their homogeneous dispersion into the salt matrix. If the nanoparticles agglomerate, the surface available to interact with the salt ions will reduce. Controlling this fact is the key to obtain a successful nanofluid.

The synthesis technique known as "the hot plate method", first used by Shin and Banerjee [56], has been the most usual procedure to develop MSBNFs. In general terms, this process involves the following four steps:

- <u>Salt dissolution</u>. Mixture of the inorganic salts in the solid state to produce the required composition. Addition of a certain quantity of distilled water to dissolve the salt.
- <u>Nanoparticle addition</u>. Addition of the solid nanoparticles to the salt solution.
- <u>Stabilization</u>. Production of a stable suspension of nanoparticles into the solution with ultrasounds.

- <u>Drying</u>. Pouring the dispersion on a Petri dish to evaporate the water onto a hot plate.

The principal concern of this method is the low scalability of the process. Despite the inorganic salts are highly soluble in water, the dispersion of the nanoparticles with ultrasonic power requires a great quantity of liquid (the usual ratio of solid salt and water is 1:100). In summary, the large water and energy consumption needed to stabilize the nanoparticles and, subsequently, to remove the employed high amount of water are the main barriers to its industrial implementation. This situation led some authors to modify the technique. However, these are minor modifications, such as changing the drying temperature [56], the drying surface [65], evaporate the water by spray drying or low temperature vacuum [32], or tuning the power of sonication energy [120]. Several authors developed the following synthesis methods, different from the "hot plate method": the direct addition of the solid nanoparticles into the molten salt [37,66,110], the in situ production of nanoparticles inside the molten salt by using a precursor [115] and the solid milling of nanoparticles and solid salt with metal balls [31,32,35]. The results obtained in these works in relation to the thermal properties of the MSBNFs have been gathered in Table 4-1.

Table 4-1. The MSBNFs synthesis methods published in the scientific literature different from the hot plate method. Comments on the main features and the specific heat determined In comparison to that obtained by the hot plate method.

METHOD	REFERENCE	CHARACTERIZATION	COMMENTS
HOT PLATE MODIFICATIONS			
Drying temperature and surface	Shin and Banerjee [56]	Specific heat, TEM	Specific heat increases by drying in a hot plate at 60 ºC, rather than in a bottle at 100 ºC. Higher agglomeration reported on the latter condition.
Drying surface	Jo and Banerjee [65]	Specific heat, molecular dynamics simulation	Drying the material in a larger surface (hot plate) increases the specific heat in comparison to drying it in a bottle (reduced area).
Spray-drying	Schuller et al. [32]	Specific heat, melting temperature, heat of fusion	Spray-drying increased the specific heat in comparison to hot-plate drying. The melting temperature was not affected, while the required heat of fusion decreased.
Low temperature vacuum	Schuller et al. [32]	---	The method was discarded due to the violent boiling of the solution in vacuum.
Sonication energy	Riazi [120]	Nanoparticle size distribution	The sonication energy was tuned until the particle-size was nanometric, which increased the specific heat.

METHOD	REFERENCE	CHARACTERIZATION	COMMENTS
NEW METHODS			
Addition to molten salt (extrusion at high temperature)	Chieruzzi et al. [37]	Specific heat, melting temperature, heat of fusion, SEM	The material produced by the hot plate method has higher specific heat, similar melting temperature, higher heat of fusion and a more homogeneous nanoparticle dispersion than the extrusion at high temperature method.
Solid milling	Schuller et al. [32]	---	The method was discarded due to the low homogeneity observed after milling.
	Lasfargues [31]	Specific heat	The absolute values of specific heat were similar both in the solid milling and the hot plate method.

According to the available published articles, there is a lack of systematic research regarding the relationship between the nanoparticle size and the production route, despite the importance of controlling the nanoparticle size to obtain the desirable thermal behaviour. Additionally, there is also an urgent need to research synthesis methods suitable to be industrially scalable and reproducible. This research aims to give some insight in the relationship between the synthesis method and the thermal properties by comparing three synthesis procedures of Solar Salt-based nanofluids: the traditional hot plate method and two novel procedures developed in this work, named as "sprayed nanoparticles" and "low-water hot plate". In the first part of this research, the materials obtained by the three processes are compared in terms of nanoparticle size and the specific heat. Then, the procedure with the best results has been optimized.

4.2.2   Materials

Two different batches of Solar Salt with the composition 60:40 wt% of $NaNO_3:KNO_3$ were prepared, each one of different purity, labelled as ASS (analytical grade solar salt) and RSS (refined grade solar salt). To do it, the following materials were employed:

- To produce the Analytical grade, ASS: Labkem, $NaNO_3 \geq 99.5$ wt% and Labkem, $KNO_3 \geq 99.8$ wt%. Both salts have an extremely low level of impurities and have been selected to synthetize nanofluids comparable to those reported on the literature (which include salt of this purity).
- To produce the Refined grade, RSS: SQM, $NaNO_3 \geq 99.5$ wt% and SQM, $KNO_3 \geq 99.6$ wt% These materials correspond to those empoyed to produce the salt used in the CSP plants.

In both cases, the raw nitrates were ground in a mortar, dried in an oven at 100 ºC to remove the moisture and mixed in the mentioned proportions. Then, these mixtures were melted in a furnace at 396 ºC for 30 minutes to ensure their homogeneity. Once this thermal program was finished,

the salts cooled down at room temperature until their solidification outside the furnace. Finally, they were grounded in a mortar to obtain a fine powder. The base materials ASS and RSS were ready to be further mixed with the nanoparticles.

Two types of ceramic nanoparticles were added to the base salts:

- <u>Alumina Nanoparticles (ANPs)</u>. They were purchased from Kawaken Chemicals. The material consists of an industrial water-based nanofluid, Alumisol-10A, containing fiber-shaped boehmite nanoparticles (L=50 nm, ϕ=10 nm) at 10 wt% according to the manufacturer. The boehmite (aluminium oxyhydroxide, AlOOH) is a precursor of the γ-Al_2O_3.

- <u>Silica Nanoparticles (SINPs)</u>. Two type of silica nanoparticels were employed. On one side, solid crystalline silica nanoparticles (Silica nanopowder, Sigma-Aldrich, St. Louis, MO, USA) were used to replicate the traditional hot plate method. On the other side, a dispersion of colloidal silica at 30 wt%, LUDOX® SM-30, from Sigma-Aldrich was used as a source of spherical SiNPs in the novel methods.

4.2.3   Synthesis methods

This section describes in detail the three nanofluid fabrication processes evaluated in this work. The Table 4-2 shows the nanofluid materials and composition produced by each of these procedures.

Table 4-2. Designation and composition of the nanofluids produced with each synthesis method.

Base salt	Nanoparticle	Nanoparticle amount, wt%	Designation	Method
ASS	Silica nanopowder	1	ASS1Si_1	Traditional hot plate
	LUDOX® SM-30	1	ASS1Si_2	Low-water hot plate
RSS	LUDOX® SM-30	1	RSS1Si_1	Sprayed nanoparticles
	LUDOX® SM-30	1	RSS1Si_2	Low-water hot plate
	Alumisol-10A	1	RSS1A_1	Sprayed nanoparticles
	Alumisol-10A	1	RSS1A_2	Low-water hot plate

4.2.3.1 The traditional hot plate method

In this research, the traditional method has been used only for comparative purposes. The crystalline SiNPs were added to the ASS in a concentration of 1 wt% (ASS1Si_1) by following the next experimental steps.

- <u>Salt dissolution</u>. Initially, the ASS was dried in an oven at 100 ºC for at least 2 hours to remove the moisture which may contain. Then, the required quantity of the salt to produce 1 g of nanofluid (0.99 g) was precisely weighed in a balance. Deionised water was added to this solid salt in an amount of 100 mL per gram of salt (100 mL) and the combination was stirred until the complete dissolution.

- <u>Nanoparticle addition</u>. The corresponding quantity of SiNPs (1 wt%) was weighed and added to the former mixture (0.01 g).

- <u>Stabilization</u>. An ultrasonic probe (UP200St, Heilscher) was used to achieve a correct dispersion of the SiNPs in the salt dissolution. The working conditions were fixed at 70% of power with 1 cycle/s during five minutes. After this slot of time, the dissolution was clear and transparent which was indicative of the complete dispersion of the nanoparticles.

- <u>Drying</u>. The solution was poured onto a glass Petri dish (ϕ = 15 cm) and heated at 100 ºC overnight until the water was completely removed. The solid material was finally recovered from the Petri dish by scratching its surface and kept in a dry place until their characterization.

4.2.3.2 The sprayed nanoparticles technique

This method is proposed with the objective of finding a process suitable to be industrially scalable. It is designed with the focus of potential implementation on the mining industries which currently provide the Solar Salt to the CSP industry. The nanoparticles could be added to the solid salts during the last stage of the purification process presently carried out in these companies, thus minimizing the costs and enabling the potential commercialization of this product for thermal storage.

The addition of anti-sticking agents to the Solar Salt, among other compounds, is common in the mining industry. The production process, among other stages, includes a drying stage which basically consists of a conveyor belt where the solid nitrates are fed to a rotary kiln where will be further dried. Diverse additives are sprayed onto the nitrate crystals in the course of this route. In the same manner, the commercial aqueous nanofluids used in this research (as the source of nanoparticles), Alumisol-10A or LUDOX® SM-30, can be added at this point of the treatment (Figure 4-1).

Two nanofluids composed of RSS-1 wt% of SiNPs (RSS1Si_1) and RSS-1 wt% of ANPs (RSS1A_1) were produced with this process. A simple configuration was devised to replicate the industrial method at a laboratory level, taking special care to ensure that the critical aspects resemble those of the industrial process. First, 300 g of the solid salt RSS were spread in a rectangular Pyrex glass container of 40 x 27 cm (length x width). The necessary amount of Alumisol-10A or LUDOX® SM-30 was sprayed onto the solid salt on each case. The samples

were then dried in an oven at 100 ºC overnight. The doped salts were recovered, milled and homogenized prior to their analysis.
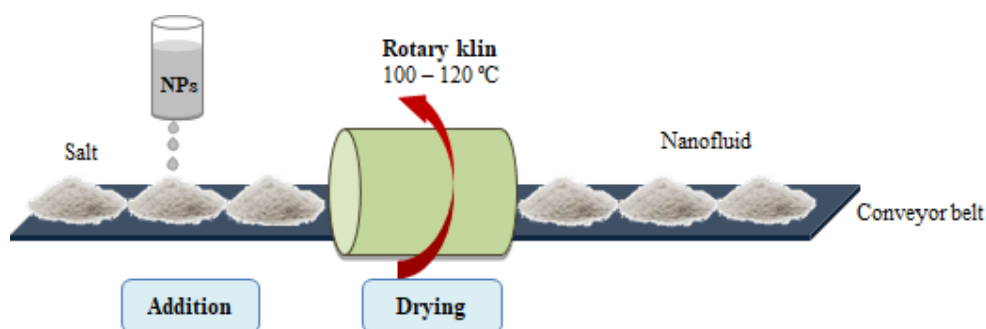
Figure 4-1. Schematic drawing of the proposed sprayed nanoparticles technique.

4.2.3.3 The low-water hot plate method

The following procedure is based on the traditional hot plate method. However, there are two significant differences in this case: ultrasounds are not required and the amount of water is substantially reduced. The method comprises four steps (Figure 4-2):

- Salt dissolution. First, the Solar Salt (of the desired purity) was dried in an oven at 100 ºC for at least 2 hours to remove any trace of moisture. Then, the required amount of the salt to produce 10 g of nanofluid (9.9 g) was precisely weighed in a weight-scale. A concentrated solution (50 wt%) is produced by dissolving the Solar Salt in a "deionized modified water" (9.9 mL) under mechanical stirring and mild temperature (≈50 ºC). The "deionized modified water" consists of deionized water were sodium hydroxide or diluted nitric acid have been added to achieved the pH of stability of each nanoparticle (pH=2 for the ANPs and pH=9 for the SiNPs). The pH suitable to stabilize each type of nanoparticle was experimentally determined according to measurements of Zeta Potential of the Alumisol-10A and LUDOX® SM-30 products.

- Nanoparticle addition. The necessary quantity of nanoparticle dispersion (1 g of Alumisol-10A or 0.33 g of LUDOX® SM-30) was precisely weighed and added to the previous solution. Mild stirring was applied to properly mix both materials, but avoiding clustering of nanoparticles due to physical impacts. After some minutes, the solution was carefully poured drop by drop onto a glass Petri dish (ϕ = 15 cm) with the aid of a plastic Pasteur pipette. Immediately after stopping the stirring, the crystallization of the nitrates was observed. The solution was near its saturation point and the nanoparticles act as nucleation points.

- Drying. The Petri dish with the solution is carefully covered with a filter paper to avoid contamination. It was subsequently heated in an oven at 100 ºC where it remained overnight to

remove any water trace. The solid sample was then recovered by scrapping the Petri dish surface with a metallic spatula.

- <u>Melting</u>. Finally, the solid material was put into a glass flask and melted in a furnace at 396 ºC for 30 minutes. The flask was then removed out from the furnace and left to cool down at room temperature. This final solid sample was crushed and milled in a mortar until a fine powder was obtained.
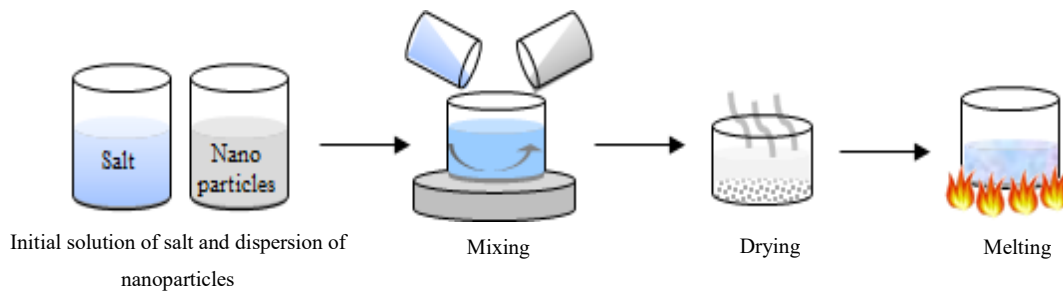
Figure 4-2. Steps of the low-water hot plate method for nanofluid synthesis.

Three nanofluids were synthetized with this procedure, one to compare with those of the traditional method (ASS1Si_2) and two more analogous to those from the sprayed nanoparticles technique (RSS1Si_2 and RSS1A_2).

4.2.4   Characterization

4.2.4.1 Nanoparticle size distribution

The size of the ANPs and SiNPs was measured on each nanofluid with the aim of establishing a relationship between the size and the thermal properties. The nanofluids were characterized using the Dynamic Light Scattering method (DLS, ZetaSizer Nano ZS, Malvern Instruments, Ltd. Malvern, UK). The nanoparticle size distribution of these nanofluids was thus obtained as the number of nanoparticles at each size-range, between 0.4 and 10,000 nm. The results obtained include the most frequent size of the distribution (the mode) and the particle diameter below which 90% of the nanoparticles (D90) are found.

4.2.4.2 Specific heat

A Differential Scanning Calorimeter (DSC, Q1000 TA Instruments with autosampler) was used to determine the specific heat, by using the Modular Differential Scanning Calorimetry (MDSC) under an isothermal procedure. Around 30 mg of the sample were introduced in an aluminium crucible, which was hermetically sealed afterwards. The sample was first stabilized at the desired temperature for an isothermal period of 10 min to achieve the material thermal equilibrium. The data collection was carried out for 20 min at the same temperature. Nitrogen was used as inert gas inside the device. The specific heat was measured at 196 °C (solid state), 296 ºC and 396 °C (both

in liquid state). These temperatures correspond to the working temperatures of the SS in real conditions on CSP facilities. The temperature modulation of the DSC technique was set-up to 0.6 °C of amplitude and a period of 110 s in order to provide good sensitivity. Three different portions of each sample were measured to obtain a representative result. This measurement method proved a high accuracy [157,158].

4.2.5 Results and discussion

4.2.5.1 Determination of the best synthesis method

4.2.5.1.1 Nanoparticle size distribution

The Figure 4-3 gathers the size distribution of each nanofluid analysed in this study. The mode of each distribution is pointed out over each curve. The aim is to study the evolution of the nanoparticle size-distribution in the different stages of the process. As a result, measurements were carried out after each stage, and the curves included on the Figure 4-3 correspond to these stages: 1) the initial nanoparticles dispersed in water, 2) after mixing the nitrates and the nanoparticles, 3) after drying the solution and 4) after melting the nanofluid. It is worth mentioning that some of these stages were not followed in some cases. Specifically, the nanofluid made under the traditional hot plate method was not melted in order to resemble the process reported in the literature. Also, the sprayed nanoparticles method does not include the stage 2) of mixing.

The ASS1Si_1, Figure 4-3 up left, shows a distribution of the initial solid SiNPs out of the nanometric range (<100 nm), as could have been foreseen due to the difficulty on breaking the initial solid nanoparticle agglomerates, even with the application of ultrasounds. Once the nitrates were added to the solution, the distribution remains almost identical. However, some agglomerates are observed with sizes around 700 nm, as a result of the high agglomeration due to the screening by the salt ions of the electrostatic repulsion forces between the nanoparticles. During the nanofluid drying stage, these agglomerates act as nucleation points and attract the nanoparticles towards then, ending on the final distribution with its highest percentage at 712 nm.
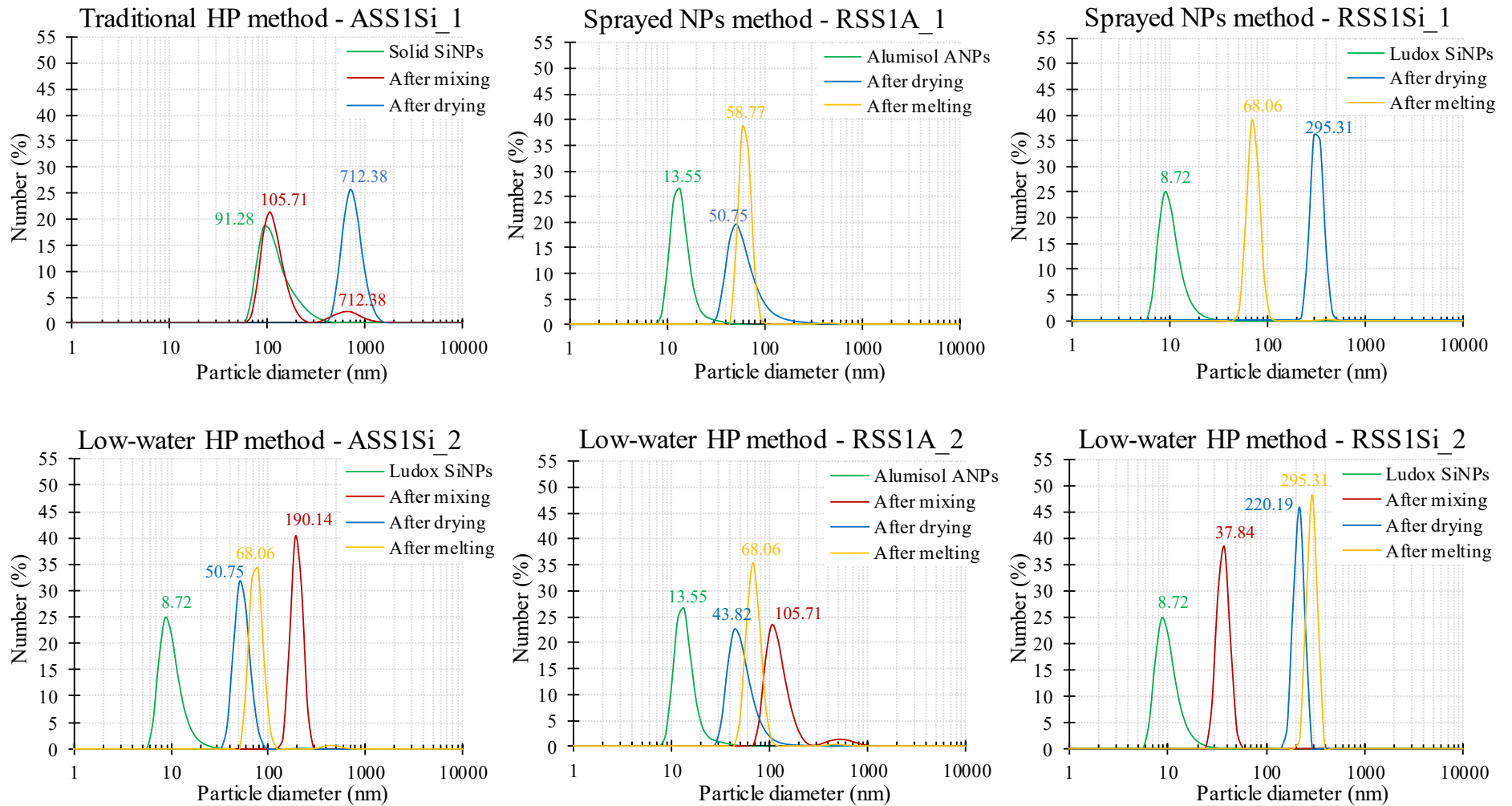
Figure 4-3. Nanoparticle size distribution of the nanofluids synthetized by the three different methods. The mode of each distribution has been depicted on top of each curve.

There are not many references in the literature about the nanoparticle size of the MSBNFs and therefore the comparison of the results obtained in this work is limited to those few ones. Andreu-Cabedo et al. [113] studied the Solar Salt with 0.5 wt% of SiNPs. These researchers found a nanoparticle size-distribution with the largest percentage of nanoparticles at 240 nm. This value is smaller than the value encountered in this study but the nanoparticle concentration in their nanofluid is lower, which could be responsible for the difference. Miliozzi et al. [78] also used a DLS device to measure nanoparticle size-distribution on nanofluids of Solar Salt with 1 wt% of SiNPs, among others. They obtained a Z-ave of 900 nm, a parameter which can be equivalent to the mode of the distribution in some cases. Riazi et al. [120] showed the dependence of the sonication energy with the nanoparticle sizes in a nanofluid equivalent to ours. They found distributions with a mode around 300 nm after dispersing the nanoparticles with the optimum sonication energy.

Regarding the two nanofluids made by the sprayed nanoparticles method (RSS1A_1 and RSS1Si_1, Figure 4-3 up centre and up right), it is remarkable the low size of the initial nanoparticles, both for the ANPs and the SiNPs. This is the great advantage on using water-based nanofluids as a source of nanoparticles (Alumisol-10A and LUDOX® SM-30) and the main difference with the previous nanofluid. After spraying these dispersions over the nitrate particles and during the mixture, most of the ANPs remained with a nanometric size while the SiNPs grew until 300 nm. This fact may be related to the higher viscosity of the Alumisol-10A ($\leq$50 cp [141]) compared to that of LUDOX® SM-30 (4.8-6.8 cp [198]). During the drying step, the water is removed more slowly in the nanofluid which contains ANPs, which allows an ordered nucleation and growth of the nanoparticles. In this synthesis method, the homogeneous impregnation of the nanoparticles-aqueous-dispersion onto the solid salt is the most critical point. In order to have reliable conclusions, the nanoparticle size distribution after the drying step was studied on five replicas of 5 g extracted from the total amount of solid material (300 g). The Figure 4-4 shows the most frequent size on each of these samples, both for the nanofluid RSS1A_1 and RSS1Si_1. In the first case (Figure 4-4, left), the ANPs sizes range from 50 to 100 nm with the exception of one replica at 875 nm. On the case of the nanofluid RSS1Si_1 (Figure 4-4, right), the most frequent sizes measured on the different replicas are not so close to each other and the determined mode values are comprised in the range 175 – 422 nm.

With respect to the last step of melting, the Figure 4-3 shows that the size-distribution width of these nanofluids shortens in comparison to the previous distributions. This could be related to the formation of big agglomerates (micron-sized) when the sample is submitted to high temperatures. Since in this last stage of melting the nanofluids are melted during a significant time, the formed big agglomerates may settle down and, as a result, they would not have been detected by the DLS.

The results obtained by the low-water hot plate method are shown on Figure 4-3, second row. In the case of the nanofluid ASS1Si_2, differences with the results obtained by the traditional method can be found in every synthesis stage. The initial nanoparticle distribution is in the nanometric range since the SiNPs are well dispersed and stabilized in the LUDOX® SM-30. These nanoparticles experience a noticeable size increase when are added to the dissolved nitrates because of the high ionic strength of this medium. After the mixture is dried, the solid material has a narrow distribution with a maximum at 50.75 nm. The comparison of the nanofluids RSS1A_1 (produced by spraying the nanoparticles) and the RSS1A_2 (low-water hot plate method) gives very similar distributions after the mixing and drying steps. However, after being melted, the particle size of the nanofluid RSS1Si_2 (mode of 295 nm) is bigger than the RSS1Si_1 particle size (mode of 68 nm).

The homogeneity of the nanofluids RSS1A_2 and RSS1Si_2 after the drying step is plotted on the Figure 4-4, together with the homogeneity obtained on the sprayed nanoparticles method (RSS1A_1 and RSS1Si_1). The nanofluid with ANPs produced by the low-water hot plate procedure, RSS1A_2, has smaller sizes (mode around 30 nm) and lower data dispersion. The mode of the nanoparticles in the nanofluid RSS1Si_2 is close to 400 nm, with a higher repeatability between the replicas than the RSS1Si_1, produced by the sprayed nanoparticles method. Similarly, Schuller et al. [32] used the spray drying method to remove the water of the solutions of salts and nanoparticles and also found a low homogeneity on the produced nanofluids.
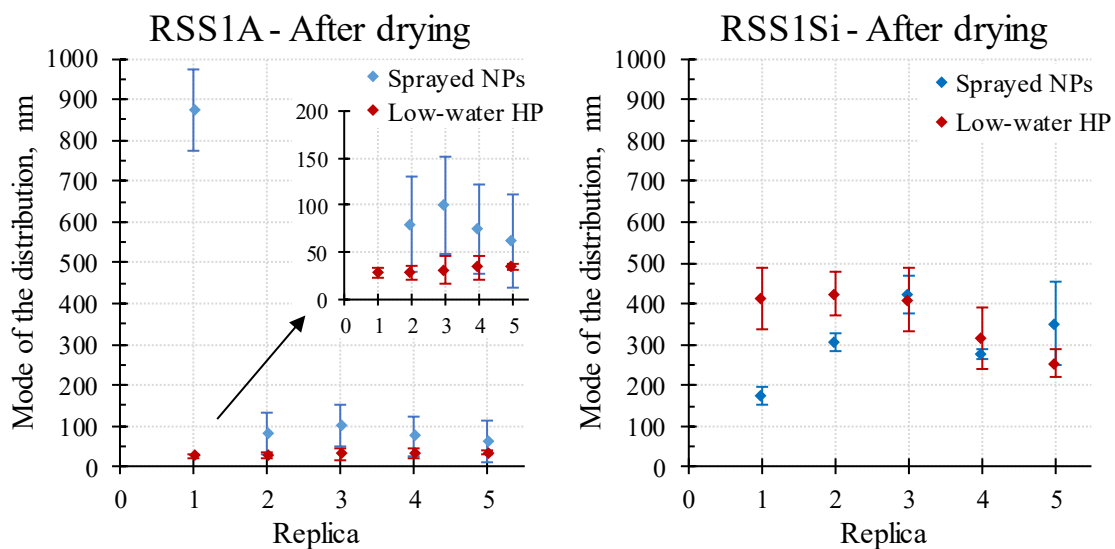
Figure 4-4. Nanoparticle size-distribution of the nanofluids RSS1A and RSS1Si synthetized by two methods. Five replicas of each nanofluid were analysed by DLS to determine their homogeneity. The mode values and their standard deviation (vertical bars) have been plotted on these graphs

The comparison of the nanoparticle sizes on the nanofluids synthetized by the three methods lead to the following conclusions:

- The use of water-based nanofluids as the source of nanoparticles is beneficial in comparison to solid nanoparticles in order to obtain dispersions in the nanometric range from the beginning.
- The materials produced by the traditional hot plate method show large nanoparticle agglomerates, often several hundreds of nanometres size, once the water is removed. As a result, this technique is not recommended to produce this type of materials.
- The sprayed nanoparticles method has a better control of the nanoparticle agglomeration through the entire process. However, the materials produced by this procedure are poorly homogeneous (large scattering on the results obtained from different samples). This heterogeneity is deemed on the high variability found between different portions of the same nanofluid. Further research is required to modify the procedure in order to make it feasible for industrial implementation.
- The low-water hot plate method is presently the best option to avoid the formation of large nanoparticles agglomerates during the synthesis procedure.

4.2.5.1.2   Specific heat

The specific heat of the nanofluids and its increment in comparison to the base salt have been determined. The results from each nanofluid and their base salts are gathered on the Figure 4-5, where the increments have been included as well.

On one side, the specific heat of the nanofluids based on ASS and SiNPs is clearly larger when they are produced by the low-water hot plate procedure, while decrements are observed in those from the traditional hot plate method. The reason is maybe directly linked with the big size of the nanoparticles observed in the traditional procedure (ASS1Si_1) according to the particle size distribution in the previous section.

On the other side, the specific heat of nanofluids based on RSS was always increased both for the sprayed nanoparticles and the low-water hot plate method. These increments were higher for the nanofluids from the sprayed nanoparticles procedure, especially for those containing SiNPs. The maximum difference of specific heat between the two methods was found in the solid state for the nanofluid RSS1Si (13% vs. 3%). The origin of these differences is not clear, as it is not directly related to the nanoparticle size distribution (very similar in both methods).
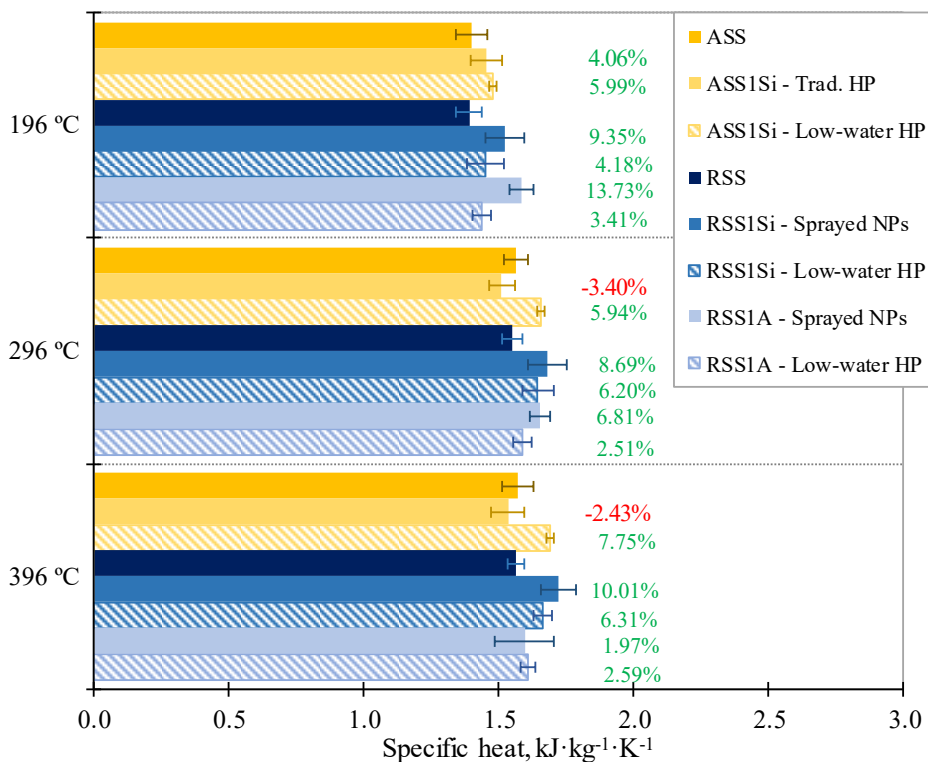
Figure 4-5. Specific heat of the nanofluids (synthetized by the three methods) and the base salts (ASS and RSS). The specific heat increment (%) In comparison to that of the original salt is indicated on each case.

4.2.5.1.3   Global analysis

In general, the materials produced by the traditional hot plate method gave worse results on the characterized parameters than those produced by the two new methods developed in this investigation. The sprayed nanoparticles procedure generated nanofluids with a promising potential, although further research is required in order to reduce the heterogeneity of these materials. In addition, it should be mentioned that the economic feasibility for the industrial implementation of this technique will rely on their adoption by the current suppliers of the Solar Salt. Therefore, at this moment, the low-water hot plate method renders the best performance between the three studied procedures. The most remarkable differences of this procedure compared with the traditional hot plate are the following ones:

- The use of ultrasound to disperse the nanoparticles is avoided. This is possible due to the use of commercial aqueous nanofluids (where nanoparticles are still well dispersed) instead of solid nanoparticles.
- The amount of water needed to disperse the nanoparticles and dissolve the salts is reduced by a hundred times.
- This method ends by melting the nanofluid as an additional step to homogenise the sample before using it.

The two first points have a direct incidence on the synthesis cost of the MSBNFs. In addition to

the cost reduction, using salts of non-analytical grades and commercial nanofluids as the source of nanoparticles, enhances the possibility of producing this material at an industrial scale.

4.2.5.2 Optimization of the low-water hot plate method

This section aims to tune up the synthesis conditions of the Solar Salt-based nanofluids in terms of the nanoparticle size distribution in a nanofluid of RSS with 1 wt% of ANPs. This composition was selected because the RSS is currently used in the CSP plants and the ANPs represents the worst case, because they are thought to have higher agglomeration than SiNPs.

As described in Section 4.2.3.3, this procedure is composed of several stages: salt dissolution, nanoparticle addition, drying and melting. The influence of several factors at each of these production stages has been analysed:

- <u>Salt dissolution.</u> The salt concentration on the initial dissolution.
- <u>Nanoparticle addition</u>. The temperature and the mixing speed of the solution during the nanoparticle addition and mixing with the salt.
- <u>Drying.</u> The drying temperature and the ratio S/V (surface of drying to volume of solution). The ratio S/V is important since the increase of the drying surface (with the same volume of solution) will reduce the drying time and consequently, the nanoparticle agglomeration.
- <u>Melting.</u> Even though the melting stage of the materials can lead to some differences on the behaviour of the materials, no variables were studied at this stage and the nanofluid was always melted at 396 ºC for 30 minutes. These parameters were carefully selected. On one side, the hot thermal storage tank in the CSP plants is at this temperature. On the other side, the melting time was the minimum to guarantee the complete melting of the whole amount of nanofluid and to avoid an excessive nanoparticle agglomeration. The stability of the nanoparticles in the molten salt is outside the scope of this investigation, which only analyses the influence of the synthesis procedure of the nanofluid and not their further behaviour under working conditions (the nanofluid will be in the molten state between 296 ºC and 396 ºC for several years). The material was heated under a controlled thermal program to avoid possible projections of material by the flash evaporation of the water trapped inside the salt crystals.
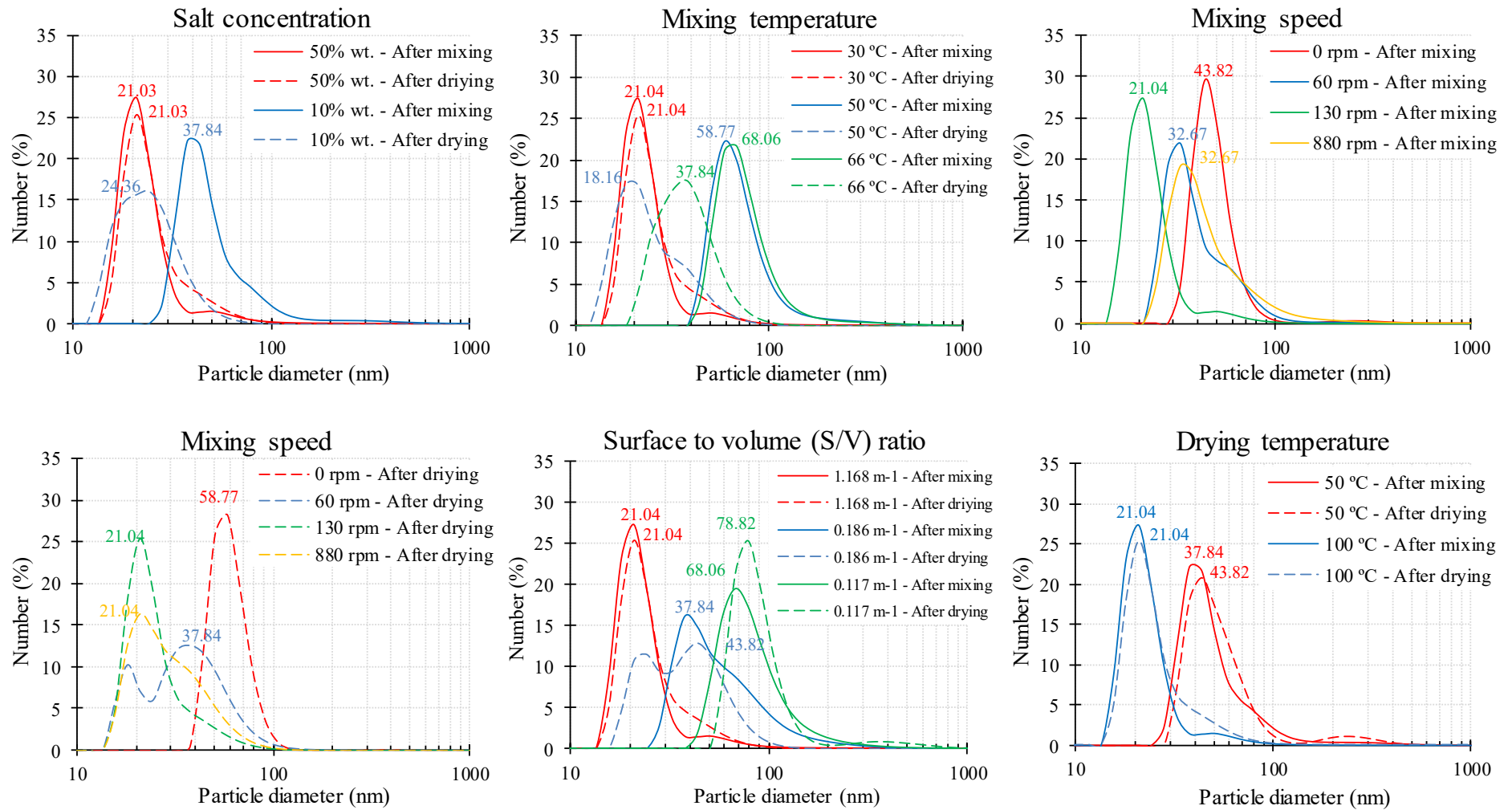
Figure 4-6. Nanoparticle size distribution during the synthesis of the RSS1A nanofluid by the low-water hot plate procedure. The mode of each distribution has been added on top of each curve.

Table 4-3. Nanoparticles size-distribution as a function of the low-water hot plate process variables evaluated in this study. SC: Salt Concentration, MT: Mixing Temperature, MS: Mixing Speed, S/V: Surface to Volume ratio, DT: Drying Temperature. The best conditions found are in bold.

Analysed parameter	Experimental conditions					Mode			D_n90		
	SC, %	MT, ºC	MS, rpm	S/V, m^{-1}	DT, ºC	Value, nm	SD, nm	RSD, %	Value, nm	SD, nm	RSD, %
SC	10	30	130	1.168	100	24.36	5.80	23.80	40.90	7.47	18.30
	50	**30**	**130**	**1.168**	**100**	**21.04**	**1.88**	**8.93**	**34.30**	**2.76**	**8.05**
MT	**50**	**30**	**130**	**1.168**	**100**	**21.04**	**1.88**	**8.93**	**34.30**	**2.76**	**8.05**
	50	**50**	**130**	**1.168**	**100**	**18.16**	**4.38**	**24.12**	**38.50**	**2.47**	**6.44**
	50	66	130	1.168	100	37.84	9.01	23.81	60.80	9.37	15.40
MS	50	30	0	1.168	100	58.77	7.05	11.99	90.20	13.10	14.50
	50	**30**	**60**	**1.168**	**100**	**37.84**	**5.65**	**14.93**	**66.70**	**15.10**	**22.60**
	50	**30**	**130**	**1.168**	**100**	**21.04**	**1.88**	**8.93**	**34.30**	**2.76**	**8.05**
	50	30	880	1.168	100	21.04	5.22	24.80	56.30	15.60	27.60
S/V	50	30	130	0.117	100	78.82	8.10	10.29	138.00	19.10	13.80
	50	30	130	0.186	100	43.82	8.41	19.19	66.00	15.70	23.70
	50	**30**	**130**	**1.168**	**100**	**21.04**	**1.88**	**8.93**	**34.30**	**2.76**	**8.05**
DT	50	30	130	1.168	50	43.82	8.97	20.47	71.00	20.90	29.50
	50	**30**	**130**	**1.168**	**100**	**21.04**	**1.88**	**8.93**	**34.30**	**2.76**	**8.05**

4.2.5.2.1 Influence of the salt concentration

Figure 4-6 up left, shows the nanoparticle size-distribution of two nanofluids of RSS1A obtained with different salt concentrations (50 wt% and 10 wt%). After the mixing stage, the nanoparticle sizes for the lower nitrate salt concentration (10 wt%) are higher than those ones for the higher concentration (50 wt%). After the drying stage, both experiments showed similar mean nanoparticle sizes, however the size distribution is wider for the lower nitrate salt concentration (10 wt%).

The reason of this difference is that the nitrates are fully dissolved and strongly linked to the water molecules. In the saturate solution (50 wt%), almost all of them are restricted to interact with the nanoparticle suspension (Alumisol-10A), which is added drop by drop. This causes these drops to remain unmixed with the bulk solution, forming a sort of "micelles" (Figure 4-7). As the nanoparticles are isolated from the dissolved salt, their size distribution is very similar after the drying step.

The nanoparticles are clearly bigger when working with the diluted solution at 10 wt% The mode size after drying is similar but the distribution of sizes is wider than in the former case (50 wt%). According to the Table 4-3, the 90% of the nanoparticles are below 40 nm after drying the diluted solution and under 34 nm for the saturated one.

Figure 4-7. Mixing of the ANPs in a saturated RSS solution (50 wt%). "Micelles" of ANPs are observed after adding the nanoparticle suspension drop by drop.

These findings are important regarding the reduction of the amount of water needed to perform the synthesis, which is one of the main objectives of this research. The advantage of using a salt concentration near their saturation point (65 wt%) is interesting in terms of water reduction. As drawback, this amount of salt needs more time to be dissolved at room temperature but this time can be diminishing by increasing the mixing temperature.

4.2.5.2.2   Influence of the mixing temperature

Three different nanofluids of RSS1A were made from aqueous mixtures of salt and nanoparticles at different temperatures: 30 ºC, 50 ºC and 66 ºC. (Figure 4-6, up centre). The experiments were done with a salt concentration of 50 wt%, since was the best conditions from the previous experiments. During the mixing step (continuous lines), there is a clear influence of the temperature. The nanoparticle size-distribution obtained at 30 ºC is narrower and the mode is also lower than those at 50 ºC and 66 ºC. This behaviour may be due to the rupture of the aforementioned "micelles" when the temperature increases. After drying the samples, the differences are greatly reduced and the curves for 30 ºC and 50 ºC are very similar in terms of the mode size and the distribution width. According to the Table 4-3, the 90% of the nanoparticles are below 34 nm for the mixing process carried out at 30 ºC, 30 nm when it was carried out at 50 ºC and 60 nm for the samples produced at 66 ºC respectively.

The smaller nanoparticle sizes were found when the aqueous solution was mixed at the lowest temperature (30 ºC). This fact is very interesting in terms of energy savings during the production process, which results in cost reduction of the entire fabrication method.

4.2.5.2.3   Influence of the mixing speed

Figure 4-6, shows the nanoparticles size-distribution of the nanofluids produced using different mixing speeds (0 rpm, 60 rpm, 130 rpm, 880 rpm). After the mixing stage (Figure 4-6 up right), the nanoparticles sizes have a high dependence of the mixing velocity. The highest sizes are found when the nanoparticles are added under static condition (0 rpm). The application of mild agitation (60 rpm and 130 rpm) reduced the nanoparticles sizes. However, extremely large mixing speed causes the agglomeration of the large particles, while small particles are also present, thus resulting on a broad distribution. The same type of broad size-distribution remained after drying the mentioned samples, as showed in Figure 4-6 down left and Table 4-3. The 90% of the nanoparticles (D90) are under 90 nm, 66 nm, 34 nm and 56 nm for mixing speeds of 0 rpm, 60 rpm, 130 rpm and 880 rpm respectively.

4.2.5.2.4   Influence of the surface to volume ratio

Figure 4-6 down centre, shows the distribution of nanofluids dried with different surface to volume ratios (1.168 m^{-1}, 0.186 m^{-1} and 0.117 m^{-1}). This parameter correlates the surface of the container with the volume of the solution to be dried. The water removal should be as fast as possible to minimize the nanoparticle agglomeration during this step. However, the boiling of water must be avoided in order to minimize the physical collisions of nanoparticles that may lead to their agglomeration. In this way, the boiling temperature of the solution must not be reached during drying. As detailed in the method description, 15 cm diameter glass Petri dishes are used to dry the nanofluid. Their total surface is equal to 0.017 m^2. The volume of the solution inside the glass Petri dish was measured before drying, so that the parameter S/V was calculated. The volume of the prepared solution changed while the drying surface was constant by using the same glass Petri dish. In such way, the experiments were done with S/V ratios of 1.168, 0.186 and 0.117 m^{-1}.

The mixing step was done under the best conditions from the previous sections: 50 wt% of salt concentration, 30 ºC and 130 rpm. In principle, the size distributions after the mixing step under these conditions should not be influenced by the S/V ratio. However, the lower the S/V ratio the higher the nanoparticle sizes were. This is probably due to the higher time needed to add the nanoparticles to the solution (higher volume), giving more chances to their agglomeration. Particle sizes out of the nanometric range (>100 nm) were measured on the distribution of the experiments with 0.186 m^{-1} and 0.117 m^{-1}.

The dashed lines on the Figure 4-6 are the DLS analysis after drying these samples. They follow the same trend described before and the 90% of the nanoparticles are smaller than 138 nm, 66 nm and 34 nm for the S/V of 0.117 m^{-1}, 0.186 m^{-1} and 1.168 m^{-1} respectively (Table 4-3).

The relationship between the nanoparticle size distribution and the S/V ratio is asymptotically inverse (Figure 4-8). The result from the $S/V = 0.186$ m^{-1} is very near from the change of tendency of the curve. More tests should be done with intermediate or higher S/V ratios to confirm this trend, since only three points have been tested. The results obtained here constituted a first step to further optimize at an industrial level this parameter of the S/V ratio.
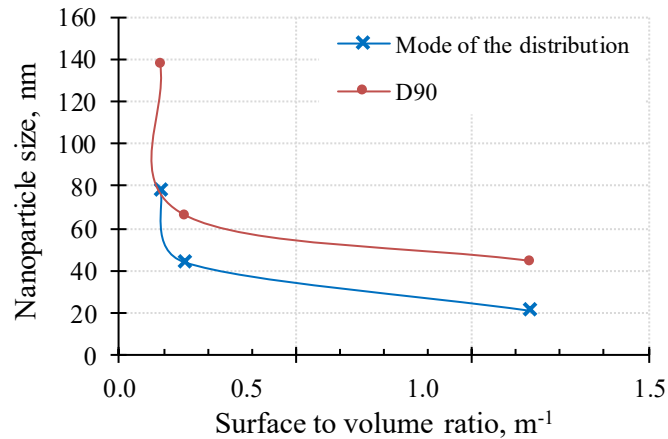
Figure 4-8. Relation between the nanoparticle size (in terms of mode or D90) and the surface to volume ratio during the synthesis of nanofluids by the low-water hot plate method.

4.2.5.2.5 Influence of the drying temperature

Figure 4-6 down right, shows the nanoparticles size-distribution of nanofluids produced at different drying temperatures: 50 ºC and 100 ºC. As mentioned earlier, if the drying step is too long, the agglomeration of the nanoparticles on the aqueous solution may occur. In this sense, at 100 ºC the drying speed will be faster than at 50 ºC. However, the results indicate that the difference on the size-distributions between the mixing stage (continuous line) and the drying stage (dashed line) is not significant for neither of the two temperatures. The 90% of the nanoparticles are under 71 nm and 34 nm when the solution was dried at 50 and 100 ºC respectively (Table 4-3).

The results found in this stage reveals that it is possible to dry the aqueous solutions at 50 ºC with the subsequent saving of energy or at 100 ºC, which is time-saving. In both cases, the size distributions are inside the nanometric range.

4.2.5.2.6 Summary of the results

The Table 4-3 summarizes the results of every studied variable on the nanofluid preparation. As an outline of the previous paragraphs, the following conditions can be established for each synthesis step:

- <u>Salt dissolution.</u> The influence of the salt concentration on the final nanoparticles size-distribution was analysed at concentrations of 10% and 50 wt% With these values, the salt concentration of the initial dissolution did not to affect the final nanoparticle size distribution. Since from an industrial and social point of view reducing the amount of water to be added is of crucial importance, the optimization of the process leads to select the minimum water percentage in the mixtures.

- <u>Mixing temperature.</u> The influence of the mixing temperature on the final nanoparticles size-mode was evaluated at 30 ºC, 50 ºC and 66 ºC. The size-distribution mode obtained on both conditions were very similar at 30 ºC and 50 ºC, while it reaches higher values at 66 ºC.

- <u>Mixing speed.</u> The influence of the mixing speed on the final nanoparticles size-distribution was evaluated by performing experiments on a wide stirring range from 0 to 800 rpm, executing experiments under four different stirring rates on this range. The results indicate a certain stirring (>0 rpm) was needed in the process as well as avoiding an excessive speed (<800 rpm) to maintain narrow distributions. The results were analogous with mild stirring (60 and 130 rpm).

- <u>Surface to volume ratio on the drying stage.</u> The surface to volume ratio (S/V) significantly affected the agglomeration of the nanoparticles. It was preferred to remove the water with a S/V as high as possible, at least with a value of 1.168 m^{-1}. However, the minimum value of S/V in order to achieve a nanometric size distribution (0-100 nm) was 0.186 m^{-1}.

- <u>Drying temperature.</u> The drying temperature should be lower than the boiling temperature of the solution to avoid bubbling (>100 ºC due to the increased boiling point of concentrated salt solutions). The nanoparticles size remained in the nanometric range when drying takes place at 100 ºC, while a small agglomeration was determined when they are dried at 50 ºC. This is probably due to the drying time increment required to carry out the drying at a lower temperature. Therefore, to optimize the process a temperature as large as possible is preferred in order to shorten the drying time, to prevent agglomeration and reduce processing time.

4.2.6 Conclusions

This research analyses the relationship between the synthesis method and the nanoparticle size and specific heat of Solar Salt-based nanofluids. The study was scheduled to take into account the industrial viability of the method as well as their suitability to avoid the nanoparticle agglomeration.

Three methods of production have been compared in terms of the nanoparticle size-distributions and the specific heat. Two of them have been developed on the present work ("sprayed nanoparticles" and "low-water hot plate") while the third one corresponds to the method most widely encountered on the published literature ("traditional hot plate").

The low-water hot plate procedure developed in this work demonstrated to be the most convenient and advantageous: agglomeration of nanoparticles through the synthesis steps was prevented to a large extent, and nanoparticles were homogeneously dispersed into the salt matrix. The specific heat of these materials were significantly higher than those of the base-salt.

In the second part of this investigation the influence of several processing variables on each step of this procedure has been evaluated. The best processing conditions on the analysed range were: salt concentration of 50 wt%, mixing temperature between 30 ºC and 50 ºC, mixing speed between 60 rpm and 130 rpm, ratio S/V higher than 1.168 m^{-1} and a drying temperature of 100 ºC. However, some of these variables should be further analysed if the process is industrially implemented. A statistical design of experiments would be advisable on that case.

These results indicate that a promising processing route is feasible although there is still a long way to industrialization in this particular field. A systematic research is needed in this sense, looking for the industrial consideration of the synthesis procedure as a way to push forward the future use of MSBNFs in the CSP thermal storage and heat transfer.

4.3 CONFERENCE CONTRIBUTION 4: THE INFLUENCE OF MIXING WATER ON THE THERMOPHYSICAL PROPERTIES OF NANOFLUIDS BASED ON SOLAR SALT AND SILICA NANOPARTICLES

Authors: Belén Muñoz-Sánchez, Javier Nieto-Maestre, Iñigo Iparraguirre-Torres, José Ángel Sánchez-García, José Enrique Juliá and Ana García-Romero

Abstract: The use of nanofluids (NFs) based on Solar Salt (SS) and nanoparticles (NPs), either as Thermal Energy Storage (TES) material or as Heat Transfer Fluid (HTF), is attracting great interest in recent years. Many authors [36,113] have reported important improvements on the thermophysical properties (specific heat capacity c_p, thermal conductivity k) of NFs based on SS and ceramic NPs. These improvements would lead to important savings and better performance of TES facilities on new Concentrated Solar Power (CSP) plants due to lower quantities of material required and smaller storage tanks. To achieve these advantageous features in the final NFs, it is essential to avoid NP agglomeration during their preparation. Different synthesis procedures have been reported: mixing of solid NPs within a SS solution by means of ultrasounds [36,63,113], direct mixing of solid NPs and molten salt [66]. In this work, NFs based on SS and silica NPs were synthetized from a SS-water solution and a commercial water-silica NF called LUDOX® SM-30 (Sigma-Aldrich). The influence of the *mixing water* volume (MW) on the c_p of NFs was evaluated. With this aim, the c_p of these samples was measured by Differential Scanning Calorimetry (DSC) both in the solid and the liquid state. In addition, the distribution of sizes was measured during the whole preparation process by Dynamic Light Scattering (DLS). Further information about sizes and uniformity of the final NFs was obtained from Scanning Electron Microscopy (SEM) images. X-ray Diffraction (XRD) patterns of the SS and final NF were performed.

4.3.1 Introduction

CSP plants require more and more efficient TES in order to supply energy during nights or cloudy periods. When using SS as TES material or HTF, an enhancement in c_p would lead to important savings in the cost of the whole process. The use of SS-based NFs is attracting great interest in recent years.

Different authors [36,63,113] have reported an increase in the c_p of SS by addition of a small amount of NPs. The dispersion of NPs within a base fluid is known as *nanofluid* (NF). The most employed method for preparing salt based NFs consists of three steps: (1) mixing solid salt and NP, (2) adding water, (3) sonication and (4) drying. Sonication helps to achieve nanometric sizes and a uniform mixture. Other authors [66] have directly mixed the NPs within the molten nitrate salt under stirring. Table 4-4 shows the method of preparation and the total amount of water in every case.

Table 4-4. Preparation methods for different authors and the total amount of water used (mL·g^{-1}). Enhancements of c_p with respect to the base salt were comprised within 19 and 34% in the liquid state for the different authors. NP: nanoparticles, US: ultrasounds

Author	Year	Salt wt%	NP wt%	Method of preparation	Total amount water (mL·g-1 NF)	Ref.
Chieruzzi et al.	2013	NaNO$_3$ (60%) + KNO$_3$ (40%)	SiO$_2$, Al$_2$O$_3$ TiO$_2$ (0.5 – 1.5%)	Salt + NP + water US and drying	100	[36]
Shin and Banerjee	2011	BaCl$_2$ (34%) + NaCl (13%) + CaCl$_2$ (40%) + LiCl (13%)	SiO$_2$ (1%)	Salt + NP + water US and drying	100	[63]
Andreu-Cabedo et al.	2014	NaNO$_3$ (60%) + KNO$_3$ (40%)	SiO$_2$ (0.5 – 2.0%)	Salt + NP + water US and Drying	10	[113]
Ho and Pan	2014	NaNO$_3$ (7%) + KNO$_3$ (53%) + NaNO$_3$ (40%)	Al$_2$O$_3$ (0.016 – 1%)	Adding NP within melted salt under stirring	---	[66]

An adequate control of the distribution of NP sizes during the preparation steps is essential to achieve an improvement of the c_p for the final NFs. The higher the NP available surface (S_a) in the molten salt media, the higher the interaction between the NPs and the ions within the molten medium. A high S_a can only be achieved by keeping particle sizes at the nanometric scale (< 100 nm), even in the molten state. Therefore, agglomeration and sedimentation of NPs must be avoided. During the preparation of NFs, water can prevent the agglomeration of NPs by maintaining them adequately solvated. However, two factors may be taken into account: on one hand, the more the total amount of water, the less the agglomeration of NPs. On the other hand, from the point of view of technical and economic feasibility, the use of big quantities of water will increase the overall cost of the process. A commitment between these two factors must be reached. The lower amount of water that guarantees the good performance of final NFs at a reasonable industrial cost must be used.

In this work, a novel procedure for preparing SS-based NFs is proposed starting from a water dispersion of NPs, rather than from solid NPs (as those exposed in Table 4-4). A thorough control of the distribution of sizes was performed in order to achieve NFs with enhanced c_p. A correlation between the distribution of sizes for the NFs (in terms of S_a) and the c_p was found. The influence of the total amount of water on the distribution of NP sizes and the c_p of final NFs was analyzed.

4.3.2   Experimental

4.3.2.1 Synthesis procedure

4.3.2.1.1   Materials

The materials used for the synthesis of NF were the following: sodium nitrate (SQM, Industrial grade, prills), potassium nitrate (HAIFA, Multi-K, prills) and LUDOX® SM-30, a commercial colloidal dispersion of silica NP in water provided by Sigma-Aldrich. All the chemical products were used as received.

4.3.2.1.2   Preparation of solutions

SS was prepared by mixing 60 wt% sodium nitrate and 40 wt% potassium nitrate, followed by melting at 450 ºC for ½ hour to ensure the homogeneity of the mixture.

Starting from the SS prepared as explained in the previous paragraph, two aqueous solutions of SS were prepared: 15 wt% and 50 wt% (SS/water). As the second concentration was near the saturation limit, SS was slowly added to warm water (about 50 ºC) under smooth stirring.

A diluted dispersion of silica NP of 1 wt% was prepared by simple dilution of LUDOX® SM-30 with an alkaline water at pH 9 (The pH of water was set at 9 with NaOH).

4.3.2.1.3   Preparation of nanofluids

SS-based NFs were prepared following the scheme shown in Figure 4-9:
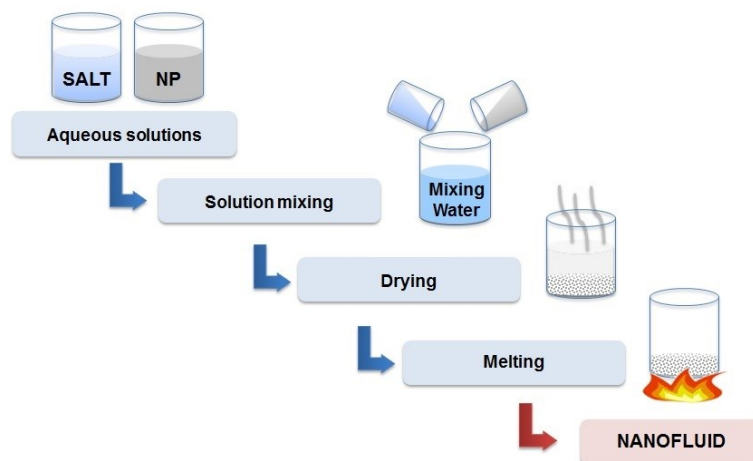
Figure 4-9. Preparation of NFs

Many variables can be modified during this preparation procedure (drying and melting temperature and time...). A complete study of these variables would be of interest, but it is beyond the scope of this paper.

The amount of Mixing Water (MW) in the solution mixing step (Figure 4-9) is a variable of great

importance to control the degree of agglomeration. Water coming from salt solution and NP dispersion was also considered in the total amount of water. During the preparation of NFs, an adequate grade of solvation will prevent silica NP from agglomeration.

Starting from a solution of SS 15 wt% and a diluted dispersion of silica NP at 1 wt%, two trials were performed: (1) with MW 25 mL and (2) with no MW. In an attempt to set the water content to a minimum, an additional trial was done, starting from SS 50 wt% and LUDOX® SM-30 with no MW (3). The order of addition in the trial 1 was the following: first the silica dispersion and second the nitrate solution. Both solutions were added within the initial MW. For the trial 2 and 3, the silica dispersion was added directly into the nitrate solution, as no mixing water was used. The additions were performed, all at once, and under smooth stirring.

Drying was performed inside an oven (trade Raypa), at 100 ºC in a glass Petri dish of 150 mm x 30 mm (diameter x width), covered with a filter paper, for the needed time to complete drying of the sample. Drying volume was the same for the three trials. All samples were dried in the same conditions. Melting was performed in a furnace (Nabertherm) at 450 ºC for ½ hour. After melting, all samples were rapidly cooled at room temperature until their complete solidification.

4.3.2.2 Characterization

4.3.2.2.1   Dynamic Light Scattering

During the synthesis procedure shown in Figure 4-9, monitoring of the NP sizes was performed by Dynamic Light Scattering. For this purpose, a ZetaSizer nano ZS, supplied by Malvern Instruments (UK) was used. Prior to the measurement, a dilution of the sample at a concentration of 0.1 mg·mL^{-1} was done, in agreement with Malvern experts' advices. The S_a of the dispersed NPs was calculated considering that NPs were spherical, according to DLS measurement assumptions.

4.3.2.2.2   Scanning Electron Microscopy

The dispersion of NPs in the solid samples was evaluated using a field emission Scanning Electron Microscope SEM (JEOL, 7001F). Specimens were metallized in a thermal evaporator. Secondary Electron (SE) and Quadrant Back Scattering Electron Detector (QBSD), attached to an Energy Dispersive X-Ray Spectroscopy system (EDX) were used to measure the size and composition of NP clusters in the solid salt.

4.3.2.2.3   X-Ray Diffraction

A XRD device Bruker D8 Advance was used to evaluate the crystallinity of the samples. XRD patterns of the SS and SS doped with silica NPs from the three trials were taken.

4.3.2.2.4   Differential Scanning Calorimetry

A DSC device TA Instruments Q100 (US) was used to measure the specific heat (c_p) of the different samples through Modular Differential Scanning Calorimetry (MDSC) with an isothermal procedure. Three temperatures, 196 ºC (solid state), 256 ºC and 396 ºC (liquid state) were tested. Some milligrams of the sample were introduced in a pan and then hermetically sealed. All the samples were first stabilized at the desired temperature, and then subjected to an isothermal period of 10 minutes in order to achieve the salt thermal equilibrium prior to data collection (20 minutes). The modulation was set up with 0.6 ºC of amplitude and a 110 seconds period according to the TA Instruments expert advices. The explained isothermal program was always performed from the highest to the lowest temperature. Thus, a complete melting of the sample was achieved at the beginning of the experiment (melting temperature 220 ºC). In this way, the sample within the crucible in the solid state behaves as a compact piece rather than the initial fine powder. First, the sapphire sample commonly used as the reference material was measured under the same protocol to find out the possible device divergence and correct the final sample results. Three replica were measured for each sample. The average and the standard deviation (SD) for the three measurements were obtained. Results were discussed in relation to the degree of agglomeration and the preparation procedure for every sample.

4.3.3   Results and discussion

4.3.3.1 Preparation of samples

All the samples (trials 1, 2 and 3) were prepared as shown in Figure 4-9. Table 4-5 shows the total amount of water per gram of final NF, including MW and water from the starting SS solution and NP dispersion.

Table 4-5. Preparation conditions for trials 1 to 3.

| Trial | Preparation conditions | | |
	SS concentration (wt%)	Mixing Water MW (mL)	Total amount water (mL·g^{-1} NF)
1	15	25	31.60
2	15	0	6.50
3	50	0	0.97

4.3.3.2 Dynamic Light Scattering

During the NF preparation process, silica NPs tended to agglomerate. As a consequence, the distribution of sizes measured by DLS moved towards higher sizes. In Figure 4-10, the distribution of sizes after every step of the preparation process is shown. The three trials are compared.

In the first step, *silica dispersion*, the distribution of sizes for the trials 2 and 3 (Figure 4-10a) are identical (same S_a 1.23 $m^2 \cdot g^{-1}$ Table 4-6), as they were measured directly from diluted silica dispersion. Though, the distribution of sizes was slightly moved towards higher values for the trial 1 (S_a 1.02 $m^2 \cdot g^{-1}$ Table 4-6). In this case, the silica dispersion was added to 25 mL of water under smooth stirring. Silica NPs were slightly agglomerated by simple collision under forced convection.

As long as silica NPs were adequately dispersed in water, none or very little agglomeration occurred. When this NP dispersion was mixed within the *nitrate solution*, higher NP sizes were found for trials 2 and 3 (lower S_a with respect to the previous step, silica dispersion). Higher degree of agglomeration, also shown by a notable decrease in S_a of 63% (Table 4-6), was observed in trial 3, where a concentrated nitrate solution (50 wt%) received a silica NP dispersion (30 wt%). In this case, the quantity of water, coming from nitrate solution and NP dispersion, was not enough to keep ions solvated and NPs dispersed, silica NPs collided by Brownian movement or forced convection and higher NP sizes were observed in DLS measurements (Figure 4-10b). In the case of trial 1, the quantity of water was enough to maintain ions adequately solvated and NPs dispersed at the same time (S_a remained constant in 1.02 $m^2 \cdot g^{-1}$, Table 4-6). A wider distribution of sizes was observed for trial 2 that is also an indication of a certain degree of agglomeration (S_a decreased 30%, Table 4-6).

A notable increase in the degree of agglomeration occurred during the *drying step*. As water was being removed from the solution of SS, this became more and more concentrated in solvated ions. Then, there was less water to maintain silica NPs dispersed and agglomeration took place. Higher degrees of agglomeration would be expected for the more concentrated solutions (Trial 2 and 3). However, the experimental results showed the contrary effect. These trials (2 and 3) required less time to get dried. Therefore, there was less time for agglomeration. The shorter the duration of the drying step, the lower the degree of agglomeration of NPs in the drying solution. This is an important result for the scaling-up of this method that would lead to considerable savings in production cost as the requirement of water can be reduced to a minimum.

After the *melting step*, narrower distributions of sizes were obtained with respect to the drying step. This can also be deduced from the increase in the S_a for the three trials (Table 4-6), more significant for trials 1 and 3. The loss of intramolecular water from silica NPs, not removed during the drying step, may be the responsible for the decrease in size of silica NPs. Stronger interactions between nitrate ions (and counterions) with silica NP may be another reason for this experimental result.
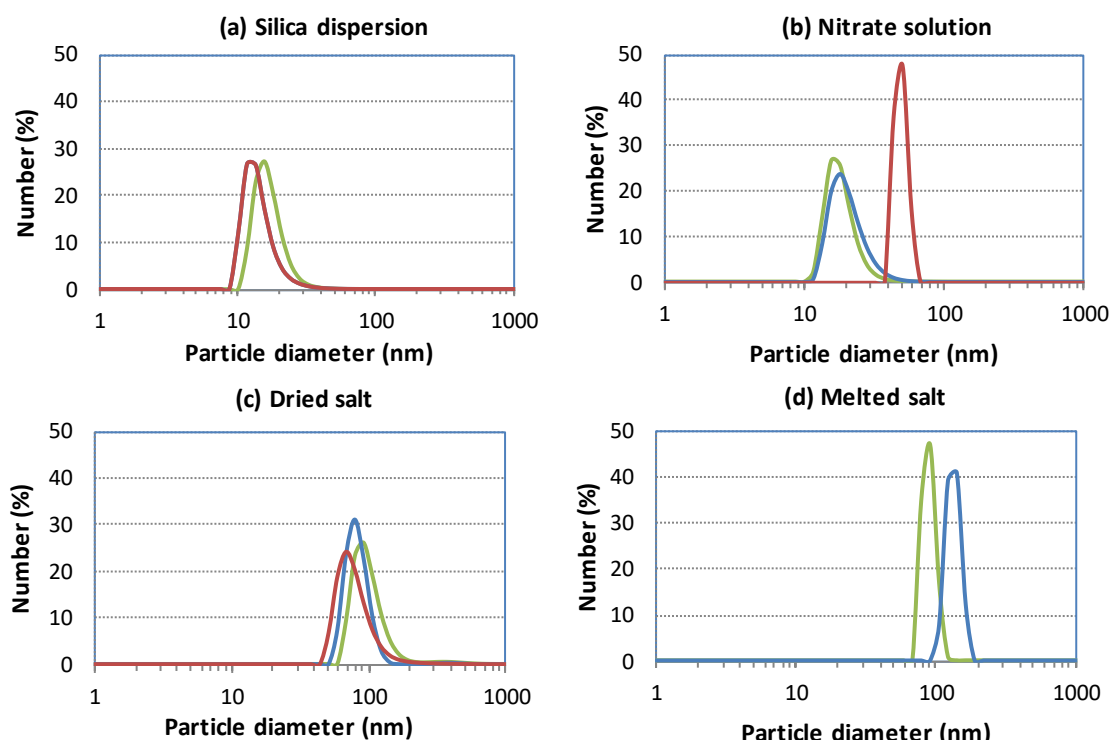
Figure 4-10. Distribution of sizes for the three samples of SS doped with silica NPs (—— Trial 1; —— Trial 2; —— Trial 3). Preparation steps: (a) Solution mixing – Silica dispersion, (b) Solution mixing – Nitrate solution, (c) Drying, (d) Melting.

Table 4-6. Available particle surface (S_a) through the different synthesis steps.

| | Preparation conditions | | S_a (m^2·g^{-1}) | | | |
Trial	MW (mL)	C. SS (wt%)	Silica dispersion	Nitrate solution	After drying	After melting
1	25	15	1.02	1.02	0.12	0.25
2	0	15	1.23	0.85	0.15	0.16
3	0	50	1.23	0.45	0.17	0.23

4.3.3.3 Scanning electron microscopy

Figure 4-11 shows SEM images for the three trials and EDX analysis. The differences in bright and contrast can be associated to changes in composition in QSBD images. Sodium (dark) and potassium (bright) nitrate crystals can be easily identified by variations in the grey tone. Silica NPs are distinguishable as a cotton-shaped structure, proved by the presence of silicon element. The EDX analysis covered an area of 1-5 μm^3, so it gave an approximate idea of the composition of the selected point, but X-Rays coming from adjacent areas were also captured. Oxygen was calculated by the software considering that the chemical compounds are oxides.

(a)

TRIAL 1	
Element	**Weight (%)**
Si	11.06
K	62.48
Zn	0.87
O	25.59
Totals	100.00

(b)

TRIAL 2	
Element	**Weight (%)**
Na	17.25
Si	0.11
K	63.53
O	19.12
Totals	100.00

(c)

TRIAL 3	
Element	**Weight (%)**
Na	11.24
Mg	3.36
Si	10.92
S	0.81
Cl	3.33
K	41.98
O	28.37
Totals	100.00
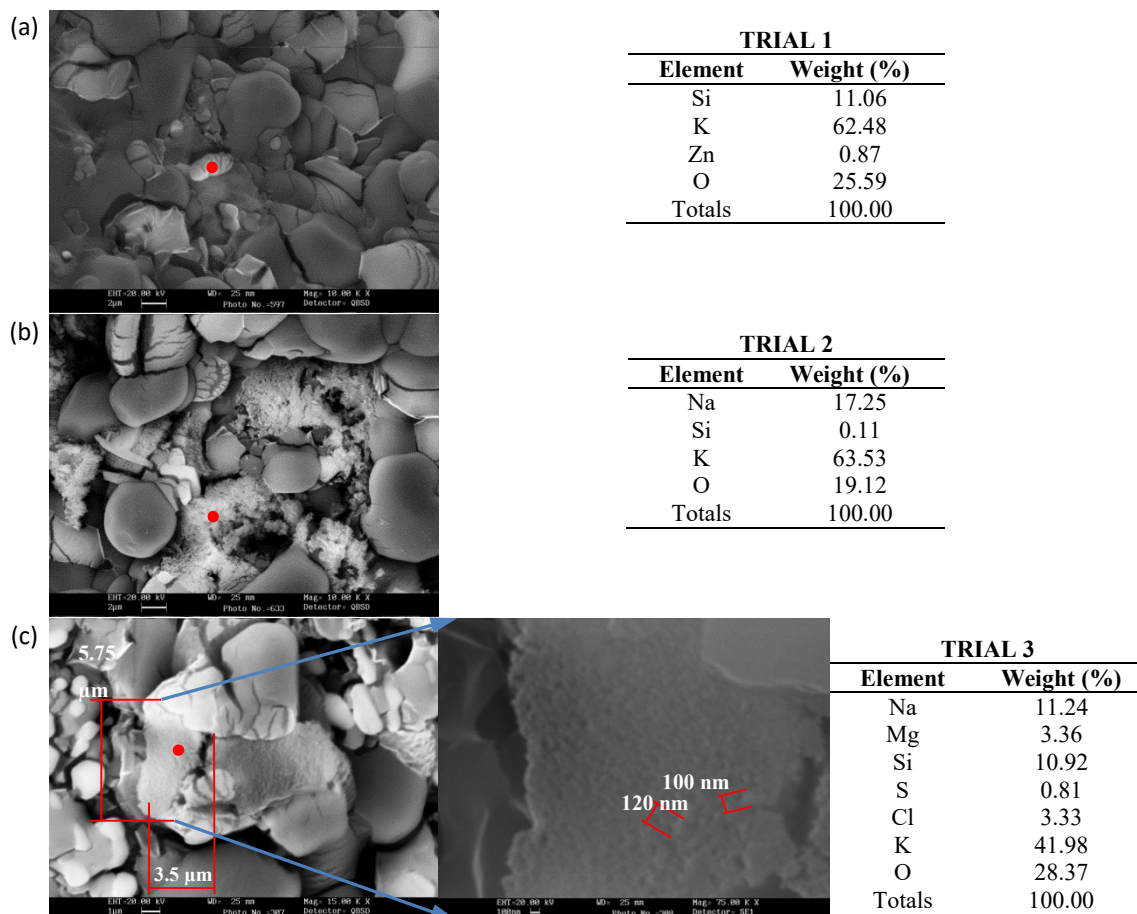
Figure 4-11. (a) Trial 1 QBSD image and composition EDX. (b) Trial 2: QBSD image and Composition EDX. (c) Trial 3: QBSD image and SE image with Composition EDX.

An estimation of the cluster size was performed for Trial 3 (Figure 4-11). The cluster seemed to be grouped in agglomerates of ~100 nm (Figure 4-11). Clusters were probably divided into these agglomerates when solved in water.

Useful information about the uniformity and sizes of NPs has been obtained from SEM images interpretation. However, the SEM technique has only given an approximate idea of the agglomerate size distribution.

4.3.3.4 Differential Scanning Calorimetry

Table 4-7 shows the c_p and SD for the three trials at three temperatures (196 ºC, 256 ºC and 396 ºC). Comparing the c_p values (Table 4-7) with the S_a calculated in Table 4-6, a relation between these two variables can be deduced, as shown in Figure 4-12. The higher the S_a, the higher the c_p. This fact can be explained by the increase in the interactions between the surface of NPs and the nitrate salt media. There is not an important difference in c_p in the liquid state, 256 ºC and 396 ºC (0.4% and 2.4% respectively) between the trial 1 (0.25 $m^2 \cdot g^{-1}$) and trial 3 (0.23 $m^2 \cdot g^{-1}$). The difference in S_a between both trials is not high enough to affect the c_p in the liquid state.

Table 4-7. c_p results for NF based in SS and silica NP in the solid (196 ºC) and the liquid state (256 ºC and 396 ºC)

Trial	Preparation conditions		c_p (kJ·kg^{-1}·K^{-1})		
	MW (mL)	C. SS (wt%)	196 ºC (solid)	256 ºC (liquid)	396 ºC (liquid)
1	25	15	1.773 ± 0.014	1.627 ± 0.007	1.613 ± 0.004
2	0	15	1.289 ± 0.084	1.440 ± 0.083	1.384 ± 0.079
3	0	50	1.471 ± 0.033	1.620 ± 0.035	1.575 ± 0.034

Taking into account that preparation of trial 1 with S_a 0.25 m^2·g^{-1} required a total amount of water of 31.6 mL·g^{-1} NF and trial 3 with S_a 0.23 m^2·g^{-1} required a total amount of water of 0.97 mL·g^{-1} NF (Table 4-5), the total amount of water does not seem to affect the degree of agglomeration in the melting state. Final available surfaces are almost the same value for both trials, and moreover, the c_p values in the melted state are very similar in both cases. Therefore, the total amount of water can be reduced to a minimum during NF preparation, maintaining a good thermophysical performance of the final NF.
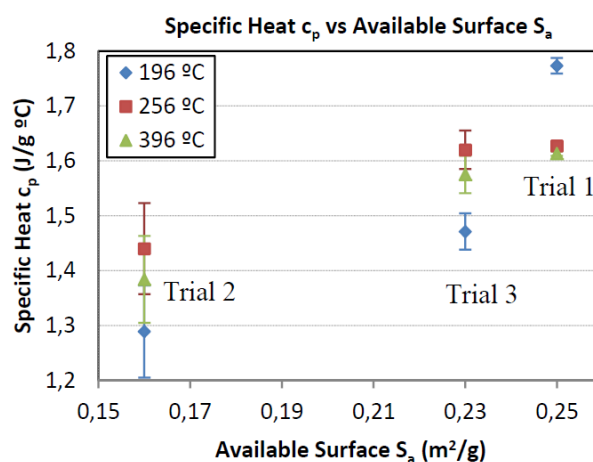
Figure 4-12. c_p (kJ·kg^{-1}·K^{-1}) vs S_a (m^2·g^{-1}) for SS doped with NP of silica.

4.3.3.5 X-Ray Diffraction

Figure 4-13 shows the XRD diffractograms obtained for the three trials and the starting SS. The position of peaks (vertical lines) corresponding to $NaNO_3$ (blue lines), KNO_3 (green lines) and crystalline silica (yellow lines) are displayed in order to follow better the results. As it can be seen in Figure 4-13, the three trials and starting SS show the sodium and potassium nitrate peaks, as it was expected. The differences in peak intensity are not relevant because they could be related to random orientation of nanocrystals in powder samples, since the weight ratio of SS/silica is constant for the three trials (100:1). In addition, there is not peak broadening that can be associated with differences in the size of crystals. Although silica is usually in amorphous state, a small proportion of NPs are shown in crystalline way. As it can be seen, it shows a peak at 21° associated with crystalline phase SiO_2.
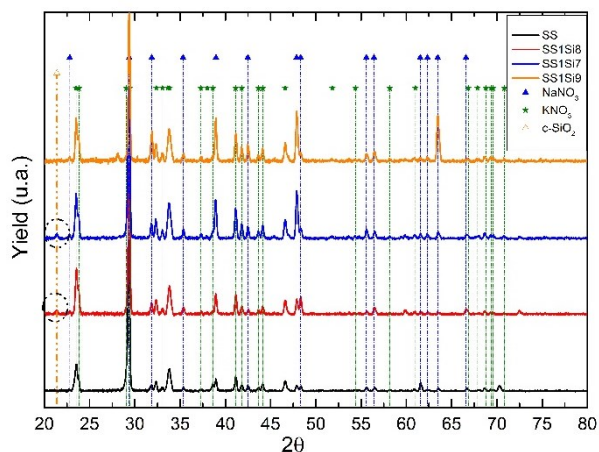
Figure 4-13. X-Ray diffraction patterns for Trials 1 to 3 and starting SS.

4.3.4   Conclusions

A novel method for preparation of NFs based in SS and silica NPs is exposed. The key feature of this procedure consists of starting from a stabilized water dispersion of silica NPs, rather than solid nanoparticles. In this way, the use of US is not required, as NPs are well dispersed and less agglomerated in the raw material. The preparation procedure consists of the following steps: (1) addition of silica dispersion, (2) addition of nitrate solution, (3) Drying and (4) Melting. The influence of the total amount of water on the distribution of sizes was evaluated. The nanoparticle sizes after drying does not seem to be affected by the total amount of water. Shorter drying times and therefore, less time for agglomeration, may be responsible of this fact. In the melting step, a general increase in S_a, and consequently decrease in NP sizes was observed. The final S_a was similar for the minimum total amount of water (0.97 mL·g^{-1} NF) and the maximum one (31.6 mL·g^{-1} NF): 0.23 and 0.25 m^2·g^{-1} respectively. For economic reasons, the use of the minimum total amount of water is preferred (0.97 mL·g^{-1} NF): no MW, starting from a nearly saturated SS solution (50 wt%) and a non-diluted commercial silica dispersion called LUDOX® SM-30.

The results from SEM analysis show that, in the solid state, nanoparticles are covering the nitrate crystals forming *clusters* of micrometric sizes. These clusters are formed by smaller agglomerates of ~100 nm in size. These results agree with the distribution of sizes measured by DLS, as *clusters* may be divided into nanometric agglomerates in water solution.

The higher the S_a (lower agglomeration), the higher the c_p of NFs. This can be explained by higher interaction surface between NPs and the molten salt medium. As stated in the previous paragraph, S_a was similar for the minimum and maximum total amount of water, 0.23 and 0.25 m^2·g^{-1} respectively. In the liquid state (256 ºC and 396 ºC), the c_p of final NFs are also in the same order of magnitude, around 1.6 kJ·kg^{-1}·K^{-1}. This means that the total amount of water can be reduced to a minimum with no effect on the final c_p of the NF.

NFs with very low degree agglomeration and adequate c_p to be used as TES materials can be prepared by means of the proposed method. The lower amount of water used with respect to other methods reported in literature, and the avoidance of US, would lead to lower fabrication costs at an industrial scale.

Chapter 5

THERMAL PROPERTIES OF SOLAR SALT-BASED NANOFLUIDS

5 THERMAL PROPERTIES OF SOLAR SALT-BASED NANOFLUIDS

5.1 INTRODUCTION

This Chapter analyses the specific heat and the thermal conductivity of Solar Salt-based nanofluids containing alumina and silica nanoparticles. In the first section, the Journal Contribution 4 studies the specific heat of these materials, both experimentally and considering the mechanisms proposed in the literature. Following, the Journal Contribution 5 gathers the thermal conductivity results of these nanofluids obtained with the LFA method. In the same manner, the experimental data have been compared to the existing theoretical models in order to give a better understanding of the enhancements obtained.

5.2 JOURNAL CONTRIBUTION 4: FACTORS INFLUENCING THE SPECIFIC HEAT ENHANCEMENTS OF SOLAR SALT-BASED NANOFLUIDS

Authors: Belén Muñoz-Sánchez, Javier Nieto-Maestre and Ana García-Romero
Abstract: The exceptional specific heat showed by inorganic salts with nanoparticles (called Molten Salt-based Nanofluids, MSBNFs) is currently a matter of controversy in the scientific community. The acquisition of a deep knowledge in this issue on several Solar-Salt based nanofluids was the core of this research. Specifically, the influence of the concentration of nanoparticles (0.5 – 1.5 wt% alumina or silica) and the purity grade of the base salt (analytical, refined or industrial grade) on the specific heat of final nanofluids was studied. The lack of repeatibility on results was due to the inherent heterogeneity of the nanofluids and their tiny amount of sample filled inside the DSC crucibles. Theoretical rules' predictions for specific heat enhancements were not aligned with the experimental data. No clear correlation between the specific heat and the available surface of nanoparticles was found, as opposed to other researchers. The SEM images were useful to have information on the nanoparticle dispersion and to prove the existence of a special nanostructure constituted by the nanoparticles and the ions of the molten salt.

5.2.1 Introduction

In 1995, Choi and Eastman [42] defined for the first time the concept of nanofluid as a suspension of colloidal particles with a size under 100 nm in a base fluid. The main attribute of these new materials is their enhanced thermal conductivity in comparison to their base fluid. In addition, the nanometric size of the particles allows overcoming their instability in the fluid, which occurs with the micrometric particles. This important discovery has diverse applications on industries involving thermal transfer and storage. One of the fields where the nanofluids present a high potential is the Concentrated Solar Power (CSP) technology.

In this kind of industry, the thermal energy coming from the sun needs to be transferred to the water-steam circuit through a Heat Transfer Fluid (HTF). This fluid is currently an inorganic molten salt at the new generation of CSP plants (power tower) with working temperatures between 400 ºC and 550 ºC. Moreover, the same molten salt is also used as Thermal Energy Storage (TES) material in order to harvest the heat (as sensible storage, 300-400 ºC) for being further used in cloudy periods or at night. The main drawback of this salt is its low specific heat and thermal conductivity, which restraints the heat transfer rate.

In view of this scene, the use of nanoparticles together with the molten salts is highly beneficial. These new composite materials are known as Molten Salt-Based Nanofluids (MSBNFs) and Shin and Banerjee [56] were the pioneers on their study in 2010. Since then, many researchers have addressed this issue. Most of them have analysed the enhancements of the specific heat of this materials compared with the base salt. The studied nanofluids include several combinations of inorganic salts and nanoparticles, but the majority are composed of Solar Salt (a mixture of $NaNO_3$ (60 wt%) and KNO_3 (40 wt%) commonly used in CSP Plants) and Alumina Nanoparticles (ANPs) [32,36,37,61,74,97] or Silica Nanoparticles (SiNPs) [31,36–38,62,64,74,78,104–106,112,113,120]. The improvement of specific heat is strongly influenced by several factors such as the concentration [31,32,36,37,61,62,64,74,78,97,112,113] or the size [61,104–106,120] of the nanoparticles. Other studies have also studied the effect of the nanoparticle type, comparing ANPs with SiNPs when added to the Solar Salt [36,37,74]. The role of the synthesis method has been considered by Schuller et al. [32] and Chieruzzi et al. [37] for Solar Salt and ANPs as well as Muñoz-Sánchez et al. [126], Riazi et al. [120] and Chieruzzi et al. [37] with the addition of SiNPs.

The amount of nanoparticles dispersed into the molten salt is considered the factor with the highest influence on the results and, consequently, the most studied so far. The Figure 5-1 is gathering the specific heat increments of Solar Salt-based nanofluids with different percentages of ANPs (Figure 5-1, left) and SiNPs (Figure 5-1, right), respectively [31,32,36,37,61,62,64,74,78,97,112,113]. These figures evidence the inconsistencies between the results from different authors for the same nanofluid. These differences could be attributed to changes on some of the mentioned factors, such as the synthesis procedure or the initial size of the nanoparticles. In addition, it seems that the crystal structure of the nanoparticles may be another factor to be considered [112].
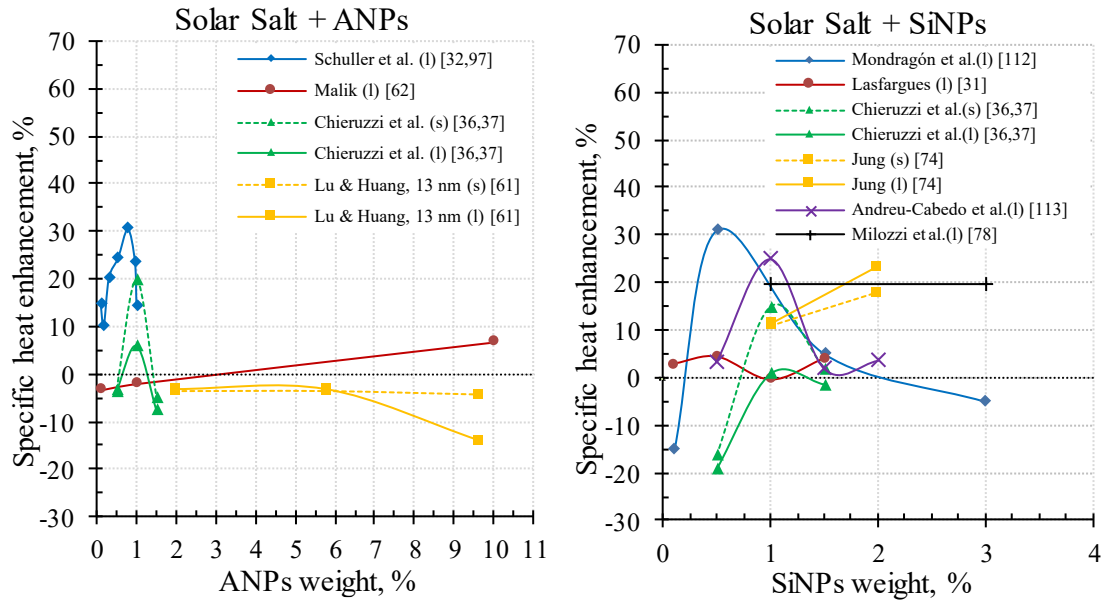
Figure 5-1. Specific heat enhancements from the literature of Solar Salt with different percentages of ANPs (left) and SiNPs (right). The solid lines represent the results of the nanofluid (liquid state) and the dashed lines those of the nanocomposite (solid state).

Apart from the experimental work, other authors developed theoretical models and simulations to explain the extraordinary thermal properties of the MSBNFs. In general, the prediction of the specific heat of nanofluids is usually made through the assumption of a thermal equilibrium between the nanoparticles and the surrounding fluid. The mathematical model from the Eq. 5-1 was proposed by Zhou et al. in 2008 [60] to match their experimental results of water-based nanofluids with ANPs. This expression takes into account the amount of the base fluid and the nanoparticles and the value of their respective specific heat.

$$c_{p,nf} = \frac{\phi \rho_{np} c_{p,np} + (1-\phi)\rho_{bf} c_{p,bf}}{\phi \rho_{np} + (1-\phi)\rho_{bf}}$$

Eq. 5-1

where c_p is the specific heat (kJ·kg^{-1}·K^{-1}), ϕ is the volume fraction of nanoparticles and ρ is the density (kg·m^{-3}). Subscripts nf, np, and bf denote nanofluid, nanoparticle and base fluid, respectively.

The Eq. 5-1 is not able to predict the experimental enhancements of the specific heat in MSBNFs, as described in several works [37,56,61–64]. In view of this discrepancy, Shin and Banerjee [63] proposed three different hypothesis to explain these enhancements: 1) the nanoparticles have larger specific heat than normal size particles due to their reduced size, 2) the interfacial thermal resistance between the nanoparticles and the molten salt is very large due to the high interface/volume relationship and 3) a nanolayer of the molten salt molecules surrounds the nanoparticle surface, which is supposed to have a specific heat higher than that of the nanoparticles or the salt. These authors were pioneering on proposing an explanation on this

particular issue though unfortunately, they did not provide any mathematical expression related to these assumptions. However, other authors obtained experimental results that can support the first model, the increase of the specific heat of a nanomaterial compared with that of the bulk material. Focusing on the nanoparticles most commonly used, the ANPs are supposed to experience an enhancement of 25% of the specific heat [71], while this phenomena is increasing by 10% the specific heat of the SiNPs [199]. On the other side, the existence of a nanolayer or a nanostructure (including both the nanoparticles and the ions of the molten salt) has also been demonstrated by Scanning Electron Microscope (SEM) images [30,99].

This investigation aims to determine the factors involved on the specific heat enhancement of Solar Salt-based nanofluids. With this objective, the nanoparticle concentration (0.5, 1 or 1.5 wt%), the purity of the Solar Salt (analytical, refined or industrial grade) and the nature and shape of the nanoparticle (fiber-shaped ANPs or nearly round-shape SiNPs) was studied as influencing factors on the specific heat of the nanofluids. In addition, the repeatability of the results is determined. The theoretical increment of specific heat is also calculated with the published methods and compared with the experimental results. The relationship between the specific heat and the available surface of the nanoparticles to interact with the molten salt is examined. Finally, the existence of a nanostructure on the studied nanofluids is verified by SEM images.

5.2.2 Experimental

5.2.2.1 Materials

Three Solar Salts (60:40 wt% of $NaNO_3:KNO_3$) of different purity were prepared: the analytical grade, ASS (Labkem, $NaNO_3 \geq 99.5$ wt%; Labkem, $KNO_3 \geq 99.8$ wt%); the refined grade, RSS (SQM, $NaNO_3 \geq 99.5$ wt%; SQM, $KNO_3 \geq 99.6$ wt%) and the industrial grade, ISS (SQM, $NaNO_3 \geq 98.0$ wt%; Haifa Multi-K GG, $KNO_3 \geq 95.0$ wt%).

The raw nitrates were ground in a mortar, dried in an oven at 100 ºC to remove the moisture and mixed in the mentioned proportions. Then, these mixtures were melted in a furnace at 396 ºC for 30 minutes, to ensure their homogeneity. Once this melting program was finished, the salts were cooled at room temperature until their solidification and finally grounded in a mortar to obtain a fine powder. As a result, the ASS, RSS and ISS were ready to be further mixed with the nanoparticles. Each of these salts was prepared in several batches of approximately 100 g which were identified, characterized and used to prepare the nanofluids. This procedure allowed a more precise comparison of the thermal properties of the nanofluids with their specific base salt.

Two types of ceramic nanoparticles were selected, ANPs (Figure 5-2, left) and SiNPs (Figure 5-2, right). ANPs were purchased from Kawaken Chemicals as an industrial water-based nanofluid, Alumisol-10A, containing fiber-shaped boehmite nanoparticles (L=50 nm, ϕ=10 nm) at 10 wt%

according to the manufacturer. The boehmite (aluminium oxyhydroxide, AlOOH) is a precursor of the γ-Al$_2$O$_3$. On the other side, a dispersion of colloidal silica at 30 wt%, LUDOX® SM-30, from Sigma-Aldrich was used as a source of spherical SiNPs.
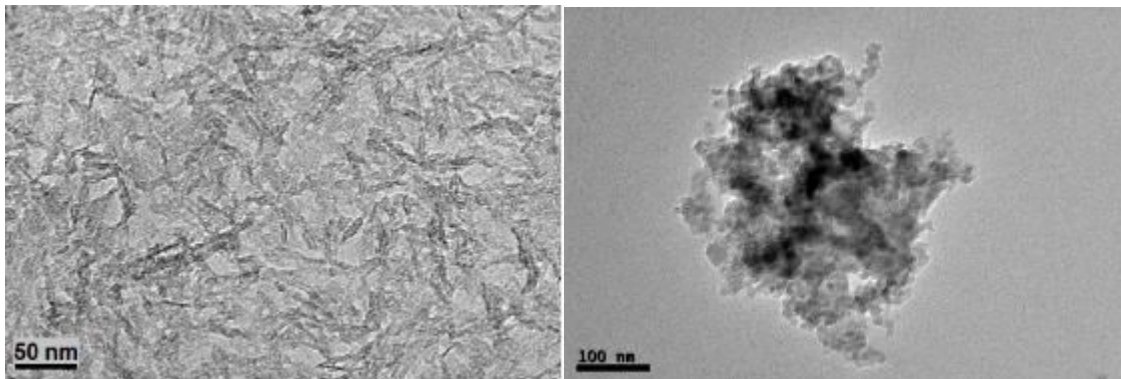
Figure 5-2. TEM images of the ANPs (left) and the SiNPs (right).

5.2.2.2 Synthesis of the nanofluids

Several nanofluids were synthetized with contents of 0.5%, 1% and 1.5 wt% of nanoparticles and the three mentioned Solar Salts (Table 5-1) to study the influence of these variables on the specific heat. The nanofluids were prepared by the well-known hot plate method for MSBNFs. First, the Solar Salt of desired purity was dissolved in distilled water (50:50 wt%) and then the proper quantity of Alumisol-10A or LUDOX® SM-30 was added respectively drop by drop under mild stirring. This solution was poured carefully into a hot plate (ϕ = 15 cm) and the water was then removed by heating at 100 ºC in an oven for at least 2 hours. The dried material was scrapped off from the hot plate, melted at 396 ºC for 30 minutes and cooled down at room temperature. The solid material was milled and a representative sample was taken to be further characterized.

Table 5-1. Name and composition of the nanofluids used in this study.

	ASS, wt%	RSS, wt%	ISS, wt%	ANPs, wt%	SiNPs, wt%
ASS	100.0	–	–	–	–
ASS05A	99.5	–	–	0.5	–
ASS1A	99.0	–	–	1.0	–
ASS15A	98.5	–	–	1.5	–
ASS05Si	99.5	–	–	–	0.5
ASS1Si	99.0	–	–	–	1.0
ASS15Si	98.5	–	–	–	1.5
RSS	–	100.0	–	–	–
RSS05A	–	99.5	–	0.5	–
RSS1A	–	99.0	–	1.0	–
RSS15A	–	98.5	–	1.5	–
RSS05Si	–	99.5	–	–	0.5
RSS1Si	–	99.0	–	–	1.0
RSS15Si	–	98.5	–	–	1.5

	ASS, wt%	RSS, wt%	ISS, wt%	ANPs, wt%	SiNPs, wt%
ISS	–	–	100.0	–	–
ISS05A	–	–	99.5	0.5	–
ISS1A	–	–	99.0	1.0	–
ISS15A	–	–	98.5	1.5	–
ISS05Si	–	–	99.5	–	0.5
ISS1Si	–	–	99.0	–	1.0
ISS15Si	–	–	98.5	–	1.5

5.2.2.3 Thermogravimetric analysis

This technique was used to verify the absence of any thermal degradation at the working temperatures in the CSP plant (≤550 ºC). About 20 mg of solid sample was put in a platinum crucible and heated in the TGA device (SETARAM SETSYS Evolution –1750, Setaram Instrumentation, France). The heating program consisted of a first heating from 20 to 90 ºC at 5 ºC/min to remove humidity followed by a second stage from 90 to 550 ºC at 2 ºC/min. Then, the sample was maintained at the highest temperature for 3 hours. Finally, it was submitted to two thermal cycles of heating and cooling between 90 and 550 ºC to know if possible changes were reversible or not. The analyses were always done under ambient atmosphere. The weight loss of the sample was precisely registered along the time with the thermobalance. Five materials were submitted to this thermal test: the ANPS, the SiNPs, the ISS and the nanofluids ISS1A and ISS1Si.

5.2.2.4 Specific heat

A Differential Scanning Calorimeter (DSC, Q1000 TA Instruments with autosampler) was used to determine the specific heat, by using the Modular Differential Scanning Calorimetry (MDSC) under an isothermal procedure. Around 30 mg of the sample were introduced in an aluminium crucible, which was hermetically sealed afterwards. The sample was first stabilized at the desired temperature for an isothermal period of 10 min to achieve the salt thermal equilibrium. The data collection was carried out for 20 min at the same temperature. Nitrogen was used as inert gas inside the device. The specific heat was measured at 196 °C (solid state), 296 °C and 396 °C (both in liquid state). These temperatures correspond to the working temperatures of the SS in real conditions. The temperature modulation of the DSC technique was set-up to 0.6 °C of amplitude and a period of 110 s in order to provide good sensitivity. Three different portions of each sample were measured to obtain a representative result. This measurement method was proved to achieve a high precision [157,158].

The specific heat of each nanofluid and its base salt (owing to the same batch of Solar Salt) were always measured consecutively to assure a proper comparison.

5.2.2.5 Nanoparticle size distribution

The size of the ANPs and SiNPs was measured on each nanofluid with the aim of establishing a relationship between these sizes and the thermal properties. The nanofluids were characterized using the Dynamic Light Scattering method (DLS, ZetaSizer Nano ZS, Malvern Instruments, Ltd. Malvern, UK). The nanoparticle size distribution of these nanofluids was thus obtained as the number of nanoparticles at each size between 0.4 and 10,000 nm. The available surface of the nanoparticles to interact with the molten salt can be inferred from this data by using the following relation (Eq. 5-2):

$$S_a = \frac{6 \cdot \varphi_{NP}}{\rho_{NP}} \sum_{i=1}^{n} \frac{N_i}{D_i}$$

<div align="right">Eq. 5-2</div>

where S_a is the available surface of nanoparticles per gram of nanofluid ($m^2 \cdot g^{-1}$), φ_{NP} is the fraction of nanoparticles in the nanofluid, ρ_{NP} is the density of the nanoparticles, n is the number of size classes in the distribution, N_i is the number of nanoparticles of each size and D_i is the diameter of each nanoparticle.

5.2.2.6 Nanofluid microstructure

The physical distribution of the nanoparticles in the matrix of Solar Salt was evaluated in the solid samples by using a Field Emission Scanning Electron Microscope (FESEM LEO 440i, Leica-Zeiss). The specimen preparation involves placing the solid sample on a microscopy slide covered with a graphite layer. After this, the specimens were metalized with platinum in a thermal evaporator prior to their characterization. Secondary Electrons (SE) images were useful on giving quantitative information of the nanoparticle and agglomerate sizes. The Energy-dispersive X-ray spectroscopy (EDX) technique was used to know the atomic composition in certain areas of the pictures.

5.2.3 Results and discussion

5.2.3.1 Thermogravimetric analysis

The thermogravimetric profile of ANPs (based on boehmite nanoparticles) is analysed in Figure 5-3, up left and reveals three different stages in the studied temperature range. The first weight loss (Δm=-11.3 wt%) occurs between 20 and 90 ºC with a minimum around 80 ºC, due to the loss of humidity of the sample. A second step of dehydration (Δm=-13.3 wt%) is observed in the range of 90-400 ºC with an endothermic peak at 390 ºC related to the desorption of intralaminar water located between boehmite nanoparticles. Finally, the boehmite starts the transformation in γ-Al_2O_3 that accounts the 5.6% of the mass loss. These changes are irreversible, as confirmed by

the absence of weight change on the second and the third cycle of the thermal treatment. These results are in agreement with the specialized literature on this subject [186,187].

The TGA and DTG curves of the SiNPs are reported in Figure 5-3, up right. The weight loss of the sample is characterized by two stages. The first region (from room temperature to 90 ºC) is linked with the loss of physically absorbed water from the surface of the nanoparticles (-6.3 wt%). On the other hand, from 90 ºC to 550 ºC there is a lower mass loss (-2.5 wt%) due to the chemically adsorbed water bonded to Si–OH through hydrogen bond. These results are in agreement with the thermal degradation of amorphous silica studied by Zhuravlev [188] and Liu and his co-workers [189].

Figure 5-3 middle, is showing the evolution of the weight of ISS under the thermal treatment described above. As expected, the weight loss in this temperature range is minimum because the nitrates are thermally stable until 600 ºC [31,33,113,180]. According to this Figure 5-3 middle, the Solar Salt suffered only a tiny weight loss of 0.6 wt% related to the start of its thermal decomposition near 550 ºC. Although only the ISS have been analysed, it is considered that ASS and RSS are thermally stable in the same range of temperatures.

The nanofluid ISS1A (Figure 5-3, down left) reduces its mass in 1.2 wt% between 20 ºC and 550 ºC (two fold the weight loss of the ISS), reaching a total loss of 5.5 wt% after the first cycle (3 hours at 550 ºC). In the second and the third cycle, where the sample was a few minutes at 550 ºC, the additional mass reduction is only around 0.5 wt% on each case. It is significant that most of the weight loss occurs at the isothermal step of 550 ºC (4.3% over a total of 6.8%). This could be related to some kind of degradation caused by the ANPs in contact with the molten nitrates at the mentioned temperature, promoting the decomposition of nitrates in nitrites and oxygen. A similar trend is observed in the thermogram of the ISS1Si (Figure 5-3, down right), although the weight loss is smaller than in the previous nanofluid (-3.3 wt%) and only after the isothermal step. It is though that the SiNPs are also reducing the thermal degradation temperature of the Solar Salt, as the ANPs. The degradation of nanofluids of Solar Salt with SiNPs were described by Schuller et al. [32] by registering a lower specific heat when the sample was submitted to thermal cycles until 450 ºC.

In view of these findings, the use of Solar Salt-based nanofluids as HTF (working temperature of 550 ºC) is not recommended due to the high weight loss registered when the nanoparticles are in contact with the molten nitrates at this high temperature. This limitation should be checked with other nanoparticles and base salts as a first step before performing any other characterization. As a result, the nanofluids on this study are considered only as TES material, which implies the use of lower temperatures (≤400 ºC).
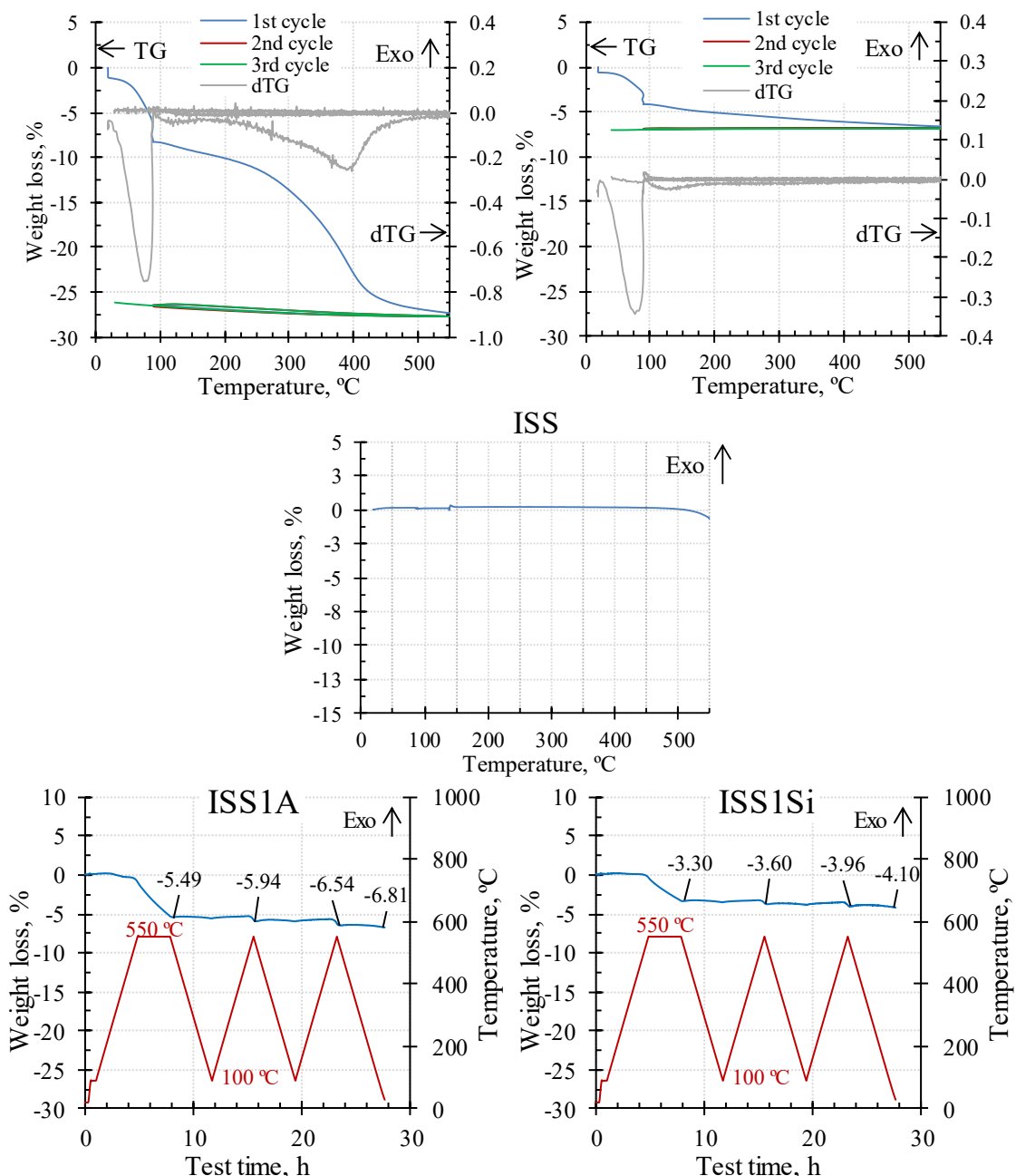
Figure 5-3. TGA measurement between 20 ºC and 500 ºC of the ANPs (up, left), SiNPs (up, right), ISS (middle), ISS1A (down, left) and ISS1Si (down, right).

5.2.3.2 Specific heat

Figure 5-4 gathers the increments of the specific heat in the solid (196 ºC) and the liquid state (296 ºC and 396 ºC) of every synthetized nanofluids. It is important to remark the high variability found between the results of equivalent nanofluids (with the same base salt, type and concentration of nanoparticles) prepared independently. In addition, the inconsistencies also occur when the same nanofluid was tested again, as explained at the end of this section. Thus, the conclusions included in the following discussion should be considered with caution.
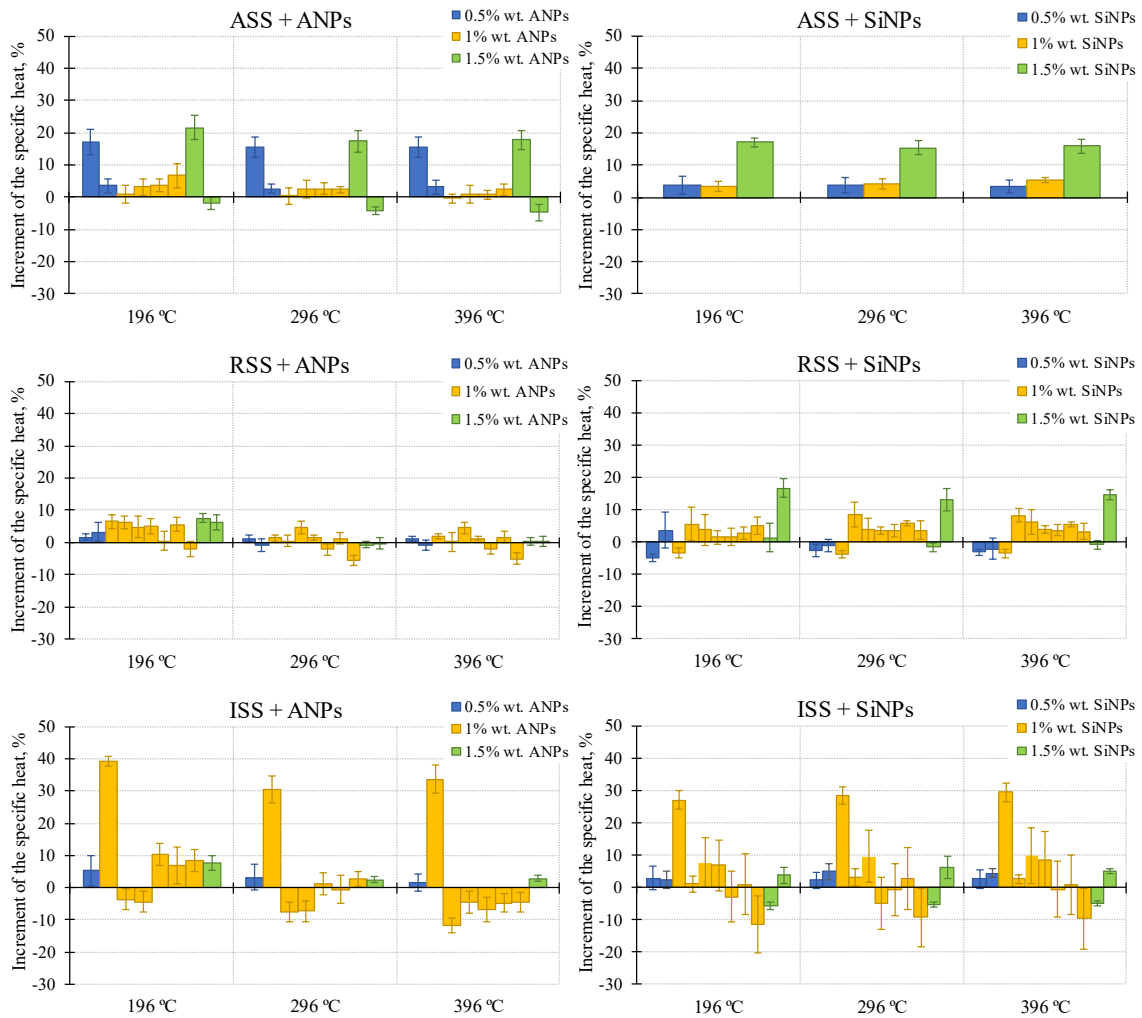
Figure 5-4. Increment of the specific heat of nanofluids with ANPs (left column) and SiNPs (right column) added respectively in different percentages to the ASS (up row), RSS (middle row) and ISS (bottom row). The error bars displayed are calculated as the sum of the experimental errors in the specific heat determination of the base salt and the nanofluid on each case. The existence of several bars of the same nanofluid is referred to the analysis of different replicas prepared independently.

The results of the Figure 5-4 can be analysed under several criteria: the nanoparticle concentration, chemical composition and shape; the test temperature and the base salt. The amount of nanoparticles added into the Solar Salt does not seem to be directly related to a higher increase of the specific heat. Although the maximum enhancements were obtained at 1.5 wt% of nanoparticles in some cases (ASS15A, ASS15Si, RSS15Si), the nanofluid ASS05A, containing only 0.5 wt% of ANPs showed similar improvements. The ISS-based nanofluids had noticeable enhancements (around 30%) with 1 wt% of both ANPs and SiNPs only in some cases, while very modest increases were experienced by these nanofluids with 0.5% and 1.5 wt% of nanoparticles. The presence of impurities in the base salt seems to play an important role in the interactions between the nanoparticles and the molten salt, and thus, a possible effect on the specific heat of the molten salt.

The impact of the nanoparticle mass concentration on the specific heat of nanofluids may be due to two opposite phenomena. On one side, a minimum quantity of nanoparticles is needed to achieve an enhancement on the specific heat of the molten salt. This needs the development of a high thermally conductive-nanolayer on their surface as suggested by Shin and Banerjee [63] or dendritic structures as proposed by Tiznobaik et al. [99]. This minimum quantity has not been determined yet by any author and may be different depending on the base salt and the feature of the nanoparticles such as their initial size and shape or their crystal structure. On the other side, the presence of a large amount of nanoparticles greatly increases their chances of agglomeration, reducing the surface available to develop the nanolayers. As a consequence, in this case the increments of the specific heat would be smaller and even absent. As detailed in the introduction (Figure 5-1), the influence of the nanoparticle percentage on the specific heat of Solar Salt-based nanofluids has been addressed by several authors. Although there is not a common trend when their results are compared, the highest increments were obtained with 1 wt% of nanoparticles in three investigations [32,36,113] while minimum impacts were observed at 0.5% and 1.5 wt% of concentration.

The effect of the Solar Salt purity on the results is similar to that found for the mass percentage of nanoparticles. The difference between the three types of Solar Salt employed as base fluids in this study (ASS, RSS and ISS) is their increasing amount of impurities, which are either dissolved or dispersed in the molten salt. Having this into account, it is thought that the presence of solid impurities may accelerate the agglomeration and settling of the nanoparticles, reducing the chances of rising the specific heat of the base salt.

The ASS-based nanofluids (Figure 5-4 first row), which only have the nanoparticles as solid material dispersed into the molten salt, showed increments of around 20% in three of the nine analysed nanofluids. In addition, their global data dispersion (the sum of the scattering of the Solar Salt and that of the nanofluid) is below 5% in any case. The other ASS-based nanofluids had weak increments around 3% and only one of them showed a decrement of the specific heat.

For the RSS-based nanofluids (Figure 5-4 middle row), the raise of the specific heat is lower than the previous nanofluids (<7%), with the exception of one of those containing 1.5 wt% of SiNPs (≈15%). There are also diminutions compared to the base salt (up to -5%) in six of these 22 nanofluids. Finally, the nanofluids with the ISS as their base salt (Figure 5-4 bottom row) are those with the higher variability in the results. The maximum enhancements are around 30% in two of the 19 nanofluids while the most frequent result is between 5% and 10% (in eight of them). These nanofluids have a higher dispersion on the results, a fact probably related to the increment on the impurities of the base Solar Salt and, consequently, the low homogeneity of the sample. The same reason could be behind the increased variability with the temperature of the specific

heat of these nanofluids. The impurities may speed up the settling of the nanoparticles when they are dispersed into the molten salt (at 296 °C and 396 °C). They may be accumulated at the bottom of the crucible, generating a layer with lower specific heat (as the specific heat of the nanoparticles is smaller than that of the molten salt). The exceptional specific heat enhancements observed in some cases (for example ISS1A) can be related to the presence of remaining low size nanoparticles in the bulk of the molten salt after the settlement of the bigger ones. This effect may be subjected to a high variability. However, the nanoparticles suspended in the molten salt are very unstable and these enhancements are not expected to remain in the time.

5.2.3.2.1 Repeatability of the results

As described in the Section 5.2.2.4, the results and the data scattering were obtained by analysing three crucibles in the DSC device for each prepared nanofluid. This method is highly precise as demonstrated in an earlier publication [157]. This procedure is referred to the repeatability of the measurements performed on the same nanofluid. According to the Figure 5-4, the variability between several replicas of equivalent nanofluids (same base salt and nanoparticle concentration and type) is quite high. To verify these results, five replicas of three particular nanofluids (RSS1A, RSS1Si and ISS1Si), fifteen nanofluids in total, were analysed again by filling and measuring three new crucibles. In the Figure 5-5 (first row and second row, left), the enhancements obtained from the former and these new DSC tests are depicted. The result of each test is the mean specific heat of the analysis with three crucibles. According to the three first graphs (RSS1A, RSS1Si and ISS1Si), the difference of the results between the two tests is evident and any clear pattern can be inferred from them. This means a low homogeneity of the nanofluids, which may be caused by the agglomeration of the nanoparticles and the presence of impurities on the base salts RSS and ISS. In general, most of the nanofluids based on RSS (with both nanoparticles) shows specific heat enhancements or decrements with independency of the temperature. That means that results are not conditioned by the solid or liquid state of the salt. Half of the nanofluids of RSS1A have specific heat enhancements, while this is seen for a 70% of the RSS1Si. This trend could be due to the easiness of the ANPs to agglomerate. The results are highly inconsistent in the nanofluid ISS1Si, which could be related to the greater amount of impurities of the ISS in comparison to the RSS.

In addition, another experiment was done to check the important enhancements of the nanofluids ISS1A ($\approx$35%) and ISS1Si ($\approx$30%). After six months of this first test, the same crucibles were measured again. In addition, a new set of three crucibles were filled with these nanofluids and analysed, in the same manner as the previous experiment. The results are gathered in Figure 5-5, down right, where the solid colour bars are referred to the ISS1A and the line pattern bars are the results of the ISS1Si. The red bars correspond to the old crucibles and the yellow bars to the new

ones. As showed by this figure, the improvements of the specific heat are not maintained after this period of time, either in the samples contained in the old or the new crucibles. The most plausible reason could be the absorption of the ambient humidity of the solid materials along the time, changing their crystalline structure. Thus, a different material with different properties is being compared with the initial one. Only Schuller et al. [32] performed a similar research. They repeated the measurements of specific heat of Solar Salt and ANPs after one and two months and did not found any variations on the results.
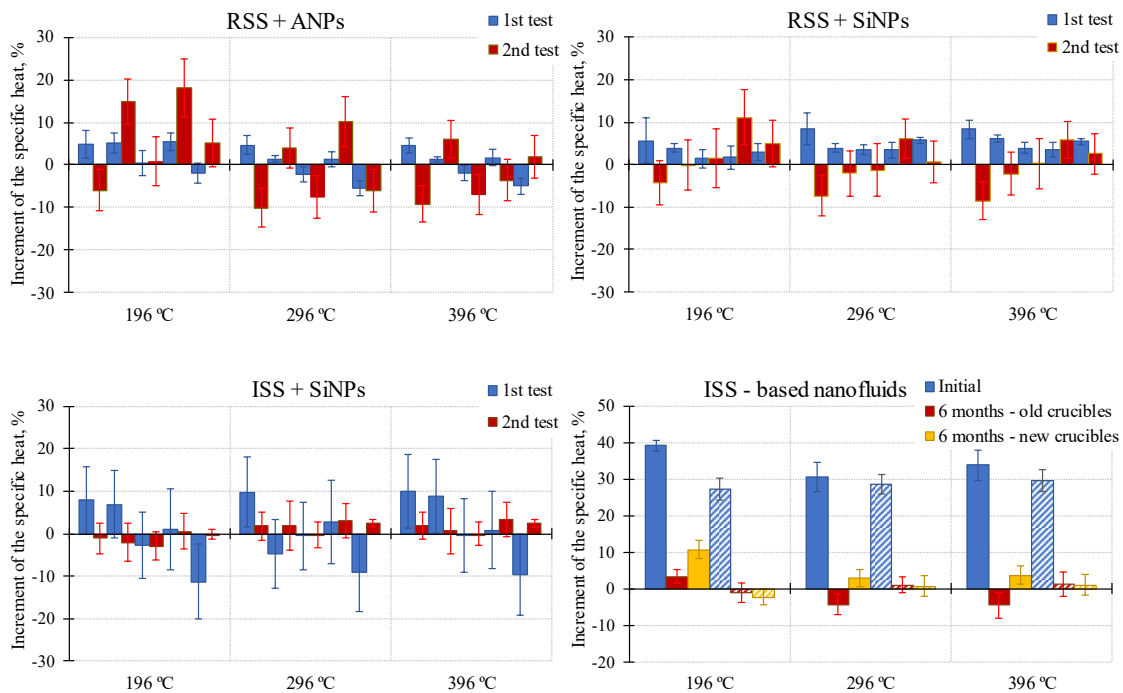
Figure 5-5. Specific heat increments of RSS1A (up left), RSS1Si (up right), ISS1Si (down left) and ISS1A (down right). The first and the second test results were obtained from two sets of three DSC crucibles. In the last graph, the solid color is the ISS1A nanofluid and the line pattern is the ISS1Si.

5.2.3.2.2   Theoretical models

In order to compare these theoretical predictions with our experimental results, the specific heat enhancement of the nanofluids was calculated according to the Eq. 5-1 proposed by Zhou et al. [60]. In addition, the increment of the specific heat of the nanoparticles proposed by Shin and Banerjee (first model) [63] was also computed. The density values considered were 3,950 $kg \cdot m^{-3}$ and 2,650 $kg \cdot m^{-3}$ for the ANPs and the SiNPs respectively [200]. The density of the Solar Salt was determined as 1,974 $kg \cdot m^{-3}$, 1,906 $kg \cdot m^{-3}$ and 1,838 $kg \cdot m^{-3}$ at the temperatures of 196 ºC, 296 ºC and 396 ºC according to the expression proposed by Janz et al. [201]. The specific heat of the nanoparticles was experimentaly determined at the temperatures of interest with the same method used with the salt and the nanofluids (Table 5-2).

Table 5-2. Specific heat (c_p) and data dispersion (SD) of the nanoparticles at the three tested temperatures.

	196 °C		296 °C		396 °C	
	c_p, kJ·kg⁻¹·K⁻¹	SD, kJ·kg⁻¹·K⁻¹	c_p, kJ·kg⁻¹·K⁻¹	SD, kJ·kg⁻¹·K⁻¹	c_p, kJ·kg⁻¹·K⁻¹	SD, kJ·kg⁻¹·K⁻¹
ANPs	1.195	0.039	1.237	0.009	1.471	0.031
SiNPs	0.970	0.112	0.943	0.243	1.157	0.143

The Table 5-3 gathers the experimental and theoretical results according to the models discussed in the introduction. In general, it is seen that the increments predicted by the models are quite tiny or even non-existent compared to the empirical ones. Thus, there must be additional factors involved on the heat transfer of the MSBNFs that have not been taken into account. The third model of Shin and Banerjee [63], which considers the existence of a solid salt-layer around the nanoparticles with a considerably larger specific heat could be playing an important role. Unfortunately, the evaluation of this model cannot be made by experimental methods, but solely by modelling and simulation tools.

Table 5-3. Enhancements of specific heat of the nanofluids according to the temperature. The mean experimental results are compared with the calculations made with Eq. 5-1 (Zhou et al. [60]) and the first model proposed by Shin and Banerjee [63].

	196 °C			296 °C			396 °C		
	Δc_p (exp.)	Δc_p (Zhou)	Δc_p (Shin)	Δc_p (exp.)	Δc_p (Zhou)	Δc_p (Shin)	Δc_p (exp.)	Δc_p (Zhou)	Δc_p (Shin)
ASS05A	10.29	-0.18	0.09	9.11	-0.28	-0.01	9.35	-0.09	0.25
ASS1A	3.58	-0.35	0.17	1.94	-0.53	-0.02	0.87	-0.17	0.47
ASS15A	9.85	-0.50	0.25	6.58	-0.77	-0.03	6.46	-0.25	0.69
ASS05Si	3.84	-0.38	-0.30	3.80	-0.53	-0.45	3.41	-0.38	-0.27
ASS1Si	3.28	-0.76	-0.58	4.28	-1.05	-0.89	5.25	-0.75	-0.54
ASS15Si	17.09	-1.12	-0.86	15.39	-1.55	-1.31	15.84	-1.10	-0.79
RSS05A	2.47	-0.14	0.14	0.24	-0.24	0.03	0.21	-0.06	0.28
RSS1A	3.80	-0.27	0.26	0.21	-0.47	0.05	0.38	-0.12	0.55
RSS15A	6.83	-0.39	0.38	-0.50	-0.69	0.08	0.25	-0.17	0.79
RSS05Si	-0.58	-0.35	-0.04	-1.90	-0.51	-0.20	-2.61	-0.36	0.12
RSS1Si	2.42	-0.69	-0.09	3.56	-1.00	-0.40	3.88	-0.70	0.23
RSS15Si	9.06	-1.02	-0.13	5.72	-1.48	-0.58	6.88	-1.03	0.33
ISS05A	5.22	-0.19	0.07	3.23	-0.26	0.01	1.61	-0.09	0.25
ISS1A	9.46	-0.37	0.14	3.22	-0.51	0.01	0.29	-0.17	0.48
ISS15A	7.76	-0.54	0.20	2.51	-0.74	0.01	2.85	-0.24	0.70
ISS05Si	2.75	-0.40	-0.13	3.69	-0.52	-0.23	3.61	-0.38	0.07
ISS1Si	4.29	-0.78	-0.25	4.24	-1.03	-0.46	5.99	-0.74	0.14
ISS15Si	-0.86	-1.15	-0.37	0.51	-1.52	-0.67	0.26	-1.09	0.20

5.2.3.2.3 Available surface of nanoparticles

In agreement with the previous results, the existence of a nanolayer around the nanoparticles with a significant heat transfer rate seems reasonable to explain the obtained specific heat increments. In order to maximize the impact of this nanostructure, it is important to promote the development

of a high amount of this material. In this sense, the interest is having a high available surface of nanoparticles where the nanolayer will be further developed. This parameter can be easily calculated from the nanoparticle size distribution (Eq. 5-2).

In the Figure 5-6, the available surface of the nanoparticles (S_a) of each nanofluid is displayed together with its specific heat enhancement. In general, the S_a of the nanofluids containing ANPs is bigger than those with SiNPs in its composition. This difference is attributable to the needle-shape of the first versus the nearly spherical-shape of the latter. The DLS device is measuring the hydrodynamic diameter of the nanoparticles or clusters, assuming that they are perfect spheres. The high aspect ratio of ANPs (L=50 nm, ϕ=10 nm) compared to the SiNPs may cause the big values of S_a of the first. Consequently, the results of nanofluids containing ANPs should be considered with caution. According to the graphs in Figure 5-6, there is not a clear correlation between the S_a and the specific heat enhancement. However, some trends can be inferred from each of the nanofluids. The specific heat of the ASS with ANPs seems to decline with increasing available surface of the nanoparticles, which is in contradiction with our hypothesis. A plausible explanation can be that a great S_a also implies more isolated nanoparticles and the high c_p-nanostructures are very far from one another to produce a real impact on the global c_p. The samples with the higher enhancements (16%; 0.08 m^2·g^{-1} and 18%; 0.3 m^2·g^{-1}) are out of this trend. However, these samples correspond to ASS05A and ASS15A. Therefore, the concentration of nanoparticles is responsible of these enhancements. The nanofluids of ASS with SiNPs have a direct correlation between these two variables (S_a and c_p). A maximum enhancement of c_p is found for the ASS15Si nanofluid, which also has the highest S_a.

The nanofluids based on RSS have different behaviours depending on the nanoparticle. Those containing ANPs have a direct increment of the c_p with the S_a for values lower than 0.07 m^2·g^{-1} and beyond this point, the improvements of c_p are independent on the available surface of nanoparticles. This independence could be caused by the impurities contained in the RSS, which may hinder the correct development of highly conductive-nanostructures. They are probably located over the nanoparticle surface, with a possible overestimation of the S_a when the sample is measured in the DLS. Hence, for values of S_a higher than 0.07 m^2·g^{-1}, no more nanostructures between the nanoparticles and the salt ions are created, maybe because these surfaces are still impeded with the impurities. In the nanofluids of RSS with SiNPs there is a maximum increment of the specific heat at 0.06 m^2·g^{-1}. Only two of these nanofluids have a S_a higher than 0.10 m^2·g^{-1}, while there were four when the ANPs were present. The nanofluid RSS15Si is reaching a notable enhancement of the specific heat (around 15%) but it has not the highest S_a (0.23 m^2·g^{-1} compared to 0.39 m^2·g^{-1} for the nanofluid RSS1Si). As described previously for the ASS-based nanofluids, the concentration of nanoparticles seems to influence the thermal improvements more than the available surface.

Finally, the results of the ISS-based nanofluids are analysed. On one side, those with ANPs in their composition have an inverse dependence between the c_p and the free surface of the nanoparticles. Only one of the nanofluids, ISS1A, is outside this rule with a remarkable enhancement of 34% (in the liquid state) and a S_a of 0.26 $m^2 \cdot g^{-1}$. On the other side, the nanofluids which contains SiNPs do not show any clear dependence between these two variables. The nanofluid with the biggest available surface of nanoparticles, 0.36 $m^2 \cdot g^{-1}$, has also the biggest increment of specific heat (30%).

As remarked before, these results are conditioned by the overestimation of the ANPs size and the existence of impurities on the base salts (RSS and ISS). These factors may be behind the absence of a clear correlation between the c_p and the S_a in most of the pairs nanoparticle + salt. The distribution of sizes of the ASS-based nanofluids doped with SiNPs may be more accurated due to the spherical nature of SiNPs. In conclusion, there should be more unknown factors playing a role into the c_p enhancements.
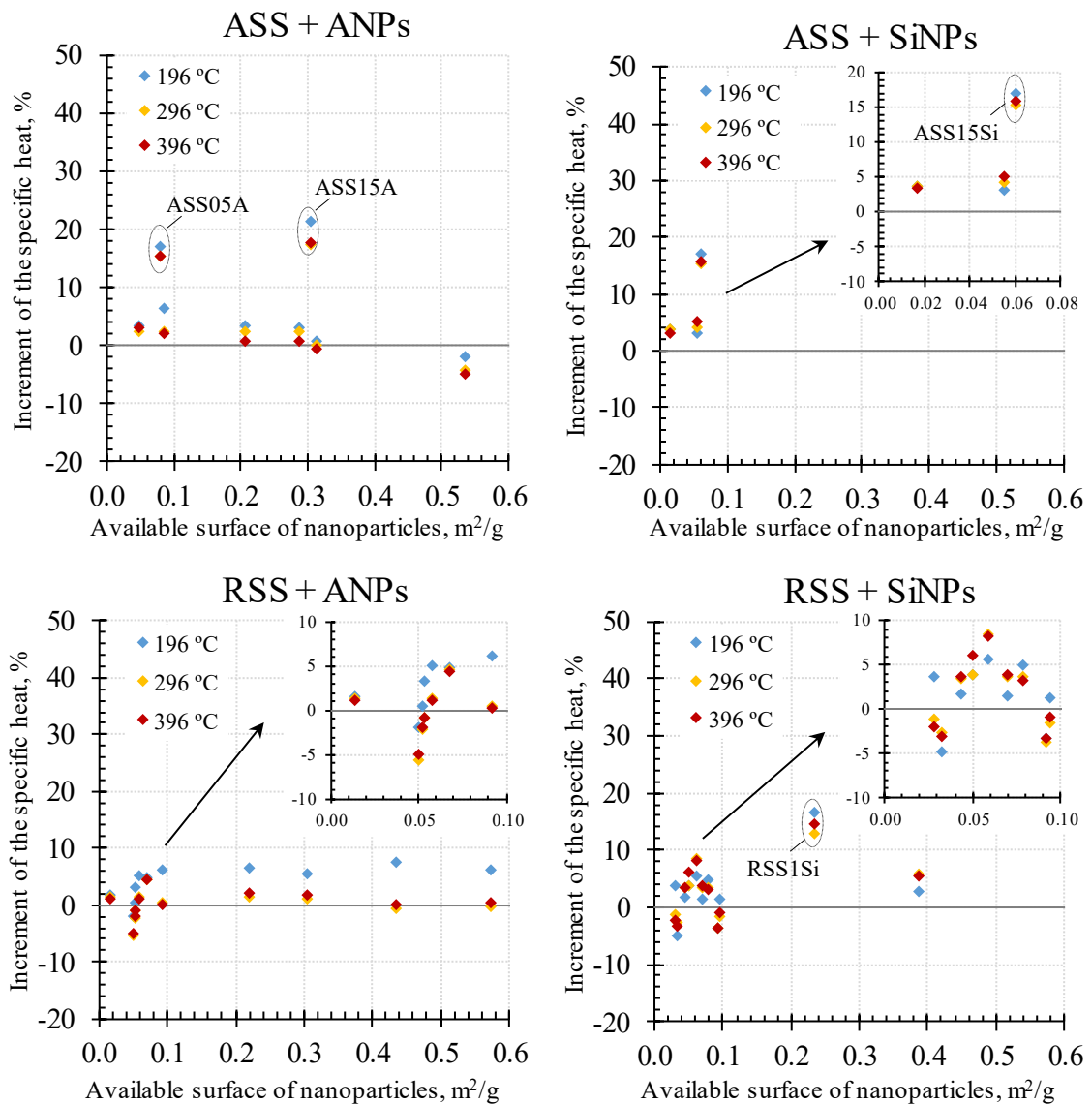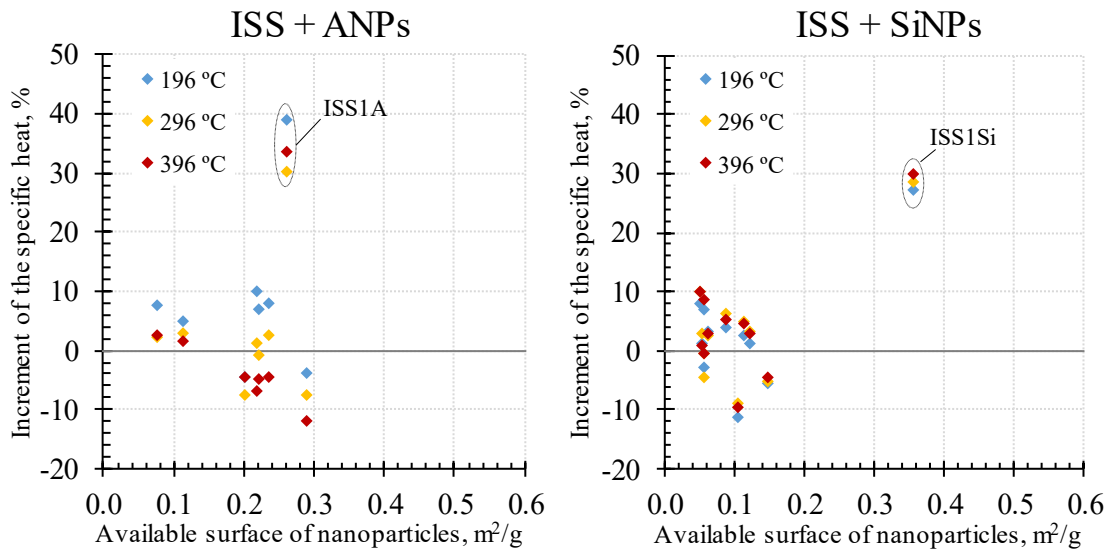
Figure 5-6. Increment of the specific heat of nanofluids versus their available surface. Nanofluids with ANPs (left column) and SiNPs (right column) added respectively to the ASS (up row), RSS (middle row) and ISS (bottom row).

5.2.3.3 Nanofluid microstructure

The analysis of the nanofluids by SEM is very helpful for several purposes. The use of this technique allows to confirm the presence of the special nanostructures responsible of the enhanced specific heat. Moreover, the nanoparticle or cluster sizes can be quantitatively estimated as well as the homogeneous dispersion of the nanoparticles in the matrix of the base salt.

The Figure 5-7 shows two SEM images of the ISS without nanoparticles. They revealed that the crystals are rounded-shape and with a smooth surface. In these images, the sodium nitrate crystals appear in darker grey and the potassium nitrate ones in a brighter tone. The white and brilliant tiny particles are presumably chloride crystals coming from the impurities of the ISS. It is considered that the other base salts ASS and RSS have a similar aspect. The obtained SEM images are alike others described in diverse publications [31,74].
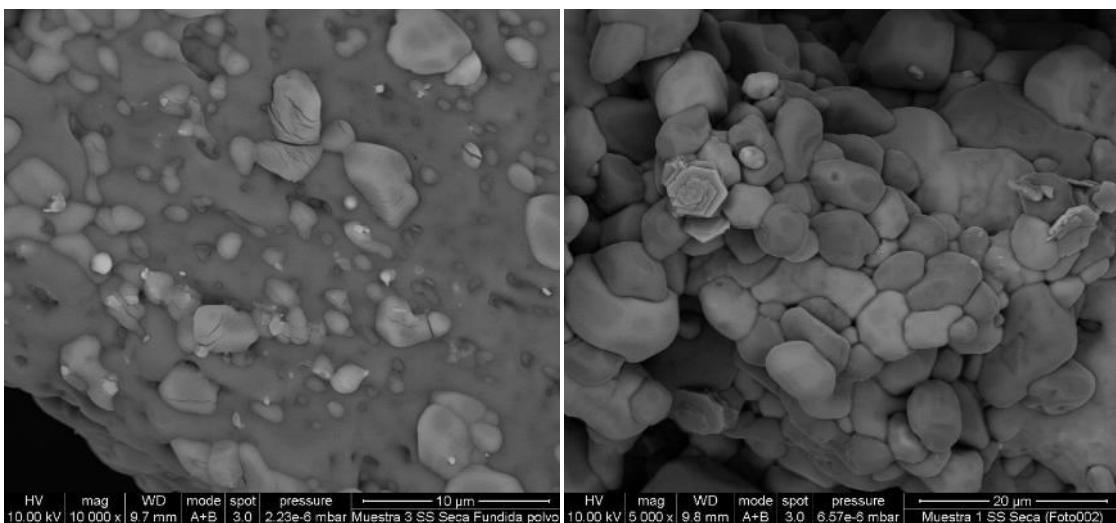
Figure 5-7. SEM images of the ISS done under QBSD with 10,000x (left) and 5,000x (right) of magnification.

The Figure 5-8 gathers the images of four different nanofluids, with the RSS as the base salt (RSS1A and RSS1Si) and their analogous with the ISS (ISS1A and ISS1Si). Every of these images shows the distinctive matrix of Solar Salt covered by individual or clustered nanoparticles. In the Figure 5-8 left side, it is evident the fibre shape of the ANPs and their agglomerates. The high number of isolated nanoparticles with a high aspect ratio is significant in the nanofluid ISS1A (Figure 5-8 left side, down). The two pictures on the right side are clearly showing the near spherical shape of the SiNPs. When these nanoparticles are agglomerated, they look like pieces of cotton.
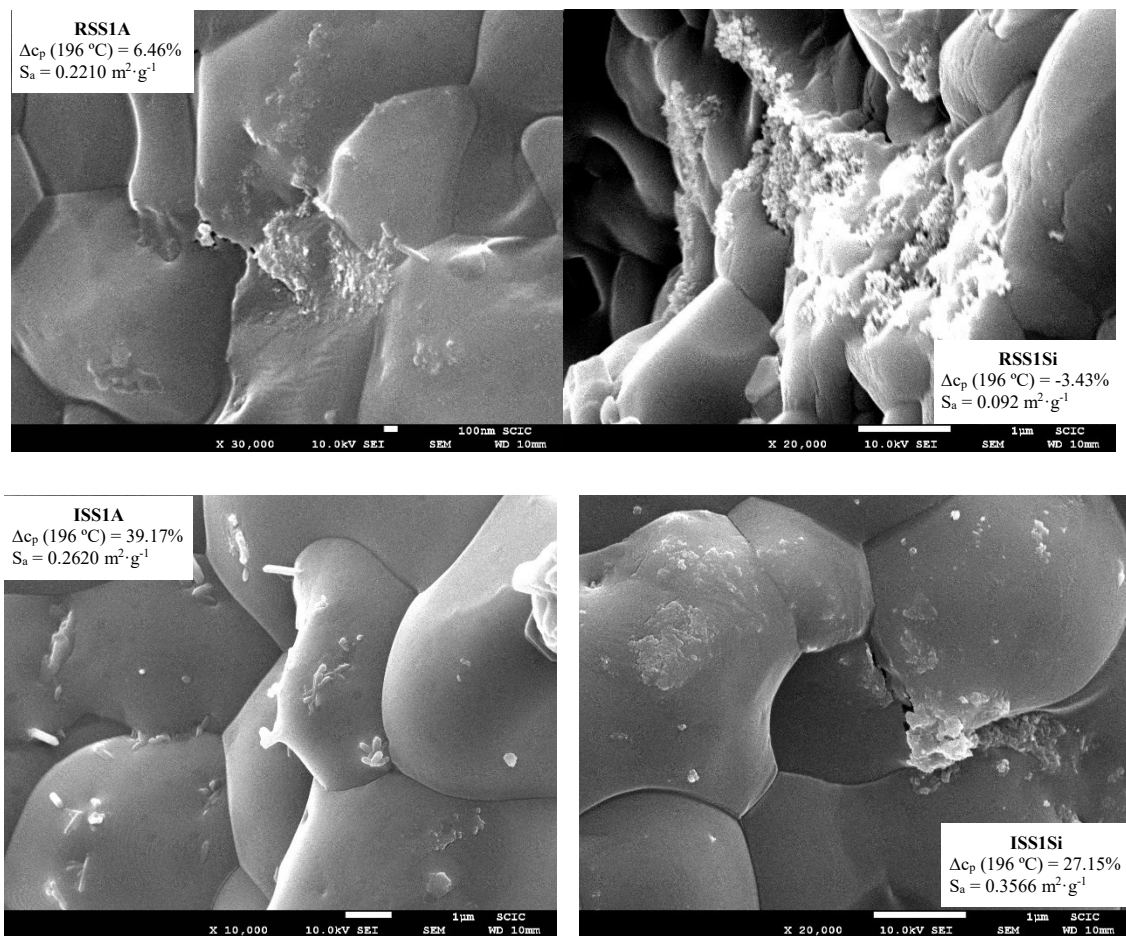
Figure 5-8. SEM images of four representative nanofluids based on RSS (up) and ISS (down). The images were done under Secondary Electrons (SE) with 30,000x (RSS1A), 20,000x (RSS1Si and ISS1Si) and 10,000x (ISS1A) of magnification. The specific heat enhancements and the surface available of nanoparticles is written on each image.

Finally, the elemental composition of the ISS1A nanofluid was analysed with EDX. This nanofluid was selected for its high increment of the specific heat (39.17%). The two images in Figure 5-9 reveals the existence of the nanostructure theorized by Shin and Banerjee [63] and demonstrated experimentally in [30,99]. The composition of the indicated area on each picture is described in Table 5-4, where the aluminium has an important percentage but the sodium, potassium, nitrogen and oxygen coming from the ISS are also present. The chloride is coming from the impurities of the ISS.
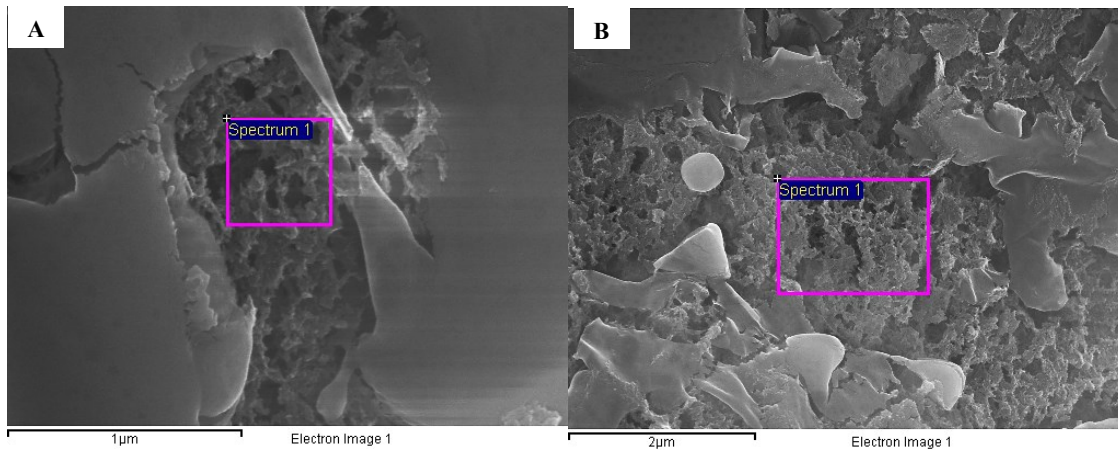
Figure 5-9. SEM images of a ISS1A nanofluid including the area where the EDX analysis have been performed (see Table 5-4).

Table 5-4. Results of the EDX analysis of the pictures showed in Figure 5-9.

Element	ISS1A Δc_p (196 ºC) = 8.30% ; S_a = 0.2367 $m^2 \cdot g^{-1}$	
	Amount, wt%	
	A	B
O	30.81	53.46
N	---	14.67
Na	43.13	6.31
K	10.77	18.75
Al	15.29	6.24
Cl	---	0.58
Total	100	100

5.2.4 Conclusions

This research has deeply studied how the specific heat of Solar Salt is improved by the addition of nanoparticles and the factors which impact on this property. The thermogravimetric tests determined that the mixture of the Solar Salt and ANPs or SiNPs is thermally degraded at 550 ºC, which restrain the use of these nanofluids only as TES material (maximum temperature 400 ºC). Regarding the specific heat results, the influence of the nanoparticle percentage seems to be related to the purity of the base salt. The highest enhancements were obtained at 1.5 wt% if the ASS and the RSS were the base salt, while the addition of only 1 wt% of nanoparticles to the ISS achieved great increments. However, these results had no repeatability: either between equivalent nanofluids which were synthetized independently or with repeated measurements on the same material. Theoretical models revealed insufficient to explain the experimental results, since they predicted very low or inexistent increments. The relationship between the specific heat and the available surface of the nanoparticles is erratic and did not provide any clear conclusion. Finally, the microstructure of the nanofluids is useful to know the dispersion of the nanoparticles and the existence of a nanostructure which may be the responsible of the improvement of the thermal properties.

Along the authors' opinion, there is still a huge research work to be done in this field. First, the inconsistencies between the experimental results should be greatly reduced. Second, the development of simulation and modelling tools for these materials is essential to perform a more effective experimental work.

5.3 JOURNAL CONTRIBUTION 5: ANOMALOUS THERMAL CONDUCTIVITY RISING OF MOLTEN NITRATES BY THE ADDITION OF NANOPARTICLES

Authors: Belén Muñoz-Sánchez, Javier Nieto-Maestre, Nuria Navarrete, José Enrique Juliá, Helena Navarro, Yulong Ding and Ana García-Romero

Abstract: This research experimentally analyses the thermal conductivity on Solar Salt-based nanofluids for the first time. Silica and alumina nanoparticles were added respectively in concentrations of 0.5, 1 and 1.5 wt% to the Solar Salt. The specific heat of these nanofluids was precisely measured by Differential Scanning Calorimetry (DSC) and the results were used to determine the thermal conductivity from the thermal diffusivity obtained in a Laser Flash Analyser (LFA) device. Important enhancements on both the specific heat (up to 17%) and the thermal conductivity (up to 60%) were obtained on the nanofluids with 1 and 1.5 wt% of silica or alumina nanoparticles. Theoretical models were not able to predict these large improvements of the thermal properties. Finally, the influence of the available nanoparticle surface on the specific heat and the thermal conductivity of the nanofluids was analysed. A parabolic correlation was found between these thermal properties and the available surface of nanoparticles in the nanofluids containing silica nanoparticles.

5.3.1 Introduction

The worldwide increasing energy demand compels to use and develop new technologies based on renewable resources. The main disadvantage of these sustainable energy sources is their intermittence and thus, their low availability on demand in comparison to the non-renewable energy resources. In this context, the Concentrated Solar Power (CSP) technology is of high importance due to its proven dispatchability and efficiency. The use of a Thermal Energy Storage (TES) system in the current CSP plants allows to extend the plant operation time by some hours when the sun is not available (cloudy weather or at night). The presently employed TES systems store the energy as sensible heat. They consist of two tanks at different temperatures (around 300 ºC and 400 ºC, respectively) filled with a molten salt. This salt is a mixture of sodium and potassium nitrate (60:40 wt%) known as Solar Salt (SS). In addition, the working temperature in the solar field is becoming increasingly higher in modern central receiver plants (tower), and Heat Transfer Fluids (HTFs) with a higher range of thermal stability are required. Thermal oils (Dowtherm™, Therminol® VP-1) have been mostly used until now as HTFs in parabolic trough plants. However, their degradation temperature is very low (400 ºC). Hence, SS represents a great alternative to these oils due to its wider range of working temperature (220 ºC – 600 ºC).

Despite the advantages shown by the SS (low cost, thermal stability, environmentally friendly), its thermal properties (the specific heat and the thermal conductivity) are poor and there is still

potential to improve them. A simple and a cost-effective way consists of adding nanoparticles to the SS. This new type of materials is known as Molten Salt-Based Nanofluids (MSBNFs) and has attracted great interest by the scientific community in recent years [57,58]. The main feature of these nanofluids is the relevant increase of the specific heat compared to the base salt, which has been systematically observed [31,36,98,112,113]. The amount of stored heat is directly related to the specific heat, so the enhancement of this property allows storing more energy and thus extending the CSP plant production. In addition, the enhancement of the specific heat has only been reported to take place in MSBNFs, while nanofluids based on water or oils have not shown it [202]. However, the mechanisms which govern the interaction between the nanoparticles and the molten salt are not still well-known, neither understood. Due to these reasons, most of the scientific research on the field has been devoted to the study of the specific heat, while other properties have received very little attention.

Another significant property related to heat storage and transfer is the thermal conductivity. Very few studies on MSBNFs consider this property [30,32,102], and they only measured the material on the solid state due to technical issues. In addition, these investigations found opposite trends when nanoparticles were added to the inorganic salts.

The experiments from Shin et al. [30,102] revealed significant enhancements on the thermal conductivity of nanofluids of carbonates (Li_2CO_3–K_2CO_3 62:38 mol) with 1 wt% of silica nanoparticles in the solid state (between 47% and 37% increment of the thermal conductivity at 150 ºC and 350 ºC). In contrast, Schuller et al. [32] observed a decrease of the thermal conductivity of the SS mixed with 1 wt% of Silica Nanoparticles (SiNPs). These decrements were independent of the nanoparticle concentration (0.09 wt%–1.19 wt%) and ranged between -13.11% and -27.87% at 145 ºC. In both investigations, the thermal diffusivity was measured by a Laser Flash Analyser (LFA) and the thermal conductivity was further calculated with this value together with the density and the specific heat of the nanocomposite.

The theoretical models of Hamilton-Crosser and Maxwell-Garnett were analysed by Shin et al. [30,102] but they did not forecast any increase of the thermal conductivity. The authors suggested that the unexpected great experimental results are related to the percolation networks observed on the SEM images of the nanocomposites.

The scarcity of studies on the thermal conductivity of MSBNFs does not allow having a real image of their potential as thermal storage and heat transfer materials, or comparing their thermal behaviour with the low temperature nanofluids (based on water or oils).

In this investigation, the specific heat and the thermal conductivity of nanofluids based on SS with Alumina Nanoparticles (ANPs) and SS with Silica Nanoparticles (SiNPs) have been determined. The influence of the nanoparticle concentration has been analysed on each of these

nanofluids, as well as the impact of the temperature on this property.

5.3.2 Materials

To synthetize the SS, sodium and potassium nitrate of refined grade were acquired from the Chilean company SQM (purity of the $NaNO_3 \geq 99.6$ wt% and the $KNO_3 \geq 99.8$ wt%). The salts were first crushed in a mortar, dried in an oven at 100 ºC to remove the moisture and mixed in the required proportions.

Two kinds of ceramic NPs were used as addition to the SS. On one side, the source of ANPs was an industrial water-based nanofluid (Alumisol-10A, Kawaken Chemicals) containing fiber-shaped boehmite nanoparticles (L=50 nm, ϕ=10 nm) at 10 wt% according to the manufacturer. The boehmite (aluminium oxyhydroxide, AlOOH) is a precursor of the γ-Al_2O_3. On the other side, a dispersion of amorphous colloidal silica at 30 wt% (LUDOX® SM-30, Sigma-Aldrich) was used as the origin of spherical SiNPs (mean diameter 7 nm).

5.3.3 Synthesis of the nanofluids

Six nanofluids (Table 5-5) were prepared by dissolving the SS in water (50:50) and then adding the proper quantity of Alumisol-10A or LUDOX® SM-30 to the solution under stirring in order to achieve the desired NPs concentration (0.5, 1 or 1.5 wt%). The water was then removed by heating at 100 ºC in an oven. The dried material was melted at 396 ºC for 30 minutes and cooled down at room temperature. The solid material was milled and a representative sample was taken.

Table 5-5. Name and composition of the samples used in this study.

	SS, wt%	ANPs, wt%	SiNPs, wt%
SS	100.0	–	–
SS05A	99.5	0.5	–
SS1A	99.0	1.0	–
SS15A	98.5	1.5	–
SS05Si	99.5	–	0.5
SS1Si	99.0	–	1.0
SS15Si	98.5	–	1.5

5.3.4 Characterization

5.3.4.1 Specific heat

A Differential Scanning Calorimeter (DSC, Q1000 TA Instruments with autosampler) was used to perform the specific heat measurements with Modular Differential Scanning Calorimetry (MDSC) under an isothermal procedure. Around 30 mg of the sample were introduced in an aluminium crucible, which was hermetically sealed afterwards. The sample was first stabilized at the desired temperature by an isothermal period of 10 min to achieve the salt thermal equilibrium. The data collection was carried out during 20 min at the same temperature. Nitrogen was used as inert gas inside the device. The specific heat was measured at 196 °C (solid state), 296 °C and 396 °C (both in liquid state). These temperatures have been employed because they correspond to the working temperatures in real conditions. The measurement was carried out under modulation (Modulated DSC) with 0.6 °C of amplitude and a period of 110 s in order to provide good sensitivity. Three different portions of each sample were measured to obtain a representative result. This measurement method is proven to achieve a high precision [157,173].

5.3.4.2 Thermal conductivity

The thermal conductivity of the salts was determined by a LFA. This device works by sending a pulsed laser to the sample, leading to a temperature rise at its surface and to the propagation of the heat by conduction. The temperature distribution inside the sample depends on the thermal diffusivity of the material. This parameter has a direct relationship with the thermal conductivity as given by Eq. 5-3:

$$k = \alpha \cdot \rho \cdot c_p \qquad \text{Eq. 5-3}$$

where k is the thermal conductivity (W·m^{-1}·K^{-1}), α is the thermal diffusivity (m^2·s^{-1}), ρ is the density (kg·m^{-3}) and c_p is the specific heat (kJ·kg^{-1}·K^{-1}).

The specific heat was precisely determined by the method detailed before. The density values of the salts were obtained from the specialized literature [203] for the test temperatures (196 ºC, 296 ºC and 396 ºC). The tests were conducted under inert atmosphere (N$_2$, 100 mL·min^{-1}) using a laser voltage of 500 V and a pulse of 0.80 ms. A platinum holder (ϕ = 12.7 mm) was used to contain the molten salt. Figure 5-10, left shows this holder prior to the measurements. An external graphite coating (Figure 5-10, right) is necessary to increase both the absorption of the laser on the sample's front surface and the surface emissivity. The device employs a mathematical model considering a composite material structured on three layers (platinum + sample + platinum) to calculate the thermal diffusivity [160].
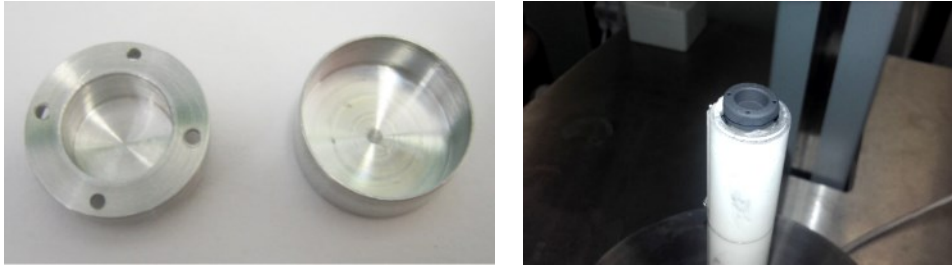
Figure 5-10. Platinum holder used to contain the salt, empty (left) and the coated holder before the analysis (right).

5.3.4.3 Nanoparticle size distribution

The size of the ANPs and SiNPs on the nanofluids was measured with the aim of establishing a relationship between the available nanoparticle surface and the thermal properties. The initial NPs dispersion (SiNPs, ANPs) and the produced nanofluids (SS05A, SS1A, SS15A, SS05Si, SS1Si and SS15Si) were characterized using the Dynamic Light Scattering method (DLS, ZetaSizer Nano ZS, Malvern Instruments, Ltd. Malvern, UK).

The measurement involves the dissolution of a few milligrams of the solid material into distilled water previously adjusted at the pH of stability of each of the nanoparticles (2 for the ANPs and 9 for the SiNPs), evaluated trough the Z potential. The sample was analysed just after being dissolved, to avoid the nanoparticle agglomeration in the meantime. The number of nanoparticles of each diameter was obtained as the result of this test.

The available surface of the nanoparticles to interact with the salt can be inferred from this data by using the following relation (Eq. 5-4):

$$S_a = \frac{6 \cdot \varphi_{NP}}{\rho_{NP}} \sum_{i=1}^{n} \frac{N_i}{D_i} \qquad \text{Eq. 5-4}$$

where S_a is the available surface of nanoparticles per gram of nanofluid ($m^2 \cdot g^{-1}$), φ_{NP} is the fraction of nanoparticles in the nanofluid, ρ_{NP} is the density of the nanoparticles, n is the number of size classes in the distribution, N_i is the number of nanoparticles of each size and D_i is the diameter of each nanoparticle.

It has not been possible to determine the nanoparticle size distribution of the nanofluids in the molten state due to the inexistence of devices which could take measurements at these high temperatures.

5.3.5 Results and discussion

5.3.5.1 Specific heat

5.3.5.1.1 Experimental determination

According to the Table 5-6, the specific heat of the pure SS is around 1.3 kJ·kg^{-1}·K^{-1} in solid (196 ºC) and 1.5 kJ·kg^{-1}·K^{-1} in the molten state (296 ºC and 396 ºC). These values are in agreement with the results published by other authors [86,180]. The specific heat of the SS is affected by the addition of ANPs or SiNPs (see Table 5-6 and Figure 5-11). The error bars in the Figure 5-11 are accounting the error propagation into the final results.

In the solid state (196 ºC), specific heat increments are seen with independency of the kind or amount of nanoparticles. The maximum enhancements obtained are around 6% for SS1A and SS15A and nearly 17% for the SS15Si nanocomposite. However, the results are different when the salt is in the liquid state (at 296 ºC and 396 ºC). On one side, the specific heat of SS-based nanofluids doped with ANPs is similar to that of the undoped SS. The scattering of the c_p results for these nanofluids is high due to their heterogeneity. On the other side, the addition of 0.5 wt% SiNPs to the SS (SS05Si) causes slight specific heat decrements in comparison to the molten SS (around 1.5%). If a higher amount of SiNPs is added, these decrements are reverted into improvements around 3% in SS1Si, and these values are three times higher (15%) in SS15Si.

As a summary, the ANPs seem to increase the specific heat of the SS only when the salt is solid while the results remain unchanged in the molten state. This may be related to a better heat conduction across the needles of alumina when they are in contact with the solid salt. The agglomeration and the sedimentation of the ANPs in the molten SS may hinder the enhancement of the specific heat in the liquid state (296 ºC and 396 ºC). The addition of the SiNPs to the SS is very effective on improving the specific heat of the undoped salt both in solid and liquid, particularly at the highest concentration of 1.5 wt%

Table 5-6. Specific heat (c_p) and Standard Deviation (SD) of the undoped SS and the nanofluids at the three tested temperatures. The samples SS (1) and SS (2) denote the initial mixture of SS used for the nanofluids with ANPs and SiNPs respectively.

	196 ºC		296 ºC		396 ºC	
	c_p, kJ·kg^{-1}·K^{-1}	SD, kJ·kg^{-1}·K^{-1}	c_p, kJ·kg^{-1}·K^{-1}	SD, kJ·kg^{-1}·K^{-1}	c_p, kJ·kg^{-1}·K^{-1}	SD, kJ·kg^{-1}·K^{-1}
SS (1)	1.236	0.024	1.420	0.024	1.436	0.023
SS05A	1.276	0.016	1.408	0.007	1.424	0.006
SS1A	1.312	0.005	1.427	0.009	1.439	0.027
SS15A	1.311	0.012	1.416	0.006	1.440	0.000
SS (2)	1.348	0.015	1.526	0.019	1.557	0.014
SS05Si	1.398	0.043	1.510	0.014	1.524	0.029
SS1Si	1.416	0.020	1.581	0.023	1.607	0.021
SS15Si	1.574	0.021	1.725	0.028	1.785	0.010
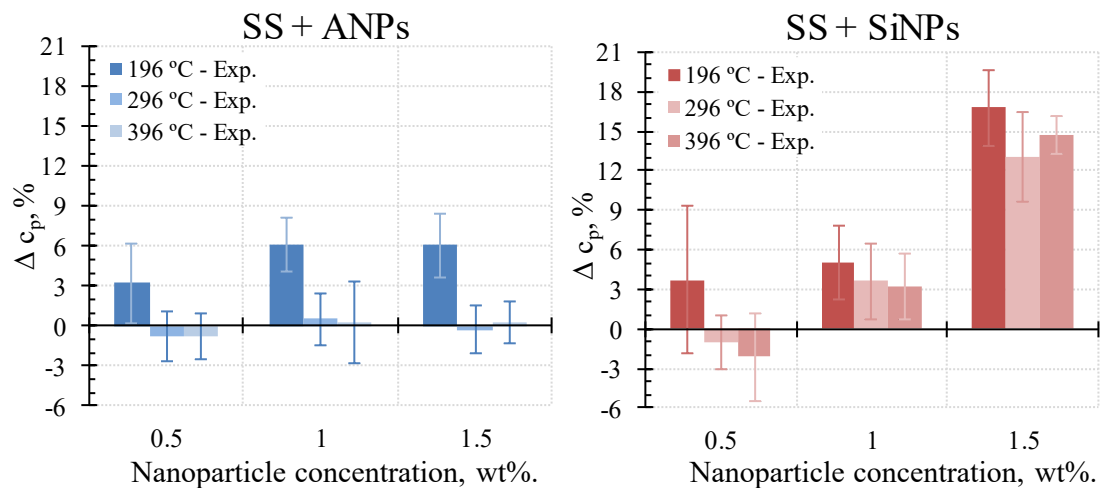
Figure 5-11. Experimental increment of the specific heat of the nanofluids with ANPs (left) and SiNPs (right). Evolution with the nanoparticle concentration and the temperature.

The influence of the nanoparticle concentration on the specific heat of these nanofluids has been studied by several authors in the recent literature (Figure 5-12). In the nanofluids with ANPs (Figure 5-12, left) Chieruzzi et al. [36] found the highest increments with 1 wt% of nanoparticles both at solid and liquid state. The results in the solid state are better, similarly to ours. Schuller et al. [32] also determined a similar increase with 1 wt% ANPs. The ANPs used in these studies were spherical particles while those employed in the present work are needles, which may easily settle down when dispersed into the molten salt. In addition, it is also possible that the ANPs employed in different articles correspond to different crystalline phases (information about this important feature is generally not reported). This could strongly influence the final results.

The results of the nanofluids with SiNPs reported by different authors are conflicting with each other as seen in Figure 5-12, right. Chieruzzi et al. [36] found the same trend as with the previous

nanofluids, similarly to Andreu-Cabedo et al. [113] but with noticeably higher increments when 1 wt% of SiNPs were used (25% increment) in the latter case. An opposite trend is described by Lasfargues [31], who reported improvements when 0.5 wt% and 1.5 wt% of SiNPs were added to the SS. A very interesting pattern was observed by Mondragón et al. [112] depending on the crystallinity of the SiNPs. The nanofluids containing amorphous SiNPs showed higher specific heat when higher contents of nanoparticles were employed, which is the same trend observed in our experiments (our SiNPs are amorphous).
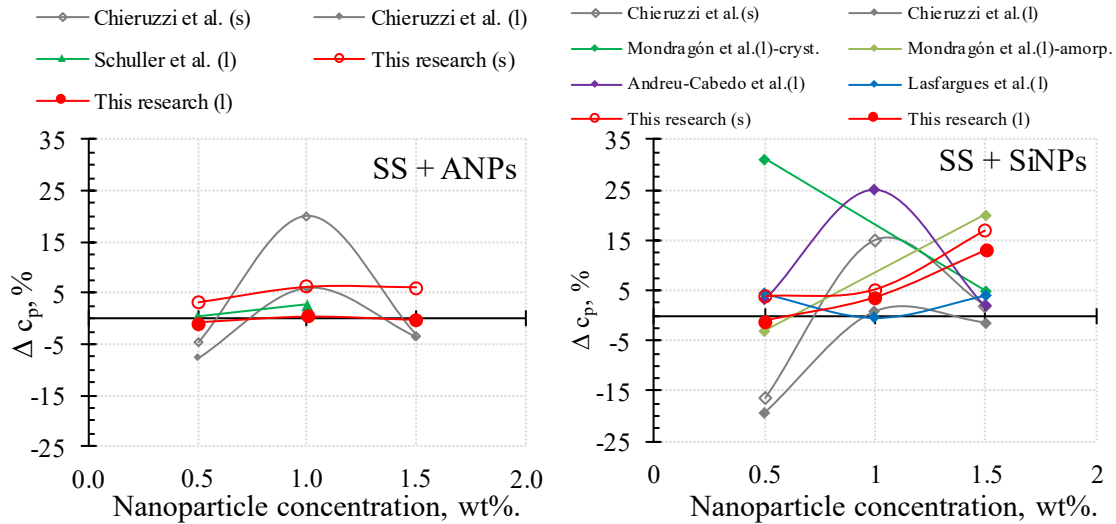
Figure 5-12. Influence of the nanoparticle amount on the specific heat increment of SS-based with ANPs (left) and SiNPs (right). Results from the literature and this work.

5.3.5.1.2 Analysis according to theoretical models

Several models to predict the specific heat of nanofluids have been developed. They are usually based on the assumption of a thermal equilibrium between the nanoparticles and the surrounding fluid. The mathematical model in Eq. 5-5 was proposed by Zhou et al. in 2008 [60] to match their experimental results of water-based nanofluids with ANPs. This expression takes into account the amount of the base fluid and the nanoparticles and the value of their specific heat.

$$c_{p,nf} = \frac{\phi \rho_{np} c_{p,np} + (1-\phi)\rho_{bf} c_{p,bf}}{\phi \rho_{np} + (1-\phi)\rho_{bf}} \qquad \text{Eq. 5-5}$$

where c_p is the specific heat (kJ·kg^{-1}·K^{-1}), ϕ is the volume fraction of nanoparticles and ρ is the density (kg·m^{-3}). Subscripts nf, np, and bf denote nanofluid, nanoparticle and base fluid, respectively.

The Eq. 5-5 is not suitable to predict the specific heat increment experimentally determined on MSBNFs, as described in several works [37,56,61–64]. Shin and Banerjee [63] proposed three theoretical models to explain why the equation was unable to predict the behaviour: the first model

considers a higher specific heat of the nanoparticles due to their reduced size, a second model takes into account the interfacial thermal resistance between the nanoparticles and the molten salt and the third model includes the formation of a molten salt nanolayer on the nanoparticle surface. The first model is able to predict the increase of the specific heat of a nanomaterial compared with that of the bulk material. The model forecasts an specific heat enhancement of 25% when ANPs are employed [71] and an increment of 10% when SiNPs are used [199].

These models have been employed to analyse our experimental results. The specific heat of the nanofluids produced in this work were calculated according to the Eq. 5-5 proposed by Zhou et al. [60] and the specific heat increment of the particles in the nanometric range proposed by Shin and Banerjee (first model) [63]. The results have been included on Figure 5-13. To do these calculation, the values employed for the density were extracted from the literature [200]. A density of 3,950 $kg \cdot m^{-3}$ was used for the ANPs and 2,650 $kg \cdot m^{-3}$ for the SiNPs. The density of the SS was determined as 1,974 $kg \cdot m^{-3}$, 1,906 $kg \cdot m^{-3}$ and 1,838 $kg \cdot m^{-3}$ at the temperatures of 196 ºC, 296 ºC and 396 ºC according to the expression proposed by Janz et al. [201]. The specific heat of the nanoparticles were experimentally determined at the temperatures of interest with the same method used with the salt and the nanofluids (Table 5-7).

Table 5-7. Specific heat (c_p) of the nanoparticles at the three tested temperatures and Standard Deviation (SD) of the meaasurements.

	196 ºC		296 ºC		396 ºC	
	c_p, $kJ \cdot kg^{-1} \cdot K^{-1}$	SD, $kJ \cdot kg^{-1} \cdot K^{-1}$	c_p, $kJ \cdot kg^{-1} \cdot K^{-1}$	SD, $kJ \cdot kg^{-1} \cdot K^{-1}$	c_p, $kJ \cdot kg^{-1} \cdot K^{-1}$	SD, $kJ \cdot kg^{-1} \cdot K^{-1}$
ANPs	1.195	0.039	1.237	0.009	1.471	0.031
SiNPs	0.970	0.112	0.943	0.243	1.157	0.143

As seen on Figure 5-13, the expression proposed by Zhou et al. [60] did not predict the experimentally determined increment of the specific heat of any of the nanofluids. This is because the specific heat of the nanoparticles is smaller than the specific heat of the SS and this model solely includes those values for the prediction. A small enhancement of the specific heat (0.5% – 1%) was forecasted by the first model of Shin and Banerjee [63] for the nanofluids with ANPs, very small in comparison to the experimentally encountered values.

Consequently, it is clear that these theoretical models are unable to predict the enhancements which were experimentally determined. Thus, another effects should be taken into account. In this sense, the third model proposed by Shin and Banerjee [63] considering a nanolayer around the nanoparticles with enhanced thermal properties could be playing an important role. Unfortunately, the features of this nanolayer cannot be made by experimental methods but modelling and simulation tools are needed.
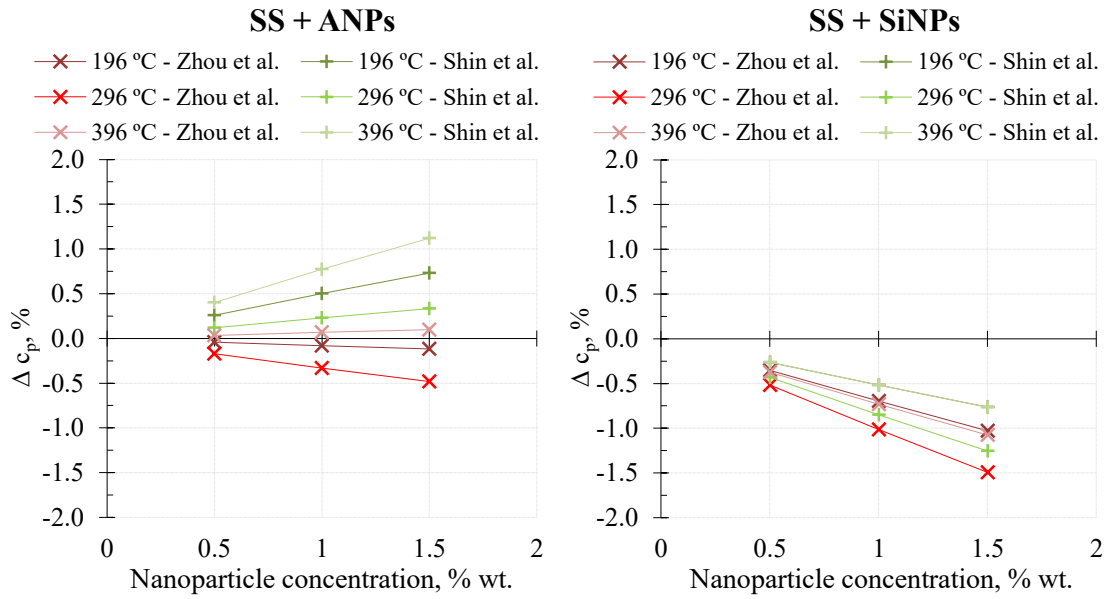
Figure 5-13. Theoretical increment of the specific heat of the nanofluids with ANPs (left) and SiNPs (right) according to Eq. 5-5. Evolution with the nanoparticle concentration and the temperature.

5.3.5.2 Thermal conductivity

5.3.5.2.1 Experimental determination

The thermal conductivity (k) of the nanofluids and the undoped SS was calculated with Eq. 5-3, considering the specific heat results and the thermal diffusivity (α) measured with the LFA device. As mentioned in the previous section, the density of the SS was calculated according to Janz et al. [201] for the three tested temperatures while the density of the nanoparticles were found in [200]. The density of the nanofluids were calculated considering the nanoparticle and the salt concentration on each case.

First, the analysis of the results of thermal diffusivity (Table 5-8) led to several observations. On one hand, the thermal diffusivity values of the initial SS are higher than those of the literature [180] (0.165 mm^2·s^{-1} at 296 ºC and 0.180 mm^2·s^{-1} at 396 ºC), The differences could be attributed to the different techniques used by other authors and the non-analytical grade of the SS. On the other hand, the highest increments of this property are found in the nanofluids containing 1% and 1.5 wt% of ANPs and 1% of SiNPs. On the other hand, moderate decrements were obtained for the nanofluid with 0.5 wt% of SiNPs. In the solid state the enhancements of the thermal diffusivity were softer and the reductions were higher than the results in the liquid state.

Table 5-8. Thermal diffusivity (α) and SD of the undoped SS and the nanofluids at the three tested temperatures and change with respect to the SS. The samples SS (1) and SS (2) denote the initial mixture of SS used for the nanofluids with ANPs and SiNPs respectively.

	196 ºC			296 ºC			396 ºC		
	α, $mm^2 \cdot s^{-1}$	SD, $mm^2 \cdot s^{-1}$	$\Delta\alpha$, %	α, $mm^2 \cdot s^{-1}$	SD, $mm^2 \cdot s^{-1}$	$\Delta\alpha$, %	α, $mm^2 \cdot s^{-1}$	SD, $mm^2 \cdot s^{-1}$	$\Delta\alpha$, %
SS (1)	0.2030	0.0092	---	0.2015	0.0093	---	0.2120	0.0240	---
SS05A	0.1585	0.0173	-21.92	0.2055	0.0279	1.98	0.2325	0.0485	9.67
SS1A	0.2170	0.0054	6.89	0.2405	0.0191	19.35	0.2430	0.0249	14.62
SS15A	0.2170	0.0096	6.89	0.2700	0.0266	33.99	0.2890	0.0236	36.32
SS (2)	0.2030	0.0092	---	0.2015	0.0093	---	0.2120	0.0101	---
SS05Si	0.1625	0.0040	-19.95	0.1615	0.0104	-19.85	0.1745	0.0229	-17.69
SS1Si	0.2095	0.0240	3.20	0.2530	0.0059	25.56	0.2860	0.0050	34.91
SS15Si	0.1925	0.0062	-5.17	0.2055	0.0028	1.98	0.2185	0.0028	3.07

The thermal conductivity results of the SS lie between 0.47 $W \cdot m^{-1} \cdot K^{-1}$ and 0.60 $W \cdot m^{-1} \cdot K^{-1}$ depending on the temperature, which are in the range of the data published in the literature [86,174]. The changes of the thermal conductivity of the nanofluids in comparison to the base salt depend on the test temperature and the nanoparticle concentration (see Table 5-9 and Figure 5-14).

In the solid state (196 ºC), the nanomaterials SS05A and SS05Si have a lower thermal conductivity than the SS (-15%). Increments of the thermal conductivity are found for the nanocomposites SS1A, SS15A, SS1Si and SS15Si (the increment is higher than 12%).

In the liquid state, there are noticeable increments of the thermal conductivity, with the exception of the nanofluid SS05Si (≈-18%). The maximum increment is found for the nanofluid SS15A (60%). When the SiNPs are present, the highest increase is 45% for the SS1Si.

These thermal conductivity results are following a very similar trend than those of the thermal diffusivity, which implies that they are mainly influenced by them rather than those of the specific heat.

Table 5-9. Thermal conductivity (k) and SD of the undoped SS and the nanofluids at the three tested temperatures and change with respect to the SS. The samples SS (1) and SS (2) denote the initial mixture of SS used for the nanofluids with ANPs and SiNPs respectively.

	196 ºC		296 ºC		396 ºC	
	k, W·m⁻¹·K⁻¹	SD, W·m⁻¹·K⁻¹	k, W·m⁻¹·K⁻¹	SD, W·m⁻¹·K⁻¹	k, W·m⁻¹·K⁻¹	SD, W·m⁻¹·K⁻¹
SS (1)	0.4775	0.0332	0.5348	0.0333	0.5348	0.0333
SS05A	0.4056	0.0333	0.5709	0.0349	0.6429	0.0545
SS1A	0.6001	0.0104	0.7128	0.0281	0.7159	0.0519
SS15A	0.6287	0.0216	0.8339	0.0326	0.8960	0.0236
SS (2)	0.4775	0.0332	0.5747	0.0283	0.6060	0.0241
SS05Si	0.4408	0.0470	0.4653	0.0244	0.4991	0.0519
SS1Si	0.5867	0.0440	0.7788	0.0289	0.8812	0.0260
SS15Si	0.6106	0.0272	0.7041	0.0308	0.7637	0.0128
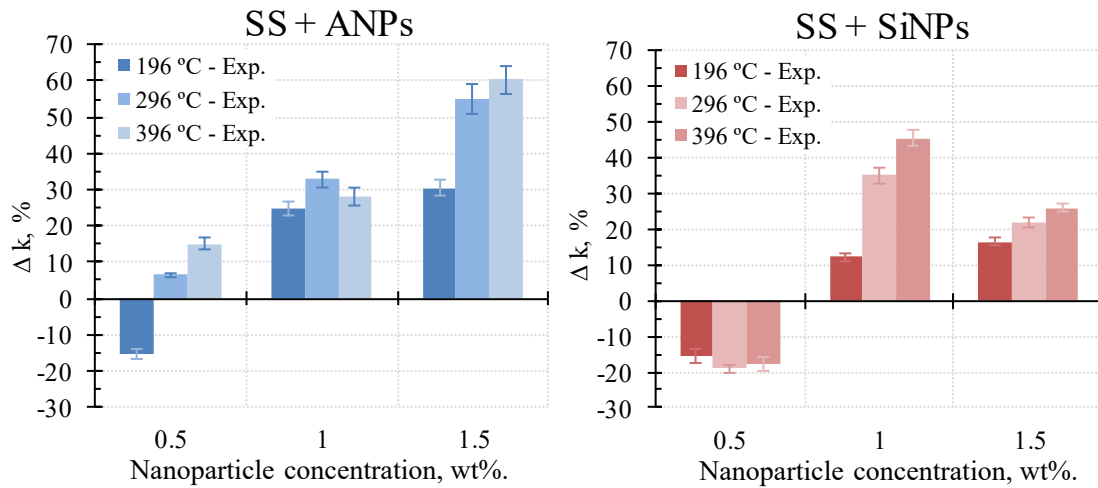
Figure 5-14. Changes on the experimental thermal conductivity of the nanofluids according to the nanoparticle concentration and the test temperature.

5.3.5.2.2 Analysis according to theoretical models

The determined thermal conductivity values were compared with the conventional theoretical model of Hamilton-Crosser [204]. This model considers Brownian motion and states a dependence of the effective thermal conductivity of solid-liquid mixtures on the nanoparticle shape,

$$k_t = k_b \left[\frac{k_{np} + (n-1)k_b - (n-1) \cdot \phi(k_b - k_{np})}{k_{np} + (n-1)k_b + \phi(k_b - k_{np})} \right]$$

Eq. 5-6

where k, n, and ϕ are thermal conductivity, empirical shape factor, and volume fraction of the

nanoparticles, respectively. Subscripts t, b, and np denote total value for the nanocomposite, the base fluid and the nanoparticle, respectively. The empirical shape factor (n) is related to the sphericity (ψ), which is the ratio of the surface area of a sphere (with the same volume as the given particle) to the surface area of the particle: $n = 3/\psi$. In this work, the ANPs are fibres with 10 nm of diameter and 50 nm length ($\psi = 0.70$; $n = 4.28$) and the SiNPs are spherical ($\psi = 1$; $n = 3$). The thermal conductivity values employed for the nanoparticles were extracted from the literature, 40 W·m^{-1}·K^{-1} [45] and 1.4 W·m^{-1}·K^{-1} [107] for the ANPs and the SiNPs respectively.

The enhancements of the thermal conductivity calculated with the Eq. 5-6 are depicted in Figure 5-15. The increments are proportional to the nanoparticle concentration and the temperature. The nanofluids with SiNPs have a higher enhancement than those with ANPs, due to the smaller difference between the thermal conductivity of the SiNPs and that of the SS.

Although these theoretical estimations predict an increase of the thermal conductivity whatever the temperature or the nanoparticle amount, the experimental determination of the thermal conductivity gave higher values than those predicted. Thus, other effects in addition to the Brownian motion of the nanoparticles should be considered to explain the empirical results. In this sense, the review of nanofluids from Goharshadi et al. [45] gathers several potential mechanisms that have been proposed so far to explain the enhancement of the thermal conductivity. Among them, the existence of an ordered layer of salt ions at the nanoparticle surface and the nanoparticle clustering creating a percolation network are considered to be the most influencing factors on this phenomenon.
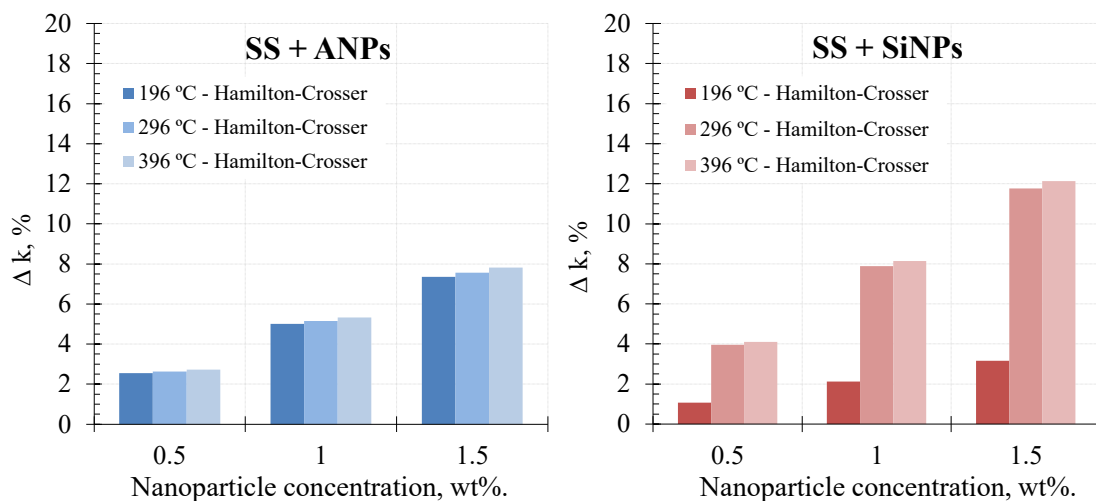
Figure 5-15. Theoretical predictions with the Hamilton-Crosser model of the thermal conductivity of the nanofluids.

5.3.5.3 Available surface and thermal properties

Figure 5-16 shows the size of the ANPs and the SiNPs both in the initial dispersions and in the prepared nanofluids. The Table 5-10 includes the available surface of the nanofluids calculated from these distributions, accounting the sizes and their frequency (Eq. 5-4).

The size range of the initial nanoparticles is mostly under 100 nm, which indicates that these initial suspensions contain individual nanoparticles which are not agglomerated. However, after the synthesis of the nanofluid these nanoparticles form clusters and increase their size. The degree of agglomeration depends on the nanoparticle percentage in the nanofluid. The cluster sizes are higher in the nanofluids containing SiNPs (around 400 nm is the most frequent size) while those with ANPs registered smaller size (notice for example the distribution of the SS15A nanofluid on the Figure 5-16). Regarding the available surface of the nanoparticles to interact with the ions of the molten salt, the results ($0.030 - 0.080$ m$^2 \cdot$g^{-1}) are very similar to those obtained by Andreu-Cabedo et al. [113], who studied the relationship between the specific heat and the available nanoparticle surface of SS-based nanofluids with SiNPs ($0.025 - 0.080$ m$^2 \cdot$g^{-1}).
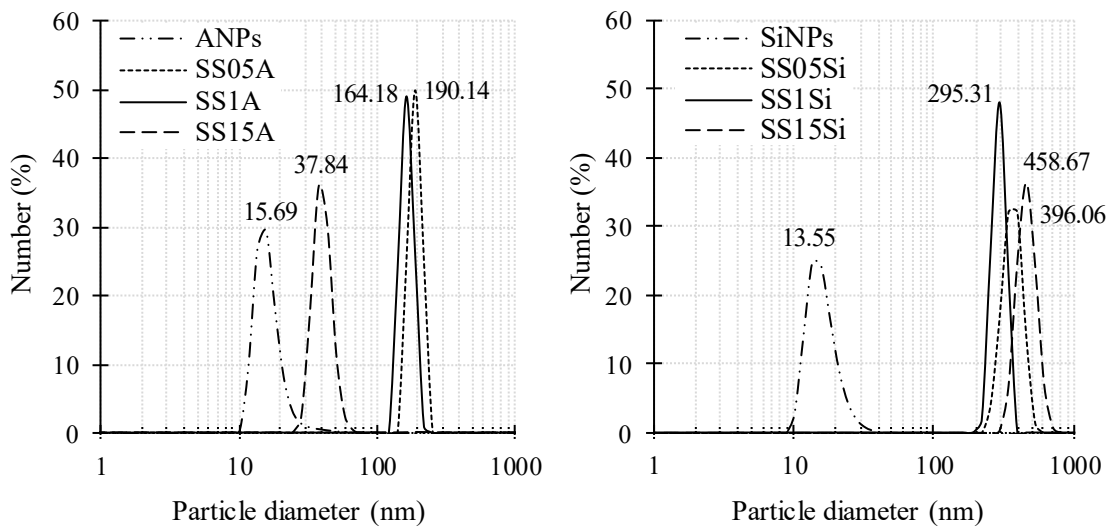
Figure 5-16. Nanoparticle size distribution of the initial nanoparticles and the nanofluids, including the mode of the distribution.

Table 5-10. Available surface (m^2 of nanoparticle surface/g of material) of the nanofluids with ANPs and SiNPs.

	SS05A	SS1A	SS15A	SS05Si	SS1Si	SS15Si
Available surface, m$^2 \cdot$g^{-1}	0.0402	0.0926	0.5743	0.0323	0.0795	0.0763

Andreu-Cabedo [113] et al. and Ho and Pan [66] found a direct dependence between this available surface and the enhancement of the specific heat of the nanofluid. Figure 5-17 shows this relationship according to our experimental data both for the specific heat and the thermal conductivity at 396 ºC.

The nanofluids containing ANPs do not experience any increment of specific heat (Figure 5-17, left) in comparison to the base material and, as a result, they are independent on the nanoparticle available surface. However, they experience a relevant increment of the thermal conductivity (Figure 5-17, right) which fits into a potential relationship with the available surface. The highest enhancement (60%) is for the nanofluid containing 1.5 wt% of ANPs.

Regarding the nanofluids with SiNPs, a parabolic trend between the specific heat and the available nanoparticle surface (Figure 5-17, left) can be plotted. The maximum enhancement (14.64%) is obtained by the nanofluid with 1.5 wt% of SiNPs (0.0763 m$^2 \cdot$g^{-1}), which has a similar available surface than that with 1 wt% of SiNPs (0.0795 m$^2 \cdot$g^{-1}). This could be due to differences on the nanoparticle size between the sample measured in the DLS and that one of the specific heat tests. Moreover, the increment of the thermal conductivity (Figure 5-17, right) follows the same trend as the specific heat versus the available surface. The biggest increment (45%) is for the nanofluid with 1 wt% of SiNPs in this case.
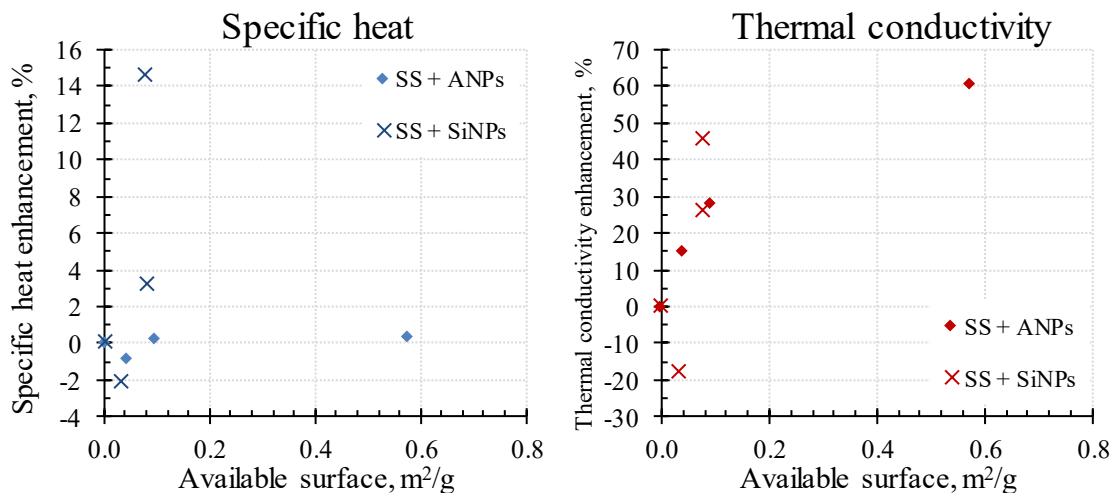
Figure 5-17. Left: Specific heat enhancement at 396 ºC versus the available surface of the nanofluids with ANPs (diamond symbols) and SiNPs (cross symbols). Right: Thermal conductivity enhancement at 396 ºC versus the available surface of the nanofluids with ANPs (diamond symbols) and SiNPs (cross symbols).

As a summary, the increment of the thermal properties of the SS-ANPs nanofluids did not follow any clear pattern, while a direct correlation (parabolic) was found for those with SiNPs. It is important to remark that these results are conditioned by the possible overestimation of the size in ANPs due to their non-spherical shape (the DLS device is measuring the hydrodynamic diameter). This could explain the absence of a clear correlation between the specific heat and the available surface. The nanoparticle sizes in the nanofluids with SiNPs may be the most similar to the real ones. In this case, a minimum surface of nanoparticles is needed to achieve enhancements of the thermal properties. There is also a maximum surface which generates different increments of the specific heat and the thermal conductivity. Thus, it should be more unknown factors apart from surface interactions which are influencing the value of these properties.

5.3.6 Conclusions

This study is pioneering on analysing the thermal conductivity of the MSBNFs in the liquid state. More in detail, the specific heat and the thermal conductivity of six nanofluids of Solar Salt with different contents of alumina and silica nanoparticles were measured. Enhancements higher than 20% were found for the specific heat and the thermal conductivity of the nanofluids with 1 wt% and 1.5 wt% containing both types of nanoparticles, respectively. The most promising nanofluids were that with 1.5 wt% of silica nanoparticles (14% of specific heat increment) and 1.5 wt% of alumina nanoparticles (60% of thermal conductivity increment).

The theoretical models to calculate the improvement of these thermal properties are unable to predict the obtained experimental results. Complex models requiring high computing power are needed to go deeper into the reasons of these spectacular enhancements. Finally, the available nanoparticle surface, which interacts with the ions of the molten salt, was estimated from the measurement with the DLS technique. A direct correlation (parabolic) was found between this parameter and the high specific heat and thermal conductivity of the nanofluids with silica nanoparticles, which confirms a main thermal transfer role to the nanoparticle size.

The obtained increase of both, the specific heat and the thermal conductivity, in the studied nanofluids is a significant step towards the achievement of real savings in the TES systems of the CSP plants. More experimental and modelling research is needed in this particular field to corroborate the results published up to date and to optimize the system.

Chapter 6

THERMAL PROPERTIES OF SODIUM

NITRATE-BASED NEPCMS

6 THERMAL PROPERTIES OF SODIUM NITRATE-BASED NANO-ENHANCED PHASE CHANGE MATERIALS (NEPCMS)

6.1 INTRODUCTION

The present Chapter deals with the determination of the thermal properties of NePCMs based on Sodium Nitrate: the specific heat, the latent heat, the phase change temperature and the thermal conductivity. Following is the Journal contribution 6, which gathers an interesting comparison between experimental and simulation results on this subject.

6.2 JOURNAL CONTRIBUTION 6. EXPERIMENTAL AND SIMULATION STUDY OF THE THERMAL PROPERTIES OF SODIUM NITRATE-BASED NANO-ENHANCED PHASE CHANGE MATERIALS (NEPCMS)

Authors: Belén Muñoz-Sánchez, Javier Nieto-Maestre and Ana García-Romero
Abstract: Sodium Nitrate-based Nano-Enhanced Phase Change Materials (NePCMs) are a new kind of PCM of high temperature developed in this investigation for the first time. As other salts containing nanoparticles, these NePCMs have a potential to improve the thermal properties of the Sodium Nitrate. With this aim, the influence of the nanoparticle type (silica or alumina), its concentration (0.5, 1 or 1.5 wt%), as well as the purity of the Sodium Nitrate (analytical, refined or industrial grade) was analyzed. The specific heat of the NePCMs showed a strong dependence on the salt purity, with little decrements ($\approx$-3%) in those based on the analytical grade and increments in those containing the refined or industrial grade ($\approx$3%). The latent heat of fusion and crystallization decreased with the addition of nanoparticles to the Sodium Nitrate of analytical grade, while remain unchanged in the NePCMs containing the salt of refined or industrial grade. The phase change temperatures (both fusion or solidification) of the Sodium Nitrate were not affected by the presence of the nanoparticles. The onset temperature of fusion followed the same trend of the latent heat. The thermal conductivity of the Sodium Nitrate of analytical grade was sensibly increased by the addition of 1 wt% of alumina nanoparticles, both in the solid (97%) and the liquid state (124%). The modelling of Sodium Nitrate with 0.5, 1 or 1.5 wt% of alumina nanoparticles in FLUENT predicted the improve of the thermal conductivity and dynamic viscosity and the reduction of the latent heat and specific heat with increasing the amount of nanoparticles. Consequently, the addition of nanoparticles should have a negative effect in the total energy storage capacity of the material, though the duration of the charging and discharging cycles could be reduced. The disagreement found between the experimental and simulation results of specific heat, latent heat and thermal conductivity suggests that some mechanism such as the nanoparticle agglomeration or sedimentation may influence the empirical measurements.

6.2.1 Introduction

Nitrate salts are commonly used in Concentrated Solar Power (CSP) plants either as a sensible Thermal Energy Storage Material (TESM) or as a Heat Transfer Fluid (HTF) [24]. In recent years, a great research effort has been dedicated to the development of new TES systems using Phase Change Materials (PCM) of high temperature [33,205,206]. Sodium Nitrate ($NaNO_3$) is considered as a suitable PCM for Direct Steam Generation (DSG) applications in CSP due to the good match between its melting temperature (306 ºC) and the phase change temperature of the saturated steam from the solar field (310 ºC at a pressure of 100 bar) [33,34]. In this sense, an extense study of its thermophysical properties as PCM were reviewed by Bauer [33] and experimental TES systems have been developed with this salt [207].

The Sodium Nitrate has several advantages over other TESMs including thermal oils, alloys or liquid metals [208] in terms of costs, thermal stability, availability and eco-friendliness. However, its low conductivity ($0.57 \ W \cdot m^{-1} \cdot K^{-1}$ at 307 ºC [209]) is a serious drawback in order to use this material as PCM, especially during discharge cycles where the heat transfer through the solid layer is only by conduction. To overcome this problem, D. Laing et al. [207,210] proposed the use of aluminium fins to improve the heat transfer, and Wu and Zhao [211] proposed metallic foams and expanded graphite to increase the thermal conductivity of Sodium Nitrate. These solutions require complicated TES devices to achieve an adequate heat transfer rate. In this context, other attempts have used the nanotechnology to improve the thermal performance of inorganic salts, as explained below.

The new materials are known as Nano-enhanced PCMs (NePCMs) and are created by adding nanoparticles to an inorganic salt. The inclusion of the nanoparticles is presumed to enhance the thermal properties (specific heat and thermal conductivity) of the base salt, as demonstrated by several researches [36,37,64,74,112,113]. Despite the importance of these properties on the heat and transfer processes, there are others implied on the phase change (latent heat, onset and melting temperature) which have been much less studied [31,32,35–40]. In general, the accomplished results of the thermal properties showed to be inconsistent between different research groups analysing the same NePCM, impeding their comparison. The novelty of this field make difficult the standardization of the synthesis procedures, source materials and analytical procedures, which are the main factors influencing the results.

The experimental investigation of these materials is still limited due to the high melting temperatures and the corrosive nature of the salts and the physical limitations (working temperatures, compatibility) of the analytical devices. In this sense, the validation of models through the use of simulation software is an important tool to advance into the knowledge of these complex mixtures. Unfortunately, the scientific literature of this subject is still very scarce

[30,63,65,74–78].

None of the previous investigations addresses the study of NePCMs with the Sodium Nitrate as the base salt, though it is considered a plausible PCM in the CSP plants. This research aims to cover this gap by developing and characterizing several NePCMs. The influence of the nanoparticle concentration (0.5%, 1% or 1.5% by weight), the shape and nature of the nanoparticles (alumina or silica) and the purity of the Sodium Nitrate (analytical, refined or industrial grade) were studied. The latter factor is justified by the economical unfeasibility of using Sodium Nitrate of analytical grade into the CSP facilities (required amount of 14 tons [207]).

On one hand, a complete thermophysical characterization of the NePCMs was performed. The specific heat (solid and liquid), the latent heat of fusion and crystallization, the phase change and the onset temperatures, the thermal conductivity and the thermal cycling resistance were determined. On the other hand, the nanoparticle size distribution was measured by DLS and the microstructure analysed by SEM. The influence of the nanoparticle size on the final thermophysical properties was discussed.

Finally, the thermophysical behaviour of these NePCMs was predicted by means of the FLUENT Software, and compared with the experimental results. The divergences were explained by agglomeration/sedimentation processes not considered in the initial model.

6.2.2 Experimental study

6.2.2.1 Materials

The raw Sodium Nitrate was used in different purities: the analytical grade, ASN (Labkem, $NaNO_3 \geq 99.5$ wt%); the refined grade, RSN (SQM, $NaNO_3 \geq 99.5$ wt%) and the industrial grade, ISN (SQM, $NaNO_3 \geq 98.0$ wt%).

Two types of ceramic nanoparticles were selected, Alumina Nanoparticles (ANPs) Figure 6-1, left and Silica Nanoparticles (SiNPs) Figure 6-1, right. ANPs were purchased from Kawaken Chemicals as an industrial water-based nanofluid, Alumisol-10A, containing fiber-shaped boehmite nanoparticles (L=50 nm, ϕ=10 nm) at 10 wt% according to the manufacturer. The boehmite (aluminium oxyhydroxide, AlOOH) is a precursor of the γ-Al_2O_3. On the other side, a dispersion of colloidal silica at 30 wt%, LUDOX® SM-30, from Sigma-Aldrich was used as a source of spherical SiNPs.
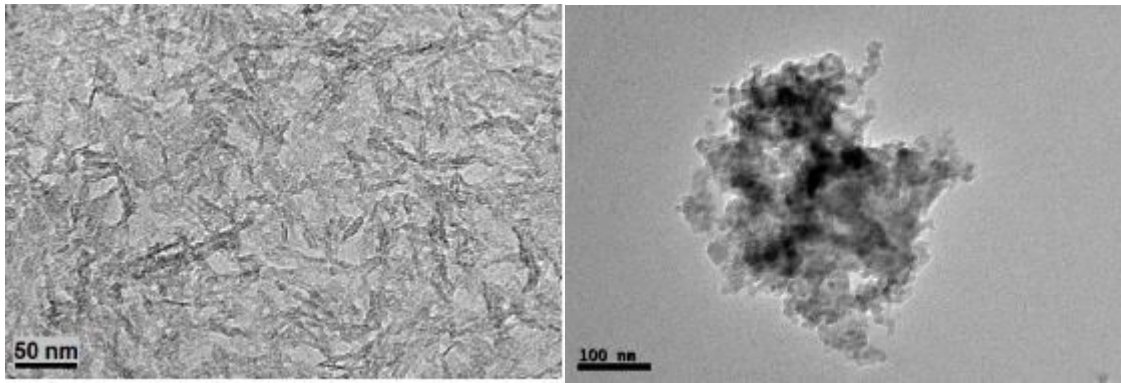
Figure 6-1. TEM images of the ANPs (left) and the SiNPs (right).

6.2.2.2 Synthesis of the NePCMs

Several NePCMs were synthetized with contents of 0.5, 1 or 1.5 wt% of nanoparticles and the three Sodium Nitrates (Table 6-1) to study the influence of these variables on the thermal properties. The NePCMs were prepared according to the well-known hot plate method developed for this kind of materials [56]. First, the Sodium Nitrate of desired purity was dissolved in distilled water (50:50 %wt) and then the proper quantity of Alumisol-10A or LUDOX® SM-30 was added respectively drop by drop under mild stirring. This solution was poured carefully into a hot plate (ϕ = 15 cm) and the water was then removed by heating at 100 ºC in an oven for at least 2 hours. The dried material was scrapped off from the hot plate, melted at 396 ºC for 30 minutes and cooled down at room temperature. The solid material was milled and a representative sample was taken to be further characterized.

Table 6-1. Name and composition of the NePCMs used in this study.

	ASN, wt%	RSN, wt%	ISN, wt%	ANPs, wt%	SiNPs, wt%
ASN	100.0	–	–	–	–
ASN05A	99.5	–	–	0.5	–
ASN1A	99.0	–	–	1.0	–
ASN15A	98.5	–	–	1.5	–
ASN05Si	99.5	–	–	–	0.5
ASN1Si	99.0	–	–	–	1.0
ASN15Si	98.5	–	–	–	1.5
RSN	–	100.0	–	–	–
RSN05A	–	99.5	–	0.5	–
RSN1A	–	99.0	–	1.0	–
RSN15A	–	98.5	–	1.5	–
RSN05Si	–	99.5	–	–	0.5
RSN1Si	–	99.0	–	–	1.0
RSN15Si	–	98.5	–	–	1.5
ISN	–	–	100.0	–	–
ISN05A	–	–	99.5	0.5	–
ISN1A	–	–	99.0	1.0	–
ISN15A	–	–	98.5	1.5	–
ISN05Si	–	–	99.5	–	0.5
ISN1Si	–	–	99.0	–	1.0
ISN15Si	–	–	98.5	–	1.5

6.2.2.3 Methods

6.2.2.3.1 Nanoparticle size distribution

The size of the nanoparticles (ANPs and SiNPs) was measured on each nanofluid with the aim of establishing a relationship between these sizes and the specific heat. The NePCMs were characterized using the Dynamic Light Scattering method (DLS, ZetaSizer Nano ZS, Malvern Instruments, Ltd. Malvern, UK). The nanoparticle size distribution of these NePCMs were thus obtained as the number of nanoparticles at each size between 0.4 and 10,000 nm. It is important to mention that the nanoparticle size measured by the DLS device is the hydrodynamic diameter. This magnitude is considering the diameter of a sphere with the same movement as the particle being measured. In this sense, due to the fibrilar structure of the ANPs the real distributions could be different.

The available surface of the nanoparticles to interact with the molten salt can be inferred from the distribution by using the following relation (Eq. 6-1):

$$S_a = \frac{6 \cdot \varphi_{NP}}{\rho_{NP}} \sum_{i=1}^{n} \frac{N_i}{D_i}$$

Eq. 6-1

where S_a is the available surface of nanoparticles per gram of nanofluid ($m^2 \cdot g^{-1}$), φ_{NP} is the fraction of nanoparticles in the nanofluid, ρ_{NP} is the density of the nanoparticles, n is the number of size classes in the distribution, N_i is the number of nanoparticles of each size and D_i is the diameter of each nanoparticle.

6.2.2.3.2 Thermogravimetric analysis

The following procedure was employed to determine the thermal stability of the raw Sodium Nitrate and the NePCMs. About 20 mg of the dried sample was introduced in a platinum crucible specifically supplied for the TGA measurements. The crucible is placed in the TGA device (SETARAM SETSYS Evolution –1750, Setaram Instrumentation, France) and subjected to the following heating program. First, a heating-ramp from 20 ºC to 90 ºC at 5 ºC/min to remove humidity. This ramp is followed by a second heating-ramp from 90 ºC to 400 ºC at 2 ºC/min. Then, the sample is hold at the highest temperature for 3 hours and cooled again until 90 ºC (2 ºC/min). Finally, two additional heating and cooling cycles between 90 ºC to 400 ºC were applied in order to know if the weight losses were reversible or not.

The analyses were always carried out under air atmosphere instead of an inert one, to account the worst scenario. The weight loss of the sample was precisely registered along the time with the thermobalance.

6.2.2.3.3 Specific heat

The apparatus employed in this work to determine the specific heat of the Sodium Nitrate and the NePCMs was a Differential Scanning Calorimeter Q100 (TA Instruments) with autosampler. It was used to perform the specific heat measurements with MDSC under an isothermal procedure. First, the solid material was dried at 100 ºC at least for 2 hours in an oven to remove the ambient humidity. Then, around 30 mg of the sample were introduced in a T-zero aluminium crucible which was heated on a hot plate before being hermetically sealed afterwards. The crucible filling and sealing was developed inside a glove box filled with argon. Once inside the DSC, the sample was first stabilized at 326 ºC (liquid state) for an isothermal period of 10 min to achieve the salt thermal equilibrium. The data collection was carried out for 20 min at this temperature. Nitrogen was used as inert gas inside the device. The specific heat was then measured at 308 ºC (solid state). The temperature modulation of the DSC technique was set-up to 0.6 °C of amplitude and a period of 110 s in order to provide good sensitivity. Three crucibles with different portions of each sample were measured to obtain a representative result. This measurement method proved to achieve a high precision, as demonstrated in [157,158].

6.2.2.3.4   Latent heat and phase change temperature

The phase change properties (latent heat and melting temperature) of the Sodium Nitrate and the NePCMs were measured with the DSC just after measuring the specific heat, in the same crucibles. The sample was first melted by increasing the temperature up to 350 ºC, followed by two heating and cooling cycles between 350 ºC and 200 ºC at a heating/cooling rate of 10 ºC/min. The results of the latent heat and melting temperature were obtained from the second thermal cycle.

6.2.2.3.5   Thermal conductivity

The thermal conductivity of the base salts and the nanofluids were indirectly calculated by means of the thermal diffusivity, which was measured in the Laser Flash Analyzer (LFA) technique. This device works by shining a pulsed laser on the sample surface, leading to a an increase of its temperature and the propagation of the heat by conduction. The temperature distribution inside the sample depends only on the thermal diffusivity of the material if other conditions remain invariable. Further comprehensive information on this technique can be found elsewhere [160].

The relationship between the thermal conductivity (k) and the thermal diffusivity (α) can be calculated from the Eq. 6-2:

$$k = \alpha \, \rho \, c_p \qquad\qquad \text{Eq. 6-2}$$

where k is the thermal conductivity ($W \cdot m^{-1} \cdot K^{-1}$), α is the thermal diffusivity ($m^2 \cdot s^{-1}$), ρ is the density ($kg \cdot m^{-3}$) and c_p is the specific heat ($kJ \cdot kg^{-1} \cdot K^{-1}$).

The specific heat of this Eq. 6-2 was calculated with the DSC, as detailed in the precedent section. The density was calculated for each temperature and salt according to the values reported in the literature [161].

A laser flash device model LFA427 from Netzsch, with a temperature range from -150 ºC to 2000 ºC was used to measure the thermal diffusivity (α). The tests were conducted under a nitrogen atmosphere with a flow rate of 100 mL/min, a laser voltage of 500 V and a pulse period of 0.80 ms. A platinum holder (ϕ = 12.7 mm, Figure 6-2, left) suitable to contain the molten salt was used in this work. Figure 6-2, left shows the empty holder prior to the measurements. An external graphite coating (Figure 6-2, right) is necessary to increase both the absorption of the laser on the sample's front surface and the surface emissivity. A mathematical model considering a composite material structured on three layers (platinum + sample + platinum) is used by the device to calculate the thermal diffusivity [160]. The platinum holder was filled with a sample of approximately 92 mg. Two portions of each salt or nanofluid were analysed in the LFA. Each of these portions were analysed at 256 ºC (solid) and 326 ºC (liquid) twice. Then, all these data were

used to calculate the mean thermal diffusivity and its Standard Deviation (SD), as well as the thermal conductivity results.
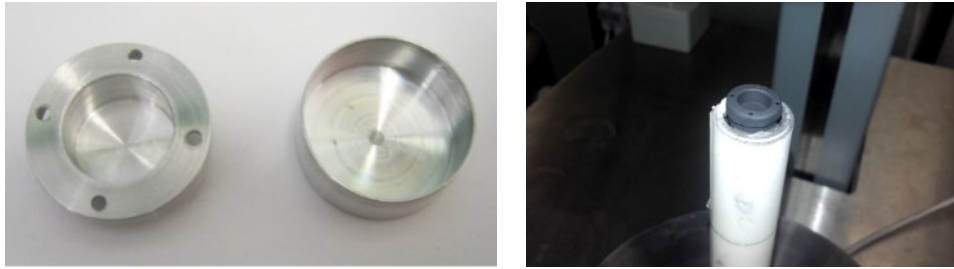
Figure 6-2. Platinum holder (pan and lid) used to contain the salt, empty (left) and coated before the analysis (right).

6.2.2.3.6   Microstructure

The physical distribution of the nanoparticles in the matrix of Sodium Nitrate was evaluated in the solid samples by using a Field Emission Scanning Electron Microscope (FESEM LEO 440i, Leica-Zeiss). The specimen preparation involves placing the solid sample on a microscopy slide covered with a graphite layer prior to their characterization. Secondary Electrons (SE) images were useful on giving quantitative information of the nanoparticle and agglomerates sizes. The Energy-dispersive X-ray spectroscopy (EDX) was used to know the atomic composition in certain areas of the pictures.

6.2.3   Simulation study

A numerical study about variations of thermo-physical properties of Sodium Nitrate doped with ANPs was performed. In particular, we focus on numerical investigation of the melting and solidification of Sodium Nitrate-based NePCMs with three different concentrations of ANPs (0.5, 1 or 1.5 wt%) which are heated or cooled from one side of a square enclosure of dimensions of 1 cm × 1 cm. The integrated simulation system ANSYS Workbench 15.0 for the numerical study was used including mesh generation tool ICEM and FLUENT software. In FLUENT, the melting and solidification model with Volume of Fluid (VOF) that includes the physical model to disperse the ANPs in the Sodium Nitrate and their interactions is applied. During melting and solidification processes, the enhancement of the heat transfer is considered. With this aim, the thermophysical properties of both starting materials (Sodium Nitrate and ANPs) were required as inputs. The values (Table 6-2) were obtained both from existing literature and our experimental results.

Table 6-2. Thermophysical properties of Sodium Nitrate from existing literature or experimentally measured.

Property	Sodium Nitrate	Ref	ANPs	Ref
Density (kg·m^{-3})	2320 – 0.715·T(K)	[203]	3980	[212]
Specific heat (kJ·kg^{-1}K^{-1})	2.431 (256 ºC)*		1.195 (196 ºC)*	
	1.776 (326 ºC)*		1.237 (296 ºC)*	
			1.471 (396 ºC)*	
Conductivity (W·m^{-1}·K^{-1})	0.570 (250 ºC, solid)	[213]	26.4 (127 ºC)	[214]
	0.514 (306 ºC, liquid)	[215]	20.2 (227 ºC)	
			15.8 (327 ºC)	
			12.6 (427 ºC)	
Viscosity (mPa·s, cp)	$0.1041 \cdot e^{(1.63 \cdot 10\text{-}4/(8.314 \cdot T))}$	[203]		
Latent heat of fusion (kJ·kg^{-1})	180*			
Melting temperature (ºC)	308	[33]		

* Experimental measurements (The data for Sodium Nitrate are those of the ASS).

The square enclosure contains Sodium Nitrate or Sodium Nitrate with different concentrations (0.5, 1 or 1.5 wt%) of ANPs. For the charging process, the Sodium Nitrate (or the NePCM) is at an initial temperature of 298 ºC, two wall sides are at a constant temperature of 318 ºC and the other two walls are adiabatic. For the discharging process, the Sodium Nitrate (or the NePCM) is at an initial temperature of 318 ºC, two wall sides are at a constant temperature of 298 ºC and the other two walls are adiabatic.

Assumptions made:

- The flow is Newtonian, incompressible and laminar.
- The viscous dissipations are negligible.
- The physical properties of PCM are temperature-dependent.
- Heat transfer is both conduction and convection controlled.
- The volume variation resulting from the phase change is neglected.
- 2D model is used, neglecting 3D convection. With this hypothesis, the results may be considered almost real because the 3D convection duration is very short compared with the whole melting process.

Storage System: Fluid flow, heat transfer and phase change of the Sodium Nitrate and the NePCMs are regarded in the storage system [216,217]. The governing conservation equations [218] are:

Continuity equation:

$$\frac{\partial \rho}{\partial t} + \nabla \cdot \left(\rho \vec{U} \right) = 0$$

Eq. 6-3

Momentum equation:

$$\frac{\partial}{\partial t}\left(\rho\vec{U}\right)+\nabla\cdot(\rho\vec{U}\vec{U})=-\nabla\cdot P+\rho\vec{g}+\nabla\cdot\vec{\tau}+\vec{F}$$ Eq. 6-4

Where P is the static pressure, $\vec{\tau}$ is the stress tensor, and $\rho\vec{g}$ and $\vec{F}$ are the gravitational body and external body forces, respectively.

Energy equation:

$$\frac{\partial(\rho H)}{\partial t}+\nabla\cdot(\rho\vec{U}H)=\nabla\cdot(K\nabla T)+S$$ Eq. 6-5

where H is the enthalpy, T is the temperature, ρ is density, K is the thermal conductivity, $\vec{U}$ is the velocity and S is volumetric heat source term and is equal to zero in the present study.

The total enthalpy H of the Sodium Nitrate or the NePCMs is computed as the sum of the sensible enthalpy, h and the latent heat, ΔH. The latent heat content, in terms of the latent heat of the NePCM, L is:

$$\Delta H = \beta L$$ Eq. 6-6

Where β is liquid fraction and is defined as:

$$\beta = 0 \quad \text{If} \quad T < T_{solid}$$

$$\beta = 1 \quad \text{If} \quad T > T_{solid}$$

$$\beta = \frac{T - T_{solid}}{T_{liquid} - T_{solid}} \quad \text{If} \quad T_{solid} < T < T_{liquid}$$ Eq. 6-7

The solution for temperature is essentially an iteration between the energy Eq. 6-5 and the liquid fraction Eq. 6-7. The enthalpy-porosity technique treats the mushy region (partially solidified region) as a porous medium. The porosity in each cell is set equal to the liquid fraction in that cell. In the fully solidified region, the difference in the solidus and liquid temperatures defines the transition from the solid to liquid phases during the melting of the Sodium Nitrate or the NePCMs. The density, specific heat capacity and latent heat of the Sodium Nitrate or the NePCMs are defined as follows [219]:

$$\rho_{npcm} = \phi\rho_{np} + (1-\phi)\rho_{pcm}$$ Eq. 6-8

$$c_{p\,npcm} = \frac{\phi(\rho c_p)_{np} + (1-\phi)(\rho c_p)_{pcm}}{\rho_{npcm}}$$

Eq. 6-9

$$L_{npcm} = \frac{(1-\phi)(\rho L)_{pcm}}{\rho_{npcm}}$$

Eq. 6-10

Where φ is volumetric fraction of nanoparticle. The dynamic viscosity and thermal conductivity of the NePCM are given by the following [219]:

$$\mu_{npcm} = 0.983^{e^{(12.958\phi)}}$$

Eq. 6-11

Thermophysical Properties: The effective thermal conductivity of the NePCMs, which includes the effects of particle size, particle volume fraction and temperature dependence as well as properties of the Sodium Nitrate and the particle subject to Brownian motion, is given by:

$$K_{npcm} = \frac{K_{np} + 2K_{pcm} - 2(K_{pcm} - K_{np})\phi}{K_{np} + 2K_{pcm} + (K_{pcm} - K_{np})\phi}K_{pcm} + 5\times10^4 \beta_k \varsigma\phi\rho_{pcm}C_{p\,pcm}\sqrt{\frac{BT}{\rho_{np}d_{np}}}f(T,\phi)$$

Eq. 6-12

where B is the Boltzmann constant = 1.381×10^{-23} J/K and

$$\beta_k = 8.4407 * (100\phi)^{-1.07304}$$

Eq. 6-13

$$f(T,\phi) = (2.8217\times10^{-2}\phi + 3.917\times10^{-3})\frac{T}{T_{ref}} + (-0.669\times10^{-2}\phi - 3.91123\times10^{-3})$$

Eq. 6-14

Where T_{ref} is the reference temperature. The first part of Eq. 6-12 is obtained directly from the Maxwell model while the second part accounts for Brownian motion, which causes the temperature dependence of the effective thermal conductivity. Note that there is a correction factor ς in the Brownian motion term, since there should be no Brownian motion in the solid phase. Its value is defined as the same as for liquid fraction, β in Eq. 6-7.

For the numerical study, the integrated simulation system ANSYS Workbench 15.0 is used. The platform includes mesh generation tool ICEM and FLUENT software. In order to reduce the computational time, first, a fine structured mesh near the boundary layer and an increasingly coarser mesh in the rest of the domain is generated, and then the mesh is exported into FLUENT for solving the governing equations. To investigate both about dispersed nanoparticles in the PCM that about their interactions, in FLUENT, the melting model together to Volume Of Fluid (VOF) model are applied. For modelling the melting process, the enthalpy-porosity technique is used. In

this technique, the melt interface is not tracked explicitly. The liquid fraction indicating the fraction of the cell volume that is in liquid form is computed at each iteration, based on an enthalpy balance. The mushy zone is the region where the porosity increases from 0 to 1 as the PCM melts. To account for temperature dependence, the input parameters of Sodium Nitrate and of ANPs were defined using different user- defined functions (UDF) written in C++ language. The PRESSURE BASED method with the FIRST ORDER UPWIND differencing scheme are used for solving the momentum and energy equations, whereas the PRESTO scheme is adopted for the pressure correction. The under-relaxation factors for the velocity components, pressure correction and thermal energy are 0.5, 0.3 and 1 respectively. Grid dependence test showed that the maximum difference of the PCM temperature at an identical time is within 0.01% between using 4000 cells and 4800 cells with a time step of 0.1 s. After mesh independence study, considering both accuracy and computing time, 4400 cells with a time step of 0.1 s are used in the computations.

6.2.4 Experimental results

6.2.4.1 Nanoparticle size distribution

The size distributions of the eighteen NePCMs analysed in this study are gathered in the Figure 6-3. The mode of each distribution is pointed out over each curve. In view of these distributions, most of them are in the nanometric range (<100 nm) or very near from it. This fact is indicative that little agglomeration took place during the synthesis procedure. The maintaining of small sizes may favour the heat transfer improvement since a higher surface of the nanoparticles is free to interact with the salt ions, as theorized by Shin and Banerjee [63].

This available surface of the nanoparticles has been computed from the distributions (Eq. 6-1) and the results are showed in the Table 6-3. The available surface in the NePCMs based on ASN and RSN increases directly with the amount of nanoparticles, for both nanoparticles (ANPs and SiNPs). On the contrary, those based on ISN and ANPs have the opposite behaviour. Finally, the NePCMs of ISN and SiNPs have a maximum value at 1 wt% of nanoparticle concentration. The differences between the ISN-based NePCMs and the others could be attributable to a higher nanoparticle agglomeration in these materials caused by the impurities of the base salt.
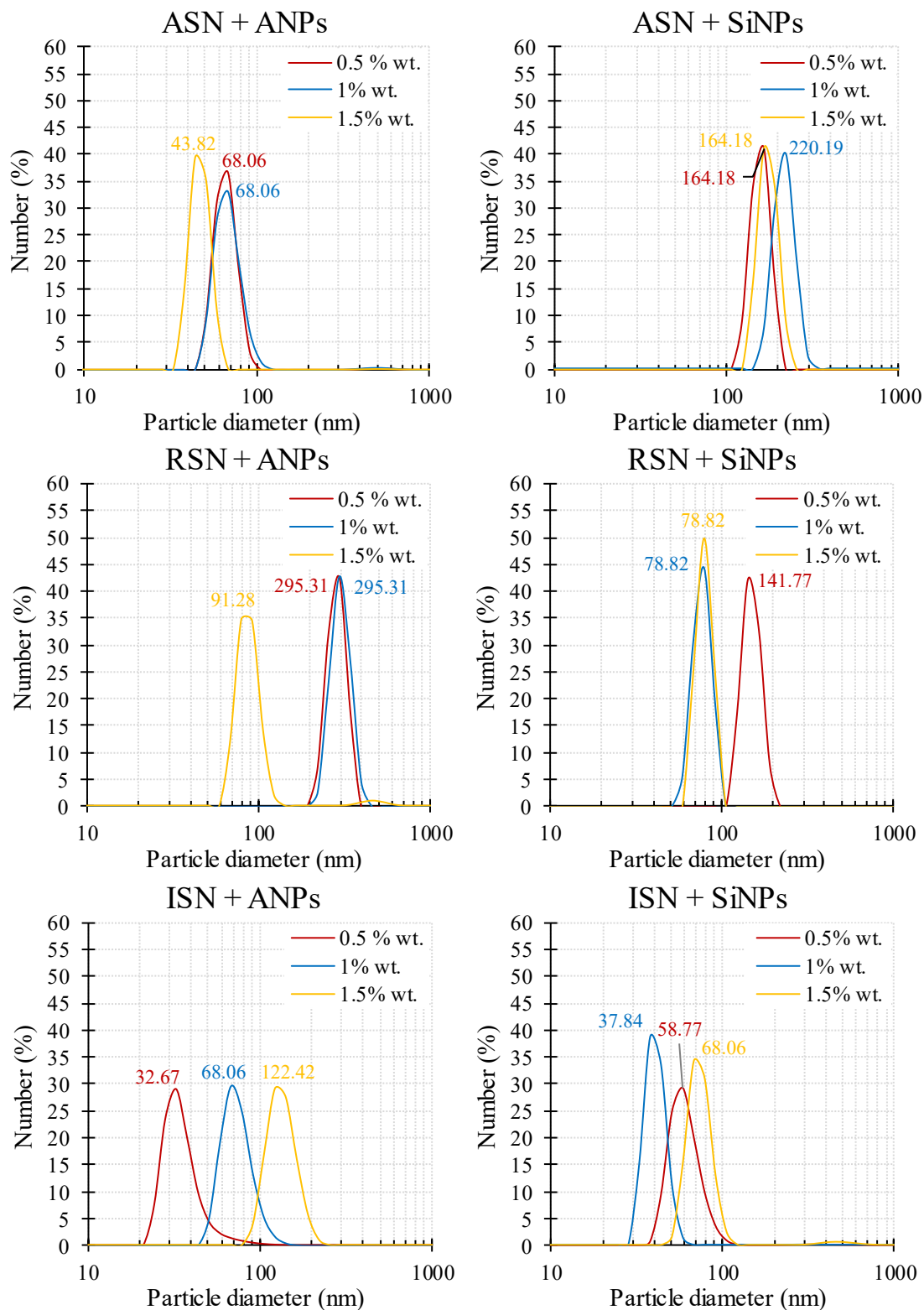
Figure 6-3. Nanoparticle size distributions of the NePCMs synthetized with the three Sodium Nitrates. The mode of each distribution is signaled on each curve.

Table 6-3. Avalaible surface of nanoparticles for each of the NePCMs calculated with the Eq. 6-1

| | Available surface of nanoparticles, S_a (m²·g⁻¹) | | | | | |
| | ANPs | | | SiNPs | | |
	0.5 wt%	1 wt%	1.5 wt%	0.5 wt%	1 wt%	1.5 wt%
ASN	0.116	0.226	0.492	0.049	0.072	0.133
RSN	0.027	0.051	0.263	0.052	0.201	0.291
ISN	0.224	0.211	0.174	0.129	0.379	0.310

6.2.4.2 Thermogravimetric analysis

The weight loss of the two NePCMs ISN1A and ISN1Si with the thermal program described in the method section is showed in the Figure 6-4. First important issue to be noticed is that both samples have little weight losses after the thermal treatment (1.62% for ISN1A and 0.65% for ISN1Si). It means that, in principle, the addition of nanoparticles to the ISN does not affect their performance under thermal cycling. It may be interesting to perform an extended durability test with a high number of thermal cycles to confirm this behaviour. In the other hand, the higher weight loss of the NePCM containing ANPs is explained by the change of this nanoparticle with the temperature. The ANPs are constituted by the boehmite, a precursor of the γ-Al_2O_3. According to our self-measurements [127], the desorption of intralaminar water located between the nanoparticles starts at temperatures higher than 300 ºC. Following this process, the boehmite starts the transformation in γ-Al_2O_3.

There are several researches which evaluates the thermal stability of NePCMs based on inorganic salts [32,64,89,113]. However, the test results are measuring the change of the specific heat before and after the thermal cycling, not the weight loss. This makes impossible to compare our results with those of the literature.
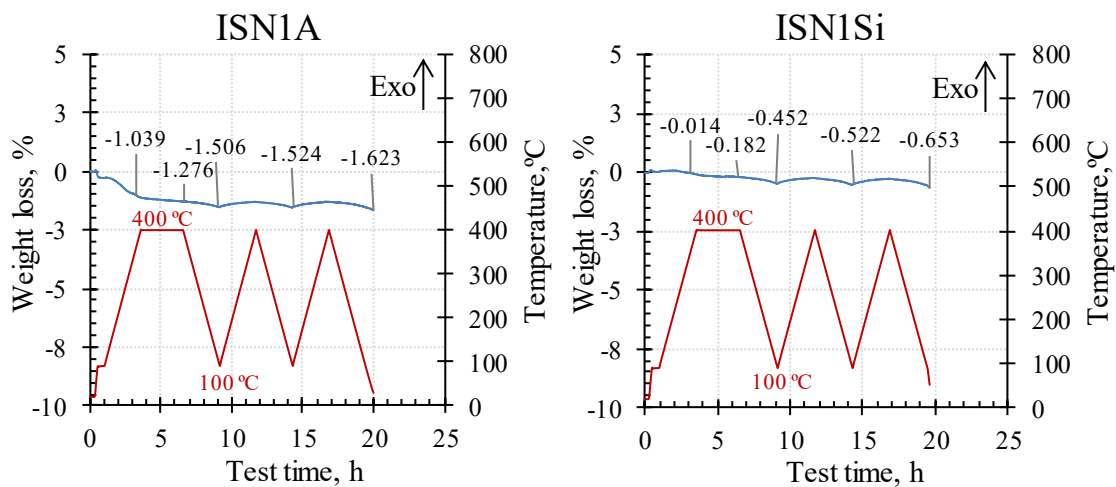
Figure 6-4. TGA measurement between 20 ºC and 400 ºC of the NePCMs ISN1A (left) and ISN1Si (right).

6.2.4.3 Specific heat

In the Figure 6-5, the specific heat results in the solid (256 ºC) and the liquid phase (326 ºC) are depicted. First, the results of the pure Sodium Nitrate salts (ASN, RSN and ISN) are in agreement with the published ones [33] (1.7 $kJ \cdot kg^{-1} \cdot K^{-1}$ as average value at 326 ºC). The higher c_p in the solid state is due to the proximity of the melting point.

Regarding the NePCMs, there are different trends depending on their base salt. Those containing ASN show a reduction of the specific heat linked to the nanoparticle concentration. This decrement is higher in the NePCMs containing ANPs. This behaviour could be attributable to a higher agglomeration tendency of these nanoparticles compared to that of the SiNPs, mainly due to their shape and higher density difference with the molten Sodium Nitrate (3,950 $kg \cdot m^{-3}$ of the ANPs [200], 2,650 $kg \cdot m^{-3}$ of the SiNPs [200] vs. 1,980 $kg \cdot m^{-3}$ of the liquid salt [201]). The sedimentation rate may be faster for the ANPs than the SiNPs. Lower enhancements of specific heat were obtained with RSN-based NePCMs, with ANPs compared with those containing SiNPs. The materials containing ISN and ANPs obtained small enhancements of the specific heat, while those with SiNPs had lower values than the base salt.

The specific heat of Sodium Nitrate-based NePCMs is not appearing in the scientific literature, which makes infeasible the comparison of our experimental results. The specific heat of similar mixtures such as those based on Solar Salt (60 wt% $NaNO_3$ – 40 wt% KNO_3) [31,35–37,115] or KNO_3 [37,39] revealed inconsistencies between them due to divergences on the synthesis method, materials or the analytical procedure. There is not a complete agreement on the effect of the nanoparticles in the specific heat of the salts yet.
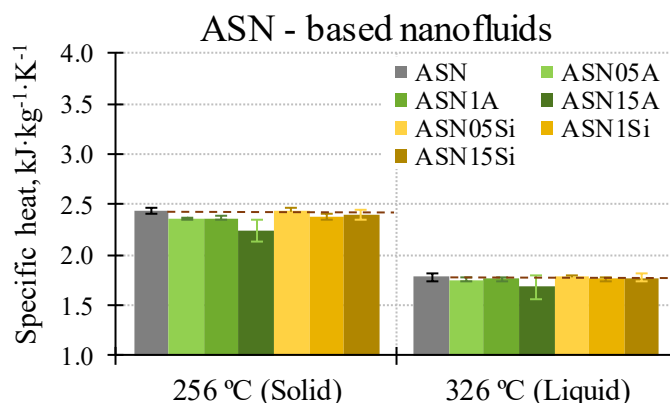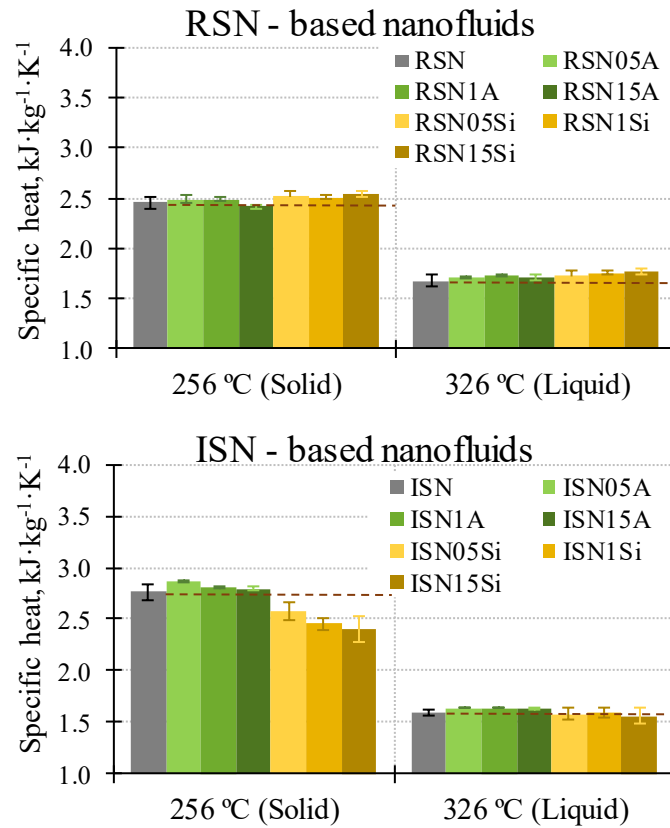
Figure 6-5. Specific heat of the Sodium Nitrate salts (ASN, RSN and ISN) and their nanofluids measured in the solid (256 ºC) and the liquid state (326 ºC).

6.2.4.4 Latent heat and phase change temperature

The latent heat of fusion and crystallization of the Sodium Nitrate and the NePCMs are gathered in Table 6-4. The first issue to be noticed is the difference of the latent heat (fusion or crystallization) between the three Sodium Nitrates without nanoparticles. The ASN has the highest values of latent heat in agreement with the literature (178 kJ·kg⁻¹ [33]), followed by the RSN (with 18 kJ·kg⁻¹ less) and finally the ISN, diminished by 55 kJ·kg⁻¹ compared to the ASN. These differences are due to the internal crystalline structure of the salts. The RSS and ISS contain impurities which impede the existence of a high-ordered structure as shown by the ASS.

Regarding the latent heat of the NePCMs, two trends are easily identified. On one side, the addition of nanoparticles to the ASS is lowering the value of this property in a direct relation with the percentage of nanoparticles. This observation is valid for the two nanoparticles (ANPs and SiNPs) and both the fusion and solidification processes. The reason of this reduction may be the disordered caused by the introduction of the nanoparticles into the well-defined crystal structure of the ASS. More in detail, it is seen that the decrease is depending on the nanoparticle, with higher decrements of the SiNPs. This observation is related to the nanoparticle shape and density. The ANPs, with a fibrilar shape (see Figure 6-1) and a density of 3,950 kg·m⁻³ (compared to 1,980

kg·m⁻³) may be easily agglomerated and settled down at the bottom of the crucible from the first heating ramp. In comparison, some of the SiNPs may be less agglomerated and remain dispersed into the molten salt due to their rounded shape (see Figure 6-1) and similar density to the molten salt (2,650 kg·m⁻³ vs. 1,980 kg·m⁻³). Thus, more SiNPs than ANPs may be embedded into the ASN, creating a higher entropy in its ordered structure. Concerning the NePCMs based on RSN and ISS, their latent heat (fusion or solidification) does not change with the addition of the nanoparticles and is independent of their concentration. This is related to the presence of impurities on the base salts, which generates entropy into their crystalline structure during the solidification process. Thus, the phase change process is not affected by the introduction of new additives in low quantities, such as the nanoparticles.

Table 6-4. Latent heat of fusion and crystallization of the ASN, RSN, ISN and the NePCMs synthetized from them. The variation of the results compared with the initial Sodium Nitrates is included.

| | | ANPs | | | | SiNPs | | | |
| | | Fusion | | Crystallization | | Fusion | | Crystallization | |
	% NPs	ΔH_f, kJ·kg⁻¹	$\Delta\Delta H_f$, %	ΔH_c, kJ·kg⁻¹	$\Delta\Delta H_c$, %	ΔH_f, kJ·kg⁻¹	$\Delta\Delta H_f$, %	ΔH_c, kJ·kg⁻¹	$\Delta\Delta H_c$, %
ASN	0	**180.53 ± 1.15**	---	**181.43 ± 1.15**	---	**180.53 ± 1.15**	---	**181.43 ± 1.15**	---
	0.5	178.57 ± 0.23	-1.09	179.00 ± 0.46	-1.34	176.73 ± 1.39	-2.10	177.40 ± 1.31	-2.22
	1	176.84 ± 0.52	-2.04	177.58 ± 0.74	-2.13	172.73 ± 2.10	-4.32	173.57 ± 1.75	-4.34
	1.5	170.73 ± 2.90	-5.43	171.47 ± 3.15	-5.49	167.73 ± 1.96	-7.09	169.73 ± 0.76	-6.45
RSN	0	**161.65 ± 3.04**	---	**163.20 ± 0.85**	---	**161.65 ± 3.04**	---	**163.20 ± 0.85**	---
	0.5	165.03 ± 0.98	2.09	165.77 ± 1.68	1.57	162.87 ± 0.45	0.75	165.30 ± 0.85	1.29
	1	163.17 ± 0.64	0.94	164.27 ± 0.46	0.65	162.80 ± 0.72	0.71	164.63 ± 0.90	0.88
	1.5	164.75 ± 0.92	1.92	166.05 ± 0.78	1.75	159.03 ± 0.51	-1.62	160.80 ± 0.10	-1.47
ISN	0	**124.67 ± 3.06**	---	**126.37 ± 3.27**	---	**124.67 ± 3.06**	---	**126.37 ± 3.27**	---
	0.5	125.23 ± 1.42	0.45	128.30 ± 1.56	1.53	132.90 ± 3.41	6.60	131.37 ± 0.93	0.93
	1	125.47 ± 0.61	0.64	128.47 ± 1.16	1.66	130.13 ± 1.72	4.39	128.20 ± 1.13	1.13
	1.5	124.87 ± 1.36	0.16	125.20 ± 2.08	-0.92	128.90 ± 0.78	3.40	126.23 ± 1.86	1.86

The fusion and crystallization temperatures were also analysed (Table 6-5). For the raw salts, the phase change temperature is reduced in the order ASN>RSN>ISN by the higher entropy into the crystalline structure, as detailed before. However, in opposition to the latent heat results, the phase change temperature is not particularly affected by the introduction of nanoparticles. In general, it can be seen a decrease in the ASN-based NePCMs and a tiny increment in the RSS- and ISN-based NePCMs. It is worth mentioning the subcooling observed both for the initial salts and the NePCMs (about 10 ºC for the ASN, RSN and their NePCMs and near 8 ºC for the RSN and its NePCMs).

Table 6-5. Temperatures of the fusion and crystallization processes of the ASN, RSN, ISN and the NePCMs synthetized from them. The variation of the results compared with the initial Sodium Nitrates is included.

	% NPs	ANPs Fusion T_f, ºC	ΔT_f, %	Crystallization T_c, ºC	ΔT_c, %	SiNPs Fusion T_f, ºC	ΔT_f, %	Crystallization T_c, ºC	ΔT_c, %
ASN	0	**310.98 ± 1.03**	---	**300.79 ± 0.42**	---	**310.98 ± 1.03**	---	**300.79 ± 0.42**	---
	0.5	309.84 ± 0.11	-0.37	300.64 ± 0.17	-0.05	310.13 ± 0.39	-0.27	300.52 ± 0.18	-0.09
	1	310.48 ± 0.25	-0.26	300.53 ± 0.05	-0.04	309.35 ± 0.46	-0.52	300.48 ± 0.04	-0.10
	1.5	310.17 ± 0.27	-0.69	300.67 ± 0.15	-0.02	309.51 ± 0.55	-0.47	300.13 ± 0.34	-0.22
RSN	0	**307.07 ± 0.00**	---	**296.28 ± 0.35**	---	**307.07 ± 0.00**	---	**296.28 ± 0.35**	---
	0.5	309.98 ± 2.82	0.95	297.62 ± 0.19	0.45	309.45 ± 1.06	0.78	298.03 ± 1.45	0.59
	1	309.15 ± 1.17	0.68	298.34 ± 0.15	0.70	309.17 ± 1.46	0.68	298.35 ± 0.74	0.70
	1.5	309.26 ± 0.99	0.71	298.52 ± 0.26	0.76	307.82 ± 0.11	0.25	298.23 ± 0.32	0.66
ISN	0	**300.01 ± 0.27**	---	**292.19 ± 0.81**	---	**300.01 ± 0.27**	---	**292.19 ± 0.81**	---
	0.5	297.84 ± 4.64	-0.72	292.60 ± 0.38	0.14	300.79 ± 0.20	0.26	292.84 ± 0.06	0.22
	1	300.35 ± 0.17	0.11	292.65 ± 0.21	0.16	300.51 ± 0.10	0.17	292.06 ± 1.19	-0.04
	1.5	300.44 ± 0.18	0.14	292.77 ± 0.09	0.20	300.51 ± 0.11	0.17	292.69 ± 0.36	0.17

The onset temperatures of fusion are gathered in the Table 6-6. This variable determines the starting point of the fusion process. The results depend on the purity degree of the base salt, as seen in the previous analysis. In this sense, the onset temperature experiences a little reduction with the increasing amount of nanoparticles in the ASN-based NePCMs. The results are very similar for the RSN and its NePCMs and an increase of this property is seen in the materials which have the ISN as the base salt. It is though that these differences are related to the entropy of the internal structure of the base salt in the same line as detailed before.

In the literature there is not any study of the phase change properties of NePCMs with SN as the base salt. However, we can compare our results (only those based on ASN) with other very similar NePCMs based on Solar Salt [31,35–37,115] or KNO_3 [37,39]. In the same trend of our results, the latent heat was found to decrease proportionally to the nanoparticle content [31,35,115]. Other researchers found an increase at certain percentages of addition [36,37,39]. These authors suggest that the nanoparticle agglomerates may have solid salt entrapped which require more energy to be melted, causing an increase of the latent heat. On the other hand, these studies did not found any change on the melting temperature with the addition of the nanoparticles and all of them reported a decrease of the onset temperature. This latter trend is coincident with our result of the NePCMs based on ASN, which is logical since any of the examined publications use salts of analytical quality.

Table 6-6. Onset temperatures of fusion of the ASN, RSN, ISN and the NePCMs synthetized from them. The variation of the results compared with the initial Sodium Nitrates is included.

	% NPs	ANPs		SiNPs	
		T_o, ºC	ΔT_o, %	T_o, ºC	ΔT_o, %
ASN	0	305.75 ± 0.03	---	305.75 ± 0.03	---
	0.5	305.45 ± 0.10	-0.10	305.45 ± 0.25	-0.10
	1	305.40 ± 0.07	-0.11	305.38 ± 0.06	-0.12
	1.5	304.30 ± 0.56	-0.47	305.30 ± 0.21	-0.15
RSN	0	301.62 ± 0.00	---	301.62 ± 0.00	---
	0.5	301.73 ± 0.45	0.04	---	---
	1	---	---	301.55 ± 0.58	-0.02
	1.5	---	---	301.53 ± 0.05	-0.03
ISN	0	289.76 ± 0.66	---	289.76 ± 0.66	---
	0.5	290.07 ± 0.31	0.11	290.48 ± 0.16	0.25
	1	289.74 ± 0.33	-0.01	290.02 ± 0.42	0.09
	1.5	289.97 ± 0.25	0.07	290.13 ± 0.13	0.13

6.2.4.5 Thermal conductivity

The thermal diffusivity and the thermal conductivity of the ASN and the NePCM ASN1A were analysed by the LFA method. The results and the increments compared to the base salt ASN are gathered in the Table 6-7, as well as those of the specific heat. The densities of the ASN were calculated at each temperature according to the expression proposed by Janz et al. [201]. The densities of the ASN1A take into account the value of 3,950 kg·m^{-3} for the ANPs [200].

First, the thermal diffusivity results of the ASN without ANPs are a bit low in comparison to those of the literature (0.15 mm^2·s^{-1} at 256 ºC and 0.17 mm^2·s^{-1} at 326 ºC) [33]. Consequently, the thermal conductivity results are also below those published. This discrepancy could be due to the different crystal structure of the analysed Sodium Nitrate [33].

Regarding the data obtained for the ASN1A, both the thermal diffusivity and the thermal conductivity were highly enhanced by the addition of ANPs to the base salt. This increment of the conductivity could be related by the great thermal conductivity of the boehmite (30 W·m^{-1}·K^{-1} [220]) in comparison to that of the Sodium Nitrate (0.5 W·m^{-1}·K^{-1} [33]).

The scarce information in the literature of NePCMs about this phenomena, makes difficult the direct comparison of our results with other researches. Some researchers have studied the thermal conductivity of different pairs of salt and nanoparticles, and their results were controversial. Silica nanoparticles added to an eutectic mixture of carbonates gave enhancements around 40% [30,102] in the solid state. However, the doping of Solar Salt with these nanoparticles obtained decrements 20% in the solid state [32].

Table 6-7. Thermal diffusivity, specific heat and thermal conductivity of the ASN and the nanofluid ASN1A in the solid (256 ºC) and the liquid state (326 ºC).

		Thermal diffusivity		Specific heat		Density	Thermal conductivity	
		α, mm^2·s^{-1}	$\Delta\alpha$, %	c_p, kJ·kg^{-1}·K^{-1}	Δc_p, %	ρ, kg·m^{-3}	k, W·m^{-1}·K^{-1}	Δk, %
256 ºC (solid)	ASN	0.089 ± 0.001	---	2.431 ± 0.034	---	2.257	0.490 ± 0.035	---
	ASN1A	0.169 ± 0.003	89.08	2.365 ± 0.016	-2.69	2.274	0.969 ± 0.019	97.78
326 ºC (liquid)	ASN	0.096 ± 0.004	---	1.776 ± 0.043	---	1.892	0.321 ± 0.047	---
	ASN1A	0.195 ± 0.004	104.45	1.755 ± 0.020	-1.18	1.912	0.719 ± 0.024	124.01

6.2.4.6 Microstructure

The study of the microstructure of the NePCMs was done over a sample of ISN1A. In the Figure 6-6, several SEM images of this nanostructured material can be observed with different grades of magnification. In these images, the matrix of Sodium Nitrate is seen as a continuous surface (in dark grey) covered with rounded-shape particles (in bright grey). These particles could be either the ANPs or the impurities which are present in the ISN salt (chlorides, phosphates, sulphates, calcium, magnesium…).

The compositional analysis of the samples was done over the images appearing in the Figure 6-7, by using the EDX over several points. The results are gathered in the tables attached to the Figure 6-7. The most abundant elements are nitrogen, sodium and oxygen, as they are composing the Sodium Nitrate. In addition, the aluminium is appearing in considerable amounts when the ANPs are present in the analysed region (points 1 and 4 of the Figure 6-7A and 1 and 3 of the Figure 6-7B). From these images, it is seen that the agglomerates of the ANPs are of a few microns in size (1-3 µm). Other elements such as magnesium, chlorine and potassium are found incidentally as they are impurities from the ISN.
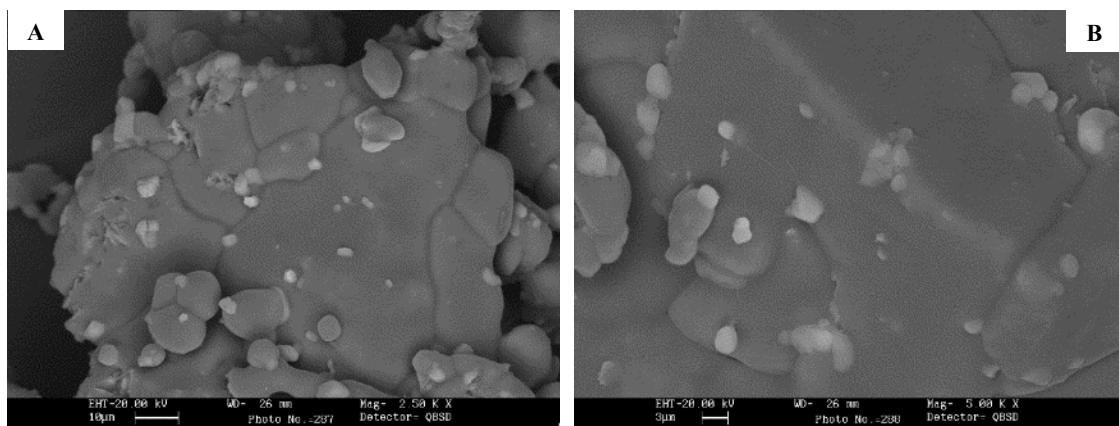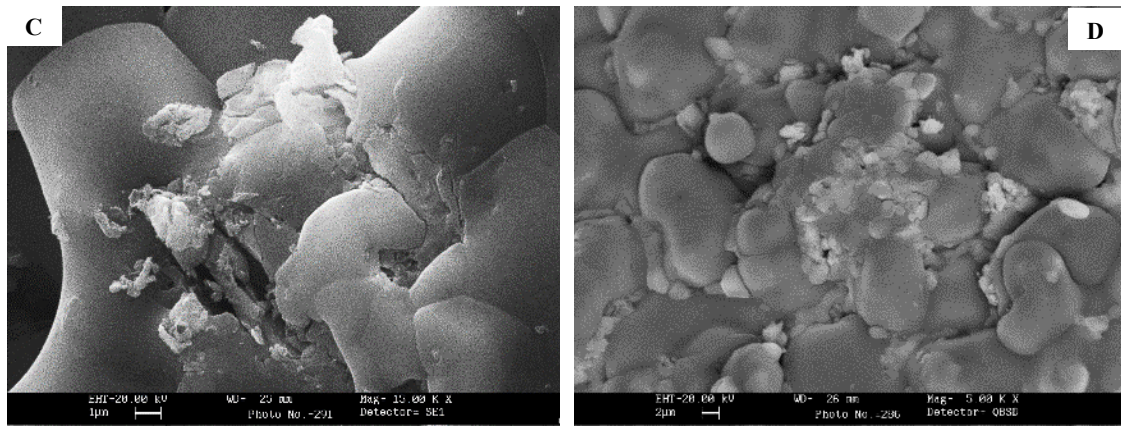
Figure 6-6. SEM images of a NePCM of ISN with 1 wt% of ANPs. The images A. B and D were done under Back-Scattered Electrons (BSE) with 2,500x (A), 5,000x (B) and 5,000x (D) od magnification. The image C was done under Secondary Electrons (SE) with 15,000x of magnification.
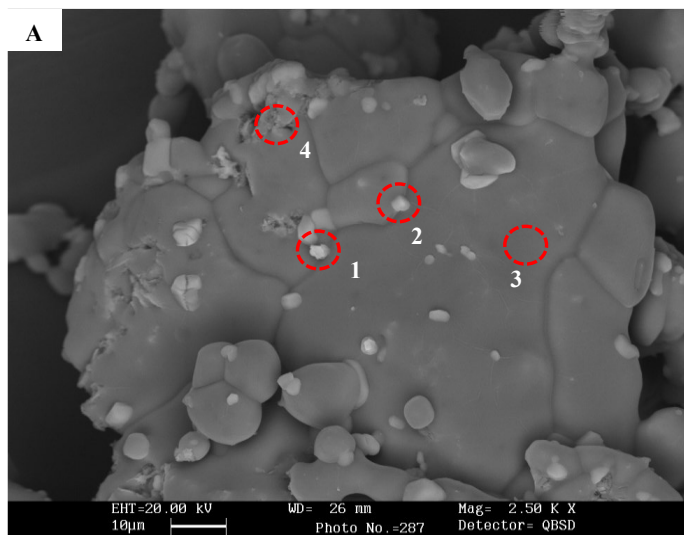
Element	Amount, % wt.			
	1	2	3	4
O	61.25	21.24		58.77
N	18.45	43.01	25.81	16.53
Na	16.57	35.75	74.19	17.51
K	1.10			1.40
Al	2.63			5.26
Mg				0.66
Cl				0.86
Total	100	100	100	100
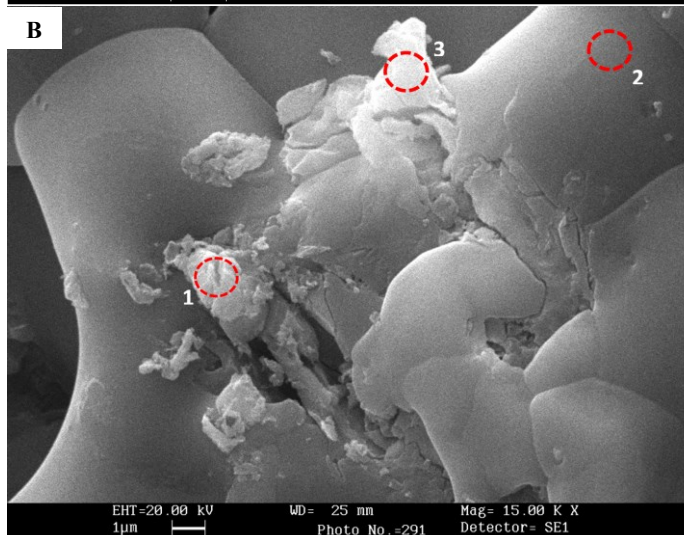
Element	Amount, % wt.		
	1	2	3
O	40.11	25.81	37.13
N			
Na	21.08	74.19	34.69
K			
Al	31.25		28.18
Mg	7.56		
Cl			
Total	100	100	100

Figure 6-7. SEM images of a ISN1A nanofluid including the area where the EDX analysis have been performed.

6.2.5 Simulation results

Transient two-dimensional numerical simulations were implemented for Sodium Nitrate and Sodium Nitrate-based NePCMs with 0.5%, 1% and 1.5% by mass of ANPs, during charging and discharging processes. The aim was examining the influence of the addition of ANPs suspended in the Sodium Nitrate in relation to the thermo-physical properties and the heat transfer rate. In addition, limitations and advantages of the addition of ANPs were analysed considering the numerical results.

6.2.5.1 Thermophysical Properties

This section is analysing the thermophysical properties of the Sodium Nitrate and the NePCMs. Essentially, the Figure 6-8 shows the thermal conductivity and the dynamic viscosity of the Sodium Nitrate (SN) and its NePCMs doped with 0.5%, 1% and 1.5% by mass of ANPs, are plotted as a function of the temperature and the nanoparticle mass concentration. The Figure 6-9 gathers the specific heat and the latent heat of the Sodium Nitrate (SN) and the NePCMs.
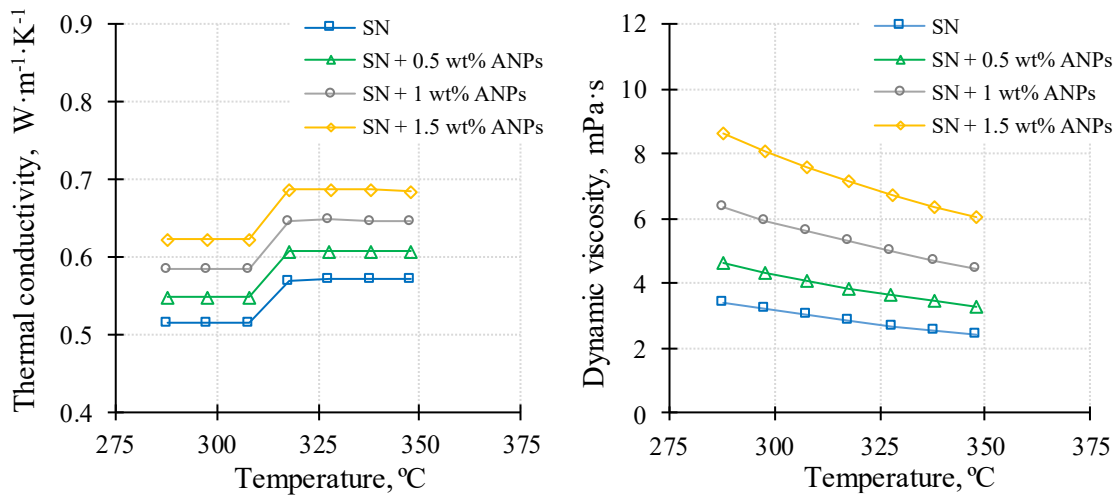
Figure 6-8. Thermal conductivity (Left) and dynamic viscosity (Right) of Sodium Nitrate-based NePCMs doped with ANPs (0.5, 1 or 1.5 wt%)

As it can be seen in Figure 6-8 left, the thermal conductivity of Sodium Nitrate doped with ANPs is higher than the base salt Sodium Nitrate. The higher the concentration of ANPs is, the higher increment of thermal conductivity. Hence, the NePCMs have higher heat transfer rate compared to the same mass of Sodium Nitrate. Nonetheless, the viscosity of Sodium Nitrate-based NePCMs increases with the mass concentration of ANPs, as shown in Figure 6-8 right. On one hand, the addition of ANPs to the Sodium Nitrate will lead to higher heat transfer rates and lower charging and discharging cycles. On the other hand, the higher dynamic viscosities for the ANPs-doped nanofluids will affect negatively to the heat transmission by convection. These two effects will be considered in the simulation of a charging and discharging cycle.
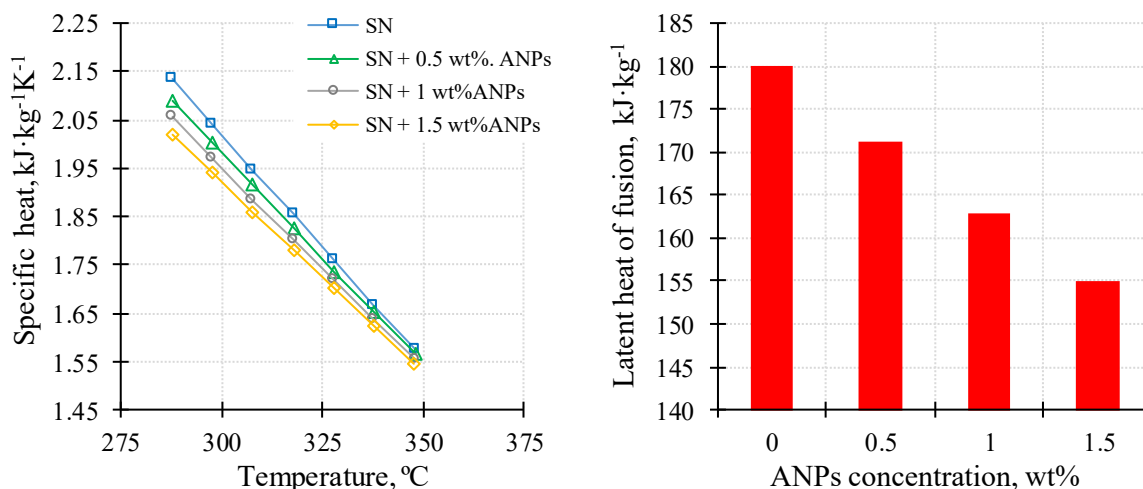
Figure 6-9. Left: Specific heat of Sodium Nitrate and its NePCMs vs concentration of ANPs and temperature. Right: Latent heat of Sodium Nitrate and its NePCMs vs concentration of ANPs.

The specific heat of Sodium Nitrate-based NePCMs is expected to decrease with the concentration of ANPs as predicted in CFD simulations (Figure 6-9). The differences are more notable at temperatures below the melting point (308 ºC). An important decrease of the ΔH_f that reached 13.9% for the higher concentration of ANPs (1.5 wt%) was predicted. Several reasons could be behind this decrease. The first one is the lower specific heat of the ANPs compared to the Sodium Nitrate (1.2 $kJ \cdot kg^{-1} \cdot K^{-1}$ vs. 2.4 $kJ \cdot kg^{-1} \cdot K^{-1}$ at 256 ºC and 1.5 $kJ \cdot kg^{-1} \cdot K^{-1}$ vs. 1.8 at 326 ºC). Consequently, the overall thermal absorbance of the NePCM will decrease with increasing mass fraction of ANPs which in turn decreases the latent heat of fusion of NePCMs. The second parameter is that the high thermal conductivity of ANPs should be quite enough to increase the thermal conductivity of NePCMs, enhancing the heat transfer characteristics of the Sodium Nitrate and accelerating the energy storage and release at a faster rate.

6.2.5.2 Heat transfer rate

Figure 6-10 shows time evolution of charging (326 ºC) and discharging (256 ºC) of the Sodium Nitrate (SN) and its NePCMs doped with ANPs at different concentrations (0.5, 1 or 1.5 wt%). These temperatures were approximately 20 ºC over the melting temperature and 50 ºC below the solidification temperature of the Sodium Nitrate, respectively.
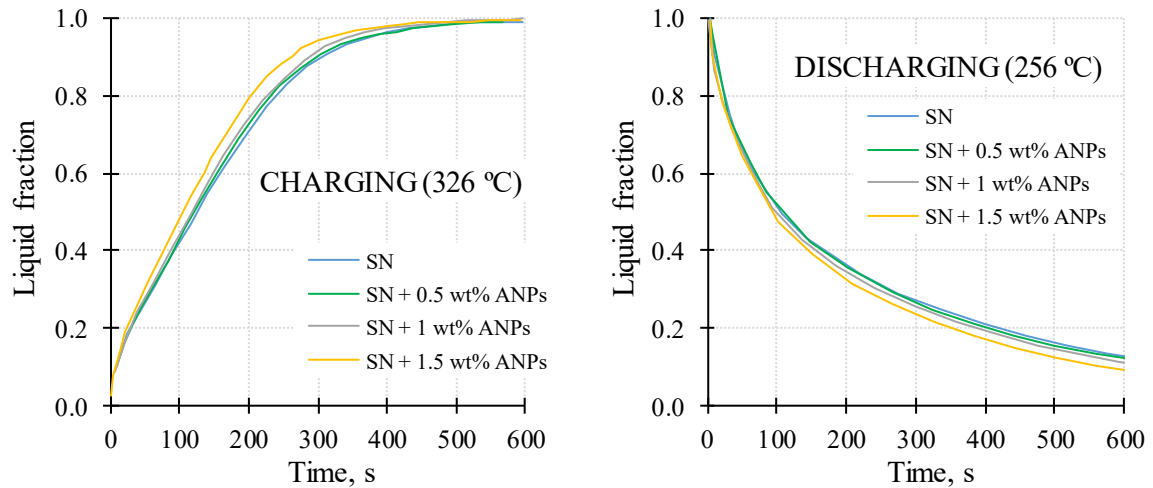
Figure 6-10. Time evolution of charging (326 ºC) (Left) and discharging (256 ºC) (Right) of Sodium Nitrate and its NePCMs doped with ANPs at different concentrations (0.5, 1 or 1.5 wt%).

The charging and discharging cycles are slightly shortened with the addition of ANPs (Figure 6-10). This is mainly due to the enhancement of the thermal conductivity with the presence of ANPs (Figure 6-8, left), despite of the lower convection heat transfer due to the higher dynamic viscosities (Figure 6-8 right) for NePCMs. Discharging cycles are normally longer than charging ones because of the formation of a solid layer of lower conductivity that becomes a barrier to the heat conduction. It is thought that these small improvements of the heat transfer performance could be considerably increased if higher volumes of NePCMs would be used in the simulation (now the domain is 1 cm x 1 cm).

6.2.6   Comparison of experimental and simulation results

In this section, the thermophysical properties predicted by the integrated simulation system ANSYS Workbench 15.0 were compared with the experimental measurements of ASN and ASN-based NePCMs. Results are shown in Figure 6-11 (c_p measurements) and Figure 6-12 (latent heat of fusion and thermal conductivity).
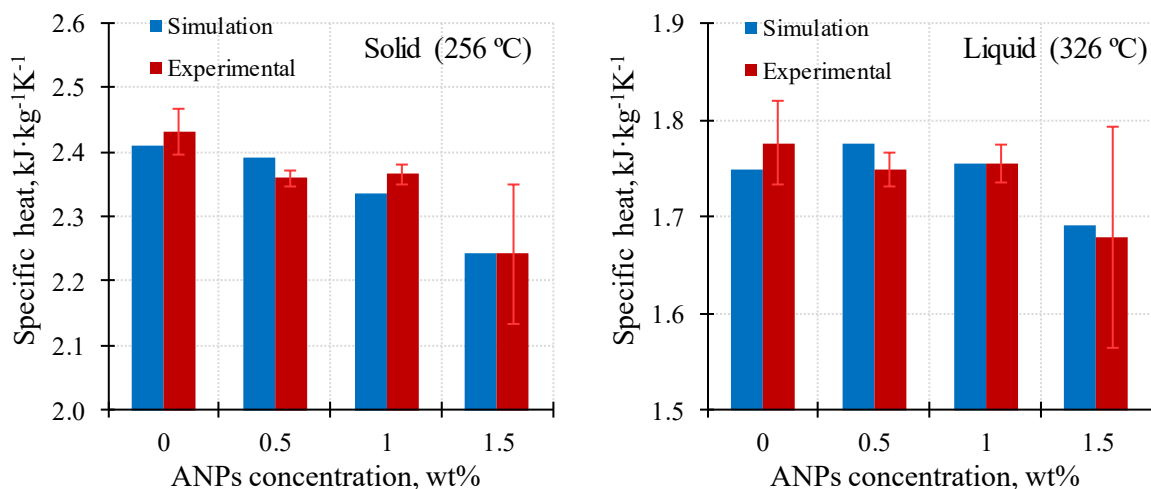
Figure 6-11. Comparison between experimental and simulation results. Specific heat of Sodium Nitrate-based nanofluids as a function of the concentration (wt%) of ANPs at 256 ℃ (Left) and 326 ℃ (Right).
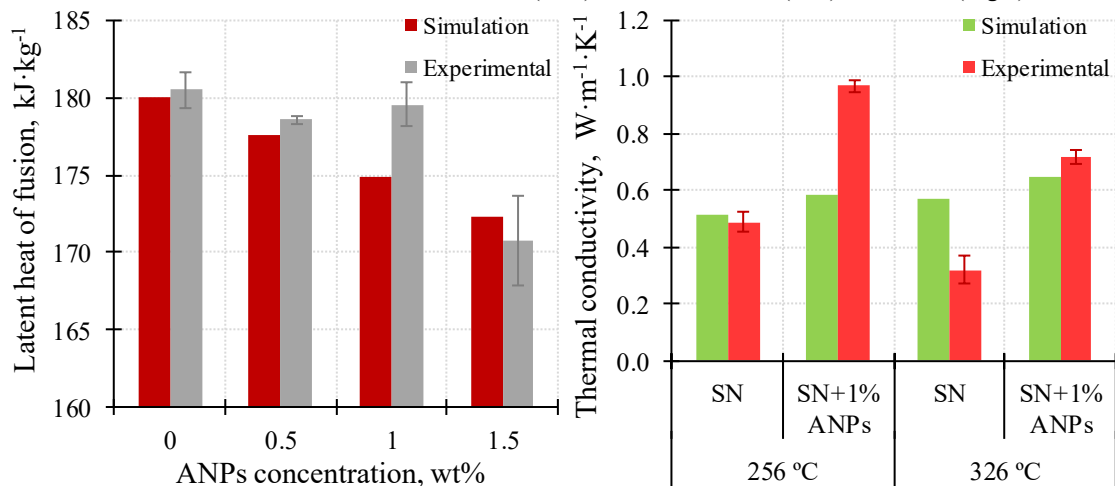
Figure 6-12. Comparison between experimental and simulation results. Left: Latent heat of fusion as a function of the concentration of ANPs. Right: thermal conductivity of Sodium Nitrate and a NePCM with 1 wt% of ANPs.

As it can be seen, the predictions of the specific heat and the latent heat of fusion are in good agreement with the experimental results for concentrations of ANPs equal or lower than 1 wt% The higher deviations were found in the case of the highest concentration tested (1.5 wt%). However, these differences are within the standard deviation of the measurements for the two thermophysical properties. The reasons of these major differences are not well known. It is possible that other processes like agglomeration and/or sedimentation of the ANPs may take place, and these are not considered in modelling.

Figure 6-11 shows that the specific heat at 256 ℃ (solid) and 326 ℃ (liquid) of Sodium Nitrate-based NePCMs doped with ANPs did not vary significantly between 0 and 1 wt% of ANPs. A strong decrease was observed when the concentration of ANPs rose from 1 wt% to 1.5 wt% of ANPs. The specific heat at 256 ℃ decreased a 3.9% by simulation results and 5.2% by experimental ones from the NePCMs with 1 wt% to 1.5 wt% of ANPs. At 326 ℃, the decrease was 3.7% by simulation results and 4.4% by experimental results.

In the case of the latent heat of fusion, Figure 6-12 left, it decreased constantly within the whole range of concentration of ANPs studied. In the simulation results, the rate of decrease was lineal and between 1.3% and 1.5% when the content of ANPs was increased by 0.5 wt%. However, the experimental results showed an unexpected increase from 0.5 wt% to 1 wt% of ANPs.

Finally, the comparison of the thermal conductivity (Figure 6-12 right), led to interesting observations. Both in the solid and the liquid state, the predicted value for the Sodium Nitrate was higher than that which was experimentally measured. This is not surprising, considering that our experimental results were low compared to those published by other researchers. However, this thermal conductivity had a huge increase with the addition of 1 wt% of ANPs to the Sodium Nitrate (98% in solid and 124% in liquid). In comparison, the enhancement was minimal when predicted by the simulation programs (around 13%). This difference could mean that other factors than those considered in the simulations are implied on the rise of the thermal conductivity, such as the surface interactions of the Sodium Nitrate ions with the ANPs.

6.2.7 Conclusions

This study has performed a global analysis of the thermal properties of Sodium Nitrate-based NePCMs. The research has obtained both experimental and simulation results, which has been then compared.

Regarding the empirical analysis, several factors affecting the thermal properties have been considered: nanoparticle concentration (0.5, 1 and 1.5 wt%), nanoparticle shape and material (ANPs or SiNPs) and the purity of the Sodium Nitrate (analytical, refined or industrial). By combining these factors, 18 NePCMs have been synthetized.

The size distribution demonstrated that most of the nanoparticles maintain their nanometric size (≤100 mm) after the synthesis procedure. The surface of the nanoparticles available to interact with the Sodium Nitrate is of high importance on their thermal properties. This surface is increasing with the nanoparticles concentration in the NePCMs based on ASN and RSN but not in those containing ISN.

The thermal stability of the Sodium Nitrate is scarcely influenced by the addition of nanoparticles at the working temperatures of these materials. The presence of ANPs generates larger mass losses in the NePCMs due to its loss of interlaminar water and its conversion into γ-Al$_2$O$_3$.

The specific heat of the NePCMs followed different trends depending on the purity of the Sodium Nitrate. In this way, those based on ASN showed decrements of this property with the addition of nanoparticles, while increments were shown if the RSN was used as the base salt. The specific heat of the NePCMs containing ISN and ANPs was increased, while the contrary occurred with

the addition of SiNPs.

A decrement on the latent heat of fusion and crystallization was observed for the NePCMs based on ASN, while this property remained unchanged or with tiny increments if the Sodium Nitrate was RSN or ISN. The phase change temperatures (of fusion or solidification) of the Sodium Nitrate were not affected by the presence of the nanoparticles in no case. Subcooling around 10 ºC was observed both for the Sodium Nitrate and the NePCMs. The onset temperature of fusion followed the same trend of the latent heat.

The thermal conductivity of a NePCM of ASN and 1 wt% of ANPs was sensibly increased compared to the initial Sodium Nitrate, both in the solid and the liquid state.

The study of the microstructure of a NePCM composed of ISN and 1 wt% of ANPs revealed that the nanoparticles are agglomerated in clusters of about 1 to 3 µm in size. The compositional analysis of the images confirmed the presence of ANPs as well as some impurities coming from the ISN, such as potassium, magnesium and chlorides.

The simulation results were performed by considering the Sodium Nitrate with addition of 0.5, 1 and 1.5 wt% of ANPs. About the thermophysical properties, the simulation predicted a direct correlation between the increase on the thermal conductivity and dynamic viscosity and a higher amount of ANPs. However, the specific heat and the latent heat of fusion followed the inverse trend. The heat transfer rate was improved with the addition of the ANPs and the charging and discharging cycles were slightly shortened.

In the final section, the experimental and simulation results were compared. The predicted and measured specific heat seem to be comparable both in the solid and the liquid state. The latent heat followed the same lineal decrement with the increasing amount of ANPs, with the exception of the NePCM containing 1 wt%. The experimental enhancement of the thermal conductivity of the NePCM with 1 wt% of ANPs was much higher than the value predicted by the simulations.

It may be interesting to perform a deeper research on the thermal cycling, thermal conductivity and simulations on these materials. In general, the results obtained with this study are promising in view of the application of the NePCMs as a new generation of TES materials in CSP.

Chapter 7

STABILITY OF SOLAR SALT-BASED NANOFLUIDS IN THE LONG TERM

7 STABILITY OF SOLAR SALT-BASED NANOFLUIDS IN THE LONG TERM

7.1 INTRODUCTION

This Chapter deals with one of the main challenges of the MSBNFs: the stability of the nanoparticles in the molten salt in the long term. This is essential to maintain the extraordinary thermal properties showed by these materials. Despite its importance, there are not references in the literature considering this topic. With the aim of contributing to the knowledge of this issue, some preliminary results are presented in this Chapter.

7.2 JOURNAL CONTRIBUTION 7: STABILITY OF CERAMIC NANOPARTICLES IN MOLTEN SOLAR SALT: THE KEY FOR THE INDUSTRIAL APPLICATION OF HIGH TEMPERATURE NANOFLUIDS

Authors: Belén Muñoz-Sánchez, Javier Nieto-Maestre and Ana García-Romero
Abstract: The stability of nanoparticles in molten salts is essential to assure the excellent thermal properties of high temperature nanofluids in the long term. This research experimentally determines the evolution of ceramic nanoparticles dispersed in Solar Salt with the time. Six different nanofluids were prepared containing Solar Salt as the base material and 1 wt% of silica or alumina nanoparticles. Three different purity grades of Solar Salt were used: analytical, refined and industrial grade. These nanofluids were maintained in liquid state for 5 hours without any external stimulus. The evolution of their physical aspect, the nanoparticle size distribution and their mass concentration was analysed. The nanoparticles present in these nanofluids were quickly agglomerated and settled, except for the combination of industrial Solar Salt and 1 wt% of silica nanoparticles, which remained stable at least for 24 hours. It is though that some impurities from the molten salt are able to create a stable colloid with the silica nanoparticles. The stability of nanoparticles in the molten salt is determined by the electrostatic repulsion and Van der Vaals attraction forces between different nanoparticles and the interactions between the molten salt ions and the surface of the nanoparticles.

7.2.1 Introduction

The research on nanofluids have gained increased attention since their discovery by Choi and Eastman [42] two decades ago. These new materials are composed of a fluid where nanometric particles (<100 nm) are homogenously dispersed. The main feature of the so-called nanofluids is their improved thermal performance in comparison to the base fluid [42,43]. This is an interesting feature in many industries, and specifically in the generation of electrical energy by the Concentrated Solar Power (CSP) technology.

The principle behind this system lies on the capture and concentration of the sun rays, heating a carrier fluid in order to produce electricity in a turbine. Thus, this Heat Transfer Fluid (HTF) requires excellent thermal properties such as high specific heat and high thermal conductivity. Molten nitrate salts are currently playing this role in the CSP plants with power tower technology, due to their broader range of working temperatures (250 – 565 ºC), especially when compared to the organic thermal oils (250 – 400 ºC) presently employed in the parabolic through systems. Nitrates offer low cost, high availability and are harmless to the environment. However, these molten nitrates have a reduced thermal specific heat (for example, Solar Salt has 1.5 kJ·kg^{-1}·K^{-1} [180]) and thermal conductivity (Solar Salt has 0.5 W·m^{-1}·K^{-1} [180]). In recent years, many authors have demonstrated that the addition of nanoparticles to these salts improves their specific heat [31,32,36,61,62,74,112,113]. These new materials are known as Molten Salt-Based Nanofluids (MSBNFs) and their research is still on an initial stage.

Currently, one of the main challenges of these materials is the stability of the nanoparticles in the molten salt along the time. Their unique thermal properties are related to the nanometric size of the nanoparticles and their homogeneous dispersion in the molten salt. Thus, the stability of the nanoparticles is of high importance to ensure that the thermal features of the MSBNFs are invariable over time.

The possible degradation factors of the MSBNFs include the collision between the nanoparticles embedded in the molten salt, due to their characteristic Brownian motion. Due to their small size, after the impacts the nanoparticles may remain together because of the Van der Waals forces of attraction, in the absence of any other repulsive forces [87]. The agglomeration process is also favoured by the minimization of the free surface energy of the nanoparticles. When these aggregates reach a certain size, they will settle down and the nanoparticles will no longer be present in the bulk of the molten salt, except of a negligible quantity.

The stability of the MSBNFs depends on the characteristics of both, the suspended nanoparticles (particle morphology, chemical structure, density) and the molten salt (density, viscosity) as well as the relationship between them. The Stokes law (Eq. 7-1) predicts the sedimentation rate of spherical particles into a fluid under stationary conditions [32].

$$V = \frac{2R^2}{9\mu} (\rho_P - \rho_L) \cdot g \qquad \text{Eq. 7-1}$$

where V is the particle's sedimentation velocity (m/s); R is the spherical particle's radius (m); μ is the liquid medium viscosity (Pa·s); ρ_P and ρ_L are the particle and the liquid medium density (kg·m^{-3}), respectively and g is the acceleration of gravity (m/s^2).

The interaction forces between the nanoparticles related to their colloidal stability are usually the electrostatic repulsion and the van der Waals attraction. In addition, other forces such as hydration and steric can also impact on the colloidal stability of the system. The van der Waals forces have three components: the attraction of permanent dipoles (Keesom), the attraction between a permanent and an induced dipole (Debye) and the force between two particles which are induced dipoles (London) [87]. The latest are the forces of attraction which are present on our system of nanoparticles and molten salt.

The colloidal stability of a system is commonly evaluated according to the DVLO theory, which is accounting the global energy of interaction between the particles with the electrostatic repulsion and the van der Waals forces of attraction [87,221]. Between two particles, there is an energy barrier that should be overcome to stick and agglomerate them. The existence of ionic components into the fluid screens the electrostatic interactions and weaken this energy barrier. In a molten salt, the ionic concentration is so high that this energetic barrier is completely supressed and all the collisions between particles lead to their aggregation. These impacts are more frequent with increasing temperature of the liquid, because of a rise on the random Brownian motion of the particles.

The DVLO theory does not consider the hydrodynamic effects (hydration and solvation forces), which are depending on the medium viscosity [87,221]. The existence of a layer of fluid around the particles may delay their agglomeration due to the high difficulty to come into contact. Thus, the roughness of the particle is also of high importance on attaching these portions of liquid on its interface. These effects have been observed in dispersions of nanoparticles in ionic liquids, which possess organic ions of big size capable of effectively surrounding the nanoparticles. However, the inorganic ions composing the molten salts are quite small to reach this scenario and thus, useless for this objective. It is also unfeasible to gain colloidal stability in this ionic liquid media (molten salts) by means of particle functionalization with polymers because of their high working temperatures (>300 ºC).

In summary, controlling the homogeneous dispersion of nanoparticles in molten salt and avoiding their agglomeration in this media is a great challenge.

According to the published literature, the colloidal interactions between (nano)particles embedded in an inorganic molten salt has been deeply analysed only by Somani [87]. This author performed turbidity measurements on the long term in MSBNFs. The nanofluids employed in this study consisted of dispersions of a molten salt with 0.1 wt% of nanoparticles. Sodium nitrate (at 350 ºC) and a mixture of NaCl-KCl (at 750 ºC) were used as molten salts. Dispersions of silica, alumina and titania nanoparticles were produced (Table 7-1). A direct correlation was found between the test temperature and the nanoparticles agglomeration rate. The silica nanoparticles

had a higher agglomeration rate but the formed clusters remained dispersed in the molten sodium nitrate. This was due to the small density difference between the nanoparticles and the molten salt. This behaviour was not achieved when the other nanoparticles were dispersed in sodium nitrate or when the mixture of chlorides was used as the base fluid.

Table 7-1. Experimental details of the published studies of the stability of MSBNFs and the properties evaluated on each case. Our experimental conditions are included as a comparison.

Molten salt	Nanoparticle (wt%)	Test time (h)	Test temp. (ºC)	Evaluated properties	Ref.
NaNO$_3$ NaCl-KCl (50:50 wt%)	SiO$_2$, Al$_2$O$_3$, TiO$_2$ (0.1)	5	350 750	Visual inspection Turbidity	[87]
Solar Salt	SiO$_2$ (0.5)	12	500	Specific heat	[112]
Solar Salt	SiO$_2$ (1) Al$_2$O$_3$ (1)	6	300 – 450 (3 cycles)	Specific heat Nanoparticle concentration	[32,38]
Solar Salt Li$_2$CO$_3$ – K$_2$CO$_3$ (64:48 wt%)	Al$_2$O$_3$ (1)	896	300 – 450 (448 cycles)	Specific heat Nanoparticle concentration	[32]
Solar Salt	CuO (0.1)	≥744	300	Visual inspection Specific heat Melting point Latent heat	[31]
Solar Salt (analytical, refined and industrial grade)	Al$_2$O$_3$ (1) SiO$_2$ (1)	5	396	Visual inspection Nanoparticle size Nanoparticle concentration	This work

Other studies evaluated the long term stability by measuring changes of the nanofluid thermal properties [31,32,38,112] (Table 7-1). Mondragon and coworkers [112] evaluated the behaviour of a nanofluid composed of Solar Salt and 0.5 wt% of silica nanoparticles at 500 ºC for 12 hours. After the test, the specific heat of the fluid on the upper part of the sample was lower than the specific heat of the liquid at the bottom area, which remained with the same initial value. The authors attributed the decrease of the specific heat to the settling of the nanoparticles. Betts and Schuller [32,38] cycled a nanofluid between two temperatures in the liquid state. The specific heat of the material was measured in the liquid extracted from three different areas of the container (up, middle and bottom). The results indicated that there was not a relevant change in this property. An interesting study was carried out by Lasfargues [31] with a nanofluid composed of Solar Salt with 0.1 wt% of CuO nanoparticles, at 300 ºC. Under static conditions, the nanoparticles settled and the specific heat was significantly reduced after 840 hours. Three different strategies were analyzed in order to avoid the settling of the nanoparticles, bubbling, forced circulation and mechanical stirring. Mechanical stirring provided a proper nanoparticle dispersion and the specific heat remained unchanged along the test time. The other evaluated

techniques were less effective on retaining the initial thermophysical properties (specific heat, melting point and latent heat of fusion).

Some other additional research works related to the stability of nanofluids have been published, mostly performing thermal cycling of the nanofluids between the solid and the liquid state [32,64,89,113]. This information, although interesting, has not been included in this analysis because is out of the scope of the herein approached research.

Due to the novelty of the MSBNFs, there are not standard or agreed procedures to evaluate their stability in the long term. Thus, the experimental conditions employed on the mentioned studies are different from each other and, as a result, it is not possible to establish a direct comparison between the obtained results.

This research aims to contribute in increasing the current knowledge about the stability of MSBNFs in the foreseen working conditions. The stability of Solar Salt-based nanofluids has been analyzed by measuring nanoparticle size and nanoparticle concentration before and after the tests. In addition, a potentially critical variable has been evaluated as well: the salt purity. The research published so far has been carried out using salts of analytical grade, which are not used in the real CSP plants due to their high cost. Salts containing solid impurities (refined and industrial grade) are actually employed in the CSP plants. Performing stability test with these salts is of special importance to understand how the impurities could affect the stability of the nanoparticles in the real application of the material. It is thought that these impurities may interfere the colloidal interactions in a positive manner by generating a "solvation sphere" around the nanoparticles and, thus slowing down their agglomeration and clustering rate.

7.2.2   Materials

To prepare the Solar Salt (60:40 wt% of $NaNO_3:KNO_3$), sodium nirate and potassium nitrate were acquired in three different levels of purity: the analytical grade (onwards named with the acronym ASS) produced with $NaNO_3$ of purity$\geq$ 99.5 wt% and KNO_3 of purity $\geq$ 99.8 wt%, both supplied by Labkem; the refined grade (onwards named with the acronym RSS) produced with $NaNO_3$ of purity $\geq$ 99.5 wt% and KNO_3 of purity $\geq$ 99.6 wt%, both supplied by SQM; and the industrial grade (onwards named with the acronym ISS) produced with $NaNO_3$ of purity $\geq$ 98.0 wt% supplied by SQM and KNO_3 of purity $\geq$ 95.0 wt% supplied by Haifa Multi-K GG.

These salts were ground in a mortar, dried in an oven at 100 ºC to remove the moisture and mixed in the mentioned proportions. Then, these mixtures were melted in a furnace at 396 ºC for 30 minutes, cooled down at room temperature until their solidification and finally grounded in a

mortar to obtain a fine powder in order to ensure their homogeneity (Figure 7-1). In this way, the ASS, RSS and ISS were ready to be further mixed with the nanoparticles.

Figure 7-1. Visual appearance of the three Solar Salts in the molten state (396 ºC). ASS (left), RSS (middle), ISS (right). Solid impurities are clearly seen in RSS and ISS.

Two types of ceramic NPs were employed, Alumina Nanoparticles (onwards named with the acronym ANPs) (Figure 7-2, left) and Silica Nanoparticles (onwards named with the acronym SiNPs) (Figure 7-2, right). ANPs were purchased from Kawaken Chemicals as an industrial water-based nanofluid, Alumisol-10A, containing fiber-shaped NPs (L=50 nm, ϕ=10 nm) at 10 wt% according to the manufacturer. A dispersion of colloidal silica at 30 wt%, LUDOX® SM-30, from Sigma-Aldrich was used as a source of spherical SiNPs.
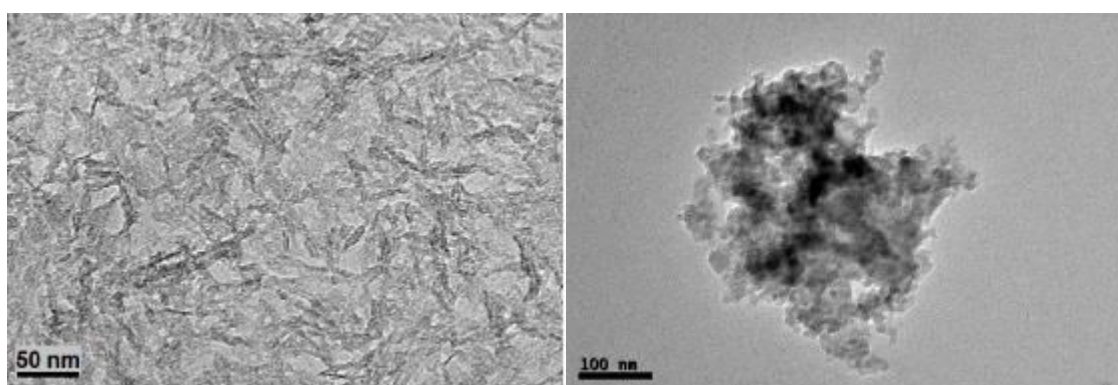
Figure 7-2. TEM images of the ANPs (left) and the SiNPs (right).

7.2.3 Synthesis of the nanofluids

Six nanofluids (Table 7-2) were prepared by dissolving the Solar Salt in water (50:50 by weight) and then adding the proper quantity of Alumisol-10A or LUDOX® SM-30 respectively to achieve the desired nanoparticle concentration (1 wt%) in the final nanofluid. All the nanofluids contained a concentration of 1 wt% of nanoparticles in the final material. The water was then removed by heating at 100 ºC in an oven. Finally, the solid material was ground in a mortar and stored in a dry place until the stability tests were done.

Table 7-2. Nomenclature and composition of the nanofluids used in this study.

	Salt purity			Nanoparticles type	
	ASS	RSS	ISS	ANPs	SiNPs
ASS1A	X			X	
ASS1Si	X				X
RSS1A		X		X	
RSS1Si		X			X
ISS1A			X	X	
ISS1Si			X		X

7.2.4 Stability tests

The nanofluids were melted inside a glass flask and maintained in the liquid state (at 396 ºC) in a furnace for a certain period to evaluate the stability of the nanoparticles. Pictures of the flasks were taken after 0.5 h, 1 h and 5 h to compare the visual appearance of the nanofluids. These periods of time were selected based on preliminary experience. In addition to this visual analysis, sampling was done at the same periods of time. As illustrated in Figure 7-3, liquids aliquots (around 5 mL) were extracted from the middle area of the flask by means of a glass pipette and were subsequently dropped onto a glass surface. Once the picture and the sample had been taken, the flask was returned into the furnace until the next sampling time. After the test, the samples were stored in a dry place for their further characterization (detailed later).

It is worth mentioning that the sampling should be done in the liquid state. Otherwise, the nanoparticles may agglomerate at the bottom during the solidification process, making it unfeasible to analyze their properties under real conditions. To determine if this assumption is correct, the nanofluid was left at room temperature after finishing the stability test until its solidification. Then, the glass flask was broken and a portion from the bottom of the sample ("sol") was extracted and characterized in the same manner as the samples extracted in the liquid state.

Four samples were extracted from the middle region of each of the six nanofluids detailed in Table 7-2, one sample after each testing period. The non-analytical Solar Salts used in this study (RSS and ISS) were also maintained in the molten state for 5 hours to analyze the stability of the contained impurities.
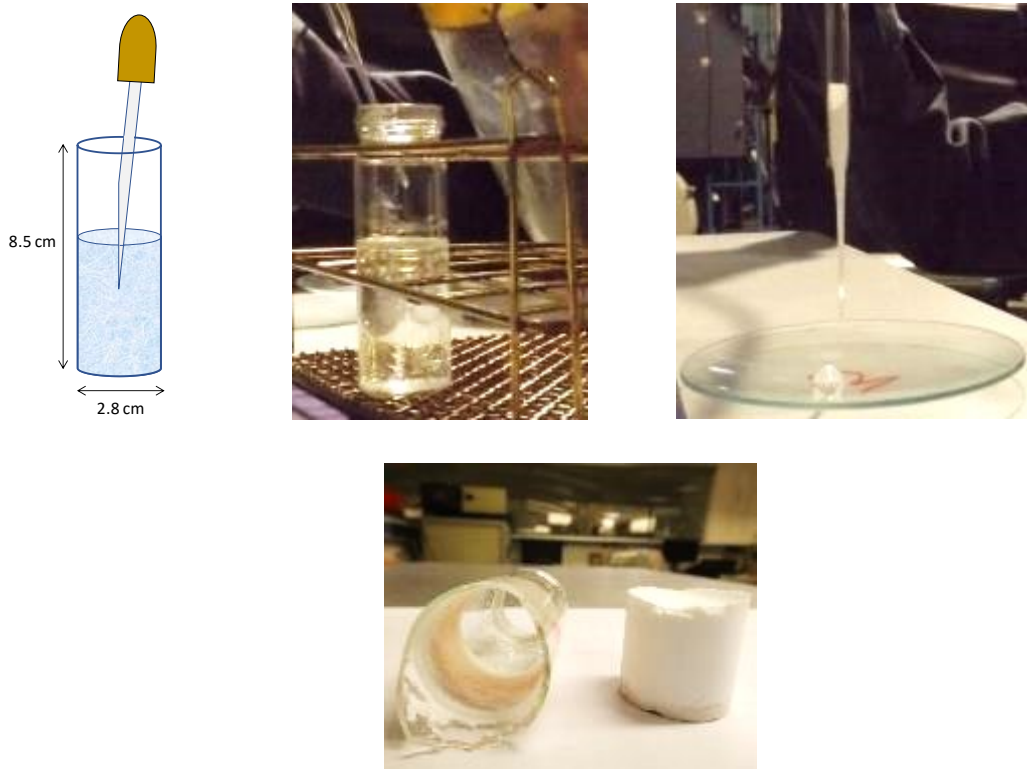
Figure 7-3. Development of the stability test: schematic representation and picture of the flask containing the nanofluid and dropping off the sample in a glass surface (up). Solid sample after the stability test (bottom).

7.2.5   Characterization

7.2.5.1 Solar Salt impurities

The main impurities contained in the supplied Solar Salts (RSS and ISS) were analysed and quantified, as they may influence the stability of the nanoparticles in the molten salts. The ASS was not considered for this analysis since its low content of impurities is outside the detection limit of the used techniques.

Specific analytical methods were carried out depending on the contaminant. Inductively coupled plasma optical emission spectrometry (ICP/OES, Thermo ICAP 7400 DUO) was used to determine sulphates, phosphates, calcium and magnesium. Ionic chromatography was employed to analyse the chlorides. The nitrites were evaluated through the colorimetric method according to the standard "4500-NO_2 –B: Nitrite by colorimetry. Standard Methods for the Examination of Water and Wastewater". Finally, the hydroxides and carbonates were analysed by titration with

HCl according to the standard UNE-EN ISO 9963-1:1996 and UNE-EN ISO 9963-2:1996, respectively.

The analysis of impurities was carried out before and after performing the stability tests (5 h in the molten state) on the solar salts (not on the nanofluids). The analysis carried out after the stability test was done over a little portion recovered from the lower side of the flask.

7.2.5.2 Nanoparticle size distribution

The size distribution of the nanoparticles was measured on the extracted aliquots with the aim of determining their agglomeration and settling in the long term. The Dynamic Light Scattering method (DLS, ZetaSizer Nano ZS, Malvern Instruments, Ltd. Malvern, UK) was employed for this purpose.

7.2.5.3 Nanoparticle concentration

The quantity of nanoparticles in the aliquots was measured to find out how many of them remained dispersed on the nanofluid after a certain period of time.

With this aim, the amount of aluminium and silicon was determined by ICP-OES (Thermo ICAP 7400 DUO) in an alkaline digestion. An amount of about 0.1 g of the solid sample was mixed with 1 g of lithium metaborate inside a platinum crucible. This mixture was melted in a furnace at 950 ºC for 20 minutes. The molten sample was then extracted in a beaker with an aqueous solution of HCl. The analysis was performed twice for each sample in order to confirm reliable results.

The mass concentration of Al_2O_3 and SiO_2 were determined from the percentages of Al and Si according to the Eq. 7-2 and Eq. 3-3, respectively.

$$\% \, Al_2O_3 = \frac{\% \, Al \cdot [Al_2O_3]_{mw}}{2 \cdot [Al]_{aw}} \qquad \text{Eq. 7-2}$$

$$\% \, SiO_2 = \frac{\% \, Si \cdot [SiO_2]_{mw}}{[Si]_{aw}} \qquad \text{Eq. 7-3}$$

where the percentages are expressed in mass fraction and *mw* and *aw* means molecular and atomic weight, respectively.

7.2.6   Results and discussion

7.2.6.1 Solar Salt

7.2.6.1.1   Visual inspection

Figure 7-4 shows the pictures of the molten salts RSS and ISS taken during the stability test. The salt ASS was not considered in this case due to its stability, as showed in Figure 7-1. As time goes by, the impurities of the molten RSS and ISS disappear from the bulk salt and concentrate at the lowest part of the flask after 5 h of test.
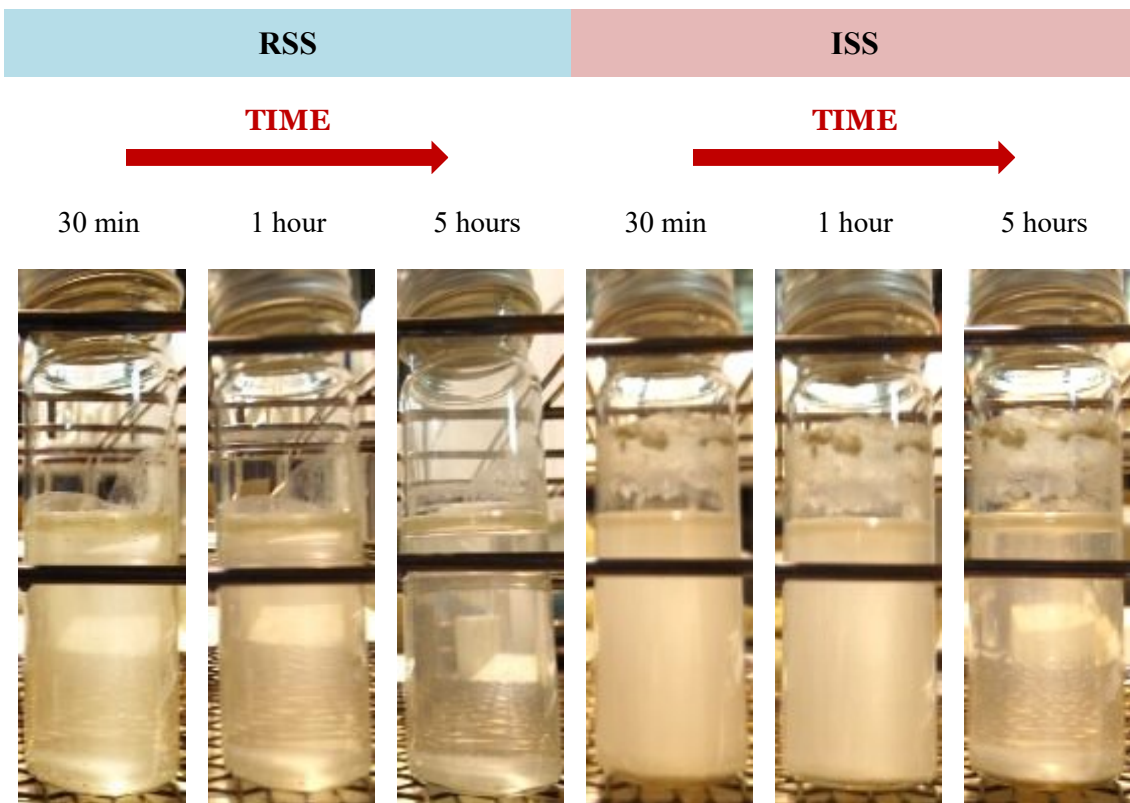
Figure 7-4. Pictures of the RSS and the ISS during the stability test. Impurities settle down at the bottom of the glass flask only after 5 h in the molten state.

7.2.6.1.2   Impurities concentration

The amount of the impurities found both in the supplied salts RSS and ISS and the samples from the bottom of the flask is gathered in Table 7-3. With the aim of comparison, these quantities are expressed in percentages and represented on the Figure 7-5. Initially, the main impurities contained both in the RSS and the ISS are chlorides and sulphates. Phosphates are more abundant in the RSS and the quantity of nitrites is very similar in the two salts. The high amount of chlorides in the ISS is the limitation to use this grade of Solar Salt in the current CSP plants, since chlorides increase the corrosion rate of the molten salt [222–224].

After being 5 hours in the molten state, the main impurities found at the bottom of the flask are phosphates and magnesium both for the RSS and the ISS. The magnesium is supposed to be initially as $Mg(NO_3)_2$ and a percentage may precipitate as MgO when heating over 330 ºC, according to the following reaction [225]:

$$Mg(NO_3)_2 \rightarrow MgO_{(s)} + 2NO_{2(g)} + \frac{1}{2}O_{2(g)}$$
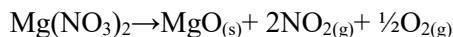
The specific reactions of other impurities that could be occurring in these molten nitrate salts during heating are not described in the literature. However, due to their ionic melt nature there will be Lux-Flood acid-base interactions between them [226].

Table 7-3. Amount of each impurity measured in the undoped RSS and ISS.

	RSS		ISS	
	Before melting (Bulk sample)	After 5 hours in the molten state (Bottom flask sample)	Before melting (Bulk sample)	After 5 hours in the molten state (Bottom flask sample)
Chlorides (total), ppm	400	500	2,460	2,300
PO_4^{3-}, ppm	230	3,200	40	800
SO_4^{2-}, ppm	1,080	1,100	780	1,000
CO_3^{2-}, ppm	<100	160	290	110
OH^-, ppm	<50	707	<50	2,350
NO_2^-, ppm	140	94	560	59
Mg^{2+}, ppm	40	500	277.2	2,300
Ca^{2+}, ppm	31.6	3,200	87.8	800
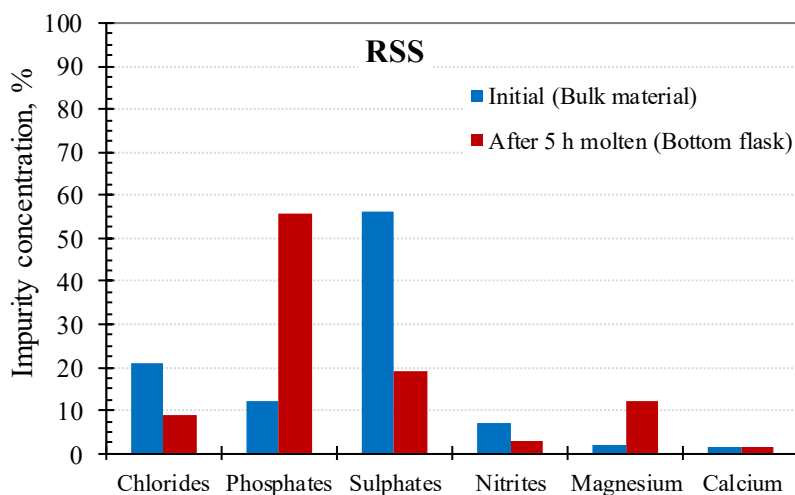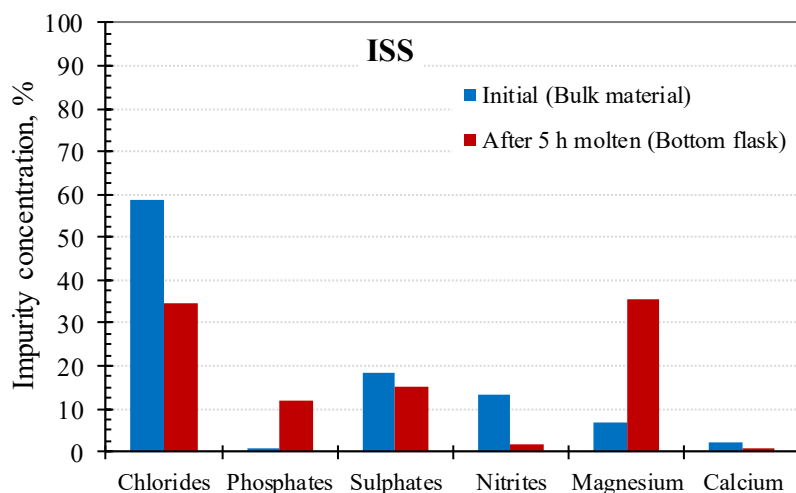
Figure 7-5. Percentage of impurities found in the bulk salt and after 5 h on the molten state in the RSS (up) and the ISS (down).

7.2.6.2 Nanofluids stability

7.2.6.2.1 Visual inspection

The pictures taken during the stability test are compared in the Figure 7-6. They are classified according to the base salt (RSS or ISS) and the nanoparticle added (ANPs or SiNPs). The ANPs settle down completely after 5 h in the molten salt. A cloud of impurities (and presumably the nanoparticles) is clearly observed at the bottom part of the flask. The nanofluids containing SiNPs show two different trends. On one side, the SiNPs are unstable in the RSS, as they sink in the molten salt after only 30 minutes of test. On the other side, a stable colloid forms between the SiNPs and the molten ISS, which is an encouraging result in comparison to the behaviour of the previous nanofluids. In view of this result, this mixture (ISS1Si) was synthetized and tested again for a longer time (24 h). Figure 7-7 shows the evolution of this second nanofluid ISS1Si along the time. The pictures are very similar to those shown in Figure 7-6 and the colloid of nanoparticles and impurities remains very stable after 24 h in the molten state. The pictures of the ISS1Si nanofluid are very alike to those presented on the Somani's doctoral dissertation [87], who studied the stability of sodium nitrate with 0.1% of SiNPs.
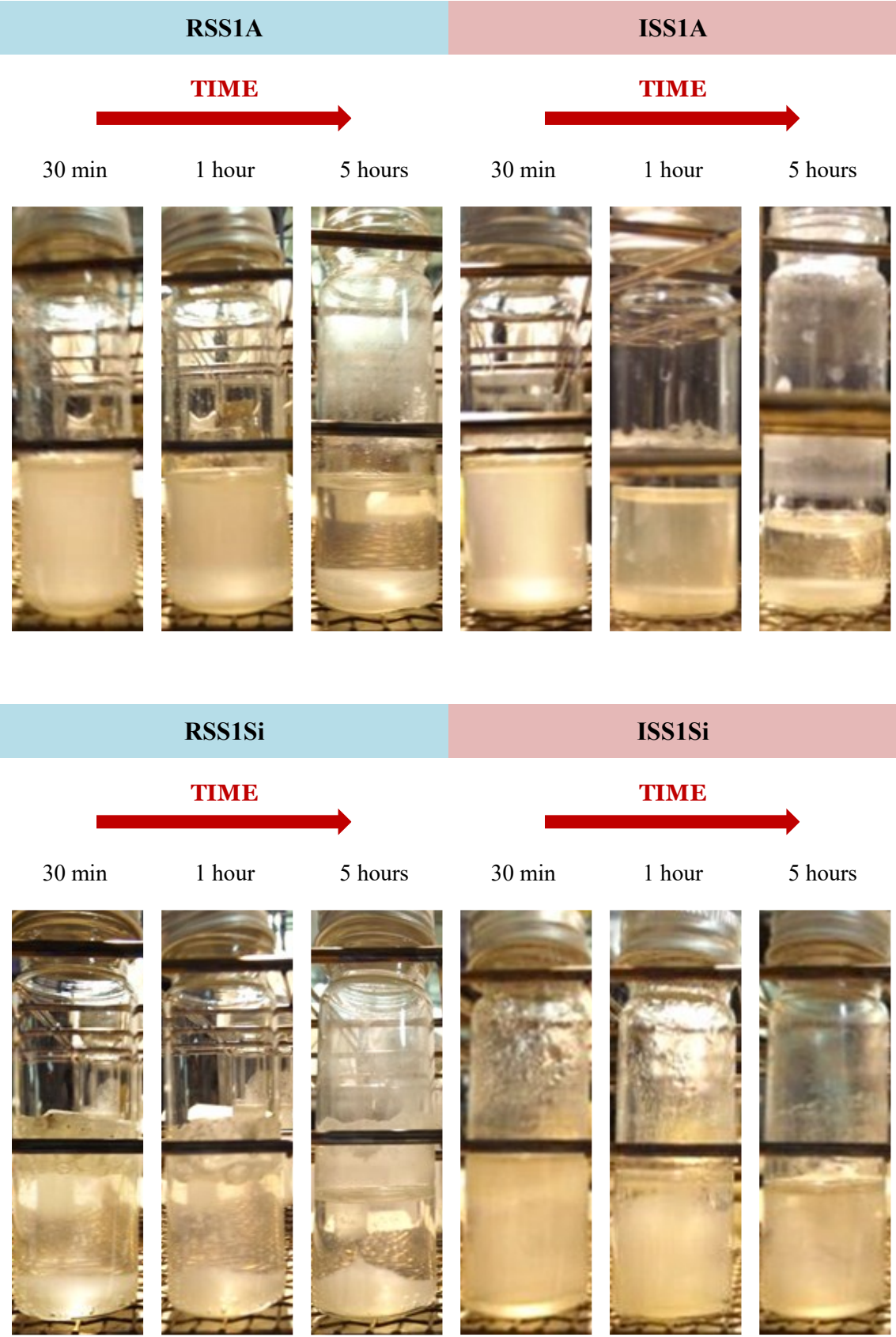
Figure 7-6. Pictures of the RSS and the ISS with ANPs and SINPs during the stability test.
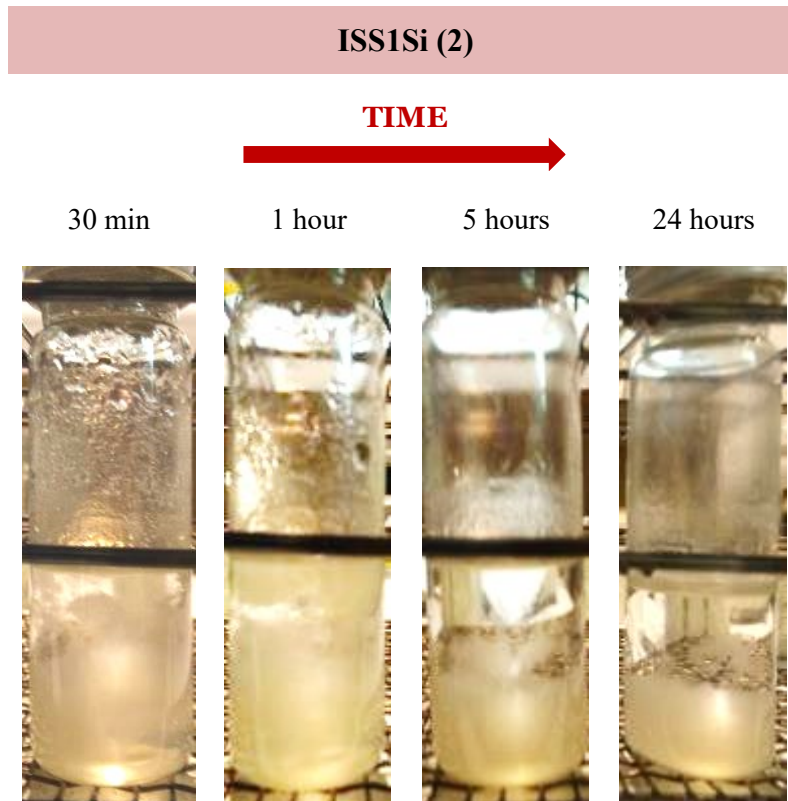
Figure 7-7. Second stability test done in the sample ISS1Si. The colloid created between the SiNPs and the impurities is still flowing into the molten salt after 24 hours.

In view of this situation, a new stability experiment was devised and performed to identify which of the ISS impurities are the responsible of this colloid stabilization. The influence of two impurities were studied: chlorides and calcium. These impurities were selected by two reasons. On one side, the amount of chlorides is near three times in the ISS (59 wt%) in comparison to the RSS (21 wt%), which led to consider that this impurity may have a high influence on the stability of the SiNPs into the ISS. On the other side, other nanofluid of HITEC XL salt with 1 wt% ANPs demonstrated high stability (unpublished results). This nitrate salt is a mixture with a high content of calcium (15 wt% of $NaNO_3$, 43 wt% of KNO_3 and 42 wt% of $Ca(NO_3)_2$).

To perform the test, four nanofluids based on ASS (without impurities) and 1 wt% of SiNPs were synthetized as explained in the Section 7.2.3. Increasing amounts of NaCl (as the source of chlorides) were included in the composition to have 0, 400, 1000 and 2000 ppm of chloride respectively, in order to emulate the concentration encountered on RSS ($\approx$ 400 ppm) and ISS ($\approx$ 2000 ppm). In addition, $Ca(NO_3)_2 \cdot 4H_2O$ (as the origin of calcium) was added to a nanofluid of ASS and 1 wt% of SiNPs in a proper amount to have 87.8 ppm of Ca^{2+} (the concentration determined in the ISS).

The pictures taken of these nanofluids along the test time are shown in Figure 7-8. The addition of chlorides seems to have no influence on maintaining the colloidal dispersion of SiNPs. All the flasks look very similar, with a white cloud at the bottom of the flask after 5 hours of test. The

addition of calcium was also ineffective on achieving a homogeneous dispersion of nanoparticles. Thus, these impurities are not the responsible of this behaviour and others or a combination between them should be tested.

Time	ASS1Si + [Cl⁻], ppm				ASS1Si + [Ca²⁺], ppm	
	0	400	1000	2000	0	87.8
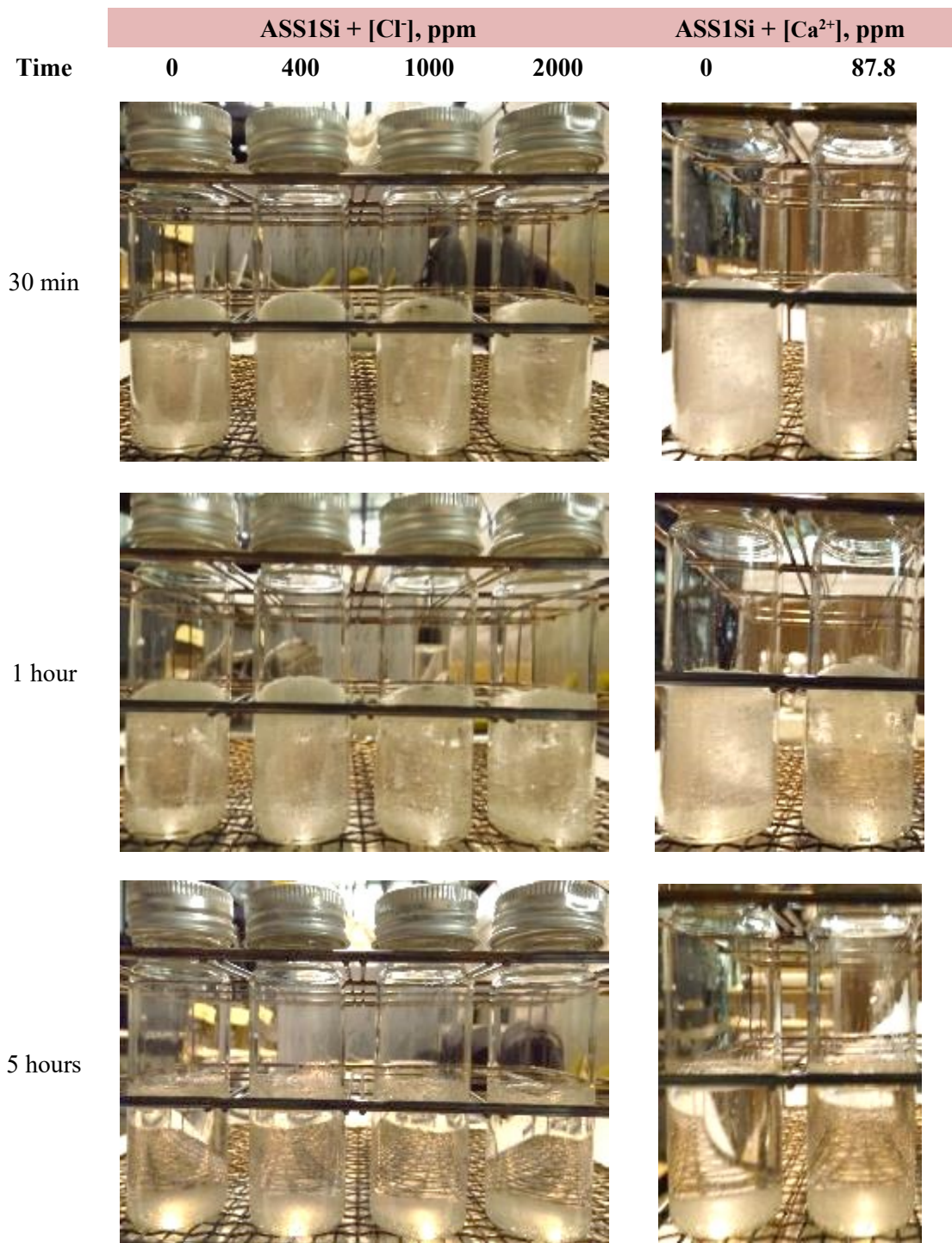
Figure 7-8. Nanofluids of ASS1Si with addition of chlorides and calcium submitted to the stability test.

7.2.6.2.2   Evolution of the nanoparticle size

The nanoparticle size distribution determined on all the nanofluid aliquots extracted from the stability tests are gathered on Figure 7-9. Different trends can be noticed in these graphs, according to the salt purity.

The ASS-based nanofluids with ANPs or SiNPs (Figure 7-9, up) have similar distributions after 30 minutes and 1 hour. In the aliquot taken after 5 hours of test, the ANPs are much bigger than the SiNPs. This fact may be related to a higher settling of the latter where only isolated small SiNPs would be dispersed in the middle of the flask. In both nanofluids, ASS1A and ASS1Si, the agglomeration of the nanoparticles is clear during the solidification process (samples called "sol"). As detailed in the methodology, these samples were taken from the bottom part of the flask after the solidification.

The nanofluid RSS1A (Figure 7-9, middle, left) shows high agglomeration (mode of 342 nm) after 30 min of starting the test. The size of these nanoparticles from the middle of the nanofluid is reducing to distributions with a mode of 220 nm (1 h) and 50 nm (5 h), which means that the largest agglomerates have settled down, and only a low amount of tiny nanoparticles remained in the bulk of the flask. The distribution of the last aliquot "sol" is into the nanometric range and very similar to that after 5 hours in the molten state. It is probable that only a tiny number of nanoparticles left suspended in the liquid and thus, they remained isolated and the crystallization process does not affect their sizes. It is also possible that the existence of a high agglomeration made more improbable to select the portion where this big agglomerates are located and led to analyse a portion with nanoparticles of small sizes. The nanoparticles on the sample RSS1Si (Figure 7-9, middle, right) follows a similar process but high agglomeration is perceived after 1 h of test. From this moment, these clusters sink into the liquid and the sizes are reduced.

Figure 7-9, bottom left, shows the evolution of the size distribution of ISS1A with the time. The nanoparticle and cluster sizes are growing in direct relation with the test time. This could be related to a certain stability of the ANPs into the ISS, due to their shape and stabilized by the impurities, despite it is not seen in the visual inspection. After the crystallization, the size distribution is smaller, as for the RSS1A. The ISS1Si (Figure 7-9, bottom, right) shows the opposite trend, where the sizes are smaller with the time and the crystallization creates big clusters of nanoparticles. This fact could be indicative of the agglomeration and settling of the SiNPs, remaining the smallest nanoparticles in suspension in the ISS. They should be in the cloud seen in the visual inspection (Figure 7-6).
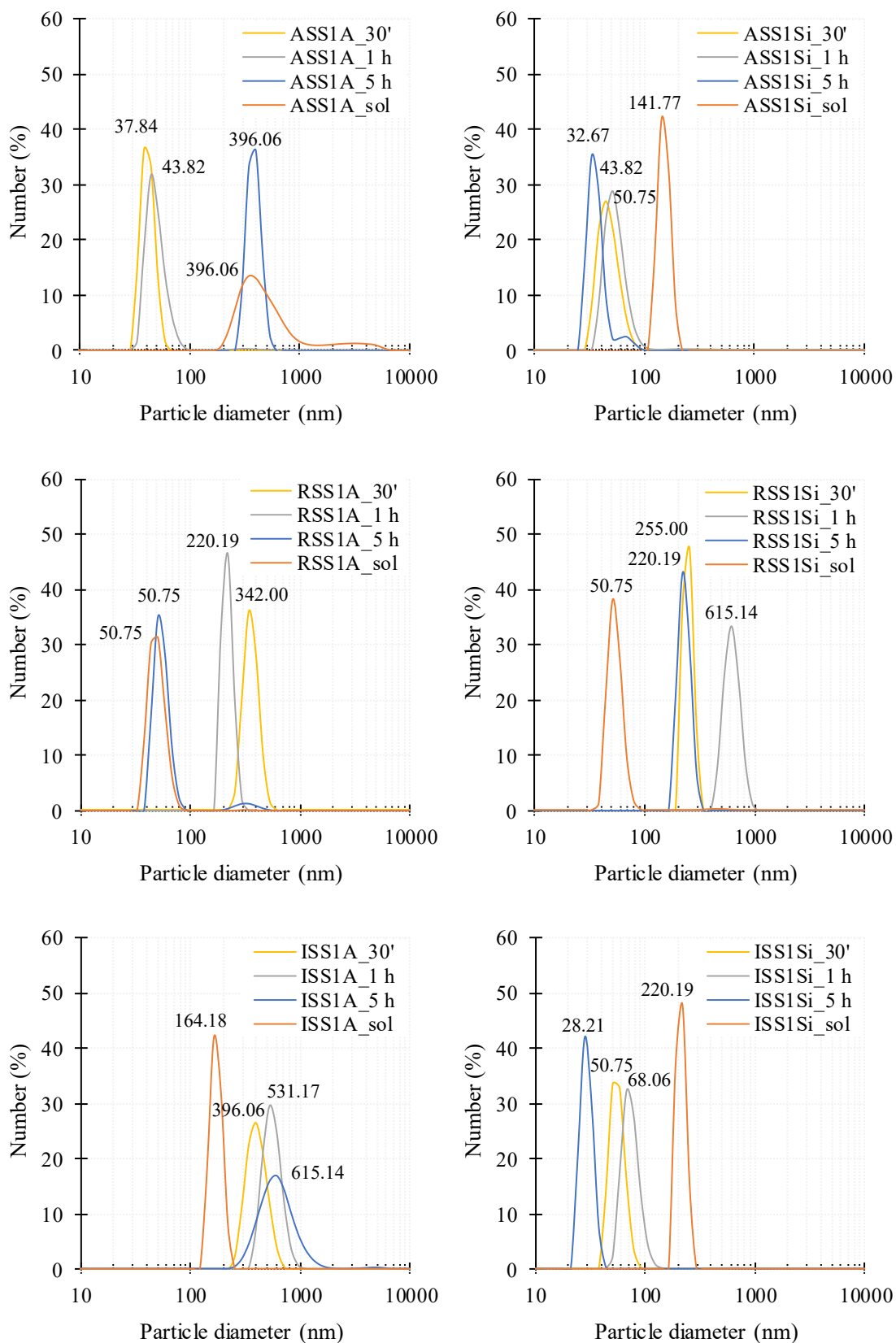
Figure 7-9. Nanoparticle size distribution of the tested nanofluids according to the sampling time. The denomination "sol" is related to those samples recovered in the solid state after the test. The mode of each distribution is indicated by a number.

7.2.6.2.3   Evolution of the nanoparticle concentration

The Figure 7-10 shows the results of the nanoparticle concentration measured by ICP for the aliquots of each of the studied nanofluids. The data missing in this graph are those samples which mass percentage of nanoparticles is below the detection limit of the technique and consequently cannot be quantified. The data with 0 wt% of nanoparticles are those detected with very low amount and in the detection limit.

The ANPs reduce very fast their concentration in the core of the molten salt. The measured concentrations in the nanofluids RSS1A and ISS1A are very low and in the detection limit of the technique only after 1 hour. It seems that at least a little amount of the ANPs in the nanofluid ASS1A are able to remain dispersed after being 5 hours in the molten salt (0.19 wt% of Al_2O_3). On the other side, the SiNPs exhibit dissimilar trends depending on the salt purity. The RSS1Si is quickly losing the nanoparticles in the molten salt core, in the same manner as the nanofluids with ANPs. The nanofluid based on ASS has a constant amount of SiNPs in the molten salt (0.3 wt%) until the end of the test. Higher concentration of SiNPs were found in the nanofluid ISS1Si, ranging from 1.33 and 0.86 along the test time. This fact confirms the enhanced stability of this pair of molten salt and nanoparticles observed in Figure 7-7 and having nanoparticles of sizes between 20 and 35 nm (Figure 7-9, down right).
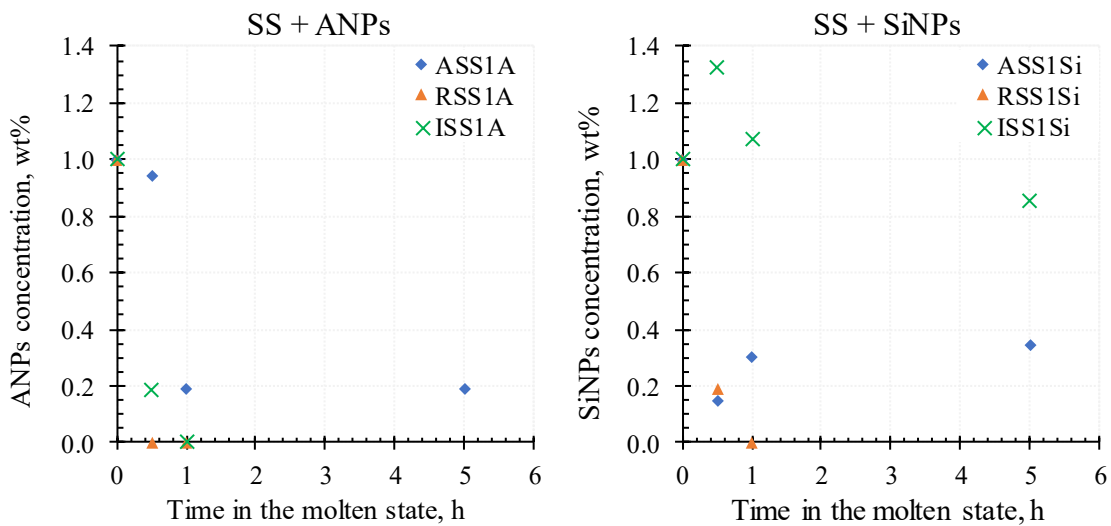
Figure 7-10. Evolution of the nanoparticle concentration versus the test time for nanofluids with ANPs (left) and SiNPs (right).

7.2.6.2.4   Estimation of the settling time

As seen in the previous discussion, the nanoparticles are agglomerated and settled in the molten salt in a short time (<5 hours). The Stokes law (Eq. 7-1) can be used to have an approximate prediction of the settling time of the nanoparticles depending exclusively on the viscosity and density of the fluid and the size and density of the nanoparticles in absence of any other external force. The settling time of the ANPs can also be analysed with the Stokes law though is valid for spherical nanoparticles, since the size obtained from DLS measurements (used for the calculations) accounts for the solvation sphere around the nanoparticle.

Table 7-4 is showing the results for each nanofluid submitted to the stability tests. The nanoparticle diameter ($D_{30'}$) consider on each case is the mode of the size distributions after 30 minutes in the liquid state (Figure 7-9). The sedimentation velocity is calculated with the Eq. 7-1 and the needed time to cover the length of the flask (4 cm) is also determined.

The computed results give an idea of the strong dependence of the nanoparticle size and the settling rate. If the diameter is in the nanometric range (<100 nm), the velocity is below 10^{-10} m/s but this value is greatly increased if the size is a hundred of nanometers. The difference of density between the nanoparticle and the molten salt is also influencing the results. This divergence is higher if ANPs are used, with the subsequent increment on their sedimentation velocity.

Our results on the settling rate of ANPs in molten SS of analytical grade (nanofluid ASS1A) are in the same order with those calculated by Schuller et al. [32] ($4.52 \cdot 10^{-10}$ m/s).

The estimated time of settling in our experimental arrangement (t_{4cm}) is not coincident with the behaviour of the samples according to the visual inspection (Figure 7-6) or the measurement of the nanoparticle amount (Figure 7-10). This contrast indicates that other phenomena are influencing the settling of the nanoparticles. These may be related to the Brownian motion and the colloidal interactions described in the introduction: the London forces created between two induced dipoles. Modelling and simulation tools are needed to perform an in-depth analysis of these forces. The scientific knowledge of this topic is very scarce and dispersed in the literature and any detailed prediction can be made in these systems with the obtained information.

Table 7-4. Estimation of the settling rate of the nanoparticles (V) according to the Stokes law. The minimum time to cover a distance of 4 cm (length of the flask) is also included.

μ_{SS} (396 °C) =	3 mPa·s	ρ_{Al2O3} =	3,960 kg·m^{-3}
ρ_{SS} (396 °C) =	1,838 kg·m^{-3}	ρ_{SiO2} =	2,650 kg·m^{-3}

	$D_{30'}$, nm	V, 10^{10} m/s	$t_{4\,cm}$, hours (years)
ASS1A	37.84	5.48	20245 (2.31)
RSS1A	342	448.31	10.33
ISS1A	396.06	601.24	7.70
ASS1Si	43.82	2.83	39267 (4.48)
RSS1Si	255	95.82	48.31
ISS1Si	50.75	3.79	29275 (3.34)

7.2.6.2.5　Global comparison of results

This final section aims to draw an overall analysis which gathers the described properties and results. There are different trends and behaviours depending on the purity of the base salt and the nanoparticle.

The nanofluids containing ASS are showing nanoparticles under 100 nm during the stability test (Figure 7-9). The nanoparticle concentration is quickly reduced (<1 hour) from the initial 1 wt% to 0.2 wt% in the molten salt in the nanofluid containing ANPs. The concentration maintains constant (0.3 wt%) in the nanofluid of ASS with SiNPs after 5 hours.

The pictures of the RSS-based nanofluids (Figure 7-6) revealed the fast settling of the nanoparticles, specially the SiNPs, in this molten salt. The sizes are in the range of 200 – 300 nm and the available surface of the nanoparticles is decreasing as the time goes on. The amount of nanoparticles dispersed into the molten salt is very little (0.1 wt%) in comparison to their initial concentration only after 1 hour of test.

The nanofluids with the ISS as the base fluid had dissimilar behaviour depending on the added nanoparticle. Along the pictures in Figure 7-6, the ANPs are quickly sunk in the molten salt while the SiNPs are arranged in a stable colloid which remains at least for 24 hours. The nanoparticle sizes are of several hundred nanometres for the nanofluid with ANPs and under 100 nm for that with SiNPs. This behaviour was directly reflected on the available surface: the nanofluid ISS1Si had the highest value of any sample analysed in this study. The unusual stability of this nanofluid is noticeable according to the high nanoparticle concentration in the molten salt (Figure 7-10). The influence of some Solar Salt impurities (chlorides and calcium) on this behaviour was discarded through visual inspection. It is though that others such as magnesium, sulphates or a combination between them could have the answer.

7.2.7 Conclusions

This study analyses the complex issue of the stability of nanoparticles in molten salts. A specific test was designed to track the time that the nanoparticles remained dispersed in the core of the molten salt. Six nanofluids containing Solar Salt of different purities (analytical, refined and industrial grade) as the base salt and two nanoparticles (silica and alumina nanoparticles) at a mass concentration of 1% were submitted to this test. The results from the characterization of the samples at different times (0.5, 1 and 5 hours) suggested discrepancies between the nanofluids depending on the base salt. After 5 hours in the molten state, the nanoparticles were agglomerated and settled down at the bottom of the flask in every of the studied nanofluids. The exception was found for the nanofluid with Solar Salt of industrial grade and 1 wt% of silica nanoparticles, which seems stable at least for 24 hours. A deep simulation and modelling work is needed to have a wider understanding of this phenomena. The inexistence of specialized publications on the interactions of ceramic nanoparticles and molten salts makes very difficult to enunciate or propose any mechanism to explain this phenomenon in detail.

At this moment, the absence of a homogeneous nanoparticle dispersion in the long term in MSBNFs is one of the main challenges to the industrial application of these materials. An external physical force such as ultrasounds or mechanical stirring of the nanofluid is needed to maintain this dispersion and avoid the nanoparticle agglomeration.

7.3   Conference contribution 5: Molten Salt Based Nanofluids Based on Solar Salt and Alumina Nanoparticles: an Industrial Approach

Authors: Belén Muñoz-Sánchez, Javier Nieto-Maestre, Luis Guerreiro, José Enrique Juliá, Manuel Collares Pereira and Ana García-Romero.

Abstract: Thermal Energy Storage (TES) and its associated dispatchability is extremely important in Concentrated Solar Power (CSP) plants since it represents the main advantage of CSP technology in relation to other renewable energy sources like photovoltaic (PV). Molten salts are used in CSP plants as a TES material because of their high operational temperature and stability of up to 600°C. Their main problems are their relative poor thermal properties and energy storage density. A simple cost-effective way to improve the thermal properties of molten salts is to dope them with nanoparticles, thus obtaining the so-called salt-based nanofluids. Additionally, the use of molten salt based nanofluids as TES materials and Heat Transfer Fluid (HTF) has been attracting great interest in recent years. The addition of tiny amounts of nanoparticles to the base salt can improve its specific heat as shown by different authors [38,72,113]. The application of these nano-enhanced materials can lead to important savings on the investment costs in new TES systems for CSP plants. However, there is still a long way to go in order to achieve a commercial product. In this sense, the improvement of the stability of the nanofluids is a key factor. The stability of nanofluids will depend on the nature and size of the nanoparticles, the base salt and the interactions between them. In this work, Solar Salt (SS) commonly used in CSP plants (60 wt% $NaNO_3$ + 40 wt% KNO_3) was doped with alumina nanoparticles (ANPs) at a solid mass concentration of 1 wt% at laboratory scale. The tendency of nanoparticles to agglomeration and sedimentation is tested in the molten state by analyzing their size and concentration through the time. The specific heat of the nanofluid at 396 ºC (molten state) is measured at different times (30 min, 1 h, 5 h). Further research is needed to understand the mechanisms of agglomeration. A good understanding of the interactions between the nanoparticle surface and the ionic media would provide the tools to avoid agglomeration and sedimentation.

7.3.1   Introduction

TES in CSP plants is an effective way to produce, store and have a high dispatchability of electricity. This is the main advantage of this technology when comparing with PV or other renewable energy forms.

In order to collect this energy and to have a higher power block efficiency, molten salts are used in CSP plants, for now mainly as a TES material, in the future more and more also as the HTF from the solar field. Their stability up to 600 °C has been proved, however there is still potential to improve their thermal properties and energy storage density. A simple cost-effective way to improve it is to dope them with nanoparticles, thus obtaining the so-called salt-based nanofluids, a topic that has been attracting great interest in recent years.

Especially relevant is the stability of this nanofluid and its heat capacity. If both features are guaranteed, this would mean that the fluid would increase the overall plant efficiency since it would increase its heat transfer capability, and thus for the same energy yield one could have a smaller storage system, and thus a higher return and a lower Levelized Cost of Electricity (LCOE). Therefore, analysing this stability on the short and medium time range is an important issue.

7.3.2 Aim

The aim of this work is the development of a nanofluid based on SS and ANPs. The heat transfer properties of this molten salt based nanofluid (MSBNF) as well as its stability under working conditions will be analysed in order to evaluate the possible application of this nanomaterial on real TES systems for CSP Plants.

7.3.3 Method

7.3.3.1 Raw Materials

7.3.3.1.1 Solar Salt

Prills of sodium nitrate (Refined grade, SQM) and potassium nitrate (Refined grade, SQM) were used as starting materials. The refined grade of purity is commonly used in TES systems for CSP Plants, due to the low chloride content (<0.1 wt%) that guarantees a good chemical compatibility with the containing materials. First of all, the prills were milled in a mortar and dried in an oven at 100 ºC for 1 hour to remove any trace of moisture. Then, sodium nitrate (SN) and potassium nitrate (PN) were mixed to obtain the composition of 60 wt% SN and 40 wt% PN. The mixture was then melted in a furnace at 396 ºC for ½ h to achieve a homogeneous base salt. After cooling it to room temperature, the salt was crushed in a mortar and stored under dry conditions.

7.3.3.1.2 Nanoparticles

A water dispersion of ANPs known as Alumisol-10A supplied by Kawaken Fine Chemicals Co. with a concentration of ANPs of 10 wt% was used as received. The initial NP size was 10 nm according to the specifications of the manufacturer.

7.3.3.2 Nanofluid Synthesis Procedure

First, the solid SS was dissolved in water. Then, the necessary amount of Alumisol-10A was added drop by drop under mild stirring. The solution was poured into a Petri Dish and the water was removed by heating at 100 ºC in an oven. The dried material was scrapped off and placed onto a glass vial to perform the stability test.

7.3.3.3 Stability Test

Two flasks containing SS and the SS-based nanofluid doped with 1% of ANPs (SS1A) were melted in a furnace at 396 ºC. The flasks were taken out from the furnace at specific times (30 min, 1 h and 5 h) for visual inspection and sampling for measuring the ANPs size distribution, their concentration and specific heat. The samples were taken from the middle of the flask in the molten state and dropped on the surface of a watchglass. Fast cooling was procured in order to avoid agglomeration of NPs during the solidification of this little portion. The solidified sample was milled and stored for further analysis.

7.3.3.4 Characterization Methods

7.3.3.4.1   Dynamic Light Scattering (DLS)

The nanoparticle size distribution of the ANPs and the sample SS1A was characterized using the DLS technique (ZetaSizer Nano ZS, Malvern Instruments, Ltd. Malvern, UK). The procedure of measurement consisted of dissolving the sample in water at a specific concentration depending on the expected sizes of the NPs in agreement with the Malvern experts' advices. In the case of the initial NP distribution of sizes, the concentration was 0.5 mg·mL^{-1}. Though, in the case of the SS doped with ANPs (SS1A), a concentration of 0.1 mg·mL^{-1} was more appropriate to perform the measurement. The method takes into account the presence of nitrates in the water dispersion. For this purpose, the refractive index (RI) and the viscosity of the base nitrate solution were introduced as parameters. The distribution of sizes, the Z_{ave} (the mean diameter obtained from the cumulative analysis of sizes) and the first peak (nm) were obtained and compared.

7.3.3.4.2   Transmission Electron Microscopy (TEM)

The size and the shape of the ANPs were observed by means of TEM using a device JEOL 2100 operating at a voltage of 100 kV.

7.3.3.4.3   Inductively Coupled Plasma (ICP)

The analysis of aluminium is carried out by inductively coupled plasma optical emission spectrometry (ICP-OES), Thermo ICAP 7400 DUO, previous alkaline fusion of the sample. The analysis was performed twice for each sample in order to obtain reliable results.

7.3.3.4.4   Differential Scanning Calorimetry (DSC)

A MDSC device (TA Instruments, Q1000) was used to measure the c_p of the SS and the MSBNF with ANPs (SS1A). An isothermal procedure was using with the MDSC method of the equipment. The modulation was set up with 0.6 ºC of amplitude and a 110 s period according to the TA

Instruments expert advices. A weight of around 25 mg of the sample was introduced in an aluminum pan, dried on a hotplate at 100 ºC and sealed hermetically under dry argon atmosphere (<0.5 ppm H_2O, <0.5 ppm O_2). A stabilization period of 10 min at 396 ºC was performed to achieve the salt thermal equilibrium prior to data collection (20 min). The same protocol was employed for the other two temperatures (296 ºC and 196 ºC). The sapphire sample commonly used as the reference material was first measured under the same protocol in order to detect possible device divergences and correct the final sample results. Three different replicas were measured for each sample, and the average c_p and the Standard Deviation (SD) were obtained.

7.3.4 Results and discussion

7.3.4.1 Nanofluid Synthesis

A nanofluid based on SS doped with 1% of ANPs was synthetized. During the preparation, the starting NP size was 10 nm, according to the TEM image (Figure 7-11a). The sizes were increased (Figure 7-11b) during the different stages of the synthesis (mixing and drying), but after the drying stage, the NP sizes are within the nanometrical range (0-100 nm).

Figure 7-12 shows the evolution of the parameters Z_{ave} and the highest peak of the distribution during the different stages of fabrication. It should be considered that the ANPs are not spherical, but flat-shaped (Figure 7-11a). The size measurements are done considering the equivalent spherical diameter of the NP. Therefore, the Z_{ave} and the highest peak data may not be the mean size of the NPs.

(a)   (b)
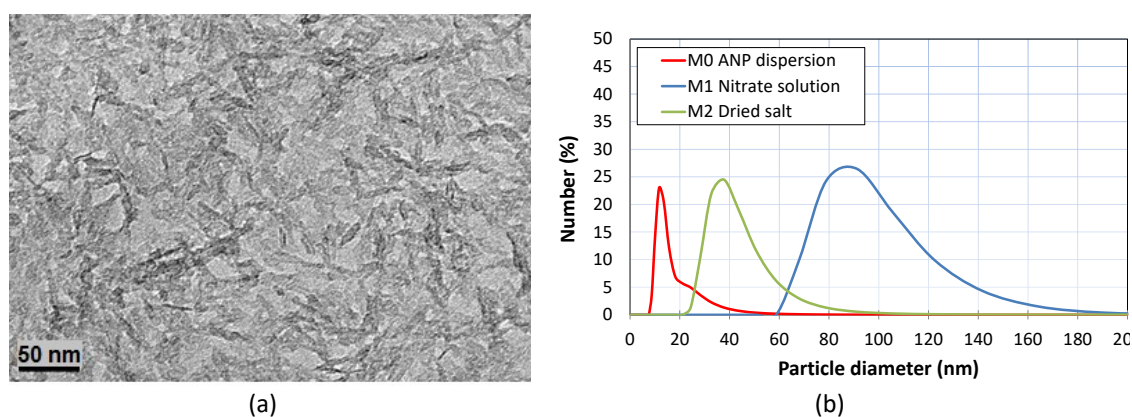
Figure 7-11. Sizes of the initial ANPs (a) and distribution of sizes during the different preparation stages (b)
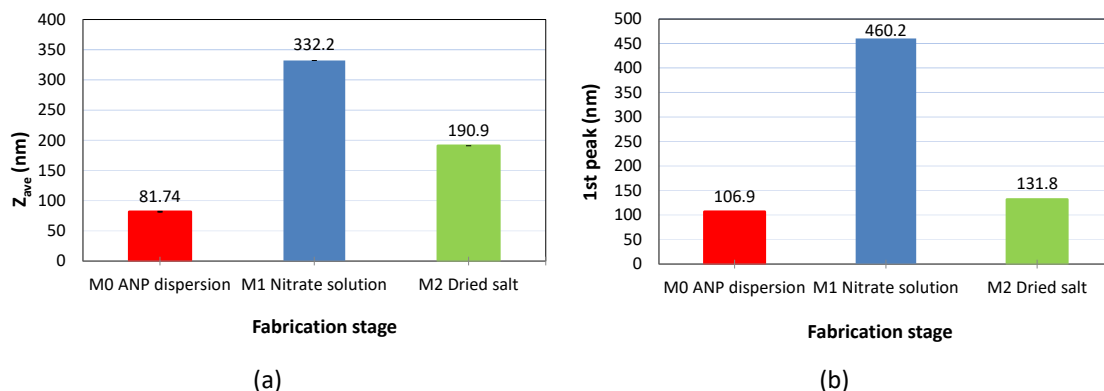
Figure 7-12. Z_{ave} measurements (a) and first peak (b) during the different preparation stages.

7.3.4.2 Stability Test

The pictures shown in Figure 7-13 show the appearance of the SS and the SS1A at different times during the stability tests at 396 ºC. A solid white layer is clearly differenced from the supernatant clear molten salt in the case of the SS doped with ANPs SS1A. This layer is not so clear in the case of the base SS. The reason is the agglomeration and sedimentation of the ANPs with time. The NPs (0-100 nm) are normally invisible, but as soon as they agglomerate to form bigger clusters, they become visible. The NPs are dispersed in the molten salt because of their nanometric sizes. The higher the available surface of the NPs, the higher the interaction with the surrounding ions that prevents them from agglomeration and sedimentation. If this interaction is not strong enough, the NPs will agglomerate. Then, sedimentation may occur as a consequence of the difference of density between the NP material [227] and the base salt [203].

In spite of starting from refined SN and PN, these salts always contain impurities that also precipitate with the time. The presence of impurities may affect the stability of the NPs. The white layer observed in the doped molten salt is probably a mixture of agglomerated NPs and insoluble impurities from the base salt.

SS 30 min SS 1h SS 5 h

SS1A 30 min SS1A 1h SS1A 5h
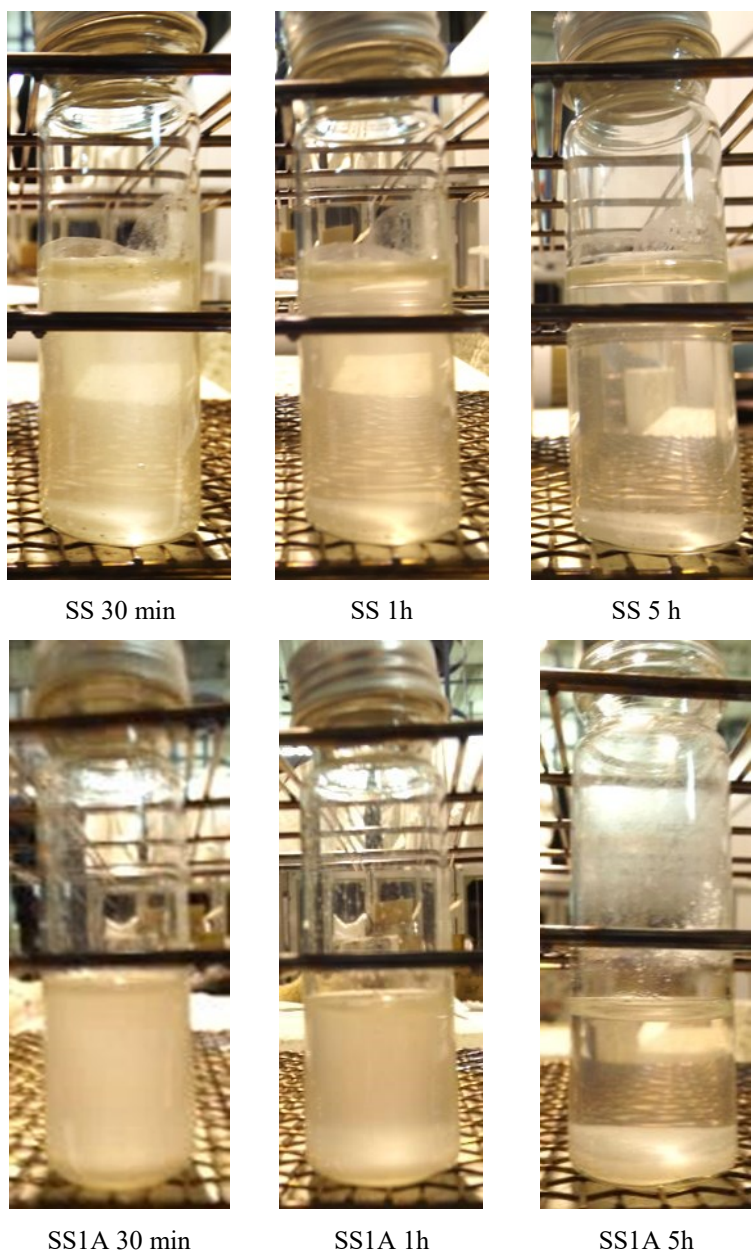
Figure 7-13. Evolution of SS and SS doped with 1% of ANPs with time (30 min, 1 h and 5h)

Figure 7-14 shows the Z_{ave} values (Figure 7-14a) and the distribution of sizes vs time (Figure 7-14b). As time goes on, the distribution of sizes is becoming narrower and moving to lower sizes. This shows an agglomeration process where the NPs grow and then fall down to the bottom of the flask. The measurement of the distribution of sizes is performed on a sample that was taken from the middle of the flask. For this reason, the sizes of NPs are becoming lower with time. As it was explained before, the Z_{ave} is a parameter provided by the device showing the mean diameter obtained from the cumulative analysis of sizes. The behaviour of Z_{ave} could seem strange: an increase in the first 1 h, and a decrease after 5 h. However, this could be a proof of the process of agglomeration plus sedimentation that takes place in the sample. The count rate in kcounts per second (kcps) is a parameter related to the duration of the measurement. The lower the count rate, the longer the duration will be. This parameter is affected by the amount of ANPs within the

sample. The lower the ANP concentration, the lower the count rate is. As it can be seen in Figure 7-15, the evolution of the count rate follows the same pattern as the Z_{ave}. A count rate of 38.7 after 5 h reveals a very low concentration of ANPs in this sample.

(a)   (b)
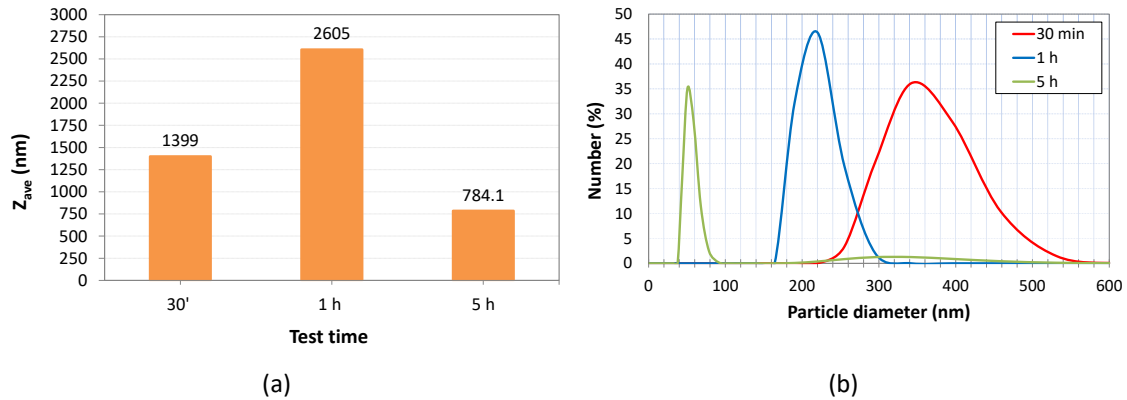
Figure 7-14. Evolution of the Z_{ave} (a) and the distribution of sizes of SS1A with time (b).
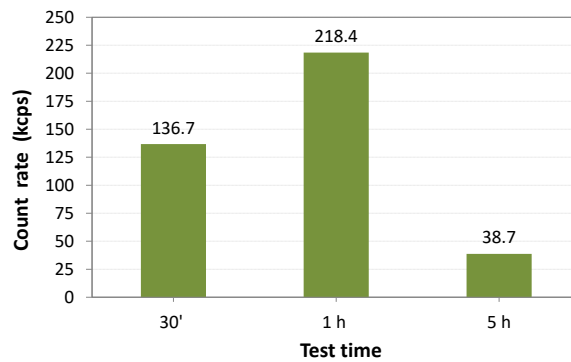
Figure 7-15. Evolution of the count rate for the size distribution of SS1A with the test time.

The result of the ICP test performed to the sample at 30 min shows a concentration of Al below the limit of detection of the device (<0.05 wt%). This means that the concentration of Al_2O_3 is very low. The process of agglomeration and sedimentation of NPs is faster than expected from the pictures and DLS measurements. The measured sizes of ANPs measured by DLS are due to a small fraction of the ANPs that still remains disperse within the molten salt after 30 min.

With regard to the c_p measurements (Table 7-5), no increment on the c_p was found on the SS-based nanofluid SS1A with respect to the base salt after 30 min. The c_p of the nanofluid resulted to be very similar to the base salt. Due to the low concentration of ANPs that remains in the nanofluid, as measured by the ICP analysis, there is almost no effect of the addition of ANPs on the c_p of the material.

Table 7-5. c_p measurements on SS, SS doped with 1% ANPs SS1A, the Δc_p (%) and the RSE (%)

c_p	SS	SS1A 30 min	Δc_p	RSE
	$kJ \cdot kg^{-1} \cdot K^{-1}$	$kJ \cdot kg^{-1} \cdot K^{-1}$	%	%
196 ºC	1.451	1.472	1.42	11.75
296 ºC	1.602	1.616	0.85	9.88
396 ºC	1.612	1.624	0.72	9.82

7.3.5   Conclusions

The study of the stability of ANPs in a molten salt with time has been analyzed. A nanofluid based on SS and 1 wt% of ANPs was successfully synthetized at a laboratory scale and the distribution of sizes of ANPs was within a nanometrical range (0-100 nm) before performing the test. However, these ANPs got quickly agglomerated and their sedimentation took place only after 30 minutes of test. In addition, the specific heat of the SS was not enhanced by the addition of the ANPs

Further research should be done to understand the mechanisms of agglomeration and sedimentation of nanoparticles in MSBNFs and to find a strategy to avoid this phenomenon. Experiments shall be made both in static and dynamic conditions for a reasonable period of time (>150 h). This is the only way to warrant a future application of the nanotechnology on TES systems for CSP Plants.

Chapter 8

RHEOLOGY OF SOLAR SALT-BASED NANOFLUIDS

8   RHEOLOGY OF SOLAR SALT-BASED NANOFLUIDS

8.1   INTRODUCTION

This Chapter describes the deep research performed on the rheological properties of the nanofluids. The Journal Contribution 9 is the result of the fruitful collaboration between different research groups to study this subject. The article is reproduced hereafter as in the original manuscript.

8.2   JOURNAL CONTRIBUTION 8. RHEOLOGY OF SOLAR-SALT BASED NANOFLUIDS FOR CONCENTRATED SOLAR POWER. INFLUENCE OF THE SALT PURITY, NANOPARTICLE CONCENTRATION, TEMPERATURE AND RHEOMETER GEOMETRY

Authors: Belén Muñoz-Sánchez, Javier Nieto-Maestre, Elisabetta Veca, Raffaele Liberatore, Salvatore Sau, Helena Navarro, Yulong Ding, Nuria Navarrete, J. Enrique Juliá, Ángel G. Fernández and Ana García-Romero

Abstract: Solar Salt-based nanofluids have attracted significant scientific interest in recent years due to their improved thermal properties, making them strong candidates as thermal energy storage materials and/or heat transfer fluids in CSP plants. There have been reports on increased specific heat due to the addition of nanoparticles, however, there is a lack of comprehensive information on other essential properties affecting the heat transfer, such as the viscosity. This article concerns the rheological behaviour of nanofluids made of Solar Salt (mass percentage at 60% $NaNO_3$ - 40% KNO_3) as the base fluid and silica or alumina nanoparticles as additives. The evolution of these nanofluids viscosity as a function of the shear rate (1 - 1000 s^{-1}) at a temperature range of 250 ºC - 400 ºC was measured and analysed. The impact of the salt purity (refined or industrial grade), the nanoparticle concentration (0.5% - 1.5 wt%) and the rheometer measuring configuration (coaxial cylinder or parallel plate) are examined. The results showed in general a Newtonian behaviour of the nanofluids with independency of the rheometer configuration. The relationship between the viscosity and the temperature follows an Arrhenius model. The influence of the nanoparticle concentration on the viscosity of the refined grade Solar Salt is analysed according to the Maron-Pierce and Kriegher-Dougherty models for the nanofluids containing alumina and silica nanoparticles respectively, due to their different shape

8.2.1   Introduction

The worldwide increasing energy demand compels to use and develop new technologies based on renewable resources. The main disadvantage of these sustainable energy sources is their intermittence and thus, their low availability on demand in comparison to the non-renewable energy resources. In this context, the Concentrated Solar Power (CSP) technology is of high

importance due to its proven dispatchability and efficiency [228–232]. Although the electricity costs are still high, they are expected to decrease consistently in the years to come [233]. The use of a Thermal Energy Storage (TES) system in the current CSP plants allows to size the storage system according to the requested plant operation time. For example, at the moment Termosol 1 and 2 (solar trough technology) in Spain reach 9 hours of thermal storage [234] and Gemasolar (solar central receiver system) even reachs 15 hours, allowing in some periods the daily continuity production [235,236]. The presently employed TES systems store the energy as sensible heat. They consist of two tanks filled with a molten salt at different temperatures: the "cold" tank is around 300 ºC and the "hot" tank at 400 ºC in the solar plants with parabolic through technology, and 565 ºC in the plants with power tower technology, respectively. This salt is a mixture of sodium and potassium nitrate (60:40 wt%) known as Solar Salt, with a melting point of 238 ºC [140,237]. This mixture is used instead the eutectic one ($NaNO_3$:KNO_3 50:50 wt%) to reduce the material costs [174]. Presently, the working temperature in the solar field is becoming increasingly higher in modern central receiver plants (tower), and therefore, Heat Transfer Fluids (HTFs) with a broader range of thermal stability are required. So far, thermal oils (Dowtherm™, Therminol® VP-1) have been mostly used as HTFs in parabolic trough plants. However, their degradation temperature is very low (400 ºC). However, they have many drawbacks such as their toxic nature, high cost, low degradation temperature (400 ºC) and the need of working under pressure to avoid their degradation. Hence, Solar Salt represents a great alternative to these oils with a wider range of working temperatures (250 ºC – 600 ºC), low cost and harmless for the environment.

Despite these advantages, its thermal properties (specific heat and thermal conductivity) are poor and there is still a large potential to improve them and/or to decrease their minimum working temperature, limiting the nocturnal losses and making the Operation & Management tasks easier [238–241]. A simple and cost-effective way to enhance their thermal conductivity and specific heat consists of adding nanoparticles to the Solar Salt. This new type of materials is known as Molten Salt-Based Nanofluids (MSBNFs) and has attracted great interest on the scientific community in recent years [57,58]. The main feature of these nanofluids is the relevant specific heat increment In comparison to the base salt, which has been systematically observed [31,36,98,112,113]. The amount of stored heat is directly related to the specific heat and as a result, the enhancement of this property allows storing more energy per unit volume, thus extending the duration of CSP plant production. Incidentally, only MSBNFs show the enhancement of the specific heat, while nanofluids based on water or oils as the base fluid do not show it [202]. The mechanisms which govern the interaction between the nanoparticles and the molten salt are not still well-known, although some hypotheses have been proposed in the literature [63,99]. Due to the encountered evidences, most of the scientific research on this field,

including the analysis of new molten salts mixtures, has been devoted to the study of the specific heat and only some few works deal with the thermal conductivity [242–245], while other properties have received very little attention.

Apart from the MSBNFs thermal properties, their rheological performance is of high importance for their industrial implementation as HTFs or in the TES system [31,74,84,95,114]. The introduction of the nanoparticles into the molten salt leads to the rise of the viscosity. This will increase the pumping energy required and could occasionally require design changes of some elements. A commitment should be reached between the larger heat transfer rates achieved by the MSBNFs and the higher costs associated to the pumping [74]. In addition, heat transfer is directly affected by viscosity because the Reynolds number changes. In spite of the industrial relevance of the rheological properties of the MSBNFs, the research on these properties is still very scarce [31,74,84,95,114].

8.2.1.1 *Factors influencing the viscosity*

The viscosity of the MSBNFs depends on many factors, such as the shear rate, the temperature and the nanoparticle concentration. Besides, the geometry of the rheometer is also a factor to be considered in non-Newtonian fluids, which is typical of colloidal systems [183,184]. Even though the dependence of the viscosity on the shear rate and the temperature is of general knowledge, a brief review has been included in Appendix A to help in the understanding of this article. The influence of the nanoparticle concentration is detailed hereafter, as a significant property owned by the nanofluids.

Several models are proposed in the literature to estimate the fluid increment of viscosity due to the presence of solid particles (a two-phase mixture) [45,246]. These models take into account the particle concentration and their shape, as well as their agglomeration caused by the flowing fluid. They have been developed from the pioneering model by Einstein (Eq. 8-1), which considers the existence of non-interacting hard spheres on a fluid with a volume fraction smaller than 1%.

$$\mu_R = 1 + 2.5 \cdot \varphi \qquad\qquad \text{Eq. 8-1}$$

where μ_R is the relative viscosity (viscosity of the dispersion/viscosity of the base fluid) and φ is the volume concentration of particles.

On the limited literature about the rheology of MSBNFs, the Krieger and Dougherty (K-D) model [74,84,95] and the Maron – Pierce (M-P) model [247] have been used to explain the viscosity increments of the nanofluids. The K-D model (Eq. 8-2) is suitable for nanofluids which contain

spherical nanoparticles. It takes into account their agglomeration to estimate the viscosity.

$$\mu_R = \left(1 - \frac{\varphi_a}{\varphi_m}\right)^{-[\mu]\varphi_m} \qquad \text{Eq. 8-2}$$

where μ_R is the relative viscosity, φ_a is the volume fraction of aggregates, φ_m is the maximum volume fraction at which flow can occur and μ is the intrinsic viscosity. Considering $\varphi_m = 0.605$, $[\mu] = 2.5$ and $\varphi_a = \phi\,(a_a/a)^{3-D}$ with $D = 1.8$, the K-D modified model is obtained (Eq. 8-3) [74,84,95].

$$\mu_R = \left(1 - \frac{\phi}{0.605}\left(\frac{a_a}{a}\right)^{1.2}\right)^{-1.5125} \qquad \text{Eq. 8-3}$$

where μ_R is the relative viscosity, ϕ is the volume concentration of nanoparticles, a_a is the size of aggregates and a is the size of the primary nanoparticles.

The M-P model (Eq. 8-4) is suitable to predict the viscosity of nanofluids with fibre-shaped nanoparticles [247].

$$\mu_R = \left(1 - \frac{\varphi_a}{\varphi_m}\right)^{-2} \qquad \text{Eq. 8-4}$$

where μ_R is the relative viscosity, φ_a is the volume fraction of aggregates, φ_m is the maximum volume fraction at which flow can occur. This parameter can be evaluated according to the aspect ratio of the nanoparticles, r, as explained in [247] (Eq. 8-5).

$$\varphi_m = \frac{2}{0.321r + 3.02} \qquad \text{Eq. 8-5}$$

8.2.1.2 Rheology of Solar Salt and MSBNFs

The viscosity of MSBNFs made of molten carbonates with multi-Wall Carbon Nanotubes (MWCNTs) accounting for 1, 2 or 5 wt% was studied by Jo and Banerjee [84]. Jung et al. [74,95] and Lasfargues et al. [31,114] studied the viscosity of the molten Solar Salt with silica nanoparticles (0.5 and 1 wt%) and molten Solar Salt with copper oxide nanoparticles (0.1 wt%). The viscosity increase due to the presence of the nanoparticles is described in all these works: 11%, 93% and 1130% for the MWCNTs mass concentrations of 1%, 2%, and 5%, respectively [84]. Jung [74] found a viscosity increment between 39% to 65% when silica nanoparticles were added to obtain a concentration of 0.5% and an increment between 57% to 68% when 1% concentration was produced. The viscosity increment reported by Lasfargues et al. [114] at the

temperature range from 250 ºC to 450 ºC was comprised between 4.7% and 18.3%. Finally, Jo et al. [95] determined a viscosity increment of 63% at 300 ºC and 79% at 400 ºC. The reviewed literature, indicates that there is not an agreement on the Newtonian [31,114] or non-Newtonian behaviour [74,84,95] of the nanofluids though the well-known Newtonian nature of the molten salts [31,74,95,114]. The nanoparticle agglomeration during the tests may influence the results, as well as the measuring method employed.

The viscosity of the Solar Salt has been measured by several authors in different conditions, as gathered in Table 8-1. Most of them analyses the equimolar mixture of sodium and potassium nitrate (45.7:54.3 wt%) instead of the industrial Solar Salt composition (60:40 wt%) [164,185,201,248,249]. The rheology of both mixtures is supposed to be very similar according to the findings reported by Serrano-Lopez et al. [86] and Jin et al. [164], where the viscosity of both compositions have been compared. These studies include different testing methods and temperatures, while the influence of the shear rate on the rheological properties has not been extensively investigated. Table 8-1 also includes the most relevant testing conditions employed on the publications about the rheological behaviour of Solar Salt-based nanofluids [31,74,95,114] and the conditions employed in this work for the sake of comparison.

All these research works have been carried out with high purity Solar Salt. However, this salt is very expensive to be used in the storage tanks at CSP plants. Instead, due to economic reasons [250], these tanks are filled in with non-analytical grade Solar Salt, which contains several dissolved and solid impurities [135,138]. As above remarked, it is well-known that the rheology of dispersions is different from that of pure fluids [183,184], and therefore the presence of the impurities could influence it.

In this context, this research aims to cover the existing gaps on the rheological properties of the commercial grade Solar Salt, as well as the properties of the nanofluids based on it, produced with silica nanoparticles and with alumina nanoparticles. Our research includes the viscosity dependence on a wide range of shear rates (10–1000 s^{-1}) and the definition of their rheological profile. Besides, the evolution of the viscosity with the temperature in the working range (250–400 ºC) and the influence of the nanoparticle concentration (0.5–1.5 wt%) has also been studied. The nanofluids were tested in two different rheometers using two different measuring systems, a coaxial cylinder and a parallel plate, to study their influence on the viscosity values. The samples were also tested in a third rheometer with the parallel plate configuration to study the behaviour at higher shear rates (>250 s^{-1}).

Table 8-1. Studies and measurement conditions to determine the viscosity of the Solar Salt.

Author	Method	Temp. range, ºC	Shear rate range, s⁻¹	Salt composition NaNO₃/KNO₃ wt%	Salt purity
Murgulescu and Zuca [248]	Damped oscillating sphere method	250 – 450	---	45.7/54.3	Analytical grade
Janz et al. [201]	Oscillating sphere	247 – 447	---	45.7/54.3	Analytical grade
Nissen [185]	Oscillation cup method	275 – 600	---	45.7/54.3	Analytical grade
Coscia et al. [249]	Coaxial cylinder	222 – 547	---	45.7/54.3	Analytical grade
Jin et al. [164]	Coaxial cylinder	243 – 447	30 rpm	60/40	Analytical grade
		233 – 440	30 rpm	45.7/54.3	Analytical grade
Jung [74]	Cone-plate	300 – 400	1 - 1000	60/40 59.7/39.8/0.5 (SiO₂ NPs) 59.4/39.6/1.0 (SiO₂ NPs)	Analytical grade
Lasfargues et al. [114]	Cone-plate (self-made)	250 – 500	1 - 400	60/40 59.95/39.95/0.1 (CuO NPs)	Analytical grade
Jo et al. [95]	Cone-plate	300 - 400	1 - 1000	60/40 59.4/39.6/1.0 (SiO₂ NPs)	Analytical grade
This work	Coaxial cylinder	250 – 300	1 – 250	60/40	Refined grade
	Parallel plate	300 – 400	1 – 250		
	Coaxial cylinder	250 – 300	1 – 250	60/40	Industrial grade
	Parallel plate	300 – 400	1 – 250 100 - 1000		

8.2.2 Materials and methods

8.2.2.1 Raw materials

Sodium and potassium nitrate were acquired from the company SQM (Sociedad Química y Minera de Chile, S.A.) in two different levels of purity: the refined grade (NaNO₃ ≥ 99.6 wt%; KNO₃ ≥ 99.8 wt%) and the industrial grade (NaNO₃ ≥ 98.0 wt%; KNO₃ ≥ 95.0 wt%). The salts were ground in a mortar, dried in an oven at 100 ºC to remove the moisture and mixed to the required proportions. At this stage. the Refined grade Solar Salt (RSS) and the Industrial grade Solar Salt (ISS) were ready to be further mixed with the NPs.

Two types of ceramic NPs were selected, Alumina Nanoparticles (ANPs) (Figure 8-1, left) and Silica Nanoparticles (SiNPs) (Figure 8-1, right). ANPs were purchased as boehmite (hydrated alumina) from Kawaken Chemicals as an industrial water-based nanofluid, Alumisol-10A, containing fiber-shaped NPs (L=50 nm, φ=10 nm) at 10 wt% [127,251]. On the other side, a

dispersion of colloidal silica at 30 wt%, LUDOX® SM-30, from Sigma-Aldrich was used as a source of spherical SiNPs (7 nm) [144].
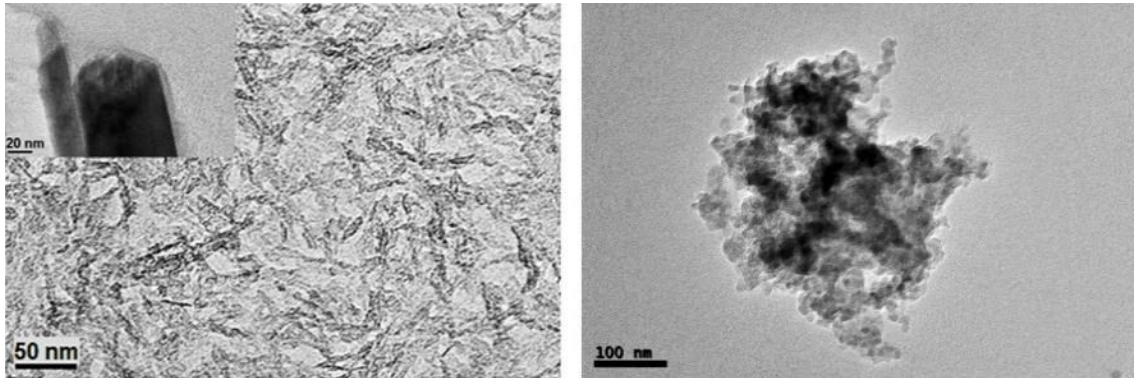
Figure 8-1. TEM images of the ANPs (left) and the SiNPs (right).

8.2.2.2 Synthesis of the nanofluids

Eight formulations were prepared by adding 0.5, 1 or 1.5 wt% of ANPs and SiNPs respectively to the RSS and the ISS salt (Table 8-2) following the common hot plate method described in the following publication [126]. The initial Solar Salt was dissolved into water and the nanoparticle suspensions were added drop by drop under constant stirring. The resulting solution was placed on a Petri dish to evaporate the water by means of heating. The dried material was scrapped off and then stored in absence of humidity until the rheological tests were performed.

Table 8-2. Reference name and composition of the samples used in this study.

	Salt purity	SS, wt%	ANPs, wt%	SiNPs, wt%
RSS	Refined	100.0	–	–
RSS05A	Refined	99.5	0.5	–
RSS1A	Refined	99.0	1.0	–
RSS15A	Refined	98.5	1.5	–
RSS05Si	Refined	99.5	–	0.5
RSS1Si	Refined	99.0	–	1.0
RSS15Si	Refined	98.5	–	1.5
ISS	Industrial	100.0	–	–
ISS1A	Industrial	99.0	1.0	–
ISS1Si	Industrial	99.0	–	1.0

8.2.2.3 Rheological tests

The viscosity and the shear stress of the salts and the nanofluids were measured under different shear rates and temperatures. The rheological study includes two approachs:

- Influence of the measuring system. Two different configurations were used: coaxial cylinders and parallel plate. The rheometer features may impact the viscosity results, as reported by Jin et al. [164]. A coaxial cylinder rheometer consists of an inner concentrically rotating cylinder with an outer stationary cylinder where the test sample is placed, according to the schema shown in Figure 8-2, left. On the other side, a parallel plate rheometer consists of two parallel disks where the sample is placed with an adjustable gap (Figure 8-2, right).

- Influence of the nanoparticle concentration. Nanofluids with RSS as the base fluid and different nanoparticles percentage were tested in one of the parallel plate rheometers. The results were evaluated with the theoretical predictions for this materials.

Table 8-3 summarizes the test conditions established for each of the three rheometers used in this study.
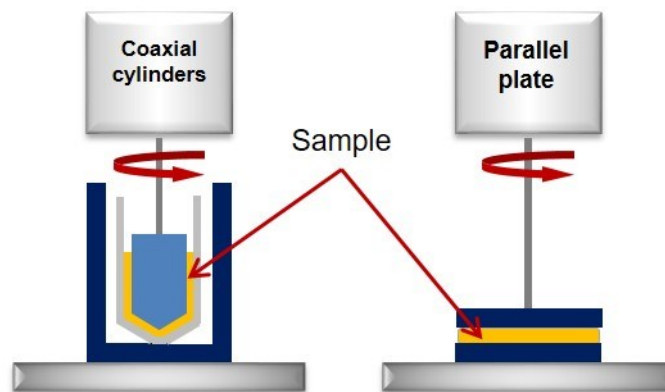
Figure 8-2. Schematic representation of the geometry of the rheometers used in this study: coaxial cylinders (left) and parallel plate (right).

Table 8-3. Experimental conditions of the viscosity measurements carried out with the three rheometers.

	Rheometer 1	Rheometer 2	Rheometer 3
Device (brand and model)	DV-III Ultra, Brookfield Inc.	AR 2000ex, TA Instruments	MCR 3502, Anton Paar
Configuration	Coaxial cylinders	Parallel plate (45 mm)	Parallel plate (35 mm)
Shear rate range, s^{-1}	1-250	100-1000	1-250
Tested temperatures, ºC	250, 270, 290, 300	300, 350, 400	300, 350, 400
Materials analysed	RSS, RSS1A, RSS1Si ISS, ISS1A, ISS1Si	ISS, ISS1A, ISS1Si	RSS, RSS1A, RSS1Si, RSS05A, RSS05Si, RSS15A, RSS15Si
Sample amount, g	9.0	2.0	1.7
Gap, mm	---	0.35	1.00
Time for thermal stabilization, min	60	5	5
Number of cycles (1 cycle = min-max-min shear rate)	3	5	2
Shear rate points per range	20	20	36
Time at each shear rate, s	10	10	--
Acquired data at each shear rate	2	1	1

8.2.2.3.1   Coaxial cylinders

The viscosity of the undoped salts, RSS and ISS, and four nanofluids based on them (RSS1A, RSS1Si, ISS1A, ISS1Si) were measured with a programmable rotational rheometer (DV-III Ultra, Brookfield Inc., USA) coupled with a furnace (maximum temperature 300 °C) and a temperature controller. The coaxial cylinders system consists of a cone spindle which is introduced in a sample chamber (Figure 8-3). This assembly is placed inside a closed thermal chamber during the high temperature measurements avoiding the evaporation of the sample. The shear rate testing range was comprised between 1 and 250 s^{-1}. The samples were tested at 250 °C, 270 °C, 290 °C and 300 °C (Test 1). The calibration of the viscometer was verified before and during the course of the measurements by measuring a reference fluid, Brookfield Viscosity Standard Fluid HT-30000 (see Appendix B).

Following the recommendations given by the rheometer manufacturer, around 9 g of the solid sample were placed inside the stationary cylinder and melted at the lowest temperature, 250 °C. After the sample was molten, the spindle was slowly inserted and put into contact with the molten flluid with special care to prevent the formation of any bubble that may alter the results. The sample was held at the test temperature for 60 minutes to reach its thermal equilibrium before collecting the data. Then, three increasing and decreasing shear rate cycles were applied to obtain the different steady state flow curves versus temperature. On each cycle, measurements were taken at 20 different shear rates, 6 points per each shear rate. Once this experimental procedure finished, a new experiment starts by heating up the same previous sample at the next target temperature, 270 °C, reproducing the same experimental procedure to obtain measurements. This process is repeated at the different temperatures until the last experiment is carried out at 300 °C. At each new temperature, the sample is thermally equilibrated again for 60 minutes prior to replicate the test. The mean shear stress, the mean viscosity and the Standard Deviation (SD) of the measurements were calculated for each analyzed shear rate. The results for very low shear rates, under 50 s^{-1}, were omitted due to their low repeatability (torque <10%), according to the Brookfield user manual [165].

These four nanofluids (RSS1A, RSS1Si, ISS1A and ISS1Si) were also tested at 300 °C (Test 2) on the same conditions as in the former Test 1, but without performing the tests at temperatures lower than 300 °C. The purpose was to determine if the previously attained results could have been influenced by nanoparticles agglomeration at the bottom of the measuring system due to the long length of the experiments on Test 1 (several hours).

Figure 8-3. Left: The spindle and the sample chamber used for the rheological tests (Rheometer 1). Right: General view of the rheometer. The spindle is hanged on the device which applies the rotational force and then immersed into the molten salt contained in the sample chamber.

The size of the NPs into the nanofluids was measured before and after performing the rheological tests with this rheometer. The NPs size gives an indication about the possible agglomeration under the dynamic forces exerted during the experiments. To do these measurements, the raw materials employed to produce the nanofluids (NPs dispersion, SiNPs and ANPs) and the four nanofluids (RSS1A, RSS1Si, ISS1A and ISS1Si) were characterized using a Dynamic Light Scattering method (DLS, ZetaSizer Nano ZS, Malvern Instruments, Ltd. Malvern, UK).

8.2.2.3.2   Parallel plate

As mentioned along the introduction, the nanofluid viscosity values may differ depending on the employed rheometer geometry [164]. Thus, with the aim to determine if this could be the case in our samples and in order to attain reliable results, two high temperature rotational rheometers with parallel plate geometry were used. In these rheometers, the tests were done at higher temperatures (300 ºC to 400 ºC) than in the coaxial cylinder device. These temperatures are in the range of the real operating conditions, as detailed in the introduction. Unfortunately, the maximum working temperature of the previous rheometer was 300 ºC. The data obtained at this temperature is further used to compare the performance of the two rheometers.

On one side, the samples ISS, ISS1A and ISS1Si were measured with a rheometer AR 2000ex, from TA Instruments (Rheometer 2, Figure 8-4, left). About 2 g of the solid sample were placed between the parallel plates with a gap of 0.35 mm. The sample is heated up to the desired testing temperature and then analysed at shear rates between 10 and 1000 s^{-1}. The testing temperatures were 300 ºC, 350 ºC and 400 ºC. Five cycles of increasing and decreasing shear rates were performed on each temperature, to find out the possible time dependency. 20 shear rate measurement-points were defined on each cycle and each measurement lasted 10 s. Because of

the little amount of sample needed, the thermal equilibrium is shortly reached. Fresh sample was put on the device to carry out the tests at each temperature. The calibration of the rheometer was done by measuring a reference fluid according to the ISO 17025 Standard (see Appendix B). The reomether was checked with the standard before testing the samples and the results were eventually corrected by using it as external reference.

Figure 8-4. The rheometers with the parallel plate configuration. Rheometer 2: AR 2000ex (left) and Rheometer 3: MCR 302 (right).

The viscosity of the samples RSS, RSS1A and RSS1Si were measured on the second parallel plate rheometer (Rheometer 3), an Anton Paar MCR 3502, where about 1.6 g of the solid sample were placed between the parallel plates of the rheometer, fixing a gap of 1 mm between them (Figure 8-4, right). The sample is heated up to the desired testing temperature, and then the test start. The shear rates employed ranged from 10 s^{-1} to 1000 s^{-1}. The testing temperatures were 300 ºC, 350 ºC and 400 ºC. The calibration of the rheometer was done by measuring the standard fluid WACKER® AK 1000000 SILICONE FLUID (see Appendix B).

It is worth mentioning that parallel plate rheometers require a precise amount of sample to attain reliable measurements (Figure 8-5). Underfilling the container may lead to errors and overfilling it may cause the loss of fluid [166]. The use of these two different rheometers was merely due to their availability on the laboratory at the time of performing the measurements. The main difference between them is the maximum possible shear rate to perform the experiments, while the rest of their features are similar and equivalent. The objective is to compare the results of the nanofluids analysed on each one with those of the coaxial cylinder rheometer.
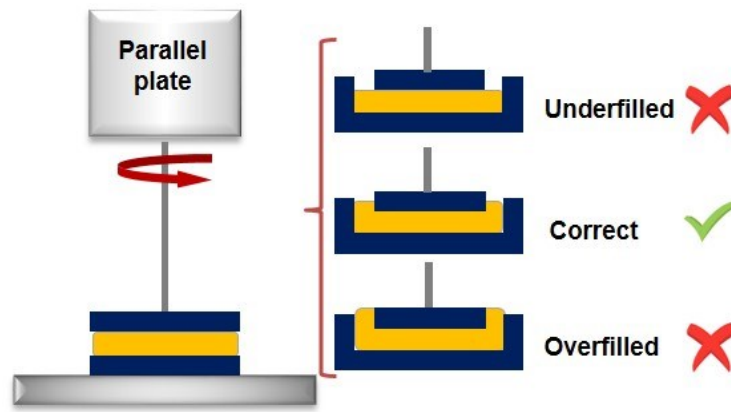
Figure 8-5. The amount of loaded sample into the parallel plate geometry is critical.

8.2.2.4 Nanoparticle size distribution

The nanoparticles size distribution of nanofluids based on RSS was characterized using the DLS technique (ZetaSizer Nano ZS, Malvern Instruments, Ltd. Malvern, UK). The produced MSBNFs solid samples were dissolved in water prior to the measurements, which were carried out at room temperature. The apparatus determines the number of nanoparticles of each diameter and calculates the modal distribution. The distributions are the results of three different measurements on the same sample. It is important to remark that the nanoparticle sizes are calculated by DLS according to their hydrodinamic diameter. This is the size of a equivalent sphere for non-spherical nanoparticles, as is the case of the ANPs. Thus, these results are always approximative and cannot be considered as absolute numbers [148].

8.2.3   Results and discussion

8.2.3.1 Coaxial cylinders configuration

8.2.3.1.1   Influence of the shear rate

Figure 8-6 shows an example of the lineal dependence between the shear stress and the shear rate at 300 ºC. The same lineal relationship was found at the other tested temperatures. A linear regression based on the Bingham rheological model fits this trend (see Appendix C, Table 8-9). The results correspond to the mean of the six data obtained at each shear rate. The Bingham rheological profile implies a constant viscosity once the yield stress has been overcome. In agreement with the high coefficients of determination ($R^2 > 0.99$) found, it can be concluded that the samples show a Bingham profile. In the case of the ISS and their nanofluids, the lineal fitting is not as good as in the previous samples. The region of low shear rates (<100 s^{-1}) and at certain temperatures (250 and 270 ºC) these materials show a shear thinning behaviour (Figure 8-6, right). This may be due to the deagglomeration of nanoparticles or impurities, followed with a plateau

where the alignment of the particles with the flow direction occurs, as observed by several authors in colloidal dispersions [182,183,247].

Figure 8-6. Dependence between the shear stress (τ) and the shear rate (γ) on undoped salts and nanofluids at 300 ºC. Solar Salt and nanofluids of Refined Grade (left) and Industrial Grade (right). The error bars are the SD of the six measurements at each shear rate.

The effect of the shear rate on the Solar Salt viscosity has been briefly studied on the scientific literature. All these studies employed analytical grade raw materials (Lasfargues et al. [31,114] and Jung et al. [74,95]). In those studies, the Solar Salt is described as a Newtonian fluid. On the contrary, the results presented in this study show that it is a Bingham fluid. The reason for these differences could be related to the purity of the raw salts, where both, RSS and ISS, contain solid impurities [135,136,138,139] which may modify their rheological profile, as pointed out by [183,184]. Other important factors responsible of the differences between our results and those obtained by other authors are the limited shear rate range employed in the present work (1-250 s^{-1}) In comparison to the wide shear rate range (1-1000 s^{-1}) used on most other articles and the rheometer configuration (a cone-plate geometry was employed on the other studies).

Regarding the rheological behaviour of Solar Salt-based nanofluids, two different trends have been reported on the literature. On one side, Lasfargues and co-workers [31,114] found that the Newtonian character of the Solar Salt was not affected after the addition of a tiny amount (0.1 wt%) of CuO nanoparticles. On the other side, Jung et al. described a shear thinning behaviour [74,95] when 1 wt% of silica nanoparticles were incorporated into the Solar Salt. The discrepancies on the results among these studies may chiefly come from the different concentration of the nanoparticles. According to these studies, the initial Newtonian character of the Solar Salt changes if the concentration of dispersed nanoparticles is over a certain percentage. Our study indicates a certain shear-thinning character on the nanofluids based on ISS at the higher

temperatures, as shown on Figure 8-6 (right). This agrees with the results obtained by Jung [74] and Jo et al. [95] with the nanofluids produced with analytical grade Solar Salt and SiNPs. However, no shear thinning behaviour was determined on the nanofluids produced with RSS in the present study.

8.2.3.1.2   Influence of the temperature

Figure 8-7 shows the mean viscosity determined for shear rates higher than 100 s^{-1} at different temperatures. It was observed that at shear rates between 100 and 250 s^{-1} the viscosity values remained constant on all the studied nanofluids with this coaxial cylinder rheometer (Table 8-3).
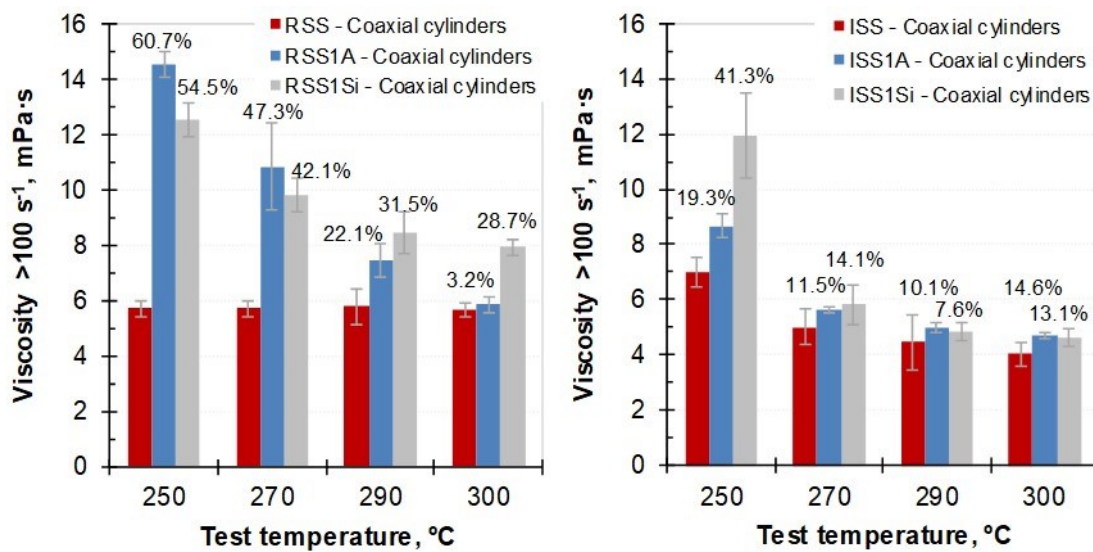
Figure 8-7. Viscosity and Standard Deviation (SD) for shear rates above 100 s^{-1}.of the undoped salts and the nanofluids at different temperatures. The error bars are the SD of the viscosity results at shear rates higher than 100 s^{-1}. The viscosity variation (%) with respect to the base salt has been included with numbers.

The viscosity of the undoped Solar Salt is around 5.70 mPa·s for the RSS grade and between 4.00 mPa·s and 7.00 mPa·s for the ISS grade. These viscosity values are higher than those reported by [164] for the analytical grade mixtures, probably due to presence of impurities on our salts. The viscosity of the RSS is independent of the test temperature, which is not in agreement with the commonly reported viscosity decrease when the temperature is risen.

The addition of the nanoparticles to the Solar Salt causes a viscosity increment in comparison to the undoped salts. This occurs whatever the temperature, the salt grade or the kind of nanoparticle employed. The nanofluids based on the RSS show higher viscosity increments than the ISS-based nanofluids. On the first case, the ANPs produce higher viscosity increment at the lower temperatures than at high temperature (61% at 250 ºC versus 47% at 270 ºC), while the SiNPs cause the largest increments at 290 ºC (31%) and 300 ºC (29%). This result is probably related to the higher agglomeration and settling of the ANPs when the temperature is increased in

comparison to the SiNPs.

Figure 8-8 shows the results of RSS and ISS and the corresponding nanofluids RSS1A, RSS1Si, ISS1A, and ISS1Si, compared to those found in the literature (undoped salts). The well-known models relating the viscosity and the temperature are detailed in Appendix A. The models of Arrhenius or Vogel, Tamman and Fulcher (Appendix A, Eq. 8-9 and Eq. 8-10) are of common use by the majority of the authors [74,164,185,248,249] but others analysed their data according to a polynomial relationship [114,185]. The results of the undoped Solar Salt show that on the case of the RSS quality the viscosity is independent of the temperature (on the evaluated temperature range), while the ISS results agree with those published by Nissen [185]. The viscosity of the nanofluids follows a similar trend to those from the literature, but presenting higher viscosity values. The mixture RSS1A is an exception, showing an inverse lineal dependence with the temperature.

As seen on Figure 8-8, our experimental results are very high In comparison to those from the literature. The reason has been attributed to the considerable amount of solid particles on the salts used in this study, compared to their absence on the analytical salts tested by other authors.

Figure 8-8. Viscosity measured with the Rheometer 1 (coaxial cylinders) versus temperature. RSS, ISS and their nanofluids compared with the published results of Solar Salt.

8.2.3.1.3   Stability of the nanoparticles during the measurements

The study of the agglomeration of the nanoparticles during the viscosity measurement is discussed in this section. Table 8-4 shows the mean viscosity and the Standard Deviation (SD) of both Test 1 and Test 2 measurements. The nanofluids based on RSS exhibit higher differences between the results obtained on these two tests than those based on ISS, which have similar values on both tests. These divergences can be related to the nanoparticle agglomeration, see the distribution on Figure 8-9. On one hand, the SiNPs experience higher agglomeration during the rheological tests in comparison to the ANPs, probably due to the fibre-shape of the latter ones, that allows the nanoparticles to align with the flow direction, remaining as individual nanoparticles rather than forming agglomerates. On the other hand, the nanoparticles size increases more after Test 1 than after Test 2, which has been attributed to the longer time spent on the former one. This circumstance confirms that the measurements of viscosity are affected by the experimental conditions.

As it can be seen in Table 8-4, the viscosity values of all the experiments carried out on the Test 2 are very similar to each other, independently of the kind of nanoparticle or the salt purity. This means that after one hour in the molten state, there is not any significant viscosity difference for any of the materials evaluated on the test.

Table 8-4. Viscosity of the different nanofluids measured at 300 ºC with the coaxial cylinder method.

	Coaxial cylinder method Shear rate range: 1-250 s^{-1}			
	Test 1 (300 ºC)		Test 2 (300 ºC)	
Sample	μ, mPa·s	SD, mPa·s	μ, mPa·s	SD, mPa·s
RSS1A	5.85	0.31	4.46	0.09
RSS1Si	7.94	0.29	4.71	0.08
ISS1A	4.72	0.10	4.23	0.05
ISS1Si	4.64	0.30	4.94	0.05
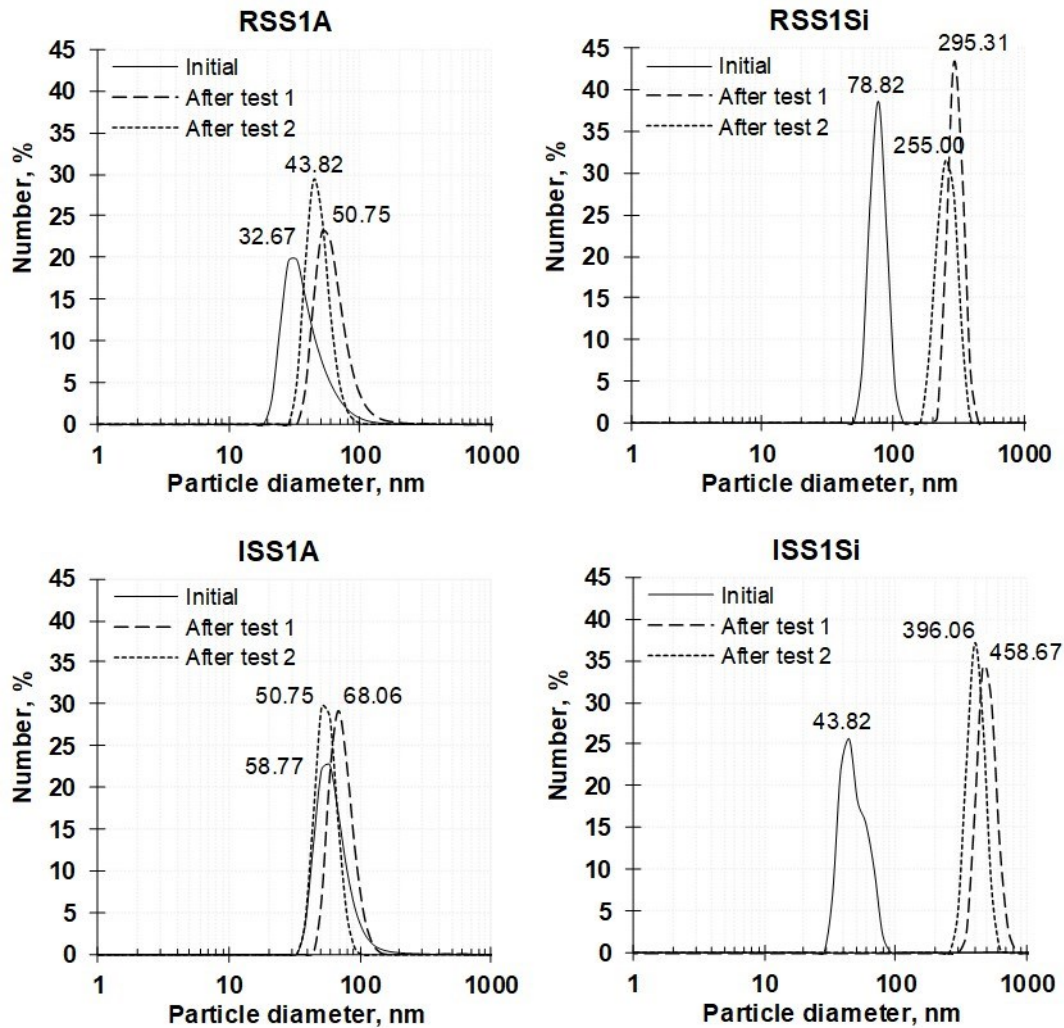
Figure 8-9. Nanoparticle size distribution of the nanofluids before and after performing the viscosity measurements. The ANPs on the left, the SiNPs on the right. Test 1 upper graphs, Test 2 below.

8.2.3.2 Parallel plate configuration

8.2.3.2.1 Influence of the shear rate

The Figure 8-10 shows the relationship between the shear stress and the shear rate when the Solar Salts and the nanofluids were tested with the parallel plate rheometers at 350 ºC. The error bars represent the SD of the different measurements performed. In general, these flow curves can be fitted to the power law fluid model (Appendix A, Eq. 8-7). According to the Figure 8-10, several rheological performances can be noticed on these flow curves.

The tests performed on the Rheometer 3 with the samples containing RSS (Figure 8-10, left) reveal two different tendencies. At low shear rate (<100 s^{-1}) the fluids show a shear thinning behaviour, while at higher rates a shear thickening behaviour is displayed. As mentioned in the analysis of the results corresponding to the coaxial cylinder geometry, this change on the rheological behaviour is related to the deagglomeration of the nanoparticles or impurities

followed by a reagglomeration beyond a certain shear rate (100 s^{-1}). No alignement of the nanoparticles with the flow has been inferred on these tests, probably due to the sample size. The good correlation of the shear thickening trend is shown on Appendix C, Table 8-10.

The samples produced with the industrial salt (ISS, ISS1A and ISS1Si) analyzed in the Rheometer 2, exhibit a clear Newtonian behaviour (Figure 8-10, right). Accordingly, suitable fittings are obtained in this case (Appendix C, Table 8-10).
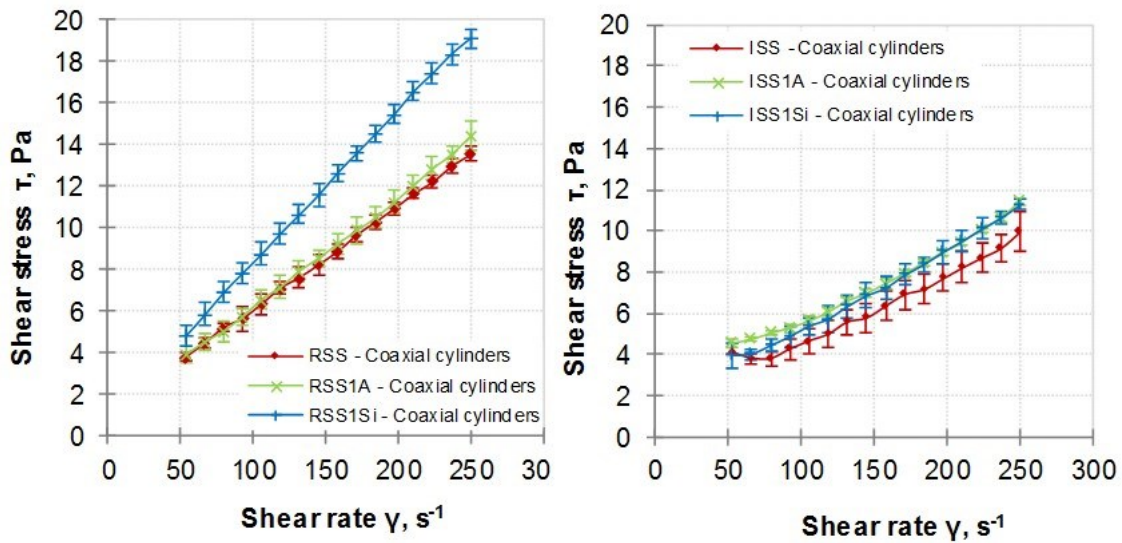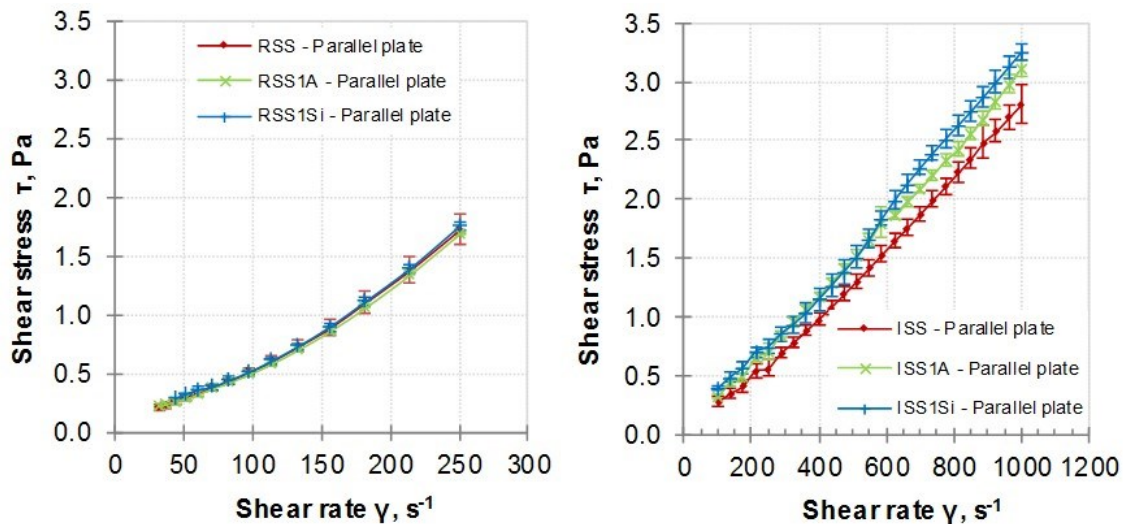

Figure 8-10. Shear stress (τ) versus shear rate (γ) on undoped salts and nanofluids at 350 ºC. Solar Salt and nanofluids of Refined Grade (left) and Industrial Grade (right). The error bars are the SD of four measurements at each shear rate point for the Refined Grade and five measurements per shear rate point for the Industrial grade respectively.

The Newtonian rheological profile of the Solar Salt proposed by Lasfargues et al. [31,114] and Jung et al. [74,95] is in agreement with the results of ISS. The upper shear rate employed on our study is the same employed by those authors (1000 s^{-1}), and the rheometer geometry (parallel plate) is more similar than the cone-plate configuration employed by them. The non-Newtonian character of the samples produced with the RSS can be explained by the strong influence of the impurities and/or nanoparticles at reduced shear rates in the small volume of sample required on the experiments. The higher shear rates used with the ISS and their nanofluids may led to the discussed Newtonian behaviour and the inexistence of a shear thickening region at high shear rates (>250 s^{-1}).

Despite the non-Newtonian profile showed by the RSS in the Rheometer 3, the proper working of this device was checked since the molten salts are Newtonian fluids. With this aim, a Solar Salt of analytical grade (Sigma Aldrich, $NaNO_3$> 99.9 wt%, KNO_3 > 99.9 wt%) was tested three times under the same conditions. Figure 8-11 is showing the mean results of shear stress versus shear rate at 300 ºC, 350 ºC and 400 ºC. This profile is similar to that found for the RSS and their nanofluids. The fitting of these data both for a Newtonian (n=1) or non Newtonian trend is gathered in Appendix C, Table 8-11. The best regression coefficients are obtained when the salt

is considered a non-Newtonian fluid at 350 ºC and 400 ºC. The results at 300 ºC have almost the same R^2. Thus, the Rheometer 3 has some kind of deviation at the higher shear rates, specially at temperatures >300 ºC.

One detail to be noticed is that the flow behaviour index (n) of the analytical Solar Salt is much close to 1 (0.9425 at 300 ºC, 1.1448 at 350 ºC and 1.1602 at 400 ºC) than that of the RSS (1.1374 at 300 ºC, 1.2866 at 350 ºC and 1.3788 at 400 ºC). This means that despite the anomaly observed with this Rheometer 3, the role of the impurities of the RSS on their non-Newtonian character is proved.
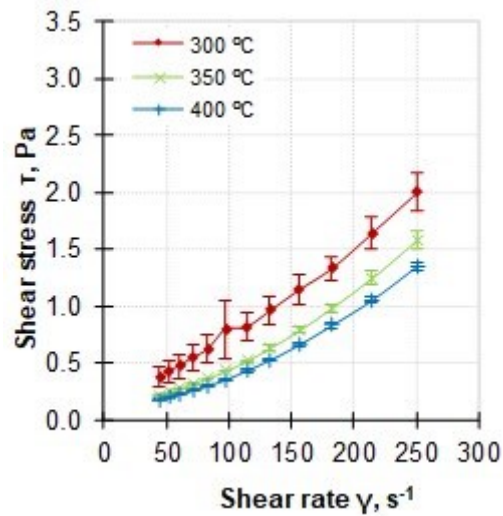
Figure 8-11. Shear stress (τ) versus shear rate (γ) of the analytical Solar Salt in Rheometer 3.

8.2.3.2.2 Influence of the temperature

On Figure 8-12 the viscosity values of the samples according to the test temperature are represented, measured at 250 s^{-1} for the RSS and its nanofluids and over 300 s^{-1} for the ISS and its nanofluids. The viscosity of the undoped RSS Solar Salt determined with the parallel plate rheometers lies in between 8.58 mPa·s and 6.43 mPa·s, and between 3.55 mPa·s and 2.17 mPa·s on the ISS grade. The RSS viscosity values determined in this work are much higher than those published in the literature [164], while those obtained with the ISS grade lie within the average viscosity reported on the literature at different temperatures. These differences lay on the selected shear rate range and the presence of impurities on the salts used in this study.

The addition of the nanoparticles to the Solar Salt affects very little to the viscosity values obtained by this technique (parallel plates). The nanofluids based on the RSS at 300 ºC even show a viscosity reduction in comparison to the undoped RSS, which could be attributed to the uncertainty of the technique and the higher data scattering induced by the presence of the nanoparticles. The maximum viscosity increment corresponds to the RSS1Si at 400 ºC (a

viscosity increment of 4%). The addition of nanoparticles (SiNPs or ANPs) produces an average viscosity increment of 11% for the ISS1A and 13% for the ISS1Si.
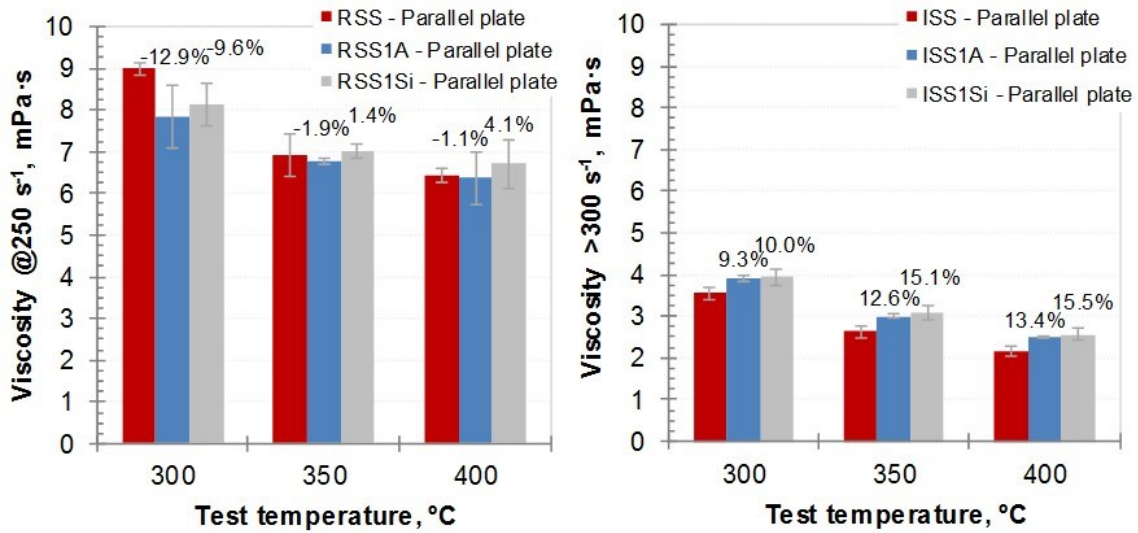
Figure 8-12. Average viscosity values and Standard Deviation (SD) at different temperatures, determined at 250 s⁻¹ (left) and between 300 s⁻¹ and 1000 s⁻¹ (right) for the undoped salts and the nanofluids. The error bars are the SD of the viscosity results. The viscosity variation (%) with respect to the base salt has been included with numbers.

The evolution of the viscosity with the temperature determined by the parallel plate configuration has been evaluated in the same way as the results attained with the coaxial cylinder geometry. Figure 8-13 shows the obtained data together with those from the literature. All the results follow a similar trend to that reported by other researchers. The absolute values of the RSS and RSS-based nanofluids are higher than those reported on the literature, while the values corresponding to the samples ISS, ISS1A, ISS1Si are in agreement. As explained before, this difference is attributed to the reduced shear rate range on the determination of the RSS and its nanofluids, while the slightly larger viscosity determined on the ISS based materials, in comparison to the viscosity reported by other authors, is most probably due to the presence of solids (impurities and/or nanoparticles) on the industrial materials employed in this study.
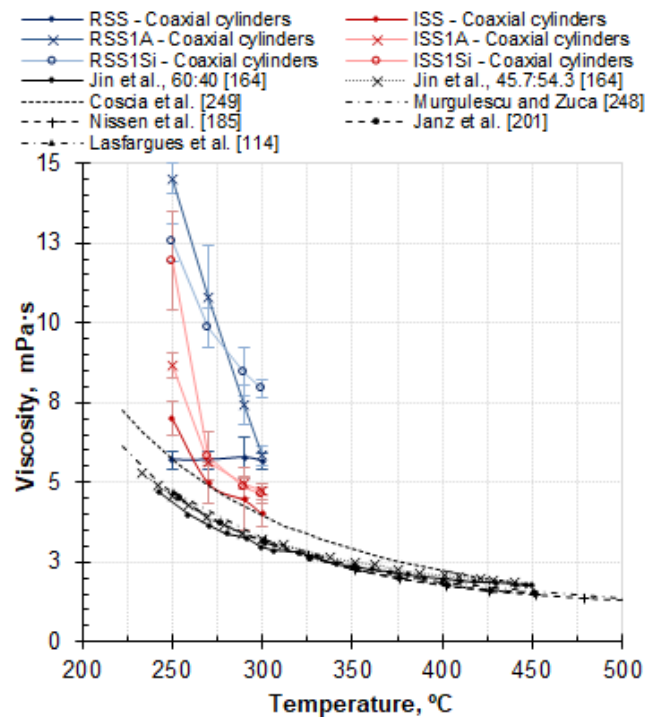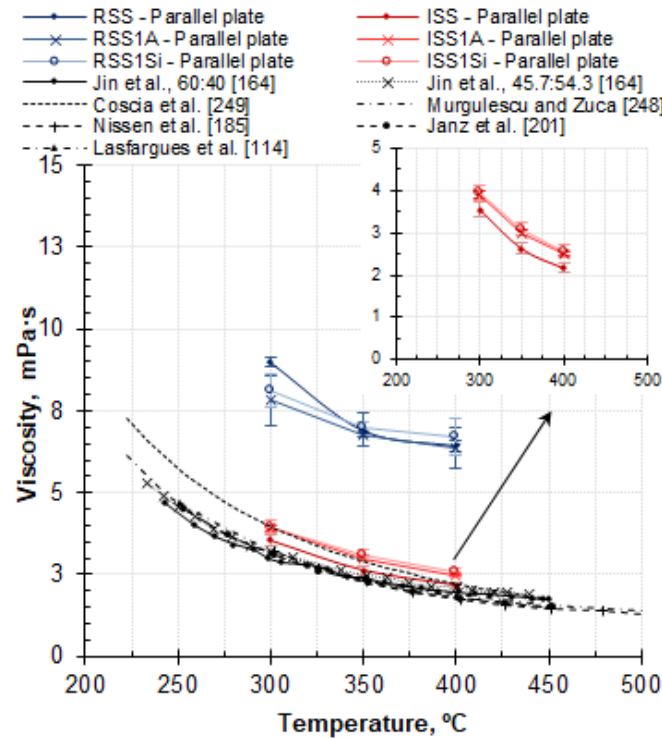
Figure 8-13. Viscosity measured with the Rheometer 2 and 3 (parallel plate) versus temperature. RSS, ISS and their nanofluids compared with the published results of Solar Salt.

8.2.3.2.3 Influence of the nanoparticle concentration

The viscosity of the nanofluids based on RSS with 0.5 wt% to 1.5 wt% of SiNPs and ANPs was determined with the Rheometer 3 (parallel plate) with the aim of analysing the influence of the nanoparticle concentration on the viscosity. These nanofluids follow a shear thinning model for shear rates under 100 s^{-1} and a shear thickening behaviour over this shear rate up to 250 s^{-1} (maximum shear rate available on the employed rheometer). This is the same behaviour previously observed on the sample containing 1 wt% of nanoparticles (Figure 8-10, left).

Table 8-5 summarizes the results obtained at 250 s^{-1} and the increment of viscosity with the addition of nanoparticles to the undoped RSS. A detailed analysis reveals a disparity of trends. On one hand, the RSS nanofluids containing ANPs have lower viscosity than the original RSS, whatever the nanoparticle concentration or the testing temperature. On the other hand, the addition of SiNPs decreases (RSS05Si) or increases (RSS15Si) the viscosity depending on the concentration.

Table 8-5. Viscosity of the RSS and RSS-based nanofluids with different nanoparticle concentration and temperatures. Measured on a parallel-plate viscosimeter at a shear rate of 250 s^{-1}. The viscosity variation with respect to the undoped RSS is included.

Sample	300 ºC			350 ºC			400 ºC		
	μ, mPa·s	SD, mPa·s	Δμ, %	μ, mPa·s	SD, mPa·s	Δμ, %	μ, mPa·s	SD, mPa·s	Δμ, %
RSS	8.98	0.13	---	6.91	0.51	---	6.43	0.16	---
RSS05A	6.60	1.51	-26.51	5.79	1.51	-16.17	5.40	0.96	-16.06
RSS1A	7.82	0.75	-12.94	6.77	0.05	-1.94	6.36	0.64	-1.15
RSS15A	7.66	0.06	-14.71	6.95	0.03	0.63	6.22	1.00	-3.32
RSS05Si	7.89	0.01	-12.14	6.56	0.00	-5.02	6.10	0.65	-5.18
RSS1Si	8.12	0.51	-9.58	7.00	0.15	1.35	6.70	0.58	4.14
RSS15Si	9.29	1.07	3.49	8.08	1.25	17.04	7.83	0.90	21.75

The models of Maron-Pierce (M-P) (Eq. 8-4) and Krieger-Dougherty (K-D) (Eq. 8-3) are used to analyze and predict the viscosity changes due to the addition of the ANPs and SiNPs, respectively. These models take into account the influence of the agglomerates on the viscosity, as detailed on the introduction. The parameter a$_a$/a in both equations (the ratio between the agglomerates size and the individual nanoparticles size) was experimentally determined by DLS (Table 8-6)Table 8-6. On the case of the nanosilica containing RSS fluids, the obtained values are similar to those proposed by Jung et al. [74] for Solar Salt based nanofluids containing 0.5 wt% and 1.0 wt% of SiNPs (32 and 20 respectively), and higher than those found by Jo et al. [95] for Solar Salt with 1 wt% of SiNPs (13.8 and 16 at 300 ºC and 400 ºC).

Table 8-6. Size of agglomerates and individual nanoparticles experimentally determined in the RSS-nanofluids by DLS technique

Sample	a$_a$, nm	a, nm	a$_a$/a	Sample	a$_a$, nm	a, nm	a$_a$/a
RSS05A	190.14	15.69	12.12	**RSS05Si**	396.06	13.55	29.23
RSS1A	164.18	15.69	10.46	**RSS1Si**	295.31	13.55	21.79
RSS15A	37.84	15.69	2.41	**RSS15Si**	458.67	13.55	33.85

Both equations (Eq. 8-3 and Eq. 8-4) need the conversion of nanoparticles mass fraction (w) to nanoparticles volume fraction (ϕ). To do so, Eq. 8-6.has been used.

$$\phi = \left(\frac{w}{\rho_{NP}} \right) \cdot \left(\frac{w}{\rho_{NP}} + \frac{(1-w)}{\rho_{BF}} \right)$$

Eq. 8-6

Where w is the mass fraction of the nanoparticles, ρ_{NP} is the density of the nanoparticles and ρ_{BF} is the density of the base fluid. The density values considered in this case were 3,950 kg·m^{-3} and 2,600 kg·m^{-3} for the ANPs and the SiNPs respectively. The density of the Solar Salt was calculated as 1,903 kg·m^{-3}, 1,869 kg·m^{-3} and 1,836 kg·m^{-3} at the temperatures of 300 ºC, 350 ºC and 400 ºC

according to the expression proposed by Janz [201].

The relative viscosity (η_R) of the nanofluids with the percentage of ANPs and temperature is depicted on Figure 8-14, left. The Maron-Pierce model was used to calculate the theoretical relative viscosity of these nanofluids according to the Eq. 8-4. The maximum volume fraction of nanoparticles was calculated from Eq. 8-5 considering the ANPs with 10 nm in diameter and 50 nm in length (aspect ratio, r = 5). The volume fraction of aggregates, φ_a, was estimated from the ratio a_a/a (on Table 8-6) and a fractal index D = 2.1, commonly used for fibre-shaped nanoparticles [247]. These theoretical results are displayed on Figure 8-14 together with the experimental results at 300 ºC. The experimental results of nanofluids with 1 wt% and 1.5 wt% of nanoparticles present a good agreement with the M-P model whereas the nanofluids with 0.5 wt% of nanoparticles have a significantly lower viscosity than that forecasted by the model.

The relative viscosity (η_R) of nanofluids at 300ºC predicted by the model with several SiNPs percentage, are presented on Figure 8-14, right, along with the experimental results attained at different temperatures. Also, the experimental and theoretical results (K-D model) of Jung [74] and Jo et al.[95] have been included on this plot.

The experimental results obtained in this work follow a second-order polynomial correlation of the type $\eta_R=A\phi^2+B\phi+1$ (see Appendix C, Table 8-12), as proposed by Batchelor et al. [252] (accounting the Brownian motion of the nanoparticles).
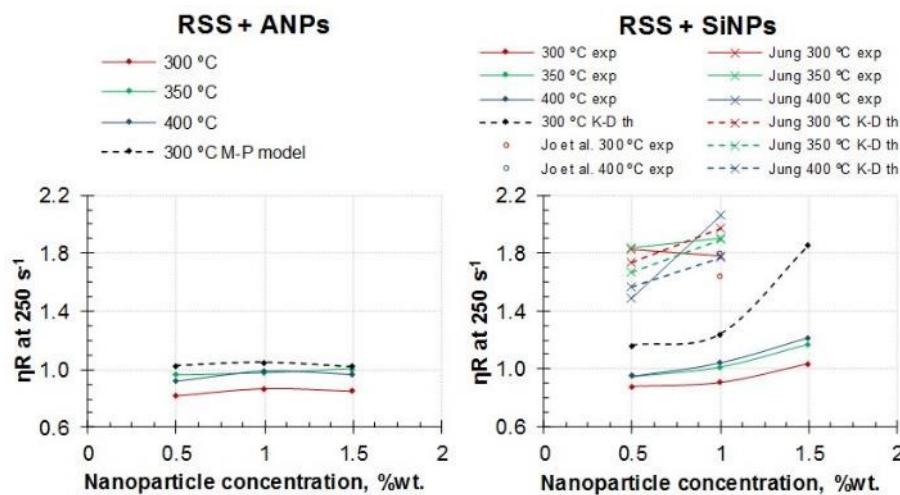
Figure 8-14. Relative viscosity (η_R) of the RSS-based nanofluids with ANPs (left) and SiNPs (right). The values predicted by the Maron-Pierce (M-P) model for the ANPs and the Kriegher-Dougherty (K-D) model for the SiNPs have also been included on the plots.

8.2.3.3 Comparative analysis of the results

This final section aims to draw a global comparison of the described trends and results. The data at 300 ºC and shear rates between 100 and 250 s^{-1} are the common features to all the performed experiments and thus, they can be directly compared to each other in these conditions.

Figure 8-15 (up) summarizes the results of the RSS and the RSS-based nanofluids with different measuring systems and a comparison with those from the literature: Jung [74] and Lasfargues et al. [31,114]. In both rheometers, a shear-thinning behaviour is observed for shear rates below 100 s^{-1}. Above this point, the coaxial cylinders rheometer indicates that all the samples are Newtonian while the measurements with the parallel plates points to a clear shear thickening behaviour. These differences could be attributed to the dissimilar amount of sample used (9 g in coaxial cylinder and around 2 g in parallel plate). The agglomeration of the nanoparticles causes a greater impact on the parallel plate configuration, generating the shear thickening profile. This explanation should be considered with caution having into account the little deviation showed by the Rheometer 3 of parallel plates at shear rates higher than 100 s^{-1}. As reported in the literature [31,182], the increase of the shear rate in suspensions implies breaking the agglomerates and thus, the reduction of the viscosity (shear thinning). This is usually followed by a plateau of stable viscosity (Newtonian behaviour) due to the alignment of the particles with the flow at higher shear rates. This situation can progress through until the collapse of the structure, leading to high agglomeration of the nanoparticles (shear thickening) and an increase on viscosity at high shear rates.

In Figure 8-15 (bottom), the results of the ISS and the ISS-based nanofluids with the two measuring systems are analysed and compared with the literature: Jung [74] and Lasfargues et al. [31,114]. The ISS and the ISS based nanofluids show a Newtonian profile in the coincident range of shear rates (100 – 250 s^{-1}) with both measuring geometries: coaxial cylinder and parallel plate. In the latter rheometer, the samples are tested in a wider shear rate (100 - 1000 s^{-1}). Thus, due to this high shear rate, the nanoparticles may be completely aligned with the flow after the first shear rate cycle, showing this Newtonian character.

In the same manner, the parallel plate rheometers show opposite trends depending on the maximum shear rate applied. At low shear rates (1-250 s^{-1}, Rheometer 3), the nanoparticles and impurities clusters are first broken (shear thinning) and then the viscosity increases due to the physical impacts between the nanoparticles. If higher shear rates are applied (100-1000 s^{-1}, Rheometer 2), the nanoparticles and impurities are quickly aligned with the flow direction and the viscosity is similar to that of the neat molten Solar Salt.

The published results [31,74,95,114] determined the Newtonian character of the Solar Salt at this temperature and shear rate range, while a shear thinning behaviour was observed by Jung [74] for the nanofluid with 1% of SiNPs (comparable to our nanofluids RSS1Si and ISS1Si). These two studies employed rheometers with a cone-plate configuration. Our results of RSS and ISS are coincident with those observed by these authors, but this is not the case of the nanofluids. The differences may come from several aspects such as the salt purity, the nanoparticle composition

and shape, the rheometer configuration or the shear rate range studied.

In summary, the rheological performance of our samples is strongly influenced by the rheometer configuration. The purity of the base salt or the presence of both ANPs or SiNPs seem insensitive to determine the rheological behaviour.
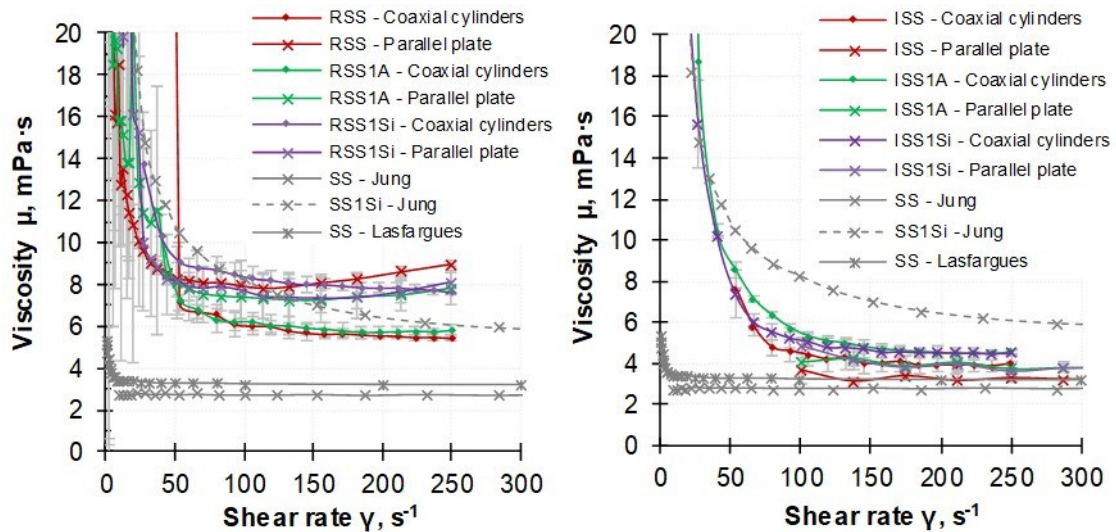
Figure 8-15. Viscosity (μ) versus the shear rate (γ) at 300 ºC of the salts and the nanofluids analysed with two rheometer geometries. RSS and their based nanofluids (up) and ISS and their based nanofluids (bottom). The experimental data from Jung et al. [74,95] and Lasfargues et al. [31,114] at 300 ºC are also displayed to compare the rheology profiles.

Regarding the viscosity results, the Figure 8-16 shows the relationship between the (average) viscosity at 300 ºC, the measuring system and the purity of the base Solar Salt. The viscosity values determined on the RSS materials by means of both rheometer configurations pose a notable difference (with exception of the RSS1Si), while the viscosity determined on the ISS materials by both techniques is very similar on all the equivalent materials and testing conditions.
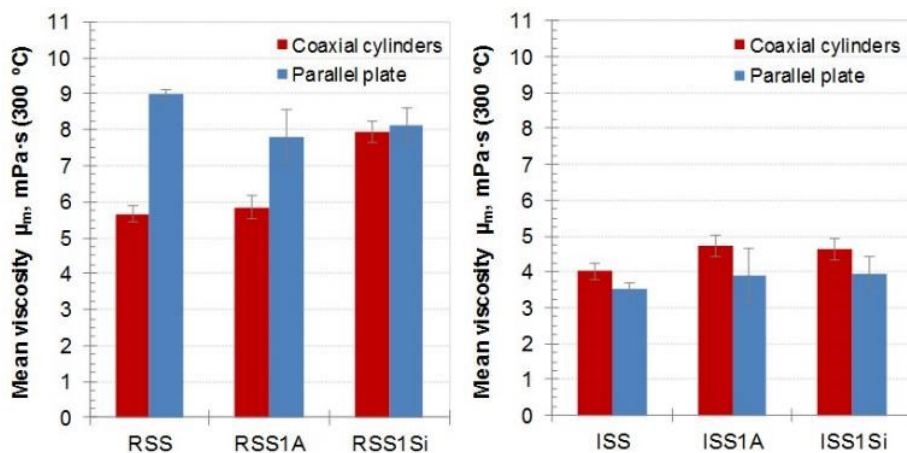
Figure 8-16. Mean viscosity and Standard Deviation (SD) at 300 ºC for the undoped salts and the nanofluids.

The differences between the rheometers configuration for the RSS and RSS-based nanofluids may come from three interrelated factors: the amount of sample used on each rheometer is different,

the time that the sample is at the molten state before being measured and the maximum shear rate applied. In this sense, in the coaxial cylinder rheometer, the sample has been in the molten state for several hours before being measured at 300 ºC and the impurities and/or nanoparticles may be agglomerated and settled at the bottom of the container. Thus, they are not dispersed in the molten salt during the measurement and the viscosity is lower than expected when taking into consideration the percentage of solids.

The samples containing ISS gave comparable results but those obtained with the parallel-plate configuration were slightly smaller. The explanation is the same detailed for the rheological performance: the wider shear rate range applied in the parallel plate may cause a higher alignment of the nanoparticles with the flow.

If these results are compared with those from other authors [31,74,95,114,164,185,203,249], a different behaviour has been observed in the present work, pointing at a dependence between the viscosity and the salt purity. The viscosity of the molten RSS at 300 ºC is higher than the viscosity published elsewhere for the analytical Solar Salt, while the viscosity of the molten ISS is near to those values. The viscosity of the nanofluid with SiNPs analysed by Jung [74] (equivalent to our nanofluids RSS1Si and ISS1Si), is between the values obtained for our RSS and ISS-based nanofluids.

In view of these comparisons, the viscosity results are highly influenced by the salt purity rather than the rheometer configuration, the presence of the nanoparticles or their chemical composition.

8.2.4 Conclusions

The viscosity of eight Solar Salt-based nanofluids containing silica and alumina nanoparticles and two commercial Solar Salts with different purity grade has been measured at different shear rates and temperatures. The tests have been carried out by using two kinds of rheometers: one corresponding to a coaxial cylinder configuration and another one with a parallel plate geometry. After a detailed analysis of the collected results, the following conclusions can be drawn:

- The rheological profile of the undoped Solar Salts and the nanofluids is influenced by the rheometer geometry. The measurements carried out with the coaxial cylinder method show that the samples have a Newtonian behaviour with a yield stress that needs to be exceeded to start the flow (Bingham profile). When the measurements are carried out with a parallel plate geometry, a shear thickening and a Newtonian behaviour are observed depending on the salt purity and the shear rate applied. This difference could be caused by some experimental deviation detected in the parallel plate system of the Rheometer 3. In both cases, the presence of nanoparticles did not change the rheological performance of the undoped Solar Salt.

- The viscosity of the undoped Solar Salt, determined by the coaxial cylinder method, is within the average value range reported by other authors. However, the results from the parallel plate configuration are clearly higher than those published by other authors when the sample is tested at low shear rates (1-250 s^{-1}) and below the average for high shear rates (100-1000 s^{-1}). This behaviour has been attributed to the dissimilar amount of sample tested on each technique (9 g in the coaxial cylinder and 2 g in the parallel plate).

- The viscosity of the nanofluids with respect to the base Solar Salt shows two different trends depending on the employed rheometer. When the coaxial cylinder method is employed, the nanofluids show an increment of viscosity in comparison to the undoped base salt, regardless of the temperature, the nanoparticle type or the salt purity. The nanofluids based on Refined Grade Solar Salt show the highest increase of viscosity in comparison to the undoped salt. On the other side, the results obtained with the parallel plate configuration reveal a similar viscosity between the undoped Solar Salt and the nanofluids, with small increments or even diminution. These results are highly influenced by the small sample size required on the latter device, far from the conditions encountered in real applications.

- The dependence of viscosity with the temperature has been observed in every tested sample. The relationship between these two variables for most samples is very similar to the mathematical expressions deduced by other researchers in the field (Arrhenius or VTF model).

- The influence of the nanoparticle concentration on the nanofluid viscosity was studied with the parallel plate geometry and the refined grade Solar Salt as the base fluid. Viscosity reductions are observed with the addition of ANPs in all the analysed concentrations. On the opposite, the addition of SiNPs led to considerable viscosity increments, except for the nanofluid with very low silica content (0.5 wt%). The theoretical model of Maron-Pierce has been used to analyse the experimental behaviour of the ANPs nanofluids and the Kriegher-Dougherty model for the SiNPs nanofluids. Results do not agree with these models. Instead, the increase of viscosity on the nanofluids containing SiNPs follows a polynomial expression similar to that proposed by Batchelor. No clear trend was found for the nanofluids containing ANPs.

The absence of published rheological studies of commercial purity Solar Salt impedes to compare and analyse the results reported in this work with equivalent materials.

The bibliographic data encountered on the literature do scarcely report the shear rate at which the measurements were performed, which could have greatly influenced the values reported on those articles and have a strong impact on the inconsistent rheological profiles reported by different researchers.

As a final remark, it is necessary to emphasize that the lack of information about the rheological properties of the high temperature nanofluids difficult the industrial implementation of these materials. In this sense, the aim of this article is to provide a step forward for the connection between the laboratory and the industry.

8.2.5 Appendix A

8.2.5.1 General factors influencing the viscosity

8.2.5.1.1 Influence of the shear rate

Generally, the rheological behaviour of fluids is evaluated by comparing the variation of the shear stress (τ) as function of the shear rate (γ). Depending of this relationship, the fluids are classified as "time-independent", "time-dependent" or "viscoelastic" fluids [182]. Most of the real fluids have a mixture of two or even three of these types.

Time-independent fluids are characterized by a specific shear stress under a certain shear rate, temperature and pressure. The flow curves of these fluids follow to the power law fluid model (Eq. 8-7) (also known as the Ostwald de Waele model) [183].

$$\tau = k \cdot \gamma^{n}$$

Eq. 8-7

where k (Pa·s^{n}) is the consistency index and n is the flow behaviour index. Power-law fluids can be subdivided into three different types of fluids based on the value of their flow behaviour index:

n < 1 → Shear thinning or pseudoplastic, decreasing viscosity with higher shear rates

n = 1 → Newtonian, constant viscosity with higher shear rates

n > 1 → Shear thickening or dilatant, increasing viscosity with higher shear rates

Viscoelastic fluids are those with a behaviour characterized by the existence of a yield stress (τ_0) which must be exceeded before the fluid will deform or flow. Among the models developed to explain this kind of fluids, the Bingham rheological model (Eq. 8-8) is widely accepted. It implies that the fluid is a rigid material under low shear stresses and has a Newtonian behaviour after overcoming the yield stress [182,183].

$$\tau = \tau_0 + \mu_0 \cdot \gamma$$

Eq. 8-8

where τ is the shear stress applied over the sample, τ_0 is the yield stress, μ_0 is the plastic dynamic viscosity and γ is the shear rate. The flow behaviour of some particulate suspensions is close to this expression [182].

The time-dependent fluids are more complex and their viscosity depends not only on the shear rate but also on the duration of shearing and their kinematic history.

8.2.5.2 Influence of the temperature

The evolution of viscosity with the temperature usually follows an Arrhenius model, as seen in Eq. 8-9, although some authors use a simple polynomial regression [114,185].

$$\mu = A_0 \exp(E_{visc}/RT)$$
<div align="right">Eq. 8-9</div>

where μ is the viscosity, A_0 is a constant, E_{visc} is the activation energy for viscous flow, R is the universal constant for the perfect gases, and T is the absolute temperature. Eq. 8-9 is commonly transformed into a lineal relationship by means of logarithms and known as the Vogel, Tamman and Fulcher (VTF) Equation (Eq. 8-10) [45].

$$\ln\mu = A + 1000\frac{B}{T+C}$$
<div align="right">Eq. 8-10</div>

These three variables have a physical meaning: A is the result of calculating $\ln\mu$ at a very high (infinite) temperature, B is the energy barrier to be overcome after any rearrangement of liquid molecules and C is the temperature at which the viscosity is infinite [45].

8.2.6   Appendix B

8.2.6.1 Calibration data of Rheometer 1

The Rheometer 1 was calibrated with a standard reference fluid Brookfield Viscosity Standard Fluid HT-30000 provided by the device manufacturer (Brookfield Inc., USA). Three samples were tested at 25, 93.3 and 149 ºC. The Table 8-7 gathers the mean values obtained and the comparison with the theoretical.

Table 8-7. Mean viscosity results at each tested temperature and comparison with the theoretical.

Temperature, ºC	Viscosity, mPa·s		
	Experimental	Theoretical	Error, %
25.0	29,120	30,000	2.93
93.3	9,175	9,000	1.94
149.0	4,600	4,500	2.22

8.2.6.2 Calibration data of Rheometer 2

The Rheometer 2 was calibrated with a standard reference fluid D10 according to the ISO 17025 Standard provided by Parangon Standard, Ltd. Four different samples of this standard fluid were tested at 40 ºC, 60 ºC and 80 ºC between 100 and 1000 s^{-1}.
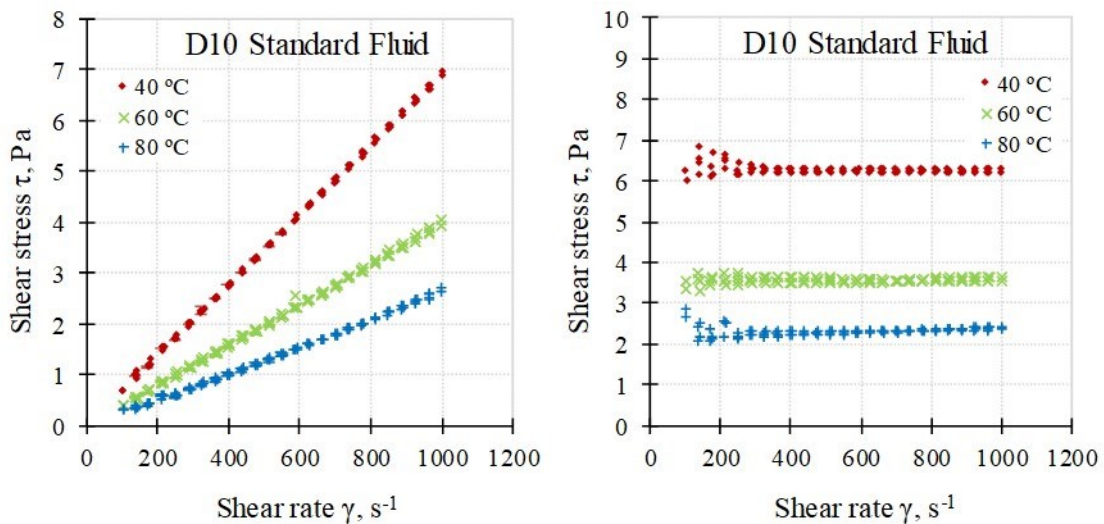
Figure 8-17. Experimental rheological profile and viscosity of the standard fluid D10 used to calibrate the Rheometer 2.

According to the Figure 8-17, this reference fluid D10 is clearly newtonian. The results of the lineal correlations of the Figure 8-17 left are showed in the Table 8-8, as well as the mean viscosity and the standard error compared to the theoretical data.

Table 8-8. Consistency index (k), flow behaviour index (n) and coefficient of determination (R^2) obtained when the experimental data are fitted to the power law fluid model (Eq. 8-7).

Temp.	k, $Pa \cdot s^n$	n	R^2	Mean viscosity, mPa·s	SD, mPa·s	Theoretical viscosity, mPa·s	Standard error, %
40 ºC	0.0069	1	0.9996	6.3036	0.1149	6.3090	0.08
60 ºC	0.0039	1	0.9985	3.5833	0.0696	3.7450	4.32
80 ºC	0.0026	1	0.9970	2.3285	0.1096	2.4730	5.84

8.2.6.3 Calibration data of Rheometer 3

The Rheometer 3 was calibrated with a standard fluid (WACKER® AK 1000000 SILICONE FLUID) provided by the device manufacturer (Anton Paar) and according to their test program.

Three different samples of this standard fluid were tested three times each one (Figure 8-18).

The theoretical fluid curve crossover (G'/G") is 120 rad/s. The experimental result of the curve crossover was 118.11 ± 1.01 rad/s with a Mean Average Error (MAE) of 2%.
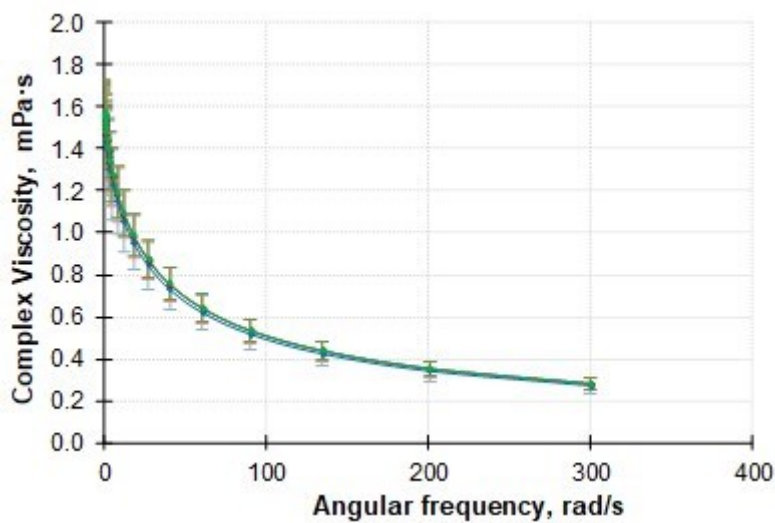
Figure 8-18. Experimental rheological profile of the standard fluid used to calibrate the Rheometer 3.

8.2.7 Appendix C

8.2.7.1 Regression of rheological results of molten salts and nanofluids

Table 8-9. Yield stress (τ_0), plastic dynamic viscosity (μ_0) and coefficient of determination (R^2) from the lineal regression according to the Bingham rheological model (Eq. 8-8).

Sample	250 ºC			270 ºC			290 ºC			300 ºC		
	τ_0, Pa	μ_0, Pa·s	R^2	τ_0, Pa	μ_0, Pa·s	R^2	τ_0, Pa	μ_0, Pa·s	R^2	τ_0, Pa	μ_0, Pa·s	R^2
RSS	0.8038	0.0568	0.9957	1.0184	0.0514	0.9954	1.7570	0.0478	0.9945	1.1302	0.0498	0.9995
RSS1A	3.6108	0.1235	0.9996	3.5279	0.0869	0.9993	1.2591	0.0666	0.9998	0.8730	0.0534	0.9987
RSS1Si	3.8560	0.1019	0.9994	1.9967	0.0866	0.9994	1.3850	0.0760	0.9984	1.0772	0.0729	0.9997
ISS	0.0680	0.4249	0.9996	0.9391	0.0590	0.9996	1.3852	0.0360	0.9930	0.8813	0.0351	0.9950
ISS1A	2.1032	0.0740	0.9991	1.5382	0.0478	0.9935	1.7356	0.0394	0.9935	1.7485	0.0370	0.9919
ISS1Si	6.1941	0.0813	0.9921	0.9521	0.0529	0.9944	0.9766	0.0428	0.9967	1.0396	0.0403	0.9977

Table 8-10. Consistency index (k), flow behaviour index (n) and coefficient of determination (R^2) obtained when the experimental data are fitted to the power law fluid model (Eq. 8-7). RSS-based nanofluids analysed between 1 and 250 s^{-1} (Rheometer 3) and ISS-based nanofluids analysed between 10-1000 s^{-1} (Rheometer 2).

Rheometer N.	Sample	300 ºC			350 ºC			400 ºC		
		k, Pa·s^n	n	R^2	k, Pa·s^n	n	R^2	k, Pa·s^n	n	R^2
3 (Parallel plate)	RSS	0.0041	1.1374	0.9972	0.0014	1.2866	0.9973	0.0007	1.3788	0.9983
	RSS1A	0.0056	1.0543	0.9972	0.0011	1.3164	0.9971	0.0014	1.2565	0.9945
	RSS1Si	0.0006	1.0451	0.9912	0.0013	1.3057	0.9975	0.0011	1.3061	0.9980
2 (Parallel plate)	ISS	0.0036	1.0000	0.9935	0.0027	1.0000	0.9916	0.0022	1.0000	0.9908
	ISS1A	0.0040	1.0000	0.9910	0.0030	1.0000	0.9983	0.0025	1.0000	0.9986
	ISS1Si	0.0040	1.0000	0.9924	0.0032	1.0000	0.9933	0.0026	1.0000	0.9934

Table 8-11. Consistency index (k), flow behaviour index (n) and coefficient of determination (R^2) obtained when the experimental data of Analytical Solar Salt (ASS) are fitted to the power law fluid model (Eq. 8-7).

Rheometer N.	Sample	300 ºC			350 ºC			400 ºC		
		k, Pa·s^n	n	R^2	k, Pa·s^n	n	R^2	k, Pa·s^n	n	R^2
3 (Parallel plate)	ASS (non-Newtonian)	0.0101	0.9425	0.9917	0.0025	1.1448	0.9871	0.0020	1.1602	0.9848
	ASS (Newtonian)	0.0770	1.000	0.9911	0.0055	1.0000	0.9530	0.046	1.0000	0.9468

Table 8-12. Correlation coefficients determined to fit the experimental results to the equation $\eta_R = A\phi^2 + B\phi + 1$ (η_R, (relative viscosity) versus ϕ (volume concentration of SiNPs nanofluids) at different temperatures).

Temperature	$\eta_R = A\phi^2 + B\phi + 1$		
	A	B	R^2
300 °C	65263.5924	-180.7771	0.9938
350 °C	51591.3605	-98.6924	0.9992
400 °C	55322.5871	-97.8576	0.9947

Chapter 9

CONCLUSIONS AND FUTURE RESEARCH LINES

9 CONCLUSIONS AND FUTURE RESEARCH LINES

9.1 INTRODUCTION

This Chapter summarizes all the conclusions obtained from the previous works according to the general objectives described in the Chapter 1. These conclusions are described in the next sections, followed by global remarks. In addition, several future research lines are proposed.

9.2 CONCLUSIONS RELATED TO THE OPTIMISATION OF THE EXPERIMENTAL METHODS

9.2.1 Specific heat

A precise method for the specific heat measurements of Solar Salt-based nanofluids and Sodium Nitrate-based NePCMs by DSC has been developed. Relative standard errors on measurements of about 5% were achieved by using this method. Parameters as the type of crucibles, the amount of sample in the crucible, and the atmosphere inside the crucible were studied.

- The use of flat-bottom crucibles (T-zero) reduced the scattering due to the better contact between the material and the crucible and, consequently, with the thermocouple of the device.

- The use of large samples (30 mg) improved the precision of the results due to a presumably lower humidity absorption percentage.

- The moisture absorbed by the sample during the manipulation to prepare the DSC specimens was the crucial factor on increase the precision of the results. The crucibles were closed under a controlled atmosphere in absence of moisture.

Thus, the optimal conditions were: the use of the T-zero type crucibles, filled in with 30 mg of the sample and sealed under an inert atmosphere. The specific heat was determined according to a MDSC method with several isothermal stages.

9.2.2 Dynamic Light Scattering (DLS)

A method for the measurement of the nanoparticle size distribution of Solar Salt-based nanofluids and Sodium Nitrate-based NePCMs by the DLS technique was developed in this tesis. An optimal dilution ratio of 0.1 mg·mL^{-1} of the solid sample into deionized water was selected. The samples were measured just after being dissolved in water to reduce the scattering on the results.

9.3 CONCLUSIONS RELATED TO THE RAW MATERIALS

9.3.1 Salts

9.3.1.1 Solar Salt

Three Solar Salts of different purity were studied: analytical grade, refined grade and industrial grade. The first one allows the comparison with the literature values, where is of common use. The second one is currently used in the CSP plants as TES and heat transfer material. The last one is analysed as a cheaper alternative to the latter.

- The main difference between the refined and the industrial grade are the amount of impurities contained on them (chlorides, sulphates, phosphates, carbonates, sodium and magnesium). The high amount of chlorides in the Solar Salt of industrial grade is limits its use as TES material, since they increase the corrosion rate of the molten salt [222–224].

- The Solar Salt of industrial grade withstood the thermal cycling between 100 ºC and 550 ºC without showing any evidence of decomposition. As expected, the weight loss in this temperature range was minimal because of the thermal stability of nitrates until 600 ºC [31,33,113,180].

- The specific heat of the Solar Salt was measured both in the solid (196 ºC) and in the liquid state (296 ºC and 396 ºC). The results were very similar for the three Solar Salts: 1.4 kJ·kg^{-1}·K^{-1} in solid and 1.5 kJ·kg^{-1}·K^{-1} in liquid, in agreement with the specialized literature [86,180].

- The thermal diffusivity and the thermal conductivity were measured by the LFA method in the Solar Salt of refined grade at these three temperatures. The results were between 0.203 mm^2·s^{-1} and 0.212 mm^2·s^{-1} for the thermal diffusivity and between 0.441 W·m^{-1}·K^{-1} and 0.499 W·m^{-1}·K^{-1} for the thermal conductivity. The differences with the literature could be attributed with the different techniques used by other authors and the presence of impurities on this Solar Salt of refined grade [180].

- The SEM images of these salts revealed an homogeneous distribution of the different crystals of sodium and potassium nitrate, similarly as those appearing in diverse publications [31,74].

- The stability in the long term of the dispersed impurities in the Solar Salts of refined and industrial grade was analysed as a previous step to understand the stability of the nanoparticles on them. The salts were kept in the molten state for five hours. The impurities sank into the molten salt at different rates. The analysis of the bottom area of the solid salt revealed a high concentration of phosphates and sulphates in the refined grade and chlorides and magnesium in the industrial grade.

- The <u>rheology</u> of the Solar Salts of refined and industrial grade was measured at different shear rates (1-1000 s^{-1}) and temperatures (250-400 ºC). Three rheometers with geometries of coaxial cylinders and parallel plate were used for the tests. The results revealed a Newtonian rheological profile of the salts, as proposed by Lasfargues et al. [31,114] and Jung et al. [74,95]. The evolution of the viscosity with the temperature followed the Arrhenius model. The geometry of the rheometers had a certain influence on the final viscosity results, related to the different amount of sample tested and the shear rate applied on each case.

9.3.1.2 Sodium Nitrate

In the same manner as the Solar Salt, three purities of Sodium Nitrate were studied: the analytical, the refined and the industrial grade. This is used as PCM of high temperature to storage the thermal energy as latent heat in the CSP plants.

- The Sodium Nitrate of industrial grade was <u>thermally cycled</u> between 100 ºC and 400 ºC (the working temperature in the solar system). The mass loss was very small (1.2 wt%), in agreement with the results of Bauer et al. [33].

- The <u>specific heat</u> of the three Sodium Nitrates was measured in solid (256 ºC) and in liquid (326 ºC). The values ranged from 2.4 kJ·kg^{-1}·K^{-1} to 2.8 kJ·kg^{-1}·K^{-1} in solid and 1.6 to 1.7 in liquid, depending on the salt purity. These results are in the range found by different researchers [33] (1.7 kJ·kg^{-1}·K^{-1} as average value at 326 ºC). The high c_p showed by the experimental results in the solid state is due to the proximity of the melting point.

- The <u>latent heat</u> (fusion and crystallization) of the three Sodium Nitrates was strongly influenced by the purity of the salt. The results were 180 kJ·kg^{-1} (reference value, 178 kJ·kg^{-1} [33]), 162 kJ·kg^{-1} and 125 kJ·kg^{-1} for the analytical, refined and industrial grade, respectively. These differences were caused by the internal crystalline structure of the salts. The refined and the industrial grade contains impurities which impede the existence of a high-ordered structure as in the analytical grade. <u>The phase-change temperature</u> (fusion or crystallization) followed the same trend. The melting temperature suffered a reduction with the increasing amount of impurities: Sodium Nitrate of analytical grade (310 ºC), refined grade (307 ºC) and industrial grade (300 ºC). The subcooling effect was observed in the three salts (10 ºC).

- The <u>thermal diffusivity and the thermal conductivity</u> of the analytical Sodium Nitrate was measured at the same temperatures as the specific heat (256 ºC in solid state and 326 ºC in liquid state). The experimental results of the thermal diffusivity (0.09 mm^2·s^{-1} in solid and 0.10 mm^2·s^{-1} in liquid) are a bit low in comparison to those of the literature [33]. Consequently, the thermal conductivity results (0.49 mm^2·s^{-1} in solid and 0.32 mm^2·s^{-1} in liquid) are also below those

published. This discrepancy could be due to the different crystal structure of the analysed Sodium Nitrate and that employed by other researchers [33].

9.3.2 Nanoparticles

9.3.2.1 Alumina nanoparticles

- The thermal cycling between 100 ºC and 550 ºC revealed three different stages related to the loss of humidity (Δm=-11.3% at 80 ºC), the desorption of the intralaminar water (Δm=-13.3% at 390 ºC) and the start of the transformation from boehmite to γ-Al_2O_3 temperature range (Δm=-5.6% at 550 ºC). These results are in agreement with the literature [186,187].

- The nanoparticle size distribution of the Alumisol-10A ranged from 10 nm to 190 nm and the most frequent size is 15.69 nm. Most of the nanoparticles (90%) are smaller than 21.70 nm. The zeta potential is inside the region of electrical stability ($\geq$35 mV) at pHs between 2 and 9.

- The specific heat of these nanoparticles is ranging from 1.195 $kJ \cdot kg^{-1} \cdot K^{-1}$ (196 ºC) to 1.471 $kJ \cdot kg^{-1} \cdot K^{-1}$ (396 ºC). These values are higher than the results from Furukawa [193] and Auerkari [194]. This could be due to the increment on the specific heat on alumina nanoparticles with respect to the bulk material, as proposed by Wang et al. [192].

- The microstructure was observed with SEM and revealed that the alumina (boehmite) nanoparticles consists of several layers arranged in a fiber-like structure. The XRD diffraction pattern obtained coincident peaks with the boehmite structure. The analysis after heating the boehmite up to 550 ºC revealed the loss of crystallinity related to the conversion from boehmite to γ-Al_2O_3, confirming the thermal cycling results.

9.3.2.2 Silica nanoparticles

- The thermal cycling between 100 ºC and 550 ºC revealed two different stages related to the loss of physically adsorbed water (Δm=-6.3% at 90 ºC), the desorption of the chemically adsorbed water bonded to Si-OH (Δm=-2.5% at 550 ºC). These results are in agreement with the thermal degradation of amorphous silica [188,189]

- The nanoparticle size distribution of the LUDOX® SM-30 ranged from 10 nm to 105 nm and the most frequent size is 13.55 nm. Most of the nanoparticles (90%) are smaller than 25.40 nm. The zeta potential is inside the region of electrical stability ($\leq$-35 mV) at pHs between 4 and 10.

- The specific heat of these nanoparticles is ranging from 0.970 $kJ \cdot kg^{-1} \cdot K^{-1}$ (196 ºC) to 1.157 $kJ \cdot kg^{-1} \cdot K^{-1}$ (396 ºC). These values are a bit lower than the results from the literature [253],

presumably due to the amorphous character of this silica.

- The <u>microstructure</u> was observed with SEM and revealed that the morphology of the silica nanoparticles consists of spheres which are clustered together forming chains. The <u>XRD diffraction pattern</u> confirmed the absence of crystallinity of this silica, as declared by the supplier of the LUDOX® SM-30.

9.4 CONCLUSIONS RELATED TO THE SYNTHESIS PROCEDURE

A detailed research about the synthesis methods of Solar-Salt based nanofluids was developed with the focus on their impact in the thermal properties. Three different methods (the traditional hot plate, the sprayed nanoparticles and the low-water hot plate) were compared by measuring the nanoparticle size distribution and the specific heat. The industrial viability of the method and the reduce nanoparticle agglomeration during the nanofluid production were the two essential factors considered to select the method.

- The <u>nanoparticle size distribution</u> was highly dependent on the synthesis method. The agglomeration in the final material was important on the traditional hot plate method (712 nm) In comparison to the low-water hot plate (68 nm). It is understandable due to the use of solid nanoparticles which need to be disaggregated in the traditional hot plate procedure. The nanofluids obtained with the sprayed nanoparticle and the low-water hot plate methods had equivalent size distributions. However, the first one generated nanofluids with a high heterogeneity.

- The <u>specific heat</u> was measured in these nanofluids in the solid (196 ºC) and in the liquid state (396 ºC). The nanofluids generated by the traditional hot plate method had decrements (-2.43% at 396 ºC) in comparison to the base Solar Salt but increments were registered in those obtained by the low-water hot plate procedure (7.75% at 396 ºC). The comparison between the specific heat of the nanofluids from the sprayed nanoparticles method and the low-water hot plate method was favourable to the first with the addition of alumina nanoparticles (10.01% vs. 6.31% at 396 ºC). The results were quite similar between these two methods if the nanofluid contained silica nanoparticles (1.97% vs. 2.59% at 396 ºC).

Despite the results of specific heat, the low homogeneity showed by the nanofluids synthetized according to the sprayed nanoparticles method impedes, at the moment, its consideration as alternative to the traditional hot plate procedure. Thus, the low-water hot plate method was revealed as a real alternative to the traditional one. Their advantages are the following:

- The use of ultrasound to disperse the nanoparticles is avoided. This is possible due to the use of commercial aqueous nanofluids (where nanoparticles are still well dispersed) instead of solid nanoparticles.

- The amount of water needed to disperse the nanoparticles and dissolve the salts is reduced by a hundred times.

- This method ends by melting the nanofluid as an additional step to homogenise the sample as much as possible before testing it.

The two first points have a direct incidence on the synthesis cost of the MSBNFs. In addition, by using commercial nanofluids as the source of nanoparticles and salts of non-analytical grades the possibility of producing it at an industrial scale is closer.

The final stage of the research was devoted to optimise the variables of this synthesis route. The best conditions found for the process were: salt concentration of 50 wt% in the initial aqueous solution, mixing temperature between 30 ºC and 50 ºC, mixing speed between 60 rpm and 130 rpm, surface to volume ration higher than 0.1168 m^{-1} and a drying temperature of 100 ºC.

9.5   CONCLUSIONS RELATED TO THE THERMAL PROPERTIES OF SOLAR SALT-BASED NANOFLUIDS

The thermal properties of Solar Salt-based nanofluids were investigated with the focus on two properties: the specific heat and the thermal conductivity.

9.5.1   Specific heat

The specific heat enhancement of Solar Salt-based nanofluids were analysed according to several factors: the salt purity (analytical, refined or industrial grade), the nanoparticle concentration (0.5, 1 or 1.5 wt%), the nanoparticle type (alumina or silica nanoparticles).

- The specific heat results were inconsistent when comparing equivalent nanofluids synthetized independently or repeated measurement on the same material. This low repeatability is due to the high heterogeneity typical of the nanofluids and it is a general issue observed in other published researches. However, some global trends were drawn from the specific heat results. The influence of the nanoparticle percentage and the purity of the Solar Salt were interrelated. The more important increments were obtained with the addition of 1.5 wt% of alumina or silica nanoparticles to the Solar Salt of analytical or refined grade. On the other hand, a mass concentration of 1 wt% of nanoparticles in the Solar Salt of industrial grade obtained the best enhancements.

- The <u>theoretical calculations</u> of the specific heat with the models of Zhou et al. [60] and Shin and Banerjee [63] were too far from the experimental results.

- The relationship between the specific heat and the <u>available surface of the nanoparticles</u> (computed from the DLS measurements) was erratic and did not provide any clear conclusion.

- The <u>SEM images</u> revealed that those nanofluids with the highest enhancements had little agglomeration between the nanoparticles, which were homogeneously dispersed. The existence of a special nanostructure was observed in a nanofluid of Solar Salt of industrial grade and 1 wt% of alumina nanoparticles. This nanostructure was considered the responsible of the specific heat improvement in this nanofluid (39.17% in the solid state).

9.5.2 Thermal conductivity

The LFA method was used to measure the thermal conductivity of several nanofluids based on Solar Salt of refined grade with different contents (0.5%, 1% or 1.5%) of alumina or silica nanoparticles. The thermal conductivity of these materials were measured for the first time in the liquid state, since there is not any precedent in the literature.

- Increments of the specific heat and thermal conductivity were found on the nanofluids with 1% and 1.5 wt% of both types of nanoparticles (alumina or silica). The results were especially remarkable for concentrations of 1.5% of silica nanoparticles (14% of specific heat increment) and 1.5 wt% of alumina nanoparticles (60% of thermal conductivity increment).

- The <u>theoretical models</u> of Zhou et al. [60] and Shin and Banerjee [63] were used to estimate the specific heat of the nanofluids and that of Hamilton-Crosser [204] to evaluate the thermal conductivity. The predictions obtained from them were very far from the experimental results, which led to suppose that additional factors are involved on the increase of the thermal properties.

- The <u>available nanoparticle surface</u> was estimated from the measurement with the DLS technique. A direct correlation (parabolic) was found between this parameter and the high specific heat and thermal conductivity of the nanofluids with silica nanoparticles, which confirms the important influence of the nanoparticle size on the thermal properties.

9.6 CONCLUSIONS RELATED TO THE THERMAL PROPERTIES OF SODIUM NITRATE-BASED NANO-ENHANCED PCMS

This study included both experimental and simulation results, which were then compared. Regarding the experimental results:

- The <u>specific heat</u> of the NePCMs was highly dependent on the salt purity. Decrements (around 3%) in comparison to the original Sodium Nitrate were found in the NePCMs containing Sodium Nitrate of analytical grade (both with alumina or silica nanoparticles) and those with Sodium Nitrate of industrial grade and alumina nanoparticles. The others NePCMs showed the opposite trend (with increments around 3%).

- The <u>latent heat of fusion and crystallization</u> decreased (up to 7% depending on the temperature) with the addition of nanoparticles to the Sodium Nitrate of analytical grade. There were not changes on this property for those NePCMs based on Sodium Nitrate of refined or industrial grade. The <u>phase change temperatures</u> (of fusion or solidification) of the Sodium Nitrate were not affected by the presence of the nanoparticles in any of the studied NePCMs. The subcooling phenomena ($\approx$10 ºC) affected both the Sodium Nitrates and the NePCMs. The <u>onset temperature of fusion</u> followed the same trend of the latent heat.

- The <u>thermal conductivity</u> was measured in a NePCM based in Sodium Nitrate of analytical grade and 1 wt% of alumina nanoparticles. It had a considerable enhancement in comparison to the initial Sodium Nitrate, both in the solid (97.78%) and in the liquid state (124.01%).

- The <u>SEM images</u> of a NePCM of Sodium Nitrate of industrial grade and 1 wt% of alumina nanoparticles revealed the existence of agglomerates of about 2 or 3 nm in size. The compositional analysis with the EDX confirmed the presence of aluminium as well as some impurities coming from the Sodium Nitrate, such as potassium, magnesium and chlorine.

- The <u>simulation results</u> considered three NePCMs with Sodium Nitrate and 0.5, 1 or 1.5 wt% of alumina nanoparticles. About the thermophysical properties, the simulation predicted enhancements and a direct correlation between the thermal conductivity and dynamic viscosity and the amount of alumina nanoparticles. The specific heat and the latent heat of fusion followed the inverse trend. The heat transfer rate was improved with the addition of the alumina nanoparticles and the charging and discharging cycles were slightly shortened.

- The <u>comparison between the experimental and the simulation results</u> revealed several trends. The specific heat results were comparable both in the solid and the liquid state. The latent heat had an inverse correlation with the content of alumina nanoparticles, with the exception of the NePCM with 1 wt%. The experimental enhancement of the thermal conductivity was much higher than the value predicted by the simulations ($\approx$13%). It is though that other mechanisms not considered in the simulations are responsible of these great increments.

9.7 CONCLUSIONS RELATED TO THE STABILITY OF SOLAR SALT-BASED NANOFLUIDS IN THE LONG TERM

The stability of nanoparticles in molten Solar Salt was analysed with a specific test designed with this objective. Six nanofluids based on Solar Salt of analytical, refined and industrial grade and 1 wt% of silica or alumina nanoparticles were maintained at 396 ºC for 5 hours.

The characterization of the nanoparticle size in these nanofluids at different times (0.5, 1 and 5 hours) suggested discrepancies between the nanofluids depending on the base salt. The visual inspection and the analysis of the nanoparticle percentage at these times revealed that they are agglomerated and settled down at the bottom of the flask in all the studied nanofluids. The exception was found for the nanofluid with Solar Salt of industrial grade and 1 wt% of silica nanoparticles, which seems stable at least for 24 hours. It is thought that some of the impurities contained in this salt were the responsible of the stabilization of the silica nanoparticles.

A deeper research is needed in this particular subject, since there is not much scientific knowledge up to now. The modelling of these systems of molten salts and ceramic nanoparticles combined with experimental research could be a great option to foster the know-how in this issue.

9.8 CONCLUSIONS RELATED TO THE RHEOLOGY OF SOLAR SALT-BASED NANOFLUIDS

The rheology of several Solar Salt-based nanofluids with 1% by weight of alumina or silica nanoparticles was studied at different shear rates and temperatures in two kinds of rheometers: coaxial cylinder and parallel plate. The collected results led to the following conclusions:

- The rheology of the Solar Salts was not changed by the addition of nanoparticles. The rheology of the initial Solar Salts and their nanofluids was influenced by the rheometer geometry. The results from the coaxial cylinder showed a Bingham profile, which is a Newtonian behaviour with an initial yield stress. The results from the parallel plate showed both a Newtonian and a shear thickening performance. The latter is possibly due to an experimental deviation of the rheometer.

- The viscosity was increased by the addition of nanoparticles to the pure Solar Salts. These increments depended on the rheometer geometry, salt purity and the kind of nanoparticle. In the coaxial cylinder method, the nanofluids based on the refined Solar Salt and 1 wt% of silica nanoparticles had the highest increments (28.7% at 300 ºC), while the industrial Solar Salt obtained similar enhancements both with silica (13.1% at 300 ºC) or alumina nanoparticles (14.6% at 300 ºC). The differences are related to the high content of impurities of the Solar Salt of industrial grade, which causes the nanoparticles to have a highest settling rate. Most of them

are at the bottom of the sample chamber and no more dispersed in the molten salt. In the parallel plate rheometer, there are little increments and even decrements for the Solar Salt of refined grade at shear rates under 250 s^{-1}. The increase at high shear rates (1000 s^{-1}) was of 9.3% for the addition of alumina nanoparticles and 10% at 300 ºC for the addition of silica nanoparticles to the Solar Salt of industrial grade. These results are highly influenced by the small sample size required on the latter device, far from the conditions encountered in real applications.

- The viscosity of the nanofluids followed an Arrhenius model with <u>respect to the temperature</u>. This relationship was found with independency of the type of nanoparticle, base salt or rheometer geometry.

- <u>The influence of the nanoparticle concentration</u> (0.5, 1 or 1.5 wt%) on the viscosity was studied with the parallel plate geometry and the refined grade Solar Salt as the base fluid. The addition of alumina nanoparticles in any concentration led to reductions on the Solar Salt viscosity (around 15%). On the opposite, the addition of silica nanoparticles led to considerable viscosity increments (up to 21% with 1.5 wt% at 400 ºC). Two theoretical models were used to analyse these results: the Maron-Pierce model for the nanofluids of alumina nanoparticles and the Kriegher-Dougherty model for those with silica nanoparticles. These models did not agree with the experimental measurements. Instead, the increase of viscosity of the nanofluids with silica nanoparticles followed a polynomial expression similar to that proposed by Batchelor. No clear trend was found for the nanofluids containing alumina nanoparticles.

9.9 GENERAL CONCLUSIONS

According to the particular conclusions developed in the previous sections, the main contributions of this doctoral dissertation are the following:

- The designing and optimisation of a precise method based on a MDSC isothermal program to determine the specific heat of molten salts and MSBNFs.

- The development and optimisation of a new synthesis method different from the traditional hot plate procedure commonly employed for the MSBNFs. This innovative method is effective on avoiding the nanoparticle agglomeration without the use of ultrasounds and reduces a hundred times the amount of water needed in the process.

- The synthesis and characterization of MSBNFs based on non-analytical grade salts is an innovation of this research and allows a more precise evaluation of the industrial application of these materials.

- The determination of the thermal properties of Solar Salt-based nanofluids with a special focus on the thermal cycling of the nanofluids, the reproducibility of the specific heat results, the thermal conductivity in the solid and the liquid state by the LFA method.

- The determination of the thermal properties of Sodium Nitrate-based NePCMs with a special focus on the thermal cycling of the NePCMs, the influence of the salt purity and nanoparticle concentration on the specific heat, latent heat and phase change temperature and the thermal conductivity in the solid and the liquid stated by the LFA method. In addition, the simulation and modelling of these materials and the comparison with the experimental results.

- The designing and execution of a specific test to evaluate the stability of the nanoparticles in the molten salt in the long term.

- The determination of the rheological properties of Solar Salt-based nanofluids with a special focus on analysing the influence of the salt purity, nanoparticle concentration, temperature and rheometer geometry on the results.

9.10 FUTURE RESEARCH LINES

Based on the previous particular and general conclusions, it seems clear that there is still a huge research work to be done in the field of MSBNFs. With this aim, several future research lines are proposed:

- Assure the reproducibility of the specific heat results by synthetizing and analysing a huge number of equivalent samples. In addition, it would be interesting to perform a round-robin test of the specific heat of one (or several) MSBNFs between different research laboratories working on the subject.

- Perform a deep study of the stability of MSBNFs under thermal cycling, by increasing the number of cycles and the nanoparticle concentration.

- Conceive and develop valid strategies to improve the stability of the nanoparticles in molten salt. A deep knowledge of the mechanisms involved in this process could be helpful, as well as modelling and simulation works in this particular subject. Regarding the experimental field, it would be interesting working with nanoparticles with a similar density to that of the molten salt or investigate the use of high temperature surfactants.

- Design of a reproducible, suitable and industrially viable method of production of these materials, with a special focus on keeping the nanoparticle size in the nanometric range and

avoiding the use of ultrasonic power or water. Ideally, this method would be performed by the mining companies that are currently selling the salt for the CSP plants in their own production lines. In this sense, the sprayed nanoparticles method described here is a great starting point to try the scalability of the procedure.

- Finally, there is a need to perform corrosion tests to assure the absence of chemical reactions between the MSBNFs and the container materials (diverse steels) of the thermal storage tanks or pipes in the CSP plants.

ANNEXES

ANNEX I. REFERENCES

[1]   G. Li, X. Zheng, Thermal energy storage system integration forms for a sustainable future, Renew. Sustain. Energy Rev. 62 (2016) 736–757. doi:10.1016/j.rser.2016.04.076.

[2]   L.E. Singer, D. Peterson, International Energy Outlook 2016, 2016.

[3]   H. Zhang, J. Baeyens, G. Cáceres, J. Degrève, Y. Lv, Thermal energy storage: Recent developments and practical aspects, Prog. Energy Combust. Sci. 53 (2016) 1–40. doi:10.1016/j.pecs.2015.10.003.

[4]   F. Wilkins, The economic and reliability benefits of CSP with thermal energy storage: recent studies and research needs, CSP Alliance Rep. (2012). doi:10.1017/CBO9781107415324.004.

[5]   EASAC, Concentrating Solar Power: It's Potential Contribution to a sustainable Energy Future, 2012. http://elib.dlr.de/79584/ (accessed January 17, 2017).

[6]   Á.F. Díaz-Carralero, Estudios físico-químicos y de corrosión a elevada temperatura para el diseño de nuevos fluidos almacenadores de energía en centrales solares de concentración, (2013). https://www.mysciencework.com/publication/show/385c89d3ba5be242ae9ace2ecb961183 (accessed February 21, 2017).

[7]   M.T. Dunham, B.D. Iverson, High-efficiency thermodynamic power cycles for concentrated solar power systems, Renew. Sustain. Energy Rev. 30 (2014) 758–770. doi:10.1016/j.rser.2013.11.010.

[8]   SolarPaces, CSP Projects Around the World, (n.d.). http://www.solarpaces.org/csp-technology/csp-projects-around-the-world.

[9]   M. Liu, N. Tay, S. Bell, M. Belusko, Review on concentrating solar power plants and new developments in high temperature thermal energy storage technologies, Renew. Sustain. Energy Rev. 53 (2016) 1411–1432. doi:10.1016/j.rser.2015.09.026.

[10]   D. Grogan, Development of Molten Salt HTF technology for Parabolic Trough Solar Power Plants - Public Final Technical Report. DOE/08GO18038., 2013.

[11]   Solutia, Therminol VP-1, (2014) 1–5. http://twt.mpei.ac.ru/TTHB/HEDH/HTF-VP1.PDF.

[12]   Dow Chemical Company, Dowtherm A - Heat Transfer Fluid, Product Technical Data, (1997).

[13] M.M. Kenisarin, High-temperature phase change materials for thermal energy storage, Renew. Sustain. Energy Rev. 14 (2010) 955–970. doi:10.1016/j.rser.2009.11.011.

[14] M. Liu, W. Saman, F. Bruno, Review on storage materials and thermal performance enhancement techniques for high temperature phase change thermal storage systems, Renew. Sustain. Energy Rev. 16 (2012) 2118–2132. doi:10.1016/j.rser.2012.01.020.

[15] L.D. Solomon, The Use of Sodium Chloride & Aluminum as Phase Change Materials for High Temperature Thermal Energy Storage Characterized by Calorimetry, (2013).

[16] C.Y. Zhao, G.H. Zhang, Review on microencapsulated phase change materials (MEPCMs): Fabrication, characterization and applications, Renew. Sustain. Energy Rev. 15 (2011) 3813–3832. doi:10.1016/j.rser.2011.07.019.

[17] R. Tamme, Thermal Energy Storage for Large Scale CSP Plants Storage for Large Scale Solar Power Plants Outline, (2009) 1–24.

[18] C.W. Robak, T.L. Bergman, A. Faghri, Enhancement of latent heat energy storage using embedded heat pipes, Int. J. Heat Mass Transf. 54 (2011) 3476–3484. doi:10.1016/j.ijheatmasstransfer.2011.03.038.

[19] S. Pincemin, X. Py, R. Olives, M. Christ, O. Oettinger, Elaboration of Conductive Thermal Storage Composites Made of Phase Change Materials and Graphite for Solar Plant, J. Sol. Energy Eng. 130 (2008) 11005. doi:10.1115/1.2804620.

[20] P. Blanco-Rodríguez, J. Rodríguez-Aseguinolaza, E. Risueño, M. Tello, Thermophysical characterization of Mg–51%Zn eutectic metal alloy: A phase change material for thermal energy storage in direct steam generation applications, Energy. (2014) 1–7. doi:10.1016/j.energy.2014.05.058.

[21] J.Q. Sun, R.Y. Zhang, Z.P. Liu, G.H. Lu, Thermal reliability test of Al–34%Mg–6%Zn alloy as latent heat storage material and corrosion of metal with respect to thermal cycling, Energy Convers. Manag. 48 (2007) 619–624. doi:10.1016/j.enconman.2006.05.017.

[22] S. Kuravi, J. Trahan, D.Y. Goswami, M.M. Rahman, E.K. Stefanakos, Thermal energy storage technologies and systems for concentrating solar power plants, Prog. Energy Combust. Sci. 39 (2013) 285–319. doi:10.1016/j.pecs.2013.02.001.

[23] J. Cot-Gores, A. Castell, L.F. Cabeza, Thermochemical energy storage and conversion: A-state-of-the-art review of the experimental research under practical conditions, Renew. Sustain. Energy Rev. 16 (2012) 5207–5224. doi:10.1016/j.rser.2012.04.007.

[24]   A. Gil, M. Medrano, I. Martorell, A. Lázaro, P. Dolado, B. Zalba, L.F. Cabeza, State of the art on high temperature thermal energy storage for power generation. Part 1—Concepts, materials and modellization, Renew. Sustain. Energy Rev. 14 (2010) 31–55. doi:10.1016/j.rser.2009.07.035.

[25]   J. Stekli, L. Irwin, R. Pitchumani, Technical Challenges and Opportunities for Concentrating Solar Power With Thermal Energy Storage, J. Therm. Sci. Eng. Appl. 5 (2013) 21011. doi:10.1115/1.4024143.

[26]   Z. Ma, G. Glatzmaier, M. Mehos, Fluidized Bed Technology for Concentrating Solar Power With Thermal Energy Storage, J. Sol. Energy Eng. 136 (2014) 31014. doi:10.1115/1.4027262.

[27]   M. Medrano, A. Gil, I. Martorell, X. Potau, L.F. Cabeza, State of the art on high-temperature thermal energy storage for power generation. Part 2—Case studies, Renew. Sustain. Energy Rev. 14 (2010) 56–72. doi:10.1016/j.rser.2009.07.036.

[28]   D. Kearney, B. Kelly, U. Herrmann, R. Cable, J. Pacheco, R. Mahoney, H. Price, D. Blake, P. Nava, N. Potrovitza, Engineering aspects of a molten salt heat transfer fluid in a trough solar field, Energy. 29 (2004) 861–870. doi:10.1016/S0360-5442(03)00191-9.

[29]   G. Glatzmaier, New Concepts and Materials for Thermal Energy Storage and Heat-Transfer Fluids, 2011.

[30]   D. Shin, Molten salt nanomaterials for thermal energy storage and concentrated solar power applications, Texas A&M University, 2011.

[31]   M. Lasfargues, Nitrate based high temperature nano-heat-transfer-fluids: formulation & characterisation, The University of Leeds, 2014. http://etheses.whiterose.ac.uk/id/eprint/7531 (accessed April 20, 2015).

[32]   M. Schuller, F. Little, D. Malik, M. Betts, Q. Shao, J. Luo, W. Zhong, S. Shankar, A. Padmanaban, Molten Salt-Carbon Nanotube Thermal Energy Storage for Concentrating Solar Power Systems Final Report, 2012. http://www.osti.gov/bridge/product.biblio.jsp?osti_id=1036948 (accessed December 17, 2013).

[33]   T. Bauer, D. Laing, U. Kröner, R. Tamme, Sodium nitrate for high temperature latent storage, in: 11th Int. Conf. Therm. Energy Storage–Effstock, 2009: pp. 14–17. http://medcontent.metapress.com/index/A65RM03P4874243N.pdf (accessed January 14, 2014).

[34]   J. Nieto-Maestre, I. Iparraguirre-Torres, Z.A. Velasco, I. Kaltzakorta, M.M. Zubieta, Novel metallic alloys as phase change materials for heat storage in direct steam generation applications, AIP Conf. Proc. 1734 (2016). doi:10.1063/1.4949130.

[35]   M. Lasfargues, Q. Geng, H. Cao, Y. Ding, Mechanical Dispersion of Nanoparticles and Its Effect on the Specific Heat Capacity of Impure Binary Nitrate Salt Mixtures, Nanomaterials. 5 (2015) 1136–1146. doi:10.3390/nano5031136.

[36]   M. Chieruzzi, G.F. Cerritelli, A. Miliozzi, J.M. Kenny, Effect of nanoparticles on heat capacity of nanofluids based on molten salts as PCM for thermal energy storage., Nanoscale Res. Lett. 8 (2013) 448. doi:10.1186/1556-276X-8-448.

[37]   M. Chieruzzi, J.M. Kenny, A. Miliozzi, Studio e sviluppo di un mezzo di accumulo a calore latente a media temperatura (200-400 °C) costituito da una miscela di sali e nanoparticelle, 2013.

[38]   M. Betts, The Effects of Nanoparticle Augmentation of Nitrate Thermal Storage Materials for Use in Concentrating Solar Power Applications, Texas A&M University, 2011. http://repositories.tdl.org/tdl-ir/handle/1969.1/ETD-TAMU-2011-05-9118 (accessed January 14, 2014).

[39]   M. Chieruzzi, A. Miliozzi, T. Crescenzi, L. Torre, J.M. Kenny, A New Phase Change Material Based on Potassium Nitrate with Silica and Alumina Nanoparticles for Thermal Energy Storage., Nanoscale Res. Lett. 10 (2015) 984. doi:10.1186/s11671-015-0984-2.

[40]   M.W. Thoms, Adsorption at the Nanoparticle Interface for Increased Thermal Capacity in Solar Thermal Systems, Massachusetts Institute of Technology, 2012.

[41]   C. Pang, J.W. Lee, Y.T. Kang, Review on combined heat and mass transfer characteristics in nanofluids, Int. J. Therm. Sci. 87 (2015) 49–67. doi:10.1016/j.ijthermalsci.2014.07.017.

[42]   S. Choi, J. Eastman, Enhancing thermal conductivity of fluids with nanoparticles, in: Int. Mech. Eng. Congr. Exhib. ASME San Fr., 1995: pp. 99–105. https://www.researchgate.net/profile/Jeffrey_Eastman/publication/236353373_Enhancing_thermal_conductivity_of_fluids_with_nanoparticles._ASME_FED/links/0f3175336e78aa9c4c000000.pdf (accessed February 17, 2016).

[43]   J. Eastman, S.U.. Choi, S. Li, L.J. Thompson, S. Lee, Enhanced thermal conductivity through the development of nanofluids, in: Mater. Res. Soc. Symp., 1996: pp. 3–12. http://journals.cambridge.org/abstract_S1946427400215996 (accessed February 17, 2016).

[44]   Y. Li, J. Zhou, S. Tung, E. Schneider, S. Xi, A review on development of nanofluid preparation and characterization, Powder Technol. 196 (2009) 89–101. doi:10.1016/j.powtec.2009.07.025.

[45]   E.K. Goharshadi, H. Ahmadzadeh, S. Samiee, M. Hadadian, Nanofluids for Heat Transfer Enhancement–A Review, Phys. Chem. Res. 1 (2013) 1–33.

[46]   A. Ghadimi, R. Saidur, H.S.C. Metselaar, A review of nanofluid stability properties and characterization in stationary conditions, Int. J. Heat Mass Transf. 54 (2011) 4051–4068. doi:10.1016/j.ijheatmasstransfer.2011.04.014.

[47]   V. Sridhara, L.N. Satapathy, Al2O3-based nanofluids: a review., Nanoscale Res. Lett. 6 (2011) 456. doi:10.1186/1556-276X-6-456.

[48]   R. Goldstein, D. Joseph, D. Pui, Convective Heat Transport in Nanofluids, in: Univ. Minnesota, 2000: pp. 99–105. http://www.aem.umn.edu/people/faculty/joseph/archive/docs/twophase.pdf (accessed February 17, 2016).

[49]   D. Singh, D. Pandey, R. Yadav, D. Singh, A study of ZnO nanoparticles and ZnO-EG nanofluid, J. Exp. Nanosci. 8 (2013) 731–741.

[50]   W. Yu, H. Xie, L. Chen, Y. Li, Investigation of thermal conductivity and viscosity of ethylene glycol based ZnO nanofluid, Thermochim. Acta. 491 (2009) 92–96. doi:10.1016/j.tca.2009.03.007.

[51]   J. Garg, B. Poudel, M. Chiesa, J.B. Gordon, J.J. Ma, J.B. Wang, Z.F. Ren, Y.T. Kang, H. Ohtani, J. Nanda, G.H. McKinley, G. Chen, Enhanced thermal conductivity and viscosity of copper nanoparticles in ethylene glycol nanofluid, J. Appl. Phys. 103 (2008) 74301. doi:10.1063/1.2902483.

[52]   E. Ettefaghi, H. Ahmadi, A. Rashidi, A. Nouralishahi, S.S. Mohtasebi, Preparation and thermal properties of oil-based nanofluid from multi-walled carbon nanotubes and engine oil as nano-lubricant, Int. Commun. Heat Mass Transf. 46 (2013) 142–147. doi:10.1016/j.icheatmasstransfer.2013.05.003.

[53]   M. Ghazvini, M. a. Akhavan-Behabadi, E. Rasouli, M. Raisee, Heat Transfer Properties of Nanodiamond–Engine Oil Nanofluid in Laminar Flow, Heat Transf. Eng. 33 (2012) 525–532. doi:10.1080/01457632.2012.624858.

[54]   R. Grena, P. Tarquini, Solar linear Fresnel collector using molten nitrates as heat transfer

fluid, Energy. 36 (2011) 1048–1056. doi:10.1016/j.energy.2010.12.003.

[55] U. Herrmann, B. Kelly, H. Price, Two-tank molten salt storage for parabolic trough solar power plants, Energy. 29 (2004) 883–893. doi:10.1016/S0360-5442(03)00193-2.

[56] D. Shin, D. Banerjee, Effects of silica nanoparticles on enhancing the specific heat capacity of carbonate salt eutectic (work in progress), Int. J. Struct. Chang. Solids - Mech. Appl. 2 (2010) 25–31.

[57] O. Arthur, M. a. Karim, An investigation into the thermophysical and rheological properties of nanofluids for solar thermal applications, Renew. Sustain. Energy Rev. 55 (2016) 739–755. doi:10.1016/j.rser.2015.10.065.

[58] H. Riazi, T. Murphy, G.B. Webber, R. Atkin, S.S.M. Tehrani, R. a. Taylor, Specific heat control of nanofluids : A critical review, Int. J. Therm. Sci. 107 (2016) 25–38. doi:10.1016/j.ijthermalsci.2016.03.024.

[59] B. Pak, Y. Cho, Hydrodynamic and heat transfer study of dispersed fluids with submicron metallic oxide particles, Exp. Heat Transf. 11 (1998) 151–170. http://www.tandfonline.com/doi/abs/10.1080/08916159808946559 (accessed February 18, 2016).

[60] S.-Q. Zhou, R. Ni, Measurement of the specific heat capacity of water-based Al2O3 nanofluid, Appl. Phys. Lett. 92 (2008) 93123. doi:10.1063/1.2890431.

[61] M.-C. Lu, C.-H. Huang, Specific heat capacity of molten salt-based alumina nanofluid, Nanoscale Res. Lett. 8 (2013) 292. doi:10.1186/1556-276X-8-292.

[62] D. Malik, Evaluation of composite alumina nanoparticle and nitrate eutectic materials for use in concentrating solar power plants, Texas A&M University, 2010. http://repositories.tdl.org/tdl-ir/handle/1969.1/ETD-TAMU-2010-05-7705 (accessed October 10, 2013).

[63] D. Shin, D. Banerjee, Enhancement of specific heat capacity of high-temperature silica-nanofluids synthesized in alkali chloride salt eutectics for solar thermal-energy storage applications, Int. J. Heat Mass Transf. 54 (2011) 1064–1070. doi:10.1016/j.ijheatmasstransfer.2010.11.017.

[64] P. Andreu-cabedo, Mejora de las propiedades térmicas de sal solar mediante adición de nanopartículas, Universitat Jaume I, 2014.

[65] B. Jo, D. Banerjee, Enhanced specific heat capacity of molten salt-based nanomaterials:

Effects of nanoparticle dispersion and solvent material, Acta Mater. 75 (2014) 80–91. doi:10.1016/j.actamat.2014.05.005.

[66]   M.X. Ho, C. Pan, Optimal concentration of alumina nanoparticles in molten Hitec salt to maximize its specific heat capacity, Int. J. Heat Mass Transf. 70 (2014) 174–184. doi:10.1016/j.ijheatmasstransfer.2013.10.078.

[67]   H. Tiznobaik, D. Shin, Enhanced specific heat capacity of high-temperature molten salt-based nanofluids, Int. J. Heat Mass Transf. 57 (2013) 542–548. doi:10.1016/j.ijheatmasstransfer.2012.10.062.

[68]   B.-X. Wang, L.-P. Zhou, X.-F. Peng, Surface and Size Effects on the Specific Heat Capacity of Nanoparticles, Int. J. Thermophys. 27 (2006) 139–151.

[69]   L. Wang, Z. Tan, S. Meng, D. Liang, G. Li, Enhancement of molar heat capacity of nanostructured Al2O3, J. Nanoparticle Res. 3 (2001) 483–487.

[70]   L. Xue, P. Keblinski, S.. Phillpot, S.U.-S. Choi, J.. Eastman, Effect of liquid layering at the liquid–solid interface on thermal transport, Int. J. Heat Mass Transf. 47 (2004) 4277–4284. doi:10.1016/j.ijheatmasstransfer.2004.05.016.

[71]   S. Oh, Y. Kauffmann, C. Scheu, W. Kaplan, M. Rühle, Ordered liquid aluminum at the interface with sapphire, Science (80-.). 310 (2005) 661–663. http://science.sciencemag.org/content/310/5748/661.short (accessed June 6, 2016).

[72]   D. Shin, H. Tiznobaik, D. Banerjee, Specific heat mechanism of molten salt nanofluids, Appl. Phys. Lett. 104 (2014). doi:10.1063/1.4868254.

[73]   K. Khanafer, F. Tavakkoli, K. Vafai, A. AlAmiri, A critical investigation of the anomalous behavior of molten salt-based nanofluids, Int. Commun. Heat Mass Transf. 69 (2015) 51–58. doi:10.1016/j.icheatmasstransfer.2015.10.002.

[74]   S. Jung, Numerical and experimental investigation of inorganic nanomaterials for thermal energy storage (TES) and concentrated solar power (CSP) applicaitons, Texas A&M University, 2012.

[75]   B. Jo, D. Banerjee, Effect of solvent on specific heat capacity enhancement of binary molten salt-based carbon nanotube nanomaterials for thermal energy storage, Int. J. Therm. Sci. 98 (2015) 219–227. doi:10.1016/j.ijthermalsci.2015.07.020.

[76]   D. Shin, B. Jo, H. Kwak, D. Banerjee, Investigation of high temperature nanofluids for solar thermal power conversion and storage applications, in: 14th Int. Heat Transf. Conf.,

2010: pp. 1–9. http://proceedings.asmedigitalcollection.asme.org/proceeding.aspx?articleid=1620722 (accessed January 14, 2016).

[77] Y. Nagaraj, Modeling and simulation of nanofluid for heat storage, University of Texas at Arlington, 2014.

[78] A. Miliozzi, E. Veca, S. Sau, R. Grena, M. Celino, M. Falconieri, F. Rondino, Individuazione e caratterizzazione di miscele di materiali a cambiamento di fase e nanoparticelle da impiegare come sistemi alternativi di accumulo termico, 2013.

[79] N.A.C. Sidik, H. a. Mohammed, O. a. Alawi, S. Samion, A review on preparation methods and challenges of nanofluids, Int. Commun. Heat Mass Transf. 54 (2014) 115–125. doi:10.1016/j.icheatmasstransfer.2014.03.002.

[80] Z. Haddad, C. Abid, H.F. Oztop, A. Mataoui, A review on how the researchers prepare their nanofluids, Int. J. Therm. Sci. 76 (2014) 168–189. doi:10.1016/j.ijthermalsci.2013.08.010.

[81] J.M. Khodadadi, L. Fan, H. Babaei, Thermal conductivity enhancement of nanostructure-based colloidal suspensions utilized as phase change materials for thermal energy storage: A review, Renew. Sustain. Energy Rev. 24 (2013) 418–444. doi:10.1016/j.rser.2013.03.031.

[82] C. Lai, W. Chang, W. Hu, Z.M. Wang, M. Lu, L. Chueh, Solar-Thermal Energy harvesting Scheme: Enhanced heat capacity of molten HITEC salt, Nanoscale. 6 (2014) 4555–4559.

[83] S. Liu, D. Wu, J. Liu, Y. Nian, P. Qiu, Development of a novel molten-salt filled with nanoparticles for concentration solar plants, 2nd IET Renew. Power Gener. Conf. (RPG 2013). (2013) 5.03-5.03. doi:10.1049/cp.2013.1884.

[84] B. Jo, D. Banerjee, Viscosity measurements of multi-walled carbon nanotubes-based high temperature nanofluids, Mater. Lett. 122 (2014) 212–215. doi:10.1016/j.matlet.2014.02.032.

[85] S.M.S. Murshed, C. a. Nieto de Castro, Superior thermal features of carbon nanotubes-based nanofluids – A review, Renew. Sustain. Energy Rev. 37 (2014) 155–167. doi:10.1016/j.rser.2014.05.017.

[86] R. Serrano-López, J. Fradera, S. Cuesta-López, Molten salts database for energy applications, Chem. Eng. Process. Process Intensif. 73 (2013) 87–102.

doi:10.1016/j.cep.2013.07.008.

[87]   V. Somani, Colloidal stability of magnetic nanoparticles in molten salts, Massachusetts Institute of Technology, 2010.

[88]   D. Shin, D. Banerjee, Enhanced specific heat capacity of molten salt-metal oxide nanofluid as heat transfer fluid for solar thermal applications, SAE Int. (2010). http://papers.sae.org/2010-01-1734/ (accessed January 14, 2016).

[89]   S. Shankar, Thermal cycling effects on the nanoparticle distribution and specific heat of a carbonate eutectic with alumina nanoparticles, Texas A&M University, 2011. http://repository.tamu.edu/bitstream/handle/1969.1/ETD-TAMU-2011-05-9483/SHANKAR-THESIS.pdf?sequence=2&isAllowed=y (accessed February 18, 2015).

[90]   D. Shin, D. Banerjee, Enhanced Specific Heat of Silica Nanofluid, J. Heat Transfer. 133 (2011). doi:10.1115/1.4002600.

[91]   D. Shin, D. Banerjee, Enhanced Specific Heat Capacity of Nanomaterials Synthesized by Dispersing Silica Nanoparticles in Eutectic Mixtures, J. Heat Transfer. 135 (2013) 32801. doi:10.1115/1.4005163.

[92]   H. Kwak, D. Shin, D. Banerjee, Enhanced sensible heat capacity of molten salt and conventional heat transfer fluid based nanofluid for solar thermal energy storage application, in: ASME 2010 4th Int. Conf. Energy Sustain., 2010: pp. 1–5. http://proceedings.asmedigitalcollection.asme.org/proceeding.aspx?articleid=1607662 (accessed January 14, 2016).

[93]   A. Padmanaban Iyer, The effect of silica nanoparticles on corrosion of steel by molten carbonate eutectics, Texas A&M University, 2011.

[94]   B. Jo, D. Banerjee, Enhanced Specific Heat Capacity of Molten Salts Using Organic Nanoparticles, in: ASME 2011 Int. Mech. Eng. Congr. Expo., 2011: pp. 1–8. http://proceedings.asmedigitalcollection.asme.org/proceeding.aspx?articleid=1645496 (accessed January 14, 2016).

[95]   B. Jo, S. Jung, D. Shin, D. Banerjee, Anomalous rheological behavior of complex fluids (nanofluids), in: ASME 2011 Int. Mech. Eng. Congr. Expo., 2011: pp. 1–6. http://proceedings.asmedigitalcollection.asme.org/proceeding.aspx?articleid=1643833 (accessed January 14, 2016).

[96]   D. Shin, D. Banerjee, Experimental investigation of molten salt nanofluid for solar thermal

energy application, in: ASME/JSME 2011 8th Therm. Eng. Jt. Conf., 2011: pp. 1–6. http://ebooks.asmedigitalcollection.asme.org/pdfAccess.ashx?url=/data/Conferences/AJ TEC2011/69610/T30024_1.pdf (accessed January 14, 2016).

[97]   M. Schuller, Q. Shao, T. Lalk, Experimental investigation of the specific heat of a nitrate–alumina nanofluid for solar thermal energy storage systems, Int. J. Therm. Sci. 91 (2015) 142–145. doi:10.1016/j.ijthermalsci.2015.01.012.

[98]   D. Shin, D. Banerjee, Specific heat of nanofluids synthesized by dispersing alumina nanoparticles in alkali salt eutectic, Int. J. Heat Mass Transf. 74 (2014) 210–214. doi:10.1016/j.ijheatmasstransfer.2014.02.066.

[99]   H. Tiznobaik, D. Banerjee, D. Shin, Effect of formation of "long range" secondary dendritic nanostructures in molten salt nanofluids on the values of specific heat capacity, Int. J. Heat Mass Transf. 91 (2015) 342–346. doi:10.1016/j.ijheatmasstransfer.2015.05.072.

[100] H. Tiznobaik, D. Shin, Experimental Study of Nanoengineered Molten Salts as Thermal Energy Storage in Solar Power Plants, in: ASME 2012 Int. Mech. Eng. Congr. Expo., 2012: pp. 1–6. http://proceedings.asmedigitalcollection.asme.org/proceeding.aspx?articleid=1751027 (accessed January 14, 2016).

[101] H. Tiznobaik, D. Shin, Investigation of Molten Salt Nanomaterials for Solar Thermal Energy Storage Application, in: ASME 2012 Summer Heat Transf. Conf., 2012: pp. 8–11. http://proceedings.asmedigitalcollection.asme.org/proceeding.aspx?articleid=1720409 (accessed January 14, 2016).

[102] D. Shin, D. Banerjee, Enhanced thermal properties of SiO2 nanocomposite for solar thermal energy storage applications, Int. J. Heat Mass Transf. 84 (2015) 898–902. doi:10.1016/j.ijheatmasstransfer.2015.01.100.

[103] H. Tiznobaik, D. Shin, Experimental validation of enhanced heat capacity of ionic liquid-based nanomaterial, Appl. Phys. Lett. 102 (2013). doi:10.1063/1.4801645.

[104] B. Dudda, D. Shin, Effect of nanoparticle dispersion on specific heat capacity of a binary nitrate salt eutectic for concentrated solar power applications, Int. J. Therm. Sci. 69 (2013) 37–42. doi:10.1016/j.ijthermalsci.2013.02.003.

[105] B. Dudda, Effect of nanoparticle dispersions in binary nitrate salt as thermal energy storage material in concentrated solar power applications, University of Texas at

Arlington, 2013.

[106] B. Dudda, D. Shin, Investigation of Molten Salt Nanomaterial as Thermal Energy Storage in Concentrated Solar Power, in: ASME 2012 Int. Mech. Eng. Congr. Expo., 2012: pp. 1–6. http://proceedings.asmedigitalcollection.asme.org/proceeding.aspx?articleid=1751811 (accessed January 14, 2016).

[107] R. Devaradjane, Utilization of molten nitrate salt nanomaterials for heat capacity enhancement in solar power applications, University of Texas at Arlington, 2013.

[108] R. Devaradjane, D. Shin, Enhanced Heat Capacity of Molten Salt Nano-Materials for Concentrated Solar Power Application, in: ASME 2012 Int. Mech. Eng. Congr. Expo., 2012: pp. 1–5. http://proceedings.asmedigitalcollection.asme.org/proceeding.aspx?articleid=1751602 (accessed January 14, 2016).

[109] R. Devaradjane, D. Shin, Nanoparticle dispersions on ternary nitrate salts for heat transfer fluid applications in solar thermal power, J. Heat Transfer. (2015). doi:10.1115/1.4030903.

[110] J. Seo, D. Shin, Enhancement of specific heat of ternary nitrate (LiNO3-NaNO3-KNO3) salt by doping with SiO2 nanoparticles for solar thermal energy storage, Micro Nano Lett. 9 (2014) 817–820. doi:10.1049/mnl.2014.0407.

[111] S. Changla, Experimental study of quaternary nitrate/nitrite molten salt as advanced heat transfer fluid and energy storage material in concentrated solar power plant, University of Texas at Arlington, 2015. http://onlinelibrary.wiley.com/doi/10.1002/cbdv.200490137/abstract (accessed September 1, 2015).

[112] R. Mondragon, L. Hernandez, L. Cabedo, S. Torro, J.E. Julia, Increment of specific heat of Solar Salt with SiO2 and Al2O3 nanoparticles, in: Eurotherm Semin. #99. Adv. Therm. Energy Storage, 2014: pp. 1–9.

[113] P. Andreu-Cabedo, R. Mondragon, L. Hernandez, R. Martinez-Cuenca, L. Cabedo, J.E. Julia, Increment of specific heat capacity of solar salt with SiO2 nanoparticles., Nanoscale Res. Lett. 9 (2014) 582. doi:10.1186/1556-276X-9-582.

[114] M. Lasfargues, H. Cao, Q. Geng, Y. Ding, Rheological Analysis of Binary Eutectic Mixture of Sodium and Potassium Nitrate and the Effect of Low Concentration CuO Nanoparticle Addition to Its Viscosity, Materials (Basel). 8 (2015) 5194–5204.

doi:10.3390/ma8085194.

[115] M. Lasfargues, A. Bell, Y. Ding, In situ production of titanium dioxide nanoparticles in molten salt phase for thermal energy storage and heat- transfer fluid applications, J. Nanoparticle Res. (2016). doi:10.1007/s11051-016-3460-8.

[116] B. Muñoz-Sánchez, J. Nieto-Maestre, I. Iparraguirre-Torres, J. a. Sánchez-García, J.E. Julia, A. García-Romero, The influence of mixing water on the thermophysical properties of nanofluids based on solar salt and silica nanoparticles, AIP Conf. Proc. 50031 (2016). doi:10.1063/1.4949129.

[117] B. Muñoz-Sánchez, J. Nieto-Maestre, I. Iparraguirre-torres, A. García-Romero, Assessment of the determination of the Specific Heat of Molten Salt doped with Nanoparticles by means of the DSC technique, in: Greenstock Conf. Beijing, 2015.

[118] B. Muñoz-Sánchez, J. Nieto-Maestre, I. Iparraguirre-torres, A. García-Romero, Nanoparticle size evaluation through Dynamic Light Scattering (DLS) technique in a nitrate salt doped with ceramic nanoparticles, in: Congr. CIIEM15. Paris, 2015.

[119] B. Muñoz-Sánchez, J. Nieto-Maestre, I. Iparraguirre-Torres, J. a. Sánchez-García, J.E. Julia, A. García-Romero, Preparation of nanofluids based on solar salt and boehmite nanoparticles: Characterization of starting materials, AIP Conf. Proc. 50030 (2016). doi:10.1063/1.4949128.

[120] H. Riazi, S. Mesgari, N. a. Ahmed, R. a. Taylor, The effect of nanoparticle morphology on the specific heat of nanosalts, Int. J. Heat Mass Transf. 94 (2016) 254–261. doi:10.1016/j.ijheatmasstransfer.2015.11.064.

[121] P. Gimenez-Gavarrel, V.D. Romanin, S. Fereres, Latent Heat of Fusion and Melting Temperature of Molten Salt Based Carbon Nanotube Suspensions Used as Phase Change Materials, in: ASME 2015 9th Int. Conf. Energy Sustain., 2015: pp. 1–5. http://proceedings.asmedigitalcollection.asme.org/proceeding.aspx?articleid=2467457 (accessed January 14, 2016).

[122] S. Mukherjee, S. Paria, Preparation and Stability of Nanofluids-A Review, IOSR J. Mech. Civ. Eng. 9 (2013) 63–69. http://iosrjournals.org/iosr-jmce/papers/vol9-issue2/I0926369.pdf (accessed January 15, 2015).

[123] W. Yu, H. Xie, A Review on Nanofluids: Preparation, Stability Mechanisms, and Applications, J. Nanomater. 2012 (2012) 1–17. doi:10.1155/2012/435873.

[124] W. Yu, D.M. France, S.U.. Choi, J.L. Routbort, Review and Assessment of Nanofluid Technology for Transportation and Other Applications, 2007.

[125] Y. Chueh, Enhanced energy harvesting scheme utilizing hierarchical nanostructures, in: IEEE Nanotechnol. Mater. Devices Conf. (IEEE NMDC 2013), 2013: pp. 3–4.

[126] B. Muñoz-Sánchez, J. Nieto-Maestre, I. Iparraguirre-Torres, J. a. Sánchez-García, J.E. Julia, A. García-Romero, The influence of mixing water on the thermophysical properties of nanofluids based on solar salt and silica nanoparticles, AIP Conf. Proc. 50031 (2016). doi:10.1063/1.4949129.

[127] B. Muñoz-Sánchez, J. Nieto-Maestre, I. Iparraguirre-Torres, J. a. Sánchez-García, J.E. Julia, A. García-Romero, Preparation of nanofluids based on solar salt and boehmite nanoparticles: Characterization of starting materials, AIP Conf. Proc. 50030 (2016). doi:10.1063/1.4949128.

[128] B. Jo, D. Banerjee, Thermal properties measurement of binary carbonate salt mixtures for concentrating solar power plants, J. Renew. Sustain. Energy. 33121 (2015). doi:10.1063/1.4922029.

[129] O. Mahian, A. Kianifar, S. a. Kalogirou, I. Pop, S. Wongwises, A review of the applications of nanofluids in solar energy, Int. J. Heat Mass Transf. 57 (2013) 582–594. doi:10.1016/j.ijheatmasstransfer.2012.10.037.

[130] Z. Han, Nanofluids with enhanced thermal transport properties, 2008. http://drum.lib.umd.edu/handle/1903/8654 (accessed March 10, 2014).

[131] P. Estellé, Comment on "Viscosity measurements of multi-walled carbon nanotubes-based high temperature nanofluids," Mater. Lett. 138 (2014) 162–163. doi:10.1016/j.matlet.2014.09.139.

[132] SQM, Sutainability Report, 2015.

[133] L. Pokorny, I. Maturana, W. Bortle, Sodium nitrate and nitrite, Kirk-Othmer Encycl. …. (2006). http://onlinelibrary.wiley.com/doi/10.1002/0471238961.1915040916151115.a01.pub2/full (accessed December 6, 2016).

[134] Labkem, Sodium Nitrate - Analytical grade, (n.d.) 8339.

[135] SQM, Sodium Nitrate Refined Grade - Thermosolar. Product Data Sheet, (n.d.).

[136] SQM, Sodium Nitrate. Industrial Grade - Thermosolar - Crystals, (n.d.).

[137] Labkem, Potassium Nitrate - Analytical grade, (n.d.) 8339.

[138] SQM, Potassium Nitrate Refined Grade - Thermosolar. Product Data Sheet, (n.d.).

[139] Haifa, Potassium nitrate. Greenhouse grade - Multi KGG, (n.d.).

[140] C.W. Bale, E. Bélisle, P. Chartrand, S.A. Decterov, G. Eriksson, A.E. Gheribi, K. Hack, I.H. Jung, Y.B. Kang, J. Melançon, A.D. Pelton, S. Petersen, C. Robelin, J. Sangster, P. Spencer, M.A. Van Ende, FactSage thermochemical software and databases, 2010-2016, Calphad Comput. Coupling Phase Diagrams Thermochem. 54 (2016) 35–53. doi:10.1016/j.calphad.2016.05.002.

[141] L. Kawaken Fine Chemicals Co., Technical Bulletin of Alumina sol, 2011.

[142] G. González Hueto, Síntesis y caracterización de películas nanoestructuradas con propiedades superhidrofóbicas, 2013. http://www.repositoriodigital.ipn.mx/handle/123456789/11093 (accessed January 6, 2015).

[143] N. Karami, M. Rahimi, Heat transfer enhancement in a PV cell using Boehmite nanofluid, Energy Convers. Manag. 86 (2014) 275–285. doi:10.1016/j.enconman.2014.05.037.

[144] W.R.G.& Co.-Conn., LUDOX® Colloidal Silica in Catalyst Applications, (2015).

[145] G.M. Technology, LUDOX® Colloidal Silica, (2012).

[146] E. Shapiro, K. Panagiotidis, T. Staffel, Coated ammonium polyphosphate, its use and manufacture, 13002805.3, 2014.

[147] Sigma-Aldrich, Silica nanopowder (718483). Product Specification, n.d.

[148] R. Shaw, Dynamic Light Scattering Training: Achieving Reliable Nano Particle Sizing, (2013). http://scholar.google.com/scholar?hl=en&btnG=Search&q=intitle:Dynamic+Light+Scattering+Training+Achieving+reliable+nano+particle+sizing#0 (accessed December 27, 2016).

[149] Christine Foster, Dynamic Light Scattering, (2015).

[150] Malvern Instruments, White paper: A basic guide to particle characterization, 2016.

[151] A. Zayid, Factors Affecting the Electrical Conductivity and Zeta Potential of Alumina

Nanofluids, (2014). https://dalspace.library.dal.ca/handle/10222/50641 (accessed December 28, 2016).

[152] Nanocomposix, Zeta Potential Analysis of Nanoparticles, Nanocomposix Publ. (2012) 1–6.

[153] Malvern Instruments, Zetasizer Nano Series User Manual, (2004).

[154] W. Pan, W. Xu, S. Li, Fundamentals of TGA and SDT, Therm. Anal. Fundam. …. (2005) 1–7. http://dialnet.unirioja.es/servlet/articulo?codigo=1986690.

[155] G. Höhne, W.F. Hemminger, H.-J. Flammersheim, Differential scanning calorimetry, 2003. http://www.springer.com/la/book/9783540004677 (accessed December 27, 2016).

[156] L. Thomas, Modulated DSC® Paper# 2 Modulated DSC® Basics; Calculation and Calibration of MDSC® Signals, 2005. http://www.tainstruments.com/pdf/literature/TP007_MDSC_2_CalculationsandCalibrations.pdf (accessed May 5, 2016).

[157] B. Muñoz-Sánchez, J. Nieto-Maestre, G. Imbuluzqueta, I. Marañón, I. Iparraguirre-Torres, A. García-Romero, A precise method to measure the specific heat of solar salt-based nanofluids, J. Therm. Anal. Calorim. (2017). doi:10.1007/s10973-017-6272-x.

[158] B. Muñoz-Sánchez, J. Nieto-Maestre, J. Gonzalez-Aguilar, J.E. Julia, N. Navarrete, A. Faik, T. Bauer, A. Bonk, M.E. Navarro, Y. Ding, N. Uranga, E. Veca, S. Sau, P. Giménez, P. Garcia, J.I. Burgaleta, Round Robin Test on the Measurement of the Specific Heat of Solar Salt, AIP Conf. Proc. 80017 (2017). doi:10.1063/1.4984438.

[159] D.A. Ditmars, S. Ishihara, T.S.S. Chang, G. Bernstein, Enthalpy and Heat-Capacity Standard Reference Material: Synthetic Sapphire (α-Al2O3) from 10 to 2250 K, J. Res. Natl. Bur. Stand. (1934). 87 (1982) 155. doi:10.6028/jres.087.011.

[160] Netzsch, Operating Instructions Laser-Flash-Apparatus LFA 427, (n.d.).

[161] G. Janz, Thermodynamic and transport properties for molten salts: correlation equations for critically evaluated density, surface tension, electrical conductance and viscosity data, J. Phys. Chem. Ref. Data. 17 (1988). http://scholar.google.com/scholar?hl=en&btnG=Search&q=intitle:Thermodynamic+and+Transport+Properties+for+Molten+Salts#0 (accessed May 5, 2016).

[162] M. Birkholz, Thin Film Analysis by X-Ray Scattering, 2006. doi:10.1002/3527607595.ch1.

[163] H. Stanjek, W. Häusler, Introduction To Powder/ Polycrystalline Diffraction, Hyperfine Interact. 154 (2004) 107–119. doi:10.1023/B:HYPE.0000032028.60546.38.

[164] Y. Jin, J. Cheng, X. An, T. Su, P. Zhang, Z. Li, Accurate viscosity measurement of nitrates/nitrites salts for concentrated solar power, Sol. Energy. 137 (2016) 385–392. doi:10.1016/j.solener.2016.08.037.

[165] B.E. Laboratories, Brookfield DV-III Ultra Instructions, n.d.

[166] L.H.O. Hellström, M. a Samaha, K.M. Wang, A.J. Smits, M. Hultmark, Errors in parallel-plate and cone-plate rheometer measurements due to sample underfill, Meas. Sci. Technol. 26 (2015) 15301. doi:10.1088/0957-0233/26/1/015301.

[167] S. Millennium, The parabolic trough power plants Andasol 1 to 3, Tech. Sol. Millenn. AG. (2008) 1–26. http://scholar.google.com/scholar?hl=en&btnG=Search&q=intitle:The+parabolic+trough +power+plants+Andasol+1+to+3#1 (accessed May 5, 2016).

[168] Enel, At priolo Enel inaugurates the "Archimede" power plant, Enel. 795 (2010) 1–2. https://servizi.enel.it/eWCM/salastampa/comunicati_eng/1634858-2_PDF-1.pdf.

[169] L. Thomas, Modulated DSC® Paper# 9 Measurement of Accurate Heat Capacity Values, TA Instruments, New Castle,. (2005) 1–11. http://www.tainstruments.com/pdf/literature/TP014_MDSC_9_MeasurementofAccurate HeatCapacityValues.pdf (accessed December 26, 2016).

[170] L. Thomas, Modulated DSC® Paper# 3 Modulated DSC® Basics; Optimization of MDSC® Experimental Conditions, 2005. http://www.tainstruments.com/pdf/literature/TP_008_MDSC_num_3_Optimization_of_ Experimental_Conditions.pdf (accessed December 27, 2016).

[171] R. Benages Vilau, Growth, Morphology and Solid State Miscibility of Alkali Nitrates, Universitat de Barcelona, 2013.

[172] R.S. France, L.A.T. México, Reference materials for calorimetry and differential thermal analysis, 331 (1999) 93–204.

[173] B. Muñoz-Sánchez, J. Nieto-Maestre, J. Gonzalez-aguilar, J.E. Julia, N. Navarrete, A. Faik, Round Robin Test on the Measurement of the Specific Heat of Solar Salt, (2016). http://elib.dlr.de/108923/ (accessed December 27, 2016).

[174] N. Pfleger, T. Bauer, C. Martin, M. Eck, A. Wörner, Thermal energy storage - overview

and specific insight into nitrate salts for sensible and latent heat storage, Beilstein J. Nanotechnol. 6 (2015) 1487–1497.

[175] ASTM International, ASTM 1269E. Standard Test Method for Determining Specific Heat Capacity by Differential Scanning Calorimetry, (2011).

[176] Modulated DSC® Paper# 1 A Simple Technique With Significant Benefits, TA Instruments. (2001).

[177] ASTM E2586-14. Standard Practice for Calculating and Using Basic Statistics, ASTM Int. (2014). doi:10.1520/E2586-14.2.

[178] Malvern Instruments, Dynamic light scattering: Common terms defined, Malvern Guid. (2011) 1–6.

[179] T. He, L. Xiang, S. Zhu, Different nanostructures of boehmite fabricated by hydrothermal process: effects of pH and anions, CrystEngComm. 11 (2009) 1338. doi:10.1039/b900447p.

[180] T. Bauer, N. Pfleger, N. Breidenbach, M. Eck, D. Laing, S. Kaesche, Material Aspects of Solar Salt for Sensible Heat Storage, (2012) 1–10.

[181] H. Zhang, Y. Zhao, J. Li, L. Shi, M. Wang, Preparation and Thermal Properties of High-Purified Molten Nitrate Salt Materials with Heat Transfer and Storage, High Temp. Mater. Process. 34 (2015). doi:10.1515/htmp-2014-0147.

[182] R.P. Chhabra, J.F. Richardson, Non-Newtonian Flow and Applied Rheology - Engineering Applications (2nd Edition), 2008. https://app.knovel.com/web/toc.v/cid:kpNNFAREAC/viewerType:toc/root_slug:non-newtonian-flow.

[183] T.F. Tadros, Rheology of Dispersions: Principles and Applications, 2010. doi:10.1002/9783527631568.

[184] N. Triantafillopoulos, Measurement of Fluid Rheology and Interpretation of Rheograms, 2000.

[185] D. Nissen, Thermophysical properties of the equimolar mixture NaNO3-KNO3 from 300 to 600 ºC, J. Chem. Eng. Data. 27 (1980) 269–273. http://www.osti.gov/scitech/biblio/6765587 (accessed January 31, 2017).

[186] W. Brostow, T. Datashvili, Chemical modification and characterization of boehmite

particles, Chem. Chem. Technol. 2 (2008).

[187] T. Tsukada, K. Okadab, Crystallinity of boehmite and its effect on the phase transition temperature of alumina, J. Mater. Chem. 9 (1999) 549–553.

[188] L.T. Zhuravlev, The surface chemistry of amorphous silica . Zhuravlev model, 173 (2000) 1–38.

[189] K. Liu, Q. Feng, Y. Yang, G. Zhang, L. Ou, Y. Lu, Preparation and characterization of amorphous silica nanowires from natural chrysotile, J. Non-Crystalline …. 353 (2007) 1534–1539. doi:10.1016/j.jnoncrysol.2007.01.033.

[190] Y. Yoon, R.M. Lueptow, Concentration of colloidal silica suspensions using fluorescence spectroscopy, Colloids Surfaces A Physicochem. Eng. Asp. 277 (2006) 107–110. doi:10.1016/j.colsurfa.2005.11.019.

[191] a Bumb, M.W. Brechbiel, P.L. Choyke, L. Fugger, a Eggeman, D. Prabhakaran, J. Hutchinson, P.J. Dobson, Synthesis and characterization of ultra-small superparamagnetic iron oxide nanoparticles thinly coated with silica., Nanotechnology. 19 (2008) 335601. doi:10.1088/0957-4484/19/33/335601.

[192] L. Wang, Z. Tan, S. Meng, D. Liang, G. Li, Enhancement of molar heat capacity of nanostructured Al_2O_3, J. Nanoparticle Res. 3 (2001) 483–487. http://www.springerlink.com/index/V36HW14166653Q21.pdf (accessed February 15, 2017).

[193] G. Furukawa, T. Douglas, R. McCoskey, D. Ginnings, Thermal properties of aluminum oxide from 0 to 1,200 K, J. Res. Natl. Bur. Stand. (1934). 57 (1956). http://nvlpubs.nist.gov/nistpubs/jres/057/2/V57.N02.A01.pdf (accessed February 16, 2017).

[194] P. Auerkari, Mechanical and physical properties of engineering alumina ceramics, Technical Research Centre of Finland, VTT Tiedotteita - Meddelanden, Espoo, 1996. http://www.vtt.fi/inf/pdf/tiedotteet/1996/T1792.pdf (accessed February 16, 2017).

[195] A.V. Coelho, G. Rocha, Specific surface area and structures of aluminas from fibrillar pseudoboehmite, Matéria (Rio …. 13 (2008) 329–341. http://www.scielo.br/scielo.php?pid=S1517-70762008000200011&script=sci_arttext (accessed August 5, 2014).

[196] S. Brühne, S. Gottlieb, W. Assmus, Atomic structure analysis of nanocrystalline boehmite

AlO (OH), Cryst. Growth …. (2008) 1–9. http://pubs.acs.org/doi/abs/10.1021/cg0704044 (accessed August 5, 2014).

[197] B. Hemingway, R. Robie, J. Apps, Revised values for the thermodynamic properties of boehmite, AlO (OH), and related species and phases in the system Al-HO, Am. Mineral. States …. 76 (1991) 445–457. http://www.osti.gov/scitech/biblio/5669396 (accessed July 20, 2015).

[198] Sigma-Aldrich, Product Specification LUDOX SM colloidal silica - 30 wt.% suspension in H2O, (n.d.) 63103. http://www.sigmaaldrich.com/catalog/product/aldrich/420794.

[199] Z.-C. Tan, L. Wang, Q. Shi, Study of heat capacity enhancement in some nanostructured materials, Pure Appl. Chem. 81 (2009) 1871–1880. doi:10.1351/PAC-CON-08-09-15.

[200] V. Romanin, S. Fereres, A Meta-Analysis of the Specific Heat Enhancement of Nanofluids, in: ASME 2014 Int. Mech. Eng. Congr. Expo., 2014: pp. 1–15. http://proceedings.asmedigitalcollection.asme.org/proceeding.aspx?articleid=2205039 (accessed January 14, 2016).

[201] G.J. Janz, U. Krebs, H.F. Siegenthaler, R.P.T. Tomkins, Molten Salts: Volume 3, Nitrates, Nitrites and Mixtures, J. Phys. Chem. Ref. Data. 1 (1972) 581–746.

[202] I.M. Shahrul, I.M. Mahbubul, S.S. Khaleduzzaman, R. Saidur, M.F.M. Sabri, A comparative review on the specific heat of nanofluids for energy perspective, Renew. Sustain. Energy Rev. 38 (2014) 88–98. doi:10.1016/j.rser.2014.05.081.

[203] G.J. Janz, U. Krebs, H.F. Siegenthaler, R.P.T. Tomkins, Molten Salts: Volume 3 Nitrates, Nitrites, and Mixtures: Electrical Conductance, Density, Viscosity, and Surface Tension Data, J. Phys. Chem. Ref. Data. 1 (1972).

[204] R.L. Hamilton, O.K. Crosser, Thermal Conductivity of Heterogeneous Two-Com Ponent Systems, I EC Fundumentals. 1 (1959) 187–191. doi:10.1021/i160003a005.

[205] S. Pendyala, Macroencapsulation of Phase Change Materials for Thermal Energy Storage, University of South Florida, 2012. http://scholarcommons.usf.edu/etd/4200/ (accessed October 10, 2013).

[206] E. Rivas, Prediseño de un módulo de almacenamiento térmico para plantas termosolares con generación directa de vapor, 2011. http://eprints.ucm.es/23159/ (accessed January 14, 2014).

[207] D. Laing, M. Eck, M. Hempel, M. Johnson, W. Steinmann, M. Meyer-, M. Eickhoff, High

Temperature PCM Storage for DSG Solar Thermal Power Plants Tested in Various Operating Modes of Water / Steam Flow, (n.d.).

[208] K. Vignarooban, X. Xu, A. Arvay, K. Hsu, A.M. Kannan, Heat transfer fluids for concentrating solar power systems - A review, Appl. Energy. 146 (2015) 383–396. doi:10.1016/j.apenergy.2015.01.125.

[209] N. Sharifi, S. Wang, T.L. Bergman, A. Faghri, Heat pipe-assisted melting of a phase change material, Int. J. Heat Mass Transf. 55 (2012) 3458–3469. doi:10.1016/j.ijheatmasstransfer.2012.03.023.

[210] D. Laing, T. Bauer, D. Lehmann, C. Bahl, Development of a Thermal Energy Storage System for Parabolic Trough Power Plants With Direct Steam Generation, (2009) 1–9.

[211] Z.G. Wu, C.Y. Zhao, Experimental investigations of porous materials in high temperature thermal energy storage systems, Sol. Energy. 85 (2011) 1371–1380. doi:10.1016/j.solener.2011.03.021.

[212] J.H.L. Iv, J.H. Lienhard, A heat transfer textbook, J. Heat Transfer. 108 (1986) 198.

[213] L.R. White, H.T. Davis, Thermal Conductivity of Molten Alkali Nitrates, J. Chem. Phys. 47 (1967) 5433–5439. doi:10.1063/1.1701811.

[214] R.W. Powell, C.Y. Ho, P.E. Liley, Thermal conductivity of selected materials, U.S. Dept. of Commerce, National Bureau of Standards; for sale by the Superintendent of Documents, U.S. Govt. Print. Off., 1966.

[215] Y. Nagasaka, A. Nagashima, The thermal conductivity of molten NaNO3 and KNO3, Int. J. Thermophys. 12 (1991) 769–781. doi:10.1007/BF00502404.

[216] M. Auriemma, Energy Storage: CFD Modeling of Phase Change Materials For Thermal Energy Storage, Int. J. Eng. Res. Appl. 6 (2016) 31–36.

[217] M. Auriemma, A. Iazzetta, Numerical Analysis of Melting of Paraffin Wax with Al2O3, ZnO and CuO Nanoparticles in Rectangular Enclosure, Indian J. Sci. Technol. 9 (2016) 1–8. doi:10.17485/ijst/2016/v9i4/72601.

[218] ANSYS Inc, ANSYS Fluent Theory Guide, 2016. doi:10.1016/0140-3664(87)90311-2.

[219] L.. Chow, J.. Zhong, J.. Beam, Thermal conductivity enhancement for phase change storage media, Int. Commun. Heat Mass Transf. 23 (1996) 91–100. doi:10.1016/0735-1933(95)00087-9.

[220] S. Duwe, C. Arlt, S. Aranda, U. Riedel, G. Ziegmann, A detailed thermal analysis of nanocomposites filled with SiO 2, AlN or boehmite at varied contents and a review of selected rules of mixture, Compos. Sci. Technol. 72 (2012) 1324–1330. doi:10.1016/j.compscitech.2012.04.015.

[221] R. Mondragón, J.E. Juliá, A. Barba, J.C. Jarque, Preparación y caracterización de nanofluidos: Influencia de variables sobre su estabilidad, estado de aglomeración y propiedades físicas, Boletín La Soc. Española Cerámica Y Vidr. 53 (2014) 101–110. doi:10.3989/cyv.142014.

[222] F.J. Ruiz-Cabañas, C. Prieto, V. Madina, a. I. Fernández, L.F. Cabeza, Materials selection for thermal energy storage systems in parabolic trough collector solar facilities using high chloride content nitrate salts, Sol. Energy Mater. Sol. Cells. 163 (2017) 134–147. doi:10.1016/j.solmat.2017.01.028.

[223] C. Prieto, J. Gallardo-González, F.J. Ruiz-Cabañas, C. Barreneche, M. Martínez, M. Segarra, A.I. Fernández, Study of corrosion by Dynamic Gravimetric Analysis (DGA) methodology. Influence of chloride content in solar salt, Sol. Energy Mater. Sol. Cells. 157 (2016) 526–532. doi:10.1016/j.solmat.2016.07.027.

[224] S.H. Goods, R.W. Bradshaw, Corrosion of Stainless Steels and Carbon Steel by Molten Mixtures of Commercial Nitrate Salts, J. Mater. Eng. Perform. 13 (2004) 78–87. doi:10.1361/10599490417542.

[225] J.E. Pacheco, Final Test and Evaluation Results from the Solar Two Project, (2002).

[226] H. Search, C. Journals, A. Contact, M. Iopscience, I.P. Address, Oxo-acidity in ionic melts, 597 (n.d.).

[227] J.H. Lienhard, I. Catton, Heat Transfer Across a Two-Fluid-Layer Region, J. Heat Transfer. 108 (1986) 198. doi:10.1115/1.3246887.

[228] Y. Chu, Review and Comparison of Different Solar Energy Technologies, annual report, Glob. Energy Netw. Inst. (2011) 56. doi:10.1002/ejoc.201200111.

[229] E. Per, L.E. Nuove, Solar Thermal Energy Production : Guidelines and Future Programmes of Enea, ENEA Rep. (2001) 1–86.

[230] A.W. Dowling, T. Zheng, V.M. Zavala, Economic assessment of concentrated solar power technologies: A review, Renew. Sustain. Energy Rev. 72 (2017) 1019–1032. doi:10.1016/j.rser.2017.01.006.

[231] R. Musi, B. Grange, S. Sgouridis, R. Guedez, P. Armstrong, A. Slocum, N. Calvet, Techno-economic analysis of concentrated solar power plants in terms of levelized cost of electricity, 160018 (2017) 160018. doi:10.1063/1.4984552.

[232] M.I. Roldán-Serrano, Concentrating Solar Thermal Technologies. Analysis and Optimisation by CFD Modelling, (2017) 88.

[233] Estela, Greenpeace, SolarPACES, Solar Thermal Electricity - Global Outlook 2016, (2016) 114.

[234] S. Patel, Solar thermal gains in UAE, Spain, and California, Power. 157 (2013). http://www.powermag.com/solar-thermal-gains-in-uae-spain-and-california/?printmode=0 (accessed September 23, 2017).

[235] M. Romero, A. Steinfeld, Concentrating solar thermal power and thermochemical fuels, Energy Environ. Sci. 5 (2012) 9234. doi:10.1039/c2ee21275g.

[236] S.S. Mostafavi Tehrani, R.A. Taylor, K. Nithyanandam, A. Shafiei Ghazani, Annual comparative performance and cost analysis of high temperature, sensible thermal energy storage systems integrated with a concentrated solar power plant, Sol. Energy. 153 (2017) 153–172. doi:10.1016/j.solener.2017.05.044.

[237] X. Zhang, J. Tian, K. Xu, Y. Gao, Thermodynamic evaluation of phase equilibria in NaNO3-KNO3 system, J. Phase Equilibria. 24 (2003) 441–446. doi:10.1361/105497103770330091.

[238] C.Y. Zhao, Z.G. Wu, Thermal property characterization of a low melting-temperature ternary nitrate salt mixture for thermal energy storage systems, Sol. Energy Mater. Sol. Cells. 95 (2011) 3341–3346. doi:10.1016/j.solmat.2011.07.029.

[239] L. Sang, M. Cai, N. Ren, Y. Wu, C. Burda, C. Ma, Improving the thermal properties of ternary carbonates for concentrating solar power through simple chemical modifications by adding sodium hydroxide and nitrate, Sol. Energy Mater. Sol. Cells. 124 (2014) 61–66. doi:10.1016/j.solmat.2014.01.025.

[240] Y. ting Wu, Y. Li, N. Ren, C. fang Ma, Improving the thermal properties of NaNO3-KNO3 for concentrating solar power by adding additives, Sol. Energy Mater. Sol. Cells. 160 (2017) 263–268. doi:10.1016/j.solmat.2016.10.013.

[241] S. Sau, N. Corsaro, T. Crescenzi, C. D'Ottavi, R. Liberatore, S. Licoccia, V. Russo, P. Tarquini, A.C. Tizzoni, Techno-economic comparison between CSP plants presenting two

different heat transfer fluids, Appl. Energy. 168 (2016) 96–109. doi:10.1016/j.apenergy.2016.01.066.

[242] M. Chieruzzi, G.F. Cerritelli, A. Miliozzi, J.M. Kenny, L. Torre, Heat capacity of nanofluids for solar energy storage produced by dispersing oxide nanoparticles in nitrate salt mixture directly at high temperature, Sol. Energy Mater. Sol. Cells. 167 (2017) 60–69. doi:10.1016/j.solmat.2017.04.011.

[243] A. Sari, A. Karaipekli, Preparation, thermal properties and thermal reliability of palmitic acid/expanded graphite composite as form-stable PCM for thermal energy storage, Sol. Energy Mater. Sol. Cells. 93 (2009) 571–576. doi:10.1016/j.solmat.2008.11.057.

[244] N. Ren, Y.T. Wu, C.F. Ma, L.X. Sang, Preparation and thermal properties of quaternary mixed nitrate with low melting point, Sol. Energy Mater. Sol. Cells. 127 (2014) 6–13. doi:10.1016/j.solmat.2014.03.056.

[245] Y. WU, Y. LI, Y. LU, H. Wang, C. MA, Novel low melting point binary nitrates for thermal energy storage applications, Sol. Energy Mater. Sol. Cells. 164 (2017) 114–121. doi:10.1016/j.solmat.2017.02.021.

[246] K. Bashirnezhad, S. Bazri, M.R. Safaei, M. Goodarzi, M. Dahari, O. Mahian, A.S. Dalkiliça, S. Wongwises, Viscosity of nanofluids: A review of recent experimental studies, Int. Commun. Heat Mass Transf. 73 (2016) 114–123. doi:10.1016/j.icheatmasstransfer.2016.02.005.

[247] P. Estellé, Comment on "Viscosity measurements of multi-walled carbon nanotubes-based high temperature nanofluids," Mater. Lett. 138 (2015) 162–163. doi:10.1016/j.matlet.2014.09.139.

[248] I. Murgulescu, S. Zuca, Viscosity of binary mixtures of molten nitrates as a function of ionic radius—II, Electrochim. Acta. 14 (1969). http://www.sciencedirect.com/science/article/pii/0013468669870374 (accessed February 22, 2017).

[249] K. Coscia, S. Neti, A. Oztekin, S. Nelle, S. Mohapatra, T. Elliott, The thermophysical properties of the NaNO3-KNO3, LiNO3-NaNO3, and LiNO3-KNO3 systems, in: ASME Int. Mech. Eng. Congr. Expo., 2012.

[250] A.B. Zavoico, Solar Power Tower - Design Basis Document, Tech. Rep. SAND2001-2100. (2001) 148. doi:10.2172/786629.

[251] L. Kawaken Fine Chemicals Co., Main features of Alumisol - 10A, (n.d.).

[252] G.K. Batchelor, The effect of Brownian motion on the bulk stress in a suspension of spherical particles, J. Fluid Mech. 83 (1977) 97. doi:10.1017/S0022112077001062.

[253] D. Lide, CRC Handbook of Chemistry and Physics, 84th Edition, 2003-2004, CRC Press, n.d.

ANNEX II. FUNDING SOURCES AND COLLABORATIONS

This thesis has been developed with the support of the University of the Basque Country (UPV/EHU) through the ZabaldUz program *"Convocatoria para personal investigador en formación en cooperación con el entorno productivo y social"*. Besides, the work has been performed in the Solar Area of the Tecnalia Research and Innovation Foundation.

The research performed has also been funded by the following projects:

- 2014-2016. "Energigune: Desarrollo de actividades de investigación en almacenamiento de energía electroquímica y térmica". Basque Governement.

- 2014-2018. "STAGE-STE: Scientific and Technological Alliance for Guaranteeing the European Excellence in Concentrating Solar Thermal Energy". Grant agreement n° 609837. European Union Seventh Framework Programme FP7/2007-2013.

- 2016-2020. "Nanouptake – Overcoming Barriers to Nanofluids Market Uptake (COST Action CA15119)". Cost Action. European Commision.

Two international research stays were successfully completed:

1) <u>Host institution</u>: Centro de Desarrollo Energético de Antofagasta. Universidad de Antofagasta (Chile).
   <u>Dates</u>: May 2016 – July 2016 (3 months).
   <u>Host researchers</u>: Dr. Ángel Gabriel Fernández Díaz-Carralero and D. Edward Fuentealba Vidal
   <u>Topic</u>: Static corrosion and rheology of Solar Salt-based nanofluids with alumina and silica nanoparticles.
   <u>Funding source</u>: "Convocatoria de ayudas para la movilidad y divulgación de resultados de investigación en la UPV/EHU (2015). Modalidad I: Movilidad de Investigadores e investigadoras en Estancias". University of the Basque Country (UPV/EHU).

2) <u>Host institution</u>: Birmingham Centre for Energy Storage (BCES). University of Birmingham (United Kingdom).
   <u>Dates</u>: February 2017 (3 weeks).
   <u>Host researchers</u>: Dr. Helena Navarro Rivero and Prof. Yulong Ding.
   <u>Topic</u>: Thermal diffusivity and rheology of Solar Salt-based nanofluids with alumina and silica nanoparticles.
   <u>Funding source</u>: "STSM: Short Scientific Missions – 1st period". Nanouptake Project. European Commision.

ANNEX II. PUBLICATIONS

II-1. JOURNALS

- B. Muñoz-Sánchez, J. Nieto-Maestre, G. Imbuluzqueta, I. Marañón, I. Iparraguirre-Torres, A. García-Romero, *A precise method to measure the specific heat of solar salt-based nanofluids*, J. Therm. Anal. Calorim. (2017). doi:10.1007/s10973-017-6272-x.

- B. Muñoz-Sánchez, J. Nieto-Maestre, I. Iparraguirre-Torres, A. García-Romero, J.M. Sala-Lizarraga, *Molten salt-based nanofluids as efficient heat transfer and storage materials at high temperatures. An overview of the literature*. Renew. Sustain. Energy Rev. (Accepted for publication)

- B. Muñoz-Sánchez, J. Nieto-Maestre, E. Veca, R. Liberatore, S. Sau, H. Navarro, Y. Ding, N. Navarrete, J.E. Juliá, A.G. Fernández, A. García-Romero. *Rheology of Solar-Salt based nanofluids for concentrated solar power. Influence of the salt purity, nanoparticle concentration, temperature and rheometer geometry*. Sol. Energy Mater. Sol. Cells. (Accepted for publication)

II-2. CONFERENCES

- B. Muñoz-Sánchez, J. Nieto-Maestre, I. Iparraguirre-torres, A. García-Romero. *Nanoparticle size evaluation through Dynamic Light Scattering (DLS) technique in a nitrate salt doped with ceramic nanoparticles*, in: Congr. CIIEM15. Paris, 2015.

- B. Muñoz-Sánchez, J. Nieto-Maestre, I. Iparraguirre-torres, A. García-Romero, *Assessment of the determination of the Specific Heat of Molten Salt doped with Nanoparticles by means of the DSC technique*, in: Greenstock Conf. Beijing, 2015.

- B. Muñoz-Sánchez, J. Nieto-Maestre, I. Iparraguirre-Torres, J. a. Sánchez-García, J.E. Julia, A. García-Romero, *Preparation of nanofluids based on solar salt and boehmite nanoparticles: Characterization of starting materials*, AIP Conf. Proc. 50030 (2016). doi:10.1063/1.4949128.

- B. Muñoz-Sánchez, J. Nieto-Maestre, I. Iparraguirre-Torres, J. a. Sánchez-García, J.E. Julia, A. García-Romero. *The influence of mixing water on the thermophysical properties of nanofluids based on solar salt and silica nanoparticles*, AIP Conf. Proc. 50031 (2016). doi:10.1063/1.4949129.

- B. Muñoz-Sánchez, J. Nieto-Maestre, I. Iparraguirre-Torres, J.E. Julià, A. García-Romero, *Silica and alumina nano-enhanced molten salts for thermal energy storage: A comparison*, AIP Conf. Proc. 80018 (2017) 80018. doi:10.1063/1.4984439.

- B. Muñoz-Sánchez, J. Nieto-Maestre, J. Gonzalez-Aguilar, J.E. Julia, N. Navarrete, A. Faik, T. Bauer, A. Bonk, M.E. Navarro, Y. Ding, N. Uranga, E. Veca, S. Sau, P. Giménez, P. Garcia, J.I. Burgaleta, *Round Robin Test on the Measurement of the Specific Heat of Solar Salt*, AIP Conf. Proc. 80017 (2017). doi:10.1063/1.4984438.

- B. Muñoz-Sánchez, J. Nieto-Maestre, L. Guerreiro, J.E. Julia, M. Collares-Pereira, A. García-Romero, *Molten Salt Based Nanofluids Based on Solar Salt and Alumina Nanoparticles: an Industrial Approach*, AIP Conf. Proc. 80016 (2017). doi:10.1063/1.4984437.

II-3. PREVIOUS PUBLICATIONS

- B. Muñoz-Sánchez, I. Iparraguirre-Torres, V. Madina-Arrese, U. Izagirre-Etxeberria, A. Unzurrunzaga-Iturbe, A. García-Romero, *Encapsulated High Temperature PCM as Active Filler Material in a Thermocline-based Thermal Storage System*, in: Energy Procedia, 2015: pp. 937–946. doi:10.1016/j.egypro.2015.03.177.

- B. Muñoz-Sánchez, M.J. Arévalo-Caballero, M.C. Pacheco-Menor, *Influence of acetic acid and calcium hydroxide treatments of rubber waste on the properties of rubberized mortars*, Mater. Struct. Constr. (2017). doi:10.1617/s11527-016-0912-7.